Swansea University
Prifysgol Abertawe

Establishing the effects of Nanocellulose-based bio-inks in an advanced 3D *in vitro* model for cartilage tissue engineering

Submitted to Swansea University in fulfilments of the requirements for the Degree of Doctor of Philosophy

Cynthia de Courcey

Abstract

Trauma, cancer or congenital conditions can lead to the loss of facial cartilage resulting in altered function and form. Tissue engineering (3D-printing) has the potential to create bespoke cartilage implants for reconstruction with biomaterials as ink carriers loaded with patient cells. There is rising interest in nanocellulose as a bio-ink candidate, but relative paucity of studies investigating an all-natural hybrid bio-ink inclusive of alginate (most common natural bio-ink material) and hyaluronic acid (HA) (native component of human extra-cellular matrix). This study aims to: i) evaluate the cytotoxic and pro-inflammatory effects of each bio-ink components individually and combined as bio-inks; ii) create an advanced 3D *in vitro* model for biocompatibility testing; and iii) apply the model for toxicity testing, refinement of bio-ink formulations and further model characterisation with differential gene expression analysis.

Six forms of nanocellulose, alginate, HA, and two cross-linker agents were investigated for their biological impact to human chondrocyte C20A4 and dermal fibroblast HFF-1 cell lines. Material sterility was determined by microbial growth assay. Cell-line characterisation and material exposures (21 days) and cross-linker exposures (7 days) were examined for cell viability, morphology and pro-inflammatory mediators (IL-6/IL-8) release. Minimum cross-linkage time and rheologically defined gelation behaviour of bio-inks with calcium chloride ($CaCl_2$) permitted completion of a standard operating procedure for the creation of an advanced 3D *in vitro* model. To mimic the implanted *in vivo* scenario, the *in vitro* model consisted of chondrocyte-encapsulated and fibroblast surface-seeded cross-linked hydrogels. RNA extraction *via* the spin column technique with optimisations were performed. Differential gene expression analysis was conducted using Nanostring against the nanocellulose-based bio-ink with the 3D *in vitro* model.

All materials maintained sterility over 21 days, except for pulp-derived nanocellulose which were excluded. Material exposures (chondrocytes: nanocellulose/alginate/HA; fibroblasts: alginate/HA) showed no significant cytotoxic effects over 21 days. Enzymatically pretreated nanocellulose (ETC) displayed the lowest pro-inflammatory effects when exposed against chondrocytes, with trends of carboxymethylated(CTC)> TEMPO-mediated oxidised(TTC)>ETC on D1-7 and TTC >CTC>ETC on D14-21. $CaCl_2$ exposure on fibroblasts demonstrated a dose- and time-dependent cytotoxicity supporting use of the lowest concentration and shortest cross-linkage time to minimise adverse cellular impact. Testing of optimised bio-inks (ETC:Alginate and ETC: Alginate:HA at 6mg/ml in media) demonstrated that nanocellulose-based bio-ink inclusive of HA was superior for chondrocyte proliferation. Heightened IL-6/IL-8 and lactate dehydrogenase release at latter timepoints indicated the need for further model development. Nanostring was successfully applied for differential gene expression analysis, which corroborated pro-inflammatory effects observed *via* cytokine quantification, as well as identified multiple areas of interest for further research.

Overall, ETC was shown to be a promising bio-ink candidate, and when combined with alginate and HA, formed a complete bio-ink formulation specific for 3D-bioprinted cartilage constructs for reconstructive purposes. Biological and rheological testing identified optimal parameters for bio-ink and *in vitro* model creation, whilst RNA extraction from chondrocytes encapsulated within cross-linked bio-ink was feasible and applicable with the Nanostring technology.

Declaration and Statements

DECLARATION

This work has not previously been accepted in substance for any degree and is not being concurrently submitted in candidature for any degree.

Signed: 

Date: 16.01.2026

STATEMENT 1

This thesis is the result of my own investigations, except where otherwise stated. Other sources are acknowledged by footnotes giving explicit references. A bibliography is appended.

Signed: 

Date: 16.01.2026

STATEMENT 2

I hereby give consent for my thesis, if accepted, to be available for photocopying and for inter-library loan, and for the title and summary to be made available to outside organisations.

Signed: 

Date: 16.01.2026

Table of Contents

Acknowledgements

I would like to extend my sincerest thanks to all who has helped make the research presented in this thesis a reality. Words alone fail to capture the expertise, time and kindness that was generously given over and over again for the past four years. For those who know me well, it is with great restraint that I keep this succinct, but please know the deepest thanks lies beneath the brevity.

To my primary supervisor Professor Martin Clift, thank you for inspiring, encouraging and challenging me, and your grounding presence when I am in deep waters. To my secondary supervisor Professor Iain Whitaker, thank you for this opportunity. You planted the seed that grew. Thank you also to the Royal College of Surgeons of England, the Blond McIndoe Research Foundation, Action Medical Research and the VTCT Foundation for funding this research, without which it could not be completed in its entirety.

To Kirsty, Josh and Sian (aka Team Clift), thank you for being the kindest and most capable teammates one could hope for. You truly brought me from zero up in the lab, showed unending patience with my many questions and are simply wonderful people. I am also extremely grateful to everyone who have gone out of their way to guide and support the following work: Dr Josie Parker (microbiology), Professor Karl Hawkins, Dr Alex Bulpitt, Sandrine Charles and Matthew Jovic (rheology), Dr April Rees, Dr Laura Thomas, Dr Haiyan An, Dr Jason Webber and Dr Iain Perry (RNA extraction and Nanostring), Dr Hamsa Naser (flow cytometry analysis) and Dr Stephen Evans (trial TEM). To the entire ReconRegen research team, thank you for welcoming me into the group and keeping my head above waters mixing bio-inks(!). A special shout-out to Octavian, Laurence, Matt, Zita, Tom, Em and Matty – thank you! To Alethea, thank you for knowing just when I needed a natter, or be fed, for my birthday courgette cakes and your friendship - you are sorely missed. For everyone on the 4th floor, especially the PhD office (old and new), it's been such a pleasure working together I feel rude not naming you all individually, but thank you for bringing so much joy to this chapter in my life.

To my family and dearest friends, your love and support keeps me smiling no matter what. To Adrian, who has read everything I have written, listened to every presentation I have given, you are my rock. Thank you for being you, and simply, thank you.

List of Tables

List of Figures

List of Equations

Abbreviations

2D	2-dimensional
3D	3-dimensional
4PL	4 parameter logistic
ALDOA	Aldolase A
ALDOC	Aldolase C
ATCC	American type culture collection
AVAP	American value added pulping
BBC3	BCL2 binding component 3
BNIP3	BCL2 interacting protein 3
BNIP3L	BCL2 interacting protein 3-like
BSA	Bovine serum albumin
Ca^{++}	Calcium
$CaCl_2$	Calcium chloride
Calcein AM	Calcein acetoxy-methyl-ester
CASP	Cysteine aspartate-specific protease
CDKN2B	Cyclin dependent kinase inhibitor 2B
cDNA	Complementary DNA
CNC	Cellulose nanocrystals
CNF	Cellulose nanofibrils
CTC	Carboxymethylated cellulose nanofibrils
CXCL8	C-X-C motif chemokine ligand 8
ddH_2O	Double-distilled water
DEG	Differentially expressed gene

dH_2O	Distilled water
DMSO	Dimethyl sulfoxide
DNA	Deoxyribonucleic acid
DPP4	Dipeptidyl peptidase 4
EB	Erythrosin B
ECM	Extra-cellular matrix
EDTA	Ethylenediaminetetraacetic acid
ELISA	Enzyme-linked immunosorbent assay
ENO1	Enolase 1
ETC	Enzymatically pre-treated cellulose nanofibrils
EthD-1	Ethidium homodimer-1
FACS	Fluorescence-activated cell sorting
FADD	Fas-associated death domain
FAP	Fibroblast activation protein alpha
FOV	Field of view
FSC	Forward scatter
FU	Fluorescence unit
G'	Storage (elastic) modulus
G"	Loss (viscous) modulus
G6P	Glucose-6-phosphate
GO	Gene Ontology
HA	Hyaluronic acid
HIF1A	Hypoxia-induced factor 1 subunit alpha
HK2	Hexokinase 2

H_2O_2	Hydrogen peroxide
HRP	Horseradish peroxidase
H_2SO_4	Sulfuric acid
ICAM-1	Intercellular adhesion molecule-1
IFN	Interferon
IFN-γ	Interferon-gamma
IHC	Immunohistochemistry
IL	Interleukin
IL-1β	Interleukin 1 beta
IL-11RA	Interleukin 11 receptor subunit alpha
IL-6R	Interleukin 6 receptor
INHBA	Inhibin subunit beta A
ISG	Interferon-stimulated gene
KEGG	Kyoto Encyclopedia of Genes and Genomes
LB	Lysogeny broth
LDH	Lactate dehydrogenase
LPS	Lipopolysaccharide
LVR	Linear-viscoelastic region
MACS	Magnetic-activated cell sorting
MFI	Median fluorescence intensity
MMP	Matrix metalloproteinase
MSC	Mesenchymal stromal cells
MW	Molecular weight
NAD^+	Nicotinamide adenine dinucleotide

NADH	Nicotinamide adenine dinucleotide (NAD) + hydrogen (H)
Nanostring	Nanostring nCounter® Analysis System
NCB	Nanocellulose blend
N-HA	Non-tyramine-substituted hyaluronic acid
NLRP3	Nucleotide-binding domain, leucine-rich-containing family, pyrin domain-containing-3
NOD	Nucleotide-binding oligomerization domain
OAS	Oligoadenylate synthetase
OD	Optical density
ORA	Over-representation analysis
PAMP	Pathogen-associated molecular pattern
PARP	Poly-ADP-ribose polymerase
PBS	Phosphate buffered saline
PC	Principal component
PCA	Principal component analysis
PCNA	Proliferating cell nuclear antigen
PCR	Polymerase chain reaction
PDK1	Pyruvate dehydrogenase kinase 1
PPI	Protein-protein interaction
PRR	Pattern recognition receptor
QC	Quality control
qRT-PCR	quantitative real-time polymerase chain reaction
RFU	Relative fluorescence unit
RIN	RNA integrity number
RNA	Ribonucleic acid

ROS	Reactive oxygen species
SEM	Standard error of the mean
SOP	Standard operating procedure
SSC	Side scatter
TB	Trypan blue
TCP	Tissue culture plate
TGF-β1	Transforming growth factor-beta one
TGF-β2	Transforming growth factor-beta two
T-HA	Tyramine-substituted hyaluronic acid
TLR	Toll-like receptor
TNF	Tumour necrosis factor
TNF-α	Tumour necrosis factor alpha
TNFAIP	Tumour necrosis factor-alpha induced proteins
TNFRSF14	Tumour necrosis factor receptor superfamily member 14
TNFRSF1B	Tumour necrosis factor receptor superfamily member 1B
TNFRSF10B	Tumour necrosis factor receptor superfamily member 10B
TNFRSF10C	Tumour necrosis factor receptor superfamily member 10C
TNFRSF10D	Tumour necrosis factor receptor superfamily member 10D
TNFRSF11B	Tumour necrosis factor receptor superfamily member 11B
TNFRSF25	Tumour necrosis factor receptor superfamily member 25
TNFRSF6	Tumour necrosis factor receptor superfamily member 6
TNFSF10	Tumour necrosis factor superfamily member 10
Triton	Triton X-100
TTC	TEMPO-oxidized cellulose nanofibrils

UV	Ultraviolet
UV-C	Ultraviolet-C
YPD	Yeast extract-peptone-dextrose

Chapter 1: Introduction

1.1 Introduction

Significant facial disfigurements, including nasal and auricular defects, from trauma, burns, cancer and congenital conditions, affect 1 in 111 people in the UK[1]. Unlike tissues with self-healing properties such as bone and liver, cartilage, which provides structural support to the nose and ear, has a low regenerative capacity[2, 3]. Current reconstructive techniques with autograft (cartilage harvested from the patient) create additional scarring, pain and are limited by donor-site availability[4-12], whilst synthetic implants are at risk of infection, extrusion, deformation and foreign-body reaction[13-15]. Neither faithfully replicates the anatomy and architecture of the lost tissue, with resultant functional limitations and asymmetry. Tissue engineering potentially offers an alternative strategy by seeding chondrogenic cells in biomimetic scaffolds to produce bespoke engineered cartilage using patient's own cells for facial defect reconstruction. Cartilage, composed of a single cell type (chondrocyte) and extracellular matrix (ECM), is avascular, aneural and alymphatic. Its simplicity in structure and composition relative to other body tissue types may allow more rapid progress from bench to bedside.

Since the early 1990s, there has been an expansive volume of research in tissue engineering, both in scope and depth addressing a variety of human tissue types[16]. Areas of research focus include the three core compositional elements (material, cell and biomolecules), methods of assembly (e.g. additive manufacturing), infrastructural and scale-up processes and technologies (e.g. bioreactors). This is paralleled by an estimated world market value of USD 9.9 billion in 2019 and a predicted rise in investment of 14.2% in ensuing years[17, 18]. Despite such promise, tissue engineered products (TEPs) have yet to be translated successfully into clinical practice. In 1997, Vacanti's landmark study entailed the implantation of a tissue-engineered, human ear-shaped cartilage made from bovine chondrocytes seeded onto polyglycolic acid (PGA)-polylactic acid (PLA) scaffolds into nude mice[19]. External stents were required to maintain form. Subsequent reports on tissue-engineered cartilage for head and neck applications by and large are limited to *in vitro* or nude mouse models[20, 21], with relative paucity of success in immunocompetent animal models or clinical studies[22-26]. This, in part, is attributed to the marked immunological response in recipient sites[27, 28]. Constructs are subjected to inflammation, fibrosis and foreign body reaction when implanted into immunocompetent animal models[29, 30]. Whilst scaffold-free cartilage

constructs implanted subcutaneously have been successfully described, involving chondrocyte suspension[31, 32], engineered cartilage sheet[33, 34], and decellularised chondrocyte extracellular matrix[35], cartilage reconstruction of the head and neck necessitate precise, specific and stable form which can withstand shrinkage and mechanical forces once implanted. These are inadequately addressed *via* the aforementioned approaches.

With regards to clinical translation, articular (joint) cartilage regeneration, a dominant focus within cartilage tissue engineering, are relatively more advanced compared with head and neck reconstruction applications. Multiple commercial products are in market, with a number of phase III clinical trials evaluating product efficacy.

Largely limited to the application of 'autologous chondrocyte implantation' for treatment of small articular cartilage defects (i.e. <2-4cm^2), these products serve as cell carriers for autologous (patient-derived) chondrocyte population expanded *ex vivo*, to be applied to the articular cartilage defect to stimulate innate cartilage regeneration. Examples of such products include MACI (bilayer collagen type I/III), NeoCart® (honeycomb bovine type I collagen), NOVOCART® 3D (bilayer type I collagen sponge containing chondroitin sulfate), CARTISTEM (hyaluronic acid-based hydrogel), Hyalograft® C (hyaluronic acid-based microfibre mesh) and Cartipatch® (agarose and alginate hydrogel)[36, 37]. Noted commonality includes the predominance of natural materials such as collagen and hyaluronic acid, but also their injectable or malleable form. The latter, with an associated low mechanical strength, are insufficient for the biomechanical requirements for head and neck cartilage reconstruction scenarios.

Over 6,000 patients were treated with NOVOCART®3D in Europe since 2003. This is a two-staged procedure, with a three-week interval for cell expansion. The phase III trial comparing NOVOCART®3D against microfracture surgery in the US which begun in 2013 involving over 200 participants[38, 39], has an estimated study completion date in December 2027. CARTISTEM, also targeted for knee cartilage repair, utilises umbilical cord blood-derived mesenchymal stem cells instead of chondrocytes, showed superior results when compared to microfracture at 5-year follow-up in a Korean randomised controlled trial involving 73 participants[37]. Microfracture surgery, the comparator intervention in both phase III trials, exposes the subchondral bone

marrow, resulting in a blood clot in the cartilage defect to stimulate innate cartilage repair. Whilst short term results are promising, outcomes from longer term studies are equivocal[40]. Alongside this, reports suggest that such scaffolds fail to maintain their structure and transform to a gel-like form following implantation and inadequate mechanical strength contributes towards the generation of fibrocartilage instead of hyaline cartilage with inferior functional properties for articular cartilage repair[41]. Therefore, indication for use of current commercial engineered cartilage products remains limited to those with early or focal cartilage damage, with cost being a defining limiting factor when compared to microfracture procedures in a pure clinical setting outside of research trials. Severe osteoarthritis, a key driver for articular cartilage tissue engineering, requires a product which supersedes current performance of artificial joints. The lifespan of a total hip replacement averages at 15 years, with 58% lasting 25 years[42]. Whilst the availability of commercial products suggests translational progress and are encouraging, tissue engineered cartilage that can withstand substantial load bearing with proven longevity remains elusive, as is the challenge of creating functional cartilage for head and neck reconstruction.

In head and neck reconstruction, a series of tracheal reconstruction utilising synthetic scaffold and non-tissue specific stem cells was a high-profile failure at the Karolinkska Institute in 2008[43-45]. Shortly after, Yanaga *et al* successfully performed ear reconstruction in four patients with microtia (congenital absence / malformation of the ear) in 2009 with a two-staged procedure. Autologous chondrocytes were injected into patients' lower abdomen which developed into a block of neocartilage. These were explanted at six months and carved into the shape of an ear before implantation[32]. Whilst cell manipulation was performed, the absence of a pre-shaped scaffold translates to a lack of control over the shape of the neo-cartilage. In 2014, autologous nasoseptal chondrocytes expanded *ex vivo* over four weeks, seeded on collagen I and III membranes, were successfully implanted in five patients with nasal alar defects[46]. However, in terms of implant volume and shape complexity, nasal alar reconstruction is significantly less demanding compared to that for total ear or tracheal reconstruction.

Distinction between head and neck reconstruction and articular cartilage repair applications include varied functional demands and implantation site. Articular cartilage is subjected to recurrent loading with micro-trauma, whilst auricular (ear) cartilage may be impacted by extreme torsion and deformational forces. Cartilage in

the head and neck are also of complex form, such as the ear and nose. Implantation site may also influence the immune and foreign body response engineered cartilage are subjected to. Constructs intended for articular repair are placed in joint spaces bathed in synovial fluid, contrasting with the vascular subcutaneous, sub-fascial or sub-muscular implantation sites of the head and neck. Despite such differences, given the volume and advances in articular cartilage tissue engineering and a common cell type (chondrocytes), learnings can be taken for head and neck applications.

Whilst not exhaustive, leading areas of focus for research in cartilage tissue engineering are the three core compositional elements - material, cell and biomolecules. Using materials as an illustrative example, the sheer number of engineered materials pose a substantial challenge in toxicological testing. Materials used as scaffolds can be categorised as natural (e.g. alginate, hyaluronic acid, collagen, chondroitin sulfate, chitosan, gelatin, fibrin, silk fibroin)[47-54] and synthetic (e.g. polyethylene glycol, poly (lactide-co-glycolic) acid [PLGA], polycaprolactone [PCL], poly(ethylene glycol) [PEG], polylactic acid [PLA])[55-59], as forms (e.g. solid, hydrogel, sponge, film, mesh, emulsion and pre-formed versus in-situ forming)[60], and be functionalised yielding altered structure-activity relationship. The vast volume of material options is further compounded by hybrid or composite materials, with differences in design to be bio-stable versus degradable, inert or biologically active[61, 62]. The heterogeneity in approach underlies an unmet need and the complexities of tissue engineering. With the focused application of a nanocellulose-based bio-ink for 3D bioprinting cartilage in mind, an overview of human cartilage and nanocellulose, the core component of the bio-ink under investigation, will be discussed.

1.2 Human cartilage

1.2.1 Extra-cellular matrix composition

Cartilage is a specialised connective tissue composed of cells and extracellular matrix (ECM). Fibres, resistant to tensile forces, are embedded within a gel-like ground substance which counteracts compression, together forming the ECM[63]. The function of ECM, whilst previously thought to be limited to providing structural support, includes modulation of cellular function and phenotype, influencing cell survival,

development, mitotic activity, migration, including that of the immune system. Ground substance is amorphous, composed of three families of macromolecules: glycosaminoglycans (GAGs), proteoglycans and cell adhesive glycoproteins.

GAGs are negatively charged, long, unbranched chains of repeating disaccharide (sugar) units. Its negative charge attracts cations (such as sodium - Na^+) and the high sodium concentration in turn draws in extracellular fluid leading to a highly hydrophilic ground substance. The high water content directly contributes to its turgor and ability to withstand compressive forces and accounts for 65-80% of the weight of hyaline cartilage[64]. Hyaluronic acid (HA) and chondroitin sulfate are key GAGs of cartilage ECM. They differ by the number of repeating disaccharide units (chondroitin <300; HA <10,000), molecular mass (chondroitin 1-3x10^4Da; HA 10^7-10^8Da) and presence of sulfation (chondroitin only)[63].

Proteoglycans, with a bottle brush-like structure, are composed of a protein core forming the linear backbone and multiple sulphated GAGs as sidechains[63]. The sulfation of chondroitin permits covalent binding (strong, 'permanent', chemical cross-linkage) to the protein core, distinct to the attachment of HA via noncovalent ionic binding reinforced by small link proteins. Aggrecan is a cartilage-specific proteoglycan, and large owing to its attachment to HA which can be up to 20μm in length. It contributes to the gel-like state of ground substance.

HA, a component part of the bio-ink under investigation, appears to have intracellular function. Synthesised at the cytoplasmic surface of cell membrane before transfer into ECM, it can be endocytosed by some cells. Independent as newly released HA, or as part of the aggrecan proteoglycan, it can act as a molecular sieve slowing movement of microbes, cancerous cells and other macromolecules whilst supporting normal cellular migration, influence microtubular activities during metaphase and anaphase stages of mitoses (cell division) affecting chromosome movement, and is involved in intracellular signalling via intra-cytoplasmic and intra-nuclear specific kinases[63].

1.2.2 Chondrocytes and low innate regenerative capacity

Chondrocytes, the key cell type in cartilage, are spheroid cells 10-13μm in diameter[65]. Cartilage has a low cellular component, constituting 2-5% of the total volume of cartilage[41, 66]. Chondrocytes are dispersed singularly or as cell clusters, located in

lucanae (cavities in ECM). ECM immediately adjacent to cells are distinct with greater amount and varied GAGs and are termed territorial matrix, interspersed amongst interterritorial matrix.

Whilst chondrocytes can produce ECM, this does not meet the requirements in the event of tissue injury or loss. Limited cellular migration to injury site due to chondrocytes fixed in lacunae and low cell density contribute to the low innate healing capacity of cartilage[3, 67]. All cartilage is avascular, and with the exception of articular cartilage and most fibrocartilage, it is encased by a vascular layer called the perichondrium. Nutrients and oxygen transport are therefore dependent on diffusion from neighbouring tissue, although compressive forces from loading enhances this process. Nonetheless, this not only limits the thickness of cartilage, but slows cell and ECM turnover.

Achieving the required number of functional chondrocytes to adequately populate a prefabricated implant and preservation of the intended phenotype relevant to end application are key challenges in cartilage tissue engineering. Limited donor cartilage (and therefore cell) availability and de-differentiation of chondrocytes during *in vitro* expansion with altered phenotype and function raises the debate between *ex vivo* and *in vivo* cell expansion. The latter, explored in greater depth in cell therapy, uses a lower seeding density and relies on adequate and appropriate cell expansion post-implantation with less assurance and control[68-70]. Injury to hyaline cartilage is notably replaced by fibrocartilage, marked by type I collagen production over type II. This poorly integrates with the damaged matrix and is not well suited to function as articular cartilage with inferior mechanical properties. Chondrocytes isolated from common donor sites such as the articular joint, costal rib and nasal septum (all hyaline cartilage) does not produce elastic cartilage[71-73], and will ultimately undergo calcification following normal developmental pathway[74-76]. Approaches to influence biochemical signals of chondrocytes to affect gene expression and collagen type I and II production to achieve the desired cartilage properties are met with various success, but include 2D versus 3D cultures, static versus dynamic culture to simulate physiologic compressive forces *in vitro* and application of growth factors or other biomolecules[77-82]. Sophisticated bioreactors integrating approaches discussed above encourage exploration of *ex vivo* chondrocyte cultivation in-situ of the prefabricated implant as an alternative mean to reduce initial seeding density requirement. This places a

spotlight on the relevance of biomaterials as scaffolds and its influence on cellular behaviour as a cell carrier.

1.3 Bio-ink and the biofabrication window paradigm

Studies in material science have sought to create tunable scaffolds that permits control over microstructure (e.g. porosity, pore size, interconnectivity), surface chemistry and topography, and physicochemical properties (e.g. stiffness, strength, viscoelasticity, wettability), tailored to specific end-applications[47, 83-85]. For 3D bioprinting, an optimal compromise is needed between biocompatibility (sustaining encapsulated cell viability pre- and post-print, and supporting host cell migration post-implantation), favourable rheological (flow for printing) and mechanical (strength and flexibility post-print) properties. This compromise is described as the 'bio-fabrication window' paradigm[86].

Two themes around biomaterials relevant to this study will first be considered: i) natural versus synthetic materials, and ii) 3D bioprinting on material demands. This is followed by discussion of the bio-ink in its form as a hydrogel and the core bio-ink component, nanocellulose.

1.3.1 Natural versus synthetic materials

The potential of biomaterials to modulate cellular and immune responses, implant integration and performance is increasingly recognised[28]. The gradual shift towards bioactive engineered natural materials to mimic native ECM contrasts with earlier paradigm of inert but 'safe' materials. Reconstruction using gold in cranial (skull) defects, as a natural inert material, dates back to 2000 BC[87]. Modern synthetic material benefits from superior mechanical strength, ability to hold its shape *in vivo* and malleable to the desired form. In the head and neck, synthetic options for ear reconstruction include silastic[88-90] and porous polyeythlene (Medpor)[91-93] implants. Whilst biostable, synthetic materials lack biological properties and heightened antigenicity from degradation products (mostly acids) causes immunogenic and inflammatory responses[94-98] placing patients at risk of implant extrusion, infection and deformation from scar tissue formation[99]. Degradation may also cause material brittleness[94]. A systematic review of biomaterials used in extrusion 3D bioprinting of 123 articles between 2006-2018 showed a predominance of natural materials (natural

58, synthetic 26, combination 39), reflecting the trend towards biomimicry[100]. The three most used materials in order of preference were: alginate, gelatin and methacrylated gelatin (GelMA) for natural materials, and polycaprolactone (PCL), poly(lactic acid) (PLA) and poly(lactic-co-glycolic acid) (PLGA) for synthetics. Nonetheless, natural materials, including those in this study, may be limited by low mechanical stability and sensitivity to processing or manufacture conditions (e.g. temperature, pH)[41].

1.3.2 3D bioprinting and material demands

Additive manufacturing describes a hosts of fabrication processes that builds 3D structures using computerised data (e.g. computer-aided design (CAD) or computed tomography (CT) data) in a layer-by-layer manner[41, 101, 102]. 3D bioprinting, a form of extrusion-based printing, deposits materials (bio-ink) through single or multi-cartridge and nozzle system driven by pneumatic, piston or screw-driven mechanisms[103]. Whilst offering control over scaffold shape and dimension, printing resolution is limited to 25-50μm[101, 104]. Standard nozzle size of the BICO Group (previously CELLINK – bioprinter used by the research group) ranges from 200μm - 840μm (27G – 18G), with precision conical nozzle available at 50, 100 and 150μm below the standard range. Although resolution can be adjusted based on printing parameters (e.g. printing pressures, shear rate, temperature) and material properties (e.g. viscosity and rheological (flow) properties), control over topographical features on the nanoscale are not feasible via the 3D printing process per se. This can, in part, be determined by material properties and behaviour, and is of great interest due to its relevance to the cell microenvironment[101, 104].

Newtonian fluids subsume under Newton's law of viscosity, maintaining a constant viscosity independent of shear forces at defined temperature and pressure (e.g. water and oil). Conversely, viscosity of non-Newtonian fluids increases or decreases with applied stresses. The latter, known as shear-thinning, is essential for materials intended as bio-inks. Nanocellulose when added to solution forms a percolating network, increasing stability and viscosity of the fluid. Extrusion forces applied to the bio-ink during printing disrupts this network, lowers material viscosity permitting flow. Crucially, upon removal of the disrupting forces on material deposition, the network is restored, returning the bio-ink to its initial state and viscosity[104].

As the printed structure builds layer-by-layer, cross-linking is a necessary stabilisation step which bonds free flowing polymer chains to each other, inducing sol-gel transition (gelation or gelling). Cross-linking can be physical (weak, reversible) or chemical (strong, permanent). Chain entanglement, hydrogen bonds, hydrophobic interactions, crystallite formation and ionic bonds (in this study: between alginate chains when exposed to calcium ions) are forms of physical cross-links. Whilst reversible in nature, physical hydrogels are insoluble in aqueous solution, but carries heterogeneities with network defects due to free polymer chain ends or loops[105]. Chemical cross-linking describes covalent bonds between polymer chains triggered through chemical or enzymatic reactions (in this study: cross-linkage of tyramine-substituted hyaluronic acid with horseradish peroxidase and hydrogen peroxide), irradiation, sulphur vulcanisation, heat, pressure and changes in pH. Covalent cross-linking is widely used to form permanent hydrogels, but toxic cross-linking agents and resultant gels with small pore size can adversely impact cell behaviour[106, 107]. During cross-linkage, the bonding of polymeric chains forms multi-dimensional networks, altering the chemical structure and increasing the molecular mass of polymers. Physical (swelling behaviour, strength, elasticity)[108] and architectural properties (pore size, density and distribution of functional groups conjugated to the polymer)[109, 110] are therefore influenced by material (the polymer – singular or hybrid) and the type and degree of crosslinking (including crosslinker concentration). Cells encapsulated within the bio-ink not only interact with the material in static conditions, but must maintain viability and critical functions during cross-linkage through the physical and chemical polymeric alterations and when subjected to dynamic forces (e.g. shear) during printing. The biological impact of such effects in the latter is outwith the remit of this research.

Despite a focused discussion on some factors relevant to material design for 3D bioprinting, it is clear that compromise between biological, rheological and mechanical demands as described in the 'bio-fabrication window' paradigm[86], whilst pivotal to successful clinical translation, is complex and challenging.

1.3.3 Hydrogels

Hydrogel is an insoluble, three-dimensional network of hydrophilic cross-linked polymers capable of retaining large amounts of water[111] and are widely used as bio-

inks for tissue engineering since it encompasses features of the human cartilage ECM. Considering the high-water content (65-80%) of native cartilage, hydrogel is an attractive scaffold option in this parallel [112]. The biphasic nature of cartilage describes a fluid and solid phase lending it its viscoelastic behaviour[113], with exudation of interstitial fluid through its porous solid matrix under mechanical loading[18]. This not only supports cartilage's pivotal function in the head and neck region (e.g. ear, epiglottis) in dissipating frequent deformational forces by permitting flexibility and limiting brittleness and breakage, but lends itself well also to additive manufacturing approaches, in particular extrusion-reliant printing methods including 3D printing.

1.4 Nanocellulose – core bio-ink component

Cellulose is the most abundant biopolymer on earth [104, 114, 115]. Cellulosic nanomaterials (CNMs), often referred to simply as nanocellulose, are defined by its morphology with at least one dimension ≤100nm[115]. This in turn confers specific physicochemical and biological properties when compared to its bulk material. Capable of being produced in large scale at >1 ton per day[116, 117], nanocellulose has a broad reach in terms of industrial applications, such as paper products, adhesives, food packaging, low-calorie food additives, supercapacitors and batteries [118-121]. In biomedicine, it is used in dialysis membrane, wound dressing, biosensor and as an excipient (inactive ingredient) in pharmaceuticals [104, 122, 123]. More recently, as a bio-ink candidate for tissue engineering, nanocellulose has been described in bone, cartilage, skin, nerve, cardiac and vascular tissue regeneration [100, 124-130].

1.4.1 Nanocellulose properties relevant for tissue engineering

There are several properties of nanocellulose which translates well when used as a bio-ink for extrusion-based 3D printing and tissue regeneration. Due to its fibrous topography, nanocellulose fibrils are considered analogous to collagen and fibronectin in native ECM[131, 132]. The interconnected framework and porosity of nanocellulose-based hydrogels have structural similarities to ECM. Such biomimetic features are considered supportive of cellular functions including cell adhesion, proliferation and differentiation[133]. Additionally, whilst its water absorption capacity supports its use in hydrogels, the nanostructured morphology of nanocellulose is associated with a high

surface area, which in turn provides added interfaces for interactions with other materials[134].

In plants, cellulose constitutes a core load-bearing polymer. The exceptional strength and flexibility of plants to overcome gravitational forces as they grow can, in part, be attributed to the cellulose in plant cell walls[135-138]. The unique mechanical properties of nanocellulose underlies its inclusion as a biomimetic reinforcing agent in hybrid bio-inks; its purpose to enhance the tensile strength and stiffness of the resultant construct[139-141]. Pomari *et al* investigated the effects of incorporating cellulose nanocrystals (CNC) at varying concentrations with chitosan. It was found that with the addition of 6% w/w CNC maximal stress was increased by 36% when compared with pure chitosan hydrogels[142]. Furthermore, the ability to tune the physical and mechanical properties with nanocellulose, such as porosity and stiffness, adds to its suitability as a bio-ink material candidate[143, 144].

Shear-thinning is an essential criterion for bio-inks to ensure printability (flow) of the bio-ink during printing and shape fidelity post-print (maintenance of form without immediate collapse of the bio-ink)[145, 146]. The viscoelastic characteristics of nanocellulose confers both shear-thinning properties and high tensile strength, and are additional factors that make nanocellulose an attractive bio-ink candidate. Its high tensile strength, which affords the 3D printed scaffold resistance against fracturing under deformative stresses[123], is particularly relevant for cartilage tissue engineering for head and neck reconstructive purposes due to the intrinsic and extrinsic forces facial cartilages are subjected to on a daily basis.

In addition to tunable mechanical properties, nanocellulose, owing to an abundance of hydroxyl (-OH) and other functional groups, are amenable to further functionalisation which imparts desired material properties. Surface modifications of nanocellulose, such as *via* oxidation, can alter surface chemistry, introduce carboxyl, hydroxyl and amino groups, and controls wettability, adhesive properties and reactivity[143, 147]. In the context of tissue engineering, nanocellulose, through functionalisation, can become electroconductive lending its place in nerve and cardiac muscle tissue engineering.

Lastly, the generally considered non-toxic profile of nanocellulose is a key factor in the rising interest of this natural biopolymer as a bio-ink candidate. Prior to discussion of the current literature regarding the biological impact of nanocellulose in the context

of 3D bioprinting, an overview of the various nanocellulose forms and their relevant features are outlined in the next section.

1.4.2 Nanocellulose forms

Microscopically, cellulose microfibrils contain a highly structured assembly of cellulose molecules. Crystalline regions are interspersed with less organised, amorphous regions[148]. The production of nanocellulose can be broadly categorised into top-down and bottom-up approaches.

The top-down production method isolates CNC and cellulose nanofibrils (CNF) from its source material by breaking down interfibrillated bonds via mechanical forces and/or enzymatic or chemical processes[149]. Nanocellulose may be isolated from plants (e.g. wood pulp, cotton, agriculture residues), algae and marine invertebrates (e.g. tunicates)[123, 129, 149, 150]. The bottom-up approach describes the synthesis of nanocellulose by bacteria, with the resultant nanomaterial termed bacterial nanocellulose (BNC).

In understanding the production methods of nanocellulose, it becomes apparent the spectrum of nanoscale features and material properties encompassed by nanocellulose materials. Its appreciation is relevant in the context of biocompatibility due to the influence of material characteristics upon their biological impact. A brief overview of the three forms of nanocellulose (CNC, CNF and BNC) and two forms of functionalisation studied in this thesis (TEMPO-mediated oxidisation and carboxymethylation) are hereby presented.

1.4.2.1 CNC

CNC are rigid, rod-like or needle-like nanoparticles, with dimensions of 3-20nm in diameter and 50-500nm in length[149, 151-153]. It is often produced through acid hydrolysis, a chemical process involving the application strong acids (e.g. sulfuric or hydrochloric acid) to cellulosic materials. This selectively removes the amorphous regions of cellulose, leaving the crystalline nanoparticles[154, 155]. As such, it has a high degree of crystallinity[151, 156]. Other production methods include enzymatic hydrolysis

(e.g. with cellulase), mechanical disintegration, deep eutectic solvent, ultrasonication, steam explosion and dual mechanical-chemical treatments[132, 157-161].

The distinct morphology of nanorods with high crystallinity grant CNC extremely high stiffness[162, 163] and the ability to achieve ordered alignment. The latter could be beneficial in applications where anisotropic feature provides directive guidance for cell migration[162, 164, 165]. For example, the work of De France *et al* and Dugan *et al* have shown that the culture of skeletal muscle myoblast in a CNC-inclusive biomaterial guided cellular differentiation into orientated myotubes[162, 165]. Furthermore, the unique dimensions of CNC, when compared with CNF and BNC, may be contributory to its ability to pass through the cell membrane[166]. This property has led to the application of CNC in drug delivery, but could be associated with its unique toxicity profile when compared to other forms of nanocellulose.

1.4.2.2 CNF

CNF are long flexible fibrils with diameters of 5-60nm and lengths of several microns[149, 167]. They are usually obtained through mechanical disintegration. High shear forces are applied to cellulosic source materials which separates cellulose fibers into nanoscale CNF[144, 168]. Mechanical disintegrative techniques involve forcing cellulose fibers through narrow channels at high velocities (microfluidisation)[169] or at high pressures (homogenization)[170]. Both creates high shear and fibrillating forces to breakdown the cellulose fibers. Other production methods include ultrasonication, cryocrushing, combined enzymatic pre-treatment and mechanical disintegration[135, 171, 172]. As such, CNF contains both crystalline and amorphous regions, with a lower crystallinity compared to CNC (>80% with CNC versus 30-80% with CNF)[154, 173-175]. Crystallinity, which denotes the proportion of crystalline region within the nanocellulose material, is one of the fundamental features which directly influence mechanical, thermal and chemical behaviours. CNF appears as an entangled fibrous network. Together with the lower crystallinity, this contribute to the flexibility, deformability and the ability of CNF to disperse more readily which is particularly useful in creating composite materials[115, 123, 176].

1.4.2.3 BNC

Discovered in 1886 by A. J. Brown, bacterial cellulose synthesised by bacteria in culture medium of glucose and xylose was found to have similar structures as plant-derived cellulose[177, 178]. BNC is produced and secreted as an exopolysaccharide[179]. The dimensions of BNC have been described in the regions of 8-10nm in diameter and 100-150nm in length[180], to diameter of 100nm and length of 100μm[179]. Reported crystallinity are between 75%-85%[123, 181]. An advantage of BNC is its high purity, reaching 99.9%[123, 181]. Distinct to plant-derived nanocellulose, BNC is free from other plant-based components such as pectin, hemi-cellulose and lignin. The commercial application of bacterial cellulose and BNC currently includes wound dressing[182, 183], artificial skin[184] and vascular or cartilage implants[185, 186]. Limitations to up-scaling and cost-effective commercialisation include the high cost of glucose as the substrate, a labour-intensive production process and relatively low yield[162, 187]. Future discussion of nanocellulose in the thesis will therefore exclude BNC.

1.4.2.4 TEMPO-mediated oxidation and carboxylmethylation

Both TEMPO-mediated oxidation and carboxymethylation are methods of functionalisation of nanocellulose.

The oxidation process introduces oxygen-containing functional groups (e.g. hydroxyl, carboxyl, carbonyl groups) to the surface of nanocellulose using an oxidising agent[188-190]. TEMPO-mediated oxidation utilises 2,2,6,6-tetramethylpiperidine-1-oxyl (TEMPO) and sodium bromide as the chemical catalysts to selectively oxidise primary hydroxyl groups to carboxylate[191-194]. Alternative chemical oxidation treatments include periodate oxidation[123].

Carboxymethylation involves substituting the hydroxyl group on the surface of nanocellulose with carboxymethyl groups using chloroacetic acids or its derivatives[195-199].

Both functionalisation imparts a negative charge to the resultant nanocellulose[200]. Common benefits include enhanced dispersibility[188, 195, 198, 201] and increased reactivity. In the context of tissue engineering, the modified surface of TEMPO-mediated oxidised nanocellulose was found to support cell adhesion and proliferation[202], and in wound dressings, superior integration with wound surfaces was observed which

promoted more rapid wound healing[123]. On the other hand, the carboxymethyl group in carboxymethylated nanocellulose provides functional sites for drug loading[123]. Similarly, both forms of functionalisation are associated with harsh reaction conditions (alkaline with carboxymethylated nanocellulose)[198, 203] and the formation of by-products[188, 198, 204, 205]. Potential degradation of cellulose structure with TEMPO-mediated oxidation and possible reduction in mechanical properties with carboxymethylation have been described[195, 198].

Further features of the functionalised nanocellulose includes enhanced stability in aqueous solution and hydrophilicity with TEMPO-mediated oxidation[188-190] and greater water solubility with carboxymethylation[195, 198]. Relevant for bio-ink applications, increasing concentrations of both forms of nanocellulose is associated with increased viscosity influencing the flow property of the bio-ink. Equally, both forms of nanocellulose carries strong viscoelastic modulus even at low concentrations, which may be a desirable feature depending on the intended tissue type for regeneration[149].

1.4.3 Biocompatibility of nanocellulose for tissue engineering

In parallel with the wide adoption of nanocellulose across multiple industries as highlighted previously, nanocellulose has demonstrated an overall favourable biocompatibility profile. *In vitro* studies available, however, are mostly focused on raw material and pulmonary models relevant to occupational exposures[206, 207]. Alternative exposure route examined included gastrointestinal exposure with relevance for food additives or packaging applications[208].

Its assessment relevant to environmental exposures confirms that nanocellulose is largely non-toxic. Dong *et al* examined the cytotoxic effects of CNC on nine cell lines using the MTT and LDH assays[209]. Six human cell lines (5 epithelial cells and 1 brain microvascular endothelial cell) and 3 murine cell types (macrophage, glial cells and brain endothelial cells) were tested in an *in vitro* setting with 0-50μg/ml CNC over 48 hours which demonstrated no cytotoxic effects. Harper *et al* employed an embryonic zebrafish model to test the biological effects of multiple forms of nanocellulose (e.g. CNC from cotton or wood pulp, sulfated and carboxylated CNC and TEMPO-

mediated oxidised CNF)[210]. CNC at 0.0003-0.172mg/ml and CNF at 0.002-0.25mg/ml were exposed to the *in vivo* model. Differences in surface chemistry were found to have minimal impact on cytotoxicity when viability, notochord malformation, developmental progression and motility were assessed. Interestingly, the study found that nanocellulose derived *via* mechanical homogenisation displayed greater toxicity than those produced by chemical processes. This may reflect differing physico-chemical properties associated with the different nanocellulose forms associated with varying production methods, rather than as a direct result of the production technique per se. A further finding of note was the uptake of fluorescently tagged CNC by the embryonic zebrafish at 0.1-0.5mg/ml during a 5-day exposure. This corroborates with an earlier comment regarding the ability of CNC to cross the cell membrane, with implications on CNC toxicity and its mechanisms of action. Lastly, when comparing the concentrations of nanocellulose tested in both studies against that of the bio-ink used in this thesis (20mg/ml), the relevant dosage for use in bio-inks with tissue engineering is noted to be much greater than those tested for environmental exposure.

Published studies examining nanocellulose-based bio-inks intended for tissue engineering purposes often subscribe to the format of bio-ink characterisation. This typically includes raw material, bio-ink (commonly multi-component) and/or scaffold (post-crosslinkage) characterisation. Morphological, mechanical, rheological and biological assessments are often encompassed to varying degrees. Analogous to the favourable biocompatibility profiles found in studies for hazards assessment in alternative exposure scenarios, nanocellulose-based bio-inks are largely found to be non-cytotoxic and is supportive of cell proliferation and tissue regeneration[128, 139-141, 211-215]. The next sections focus upon *in vitro* and *in vivo* studies examining nanocellulose-based bio-ink for tissue engineering purposes. The sub-sections aim to address: i) factors found to be influential of the biological effects of nanocellulose, thereby highlighting the complexities of studying biocompatibility in the context of tissue engineering; and ii) the patterns of test systems employed in these studies as relevant to the principles of *in vitro* toxicology.

1.4.3.1 Factors influencing the biological impact of nanocellulose-based bio-inks

Many factors act as biological cues directing cellular function and therefore impacts the biological effects of nanomaterials. Examples of such influential material

characteristics include material stiffness, surface roughness and porosity of the resultant construct[213]. This is, in part, imparted by the physico-chemical properties of nanocellulose, which differs based on its form (CNC versus CNF), material source, production methods and functionalisation as previously discussed. Further additives as part of the hybrid bio-ink formulations, or modifications as part of the biofabrication process, can further enhance or disrupt the interactions between the bio-ink material and host cells or tissue. There are a staggering number of variables associated with the successful clinical translation of a tissue engineered product (TEP), and a standardised *in vitro* model may permit a higher throughput of testing prior to *in vivo* studies, whilst controlling for bio-ink or experimental variables of interest.

Whilst not intended to be an exhaustive list, the influence of five categories (surface charge, nanocellulose content, hybrid bio-inks, model geometry and 3D bioprinting parameters) upon the biological effects of nanocellulose-based bio-ink are discussed. Cumulatively, they illustrate varying cytotoxic effects associated with the use of nanocellulose-based bio-inks, highlighting the necessity for a material-, system- and end-application specific means of investigation to achieve valid and relevant toxicity data.

1.4.3.1.1 Surface charge

The surface charge of nanocellulosic material was shown to influence cell adhesion and proliferation. Whilst Alexandrescu *et al* examined the effects of CNF with a neutral charge versus negative charge (the latter with TEMPO-mediated oxidised CNF) and found that both supported fibroblast growth[216], Kummala *et al* reported differences in cell behaviour with varying surface charges. In the latter study, comparison between material coatings with CNC and two CNFs with a high (1.50 mmol/g) or low (1.14mmol/g) surface charge was conducted against human dermal fibroblast[217]. Nanocellulose was prepared from kraft wood pulp, with TEMPO-mediated oxidation treatments with both CNF and acid hydrolysis with the CNC. Latex was used as a control coating which has previously been shown to support fibroblast attachment and growth. Interestingly, whilst cell adhesion and proliferation were seen with the CNF with the low surface charge over a 72-hour period, fibroblast surface-seeded upon both the CNC and CNF with high surface charge coatings showed both

reduced cell attachments at 24 and 72 hours, and a reduction in cell numbers from day 1 to day 3 indicating cytotoxicity.

It is noteworthy that surface charge can have direct effects on bio-ink performance which in turn, impacts cellular function. Xu *et al* discovered that the ionic interaction between TEMPO-mediated oxidised CNF and GelMA can cause phase separation, which are likely to be detrimental for cell growth[218]. To maintain bio-ink homogeneity and stability, the content of GelMA was controlled to be <1wt%.

1.4.3.1.2 Nanocellulose content

Depending on the system tested, nanocellulose content was found to have varying effects on cytotoxicity. Whilst Lan *et al* showed no difference in cytotoxicity between bio-inks with differing nanocellulose content[190], other studies showed altered cytotoxicity[219, 220]. The study by Lan *et al* examined bioprinted constructs of TEMPO-mediated oxidised CNF with alginate seeded with primary human meniscus fibrochondrocytes[190]. Live/dead assay at 24 hours demonstrated comparable cell viability of both bio-ink CNF:alginate ratios at 70:30 and 80:20. Conversely, Dutta *et al* investigated a gelatin, alginate and CNC (from cotton pulp, width 10-20nm, length 50-400nm) bio-ink seeded with human bone marrow-derived mesenchymal stem cells (hBMSCs) for bone tissue regeneration[219]. Cell viability assessed by the WST-1 assay and cell adhesion with fluorescence staining showed that the 1% CNC provided optimal result for up to day 7 when compared to 0.5%, 2% and 4% CNC. Similarly, Cheng *et al* compared four nanocellulose concentrations in a chitosan-CNF (wood pulp, diameter 3nm, length 10-20μm) hydrogel for neural tissue regeneration[220]. Cell viability assessed by fluorescence staining on day 3 and oxygen metabolism and mitochondrial function as examined by the Seahorse XFp analyser, showed that the 0.09% concentration displayed superior cell health, whilst the 0.5% CNF content (the highest concentration tested) yielded the greatest cytotoxic effects and impaired mitochondrial function.

Collectively, this illustrates that the concentration of nanocellulose within a test system must be defined despite the relative non-toxic profile of nanocellulose. Furthermore, an optimal nanocellulose concentration should be selected to maximise the biological performance of bio-inks.

1.4.3.1.3 Hybrid bio-inks

Multi-component bio-inks are common in recent research in tissue engineering. Nanocellulose may be combined with other natural or synthetic polymers, and the combined effects of the biomaterials can alter the toxicity profile of the resultant hybrid bio-ink.

Some bio-ink additives have been shown to have negative effects on cell health, such as that from Ojansivu *et al*[221]. This study examined the effects of the addition of a TEMPO-mediated oxidised CNF from softwood kraft pulp with/without bioactive glass to a gelatin-alginate bio-ink. Intended for bone tissue regeneration, cell viability and cell proliferation were tested using the Saos-2 cell line of human osteoblastic phenotype and hBMSCs. Cell viability and proliferation were unaffected with the addition of CNF to the gelatin-alginate bio-ink, as assessed by the live/dead assay (day 1,7,14) and LDH assay (day 1,4) and *via* the quantification of DNA content (day 1,7,14), respectively. Whilst non-cytotoxicity was demonstrated with CNF, the addition of bioactive glass (with or without CNF) showed a marked decreased in cell viability and proliferation. This was witnessed with both cell types.

The converse pattern was observed in studies by Cheng *et al* [220] and Ferreira *et al* [128]. As previously described, Cheng *et al* demonstrated that the addition of CNF to chitosan did not uniformly yield superior cell viability in an *in vitro* setting. The bio-ink with 0.09% CNF content outperformed the chitosan-only control, whilst the 0.5% CNF showed heightened cytotoxicity when compared to the chitosan-only control[220]. This study also included an *in vivo* study involving a zebrafish brain injury model with the implantation of constructs seeded with neural stem cells derived from adult mouse brains. The hybrid material containing both chitosan and CNF consistently outperformed the CNF-only constructs in both locomotion (swimming) on day 4 and survival rate on day 6, thereby demonstrating a biological benefit to the inclusion of CNF with the chitosan hydrogel.

Interestingly, Ferreira *et al* also examined the effect of bio-active glass with CNF (from Eucalyptus grandis) for bone regeneration. Cytotoxicity was measured by the live/dead assay (day 3) and MTT assay (day 1,2,3). Exposure involved adding the scaffolds to cells seeded on tissue culture well plates in 2D culture. In contrast to the findings from the study by Ojansivu *et al,* Ferreira *et al* showed that no cytotoxic effects were seen

with bio-inks containing bioactive glass and CNF[128]. However, differing exposure methods were noted. In the study by Ojansivu *et al* where cytotoxicity was observed with bioactive glass bio-ink formulations, direct mixing of cell suspensions with the bio-inks was performed[221].

1.4.3.1.4 Model geometry

Xu *et al* evaluated cell proliferation of human dermal fibroblast surface-seeded on TEMPO-oxidised CNF from birch kraft pulp (charge density 1.14 mmol/g)[213]. Two 3D printed scaffold model geometries were tested with a thickness of 3mm (15 layers) versus 2mm (11 layers), whilst controlling for other experimental parameters. Immunofluorescence staining showed enhanced cell proliferation with the thicker 3mm construct at 72 hours. Whilst a larger construct theoretically could provide greater spatial dimension for cell growth in 3D, the surface area available for surface-seeded fibroblast in 2D was consistent. Cell migration (from surface to core) was not investigated, and although this may explain increased 3-dimensional space for cell growth, there are other factors that could contribute to the differences observed. Scaffold characterisation in the forms of scanning electron microscopy (SEM) to visualise surface and cross-sectional topography, water absorption capacity, compression Young's modulus and shear modulus, all showed differences between the scaffolds of 2mm and 3mm thickness. Such differences in physical properties parameters may influence cell growth profiles.

1.4.3.1.5 3D bioprinting parameters

Further to inherent raw material, composite bio-ink and model factors, the biofabrication process alone can alter cell behaviour, and should be accounted for during the creation of an *in vitro* model. As previously described in section 1.4.3.1.3, Ojansivu *et al* studied the impact of the addition of a TEMPO-mediated oxidised CNF with or without bioactive glass to a gelatin-alginate bio-ink for bone regeneration[221]. DNA content was monitored to mark cell proliferation of the Saos-2 osteoblastic cell line. Constructs created by casting in a mold versus 3D printed were compared. Whilst the casted system demonstrated rising DNA content on day 1, 7 and 14 indicating continuous cell proliferation in the gelatin-alginate bio-ink both with or without CNF, in the 3D printed system, DNA content was unchanged between day 1 and 7 before a

rise on day 14. This indicates a degree of cell stress imparted from the 3D bioprinting process, such as from the shear forces, at the early and middle timepoint.

1.4.3.1.6 Section summary – factors influencing the biological impact of nanocellulose-based bio-inks

The highlighted examples illustrate the complexity of studying the biological effects of TEPs because of the numerous inter-related factors. In order to achieve advancements towards successful clinical translation, a standardised *in vitro* model may serve to exert uniformity across selected key variables. However, a pragmatic approach in experimental design remains a necessity as it is not feasible to isolate singular factors and attain absolute equivalence across all variables.

1.4.3.2 Study design

Experimental findings are specific for the material, cells and test system applied, which could influence the validity, relevance, reproducibility and interpretation of toxicity data. Broad patterns as well as heterogeneity observed in cell-based studies of nanocellulose-based bio-inks intended for tissue engineering are discussed, followed by a brief overview of *in vivo* studies.

1.4.3.2.1 Cells

Both human and animal cells were used for the testing of bio-inks for tissue engineering. Whilst there may be a greater volume of historical data involving cell lines from an animal source, the use of human cells offers greater specificity and relevance for the end-application of a clinically applicable TEP.

Regarding human cells, they can be further categorised into primary cells, stem cells and cell lines. The former two are more commonly employed. Using cartilage regeneration as an example, studies have sought to utilise primary cells isolated from the anatomical site of interest, such as with primary human meniscus fibrochondrocytes (knee meniscus)[190], auricular (ear)[211] and nasal (nose) chondrocytes[222-224]. Target tissue-derived ‘stem cells’ have also been studied, such as with cartilage stem / progenitor cells (CSPCs)[225], although the use of mesenchymal

stem cells such as those that are bone marrow-derived are more commonly reported[219, 221, 222 226]. Whilst primary cells offer specificity, the heterogeneity in patient phenotypes can impact the reproducibility of results. Currently, the Good In Vitro Method Practices (GIVIMP) from the Organisation for Economic Co-operation and Development (OECD) recommends the use of cell lines for *in vitro* toxicity testing including cell line characterisation prior to toxicity testing. Examples of human cell lines used in the testing of nanocellulose-based bio-inks include the epithelial cell line Saos-2 of osteoblastic phenotype established from adult osteosarcoma used for bone regeneration[221] and the keratinocyte cell line HaCaT for skin regeneration[214].

Animal sources offer greater availability of tissue type-specific cell lines, which may in part, explain their popularity. For studies focused on human tissue regeneration purposes, murine cell lines were more commonly used, such as the chondrogenic ATDC5 for cartilage[140], calvarial pre-osteoblast MC3T3-E1 for bone[128, 141], H9C2 for cardiac muscle as the target tissue type[212], and fibroblasts L929[212 227] and 3STS[216] for skin or general cytotoxicity testing. Less commonly adopted are animal-derived stem cells, but reports have included the use of mouse bone marrow derived-mesenchymal stem cells[228] and neural stem cells isolated from adult mouse brain[220].

As advances in complex *in vitro* models (CIVMs) continues to develop, there is a movement towards limiting the use of animal-derived products such as the use of accutase over animal-derived trypsin as a cell dissociation agent, or synthetic or human-derived media supplements over the widely used fetal bovine serum. Costs and availability are some of the limiting factors towards their adoption. With regards to cell line source, as the number of studies involving human cell lines increases with the expansion of data available with their use, human cell lines in *in vitro* toxicity testing may eventually predominate over animal sources for human-specific applications.

A further observation of reported studies includes the relative lack of co-culture models studying the cell-material and host-material interactions. Multi-cellular CIVMs are increasingly utilised for *in vitro* toxicity testing. Relevant to cartilage tissue engineering, studies involving dual cell types often explore the ratio effects of stem cells and differentiated chondrocytes upon cell expansion and ECM regeneration. To leverage advances in *in vitro* toxicology, multi-cellular *in vitro* models may offer

further insights when both target tissue cell type and the cell type reflecting the host environment are applied.

1.4.3.2.2 Exposure methods

To achieve a physiologically-relevant *in vitro* model, the exposure methodology is a core consideration. Studies generally fall under four exposure approaches, divided into direct and in-direct exposures.

Direct exposure describes: i) 2D cell culture in tissue culture plate (TCP) with constructs (usually cross-linked) directly added onto cells in TCP wells[128, 140, 229]; ii) cells surface-seeded onto un-crosslinked bio-ink or cross-linked scaffolds in TCP wells[139, 212, 213, 225, 228]; and iii) cell suspension mixed with bio-ink to create a cell-laden bio-material[190, 211, 220-224]. Some studies utilised a combination of exposure methods based on the toxicity assay[140, 219]. In cartilage and other solid organ tissue engineering, the latter approach (iii) most closely mimics the cell-laden bio-ink in the 3D bioprinting scenario when cells of the target tissue type are used, whilst surface-seeding reflects the implant-host interface.

Alternatively, the material extract dilution method was often used as an in-direct exposure method. This is described in the ISO standard 10933-5, the Biological Evaluation of Medical Devices. This involves incubating the crosslinked construct in a culture medium (e.g. for 24 hours)[225] to produce the material extract solution, which are then subsequently added to cells in 2D culture. The material extract dilution method is used by Sinna *et al* investigating cartilage regeneration[225], Cui *et al* for bone regeneration[141], Sun *et al* for cardiac muscle regeneration[212] and Alexandrescu *et al* for its effects against a mouse fibroblast cell line[216]. Whilst the material extract dilution method is an established and validated method of toxicity testing that is well-embedded in regulatory toxicological practice, it is recognised that bioactive TEPs are a relatively new entity. The ISO standard 10993-5, which was published in 2009 and most recently revised in 2022, was formed to assess medical devices that are largely designed as inert implants with varying degrees of biointegration and biodegradation, and this is arguably distinct from TEPS designed for tissue regeneration.

1.4.3.2.3 Endpoint assessment

Pro-inflammatory effects, oxidative stress and genotoxicity are considered key drivers of cytotoxicity, and together forms four key *in vitro* toxicology endpoints. Whilst cytotoxicity data is a pre-requisite for biocompatibility testing of medical devices for regulatory approval in most markets, taken on its own, it does not shed light on potential sub-lethal adverse outcomes, nor upon the possible mechanisms of action of cytotoxicity[230]. The assessment of more than one toxicology endpoint, with the use of multiple (≥2) techniques per endpoint assessment is generally recommended in *in vitro* toxicology.

As commented upon previously, most cell-based studies of nanocellulose-based bio-inks form part of a global assessment for bio-ink characterization. It is found that cytotoxicity is a commonly assessed toxicological endpoint in *in vitro* studies, with a fair number of studies employing dual methods of assessment[140, 141, 190, 212, 214, 215, 219, 220]. This most frequently involves the combination of a metabolic assay and fluorescence staining, although a number of studies reported a single mode of endpoint assessments[139, 219, 225, 231]. Metabolic assays were often performed to determine cell proliferation and included the WST-1 assay[139, 141, 219], MTT assay[225, 231], Alamar blue assay [224] and CCK8 assay[141]. The live/dead assay is also commonly adopted in multiple studies[190, 211, 223], as are immunofluorescence staining to visualize cell morphology and cell distribution[140, 212, 215, 219, 220, 228]. Alternative assays reported included the quantification of DNA content over time to determine cell proliferation rate[214] and the assessment of mitochondrial function and oxygen metabolism using the Agilent Seahorse XF Analyzer[220].

Relative to cytotoxicity, there is a comparative lack of assessment of pro-inflammatory effects, oxidative stress and genotoxicity in an *in vitro* setting for nanocellulose-based bio-inks. However, for the purpose of tissue engineering, numerous studies investigated the functional element of the cell-seeded bio-ink in terms of tissue regeneration and appropriate cell differentiation from MSCs for the target tissue type. Lan *et al* seeded primary human meniscal fibrochondrocytes in a TEMPO-mediated oxidized CNF-alginate bio-ink and demonstrated newly synthesized ECM and type I and II collagen by immunostaining[190]. Gene expression analysis by qPCR also showed that the CNF-alginate bio-ink showed up-regulation of chondrogenic genes (*COL2A1*)

and down regulation of undesirable chondrocyte hypertrophy-related genes (*COL10A1* and *MMP13*) when compared with the collagen-alginate bio-ink without CNF[190]. Chayanun *et al* also utilized immunostaining to demonstrate enhanced GAG and type II collagen production by murine ATDC5 chondrogenic cell line when a cotton-derived CNF was added to an alginate dialdehyde-gelatin bio-ink as a reinforcing agent[140]. Similarly, for bone regeneration, multiple mineralization studies with the Alizarin red S stain[141, 219] and quantification of alkaline phosphatase activity[141, 221] have shown positive results with cotton-derived CNC (diameter 10-20nm, length 50-400nm) in a CNC-gelatin-alginate bio-ink with hBMSCs, a CNF (diameter 30nm, length 1-3μm)-oxidised alginate-gelatin bio-ink with mouse calvarial pre-osteoblast cell line MC3T3-E1 and a TEMPO-oxidised CNF from softwood kraft pulp-bioactive glass-gelatin-alginate bio-ink with hBMSCs and the human osteoblast cell line Saos-2. Whilst functional assays are critical in the development of suitable bio-inks for 3D bioprinting, there may be a role in the investigation of added toxicological endpoints to illuminate the sub-lethal effects of bio-inks under investigation and possible mechanisms behind bio-ink performance to advance the field of tissue engineering.

1.4.3.2.4 Timepoints

Specifically for *in vitro* studies, timepoints investigated also varied between studies. Possibly secondary to inherent challenges and limitations to prolonged *in vitro* cell culture, acute timepoints were more commonly studied compared to chronic timepoints. Timepoints at ≤72 hours are relatively frequently employed[128, 190, 209, 213, 216, 224, 228, 232], to a slightly lesser degree, as are studies of 7 days[141, 212, 219, 223, 227, 231] and 14 days duration[139, 140, 221, 222, 225, 226]. Noticeably far fewer *in vitro* studies report upon chronic timepoints, such as 21 and 28 days[211, 220].

Cell de-differentiation over time in *ex vivo* culture is a known challenge, especially with the use of primary human chondrocytes, coupled with a relative minority of cell line use which may better tolerate long-term cell culture conditions whilst maintaining defined cellular characteristics and function. The phenomenon of positive publication bias could also limit the amount of published data. Cheng *et al* assessed cell viability of adult mouse brain neural stem cells embedded in chitosan bio-ink with varying concentrations (0, 0.06, 0.09, 0.12, 0.5 wt%) of wood pulp-derived CNF[220]. Using the CCK-8 assay, it was observed that cells embedded within the bio-ink (with or without

CNF) showed comparable cell metabolic activity on day 0 and day 3, and the incorporation of CNF enhanced cell proliferation on day 7, 14 and 21. However, on day 28, the metabolic activity measured declined across all bio-ink formulations indicating likely model inadequacy posing constraints in *in vitro* cell culture at this chronic timepoint.

1.4.3.2.5 *In vivo* studies

In vivo studies provide whole organism response that encompasses an immune system, systemic metabolic (hepatic) and excretory (renal) systems which responds to and processes an implanted foreign material or construct. The high sensitivity of *in vitro* cytotoxicity testing may, in part, be due to the artificial isolation of cells within the model system with the absence of protective biological processes that otherwise exists in a whole organism[216]. *In vivo* studies are widely employed in studies in tissue engineering across multiple tissue types, such as bone[128, 226], cartilage[222, 232], neural tissue[220] and the cornea[233]. *In vivo* experiments benefit from the study of long term timepoints, commonly up to 60-90 days[128, 222, 232, 233]. It permits analysis of multiple endpoints simultaneously, including scaffold performance and degradation, foreign body response including inflammation, and function in terms of tissue regeneration.

The calvarial bone defect model was used effectively to demonstrate that nanocellulose-based bio-ink supports bone regeneration with limited toxicity, and two studies illustrating this are hereby described. Patel *et al* reported superior bone regeneration with a PLA scaffold with 2% CNC at 3 weeks in a rat model with no evidence of inflammatory response[226]. Ferreira *et al* not only demonstrated bone formation with bioactive glass-CNF scaffold in a rat model, systemic biocompatibility was also assessed *via* the quantification of blood biochemical markers of toxicity and histopathological examination of the liver and kidney. Levels of glutamic oxaloacetic transaminase (TGO) and glutamic pyruvic transaminase (TGP) for the liver and creatinine for the kidney, and solid organ histological examination revealed no differences between the nanocellulose-based scaffold and the scaffold-free control at 56 days[128]. In a rat model investigating 3D bioprinted tunicate-derived CNF-alginate scaffolds, Apelgren *et al* in 2022 demonstrated with histological analysis that there was no evidence of acute inflammation, invasion of immune cells or extensive fibrosis at day 30 and day 90[232]. Expanded polytetrafluoroethylene (ePTFE), used in medical

devices such as stents or vascular grafts coating, are the polymer associated with the commonly recognized products such as Teflon and GoreTex. ePTFE was used as a control material. Although moderate foreign body reaction was observed with the presence of macrophage, lymphocytes and giant cells, the author concluded that in comparison to ePTFE, scaffolds inclusive of the tunicate-derived CNF was non-irritant according to the ISO standard 10993-6 for local effects after implantation. Overall, nanocellulose-based scaffolds demonstrated limited cytotoxic and inflammatory effects *in vivo*.

Considerations regarding *in vivo* studies include study design restraints associated with whole organisms. The use of immunocompetent animals is applied for the study of the host-material response of cell-free scaffolds. Whilst this provides vital information regarding the foreign body response, it does not permit assessment of human tissue regeneration. Used to illustrate the latter, the study by Apelgren *et al* in 2017 investigated alginate-CNF scaffolds seeded with human nasal chondrocytes or hBMSCs in athymic or nude mice to study the effect of adult versus stem cells on cell proliferation[222]. The opportunity to develop increasingly sophisticated CIVMs such as with organ-on-chip and microfluidic technologies may improve the functionalities and physiological relevance of such models, which are already under development in the context of drug screening and disease modelling. Such technologies may bridge the gap between more simplistic 2D monoculture *in vitro* models and *in vivo* studies, and have a role in advancing efforts within the complex field of tissue engineering.

1.4.4 Commercially available nanocellulose-based bio-inks

Commercially available, off-the-shelf nanocellulose-based bio-inks provides convenience and ease of use but may hinder customisation. UPM Biomedicals is a leading player of commercialised medical grade nanocellulose intended for medical and life sciences applications. GrowInk™ from UPM Biomedicals is marketed as an animal-free, medical-grade hydrogel of CNF from wood sources. Partnering with CELLINK, a prominent Swedish bioprinter supplier, the CELLINK Bioink consists of CNF (from UPM Biomedicals) and alginate, and is available as an accessory kit.

Distinct to both commercially available nanocellulose-based bio-inks, this thesis examined the biological effects of tunicate-derived CNFs (including various functionalisation), alginate (the most commonly used natural bio-ink candidate according to a recent systematic review[100]), and hyaluronic acid (a native component part of human cartilage).

1.5 Aims and objectives

The central hypothesis postulates that nanocellulose is a biologically compatible material for cartilage tissue engineering *via* 3D bioprinting approaches.

The aim of this thesis is to create a physiologically relevant advanced 3D *in vitro* model for the purpose of examining the cytotoxic and pro-inflammatory effects of nanocellulose-based bio-inks for cartilage tissue engineering purposes. This research builds upon previous studies investigating dual components bio-inks with wood-derived nanocellulose combined with either alginate [223, 224, 234] or hyaluronic acid (unpublished data). A secondary aim is to refine the bio-ink formulation based upon biological data generated from this thesis. The final optimal bio-ink formulation was then applied to the advanced *in vitro* co-culture model created as part of the thesis for biocompatibility testing.

The aims were met *via* the following objectives:

1. To establish material sterility and the cytotoxic and pro-inflammatory effects of nanocellulose, alginate and hyaluronic acid against human dermal fibroblast and human chondrocyte cell lines.
2. To create an advanced 3D *in vitro* model for the biological testing of nanocellulose-based bio-ink intended for cartilage tissue engineering.
3. To conduct testing for cytotoxicity and pro-inflammatory effects of optimised nanocellulose-based bio-ink using the developed advanced 3D *in vitro* model.
4. To trial RNA extraction from the advanced 3D *in vitro* model and conduct global characterisation of the advanced 3D *in vitro* model using differential gene expression analysis.

Chapter 2: Materials and Methods

2.1 Chemical and reagents

Table 2.1 List of materials used in thesis. *Bio-ink materials are denoted by *.*

Materials	**Brand (Cat No.)**
3M sodium acetate solution, pH 5.2	Thermo scientific (R1181)
Alamar Blue™ HS cell viability reagent	Invitrogen (A50101)
AllPrep® DNA/RNA mini kit	Qiagen (80204)
C20A4 cell line	Sigma-Aldrich (SCC041)
Calcium chloride dihydrate, suitable for cell culture	Sigma-Aldrich (C7902-500G)
CD15 antibody, anti-human, APC	Miltenyi Biotec (130-114-008)
CD44 antibody, anti-human, VioBlue®	Miltenyi Biotec (130-113-899)
CD44 microbeads human	Miltenyi Biotec (130-095-194)
Corgel® BioHydrogel 5% gel kit*	Lifecore Biomedical, Inc (ENG 00152)
D(+)-glucose anhydrous	Formedium (GLU03)
DMEM (1x) Dulbecco's modified eagle medium; [+] 4.5g/L D-Glucose, L-Glutamine; [-] Pyruvate	Gibco (41965)
Dimethyl sulfoxide (DMSO)	Fisher (BO231-100)
Elastosil® RT 601 A	Wacker (60003804)
Elastosil® RT 601 B	Wacker (60003815)
ErB-2 (CD340) antibody, anti-human, PE, REAfinity ™	Miltenyi Biotec (130-124-473)
Erythrosin B stain	Logos Biosystems (L13002)
Fetal bovine serum (FBS)	Gibco (10270106)
HFF-1 cell line	ATCC (SCRC-1041™)
Hydrogen peroxide solution 30% (w/w) in H2O, contains stabilizer	Sigma-Aldrich (H1009)
Human IL-6 DuoSet ELISA	R&D Systems, Inc (DY206)
Human IL-8/CXCL8 DuoSet ELISA	R&D Systems, Inc (DY208)
Lactate dehydrogenase activity assay kit	Sigma-Aldrich (MAK066-1KT)
LB Broth	Sigma-Aldrich (L3022)
LB Broth powder	Melford (L24060)
LIVE/DEAD™ viability/cytotoxicity kit	Invitrogen (L3224)
Nanocellulose blend, hydrophilic bioplus® (NCB)*	GranBio (previously American Process International LLC)
Nanocellulose crystals, hydrophilic bioplus® (CNC)*	GranBio (previously American Process International LLC)
Nanocellulose fibrils, hydrophilic bioplus® (CNF)*	GranBio (previously American Process International LLC)
Penicillin/streptomycin 100x or 10,000u/ml	Gibco (15140-122)

Peptone	Formedium (PEP03)
Phosphate buffered saline (PBS; pH 7.4 1x, $mgcl_2$ + $cacl_2$ free)	Gibco (14190-094)
Phosphate buffered saline tablet (PBS)	Sigma (P4417)
Probumin® Bovine Serum Albumin (BSA)	Millipore (82-045-1)
Qubit™ RNA HS Assay Kit	Invitrogen (Q32852)
Sodium alginate*	Sigma-aldrich (W201502)
Sodium hyaluronate - sterile research-grade (molecular weight $1.59x10^6$Da)*	Lifecore Biomedical, Inc (HA15MS; Lot 029755)
Trypan blue solution	Sigma-Aldrich (T8154)
TrypLE™ Express [-] phenol red	Gibco (12604-013)
Trypsin	Gibco (25300-062)
TuniCell CTC – carboxymethylated cellulose nanofibrils*	Ocean TuniCell AS
TuniCell ETC – enzymatically pretreated cellulose nanofibrils*	Ocean TuniCell AS
TuniCell TTC – TEMPO-mediated oxidized cellulose nanofibrils*	Ocean TuniCell AS
Yeast extract powder	Formedium (YEA03)

2.2 General materials and equipment

Table 2.2 List of materials and equipment used in thesis.

Materials and Equipment	**Brand (Cat No.)**
1ml luer syringe	BD Plastipak (303172)
1ml syringe luer-lok™ tip	BD (309628)
5ml plastic syringe (Fisherbrand)	FisherScientific (14955458)
96 well half-area plate	Greiner Bio-One (675061)
Autoclave (Classic extended; for nanocellulose)	Prestige Medical
Autoclave (VARIO 1528; portable)	Dixons
Cell culture flasks T25	Greiner Bio-One (690175)
Cell culture flasks T75	Greiner Bio-One (658175)
Cell culture flasks T175	Greiner Bio-One (660175)
Cell culture microplate, 96 well, flat and clear bottom, black, with lid (for alamar blue assay)	Greiner bio-one (655090)
Cell strainer 70um nylon	Falcon (352350)
Centrifuge (for cell culture + bio-ink material)	Hitachi (himac CT6E)
Centrifuge (for eppendorf)	Eppendorf (5810R)

Class II hood	ScanLaf Mars
Cover slips	Fisher Scientific (11961988)
Electric mixer (paint mixer)	Badger Air-brush Co. (121)
Eppendorf (200µl)	Fisher Scientific (14230225)
Eppendorf (500µl)	Fisher Scientific (14230200)
Eppendorf (1.5ml)	Greiner Bio-One (616201)
Falcon tubes (15ml)	Greiner Bio-One (188271)
Falcon tubes (50ml)	Greiner Bio-One (227261)
Filter (Millex®-GP Millipore Express® PES membrane filter unit (0.22um))	Merck Millipore Ltd (SLGP033RS)
Haemocytometer (Neubauer-improved Bright Line)	Marienfeld Superior (Counting Chamber)
Light microscope (Axiovert 40C)	Zeiss
Light microscope (CKS53 40C)	Olympus
Liquid scintillation vials (with screw cap attached)	Sigma-Aldrich (Z190535-1PAK)
LS columns (for MACS)	Miltenyi Biotec (130-042-401)
Microcentrifuge (Starlab)	Starlab Group
Microplate, 96 well, half area clear (for ELISA)	Greiner Bio-one (675061)
Mr frosty™ freezing container	Thermo Scientific (5100-0001)
nCounter Sprint cartridge	Nanostring
nCounter Sprint reagent C	Nanostring
nCounter Sprint reagent pack (contains reagent A and B and hybridisation buffer)	Nanostring (100079)
Pasteur pipette	VWR (612-4497)
pH-indicator strips (MQuant®; non-bleeding)	Merck Millipore Ltd (MC038766; 1.09584.0001)
Pipette tips (20µl)	Starlab (TipOne S1120-1810)
Pipette tips (200µl)	Starlab (TipOne S1111-1706)
Pipette tips (1000µl)	Starlab (TipOne S1111-6701)
Plate reader (FLOUstar Omega)	BMG Labtech
Qubit™ flex assay tube strips	Invitrogen (Q33252)
Rheometer (AR-G2)	TA Instruments
Scale (for mg)	Sartorius Research (R180 D)
Scale (for g)	Sartorius (TE3102s)
Serological pipettes (5ml)	Greiner Bio-One (606180)
Serological pipettes (10ml)	Greiner Bio-One (607180)
Serological pipettes (25ml)	Greiner Bio-One (760180)
Slides	RS France (BPB019)
Static eliminator	Ohaus (ION-100A)

Tissue strainers 250um (Pierce™)	Thermo scientific (87791)
Tissue well plate (Falcon; 6 well)	Corning (353046)
Tissue well plate (12 well)	Greiner Bio-One (655180)
Tissue well plate (24 well)	Greiner Bio-One (662160)
Transwell® companion plate	Corning (353502)
Transwell® inserts (falcon® permeable supports)	Corning (353091)
Waterbath (JB Nova)	Grant Instruments

2.3 Bio-ink materials

All materials used for bio-ink creation and their suppliers are listed in table 2.1, denoted by ∗. Material abbreviations, format as supplied, and chapters in which materials were applied are summarised in table 2.3.

2.3.1 Concentrations of bio-ink materials

The concentrations of bio-ink materials were based on bio-ink formulations previously investigated by Al-Sabah *et al* [223], Jessop *et al* [224] and Jovic *et al* (unpublished data). Harmonisation of material concentrations was undertaken to address small discrepancies between studies, and more crucially, the use of ratio for bio-ink components. The next section details the rationale behind the final chosen concentrations for each material: nanocellulose, alginate and hyaluronic acid.

Using the bio-ink containing nanocellulose and alginate as an example, bio-inks were created using material concentrations at 80:20, 60:40, 40:60, 20:80 and 0:100 ratios (nanocellulose:alginate) [224]. Whilst not an uncommonly adopted approach [227], this resulted in differing concentrations of nanocellulose and alginate for each bio-ink formulation (see table 2.4). Consequentially, it is difficult to attribute bio-ink performance as a result of a single variable. Therefore, decision was taken to convert ratios to concentrations, which improved clarity and facilitated the testing of concentrations as an independent variable.

Table 2.3 Summary of bio-ink material component abbreviations, form as supplied and thesis chapters in which material were applied. *Material used in final bio-ink formulations and tested in the advanced 3D in vitro model are highlighted in bold.*

Bio-ink components		**Abbreviations**	**Supplied form**	**Chapter**
Pulp-derived nanocellulose	Nanocellulose blend	NCB	Gel	3
	Cellulose nanocrystals	CNC		
	Cellulose nanofibrils	CNF		
Tunicate-derived nanocellulose	**Enzymatically pretreated**	**ETC**	**Gel**	**3,6,7**
	TEMPO-mediated oxidized	TTC		3
	Carboxymethylated	CTC		3
Alginate	**Alginate**	**Alginate**	**Powder**	**4**
HA	Tyramine-substituted HA	T-HA	T-HA as powder + HRP in solution	5
	Non-tyramine-substituted HA	**N-HA**	**Powder**	**5,6,7**

Table 2.4 Concentrations of nanocellulose and alginate in bio-inks of material ratios at 20% increments.

Concentration (mg/ml)		**Bio-ink material ratio (nanocellulose:alginate)**				
	Stock	**80:20**	**60:40**	**40:60**	**20:80**	**0:100**
Nanocellulose	30	24	18	12	6	0
Alginate	25	5	10	15	20	25

With regards to nanocellulose and alginate, 75:25 and 80:20 ratios (nanocellulose:alginate) were found to be superior, based upon the work of Al-Sabah *et al* and Jessop *et al*, respectively [223, 224]. With the work of Jovic *et al* on nanocellulose and HA supporting the 80:20 and 60:40 bio-ink formulations (unpublished data), the 80:20 ratio was chosen on the basis that it most closely reflects work investigating all three bio-ink components.

Therefore, with nanocellulose, the 80% concentration equivalent was selected as the final bio-ink concentration. As nanocellulose was supplied in 3 concentrations (see table 2.5), bio-ink containing 80% nanocellulose will yield varying final nanocellulose content if a stock concentration is not defined. This further illustrates the drawbacks of using a ratio-based approach to bio-ink formulations. In view of the technical challenges in concentrating nanocellulose gel, 80% of the lowest supply concentration was used to define the final bio-ink formulation (i.e. 80% of 25mg/ml, with final bio-ink concentration of 20mg/ml). This was used in all toxicity testing to mimic the *in*

vivo exposure dosage (chapter 3, 6, 7). However, for sterility testing, 100µl of the nanocellulose gel as supplied was used, as described by Al-Sabah *et al* [223]. The rationale to test the nanocellulose without dilution was to avoid unnecessary material handling, minimising the risk of introducing contamination and potential confounding factor should non-sterility be detected.

Moving onto alginate, as described above, the 20% concentration equivalent of a stock solution of 25mg/ml was selected. This was based on optimised material concentration for ease of material dissolution and mixing to form hybrid bio-inks and pre-cross-link shape fidelity post-print (i.e. maintenance of the 3D printed structure before cross-linkage) [223, 224]. This translated to 5mg/ml and was applied for all material testing as well as bio-ink creation in this thesis.

With HA, a two-component bio-ink using nanocellulose and HA was previously tested for material performance, printability and chondrogenic potential. Bio-ink ratios of 80:20 and 60:40 (nanocellulose:T-HA) were found to be superior in terms of chondrogenic potential, an important bio-ink performance parameter for cartilage tissue engineering (unpublished data). This equates to T-HA concentrations of 6mg/ml and 12mg/ml. Due to the lack of distinction between the two concentrations, both will be tested (chapter 5). A single final bio-ink concentration will be defined based on their cytotoxic and pro-inflammatory effects, as well as their impact on cross-linking for the creation of hydrogel discs for use in the advanced 3D *in vitro* model. Whilst recognising that the nanocellulose concentration at the 60:40 ratio was lower, the decision was taken to maintain nanocellulose at 20mg/ml (i.e. 80% equivalent), to minimise extraneous variables. This is because nanocellulose was thought to be strongly contributory towards the mechanical strength of the resultant construct, with a higher concentration being more desirable, whilst the inclusion of HA primarily supports chondrogenicity of this bio-ink.

The concentrations at which each bio-ink material was tested in this project, as well as concentrations of material as supplied and stock solution created, are listed in table 2.5.

Table 2.5 Supplied and final concentrations of bio-ink material components.

Bio-ink material		Concentration (mg/ml)		
		Supply	Stock solution	Tested in thesis
Nanocellulose	NCB	30	n/a	20
	CNC	60		
	CNF	30		
	ETC	25		
	TTC	25		
	CTC	25		
Alginate	Alginate	Powder	25	5
HA	T-HA	Powder	30	6 + 12
	N-HA	Powder	n/a	

2.3.2 Rationale behind selection of alternative material source

Each bio-ink component was tested independently (chapter 3-5) and combined as hybrid bio-inks (chapter 6-7). Based on the initial results detailed in chapters 3 and 5, alternative material sources were sought due to incompatibility of the original material for use. Whilst the basis for transition to a new material source will be expanded upon in their respective chapters, this section details the rationale behind selection of the new material source.

2.3.2.1 Nanocellulose

Studies initiated with pulp-derived nanocellulose produced *via* the American Value Added Pulping (AVAP®) technology. A chemical pre-treatment step with ethanol and sulfur dioxide is applied to wood-pulp biomass. This fractionates the raw material to remove hemicelluloses, lignin and the amorphous regions of cellulose [235]. By tuning the time and temperature of the pre-treatment step, nanocellulose of varying morphology is produced. This includes a nanocellulose blend (NCB), cellulose nanocrystals (CNC) and cellulose nanofibrils (CNF). The former, NCB, is created *in situ via* the AVAP® process and contains both nanocellulose crystals and fibrils (i.e. not a blend of CNC and CNF post-production). Being organically derived, not subjected to sterilisation as part of its production and supplied as an aqueous slurry, the pulp-derived nanocellulose was deemed unsuitable for use due to sterility issues despite in-house sterilisation (section 3.3.1).

As such, sterility was a key criterion for the selection of alternative sources of nanocellulose. Whilst commercially available nanocellulose are relatively abundant, options were significantly reduced once the sterility criterion was applied. Two sources were identified. GrowInk™ (UPM Biomedicals) is an off-the-shelf bio-ink consisting of plant-derived (birch) cellulose nanofibrils. It is available as a pure nanocellulose gel, an anionic version of the pure gel and a hybrid version pre-mixed with alginate. TuniCell, on the other hand, is marketed as a nanocellulose gel derived from tunicates (marine invertebrates). TuniCell's cellulose nanofibrils were available as three variably functionalised products: enzymatically pretreated (ETC), TEMPO-mediated oxidised (TTC) and carboxymethylated (CTC).

The final selection of TuniCell was based on its availability as a pure nanocellulose product, with reported purity of >99%. Whilst GrowInk offers convenience as a pre-made bio-ink, it is not intended for major modification, except for the addition of biomolecules to influence cell signalling, such as growth factors and adhesion proteins. TuniCell's product therefore offered greater flexibility for the purpose of bio-ink creation. The proprietary nature of GrowInk also supported the selection of TuniCell, to permit full transparency of bio-ink composition.

2.3.2.2 Alginate

In view of the longer study duration in culture conditions than previously tested (48 hours versus 21 days) [223], transition to culture grade alginate was made, using the same supplier, although UV-treatment was maintained.

2.3.2.3 Hyaluronic acid

Two forms of HA were used in this thesis. Work initiated with tyramine-substituted HA (T-HA) based on previous work on bio-inks consisting of nanocellulose and T-HA (unpublished data). The chemical modification with T-HA permitted this form of HA to be cross-linked with horseradish peroxidase and hydrogen peroxide (H_2O_2), and by extension, cross-linking of nanocellulose:T-HA bio-inks. Due to the incompatibility of T-HA to create an advanced 3D *in vitro* model, as detailed in chapter 5, an alternative source of HA was sought.

The criteria for selection of an alternative HA were: i) sterility, and ii) biomimicry. The former criterion, like nanocellulose, markedly reduced available options. In terms of

biomimicry, to more closely mimic native human cartilage, the desired form of HA would be of a higher molecular weight (MW) and devoid of chemical modifications. It was noted that the T-HA used in this project had a molecular weight of 750 kDa, below that of human cartilage. Whilst the content and MW of HA varies between tissue types and are influenced by age and disease states, the MW of HA in normal biological fluid and tissues are high, ranging from 1000-8000 kDa [236, 237]. There have been limited studies examining HA specifically in facial cartilage. In human articular cartilage, the MW of HA was greater than 2000 kDa in young adults, with lower MW found with increasing age and with inflammatory or tissue remodelling processes [236]. It was noted that with increasing MW and content of HA, viscosity and visco-elasticity are increased, producing a stronger 3D polymer network[237], a desirable characteristic for fabricating tissue-engineered cartilage. This formed the basis for which HA of a higher MW was sought. Finally, regarding chemical modifications, as native HA in the human body does not carry tyramine-substitutions, the removal of the requirement to cross-link HA led to the final criterion of an alternative HA without chemical modifications.

Two alternative HA sources were identified which were both sterile and without chemical modifications. The first was from the same supplier as T-HA, available in 11 MW ranges, from <10k to 1000-1800 kDa. A second source, from IFF N&H Norway (trading as NovaMatrix®) was available with a MW 620-1150 kDa. Therefore, the former was chosen due to the higher available MW, and will be subsequently referred to as N-HA (non-tyramine-substituted HA). Due to the custom nature of the sterile version of N-HA, the final MW of N-HA used in this project was 1590 kDa.

2.3.3 Preparation of bio-ink materials

The methodologies for the preparation of bio-ink materials, including sterilisation where needed, are detailed below. All sterile materials are handled within the tissue culture hood and in an aseptic manner when intended for cell culture or sterility testing purposes. All stock solutions were made fresh immediately prior to use for cell-based experimental purposes, and within two weeks of reconstitution for cell-free applications.

2.3.3.1 Tunicate-derived nanocellulose

Sterile tunicate-derived nanocellulose, which includes ETC, TTC and CTC, are supplied in gel format at 2.5% in cell grade, pyrogen-free water. Available in 3ml syringes, the tunicate-derived nanocellulose was used directly in sterility or material toxicity testing and for the creation of bio-inks. There were no additional sterilisation or preparatory steps. Storage was at 4°C and materials used within the expiry date (shelf-life one year). Dilution of nanocellulose was performed with sterile ddH_2O or culture media as specified.

2.3.3.2 Alginate

Alginate was supplied as a powder. Sterilisation and reconstitution to create a stock solution followed published methodology by Al-Sabah *et al* and Jessop *et al*. The alginate powder was first sterilised by UV-C application (germicidal light at 254nm) for one hour within a tissue culture hood. Sterilisation was performed with the alginate powder in a 50ml falcon tube with the lid removed. Reconstitution was undertaken immediately following UV-C application, with the application of sterile ddH_2O or cell culture media. Repeated cycles of mixing with a spatula and 10 minute placement in a waterbath at 37°C was performed until a homogenous solution was reached. Submersion in a waterbath was found to speed up the reconstitution process, and parafilm cover of the lid was used to reduce the risk of contamination. The solution was then stored at 4°C overnight and subjected to a final mixing prior to use. Stock solutions were stored at 4°C.

2.3.3.3 N-HA

N-HA was supplied as a sterile powder, stored at -20°C. It was not subjected to additional sterilisation procedures and was reconstituted in sterile ddH_2O or culture media to the desired concentrations. Mixing with spatula was initially trialled, but was challenging due to the high viscosity of the resultant gel. An electric mixer was used with success, taking care to add solvent in small aliquots. The metal mixer head was sterilised by autoclave prior to use. Centrifugation at 1000G in 5 minute cycles was performed to remove air bubbles. The stock solution was then stored at 4°C overnight and subjected to a final mixing with spatula prior to use.

2.4 Bio-ink creation

All bio-inks tested, their composition, applications and chapters in which they were applied are listed in table 2.6. The methodology for bio-ink creation is hereby described. The bio-inks were stored at 4ºC, and handled aseptically when intended for cell culture purposes.

2.4.1 Two-component bio-inks

2.4.1.1 Nanocellulose and alginate bio-inks

Pulp-derived nanocellulose (NCB, CNC, CNF) was sterilised and prepared as described in sections 3.2.1 and 3.2.2 prior to bio-ink creation. Tunicate-derived nanocellulose (ETC, TTC, CTC) was used as supplied. In both cases, dilution to achieve the desired concentration was performed with the same solvent as alginate, using either sterile ddH_2O or media. Alginate was sterilised and prepared as a stock solution, as described in section 2.3.3.2.

Mixing of the two materials was performed with repeated passages between two 5ml syringes connected with a luer-lock connector. Care was taken to avoid the introduction of air bubbles. Homogenisation was seen at around 10-13 passages with bio-ink made with media, where the phenol red in media eased visualisation of the mixing process. As such, a minimum of twenty passages was performed for bio-ink creation.

2.4.1.2 Nanocellulose and HA bio-inks

Pulp- and tunicate-derived nanocellulose were prepared in the same manner as for nanocellulose:alginate bio-inks (see section 2.4.1.1). Sterilisation and preparation of T-HA was performed as described in section 5.2.2.1. The stock solution for T-HA, consisting of T-HA and HRP, was used to create bio-inks. For N-HA, reconstitution was performed to the desired concentration with either sterile ddH_2O and media as described in section 2.3.3.3.

Table 2.6 Summary of bio-inks, their compositions and thesis chapter applied. *Bio-inks used for final toxicity testing in the advanced 3D in vitro model are highlighted in bold.*

Bio-ink Name	**Composition**						**Application**			**Chapter**
	Nanocellulose		**Alginate**	**HA**						
	Form	**Concentration** (mg/ml)	**Concentration** (mg/ml)	**Form**	**Concentration** (mg/ml)	**Solvent**	**Minimum gelation time**	**Rheological testing**	**Toxicity testing** (3D model)	
NCB:Alginate	NCB	20	5	-	-	water	✓	✓		4
CNC:Alginate	CNC	20	5	-	-	water	✓			4
CNF:Alginate	CNF	20	5	-	-	water	✓			4
ETC:Alginate (water)	ETC	20	5	-	-	water	✓	✓		4
TTC:Alginate (water)	TTC	20	5	-	-	water	✓			4
CTC:Alginate (water)	CTC	20	5	-	-	water	✓			4
ETC:Alginate (media)	**ETC**	**20**	**5**	**-**	**-**	**media**	**✓**	**✓**	**✓**	**4,6**
TTC:Alginate (media)	TTC	20	5	-	-	media	✓			4
CTC:Alginate (media)	CTC	20	5	-	-	media	✓			4
NCB:T-HA (low)	NCB	20	-	T-HA	6	water	✓			5
ETC:T-HA (low)	ETC	20	-	T-HA	6	water	✓			5
ETC:T-HA (high)	ETC	20	-	T-HA	12	water	✓			5
ETC:Alginate:T-HA (low) in water	ETC	20	5	T-HA	6	water	✓			5
ETC:Alginate:T-HA (high) in water	ETC	20	5	T-HA	12	water	✓			5
ETC:Alginate:T-HA (low) in media	ETC	20	5	T-HA	6	media	✓			5
ETC:Alginate:T-HA (high) in media	ETC	20	5	T-HA	12	media	✓			5
ETC:Alginate:N-HA (low) in water	ETC	20	5	N-HA	6	water	✓	✓		5
ETC:Alginate:N-HA (high) in water	ETC	20	5	N-HA	12	water	✓	✓		5
ETC:Alginate:N-HA (low) in media	**ETC**	**20**	**5**	**N-HA**	**6**	**media**	**✓**	**✓**	**✓**	**5,6,7**
ETC:Alginate:N-HA (high) in media	ETC	20	5	N-HA	12	media	✓	✓		5

Mixing of nanocellulose and HA was performed in the same manner as with nanocellulose:alginate bio-inks with repeated passages through two 5ml syringes joined by a luer-lock connector (section 2.4.1.1). Dilution to achieve the appropriate HA concentrations was performed using either sterile ddH_2O or media.

2.4.2 Triple component bio-inks

The only form of nanocellulose used for the triple component bio-inks was ETC. It was used as supplied without further preparatory steps.

For ETC:Alginate:T-HA bio-inks, stock solutions of alginate and T-HA were first homogenised using an electric mixer, prior to being combined with ETC. Air bubbles were removed by centrifugation at 1000G in 5 minute cycles.

With alginate and N-HA, initial trials of mixing stock solutions did not result in a homogenous mixture, potentially due to marked viscosity when combining both viscous materials. Methods trialled included the use of an electric mixer and prolonged submersion in waterbath at 37°C. As such, the triple component bio-ink with N-HA was created as follows.

Alginate powder was sterilised under UV-C as described in section 2.3.3.2. N-HA powder was then added to the UV-treated alginate powder. Solvent (sterile ddH_2O or media) was added in small aliquots and mixed initially with a spatula until a 'paste' was formed. As further solvent was added and a viscous solution was created, an electric mixer was used for further mixing until the correct volume was reached. ETC in gel form was then added, again in small aliquots, and mixed with an electric mixer until the bio-ink was created. Removal of air bubbles was achieved *via* centrifugation at 1000G in 5 minute cycles, followed by gentle mixing with a spatula.

2.5 Cross-linker reagent

Calcium chloride ($CaCl_2$) and hydrogen peroxide (H_2O_2) were used as reagents to cross-link bio-inks and create hydrogel discs. The cell encapsulated and/or surface-cell-seeded hydrogel discs were then used in the advanced 3D *in vitro* models for testing of the bio-inks. These were key reagents in the creation of the advanced *in vitro* models and therefore subjected to cross-linker toxicity testing. The rationale for the choice of concentrations of $CaCl_2$ and H_2O_2 were detailed in section 4.3.3 and 5.3.1.3, respectively.

Calcium chloride was supplied in powder form, and reconstituted in sterile ddH_2O to create solutions of 0.1, 0.5 and 1.0M. The solutions were then filtered using sterile

0.22μm Millex^{TM}-GP Filter Units, and stored at 4^{o}C. Preparation of hydrogen peroxide is described in section 5.2.4.1.

2.6 Sterility testing

All bio-ink materials were subjected to sterility testing in the forms of a microbial growth assay initially. Samples which exceeded the threshold for sterility were further examined with bacterial isolation.

2.6.1 Microbial growth assay

The microbial growth assay determines the presence of microbial contamination *via* increased optical density (OD). A rise in OD signifies turbidity of the culture medium as a result of microbial proliferation. Lysogeny broth (LB) and yeast extract-peptone-dextrose (YPD) were two culture media used, preferentially selecting for bacteria and yeast respectively. As material agglomeration in culture conditions may also cause a rise in OD, sterile PBS was introduced as a third 'culture medium', whereby a rise in OD with LB or YPD, but not in sterile PBS would more likely indicate microbial contamination.

The microbial growth assay was based on work by Al-Sabah *et al*. Material samples (100μl) were added to 10ml of LB, YPD and sterile PBS, and incubated at 37^{o}C under constant agitation on a shaker[223]. The form and concentrations of material tested are specified in each respective chapters (chapter 3-5). Samples were tested as 'stock' material with minimal material handling and therefore tested un-cross-linked. LB powder was reconstituted at 20g/L in dH_2O. YPD was made with 1% yeast extract, 2% peptone and 2% glucose (D(+)-glucose anhydrous) in dH_2O. Both LB and YPD were sterilised by autoclave (121^{o}C for 15minutes).

The study period was extended, from 48 hours[223] to 21 days, to encompass the full study period. Timepoints are as specified in the relevant sections (chapter 3-5), but broadly covers day 1, 2, 5, 7, 14 and 21. Three biological replicates were undertaken.

Optical density was determined at 600nm using a microplate spectrophotometer. Three technical replicates were undertaken for optical density readings, using 100μl of the samples in a 96 well plate. Readings were corrected by subtracting the average reading

of blank wells. The average of three technical replicates was used for each biological repetition.

Negative controls consisted of culture medium subjected to the same experimental conditions as the materials, termed ‘culture’, as well as without, termed ‘fresh’.

2.6.2 Bacterial isolation

An optical density of less than 0.1 is a widely accepted threshold for sterility. As such, samples identified as ‘contaminated’ with an optical density greater than 0.1 were subjected to bacterial isolation. Samples were inoculated and streaked on both LB and YPD agar plates, incubated at 37^{o}C and observed once daily for microbial growth. Samples were discarded if no growth were observed following 7 days of incubation. Macroscopic images were taken of positive cultures. Further delineation to identify microbes were not undertaken, as it will not alter the outcome of material exclusion from the study due to non-sterility.

2.7 Cell culture

Two cell lines were used: i) HFF-1 (human dermal fibroblast) and ii) C20A4 (human chondrocytes.

The HFF-1 cell line was kindly provided by the research department, but is available from ATCC® (SCRC-1041^{TM}). It is a human dermal fibroblast cell line, established from human skin. In the context of cartilage tissue engineering, fibroblast, a key cell type in wound healing and foreign body reaction processes, was used to investigate the material-host interaction, and will contribute towards the advanced *in vitro* co-culture model .

The C20A4 cell line was purchased from Sigma-Aldrich (SCC041). It is a human chondrocyte cell line established from rib cartilage. With chondrocyte being the primary cell type in cartilage, its application in this project was to study the material-host interaction of bio-inks intended for cartilage tissue engineering.

All cell culture work was undertaken using aseptic techniques and in a class II cabinet with laminar flow. This section details procedures relevant for 2D cell culture practices. Methodologies relating to the 3D *in vitro* model are described subsequently

in section 2.10. The same cell culture procedures were applied for both cell types, unless otherwise specified.

2.7.1 Culture media

Both the HFF-1 and C20A4 cell lines share a culture media, as recommended by their supplier. Complete media was made by adding fetal bovine serum (10%) to the base media, Dulbecco's Modified Eagle's Medium (DMEM). The addition of 1% Penicillin-Streptomycin to the complete media aimed to reduce the risk of bacterial contamination.

2.7.2 Thawing and initial seeding

Cells from liquid nitrogen were thawed in a waterbath at 37°C. The thawed cell suspension was transferred to a 15ml centrifuge tube, and pre-warmed culture media added to reach a total volume of 10ml. Cell pellet was achieved *via* centrifugation. Supernatant was discarded and the cell pellet re-suspended in 1ml of media, counted (described in section 2.8.1 and 2.8.2) and transferred to culture flask at the desired seeding density. Table 2.7 details the seeding densities for cell maintenance in 2D culture, and centrifugation parameters for each cell type. Cells were incubated in a humidified environment at 37°C and 5% CO_2.

Table 2.7 Seeding density for cell maintenance in 2D cultures and centrifugation parameters for HFF-1 and C20A4 cell lines.

		HFF-1	**C20A4**
Seeding density (cells/ml)	**T75 flask**	$6x10^5$	$1x10^6$
	T175 flask	$1.4x10^6$	$2.3x10^6$
Centrifugation parameters		270G for 5 minutes	300G for 5 minutes

2.7.3 Trypsinisation and subculturing cells

As recommended by the supplier, HFF-1 was subcultured when confluency was reached, and C20A4 at 90% confluency. Trypsinisation to dissociate cells was performed by first discarding the culture medium. The adherent cells were rinsed three times with PBS to reduce the amount of residual serum, which contain trypsin inhibitor. Pre-warmed trypsin was then added to the cells, and observed until cells were rounded and detached. Media at double the volume of trypsin was added to neutralise

the action of trypsin. The cell suspension was then transferred to a conical tube and centrifuged to achieve a cell pellet. Cells were re-suspended in media (1ml with T75, 3ml with T175), counted and plated at the desired concentration.

2.7.4 Cryopreservation

Cryopreservation was performed at the earliest passages where able. Cells were detached from culture flasks, pelleted and counted as described in section 2.7.3. HFF-1 and C20A4 were cryo-preserved at $1.2x10^6$ and $2x10^6$ cells/ml, in complete media with the addition of 10% dimethyl sulfoxide (DMSO). Cryovials were stored at -80°C for 24h in a Mr. Frosty™ freezing container, prior to transfer to liquid nitrogen for long term storage.

2.8 Cell line characterisation

Characterisation of both cell lines was conducted to understand cellular behaviour prior to exposures to bio-ink materials and cross-linkers in 2D cultures, and application in the advanced 3D *in vitro* model. Cytotoxicity and pro-inflammatory effects were assessed with the trypan blue exclusion assay and IL-6 and IL-8 release (using ELISA), respectively. This was supplemented by light microscopy assessment of cell morphology over the study period of 21 days. To avoid the potential teratogenic effects of trypan blue, a trial comparison with erythrosin B was undertaken prior to the transition to the full adoption of erythrosin B. Methodologies of the aforementioned assays and techniques will be first described, followed by results of the cell line characterisation, and comparison between trypan blue and erythrosin B.

2.8.1 Trypan blue exclusion assay

The trypan blue (TB) exclusion assay was used for both cell counting and cell viability assessment. Cell viability was assessed indirectly based on cell membrane integrity[238, 239]. The TB dye is impermeable to cell membranes of viable cells, but selectively stains non-viable cells due to uptake of the dye into cells through compromised, and therefore more permeable, cell membrane. Under brightfield microscopy, dead cells were stained blue and live cells were unstained.

The cell suspension, prepared as described in section 2.7.3, and the TB dye were mixed in 1:1 ratio (total 20µl) and 10µl was loaded onto a haemocytometer. The number of live (unstained) and dead (blue) cells were counted, and the total cell concentration, live cell concentration and cell viability were calculated as follows.

Total and live cell concentrations in cells/ml were calculated following equation 2.1 below. Dilution factor was 1 and cell suspension was of 1ml. Total cell concentration consisted of both live and dead cells, whilst live cell concentrations only of live cells. Cell viability was calculated with equation 2.2.

Equation 2-1

$$\text{Cell concentration (cells/ml)} = \text{No. of cells counted} \times \frac{\text{Dilution factor}}{\text{No. of squares counted}} \times 10^4$$

Equation 2-2

$$\text{Cell viability (\%)} = \frac{\text{No. of live cells}}{\text{No. of live + dead cells}}$$

2.8.2 Erythrosin B exclusion assay

Erythrosin B (EB), a cherry-pink food colouring, is a fluorescent dye impermeable to cell membrane[240, 241]. It can also be used in a similar manner to TB in an exclusion assay. To avoid the potential teratogenic effects of Trypan blue[242, 243], EB was introduced as a replacement of the TB exclusion assay.

2.8.2.1 Comparison of trypan blue and erythrosin B exclusion assay

The introduction of EB was undertaken shortly following the characterisation of the HFF-1 cell line, one of the first cell-based studies in the thesis. It was hypothesised that TB and EB would function equally effectively in the context of the dye exclusion assay. Comparison between the TB or EB exclusion assay was undertaken prior to the transition, and was performed as described in section 2.8.1. With the EB exclusion assay, TB was replaced by EB in the same volume. HFF-1 was seeded at $2x10^4$ cells/cm^2, the chosen cell density for the 2D model, based on results from the HFF-1 cell line characterisation (section 2.8.5). Comparison between TB and EB showed no statistically significant difference between either dye when assessing the total and live cell concentrations, and cell viability of the HFF-1 cell line over 21 days (figure 2.1). The data supported the switch towards the EB exclusion assay. As a result, all cell

counting and cell viability assays in this thesis were performed with the EB exclusion assay, with the exception of HFF-1 cell line characterisation which used TB.

2.8.3 ELISA

The enzyme linked immunosorbent assay (ELISA) is a plate-based, labelled immunoassay technique used to detect and quantify soluble substances, such as proteins, peptides and hormones. The DuoSet ELISA kits used to quantify IL-6 and IL-8 utilises the sandwich ELISA technique, which quantifies the cytokines between two antibody layers (i.e. the capture and detection antibodies), hence termed 'sandwich' ELISA. Both interleukins are pro-inflammatory cytokines[244, 245]. IL-6 is an important mediator of the acute phase response, triggering a multi-faceted response *via* its action on various target organs. Its pro-inflammatory effects include the activation of hepatocytes to produce acute phase proteins (such as the C-reactive protein), stimulating bone marrow endothelium for the release of neutrophils, and supporting the differentiation of effector T cells. IL-8 functions as a pro-inflammatory chemokine. It is involved in the local inflammatory response, attracting neutrophils to the site of injury as cells migrates along its concentration gradient. In the context of the surgically implanted tissue-engineered construct, whilst inflammation is an inevitable and necessary component in wound healing, the heightened and/or prolonged release of IL-6 and IL-8 signals a more severe degree of inflammation. This

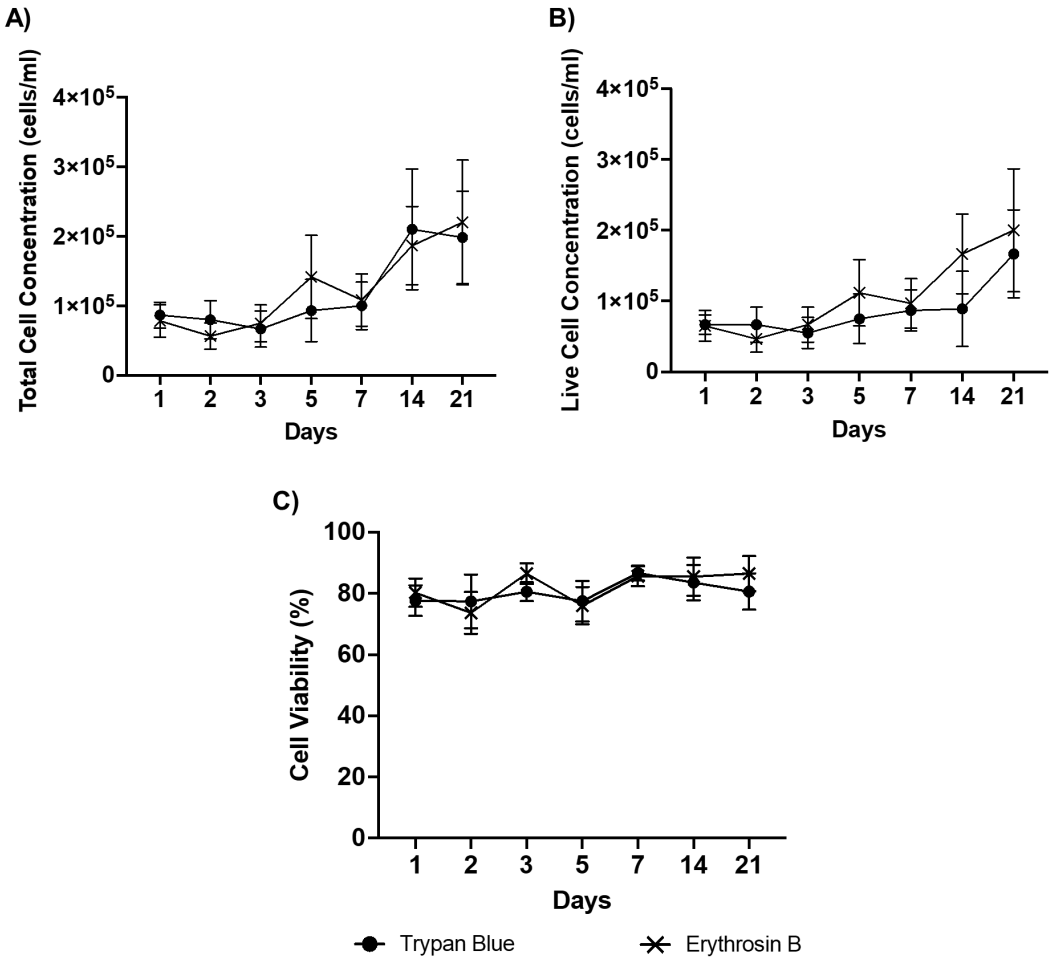

Figure 2.1 Comparison of trypan blue and erythrosin B exclusion assay for the assessment of cell population density and cell viability of HFF-1 in 2D monoculture over 21 days. *Total cell concentrations (A), live cell concentrations (B) and cell viability (C) were evaluated and the Mean±SEM is presented. N=3.*

can result in a predominance of pro-fibrotic reaction, known as the foreign body response, with scarring and impaired tissue regeneration that ultimately compromises the function and performance of the implant[245].

The ELISA procedural steps, as per manufacturer's guidance, are outlined below and depicted in figure 2.2. Reagent and standards concentrations are outlined in table 2.8. As half area plates were used, all volumes indicated in the manufacturer's instructions were halved. All procedures were performed at room temperature. The reagent diluents were 1% BSA in PBS for IL-6 and 0.1% BSA, 0.05% Tween 20 in Tris-buffered saline for IL-8. The wash step specified below consisted of the aspiration of the contents of each well, followed by three wash cycles using the wash buffer (300µl of 0.05% Tween® 20 in PBS). Culture media with which IL-6 and IL-8 were measured were

harvested, centrifuged (100G for 1 minute) to remove cellular or biomaterial debris and immediately aliquoted and stored at -20°C until use.

For IL-6 and IL-8 quantification using the ELISA, half area 96-well plates were coated with 50µl of the capture antibody and incubated overnight. Following a wash step, block buffer (50µl of 1% BSA in PBS) was added and incubated for 1 hour. Wash step was repeated. Samples and standards (50µl) were then added in triplicates and incubated for a further 2 hours, followed by another wash step. Detection antibody (50µl) was then added to each well and incubated for 2 hours again. Following a further wash step, 50µl of Streptavidin-HRP was added, shielded from direct light and incubated for 20 minutes. The wash step was repeated. Substrate solution (50µl) was added, shielded from light, placed on a shaker and incubated for a further 20 minutes. Finally 25µl of stop solution (2N H_2SO_4) was added. The plate was placed on a shaker for a further minute before determining the optical density immediately using a microplate reader. Light absorbance was recorded at 450nm and 570nm. Wavelength correction to account for optical imperfections in the plate was performed by subtracting readings at 570nm from readings taken at 450nm. A standard curve was produced with known concentration of standards, and sample concentrations determined, using a four parameter logistic (4PL) curve fit available *via* an open-source software (MyAssays.com). Values were multiplied by dilution factors where applicable.

Table 2.8 Concentrations of standards and reagents for IL-6 and IL-8 quantification with ELISA

ELISAs	**Standard concentration (pg/ml)**	**Antibody concentration**	
		Capture (µg/ml)	**Detection (ng/ml)**
IL-6	9.38-600	1	100
IL-8	31.3-2000	1	50

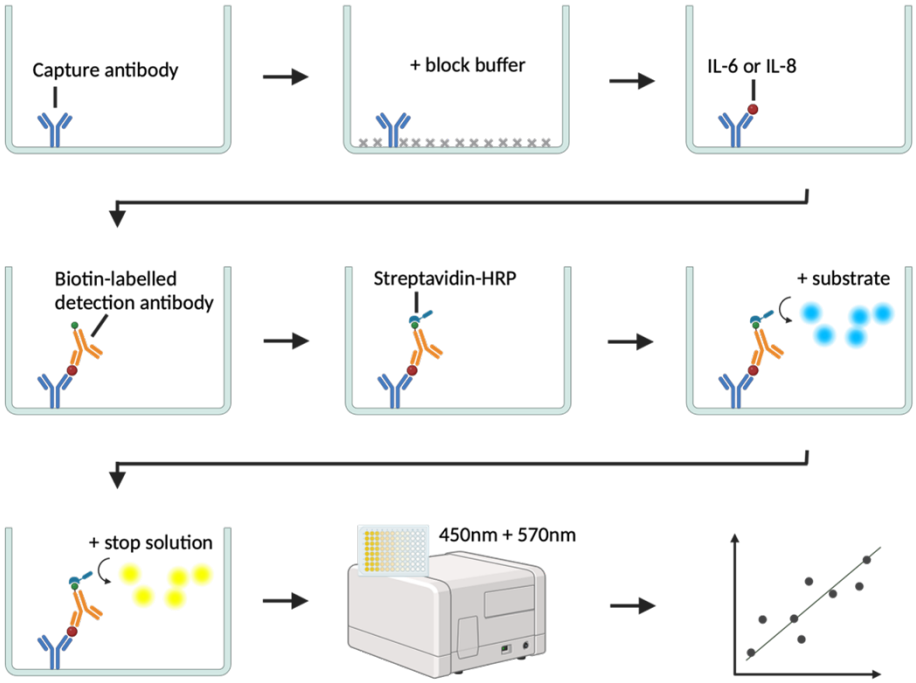

Figure 2.2 Schematic of sandwich ELISA for IL-6 and IL-8 using the DuoSet ELISA system. *Capture antibody specific for IL-6 or IL-8 was first bound to the floor of a 96 well plate, following which block buffer was added to block any non-specific binding sites. Sample was added, with IL-6 or IL-8 bound to the capture antibody. The biotin-labelled detection antibody, also specific for IL-6 or IL-8, was bound to the target analyte. This formed the antibody-antigen-antibody complex, hence 'sandwich' ELISA. This complex was then detected via the binding of Streptavidin to biotin. As Streptavidin was conjugated to the enzyme horseradish peroxidase (HRP), colour change (blue) was produced with the addition of the substrate solution. Wash steps were performed following each step, up to and including the addition of streptavidin-HRP. The final addition of the acidic stop solution halted the enzymatic reaction between HRP and substrate, turning the colour from blue to yellow. The intensity of the colour change was directly proportional to the presence and concentration of IL-6 or IL-8. Light absorbance was read using a microplate reader at 452nm, using 540nm for correction. A standard curve was produced, with which sample concentrations were defined. Created with BioRender.com.*

2.8.4 Light microscopy

Cell morphology was assessed using light microscopy. Three biological replicates were imaged for each testing condition and timepoint. Three field of views were taken per biological replicate, and representative images were shown in figures.

2.8.5 Cell line characterisation

Cell line characterisation was performed for both HFF-1 (human dermal fibroblast) and C20A4 (human chondrocyte) to understand their growth profile, baseline pro-inflammatory status and cell morphology in 2D monoculture over 21 days. This is important prior to their applications for bio-ink material and cross-linker toxicity

testing. Cell densities relevant to the *in vivo* scenario were selected as detailed below. Time points tested were day 1, 2, 3, 5, 7, 14 and 21. Cell culture procedures were detailed in section 2.7. Total and live cell concentrations, and cell viability were monitored with trypan blue exclusion assay for HFF-1 and erythrosin B exclusion assay with C20A4. The release of IL-6 and IL-8 as measured by ELISA examined cell activation for pro-inflammatory states and cell morphology was visualised with light microscopy. Methodologies for each examination are detailed in sections 2.8.1 (trypan blue exclusion assay), 2.8.2 (erythrosin B exclusion assay), 2.8.3 (ELISA) and 2.8.4 (light microscopy).

2.8.5.1 HFF-1 cell line characterisation (human dermal fibroblast)

Fibroblast was selected to represent the biomaterial-host response. Whilst there is a paucity in the literature detailing fibroblast density in the sub-dermal, subcutaneous or sub-fascial planes (in which tissue engineered constructs would be implanted), fibroblast density deduced from human skin biopsies was used as a surrogate. Gunin *et al* demonstrated that fibroblast density in interfollicular dermis in human skin biopsies decreased from 4000 cells/cm^2 to 2000 cells/cm^2 in the first ten years of childhood, following which cell density remained fairly constant[246]. With limited studies detailing fibroblast density *in vivo*, alternative studies were reviewed showing seeding densities of human dermal fibroblast ranging from 2000 cells/cm^2 [247], 3800 cells/cm^2 [248] to 4000 cells/cm^2 [249]. Indeed, these were relatively low cell densities for the purpose of cell culture. Initial seeding density, as recommended by ATCC for the HFF-1 cell line, was 8000 cells/cm^2. In an alternative study, fibroblast density was quoted as 2100-4100 cells/mm^3 [250], which translates to approximately 2.1-4.1x10^6 cells/cm^3 but this is difficult to convert to units relevant for 2D cell culture. Overall, the cell density of 2000 cells/cm^2 was thought to be most representative of the adult and older children population with which tissue engineered cartilage would serve. However, due to the low cell density, this would produce a sparse cell population with sub-optimal cell-to-cell interaction. Detection of cell effects, at such low density, was also questionable. As such, as part of the cell line characterisation, three cell densities was chosen on a log scale, and were tested with the aim of selecting the most suitable cell density for use in subsequent studies: 2000 cells/cm^2 (low), 20,000 cells/cm^2 (mid) and 200,000 cells/cm^2 (high).

2.8.5.1.1 Growth profile and cell morphology

Of the three cell densities tested, the high cell density (200,000 cells/cm^2) demonstrated an early decline in cell viability and a drop in total and live cell concentration from day 2 onwards (figure 2.3C). Whilst there was a gradual recovery of cell concentrations and cell viability between day 7 and day 21, this high cell density was unsuitable for use with over-crowding from the point of seeding and confluence reached on day 1 (figure 2.4).

In contrast, the low cell density showed sparse cell population and limited cell to cell contact up to day 5 (figure 2.4). This is supported by low levels of total and live cell concentrations, although a notable rise in cell concentrations was seen from day 7 onwards (figure 2.3A). This rise in latter timepoints was reflected by the light microscopy images, with confluency reached between day 14 and day 21 (figure 2.4).

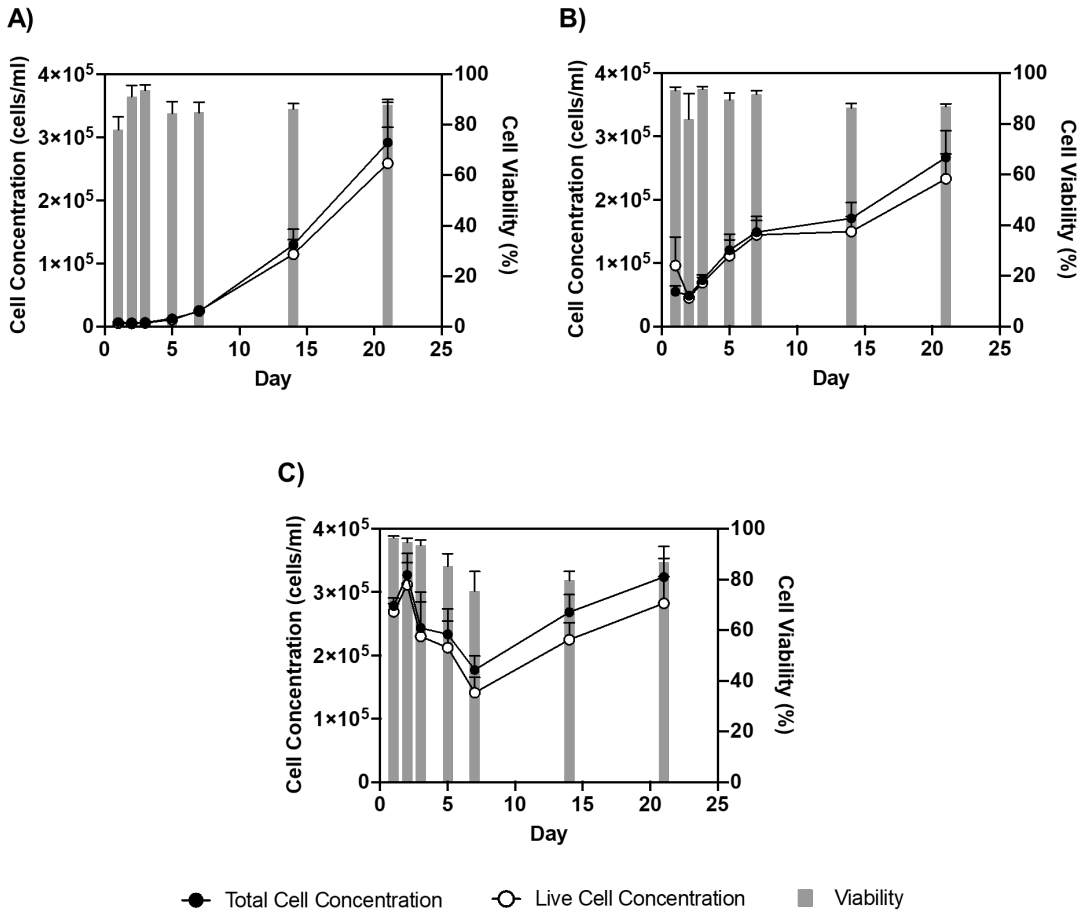

Figure 2.3 Growth profiles of three cell densities of the HFF-1 cell line in 2D monoculture over 21 days. *The total and live cell concentrations and cell viability was assessed with the trypan blue exclusion assay. Cell densities at 2,000 cells/cm^2 (low - A), 20,000 cells/cm^2 (mid – B) and 200,000 cells/cm^2 (high – C) were evaluated. Mean±SEM is presented. N=3.*

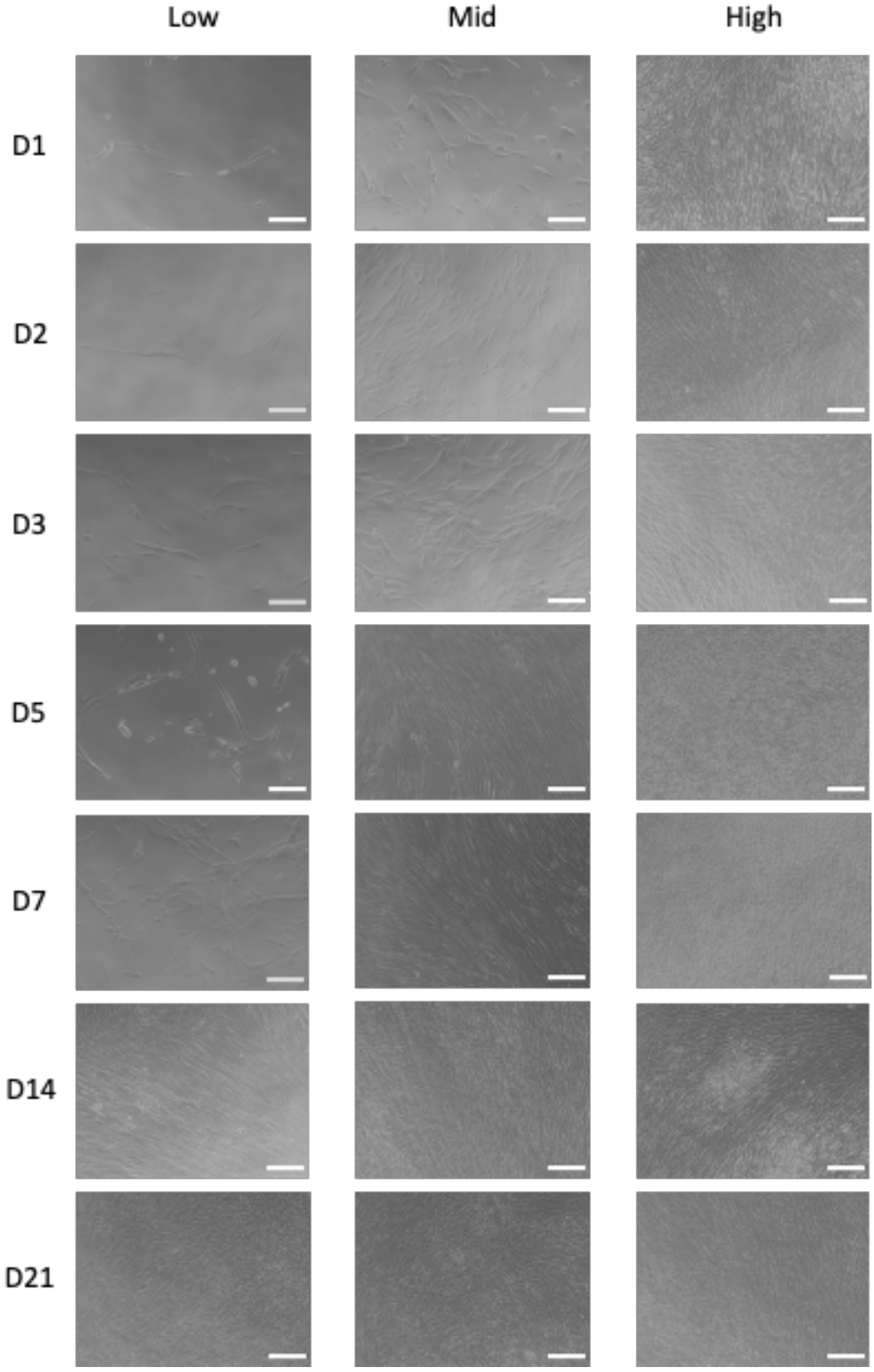

Figure 2.4 Light microscopy of HFF-1 cell line characterisation in 2D monoculture over 21 days. *Cell densities were presented as: low (2,000 cells/cm^2), mid (20,000 cells/cm^2) and high (200,000 cells/cm^2). Scale bars represent 200μm.*

The mid cell density (20,000 cells/cm^2) was deemed most suitable. Cells were suitably but not overly sparse on day 1, which supported cell to cell interaction with demonstratable cell proliferation, reaching confluency on day 7. This could be seen in both the total and live cell concentrations (figure 2.3B) and light microscopy images (figure 2.4). A decline in the rate of cell proliferation was seen between day 7 and day 14, likely reflecting the effects of contact inhibition as confluency was reached on day 7. However, following a slight drop in cell viability on day 14, cells regained their proliferative status with cell viability maintained at above 80% throughout the 21 days.

2.8.5.1.2 Pro-inflammatory status

Trends in the release of IL-6 and IL-8 revealed marked differences between cell densities, but was in the same vein when compared between IL-6 and IL-8 (figure 2.5). HFF-1's in high cell density showed elevated cytokines release which was likely due to activation from over-crowding as well as an overall higher number of cell population. This supports that the high cell density was unsuitable for use for the advanced *in vitro* model.

As to the low cell density, IL-6 was non-detectable from day 1 to day 7, and whilst IL-8 could be detected at low levels at an earlier stage, it was non-detectable between day 1 to 3. The extremely low cell population rendered cellular effects below the threshold for measure. Taken together with the sparse cell density seen in light microscopy, altered cell behaviour was deemed likely and therefore it was unsuitable for use for the *in vitro* model.

Akin to the growth profile and cell morphology visualisations, the mid cell density appeared both optimal amongst all cell densities tested, as well as being suitable for its application for the advanced *in vitro* model. It was noted that elevated IL-6 and IL-8 levels were seen at the latter timepoints on day 14 and day 21. This suggests cells were activated and was in pro-inflammatory states which indicates possible limitation of the model. This is mostly likely a direct result of over-confluency and will be taken into account when applied for material toxicity testing in chapters 4 and 5.

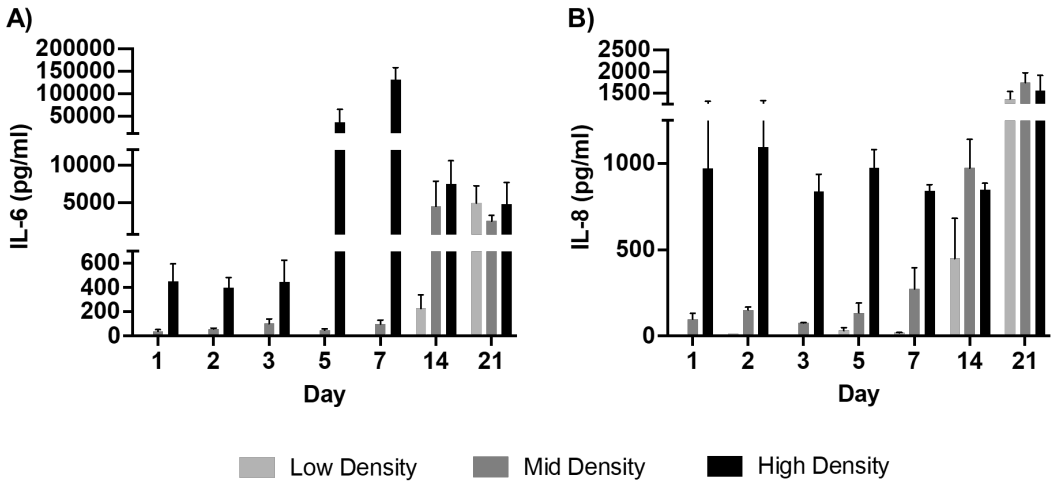

Figure 2.5 Cell line characterisation of the pro-inflammatory status of HFF-1 in 2D monoculture over 21 days. *IL-6 (A) and IL-8 (B) release were measured with ELISA. Cell densities at 2,000 cells/cm^2 (low), 20,000 cells/cm^2 (mid) and 200,000 cells/cm^2 (high) were evaluated. Mean±SEM is presented. N=3.*

2.8.5.1.3 Section summary - HFF-1 cell line characterisation

From the three cell densities tested, it was concluded that the mid cell density (20,000 cells/cm^2) was most suitable for use, based on growth profile, pro-inflammatory status and light microscopy data. This will be applied in all future studies in this thesis.

2.8.5.2 C20A4 cell line characterisation (human chondrocyte)

The selection of cell density for human chondrocyte sought to mimic the *in vivo* scenario. A wide range of cell densities had been investigated for the purpose of tissue engineered cartilage, from 2-4x10^6 cells/ml[251-254], to higher concentrations at 1-6x10^7 cells/ml[95, 255, 256].

Regarding human native cartilage, cell densities vary with location and decreases with age. Homicz *et al* examined 33 nasal septal cartilages harvested during surgery. The average chondrocyte cell density was 24.9x10^6 cells per gram of wet weight. With a range of 3.7-51.8x10^6 cells/g. A reduction of cell density at 7.4% for each decade of increasing age was seen[257]. An alternative study, which examined 24 nasal septal cartilage, showed a lower range of chondrocyte densities of 0.5-7.5x10^6 cells/g of wet weight[258]. Although cartilage wet tissue density in porcine[259] and bovine[260] cartilage has been defined in the literature (1.08g/ml), it remained difficult to translate this for

application based on the wide range of native cartilage cell densities, variance with age and location, and relative paucity of studies reporting human cartilage wet tissue density.

As such, the chosen cell density for this project was $3x10^6$ cells/ml within the cell-encapsulated bio-ink, as it most closely mimics the 3D bioprinted cartilage construct, building on earlier research[223, 224]. The work of Al-Sabah *et al* and Jessop *et al* investigated bio-inks consisting of nanocellulose and alginate with chondrocyte cell densities of $2x10^6$ cells/ml - $3x10^6$ cells/ml. Jovic *et al* examined bio-inks consisting of nanocellulose and HA with chondrocyte density of $3x10^6$ cells/ml (unpublished data). Nonetheless, cell at $3x10^6$ cells/ml would be too densely populated and incompatible with 2D cell culture. Therefore, considering the use of 100µl hydrogel discs for the advanced 3D *in vitro* model, the cell number encapsulated within the model was used instead. This translated to an initial seeding cell number of $3x10^5$ cells/well, accepting the relatively high cell density and its impact upon prolonged culture period of 21 days.

2.8.5.2.1 Growth profile and cell morphology

Cell proliferation was seen initially immediately following seeding, with a rise in total and live cell concentrations up to day 3 (figure 2.6). Following which, the threshold for over-crowding was reached, causing a decline in cell concentrations on day 5 and day 7, with a drop in cell viability on day 7 to under 80%. Corresponding light

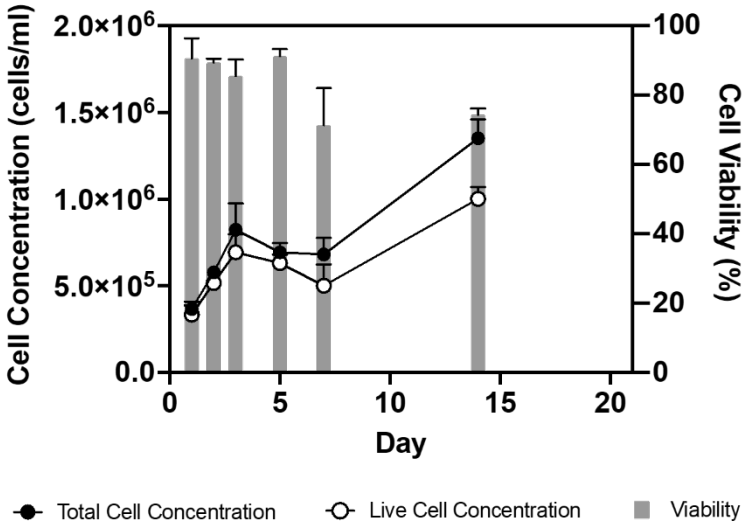

Figure 2.6 Growth profiles of the C20A4 cell line in 2D monoculture over 21 days. *The total and live cell concentrations and cell viability were assessed with the erythrosin B exclusion assay. The cell line and model were incompatible on day 21 due to auto-detachment of cell sheet. Mean±SEM is presented. N=3.*

microscopy images showed 100% confluency on day 1 as anticipated based on the high seeding density (figure 2.7A). There was an appreciable rise in cell numbers up to day 3, whereby cells were more densely packed and a higher number of cells were seen within each FOV. At latter timepoints, cell proliferation continued with concentrations approximately doubling between day 7 and 14, and whilst cell viability did not decline further, it was persistently below 80%. Cell morphology remained similar between day 3 and 14.

However, the last timepoint on day 21 could not be reached due to over-confluency and the auto-detachment of cell sheet (figure 2.7B left and middle). This was noted to occur between day 17-19. The application of the erythrosin B exclusion assay to the cell sheet and culture well contents showed the non-viability of cells with debris only seen (figure 2.7B right). Trial of larger vessels including 6 and 12-well plates and T25 flasks did not improve matters, due to the high seeding density.

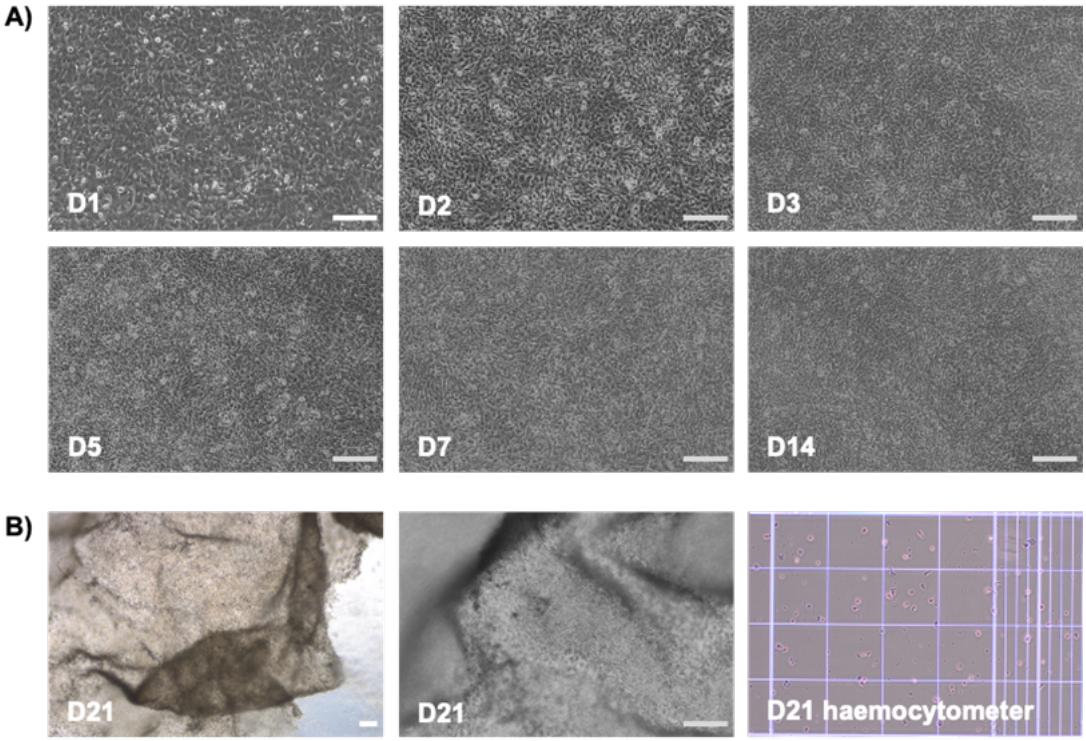

Figure 2.7 Light microscopy of the C20A4 cell line characterisation in 2D monoculture over 21 days. *(A) presents cell morphology between day 1 and day 14. (B) demonstrated cell morphology and the auto-detachment of cell sheet on day 21 (left and middle), and outcome of the erythrosin B exclusion assay on haemocytometer (right). Scale bars represent 200μm.*

2.8.5.2.2 Pro-inflammatory status

Due to the auto-detachment of cell sheet and incompatibility of the model for C20A4 cell line characterisation for day 21, the assessment of the pro-inflammatory status was only performed between day 1 and day 14.

In general, both cytokines demonstrated a static trend over the initial 3-5 days. Following which, levels of IL-8 was first to rise which peaked on day 7, and IL-6 on day 14 (figure 2.8). Both were suggestive of cell activation in their pro-inflammatory state. Interestingly, IL-8 levels fell on day 14 despite a marked rise in cell concentrations. This may reflect a degree of cellular dysfunction in conjunction with reduced cell viability.

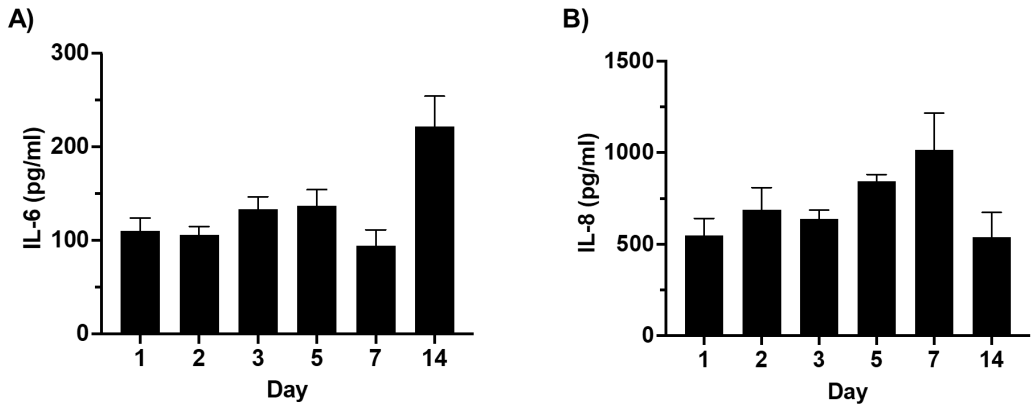

Figure 2.8 Cell line characterisation of the pro-inflammatory status of C20A4 in 2D monoculture over 14 days. *IL-6 (A) and IL-8 (B) release were measured with ELISA. Mean±SEM is presented. N=3.*

2.8.5.2.3 Section summary - C20A4 cell line characterisation

The 2D monoculture model of C20A4 permits an understanding of the growth profile and pro-inflammatory status of the cell line prior to its application for bio-ink material and crosslinker toxicity testing. The use of an end-application relevant cell density resulted in marked over-confluency which was incompatible with the model on day 21, and with limitations on day 7 and 14. Nonetheless, the model supports a period of cell proliferation, up to day 3, and an acceptable cell viability profile up to day 14.

2.9 Lactate dehydrogenase assay

The lactate dehydrogenase (LDH) assay quantifies LDH, a cytoplastic enzyme which is leaked into culture media *via* damaged cell membranes during cell stress and cell death[261, 262]. The levels of LDH acts as a surrogate marker for cytotoxicity. An advantage of the assay is the lack of manipulation of cells and the biomaterial in which the cells are encapsulated within[263], and was applied in this project as a measure of cytotoxicity of all 3D models. In the described assay, the levels of LDH were quantified *via* the measurement of NADH. The reduction of NAD^+ to NADH occurs when LDH catalyses the conversion of lactate to pyruvate. NADH was then detected and quantified through a colorimetric assay.

The assay procedure followed manufacturer's guidance. The master reaction mix was made up immediately prior to the assay, at the ratio of 48:2 of assay buffer and substrate mix, both supplied within the commercial kit. Standards (0-12.5nmole/well) and samples at 10µl volume was added to each well of a 96 well plate. The master reaction mix was then added to the 96 well plate to create a total volume of 50µl. This was incubated on a horizontal shaker for 2 minutes whilst shielded from light. The light absorbance was read at 450nm serially from 2 minutes onwards at 5 minutes interval. This was performed until the value of the most active sample exceeded that of the highest standard. The plate was shielded from light throughout and the assay was conducted at room temperature. All samples and standards were run in duplicate as recommended, with biological triplicates undertaken.

Data analysis utilised two sets of reading: the initial reading taken at 2 minutes, and the readings from the penultimate capture, i.e. where the most active samples neared but remained within the value of the highest standard concentration. Readings were corrected by the subtraction of the average reading of the lowest standard (i.e. 0 nmole/well or blank). The change in measurement between $T_{initial}$ and T_{final} (ΔA_{450}) was calculated by equation 2.3. The NADH standard curve was plotted, and the amount of NADH for each sample determined using the ΔA_{450} against the standard curve. The LDH activity was then calculated using equation 2.4, whereby B equals the amount of NADH generated between $T_{initial}$ and T_{final} (nmole). The reaction time (minutes) was calculated by equation 2.5. The volume of sample in mls added to each

well was represented by V. LDH activity therefore was nmole/min/ml (or milliunit/ml) as per the kit's instructions.

Equation 2-3 $$\Delta A_{450} = (A_{450})_{final} - (A_{450})_{initial}$$

Equation 2-4 $$\text{LDH activity (miliunit/ml)} = \frac{B}{(\text{Reaction time}) \times V} \times \text{Sample dilution factor}$$

Equation 2-5 $$\text{Reaction time} = T_{final} - T_{initial}$$

2.10 Hydrogel disc creation for 3D *in vitro* model

The creation of 100µl pellets was previously described by Al-Sabah *et al*[223] and Jovic *et al* (unpublished data) *via* the deposition of bio-inks using a 1ml syringe, shaped by the indentations of a 96 well plate lid. This results in a dome-shaped or hemi-spherical pellet. Due to the proposed work in this project, a relatively flat surface for HFF-1 surface cell seeding was sought and hence an alternative method to create hydrogel discs was created.

2.10.1 Silicon mold creation

To create standardised 8mm wide hydrogel discs for the advanced 3D *in vitro* model, donut-shaped silicon molds were created, following an in-house, previously optimised protocol using Elastosil® RT 601 A+B (unpublished). The procedure is illustrated in figure 2.9, and described as follows. The Elastosil® RT 601 was mixed by measuring the correct volume of the very viscous part A, with the fluid part B added using a pipette dropper drop by drop to achieve a part A:B ratio of 15:1. The mixture was mixed vigorously using a 1000µl pipette tip, and transferred to 12 well plates using a 5 ml syringe. A volume of 1ml was added to each well, and the mixture was left to set overnight at room temperature (figure 2.9A), whereby air bubbles within the mixture were dissipated. The silicon disc was carefully lifted out the following day, taking care to avoid damage to the disc (figure 2.9B). The central cut-out of the mold, whereby bio-ink would be placed in future use, was created using an 8mm skin biopsy punch tool (figure 2.9C), yielding a final donut-shaped mold (figure 2.9D). All molds were sterilised by autoclave prior to use in cell-based studies.

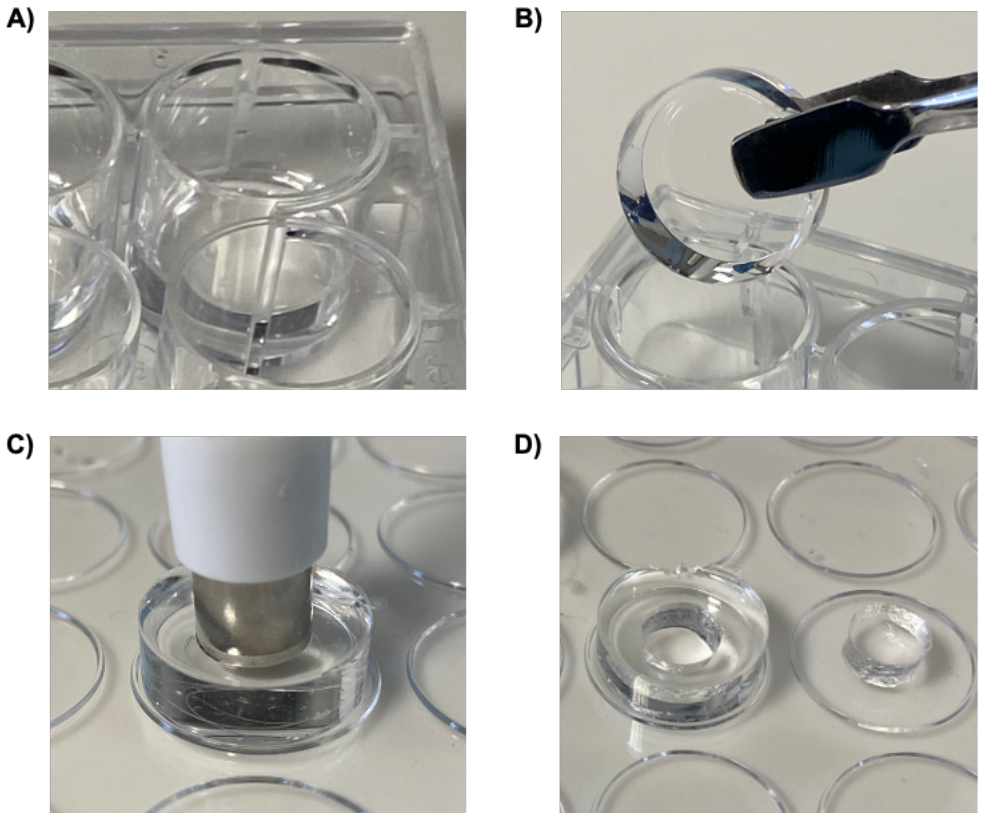

Figure 2.9 Creation of silicon molds. *Elastosil® RT 601 A+B was mixed in 15:1 ratio (A:B), with 1ml/well added to 12 well plate which set overnight at room temperature (A). The silicon discs were then lifted off the well plate (B) the following day. The mold was created by applying an 8mm skin punch biopsy tool centrally (C), creating a donut-shaped mold (D).*

2.10.2 Creation of cell-free hydrogel disc

Hydrogel discs were created by the cross-linkage of 100µl of bio-ink with the relevant cross-linker. This was applied firstly to determine the minimum gelation time required to achieve a fully cross-linked hydrogel disc and also for the creation of cell-seeded hydrogel discs used in the advanced 3D *in vitro* model for toxicity testing.

The preparation of bio-inks was described in section 2.3.3. Preparations of cross-linkers were detailed in section 2.5 for $CaCl_2$ and section 5.2.4.1 for H_2O_2. The creation of silicon molds was described in section 2.10.1.

The procedure is hereby described and illustrated in figure 2.10. The silicon molds were firmly pressed down into the centre of each well in a 6 well plate. Adherence was confirmed by holding the plate upside down, whereby the molds should stay. The addition of 100µl of bio-ink (preparation as described in section 2.4.1 for two component bio-inks, and in section 2.4.2 for triple component bio-inks) was performed using a 1ml syringe, and the bio-inks added to the centre of the silicon mold. The apical

surface was smoothened using a 200µl pipette tip, and 600µl of cross-linker was applied (figure 2.10A). Due to the slight concavity of the apical surface of the silicon mold, a larger volume of cross-linker could be applied and retained above the bio-ink and within the silicon mold. To maximise the amount of cross-linker available to the bio-ink and thereby limiting the duration of cross-linker exposure, the maximum volume of cross-linker that could be consistently applied and retained were chosen as the standardised cross-linker volume (i.e. 600µl). Upon the completion of the desired cross-linkage time, the cross-linker was removed by pipetting, and the silicon mold eased off the base of the well, and the hydrogel disc pushed off the silicon mold if needed. Each hydrogel disc was rinsed with 3 wash cycles of 1ml of PBS in a 12 well plate to remove any residual cross-linker. For the purpose of cell-seeded hydrogel disc, the basal surface (figure 2.10B) was used over the apical surface (figure 2.10C) due to the smoother surface topography.

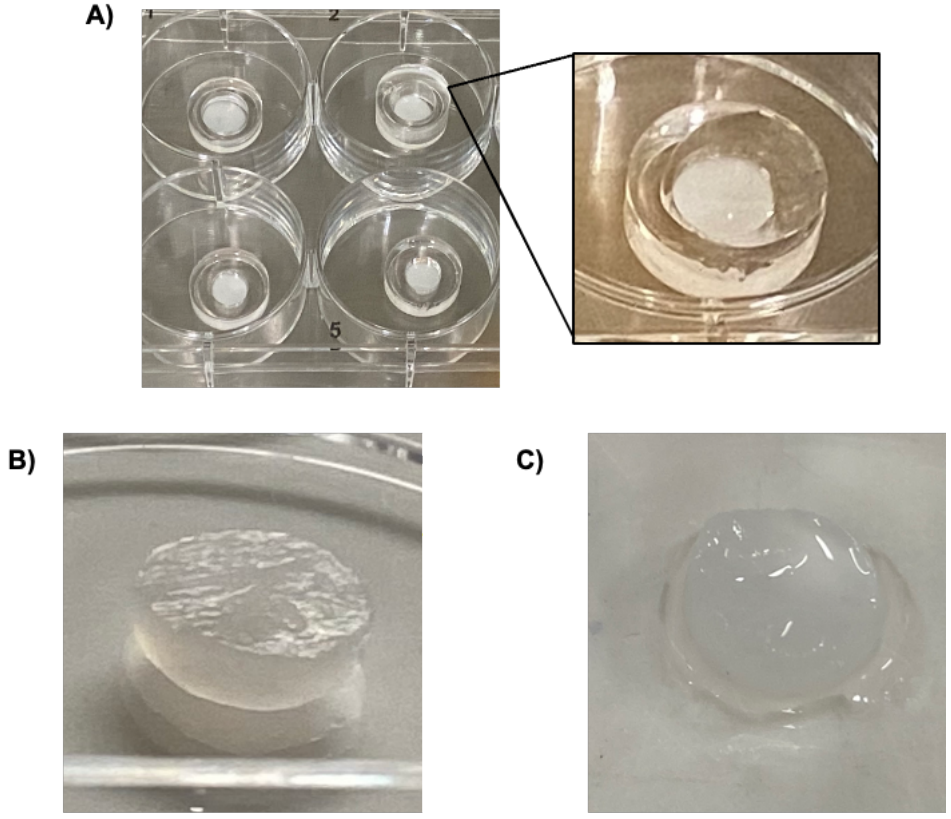

Figure 2.10 Creation of cell-free hydrogel discs. *Bio-ink (100µl) was added to the centre of silicon molds placed in a 6 well plate. Cross-linkers (600µl) was added on top of the bio-ink (A) and removed following the desired cross-linkage duration. The silicon molds were lifted from the plate and the hydrogel discs eased off the molds. The smooth basal surface (B) and apical surface (C) of the hydrogel disc are shown.*

2.10.3 Creation of cell-seeded hydrogel disc

Three forms of cell-seeded hydrogel discs were created to mimic the *in vivo* scenario of the implanted tissue-engineered cartilage implant. This included two monocultures involving HFF-1 and C20A4 cell types, and combined to create the 3D co-culture model. The fibroblast (HFF-1) was surface-seeded to mimic the material-host interaction (figure 2.11A), and the chondrocyte (C20A4) was encapsulated within the bio-ink and therefore hydrogel disc (figure 2.11B). The co-culture model was the amalgamation of the two monoculture systems, as shown in the schematic (figure 2.11C). These were applied in the advanced 3D *in vitro* model (chapter 6 + 7). All hydrogel discs and models were created and kept in sterile conditions.

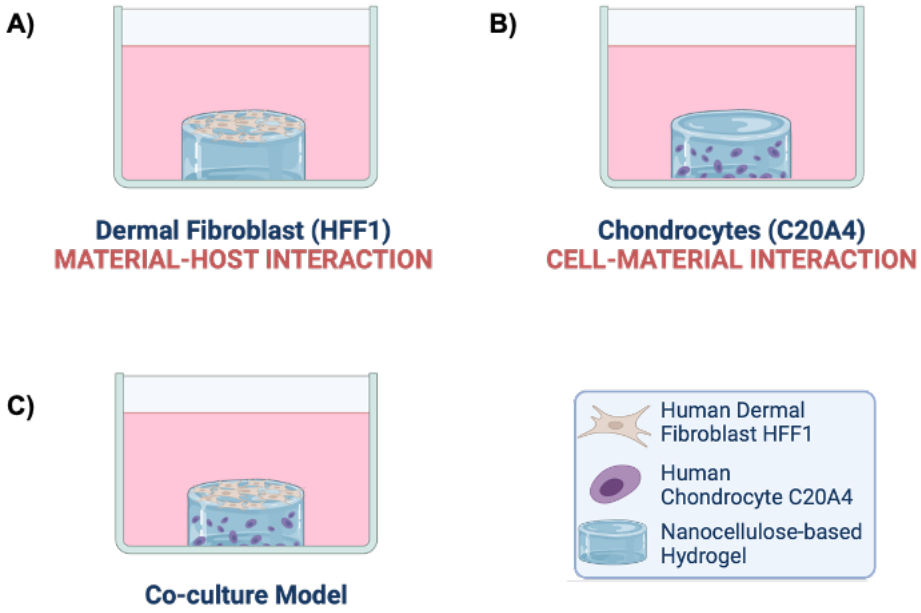

Figure 2.11 Schematic of cell-seeded hydrogel discs applied in the advanced 3D in vitro models. *(A) represents a surface-seeded hydrogel disc with human dermal fibroblasts, HFF-1, to investigate the biomaterial-host interaction. (B) illustrates a cell-encapsulated hydrogel disc with human chondrocytes, C20A4, to examine the cell-material interaction for tissue-engineered cartilage. (C) shows the co-culture model of HFF-1 surface-seeded and C20A4-encapsulated hydrogel discs.*

2.10.3.1 HFF-1 (fibroblast surface-seeded hydrogel disc)

Cell-free hydrogel discs were created as described in section 2.10.2 and were always created immediately before cell seeding. The rationale for the cross-linker choice (0.1M $CaCl_2$) and duration of application (15 and 25 minutes) were as detailed in section 4.3.3 and 5.3.1.3, for the two component and triple component bio-inks, respectively. HFF-1 was cultured as described in section 2.7. Seeding density of the hydrogel disc was 20,000 cells/cm^2, as explained in section 2.8.5.1. The surface area

of the hydrogel disc was calculated using the geometric equation for the area of a circle: πr^2, where r represents radius, and was 4mm deduced from an 8mm wide disc. To control for seeding, the hydrogel discs following PBS washes were placed back in fresh autoclaved-sterilised silicon molds secured to 12 well plates. The hydrogel discs were flipped such that the smooth basal surface during cross-linkage now became the apical surface. The cell suspension in 100µl volume of media was added to hydrogel disc. The cell suspension volume was chosen to ensure the full cell suspension remained within the central well of the donut-shaped silicon mold and not overspill onto the outer surface of the silicon mold, such as in the case with the cross-linker application. This was to ensure targeted cell seeding onto the hydrogel discs.

With a limited cell suspension volume, prolonged incubation was undesirable due to the restriction of nutrients available to cells. Therefore, initial incubation periods of 2 hours and 24 hours were tested. Following the procedure described above, the hydrogel discs topped with cell suspension were incubated at 37^{o}C for 2 hours or 24 hours. Following the defined incubation period, the cell suspension was removed by pipetting. The hydrogel disc was then carefully removed from the silicon mold, taking care to avoid handling of the cell-seeded surface, and transferred to a 24 well plate and submerged in 1ml fresh media and returned to incubation at 37^{o}C. Cells were visualised using Live/Dead staining, as described in section 6.2.3, which was comparable between the two seeding time duration (data not shown). As such, a final seeding duration of 2 hours was chosen for all future model creation.

2.10.3.2 C20A4 (chondrocyte-encapsulated hydrogel disc)

As chondrocytes were encapsulated within the hydrogel disc, the cell suspension was pre-mixed with the un-crosslinked bio-ink prior to the creation of the hydrogel disc. Cell density was $3x10^6$ cells/ml and referred to the cell-encapsulated bio-ink. Bio-inks were prepared as detailed in section 2.4.1 and 2.4.2 for the two or triple component bio-inks, respectively, and were created fresh before cell seeding.

To account for the cell suspension volume, the reconstitution volumes for alginate and HA were adjusted to ensure the correct cell density as well as material concentration in the final cell-encapsulated bio-ink. Homogenisation of the bio-ink and cell suspension was performed by passaging the bio-ink between two 5ml syringes with a luer-lock connector. Care was taken to minimise the introduction of air bubbles, to

passage slowly and gently with a minimum of 20 passages. Once the bio-ink was seeded, creation of the cell encapsulated hydrogel disc continued as described in section 2.10.2, the same as with cell-free hydrogel discs, except for the sterile conditions. Following cross-linkage, the same procedure was also followed with the removal of cross-linker, three PBS washes, transfer to a 24 well plate and submerged in 1ml of culture media.

2.10.3.3 Co-culture

This described a fibroblast (HFF-1) surface seeded, chondrocyte (C20A4) encapsulating hydrogel disc, as shown in figure 2.11C. For this, the C20A4-seeded hydrogel disc was first created as described in section 2.10.3.2. This was followed by the procedure for HFF-1 surface seeding as detailed in section 2.10.3.1.

2.11 Determination of the minimum gelation time in silicon molds

The minimum gelation time of bio-inks in silicon molds was tested with a variety of bio-inks formulations and cross-linker choices and concentrations, as specified in chapters 4 and 5. The minimum gelation time was defined as five consecutive successful cross-link without residual uncross-linked hydrogel (figure 2.12). A step-wise approach at 1 minute intervals was utilised, unless otherwise specified. The procedure for cross-linkage in silicon mold was as described in section 2.10.2.

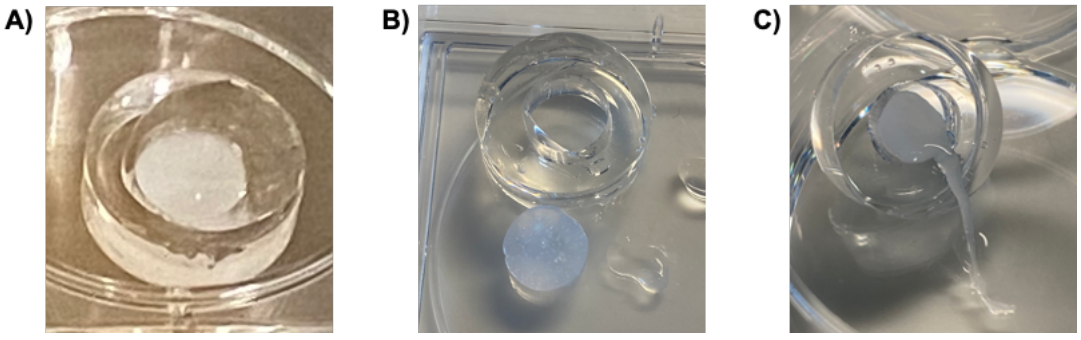

Figure 2.12 Determination of the minimum gelation time of bio-inks in silicon molds. *Bio-inks (100µl) were cross-linked in a standardised manner with the addition of 600µl of cross-linker within a silicon mold to create hydrogel discs (A). The minimum gelation time was defined as the time required (minutes) to achieve five consecutive successful cross-linkage. (B) represents a successful cross-linkage with the creation of a hydrogel disc, whilst (C) demonstrates an incomplete cross-linkage with residual un-crosslinked bio-ink.*

2.12 Rheological testing

Rheology is a branch of physics which studies the response of a material (deformation or flow) when subjected to strain or stress. In the context of this project, it provides a real-time, quantitative means of examining the change in the behaviour of bio-inks when exposed to cross-linkers. The procedure of an oscillatory time sweep is hereby described.

Oscillatory time sweeps were conducted using an AR-G2 Controlled Stress Rheometer. In principle, the bio-ink sample is sandwiched between two rheometer plates. The base plate remains stationary, whilst the upper plate oscillates and applies stress or strain to the sample, whilst rheological parameters of the sample are recorded at regular intervals. For this project, a 40mm diameter cone and plate geometry was selected, which maximises the contact surface area compared to a parallel plate.

In a time sweep, time is the variable, and the temperature, frequency and applied strain amplitude are kept constant. However, prior to the experiment, calibration was performed to set the zero gap (gap between the two rheometer plates). A strain sweep (increased levels of stress at a single frequency) was employed to determine the linear-viscoelastic region (LVR) and the critical strain for the oscillatory measurements.

It is essential that the material fully occupied the space between the two rheometer plates and with no air bubbles, all of which will distort measurements. For the setting of the zero gap, the geometry was calibrated using rotational mapping. The sample was loaded onto the centre of the base plate. The upper plate then gradually lowered onto the sample until the gap (space between the rheometer plates) was completely filled. The excess material at the periphery of the plates was removed using a spatula. To avoid the risk of mechanical damage to the material, the normal force measure at the lower plate was set at a maximum of 0.1N[234]. The volume of un-crosslinked bio-ink added for each experiment was 0.6ml.

The LVR describes the range within which the viscoelastic properties of the material is independent of the applied strain. When high levels of strain are applied, material may undergo changes to their microstructure, thereby affecting the rheological parameters measured when recorded outside the LVR. In other words, by ensuring that the applied strain was below this critical level, and therefore within the LVR, material changes recorded over time would be reflective of the material change per se, and not

impacted by the stress applied by the rheometer. All oscillatory time sweep was performed within the LVR of the samples, as indicated by the stress sweeps (data not shown).

Following a sample equilibration period of 5 minutes, with the rheometer's lower plate set at 22^{o}C, the oscillatory time sweep was conducted with a constant oscillation stress of 1Pa, at a frequency of 1Hz. A ring of cross-linker was applied to surround the bio-ink and the rheometer plate. Initial testing revealed evaporation of the cross-linker over time, and due to the geometry of the rheometer, the maximum volume of cross-linker that could be applied to surround the bio-ink and rheometer plate without overspill was 700µl. The storage (elastic) modulus, G', and loss (viscous) modulus, G", were measured every 3.5 seconds for a study period of 12 hours. Three replicates were performed.

2.12.1 Gel point

In rheological terms, hydrogel in aqueous (solution) phase exhibit low levels of polymer entanglements, permitting 'flow'. The exposure to a cross-linking agent initiates cross-links formation between polymer chains, restricting their free movement. As the amount of cross-link formation increases, a critical point is reached where gelation occurs. Also known as the gel point, this describes the transition from a liquid to solid state. An operational definition of the gel point, at which the storage (G') and loss (G") modulus at a single frequency equates, was used herein. As such, it was explored to define the point at which complete cross-linkage was reached, to aid the selection of the application time for cross-linkers for the 3D *in vitro* model creation. During an oscillatory time sweep, the gel point is the intersection point of G' and G" over time. This was examined for all bio-inks subjected to rheological testing in chapters 4 and 5.

2.12.2 Real-time monitoring of storage modulus during cross-linkage

The change of storage modulus (G') over time was assessed to understand the change in rheological properties of the bio-ink during cross-linkage. As such, the point at which the cross-linker was applied during the oscillatory time sweep was time zero.

2.12.3 Data visualisation using commercial rheometer software

Initial data visualisation was performed using TRIOS, the commercial rheometer software. Data was presented in three formats: unsmoothed (figure 2.13A), smoothed in log scale (figure 2.13B) and smoothed in linear scale (figure 2.13C). The storage and loss modulus over time was visualised to examine for the gel point, and the plateau point and pattern of change of the storage modulus during cross-linkage. Whilst approximate estimates can be deduced from the graphs produced *via* the commercial software, an alternative approach was explored for data interrogation detailed in the next section. Of note, data smoothing was performed as a function of the TRIOS software and precise methodology was proprietary knowledge.

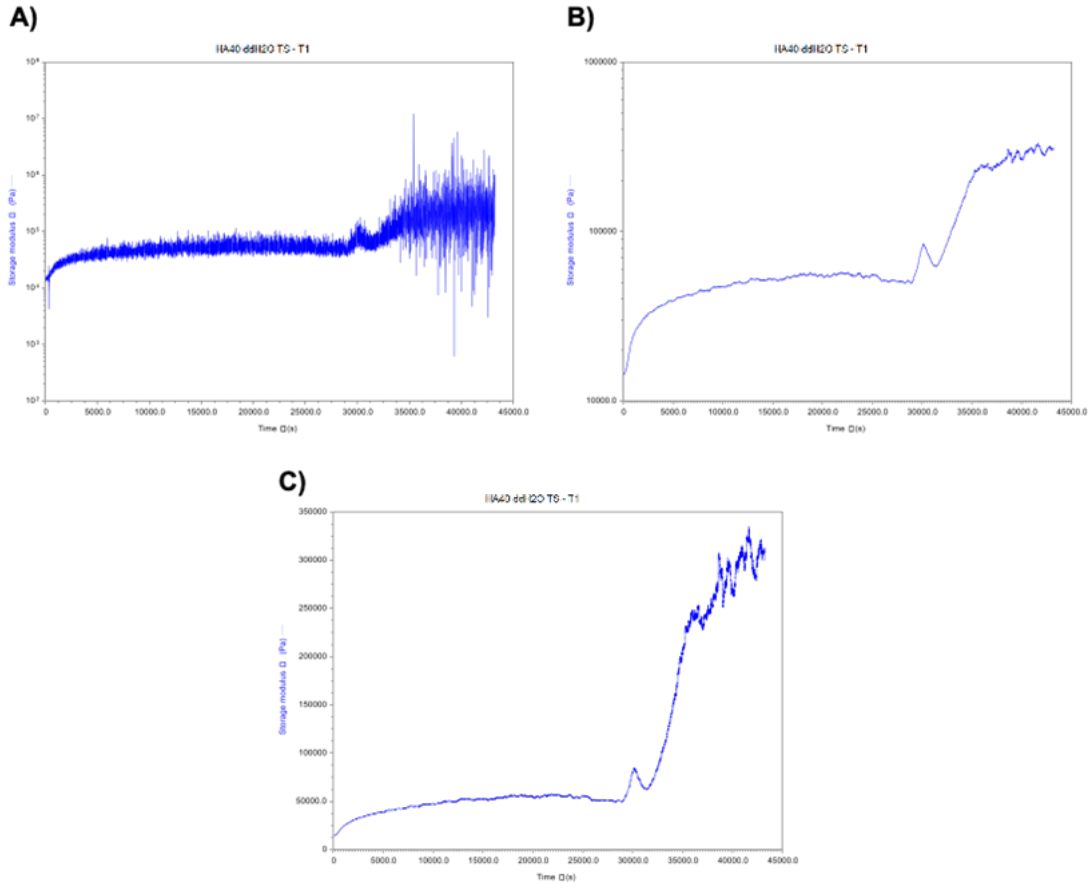

Figure 2.13 Storage modulus over time of bio-ink ETC:Alginate:N-HA (high) in ddH_2O exposed to 0.1M $CaCl_2$ processed via the TRIOS software. *The same dataset was displayed as unsmoothed in log scale (A), smoothed in log scale (B) and smoothed in linear scale (C). Data represents an oscillatory time sweep performed at 1Pa and 1Hz over 12 hours. N=1.*

2.12.4 Data analysis

Data cleaning was initially performed to remove artefacts and negative values. The study duration of the oscillatory time sweep was set at 12 hours, with the intention of extending beyond the anticipated plateau point of the storage modulus to improve the likelihood of data capture. Gross data visualisation *via* the TRIOS software revealed a sudden and marked disturbance of readings between 8-10 hours. Figure 2.14A illustrates the abrupt change in storage modulus, which was accompanied with the loss of the ring of cross-linker around the rheometer plate and sample (figure 2.14B left), alongside the gap between the rheometer plates (figure 2.14B right). It was presumed that evaporation of the 700µl cross-linker occurred during the 8-10 hour period, with the subsequent exposure of bio-ink to air which causes dehydration and material shrinkage resulting in the underfilling between the rheometer plates. This in turn caused artefacts in the data. All datapoints beyond the abrupt change in storage

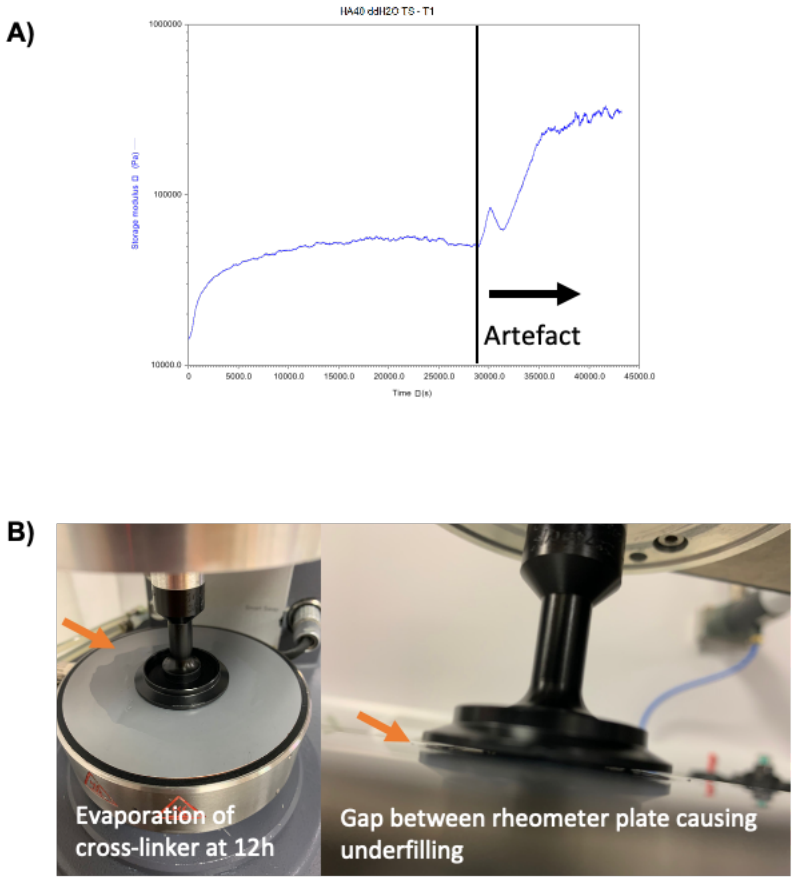

Figure 2.14 Data artefact associated with underfilling of rheometer. *(A) represents the storage modulus over time of bio-ink ETC:Alginate:N-HA (high) in ddH2O exposed to 0.1M $CaCl_2$, displayed via the TRIOS software. The data represents an oscillatory time sweep performed at 1Pa and 1Hz over 12 hours. N=1. The timepoint of the acute change in storage modulus was denoted by vertical line, and data beyond this timepoint was artefact. (B) illustrates the evaporation and loss of cross-linker surrounding the rheometer plate on the left, and the gap between the upper and lower rheometer plates demonstrating under-filling on the right.*

modulus was deemed unsuitable for data analysis. The timepoint that this occurred was deduced from visual inspection of graphs produced from the TRIOS software and datapoints were manually removed. In addition, a small volume of negative values of storage modulus was also removed as artefact.

In summary, for data cleaning, removal of the major artefact shortened the study period to be analysed from 12 hours to a minimum of 8 hours (figure 2.15A). Whilst there was a notable number of negative storage modulus values (figure 2.15B), whereby the highest number was associated with the bio-ink ETC:Alginate:N-HA (high) in media, this was proportionally an insignificant number given the very high number of datapoints captured in total (figure 2.15C). A minimum of 8000 datapoints were analysed per experiment.

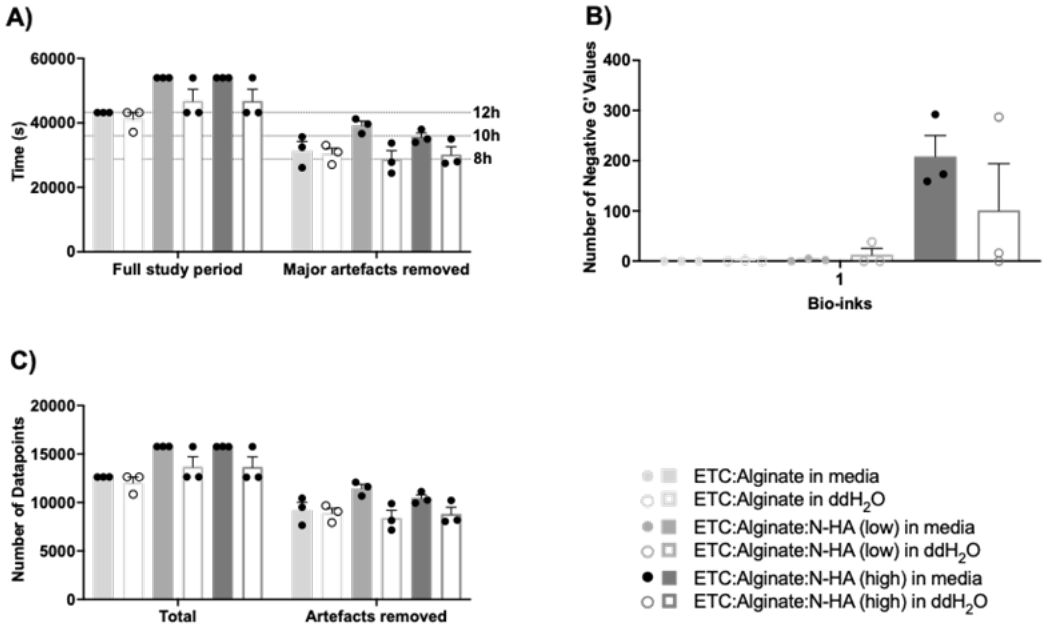

Figure 2.15 Summary of data cleaning for oscillatory time sweeps assessing the rheological parameters of bio-inks exposed to cross-linker. *Six bio-inks were examined as illustrated in the figure legend. ETC represents nanocellulose and N-HA is hyaluronic acid, which was tested in a high and low concentration and reconstituted in media or double-distilled water (ddH_2O). The difference between the full study period of a minimum of 12 hours, and the study duration following the removal of major artefacts is represented in (A). The number of negative values of the storage modulus for each bio-ink across the study period is shown in (B). The total number of datapoints collected for each bio-ink, together with the number of analysed datapoints represented by the group termed 'artefacts removed' is shown in (C). Mean±SEM. N=3.*

Data analysis was undertaken for all 'clean' datapoints, using the curve estimation function with SPSS. The cubic equation carried the highest R^2 value considering all bio-inks and triplicates combined, and was therefore selected as the best fit equation. Mathematically, due to the unsmoothed nature of the raw data where much noise

existed, an R^2 of 0.5 was deemed satisfactory, with the ideal R^2 value being one. Table 2.9 lists all R^2 values for each bio-ink tested, including replicates. The application of the curve estimation to identify the best fit equation served to both reduce the noise of the data, and permit extrapolation of data for storage modulus and time.

Table 2.9 The R^2 value of cubic equation estimation of oscillatory time sweeps. *Six bio-inks were examined. ETC represents nanocellulose. N-HA is hyaluronic acid, which was tested in a high and low concentration, and reconstituted in media or double-distilled water (ddH_2O). N=3.*

	Bio-inks					
	ETC:Alginate		**ETC:Alginate:N-HA(low)**		**ETC:Alginate:N-HA(high)**	
	media	**ddH_2O**	**media**	**ddH_2O**	**media**	**ddH_2O**
Rep 1	0.83	0.60	0.91	0.72	0.89	0.54
Rep 2	0.84	0.83	0.89	0.71	0.50	0.53
Rep 3	0.78	0.82	0.87	0.89	0.86	0.89

The cubic equation for each dataset, as identified with SPSS, was then plotted and interrogated using Wolfram Mathematica for the following: the plateau point of storage modulus (G' value and time), the time to reach 50% of the plateau of G', and G' values at 5, 15, 30 minutes, 1 and 4 hours, time of plateau, and time of plateau plus 30 and 60 minutes. These were deduced from the cubic equation directly, except for the plateau point. This was derived from the inflection point of the cubic curve, solved by the time where gradient equals zero. Figure 2.16 illustrates the curve estimates produced for one dataset following the procedure described. Figure 2.16A represents the curve estimation output from SPSS with each blue dot representing a datapoint, and the various curve estimations produced. The cubic equation from SPSS was plotted in Wolfram Mathematics as shown in figure 2.16B.

2.13 Toxicity testing

Testing for cytotoxicity and pro-inflammatory effects upon HFF-1 and C20A4 was conducted against individual bio-ink components (material – chapters 3, 4, 5), cross-linkers (chapters 4, 5) and the cross-linked bio-ink in the form of an advanced *in vitro* model (chapter 6). Following which, transcriptomics study was applied upon the 3D

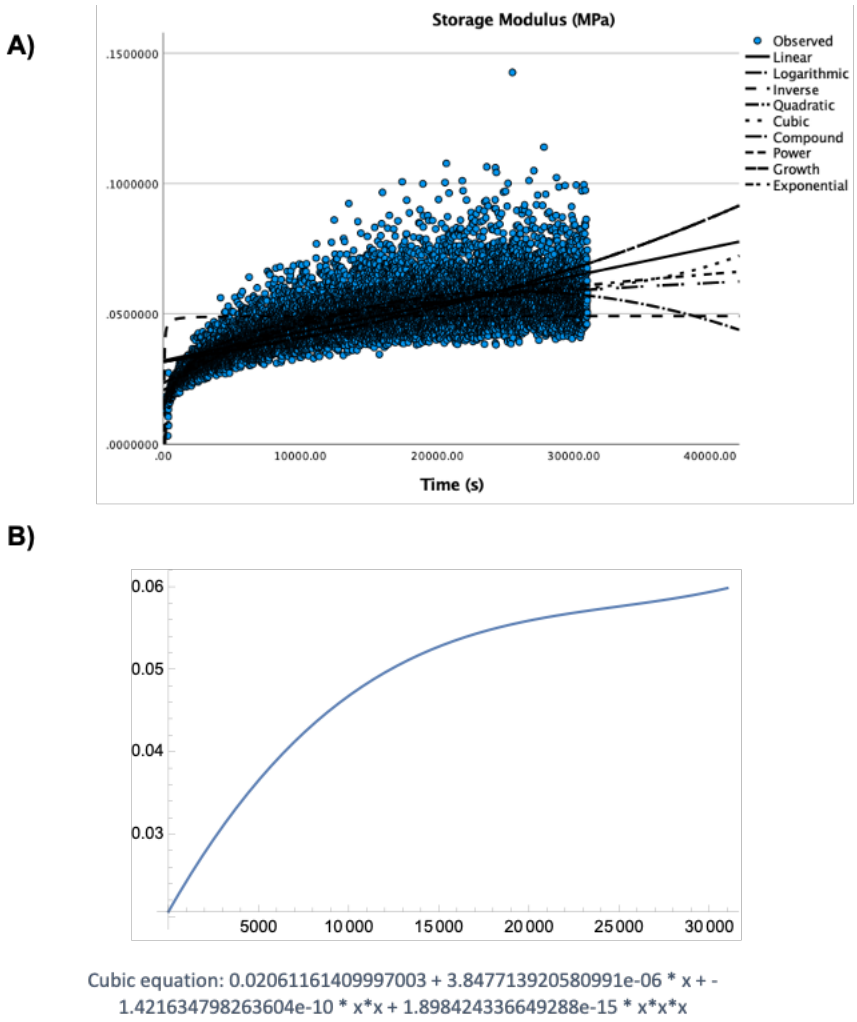

Figure 2.16 Data interpretation and visualisation of an oscillatory time sweep. *(A) represents the curve estimation output as produced with SPSS. (B) showed the cubic equation and the plot with Wolfram Mathematica. N=1.*

in vitro model (chapter 7). Table 2.10 summarises study parameters. All studies were conducted with three biological replicates.

Testing in 2D cultures was conducted against HFF-1 and C20A4 monocultures, whilst both monocultures and co-culture with both cell types were performed for 3D cultures. Exceptions are as shown in table 2.10. In 2D cultures, this was due to unfavourable toxicity profile with one cell type, which deemed further testing irrelevant and unnecessary. For 3D cultures, it was a result of incompatibility of the testing model with physiologically relevant material concentrations or cell seeding density.

Assays for cytotoxicity and pro-inflammatory response were kept consistent, except for cytotoxicity where erythrosin B exclusion assay was applied for 2D cultures and the LDH assay was used with 3D cultures, with the addition of alamar blue assay and

Table 2.10 Summary of material, cross-linker and bio-ink toxicity testing parameters. *Timepoints tested are denoted by: ♦ day 1, 2, 3, 5, 7, 14, 21; ◊ day 1, 3, 5, 7, 14, 21; # 5, 15, 30 minutes, 1, 4 hours and day 1, 2, 5, 7.*

	Cell line	**2D/3D**	**Cytotoxicity**	**Pro-inflammatory effects**	**Cell morphology**	**Timepoints***
Material toxicity testing						
Nanocellulose (ETC,TTC,CTC)	C20A4	3D	LDH assay	IL-6 + IL-8 (ELISA)	-	♦
Alginate	HFF-1 C20A4	2D	Erythrosin B exclusion assay	IL-6 + IL-8 (ELISA)	Y	♦
T-HA (0.006 + 0.012g/ml)	HFF-1	2D			Y	♦
N-HA (0.006 + 0.12g/ml)	HFF-1 C20A4	2D			Y	♦
Cross-linker toxicity testing						
$CaCl_2$ (0.1, 0.5, 1.0M)	HFF-1	2D	Erythrosin B exclusion assay	IL-6 + IL-8 (ELISA)	Y	#
$CaCl_2$ 0.1M	C20A4	2D			Y	#
H_2O_2 (5, 10, 15, 20, 25μM; 5, 10, 15, 20, 25mM)	HFF-1	2D			Y	#
Bio-ink toxicity testing						
ETC:Alginate **ETC:Alginate:N-HA (low) in media**	HFF-1 C20A4 Co-culture	3D	LDH assay Alamar blue assay Live/dead staining	IL-6 + IL-8 (ELISA)	-	♦
ETC:Alginate:N-HA (low) in media	C20A4 Co-culture	3D	Transcriptomic study with Nanostring		-	◊

live/dead staining with final testing of the bio-inks. Cell morphology was assessed with light microscopy for all 2D cultures.

Testing of materials and bio-inks was conducted over an acute (day 1, 2, 3, 5, 7) and chronic (day 14, 21) timeframe. Transcriptomic study was abbreviated to six of the seven timepoints over 21 days (exclusion of day 2), due to the 12 samples per panel

Nanostring system and cost. Cross-linker toxicity testing involved timepoints reflective of cross-linker application duration (5, 15, 30 minutes). To assess the cellular effects of potential residual cross-linker within the hydrogel disc system, intermediate timepoints included 1 and 4 hours, and chronic timepoints represents worst case scenario (day 1, 2, 5, 7).

With 2D cultures, material and cross-linker exposures were conducted 24 hours following seeding. In 3D cultures, as this primarily involved the encapsulation of chondrocytes in nanocellulose or bio-ink, seeding and exposure was considered to occur simultaneously. The day 1 timepoint refers to 24 hours following exposures.

Due to the dissolution of material (alginate and HA) in media for 2D material toxicity testing, media change was rationalised to 50:50 removal and exchange of media on day 7 and day 14. Calculations for ELISA and LDH assay therefore included a dilution factor of 2 for day 14 and of 4 for day 21. This aimed to balance the need for fresh media and nutrients for cell health, whilst recognising the unknown pharmacokinetics of the materials tested and therefore alternative dosing regimes were not feasible.

For 2D cultures, all negative controls were exposure-free, cell-only cultures treated under the same experimental and culture conditions. With 3D cultures, negative controls included a cell only 2D culture for monoculture scenarios, and a material only, cell-free control to account for material interference of assays. Negative control was not conducted for the transcriptomic study. The positive control for the erythrosin B exclusion assay was 0.1% Triton to achieve complete cell death rapidly. Lipopolysaccharide (LPS) is a component of the outer membrane of gram-negative bacteria. It is an endotoxin and is commonly used as positive control for its pro-inflammatory effects. In this project, 1μg/ml LPS was used as the positive control for all ELISAs testing for the release of IL-6 and IL-8, and was applied to both 2D and 3D culture conditions.

For the assessment of pro-inflammatory effects, cytokine release per cell were calculated where specified. This was performed to account for the varied cell concentrations seen over time, as well as between exposure or culture conditions. Total cell concentrations, as determined by the erythrosin B exclusion assay, was used for this calculation throughout. An alternative option would be to use the live cell

concentration, but this may generate low cell numbers not representative of the full study period, with the pro-inflammatory effects erroneously magnified.

Finally, as experiments were conducted in parallel, including cell-free cross-linkage studies, whilst results are presented sequentially, extra care was taken to specify the form and concentrations of material, cross-linker and bio-ink tested in each chapter. Table 2.6 tabulates the composition of each bio-ink and their assigned names are kept consistent through the thesis.

2.14 Statistical analysis

Handling of raw data was performed with Microsoft Office Excel. Statistical analysis was performed using GraphPad Prism, unless otherwise specified. Statistical analysis was undertaken for studies with a minimum of three biological replicates. The results were presented as mean ± standard error of the mean (SEM). Ordinary two-way ANOVA was performed using Tukey's multiple component test. The p-value was considered significant if $p < 0.05$.

Chapter 3: Nanocellulose – core bio-ink material: Establishing sterility and its biological effects on HFF-1 and C20A4 cell lines

3.1 Introduction

Utilising a hybrid and natural approach, the bio-inks under investigation consisted of nanocellulose and alginate, with or without hyaluronic acid (HA). Nanocellulose, being the core material component, constitutes the focus of this chapter. The purpose here was to explore the biological effects of various forms of nanocellulose with the view to select a single, most optimal form to take forward for the final bio-ink formulation, which in turn will be used in biocompatibility testing in the advanced 3D *in vitro* model (chapter 6 and 7).

Material sterility was an essential criterion, which must be met for two reasons. Firstly, to permit end-application of cartilage tissue engineering in the long term, and secondly, to achieve the project's goal of biocompatibility testing in the format of an *in vitro* cell-based model in the immediate term. As such, it was the first investigation undertaken.

Following confirmation of material sterility, the next step was to explore their biological effects in terms of cytotoxicity and pro-inflammatory effects against the human dermal fibroblast (HFF-1) and human chondrocyte (C20A4) cell lines. Six forms of nanocellulose were investigated, including pulp- and tunicate-derived nanocellulose.

The aims of this chapter were:

i) To establish the cytotoxic and pro-inflammatory effects of nanocellulose against HFF-1 and C20A4 cell lines.
ii) To identify the optimal nanocellulose form to be used in the final bio-ink formulation based on biological evaluation.

The three aims were met *via* the objectives below:

1. To establish standardised material preparatory procedures for pulp-derived nanocellulose.
2. To investigate the sterility of pulp- and tunicate-derived nanocellulose over 21 days.
3. To assess the cytotoxicity and pro-inflammatory response of HFF-1 and C20A4 cell lines when exposed to nanocellulose.

3.2 Methods

All methods used in this chapter pertaining to microbial growth assay (section 2.6), cell culture (section 2.7), LDH assay (section 2.9) and ELISA (section 2.8.3) were previously described in Chapter 2 (Material and Methods). Specific sections are referenced as detailed below.

The sterilisation and material preparation of pulp-derived nanocellulose will be described first, followed by details of sterility testing and material toxicity testing. Figure 3.1 serves as a schematic of parameters for both sterility and material toxicity testing conducted in this chapter. It outlines the nanocellulose forms investigated, assays used and testing conditions and timepoints.

3.2.1 Sterilisation of pulp-derived nanocellulose

Pulp-derived nanocellulose, in hydrogel form, was initially decanted into 50ml Falcon tubes as 40ml aliquots. A reduced volume was used to account for expansion during autoclaving and for ease of material handling and spillage avoidance during subsequent material preparation (outlined in section 3.2.2). Each aliquot was subjected to moist heat sterilisation *via* a single automated autoclave cycle at 121^{o}C.

Published sterilisation protocols using autoclaving described the use of bench-top autoclaves with slight variance of temperature and cycle duration (126^{o}C for 20min with Al-Sabah *et al*, 2019; and 121^{o}C for 30min with Jessop *et al,* 2019) [223, 224]. As both reflected the use of a single autoclave cycle, the same approach was used in this project, taking care to maintain consistency *via* the use of the same autoclave machine throughout the study period.

3.2.2 Material preparation of pulp-derived nanocellulose

The sterilised pulp-derived nanocellulose were subjected to centrifugation at 1500G for 5 minutes to achieve phase separation. The liquid supernatant was exchanged with ultrapure water at 1:1 volume ratio to reduce the amount of residual bleaching chemical and lignin fragments from the nanocellulose extraction process and material acidity.

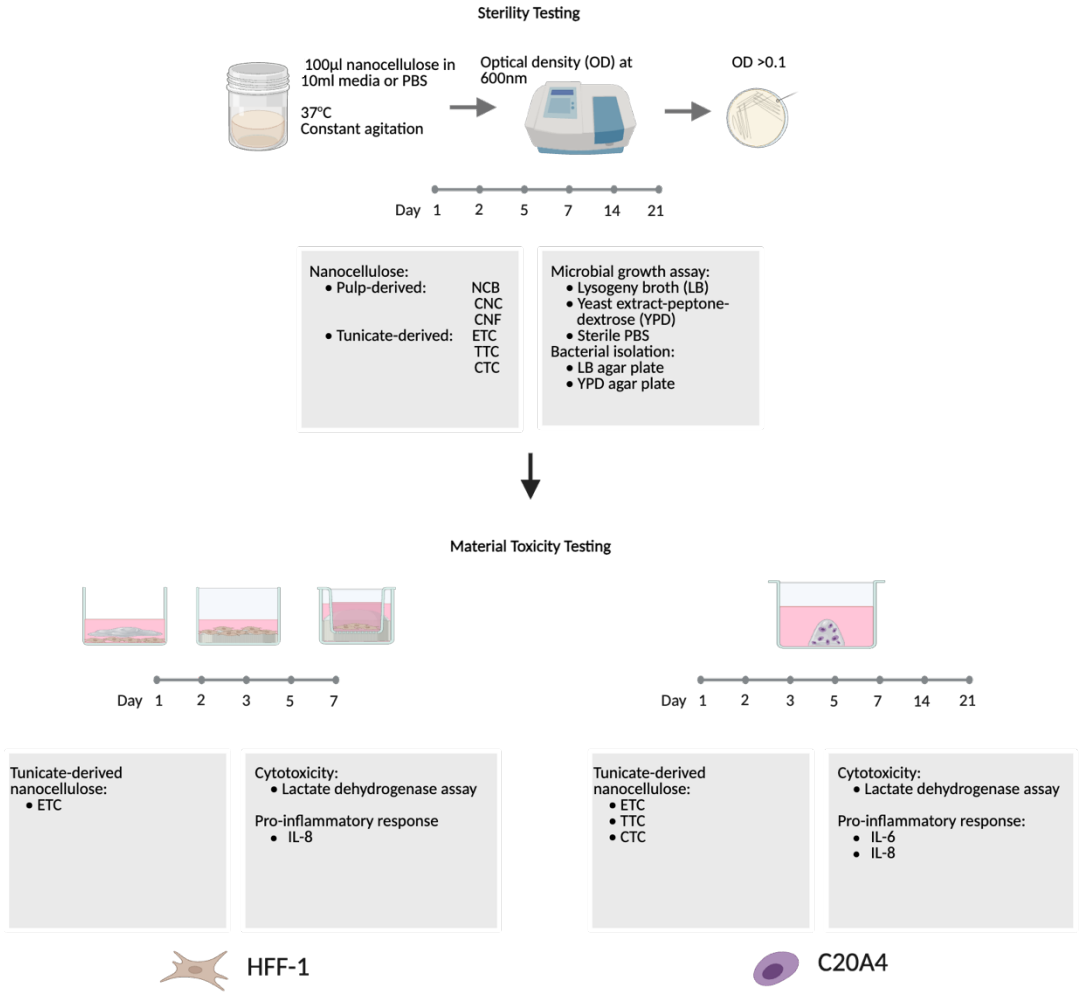

Figure 3.1 Schematic of chapter 3 workflow. *Sterility testing was conducted against pulp-derived (nanocellulose blend (NCB), cellulose nanocrystals (CNC), cellulose nanofibrils (CNF)) and tunicate-derived nanocellulose (enzymatically pretreated nanocellulose (ETC), TEMPO-mediated oxidised (TTC), carboxymethylated (CTC)). Microbial growth assay involved incubation of nanocellulose in lysogeny broth (LB), yeast extract-peptone-dextrose (YPD) or sterile PBS between 1-21 days. Optical density (OD) was measured at 600nm using spectrophotometer. Bacterial isolation of non-sterile samples with OD >0.1 were performed by streaking on LB and YPD agar plates. Material toxicity testing was conducted using ETC against HFF-1 with a trial of three models of exposures over 7 days, and C20A4 encapsulated within three types of tunicate-derived nanocellulose over 21 days. Cytotoxicity (lactate dehydrogenase assay) and pro-inflammatory effects (IL-6,IL-8) were assessed. Created with BioRender.com.*

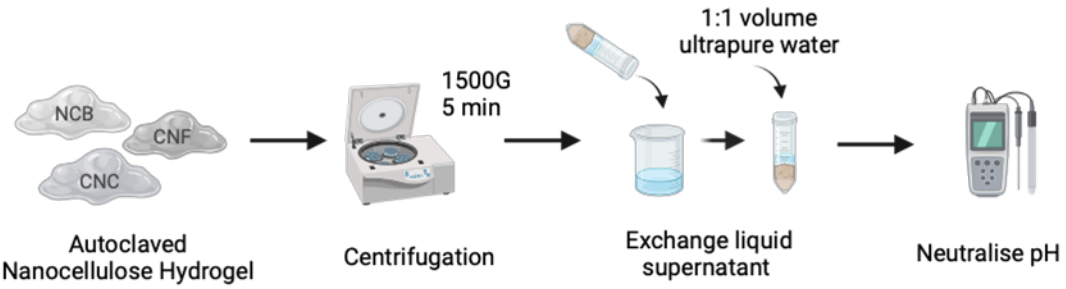

Figure 3.2 Schematic of preparation of pulp-derived nanocellulose prior to testing and use. *Centrifugation of autoclaved nanocellulose hydrogel at 1500G for 5 minutes produces liquid supernatant. This is exchanged with sterile ultrapure water in 1:1 volume to reduce residual bleaching chemicals from nanocellulose production. Alkalinisation of resultant hydrogel completes nanocellulose preparation. Created with BioRender.com.*

Following homogenisation by mixing with a spatula, neutralisation of the nanocellulose was achieved *via* drop-wise addition of sodium hydroxide until a pH of 7 was reached, confirmed using pH indicator strips. This process is depicted in figure 3.2.

The above steps were applied subsequent to sterilisation in order to minimise handling of non-sterile material in the laboratory, and thereby reduce the risk of contamination.

Published methodologies and in-house protocols were reviewed and harmonised[223, 224]. They were in effect identical, except for the exchange of supernatant following centrifugation. This was an important distinction as removal versus exchange of the liquid supernatant will alter the wt.% of the resultant nanocellulose, and therefore dose in future biological testing. Corresponding authors of the protocols were consulted, confirming the exchange of liquid supernatant and this was kept for the protocol used in this study.

3.2.3 Material sterility testing

Material sterility testing was undertaken as described in section 2.6. All materials were subjected to microbial growth assay in LB, YPD and sterile PBS (section 2.6.1). Samples with an optical density (OD) of greater than 0.1, a widely accepted threshold for sterility, were subjected to bacterial isolation (section 2.6.2).

Pulp-derived nanocellulose, which included NCB, CNC and CNF, were tested untreated as supplied and sterilised *via* autoclaving (section 3.2.1). Sterile tunicate-derived nanocellulose, which included ETC, TTC and CTC, were tested as supplied.

Testing involved 100µl of the nanocellulose gel as supplied, with sterilisation performed where indicated. Materials were not subjected to further preparatory procedures prior to being put forth for sterility testing. Timepoints of the microbial growth assay were day 1, 2, 5, 7, 14 and 21.

3.2.4 Cell culture

The culture of HFF-1 fibroblast and C20A4 chondrocyte cells were conducted as previously described in section 2.7.

3.2.5 Material toxicity testing

3.2.5.1 HFF-1 cell line (human dermal fibroblast)

This section details the pilot testing conducted to examine the feasibility of material toxicity testing with HFF-1 exposed to nanocellulose. To mimic the implant-host contact interface, models sought to create direct contact between HFF-1 and a 'surface' of nanocellulose.

A dose of 0.02g/ml was chosen to reflect the potential maximum realistic dose as this is the nanocellulose concentration of the bio-ink (as discussed in section 2.3.1). A total volume of 3ml was chosen to ensure sufficient supernatant were available for analysis following centrifugation to remove nanocellulose. This step was necessary to reduce the risk of material interference of the assays. In a total volume of 3ml, this translates to 2001µl ETC of 3 wt.% and 999µl media. The relatively large volume of nanocellulose hydrogel stock required to achieve a physiologically relevant concentration posed challenges in achieving cell culture condition. As such, three exposure methods (models 1-3) were tested, as shown in figure 3.3. This pilot testing was conducted using tunicate-derived ETC, with a sample size of 1.

In model 1, HFF-1 were seeded in the same manner as in cell line characterisation (section 2.7). Nanocellulose was added 24h after seeding to permit cell attachment. This model is the simplest in concept, with nanocellulose added directly to 2D cell culture. There were, however, concerns that the viscosity and volume of nanocellulose on top of the HFF-1 monoculture could impede cellular access to nutrient and gaseous exchange. Therefore, negative effects observed maybe a result of the model itself, and not necessarily effects from the material exposure per se.

In model 2, HFF-1 was seeded on top of the nanocellulose, which was added first to the well plate. This aimed to counteract the limited access to media and oxygen as in model 1, however, the ability for cell attachment to un-crosslinked nanocellulose were uncertain, as is the potential downstream physiological impact.

In model 3, the Transwell insert was used to primarily preserve cell culture conditions for HFF-1. Cells were added to the insert, whilst nanocellulose were added to the well plate (figure 3.3). A key limitation was the indirect contact between cells and material due to separation by the insert membrane, which did not reflect the *in vivo* scenario.

Here, cell seeding was carried out in a 500µl cell suspension, and the residual media volume to dilute the nanocellulose hydrogel stock. Nanocellulose were added 24h following cell seeding to mimic model 1.

In model 1 and 3, media were exchanged at the point of nanocellulose exposure. For each model, the negative control consisted of cell only without nanocellulose exposure, and a cell-free, material only control to account for material interference of assays.

Direct inspection of each model macroscopically was supplemented by biochemical assessment with measurement of IL-8 (methodology outlined in section 2.8.3) and LDH (section 2.9) release. Cytotoxicity was measured using the LDH assay, as the model formats were incompatible with the erythrosin B exclusion assay.

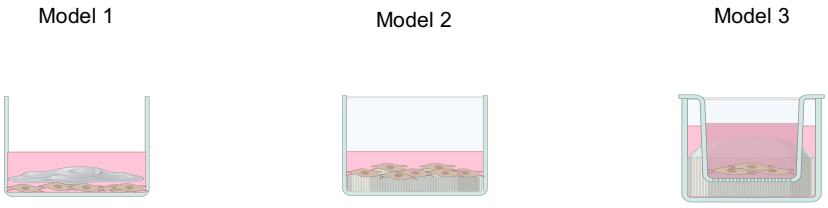

Figure 3.3 Schematic of material toxicity testing of nanocellulose against HFF-1. *Tunicate-derived enzymatically pretreated nanocellulose at 0.02g/ml were exposed to HFF-1 over 7 days, in three model set-ups. Model 1 – HFF-1 seeded on well plate and nanocellulose added 24h after seeding. Model 2 – nanocellulose first added to well plate and cell suspension applied onto nanocellulose. Model 3 – using Transwell insert, nanocellulose added to well plate and cell seeded on apical surface of insert membrane, with indirect contact between material and cells. Created with BioRender.com.*

3.2.5.2 C20A4 cell line (human chondrocyte)

In contrast to exposure against HFF-1, chondrocytes were mixed within the nanocellulose hydrogel stock at the relevant cell and material concentration (sections 2.3.1 and 2.7). Cytotoxicity and pro-inflammatory effects were assessed using the LDH assay and ELISA for IL-6 and IL-8 release, respectively (methodologies outlined in section 2.9 for LDH assay and 2.8.3 for ELISA). The 3D exposure scenario alongside negative and positive controls, as well as 2D cultures, are depicted in figure 3.4.

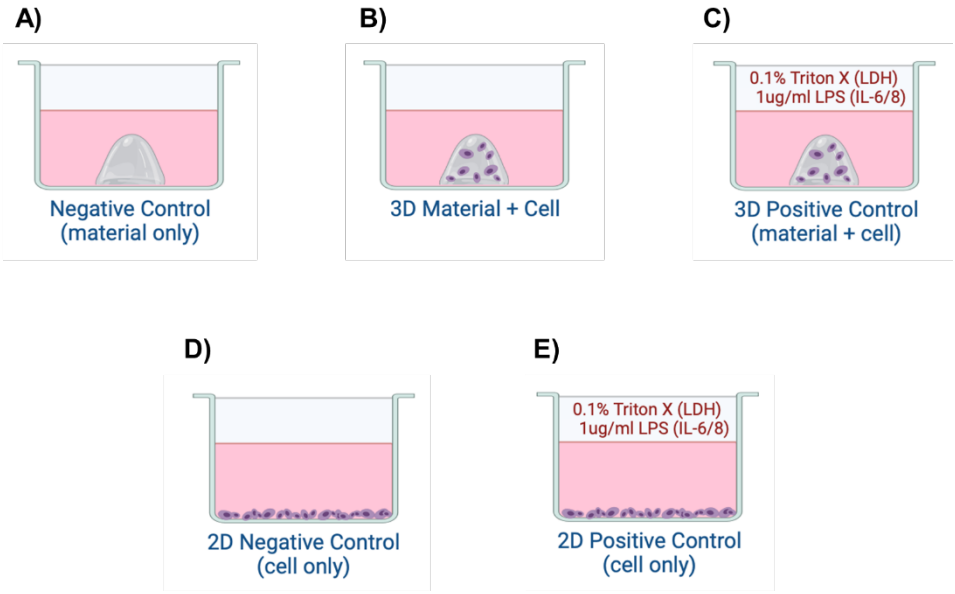

Figure 3.4 Schematic of material toxicity testing with C20A4 exposed to nanocellulose. *A/B/C (top row) represent 3D scenarios with nanocellulose, and are as follows: A) nanocellulose only without cells cultured in media to test for material interference of downstream assays; B) C20A4 exposure to nanocellulose; C) same as (B), but with addition of positive controls (0.1% Triton X for LDH assay, and 1µg/ml LPS for IL-6 and IL-8 release assessed with ELISA). D/E (bottom row) represent 2D scenarios without nanocellulose and are as follows: D) C20A4 2D monoculture; E) same as (D), but with addition of positive controls as listed for (C). Created with BioRender.com.*

3.3 Results and Discussion

3.3.1 Material sterility testing

3.3.1.1 Pulp-derived nanocellulose

Sterilised samples showed an OD of greater than 0.1, mostly at latter timepoints (figure 3.5A). CNF showed the overall highest OD values, reflecting the greatest degree of microbial growth. This was especially the case on day 14 and 21, in LB and YPD. CNC displayed variable OD across the study period, exceeding the 0.1 threshold as early as day 5. NCB was considered the best performing nanocellulose with regards to sterility, maintaining OD <0.1 in both media until day 7. It was interesting to note different microbes were isolated from NCB, CNC and CNF. Representatives were shown in figure 3.5B/C/D. However, sterilised samples with OD >0.1 did not yield macroscopically detectable microbes for up to 21 days of culture.

Regarding sterile PBS as the culture medium, OD remained less than or close to 0.1 for both sterilised and non-sterilised material up to day 21, suggesting the rise in OD in media was less likely to be due to material agglomeration alone.

3.3.1.2 Tunicate-derived nanocellulose

To permit longer term study as intended, an alternative sterile form of nanocellulose was introduced, which was the tunicate-derived nanocellulose. All three types of tunicate-derived nanocellulose were subjected to the microbial growth assay in the same manner as the pulp-derived nanocellulose. They all remained under the 0.1 OD threshold throughout the 21 day period, suggesting suitable sterility profile (figure 3.6). Whilst the OD remained below the threshold of 0.1, heightened variance was noted on day 7 with sterile PBS, and therefore additional testing were carried out for both media types and sterile PBS to bring to a total sample size of 5 on day 7. This did not alter the overall conclusion that sterility is maintained for all three tunicate-derived nanocellulose up to 21 days.

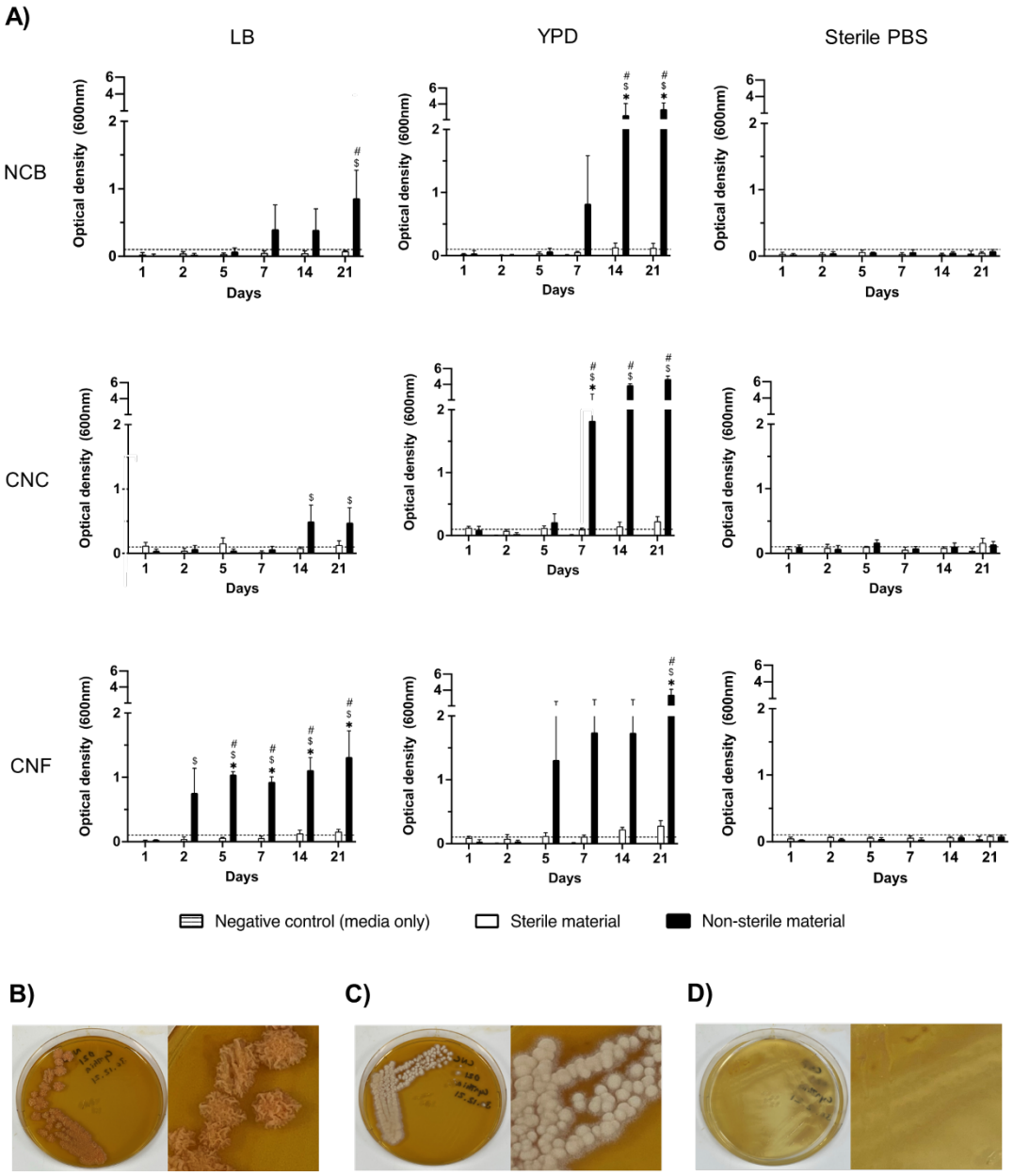

Figure 3.5 Sterility testing and bacterial isolation of pulp-derived nanocellulose. *A) Assessment of sterility and material effects on optical density in lysogeny broth (LB), yeast extract-peptone-dextrose (YPD) and sterile PBS. Three types of pulp-derived nanocellulose (nanocellulose blend (NCB), nanocellulose crystals (CNC) and nanocellulose fibrils (CNF)) were investigated. Autoclaved sterilised and non-sterilised nanocellulose in LB, YPD or sterile PBS were incubated at 37°C under constant agitation over 21 days. Media or PBS without nanocellulose served as negative control. Optical density measured at 600nm. Accepted arbitrary threshold for sterility at <0.1 denoted by horizontal dotted line. Mean±SEM is shown. N=3. Significance represented as follows: comparison of sterile and non-sterile materials at same timepoints p <0.05 (*); comparison of non-sterile materials between day 1 and day 2-21 p <0.05 (#); and comparison of non-sterile materials and cultured negative control at same timepoints p <0.05 ($). B-D) Morphology of microbial growth from non-sterile nanocellulose streaked on agar plate at day 7. Nanocellulose and culture medium as follows: B) NCB on YPD, C) CNC on YPD, D) CNF on LB.5*

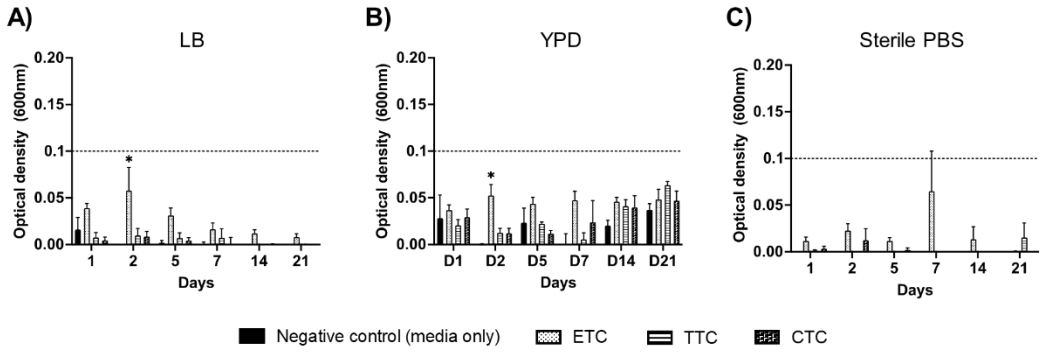

Figure 3.6 Sterility assessment of tunicate-derived nanocellulose. *Sterility assessment in lysogeny broth (LB) and yeast extract-peptone-dextrose (YPD) and material effects in sterile PBS on optical density. Three types of tunicate-derived nanocellulose (enzymatically pretreated (ETC), TEMPO-mediated oxidized (TTC) and carboxymethylated (CTC)) were investigated. Sterile nanocellulose were incubated at 37°C under constant agitation over 21 days. Media or PBS without nanocellulose served as negative control. Optical density measured at 600nm. Accepted arbitrary threshold for sterility at <0.1 denoted by horizontal dotted line. Mean±SEM is shown. N=3, except n=5 on day 7. Significance when compared to negative 'media only' control at each timepoints is denoted by ∗ ($p<0.05$).*

3.3.1.3 Section summary and discussion – material sterility testing

The project initiated with the sterility assessment of the three forms of pulp-derived nanocellulose. Each nanocellulose form, with both a sterilised and untreated version, were assessed for sterility using a microbial growth assay with two forms of media. Microbial contamination was seen in the non-sterilised samples, as anticipated. This was the case for all three forms of nanocellulose (NCB, CNC and CNF), and with both media types (LB and YPD).

The pulp-derived nanocellulose initially investigated in this project was a commercially available product from GranBio Technologies. It was supplied in a non-sterile, hydrogel format, stored at 4°C. Previous successful sterilisation with autoclave treatment permitted use in cell culture conditions for up to 48 hours [223]. Sterilisation and sterility testing in this project were therefore undertaken following published methodologies [223], but with the timeframe for testing extended to encompass the full study period of 21 days. In response to sub-optimal sterility at latter timepoints, a sterile form of nanocellulose (tunicate-derived and commercially available from Ocean TuniCell) was introduced and subjected to the same sterility testing methodologies.

Sterilisation by autoclaving was performed based on Al-Sabah *et al*'s study evaluating three sterilisation methods, which also included UV-C light and the application of 70%

ethanol [223]. The reported study investigated three pulp-derived nanocellulose from GranBio Technologies, the same as that used in the current research. Building on this work, sterilisation was undertaken in the same manner.

Whilst the threshold of 0.1 for OD to indicate sterility is arbitrary, this is well-accepted in the field of microbiology. As such, the crossing of this threshold for pulp-derived nanocellulose raised concerns regarding material sterility, despite no macroscopic microbial growth during bacterial isolation. Nonetheless, without further investigations such as enriched or prolonged culture, microbial contamination cannot be excluded. This posed two questions: 1) Were the conclusion valid regarding microbial contamination, with other causes contributing to the rise in OD?; 2) In the case of assumed or proven contamination, should this be addressed *via* attempts to optimise the sterilisation process, or to seek alternative sterile source?

The first question was addressed through an added investigation with sterile PBS as the culture medium. This did not produce a rise in OD as seen with LB or YPD, and therefore supported the notion that the rise in OD were a result of microbial contamination. However, material agglomeration can be influenced by intrinsic (e.g. material concentration) and extrinsic factors (e.g. solution conditions, temperature). Lysogeny broth, yeast extract peptone dextrose and PBS, with varying amounts of salt, chemical and protein content, may alter agglomeration behaviour leading to differing OD, unrelated to microbial growth. Ultimately, it was prudent to adopt a cautious stance regarding sterility given the overarching aim of the project. As such, autoclaved pulp-derived nanocellulose was considered unsuitable from a sterility perspective, which led to the second question listed above.

Alternative sterilisation methods or further optimisation of autoclaving were both potential avenues in response to microbial contamination. Options included ethylene oxide, gamma irradiation, and use of antibiotic or antimycotic medications [264]. However, considering the organic (plant-derived) nature, non-sterile manufacturing process and hydrogel format, which leant a greater risk of microbial growth compared to dry powder forms, a degree of microbial contamination was assumed at the point of supply. Whilst optimised sterilisation could achieve sterility, mitigation of endotoxin and defining product shelf-life would need to be addressed. This rationale led to the adoption of the second approach of identifying an alternative sterile nanocellulose

source. Sterility was confirmed *via* the microbial growth assay, establishing its suitability for further biological testing. Review of the literature suggests that no prior published studies using tunicate-derived nanocellulose from Ocean TuniCell intended for tissue engineering purposes examined material sterility as part of their investigation.

Regarding bioburden of nanocellulose, the vast majority of studies that focused on tissue regeneration application did not undertake an evaluation of sterility. Boix-Lemonche *et al* accounted for the presence of mycoplasma in an *ex vivo* cultured corneal model [265]. Alternative studies which investigated bioburden in terms of microbial contamination and endotoxin were both of nanocellulose-based wound dressings and not for tissue engineering purposes [266, 267].

In conclusion, regarding the choice of nanocellulose put forward for testing of their biological effects, sterility for the full study period of 21 days was deemed essential, given the intended goal of clinical translation. As such, pulp-derived nanocellulose were excluded for biological testing, despite NCB maintaining OD <0.1 up to day 7.

3.3.2 Material toxicity testing

3.3.2.1 Trial of HFF-1 cell line (human dermal fibroblast)

Model 1 and 2 which involved direct exposure of HFF-1 with nanocellulose, were deemed incompatible with cell culture conditions demonstrating minimal IL-8 release by HFF-1 across all timepoints (figure 3.7A), suggestive of cell non-viability. Whilst model 3 showed similar levels of IL-8 release between material exposure and cell only negative control, IL-8 release subsequently declined between day 2-7. Therefore, all three models were deemed unsuccessful and could not be used to assess material toxicity.

Furthermore, the relatively low level of LDH measured, as compared to cell only negative control, went against the presumed rise in cell non-viability for all three models. Again, this likely indicated model failure or nanocellulose interference with the LDH assay.

In culmination, it was concluded that it was not feasible to assess the material toxicity of nanocellulose against HFF-1 at physiologically relevant concentration and exposure scenarios. Non-direct contact between cells and nanocellulose in model 3 were incongruent with the end-application *in vivo* scenario and therefore further optimisation was not undertaken.

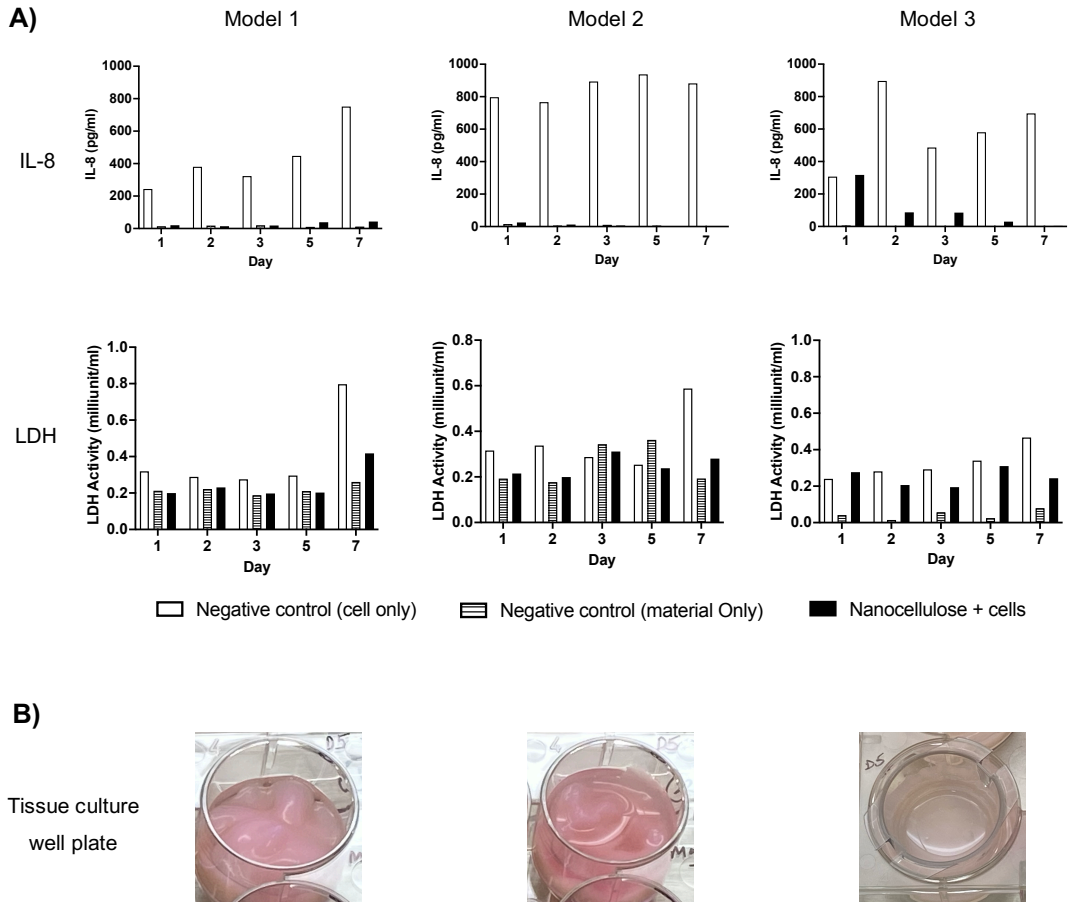

Figure 3.7 Trial testing for pro-inflammatory response and cytotoxicity of nanocellulose against HFF-1 2D monoculture over 7 days. *Three models of exposure were tested: model 1) Nanocellulose added to HFF-1 seeded on tissue culture plate (TCP); model 2) HFF-1 cell suspension added to nanocellulose in TCP; and model 3) Indirect contact exposure with nanocellulose in TCP well and HFF-1 seeded on Transwell insert. A) IL-8 release by HFF-1 and lactate dehydrogenase assay (LDH) were used to assess model feasibility. N=1. B) Images of TCP well of each model demonstrating relative volume of nanocellulose and media.*

3.3.2.2 C20A4 cell line (human chondrocytes)

3.3.2.2.1 Cytotoxicity

Chondrocytes exposed to all three forms of tunicate-derived nanocellulose exhibited a similar trend of LDH release over time. An initial stable level of LDH was observed between day 1 and 5, followed by rising levels of LDH from day 7 to 21 (figure 3.8).

Similarly, LDH levels were comparable between chondrocytes exposed to nanocellulose and chondrocyte-only 2D negative controls at early timepoints. However, from day 7 onwards, greater LDH levels were seen in 2D chondrocyte-only negative control than in cells exposed to any of the three forms of nanocellulose. Statistically significant differences were reached on day 14 and 21, and for all three forms of nanocellulose, both between timepoint comparison to day 1 and comparison between cells exposed to nanocellulose and cell-only 2D negative controls.

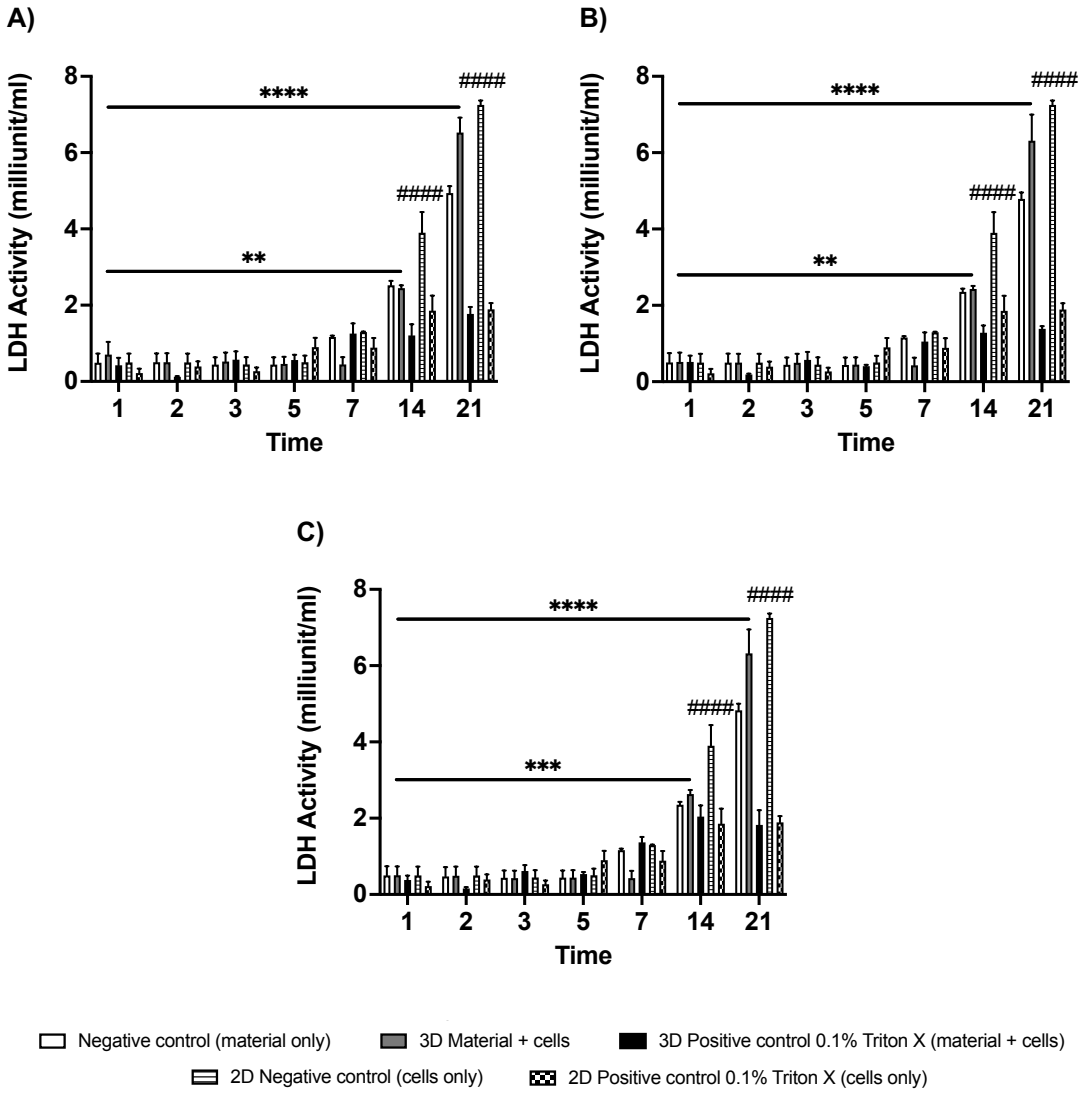

Figure 3.8 Cytotoxicity testing of tunicate-derived nanocellulose against C20A4 over 21 days. *Exposure consisted of C20A4 encapsulated within 100µl un-cross-linked nanocellulose under submerged condition. Negative control consisted of 2D cell culture without nanocellulose. Material interference of assay tested with material only, cell-free negative control. Positive control with 0.1% Triton X were applied to 3D and 2D cultures. A-C represent three types of nanocellulose tested: A) Enzymatically pretreated, B) TEMPO-mediated oxidized and C) carboxymethylated nanocellulose. Mean±SEM of lactate dehydrogenase activity is presented. Significance between day 1 and day 2-21 denoted by * for nanocellulose-exposed C20A4 (3D) and # for negative cell only control (2D): $p<0.05$ */#, $p<0.01$ **/##, $p<0.001$ ***/###, $p<0.0001$ ****/####. N=3.*

Interestingly, quantifiable levels of LDH were detected with the material only, cell-free controls. Levels of LDH between the material-only control and cells exposed to nanocellulose were similar and low, up to day 5. At latter timepoints, the levels of LDH measured in the material-only controls when compared to cells exposed to

nanocellulose were variable. They were higher on day 7, comparable on day 14 and lower on day 21, when compared to cells exposed to nanocellulose. However, this pattern was consistent across the three nanocellulose form and at each specific timepoints. Whilst detectable LDH levels in material-only, cell-free control suggests potential material interference of the LDH assay, the consistency in trends would permit comparison across the nanocellulose forms.

To aid direct comparison between the three forms of nanocellulose, figure 3.9 was compiled. There was no statistically significant difference in LDH release measured when chondrocytes were exposed to ETC, TTC and CTC. Therefore, no superiority of a specific tunicate-derived nanocellulose form was observed, based on cytotoxicity as assessed by the LDH assay.

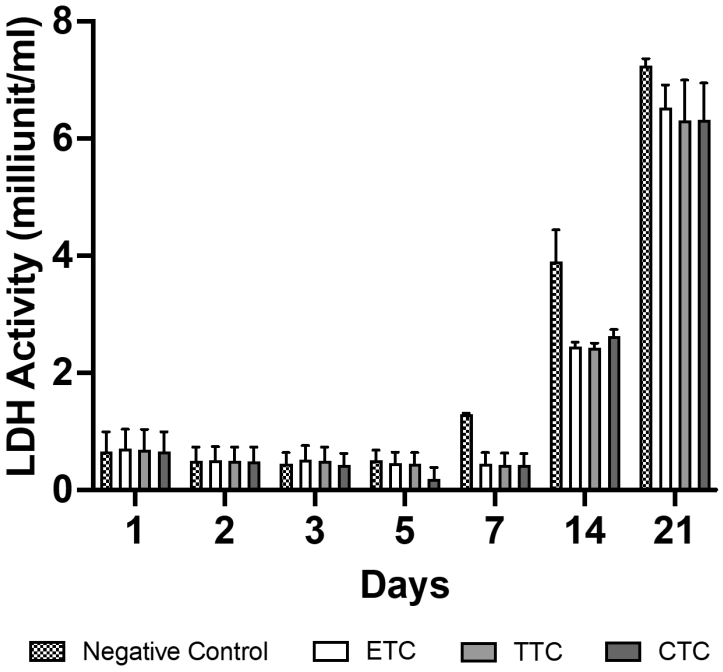

Figure 3.9 Comparison of lactate dehydrogenase (LDH) activity between three tunicate-derived nanocellulose upon exposure against C20A4 over 21 days. *Tunicate-derived nanocellulose investigated were enzymatically pretreated (ETC), TEMPO-mediated oxidised (TTC) and carboxymethylated (CTC) nanocellulose. C20A4 were encapsulated within 100µl un-cross-linked nanocellulose and cultured in submerged condition. Negative control constituted nanocellulose-free 2D cell culture. Mean±SEM of LDH activity is presented. N=3.*

3.3.2.2.2 Pro-inflammatory response

Similar to cytotoxicity, chondrocytes exposed to the three forms of tunicate-derived nanocellulose all displayed increased levels of IL-6 and IL-8 release over time (figure 3.10). This was most notable on day 14 and 21, with relatively low or non-detectable levels between day 1 to 7. Whilst model effects maybe contributory to the rise in pro-inflammatory effects at latter timepoints, differences observed between the variably functionalised nanocellulose suggests that material effects were present, which will be discussed in latter parts of this section.

Considering possible material interference on the ELISA assay, in contrast to the LDH assay, negligible or non-detectable levels of IL-6 and IL-8 were found with all three tunicate-derived nanocellulose forms at all timepoints. Whilst material interference cannot be fully excluded, this result indicates that the rise in pro-inflammatory mediators witnessed in exposure or positive control scenarios were more likely due to the exposure chemicals.

To facilitate direct comparison of the tunicate forms, figure 3.11 clearly demonstrates that ETC was the least pro-inflammatory across all timepoints. This nanocellulose form (ETC) consistently induced the lowest levels of IL-6 and IL-8 by chondrocytes, compared to TTC and CTC. This was statistically significant on day 7 for IL-6 and day 5, day 7 and 21 for IL-8. It was also interesting to note that whilst CTC induced the highest levels of IL-6 and IL-8 in the acute phase (day 1-7), this was superseded by TTC in the chronic phase (day 14-21). This indicates that the differences in physico-chemical properties between the TEMPO-mediated oxidised and carboxymethylated nanocellulose fibrils, not only produced varied biological responses, but a temporal element could also influence final biological outcomes.

The difference between the nanocellulose forms were also appreciated when reviewing comparisons between material exposure and cell-only 2D negative control, and between material exposure and 3D positive control with LPS (figure 3.10). Using the material-free, cell-only 2D negative control as the comparator, the superiority of ETC as the least pro-inflammatory was clear, as levels of IL-6 and IL-8 remained below that of the negative control throughout, except on day 21 with IL-8. Conversely, both TTC and CTC exposures led to, at times, higher levels of IL-6 and IL-8 release when

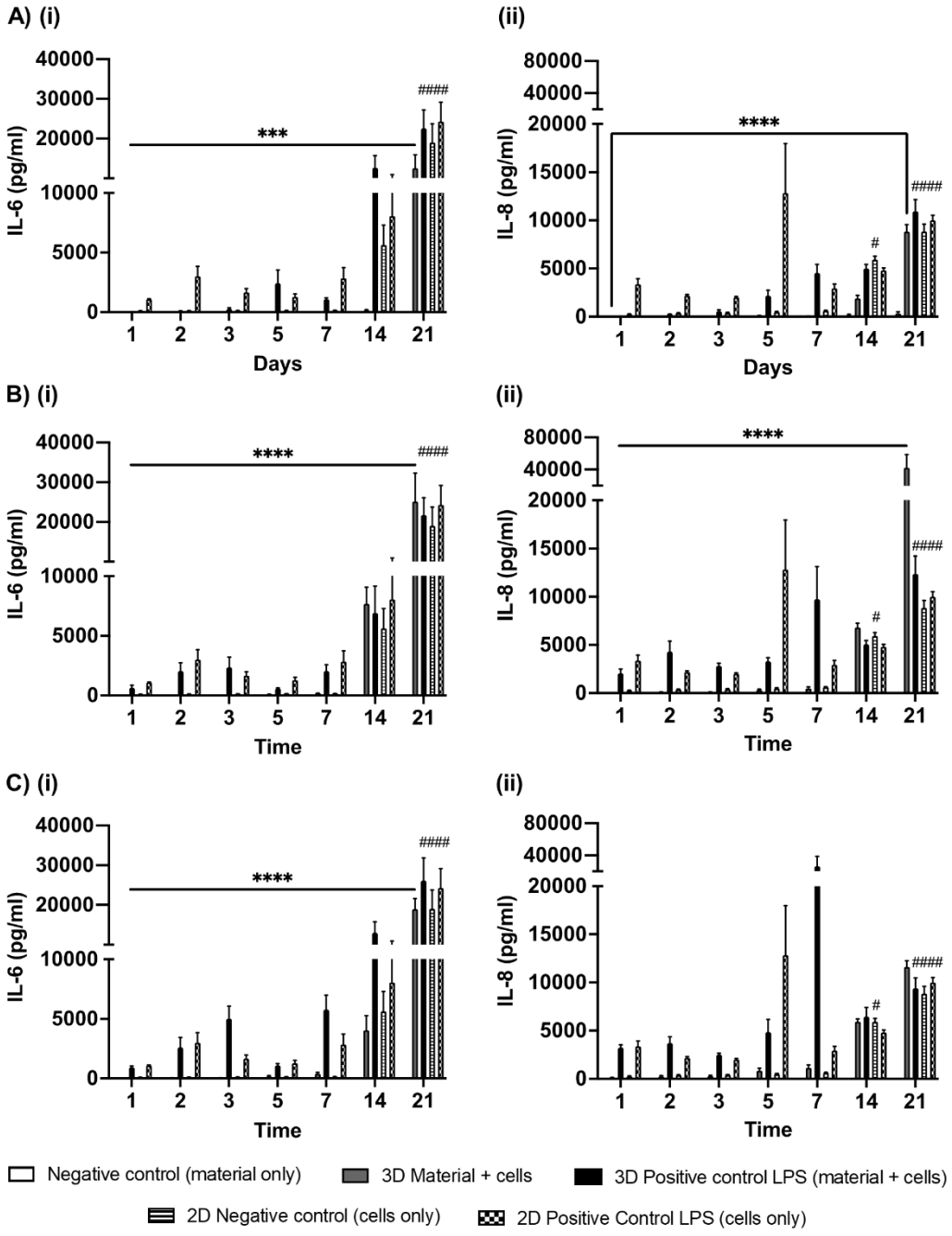

Figure 3.10 Pro-inflammatory effects of tunicate-derived nanocellulose against C20A4 over 21 days. *Exposure consisted of C20A4 encapsulated within 100µl un-cross-linked nanocellulose under submerged condition. Negative control consisted of 2D cell culture without nanocellulose. Material interference of assay tested with material only, cell-free negative control. Positive control with LPS were applied to 3D and 2D cultures. Three types of nanocellulose tested were: A) enzymatically pretreated (ETC), B) TEMPO-mediated oxidized (TTC) and C) carboxymethylated nanocellulose (CTC). Mean±SEM of IL-6 (i) and IL-8 (ii) released is presented. Significance between day 1 and day 2-21 denoted by ∗ for nanocellulose-exposed C20A4 (3D) and # for negative cell only control (2D): p<0.05 */#, p<0.01 **/##, p<0.001 ***/###, p<0.0001 ****/####. N=3.*

compared to cell-only negative controls. This difference was most marked in chronic timepoints (day 14-21) with TTC, although this was not statistically significant.

Moving onto positive controls and firstly reviewing 2D cultures, a heightened pro-inflammatory response was shown when chondrocytes were exposed to LPS, although

the effects were less marked at latter timepoints. However, when reviewing 3D cultures, the pro-inflammatory responses of chondrocytes to the addition of LPS diverged between the three nanocellulose form, again, hinting at the impact of their varied functionalisation. The nanocellulose of interest, due to its lowest pro-inflammatory effects, ETC, conferred a slight delay in the mounting of pro-inflammatory response by chondrocytes when compared to cells in 2D culture (day 21 versus day 14). This delay, in mounting a pro-inflammatory response in the 3D system when exposed to LPS, was not seen at all with TTC, whereby chondrocytes exposed to TTC mounted a similar, if not greater, pro-inflammatory response compared to the 3D positive control. Finally, the effects of CTC displayed a less clear trend, and laid somewhere between that with ETC and TTC.

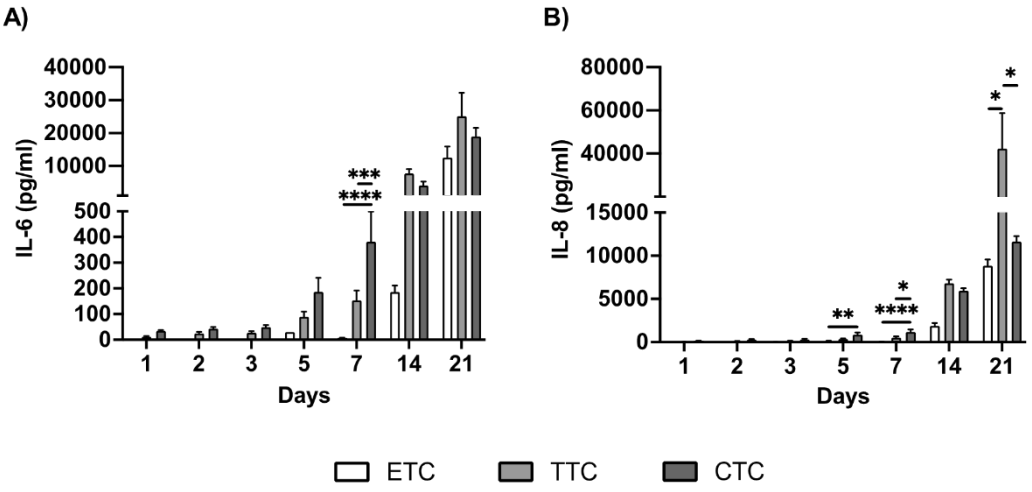

Figure 3.11 Comparison of IL-6 and IL-8 release between three tunicate-derived nanocellulose upon exposure against C20A4 over 21 days. *Tunicate-derived nanocellulose investigated were enzymatically pretreated (ETC), TEMPO-mediated oxidised (TTC) and carboxymethylated (CTC) nanocellulose. C20A4 were encapsulated within 100µl un-cross-linked nanocellulose and cultured in submerged condition. Pro-inflammatory mediators A) IL-6 and B) IL-8 were measured. Mean±SEM is presented, significance between nanocellulose types at each timepoint are denoted by * (p<0.05 *, p<0.01 **, p<0.001 ***, p<0.0001 ****). N=3.*

In summary, the un-crosslinked enzymatically pretreated form of tunicate-derived nanocellulose (ETC) was deemed the least pro-inflammatory towards chondrocytes, for up to 21 days. Carboxymethylated nanocellulose (CTC) was the most pro-inflammatory in the acute phase (day 1 to 7), whilst the TEMPO-mediated oxidised form (TTC) replaced CTC on this regard in the chronic phase (day 14 to 21).

3.3.2.3 Section summary and discussion – material toxicity testing

Firstly, it is worth noting that both pulp- and tunicate-derived nanocellulose were available in three forms from each commercial supplier. Table 3.1 summarised known physico-chemical properties of the six nanocellulose forms. Full material characterisation as recommended by Foster *et al* in a review of parameters and techniques used for the characterisation of nanocellulose was outside the remit of this study[268]. Nonetheless, the influence of varying physicochemical properties on potential structure-activity relationships and therefore biological impact was acknowledged. It was interesting to note that whilst pulp-derived nanocellulose included nanocellulose crystal (CNC), fibrils (CNF) and 'blend' (NCB) forms [234 235], tunicate-derived nanocellulose were all 'nanocellulose fibrils' but variably functionalised. Published data relating to the material characterisation of these specific forms of tunicate-derived nanocellulose is lacking and information is presented from the product specification information supplied by Ocean TuniCell.

Table 3.1 Physicochemical properties of pulp- and tunicate-derived nanocellulose. *The dimensions of all forms of nanocellulose used in the thesis and additional physicochemical characteristics are presented[223, 234].*

	Pulp-derived			**Tunicate-derived**		
	CNC	**CNF**	**NCB**	**ETC**	**TTC**	**CTC**
	Nanocellulose crystals	Nanocellulose fibrils	Nanocellulose blend	Enzymatically pre-treated	TEMPO-mediated oxidised	Carboxy-methylated
Width (nm)	4.5 ± 1.5	29 ± 18	17 ± 12	8.55 ± 3.37	6.2 ± 1.49	4.99 ± 1.28
Length (nm)	222 ± 139	1627 ± 1252	925 ± 787	2519 ± 827	2262 ± 1026	2017 ± 1063
Aspect ratio	49	55	55	296 ± 97	365 ± 17	412 ± 76
Viscosity (Pa·s)	-	-	-	96.37 ± 0.05	107.67 ± 3.33	101.75 ± 16.05
Degradation peak (°C)	-	-	-	359 (onset 325)	315 (onset 268)	296
Degree of polymerisation	-	-	-	3900 – 4200	3600 – 3900	-
Crystallinity index (%)	93	88	-	89.07 ± 1.6	86.83 ± 0.66	-
Zeta potential (mV)	Average -23.3 ± 5.4			-7.48 ~ -16.9	-40.3 ~ -57.2	-
Elemental analysis	-	-	-	C 42.72%; H 6.14%; O 48.14%; N <0.05%; S <0.01%		-

3.3.2.3.1 Tunicate-derived nanocellulose

As a relatively new product on market, there were limited published data regarding the biocompatibility of the tunicate-derived nanocellulose from Ocean Tunicell used in this study. The next section provides a focused overview of 12 published studies specific for this nanocellulose form, which differs to the broader approach taken in the discussion of the biocompatibility of nanocellulose for tissue engineering in section 1.4.3.

Of the 12 studies, the majority (9 studies) were intended for tissue regeneration applications, with 2 studies looking at wound dressings [266, 267] and 1 for microbeads purposes [269]. Only one out of nine studies assessed chondrocytes for cartilage regeneration[270]. Fat was the most common tissue type with three studies [271-273], followed by cornea (eye) [233, 265] and vascular tissue [273, 274] with two studies each. A further study utilised human dermal fibroblast to study tissue engineering applications, with no specific end-organ target stated [232].

All nine studies evaluated cross-linked constructs consisting of a hybrid material which included nanocellulose. As such, independent effects of nanocellulose were not assessed, with the approach of this chapter distinct to those reported in the literature and therefore results are not directly comparable. Of the three variably functionalised forms of nanocellulose, ETC were the most commonly studied (5 studies) [232, 272-275], followed by TTC (2 studies) [233, 265]. In two articles, the specific form of nanocellulose was not stated [270, 271], and at the point of writing, there was no published data relating to CTC. As hybrid materials, alginate was combined with nanocellulose, with or without additional additives, in all but one study where collagen was used instead [233].

Within these 9 studies, there were four *in vivo* studies, 1 *ex vivo*, 1 *in vitro* and 3 mixed studies with both *in vitro* and *in vivo* components. Of the four studies which included *in vitro* assessments, live/dead staining was uniformly employed [232, 273, 274], except in one study where only live staining was performed [233]. Oskarsdotter *et al* also assessed morphology (nuclei and actin filament on confocal microscopy) [273], whilst Xeroudaki *et al* assessed endothelial cell gene expression by HUVECs [233]. Lastly, Boix-Lemonche *et al* examined cell viability with alternative methodology using PrestoBlue in an *ex vivo* cultured porcine corneal model [265]. This quantifies the amount of resazurin converted to fluorescent resorufin by live cells.

3.3.2.3.2 HFF-1 cell line (human dermal fibroblast)

Unfortunately, in the case of nanocellulose, it had not been feasible to study the impact of nanocellulose on dermal fibroblast alone. As described in section 3.3.2.1, pilot models were trialled without success when using physiologically relevant concentrations of nanocellulose. The incorporation of Transwell inserts translated to indirect material-cell contact, which did not mimic the *in vivo* scenario. Whilst alternative measure of cytotoxicity and pro-inflammatory response could be explored, the models both in theory and supported by pilot data suggested that the critical limiting factor was incompatible culture condition. As dermal fibroblast was used to understand potential material-host interaction and was not the core cell type (i.e. chondrocytes for cartilage tissue engineering), whilst undesirable, the lack of the dermal fibroblast mono-culture and co-culture did not hinder achieving the chapter aims.

3.3.2.3.3 C20A4 cell line (human chondrocyte)

Regarding the effect of nanocellulose on chondrocytes, it was interesting to note the varying pro-inflammatory effects of the three variably functionalised tunicate-derived nanocellulose, despite comparable cytotoxic effects as measured by the LDH assay. Whilst full material characterisation data is not available, there are notable differences between the three nanocellulose forms (table 3.1). Of note, the aspect ratio differed by around 50-60 between each form, with ETC being the lowest and CTC the largest. The zeta potential of ETC was also markedly lower than that of TTC. This may potentially explain the higher OD observed with ETC when incubated with sterile PBS. The relative lower zeta potential of ETC could contribute towards greater degree of material agglomeration due to material instability. Whilst understanding structure-activity relationship is outwith the remit of this project, the data from this chapter permitted an evidence-based selection of the optimal nanocellulose form to take forward for the final bio-ink formulation. As outlined above, to date, there is a paucity of studies directly comparing the three forms of tunicate-derived nanocellulose. This study contributes towards a knowledge gap in the literature by investigating the three nanocellulose forms in terms of cytotoxicity and pro-inflammatory effects against a human chondrocyte cell line, which has not been previously reported.

3.3.2.3.4 Barriers to achieving a physiologically relevant *in vitro* model

In order to mimic the *in vivo* scenario of an implanted cell-laden cartilage tissue engineered construct, the composite bio-ink will not only be cross-linked, but interacts with chondrocytes and fibroblasts in differing manners. Whilst both cell types will be in direct contact with the material, the chondrocytes will be dispersed within the nanocellulose to mimic the cell-laden bio-ink, whilst the fibroblasts will be exposed to one surface of the nanocellulose to mimic the implant-host contact interface. This presented inherent challenges, and indeed barriers, to studying the effect of a single component of a composite bio-ink whilst respecting various parameters to achieve a realistic exposure scenario. This was particularly the case with HFF-1, whereby various models were trialled without success. However, it is helpful to characterise and understand the biological effects of nanocellulose singularly, against each cell type, prior to observing their effects when combined with alginate and/or HA, and in a co-culture system, in adherence to the pre-cautionary principle in toxicology.

3.4 Chapter Summary and Conclusion

The overarching approach of chapters 3, 4 and 5 involves understanding the impact of each bio-ink component independently and prior to cross-linkage, on both chondrocytes, dermal fibroblasts and co-culture setting. This would permit selection of the optimal material forms to refine the bio-ink and cross-linkage processes before the assessment of the cross-linked cell-laden bio-ink in the form of an advanced *in vitro* 3D model.

This chapter addressed the core bio-ink ingredient, Nanocellulose, exploring both pulp- and tunicate-derived forms. The aims were two-fold, focusing on: i) biological impact of nanocellulose, and ii) selection of an optimal form for final bio-ink formulation. Microbial growth assay tested material sterility and excluded pulp-derived nanocellulose from further testing due to non-sterility. Biological effects were assessed *via* the LDH assay and IL-6 and IL-8 release *via* ELISA for cytotoxicity and pro-inflammatory response, respectively. Testing against chondrocytes revealed comparable cytotoxic effects, whilst the three variably functionalised tunicate-derived nanocellulose produced distinct pro-inflammatory effects, with ETC deemed the least pro-inflammatory. A summary of conclusions and recommendations from this chapter to be taken forward for the project is provided in table 3.2.

Table 3.2 Summary of chapter conclusions and take-on messages.

Conclusions	
Sterility	• Only tunicate-derived nanocellulose met sterility threshold.
Cytotoxicity	• No superiority between ETC, TTC and CTC.
Pro-inflammatory effects	• TTC > CTC > ETC in pro-inflammatory effects on chondrocytes.
Recommendations	
• ETC taken forward as the biologically most suitable nanocellulose form for final bio-ink formulation.	

Chapter 4: Alginate – additive bio-ink material: Establishing sterility, its biological effects on HFF-1 and C20A4 cell lines and cross-linkage behaviour

4.1 Introduction

Tissue engineering *via* 3D bioprinting necessitate a biocompatible cell carrier, which can dually function as an 'ink', with flow properties that permits extrusion through the printer nozzle, and can be transformed post-print into a solid, stable construct for clinical implantation.

Hydrogels are networks of cross-linked polymer chains that can absorb large volumes of water, but are insoluble in aqueous condition [276, 277]. Their high-water content and porous architecture mimic the extracellular matrix of human soft tissue, leading to its broad biomedical application, including as contact lens in the 1960s, and more recently, tissue engineering scaffolds. Although nanocellulose lends favourable mechanical and rheological (flow) properties as a bio-ink component, it requires an additive material to provide cross-linking ability for hydrogel formation.

Alginate is currently the most commonly cited natural bio-material for extrusion-based bio-printing, applied either alone or combined as hybrid bio-inks [100]. When paired with nanocellulose, the hybrid bio-ink brings together benefits of each material, with the inclusion of alginate crucially permitting cross-linking, also known as gelation. The external gelation method, a widely adopted cross-linking strategy, involves adding divalent cations (such as Ca^{++} in soluble salt solution form - calcium chloride ($CaCl_2$)) to the anionic alginate. As calcium ions permeates through the alginate from outside in, non-covalent, ionic cross-linking occurs alongside hydrogel formation [278, 279].

The significance of cross-linking lies in both its requirement as a stabilisation process in polymer chemistry to achieve a solid implantable construct, and biologically, as a potential source of toxicity in tissue engineered products.

This chapter focuses on alginate, an additive material of the hybrid bio-ink under investigation. It is part of a series of three chapters (chapter 3, 4 and 5) which investigates the biological effects of each individual bio-ink components separately. Additional studies required for the creation of the SOP for the advanced 3D *in vitro* model (appendix 1), relevant to the bio-ink ETC:Alginate, are also included. Broadly, this is comprised of examination of the gelation process and the biological impact of the cross-linker agent, $CaCl_2$.

The aims of this chapter were:

i) To establish the cytotoxic and pro-inflammatory effects of alginate on HFF-1 and C20A4 cell lines.

ii) To define the optimal cross-linking process of the ETC:alginate bio-ink using $CaCl_2$, with respect to developing a 3D *in vitro* model.

The above aims were met *via* the objectives below:

1. To establish standardised material preparatory procedure for alginate.
2. To investigate the sterility of alginate over 21 days.
3. To assess the cytotoxicity and pro-inflammatory response of HFF-1 and C20A4 when exposed to alginate.
4. To assess the cytotoxicity and pro-inflammatory response of HFF-1 and C20A4 when exposed to $CaCl_2$.
5. To define the minimum gelation time required, relating to aim (ii).
6. To define the gelation point of ETC:alginate bio-ink when cross-linked with $CaCl_2$.
7. To select the optimal $CaCl_2$ concentration and duration of application, relating to aim (ii).

4.2 Methods

All methods used in this chapter were previously described in Chapter 2 (Materials and Methods), with sections referenced detailed below. Figure 4.1 outlines the workflow of this chapter.

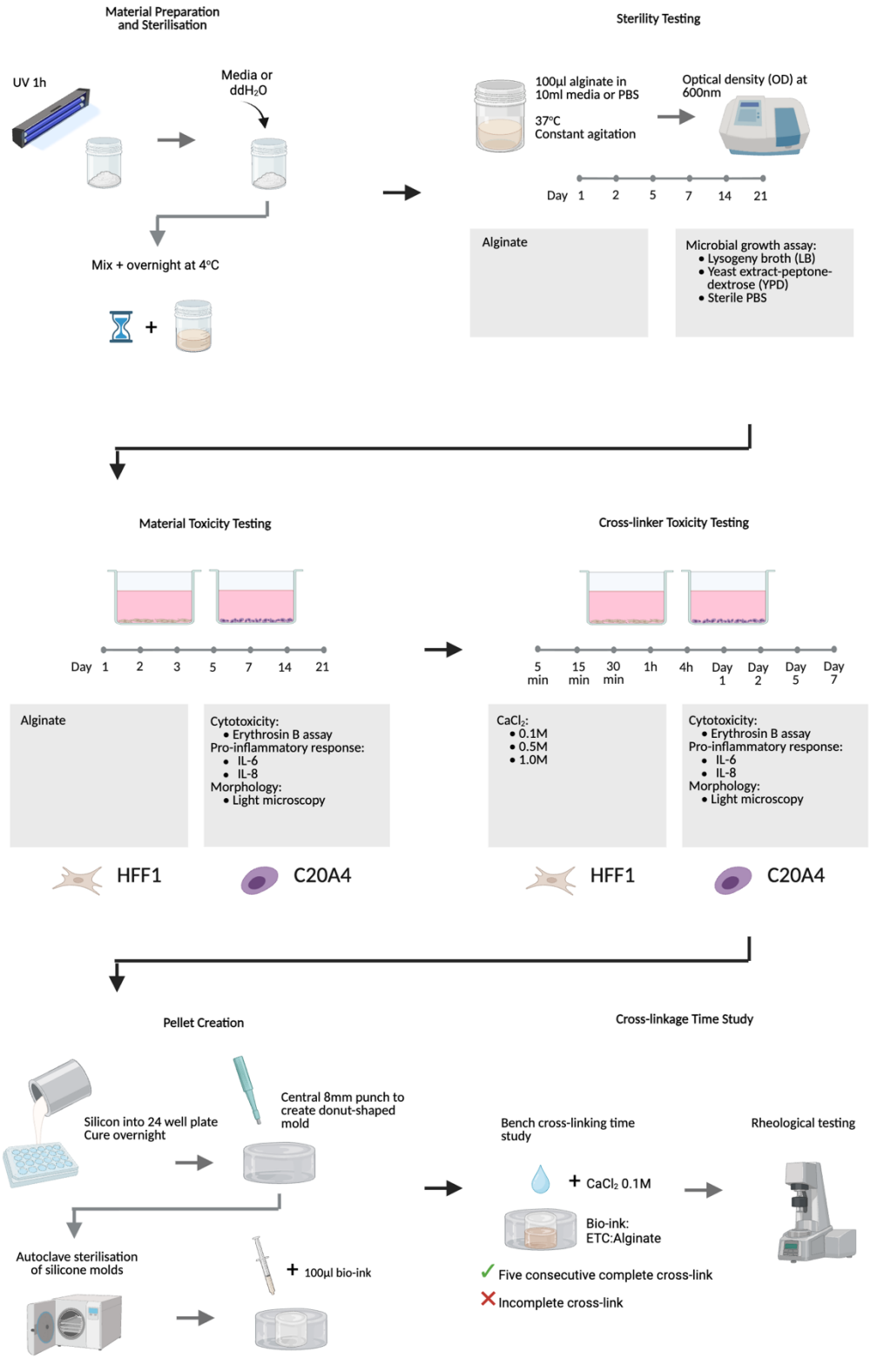

Figure 4.1 Schematic of chapter 4 workflow. *There are six components to the workflow of chapter 4. This begins with material preparation and sterilisation. Alginate was sterilised by UV irradiation for 1 hour, following which it was reconstituted in either media or double-distilled water (ddH_2O). Following dissolution and mixing, it was stored overnight at 4°C. The next step was sterility testing, which involved incubating 100µl alginate in 10ml of lysogeny broth (LB), yeast extract-peptone-dextrose (YPD) or sterile PBS, at 37°C under constant agitation. Optical density was measured at 600nm. This was then followed by material and cross-linker toxicity testing. Both involved HFF-1 and C20A4 cell lines in 2D culture exposed to alginate (material) or calcium chloride ($CaCl_2$, cross-linker). Cytotoxicity (erythrosin B assay), pro-inflammatory effects (IL-6 and IL-8 release) and morphology were assessed. The next step was pellet creation, which briefly involved the addition of silicone to 24 well plate and following curing overnight, an 8mm punch cutter was applied centrally to create a donut-shaped silicone mold. This was sterilised by autoclaving. The chapter completes with the study of cross-linkage time. This was dually assessed with bench cross-linking study to identify the minimum time required for 5 consecutive successful cross-link, and with rheological testing. Created with BioRender.com.*

4.2.1 Sterilisation and material preparation for alginate

The alginate form and concentration used in this study (sections 2.3.1 and 2.3.2.2), sterilisation methods and material preparation protocol (section 2.3.3.2), alongside rationale for their selection, were previously described in Chapter 2.

All alginate used in this study were reconstituted in cell culture media, except when otherwise specified. Sterile ddH_2O was used as the alternative solvent. This was applied for sterility testing, pilot testing of gelation studies with pulp-derived nanocellulose, and during gelation studies using ETC-based bio-ink for comparison testing between media and ddH_2O.

4.2.2 Material sterility testing

Microbial growth assay was conducted with LB, YPD and sterile PBS over 21 days to examine material sterility, as described in greater detail in section 2.6. In the same manner as sterility testing of nanocellulose, the study period was extended to 21 days. However, in contrast to ETC, where stock preparation from supplier was tested, alginate in powder form was first reconstituted in sterile ddH_2O prior to sterility testing. Sterile ddH_2O was used instead of culture media to minimise potential sources of contamination. Bacterial isolation was not conducted as all samples remained within the threshold for sterility (optical density <0.1).

4.2.3 Toxicity testing of material (alginate) and cross-linker ($CaCl_2$) on HFF-1 and C20A4 cell lines

Both alginate and $CaCl_2$ were independently tested against HFF-1 and C20A4 cell lines to elucidate their effects on cytotoxicity and pro-inflammatory response. The

parameters of both material and cross-linker toxicity testing are depicted in figure 4.1, and expanded upon in sections below.

Alginate used during *in vitro* cell culture was reconstituted in culture media [224], as opposed to sterile ddH_2O [223], to avoid the risk of cytolysis. Cells in hypotonic solution, such as ddH_2O, experience a net movement of free water into the cell *via* osmosis. This leads to increased intracellular volume and eventual cell lysis. The use of culture media over sterile ddH_2O as solvent for alginate aimed to minimise the potential confounding variable when cytotoxicity is observed.

Timepoints for alginate were designed to be consistent across all material toxicity testing. This includes the acute timeframe of day 1, 2, 3, 5 and 7, and chronic time periods of day 14 and 21.

Timepoints for $CaCl_2$ differed to reflect realistic exposure and worst-case scenarios. Shorter time course of 5min, 15min and 30min provides information of anticipated cross-linking duration. For the 3D *in vitro* model, the crosslinking agent is removed and the crosslinked pellet is washed with PBS prior to being submerged in media for culture. Whilst this process removes the majority of cross-linking agent, it is anticipated that a small amount will remain, having permeated through the hydrogel pellet. Timepoints at 1 hour, 4 hours, day 1 and 2 provide an intermediate view of the prolonged effect of $CaCl_2$ on both cell types, whilst timepoints at day 5 and 7 represent the worst case scenario.

Three $CaCl_2$ concentrations (0.1M, 0.5M and 1.0M) were tested based on published work[223, 224].

4.2.3.1 Cell culture

Cell culture methodologies for HFF-1 and C20A4 were as described in section 2.7.

4.2.3.2 Erythrosin B exclusion assay

Cytotoxicity of all 2D cultures conducted in chapter 5 was assessed using the erythrosin B exclusion assay, as detailed in section 2.8.2.

4.2.3.3 ELISA

The release of IL-6 and IL-8 by both cell types were measured *via* ELISA to assess the pro-inflammatory response induced by exposure to alginate and $CaCl_2$. Methodologies for ELISA are described in section 2.8.3, whilst the calculation for chemokine release per cell was calculated in section 2.13.

4.2.3.4 Light microscopy

Cell morphology was examined using light microscopy as detailed in section 2.8.4.

4.2.4 Gelation of Nanocellulose:Alginate bio-inks

Gelation was primarily tested against bio-ink made of tunicate-derived nanocellulose ETC and alginate, now termed 'ETC:Alginate'. Initial pilot testing was conducted with pulp-derived nanocellulose, prior to knowledge of their non-sterility. All bio-inks tested consisted of the same nanocellulose and alginate concentrations, as detailed in table 2.5. Bio-inks tested were specified to denote which nanocellulose forms were used in subsequent results sections.

Bio-inks creation followed a series of protocols described in section 2.3, which encompasses material preparation and sterilisation steps, concentrations used for both nanocellulose and alginate, and procedures for material mixing and bio-ink preparation.

4.2.4.1 Determination of minimum gelation time in silicon molds

To simulate 3D bio-printed constructs and to produce standardised pellets for the 3D *in vitro* models for future biocompatibility testing, 100µl bio-ink were cross-linked into 8mm wide disc-shaped pellets using silicon molds as described in section 2.10.2.

The purpose of the bench-top gelation study was to determine the minimum time required to achieve solidified bio-ink pellets suitable for use in an *in vitro* model. Relevant methodologies are described in section 2.11. Variables tested are summarised in table 4.1. Key distinctions between initial pilot and subsequent testing, and the rationale behind the adjustments, were:

i. Transition from pulp-derived to tunicate-derived nanocellulose, based on non-sterility of pulp-derived nanocellulose (detailed in section 3.3.1).
ii. Comparison of both solvents for alginate, as it was hypothesised that media would be more biocompatible than sterile ddH_2O.
iii. Transition to single cross-linker concentration; 0.1M was chosen due to its lesser cytotoxic effects (section 4.3.3) and permissive cross-linking ability as determined during pilot testing.

Table 4.1 Overview of bio-inks, solvents used for alginate and cross-linker concentrations tested in pilot and formal study of minimum gelation time in silicon molds. **All bio-inks used in the pilot phase were pulp-derived nanocellulose (NCB, CNC, CNF), whilst tunicate-derived nanocellulose were used subsequently (ETC, TTC, CTC).*

Pilot			**Study**		
Bio-inks*	***Solvent for Alginate***	***$CaCl_2$ concentration***	***Bio-inks****	***Solvent for Alginate***	***$CaCl_2$ concentration***
NCB:Alginate	ddH_2O	0.1M	ETC:Alginate	ddH_2O	0.1M
CNC:Alginate		0.5M	TTC:Alginate	Media	
CNF:Alginate		1.0M	CTC:Alginate		

4.2.4.2 Rheological study of gelation

Rheological study was initially employed as an attempt to define the gel point and to describe quantitatively and temporally the material behavioural change of the bio-inks when exposed to cross-linker $CaCl_2$.

Methodology for the oscillatory time sweep experiment was detailed in sections 2.12.2, 2.12.3 and 2.12.4. All rheological tests were conducted with 0.1M $CaCl_2$. Initial pilot testing was performed with pulp-derived NCB:Alginate bio-ink, whilst subsequent testing used tunicate-derived nanocellulose ETC. Two bio-inks were tested to compare the material performance between alginate reconstituted in media versus sterile ddH_2O, and are named 'ETC:Alginate (media)' and 'ETC:Alginate (ddH_2O)', respectively.

4.3 Results and Discussion

4.3.1 Material sterility testing

Both UV-treated and untreated alginate were considered sterile up to day 21, demonstrating an optical density of <0.1 in both culture media of LB and YPD (figure 4.2 A+B). As alginate remained far below the accepted threshold for sterility, whilst there was no concern regarding the effect of agglomeration impacting heightened optical density, all material were subjected to the same sterility testing methodology. In this case, alginate maintained OD of <0.1 in sterile PDS throughout the study period (figure 4.2C). These results implied that UV-sterilised alginate was suitable for use in the advanced *in vitro* model up to 21 days.

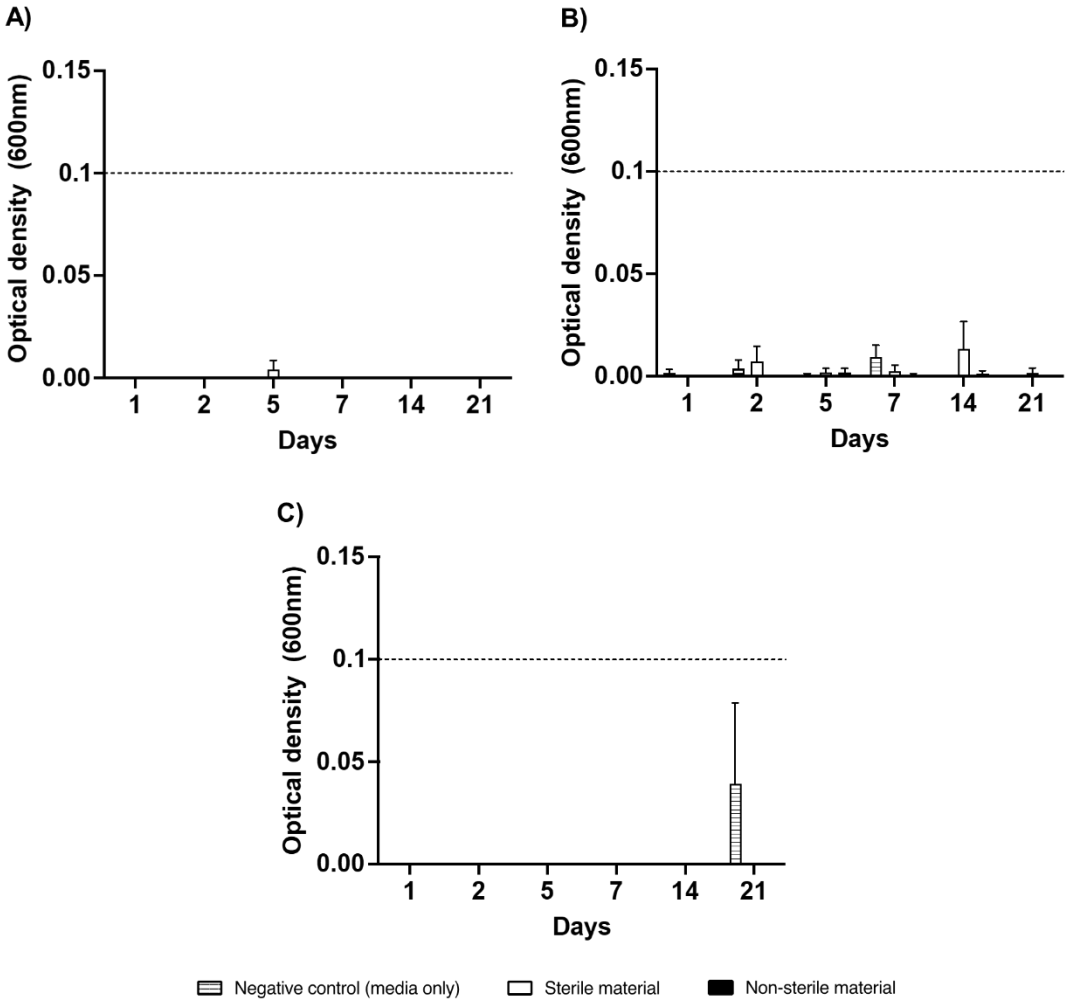

Figure 4.2 Sterility testing of alginate. *Assessment of sterility and material effects of alginate on optical density in A) lysogeny broth (LB), B) yeast extract-peptone-dextrose (YPD) and C) sterile PBS. UV-sterilised and non-sterilised alginate in LB, YPD or sterile PBS were incubated at 37°C under constant agitation over 21 days. Media or PBS without alginate served as negative control. Optical density measured at 600nm. Accepted arbitrary threshold for sterility at <0.1 denoted by horizontal dotted line. Mean±SEM is shown. N=3.*

4.3.2 Material toxicity testing

4.3.2.1 HFF-1 cell line (human dermal fibroblast)

4.3.2.1.1 Cytotoxicity

No adverse impact on cell viability was observed when alginate was exposed to HFF-1. Total and live cell concentrations of HFF-1 exposed to alginate followed similar trends to the negative control (figure 4.3A/B). There was no statistically significant difference between cells exposed to alginate versus negative control across all three measures (total and live cell concentrations, and cell viability).

A rise in total and live cell concentrations was seen between day 1 and 14, followed by a decline on day 21. The decline in cell concentration on day 21 likely reflected the impact of over-confluence, although cell viability was maintained throughout the study period. Timepoint comparison for HFF-1 exposed to alginate also demonstrated no statistically significant change of total and live cell concentrations or cell viability between all timepoints.

The application of Triton X-100 as positive control induced statistically significant cytotoxic effects at all timepoints for total cell concentration ($p<0.01$), live cell concentration ($p<0.001$) and cell viability ($p<0.0001$) (not shown in figure 4.3 A-C). Thus, confirming the vulnerability of HFF-1 to cytotoxic compounds, and measurable cytotoxic effects *via* the erythrosin B exclusion assay.

These results indicated that UV-treated alginate did not elicit cytotoxic effect on HFF-1 and therefore was suitable as a bio-ink component and for use in the 3D *in vitro* model for up to 21 days.

4.3.2.1.2 Pro-inflammatory response

Both HFF-1 exposed to alginate and negative control displayed relatively low levels of IL-6 and IL-8 release, up to day 7 (figure 4.4). This was followed by a rise in both chemokines on day 14 and 21, which was statistically significant on day 21. This is suggestive of cell activation and heightened pro-inflammatory response at latter timepoints.

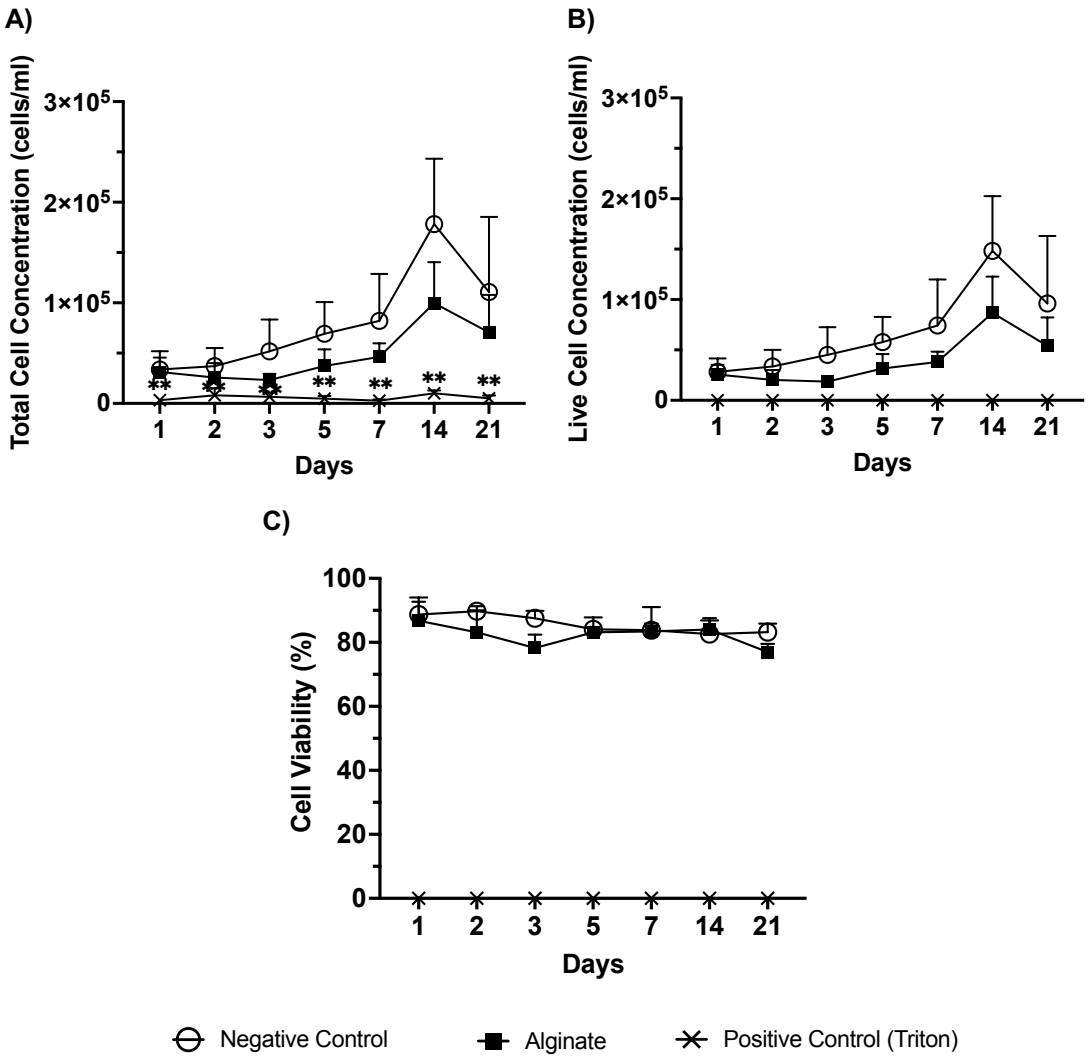

Figure 4.3 Cytotoxicity of HFF-1 2D monoculture exposed to alginate over 21 days. *Total (A) and live (B) cell concentrations and cell viability (C) assessed with erythrosin B assay. Positive control was 0.1% Triton X-100. Mean±SEM is presented. N=3.*

Whilst HFF-1 exposed to alginate displayed lower levels of IL-6 and IL-8 release when compared to negative control, there were no statistical difference at all timepoints. This implies that HFF-1 when exposed to alginate in studied conditions did not produce an exacerbated pro-inflammatory response, nor did exposure to alginate offered a protective effect.

Regarding assay validity, there was no demonstratable interference of the assay from the material with non-detectable to very low level of IL-6 and IL-8 measured with the material only negative control.

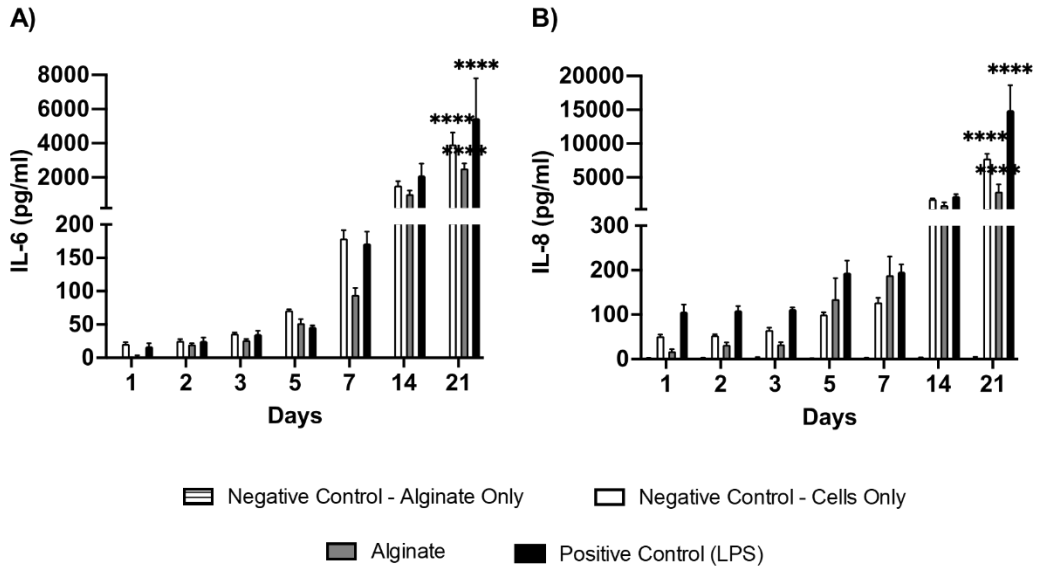

Figure 4.4 Pro-inflammatory effect of alginate on HFF-1 2D monoculture over 21 days. *IL-6 (A) and IL-8 (B) release were measured with ELISA. Negative control consisted of HFF-1 2D monoculture without material exposure. Positive control was LPS. Material interference on assay was investigated with material treated to the same experimental conditions, termed 'negative control – alginate only'. Mean±SEM is presented. N=3. Statistical significance on timepoint comparisons D1 v D2-21 of each culture conditions are denoted by: $p<0.05$ *, $p<0.01$ **, $p<0.001$ *** and $p<0.0001$ ****.*

Due to the greater total and live cell numbers of HFF-1 in negative controls compared to cells exposed to alginate, the relative high levels of chemokine release witnessed in negative controls could be attributed to greater cell number. As such, IL-6 and IL-8 released per cell were calculated to permit a more comparable assessment. Results were similar to prior comparisons. Time course comparison for all cell culture conditions showed a rise in chemokine release on day 14 and 21, which reached statistical significance on day 21 for both IL-6 and IL-8 (figure 4.5). IL-6 and IL-8 release per cell were comparable between HFF-1 exposed to alginate versus negative control at all timepoints. Statistically significant increases in IL-8 release per cell was seen with positive control (LPS) when compared to negative control at all timepoints ($p<0.05$), although not shown in figure 4.5B. Overall, the results indicates that exposure of alginate to HFF-1 in 2D culture did not elicit a pro-inflammatory response up to 21 days, and remain suitable for bio-ink creation purposes.

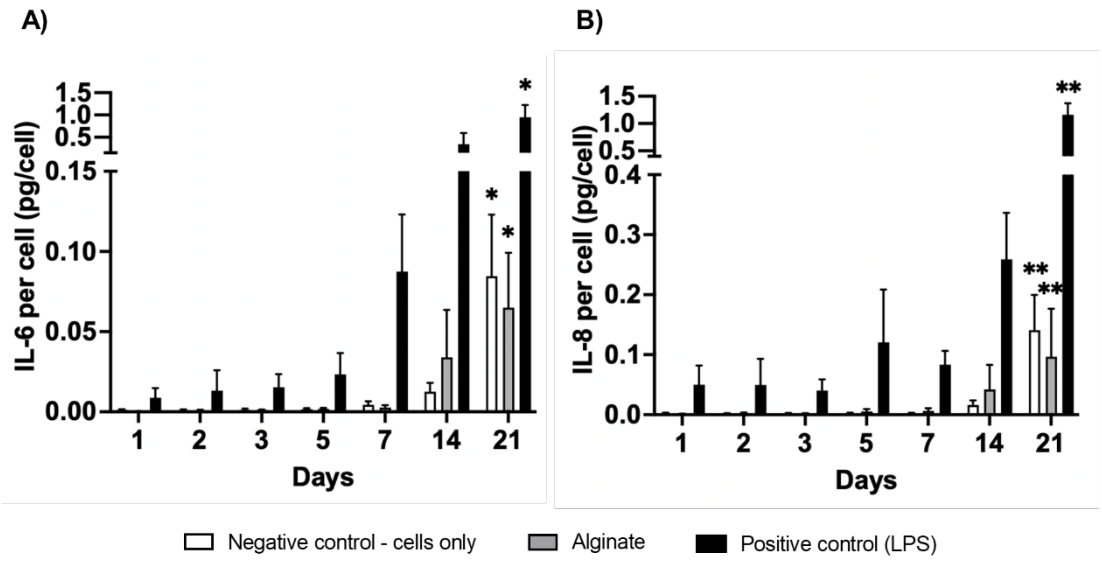

Figure 4.5 Pro-inflammatory effect per cell of alginate on HFF-1 2D monoculture over 21 days. *IL-6 (A) and IL-8 (B) release were measured with ELISA, and chemokine released per cell were calculated relative to total cell number at each timepoint. Negative control consisted of HFF-1 2D monoculture without material exposure. Positive control was LPS (1μg/ml). Mean±SEM is presented. N=3. Statistical significance on timepoint comparisons D1 v D2-21 of each culture condition are denoted by: p<0.05 *, p<0.01 **, p<0.001 *** and p<0.0001 ****.*

4.3.2.1.3 Cell morphology

Light microscopy images reflected findings from the erythrosin B exclusion assay (section 4.3.2.1.1). Cells showed increasing cell density from day 1 to 14 in the negative control, mirroring the rise in total cell concentration. A similar trend was observed with HFF-1 exposed to alginate, but at a lesser magnitude. Alginate in media appeared to have led to a cloudy appearance in light microscopy, although cell morphology remains distinguishable. This was not significantly altered compared negative control, except for the slower speed in reaching confluence. Positive control with 0.1% Triton X-100 was effective in causing near total cytotoxicity. As such, the image from day 1 was considered representative for all timepoints up to day 21.

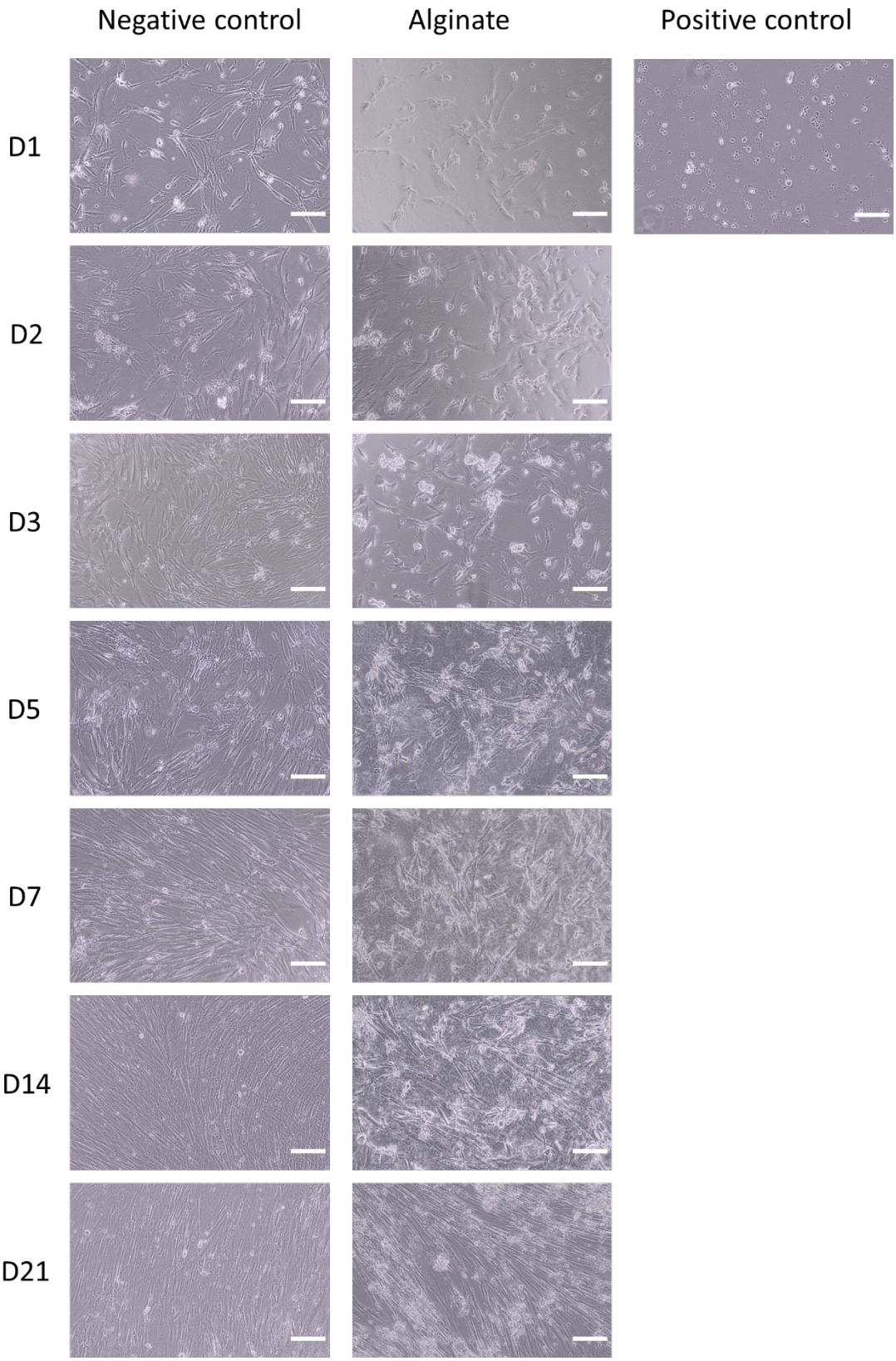

Figure 4.6 Light microscopy of alginate exposure on HFF-1 2D monoculture over 21 days. *Negative control represent cell-only culture. Positive control was 0.1% Triton X-100. Three biological replicates with 3 field of view per sample. Representative images shown. Only day 1 was displayed for positive control as significant cytotoxicity reached at first timepoint, with no significant morphological changes over time. Scale bars represent 200μm.*

4.3.2.2 C20A4 cell line (human chondrocyte)

This section focuses on the second cell type, human chondrocyte, exploring the cytotoxicity, pro-inflammatory effects of alginate and its impact on cell morphology on C20A4 in 2D culture.

4.3.2.2.1 Cytotoxicity

Total and live cell concentration, and cell viability of C20A4 exposed to alginate were not significantly different to negative control at all timepoints tested. In contrast, positive control (Triton X-100) was able to induce statistically significant reductions in total and live cell concentration, and cell viability of C20A4 at all timepoints when compared with negative control ($p<0.0001$; not shown in figure 4.7). Overall, this suggests preserved cell viability when C20A4 was exposed to Alginate.

On review of each culture condition over time, the total and live cell concentration for C20A4 exposed to alginate and negative controls remained comparable throughout the study period. There was a small decline in live cell concentration on day 21, although this was not statistically significant. Cell viability over this period, however, did show a statistically significant drop on day 21 for both C20A4 exposed to alginate and negative control ($p<0.001$). This suggests limitation of model with cell culture conditions impacting cell viability on day 21, which is consistent with the findings from cell line characterisation (detailed in section 2.8.5.2.1).

4.3.2.2.2 Pro-inflammatory response

Exposure to alginate did not elicit a heightened pro-inflammatory response in the forms of raised IL-6 and IL-8 release by C20A4 when compared to negative control over the 21 day period. In contrast, significant increase in chemokine release was seen with the positive control (LPS) when compared to negative control throughout the study period ($p<0.0001$ for IL-6 at all timepoints; $p<0.05$ for IL-8 at all timepoints; not shown in figure 4.8). This suggests that exposure to alginate did not stimulate a heightened pro-inflammatory response by C20A4.

Material interference on the assay was negligible, with non-detectable to very low level of chemokines measured across all timepoints.

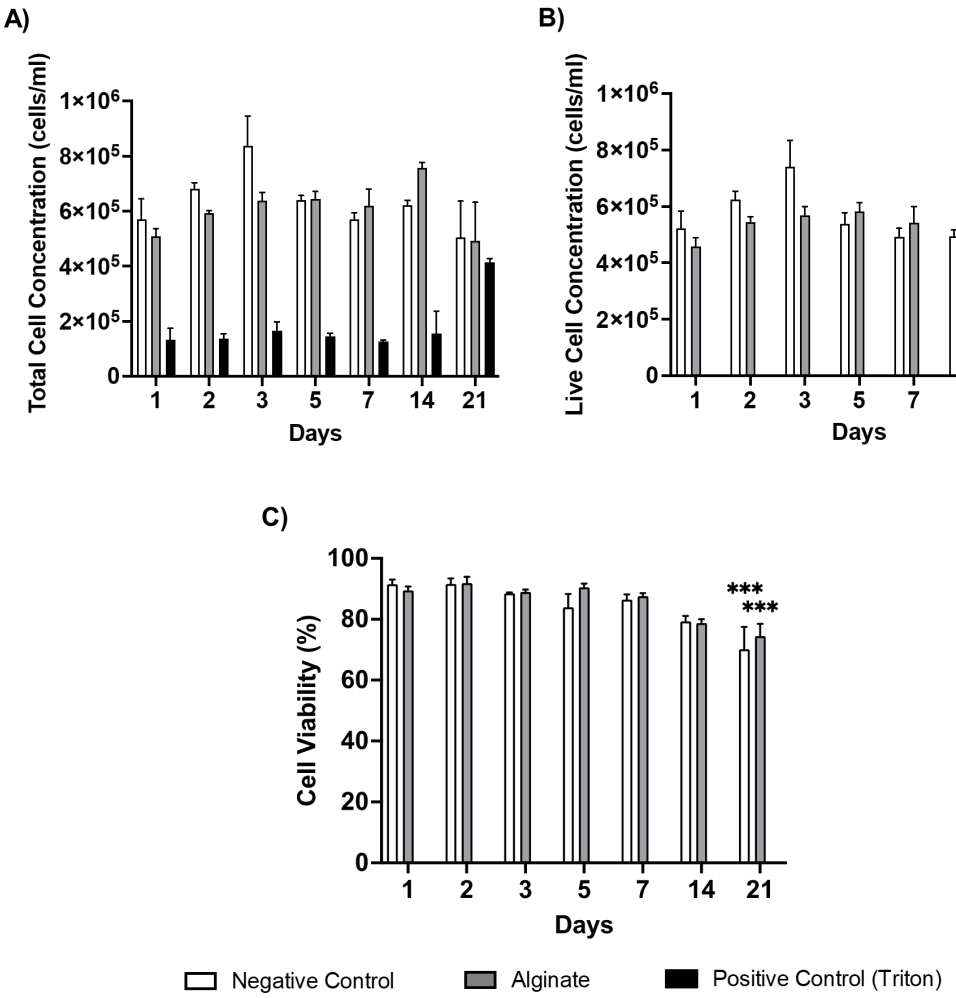

Figure 4.7 Cytotoxicity of 2D monoculture of C20A4 exposed to alginate over 21 days. *Total (A) and live (B) cell concentration and cell viability (C) assessed with erythrosin B assay. Positive control was 0.1% Triton. Mean±SEM is presented. N=3. Statistical significance on timepoint comparisons D1 v D2-21 of each cell conditions are denoted by: p<0.05 *, p<0.01 **, p<0.001 *** and p<0.0001 ****.*

There is an overall rising trend of chemokine release by C20A4 when exposed to alginate and in negative controls, reaching statistical significance on day 21 (figure 4.8). Similar to HFF-1, IL-6 and IL-8 release were less with C20A4 exposed to alginate when compared to negative control. The discrepancies of IL-6 and IL-8 release between cells exposed to alginate and negative control were most marked on latter timepoints. However, total and live cell concentration were fairly comparable between cells exposed to alginate and negative control. This suggests that the rise in chemokines was not a result of increased cell numbers. Hence, chemokine release per cell was calculated next in the same manner as with HFF-1, to provide an alternative perspective of chemokine release in the system tested.

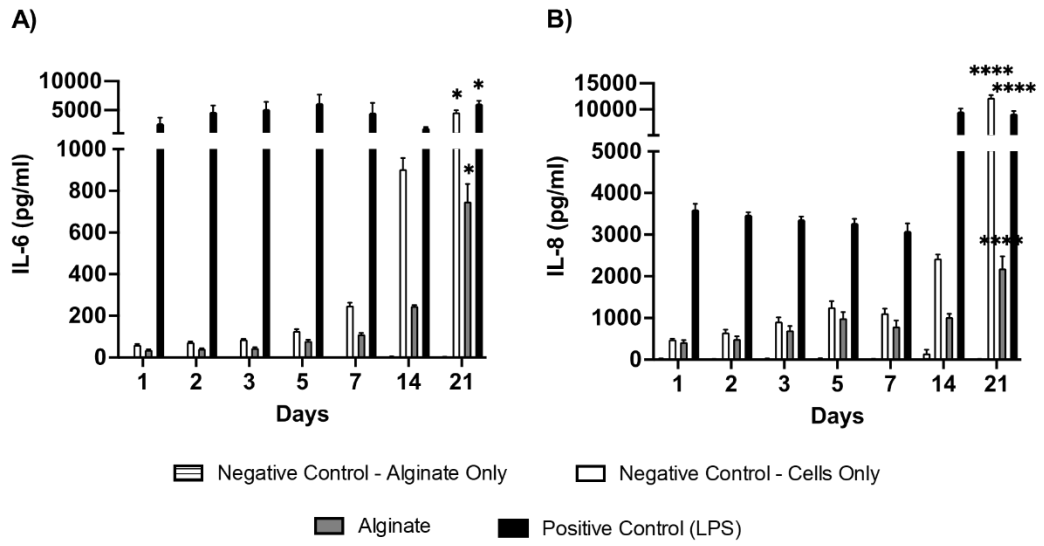

Figure 4.8 Pro-inflammatory effect of alginate on C20A4 2D monoculture over 21 days. *IL-6 (A) and IL-8 (B) release were measured with ELISA. Negative control consisted of C20A4 2D monoculture without material exposure. Positive control was LPS. Material interference on assay was investigated with material treated to the same experimental conditions, termed 'negative control – alginate only'. Mean±SEM is presented. N=3. Statistical significance on timepoint comparisons D1 v D2-21 of each culture conditions are denoted by: p<0.05 *, p<0.01 **, p<0.001 *** and p<0.0001 ****.*

Similar trends were revealed when considering chemokines released per cell. IL-6 and IL-8 levels were consistently lower with C20A4 exposed to Alginate when compared to negative control. Whilst these differences were greater on day 14 and 21, they were not statistically significant (figure 4.9). Positive control using LPS, however, was able to stimulate a pro-inflammatory response with heightened IL-6 and IL-8 release per cell when compared to negative control at all timepoints. This was statistically significant only with IL-6 ($p<0.05$; not shown in figure 4.9). Finally, considering change over time, when adjusted for cell numbers, rise in chemokine release per cell was seen in both C20A4 exposed to alginate and negative control. The greatest rise was on day 21 for both IL-6 and IL-8, which was statistically significant with IL-8.

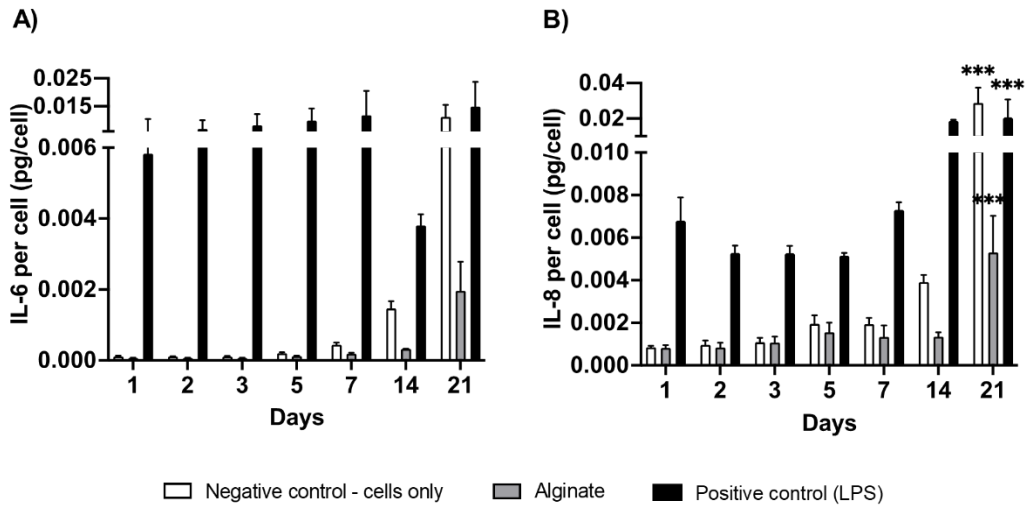

Figure 4.9 Pro-inflammatory effect per cell of alginate on C20A4 2D monoculture over 21 days. *IL-6 (A) and IL-8 (B) release were measured with ELISA, and chemokine released per cell were calculated relative to total cell number at each timepoint. Negative control consisted of C20A4 2D monoculture without material exposure. Positive control was LPS. Mean±SEM is presented. N=3. Statistical significance on timepoint comparisons D1 v D2-21 of each cell conditions are denoted by: p<0.05 *, p<0.01 **, p<0.001 *** and p<0.0001 ****.*

4.3.2.2.3 Cell morphology

The cell morphology of C20A4 when exposed to alginate at concentrations relevant to *in vivo* 3D bioprinting exposure scenarios (chondrocyte-embedded bio-inks) showed minimal change (figure 4.10). As demonstrated in the cell line characterisation, the seeding density of C20A4 achieved confluence on day 1, as was the case here both in the negative control and with alginate exposure. Arguably, due to cell over-confluency and the densely packed chondrocytes, it may be relatively more difficult to visualise subtle cell morphology alterations, especially when the chondrocytes have round or ellipsoidal shapes, unlike the fibroblast with a spindle-like morphology where morphological disturbance was more readily apparent.

A further observation is the ability to maintain 2D culture without auto-cell sheet detachment. The latter was observed during cell line characterisation with optimal media change regime. The adjusted media change to account for alginate dosing was associated with reduction in nutrients availability and in removal of cellular waste product, which were presumed to impact cell proliferation profile. The reduced total cell number overall in turn meant that the threshold where cell over-confluency leading to cell sheet detachment did not occur during the 21 day study period.

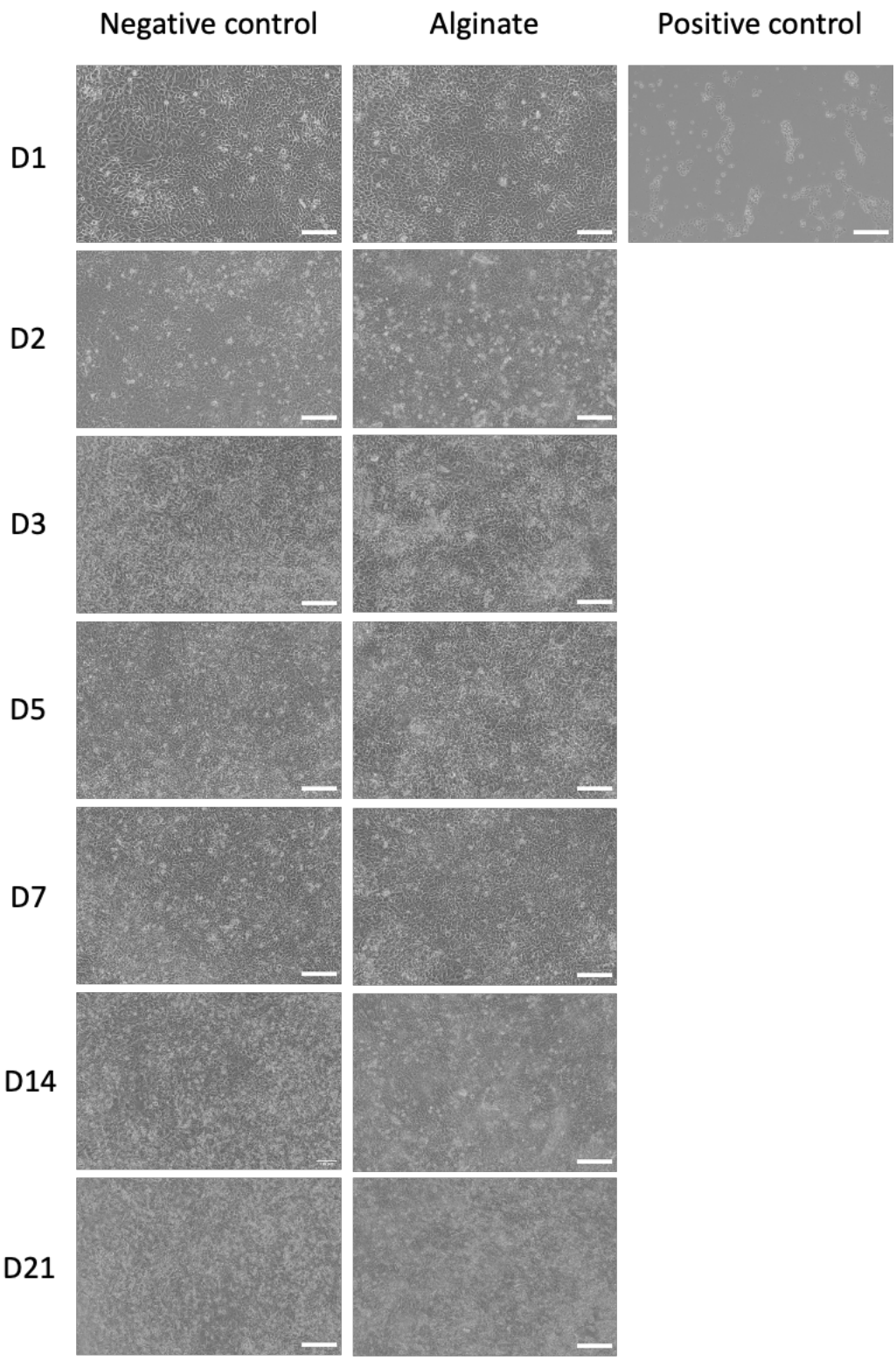

Figure 4.10 Light microscopy of the effect of alginate against C20A4 in 2D monoculture over 21 days. *Scale bars represent 200μm.*

4.3.2.3 Section summary - material toxicity testing

Alginate demonstrated no significant adverse cytotoxic or pro-inflammatory effects against both cell types in 2D culture. The results indicate that UV-treated alginate was suitable for use as a bio-ink component and as part of a 3D *in vitro* model for biocompatibility testing over a 21 day period.

4.3.3 Cross-linker toxicity testing

4.3.3.1 HFF-1 cell line (human dermal fibroblast)

4.3.3.1.1 Cytotoxicity

Direct comparison of total and live cell concentration and cell viability between 0.1M, 0.5M and 1.0M $CaCl_2$ concentrations showed no statistically significant difference across all timepoints.

However, total cell concentrations of HFF-1 were reduced when exposed to $CaCl_2$ at all time points compared to negative control. A more marked reduction was seen on day 5 and 7, which were statistically significant (figure 4.11A). Timepoint comparison showed a statistically significant rise in total cell concentration in negative control on day 5 ($p<0.0001$). This reflects increased cell proliferation, in line with previous cell line characterisation. In contrast, timepoint comparison for all $CaCl_2$ concentrations and positive control showed no statistically significant difference over time, which may indicate an inhibitory effect of $CaCl_2$ on HFF-1 cell proliferation.

Live cell concentrations of C20A4 exposed to $CaCl_2$ at all three concentrations and Triton X-100 as positive control showed statistically significant reduction at all timepoints ($p<0.0001$; figure 4.11B). This suggests that $CaCl_2$, even at the lowest concentration and at the shortest cross-linker application duration, has a significant cytotoxic effect on HFF-1. Although not statistically significant, a general downward trend of live cell concentration was seen with prolonged $CaCl_2$ exposure, suggestive of heightened cytotoxic effects with increasing duration of cross-linker application. This is mirrored in trends in cell viability. When compared to negative control, cell viability was reduced with application of $CaCl_2$. The higher the $CaCl_2$ concentration,

the shorter the amount of time required to reach statistically significant reduced cell viability (figure 4.11C).

Taken together, this data showed that $CaCl_2$ has a cytotoxic effect on HFF-1 in 2D culture. This adverse effect was greater with increasing concentration of $CaCl_2$. As such, this data supports the selection of the lowest $CaCl_2$ concentration 0.1M for future work. It could also be recommended that limiting cross-linker application duration will have lesser adverse impact on cytotoxicity.

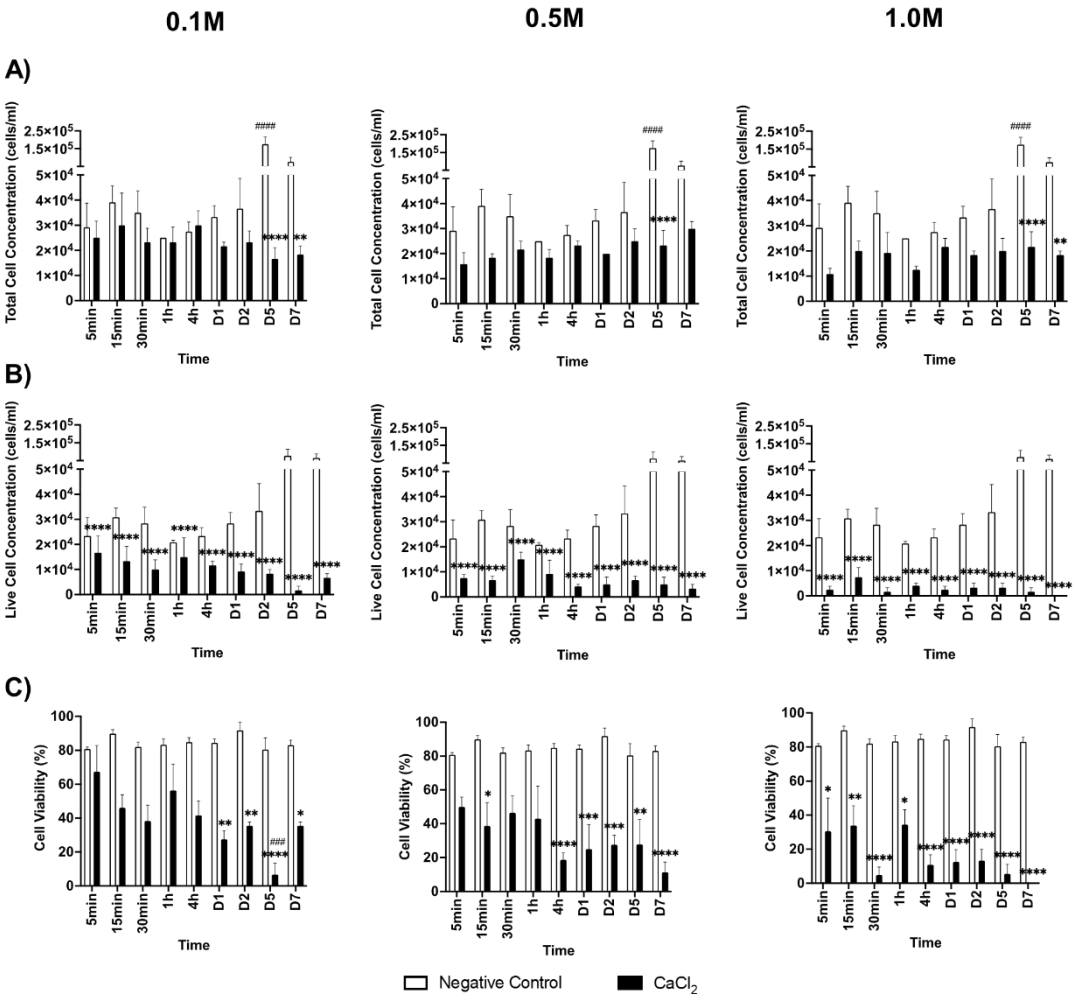

Figure 4.11 Cytotoxicity of HFF-1 exposed to cross-linker calcium chloride. *The effect of 0.1M, 0.5M and 1.0M calcium chloride ($CaCl_2$) were tested against 2D HFF-1 monocultures up to 7 days using erythrosin B assay. Total cell concentration (A), live cell concentration (B) and cell viability (C) were assessed. Positive control was 0.1% Triton X (not shown). Mean±SEM is presented. N=3. Comparison between negative control and $CaCl_2$ or positive control denoted by * and timepoint comparison of 5min v 15min to day 7 for each culture condition by #. Statistical significance is presented as: p<0.05 */#, p<0.01 **/##, p<0.001 ***/### and p<0.0001 ****/####.*

It is recognised that the worst-case scenario exposures exceed realistic dosage as the cross-linked constructs would undergo removal of crosslinker and wash steps prior to culture *in vitro.* I.e. cells were not directly exposed to $CaCl_2$ for the duration of the timepoints studied. Nonetheless, based on the external gelation method, a small amount of $CaCl_2$ which permeated the pellet would persist, and it was worthwhile to consider the effect of $CaCl_2$ on cells beyond the crosslinker application timeframe.

4.3.3.1.2 Pro-inflammatory response

Upon initial application of $CaCl_2$, HFF-1 mounted a greater pro-inflammatory response with 0.5M and 1.0M $CaCl_2$ as compared to 0.1M, with higher levels of IL-6 and IL-8 release. This was seen between 5 minutes to 4 hours although there was no statistical significance (figure 4.12A/C/E). This suggests that 0.1M yielded the least pro-inflammatory response against HFF-1 up to 4 hours.

However, beyond day 1, IL-6 and IL-8 release with 0.1M exceeded that with 0.5M and 1.0M, which was statistically significantly on day 5 and 7. This may be due to the cytotoxic effects of more concentrated $CaCl_2$, resulting in reduced number of live cells able to release chemokines. When compared to negative control, level of IL-6 released by HFF-1 exposed to 0.1M $CaCl_2$ were lower on day 5 and day 7, but this could be better interpretated when adjusted for cell numbers. On reviewing timepoint comparisons, IL-6 release in negative control showed a rising trend up to day 7, which reached statistical significance on day 5 and day 7 ($p<0.0001$). HFF-1 exposed to 0.1M $CaCl_2$ and positive control with LPS followed a similar trend, with statistical significance reached also on day 2.

IL-8 release by HFF-1 followed a similar pattern to IL-6 when exposed to $CaCl_2$ in that 0.5M and 1.0M elicited a greater release of IL-8 up to 4 hours, when compared to 0.1M. Following which, HFF-1 exposed to 0.1M $CaCl_2$ mounted a greater rise in IL-8 compared to negative control. This was statistically significant on day 5 and 7, both when compared to negative control, and for timepoint comparison to 5min (figure 4.12B).

Although statistical analysis yielded significant differences between 0.1M to 0.5M and 1.0M $CaCl_2$ on day 5 and 7, interpretation of pro-inflammatory effects must be

considered alongside the cytotoxic effects of higher $CaCl_2$ concentrations. Therefore, chemokine release per cell is now presented.

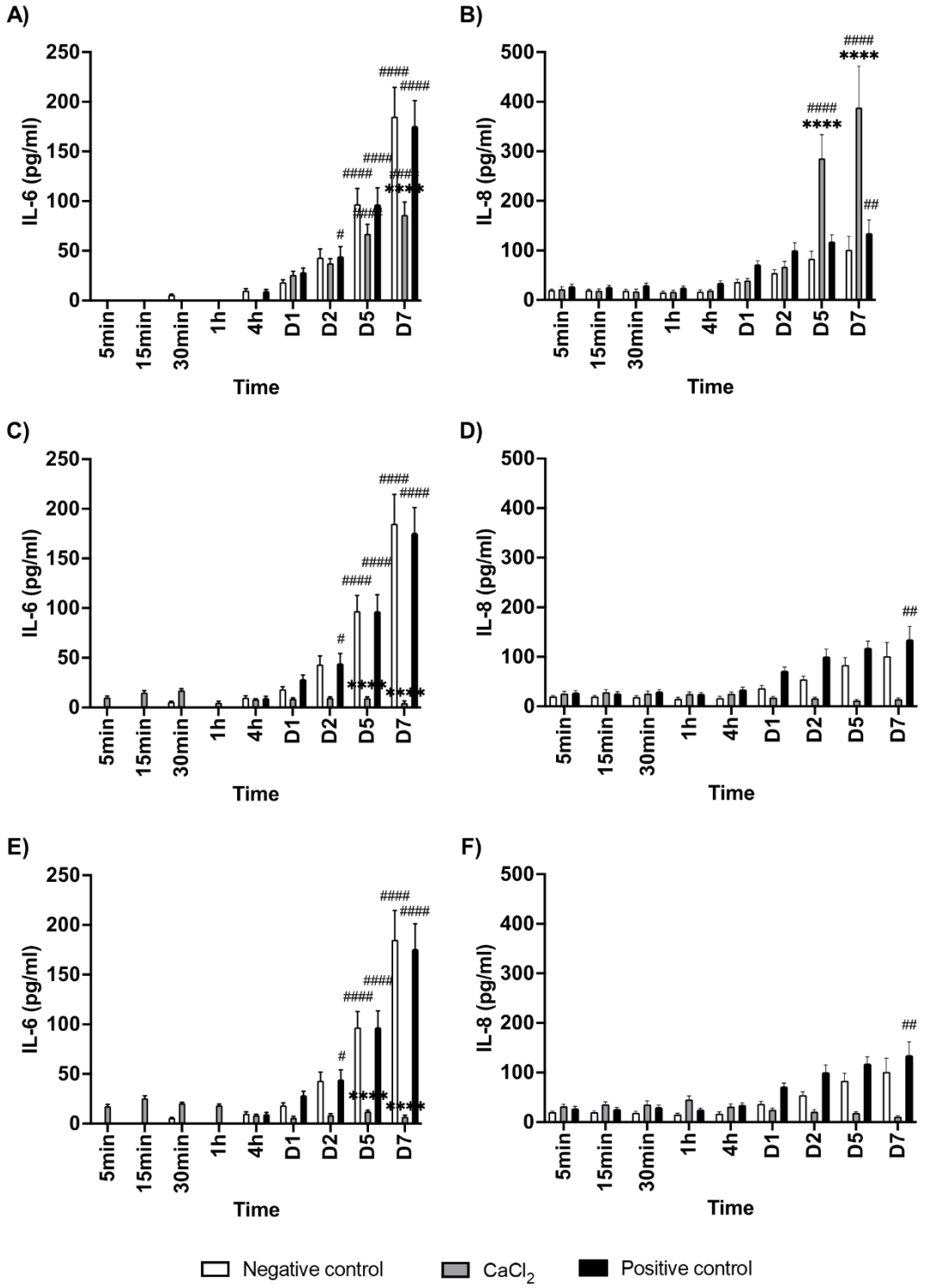

Figure 4.12 Pro-inflammatory effect of cross-linker calcium chloride ($CaCl_2$) on HFF-1 2D monoculture. *HFF-1 was exposed to $CaCl_2$ of 0.1M (A,B), 0.5M (C,D) or 1.0M (E,F) between 5 minutes and 7 days. IL-6 (A,C,E) and IL-8 (B,D,F) release were measured with ELISA. Positive control was LPS (1µg/ml). Mean±SEM is presented. N=3. Comparisons are denoted as follows: between negative control and $CaCl_2$ or positive control at each timepoint (*), timepoint comparison with 5min v 15min – day 7 for each culture condition (#) and comparison between $CaCl_2$ concentrations at each timepoint ($). Statistical significance denoted as: $p<0.05$ */#/$, $p<0.01$ **/##/$$, $p<0.001$ ***/###/$$$ and $p<0.0001$ ****/####/$$$$.*

When directly comparing IL-6 and IL-8 released per cell between HFF-1 exposed to 0.1M, 0.5M and 1.0M $CaCl_2$, there were no statistical differences (figure 4.13).

When compared against negative control, HFF-1 exposed to $CaCl_2$, at any concentration, did not elicit a statistically significant change in IL-6 or IL-8 release per cell at all timepoints tested. However, there is a dose-dependent rise in IL-6 and IL-8 release per cell with higher $CaCl_2$ concentration up to 1 hour, although this was not statistically significant. For 0.5M and 1.0M $CaCl_2$, levels of both chemokines dropped from 4 hours onwards, despite adjusting for cell numbers. This remains likely a result of cytotoxic effects of $CaCl_2$ during prolonged applications. Considering 0.1M $CaCl_2$, IL-6 and IL-8 release per cell began to rise from day 1 onwards, exceeding that of negative control.

Although there was no statistically significant rise between IL-6 and IL-8 per cell for 0.1M $CaCl_2$ when compared to negative control at all timepoints, the rise in IL-6 over time was significant on day 5 and 7. With timepoint comparisons, a statistically significant rise of IL-6 release per cell was noted in all culture conditions on day 5 and 7, including with negative and positive controls. Comparisons between negative control and positive controls at each timepoints, and timepoint comparisons of each culture conditions showed no statistical significance for IL-8 release per cell.

4.3.3.1.3 Cell morphology

The impact of the cross-linker $CaCl_2$ on the cell morphology of HFF-1 was examined with light microscopy and is illustrated in figure 4.14. Overall, it mirrors the time- and dose-dependent cytotoxicity trends observed with the erythrosin B exclusion assay. Cell morphology was relatively preserved with the lowest $CaCl_2$ concentration (0.1M) at the earliest timepoint at 5 minutes, which contrasts with the reduced numbers of live cell and numerous dead cells seen with the middle (0.5M) and highest (1.0M) concentrations. Cell morphology with 0.1M $CaCl_2$ demonstrated a gradual loss of normal cell morphology over time, especially at timepoints $\leq$24 hours. However, whilst data from the erythrosin B exclusion assay revealed a clearer trend of increasing cytotoxicity with time and cross-linker concentration, the degree of altered cell morphology and abundance of non-viable cells and cellular debris was variable over time and across the higher concentrations. Nonetheless, the findings from the cell

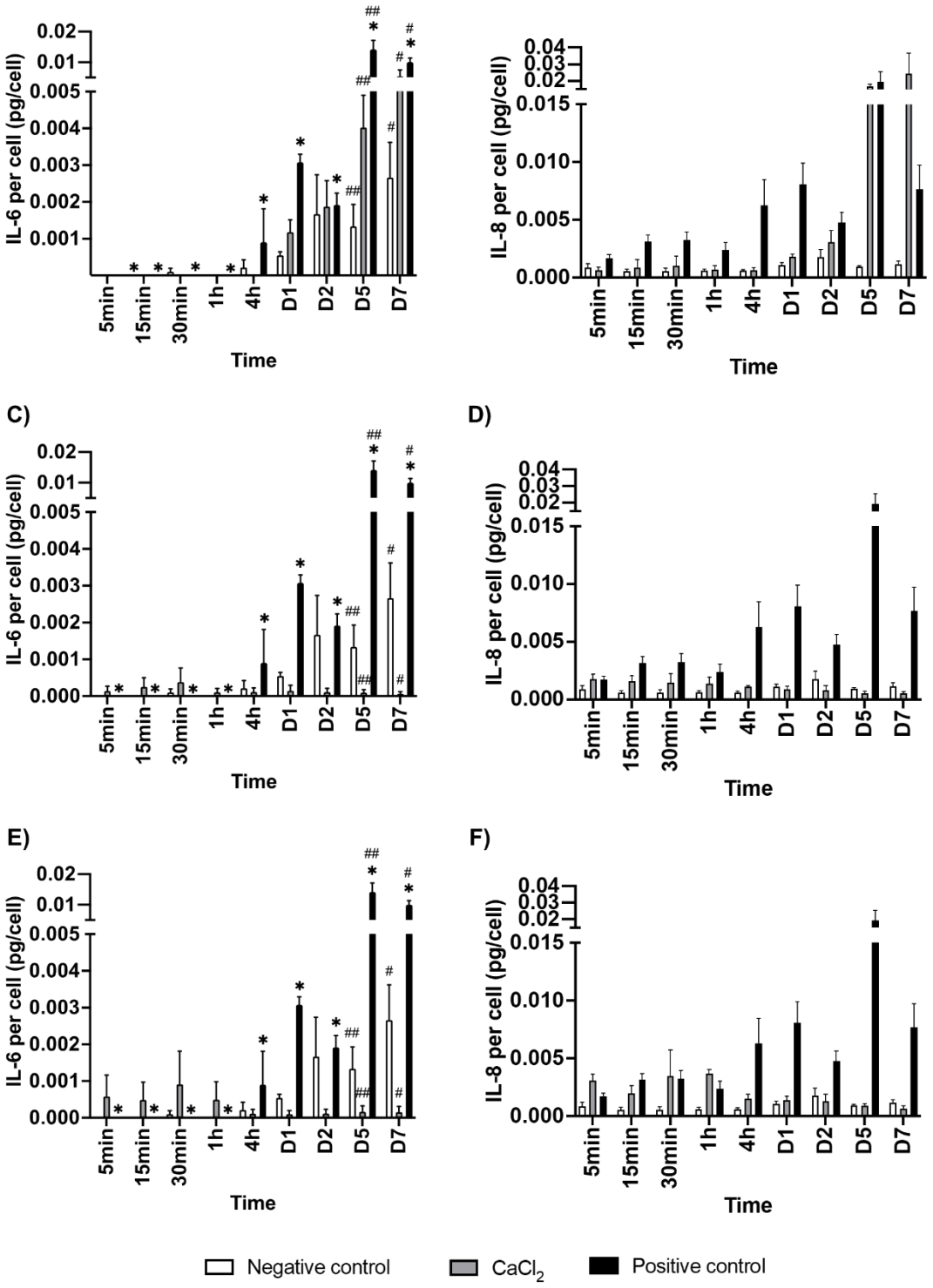

Figure 4.13 Pro-inflammatory effect per cell of 0.1M, 0.5M and 1.0M calcium chloride ($CaCl_2$) on HFF-1 2D monoculture over 21 days. *IL-6 (A,C,E) and IL-8 (B,D,F) release were measured with ELISA, and chemokine released per cell were calculated relative to total cell number at each timepoint. $CaCl_2$ concentrations are shown as: 0.1M (A,B), 0.5M (C,D) and 1.0M (E,F). Positive control was LPS. Mean±SEM is presented. N=3. Statistical significance between negative control and $CaCl_2$ or positive control are denoted by * and timepoint comparisons D1 v D2-21 of each cell conditions by #: p<0.05 */#, p<0.01 **/##, p<0.001 ***/### and p<0.0001 ****/####.*

morphology assessment supports the use of the lowest 0.1M concentration and to limit the time of cross-linker exposure.

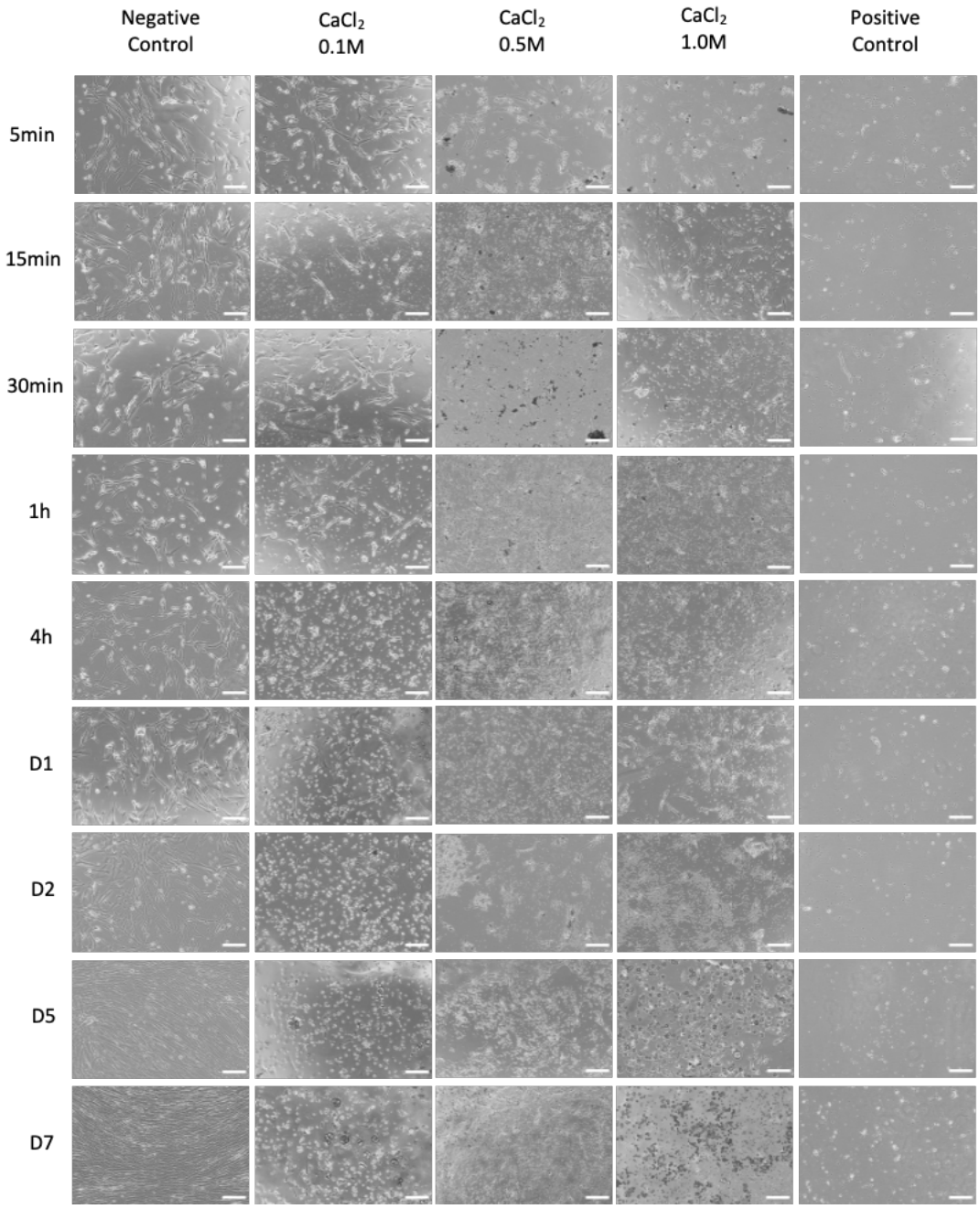

Figure 4.14 Light microscopy of the effects of 0.1M, 0.5M and 1.0M cross-linker calcium chloride against HFF-1 2D monoculture over 7 days. *Scale bars represent 200μm.*

4.3.3.1.4 Section summary - cross-linker toxicity testing on HFF-1

Overall, the data indicated that there was a time- and dose-dependent cytotoxic and pro-inflammatory effect of $CaCl_2$ on HFF-1. Based on these results, the lower $CaCl_2$ concentration of 0.1M was chosen for further testing against C20A4, as well as for rheological testing. Limiting contact time between the cross-linker and cells was also recommended, and will be taken into consideration to define the final cross-linking

time used in the SOP for *in vitro* model creation (Appendix 1), alongside results from the gelation studies.

4.3.3.2 C20A4 cell line (human chondrocyte)

4.3.3.2.1 Cytotoxicity

All measures were adversely impacted for C20A4 upon exposure to the cross-linker $CaCl_2$ at 0.1M concentration. Whilst statistically significant reductions were seen from day 1 onwards, notable reduction in total cell concentration, live cell concentration and cell viability were present from 30 minutes of cross-linker application (figure 4.15). Assessment of change over time showed that whilst there was a slight recovery in each measure at one hour, this was not preserved at the next timepoint. This is likely to indicate variability in cell behaviour. Nonetheless, an overall trend of cytotoxic effects taking hold was observed from 30 minutes onwards, with heightened effects by 4 hours and significant reduction in cell viability to less than 70% beyond this timepoint.

The time-dependent cytotoxic effect of the cross-linker on C20A4 mirrors that of HFF-1. Considering the cytotoxic effects upon both cell types, it was determined that cross-linker application duration should be kept to a minimum to preserve cell survival and function. Although acceptable level of viability was achieved at up to 4 hours, and this should be balanced against the material requirement for gelation. The data also support the use of wash steps following cross-linkage to remove exogenous $CaCl_2$. However, a residual amount of the $CaCl_2$ will be present, having permeated through the cross-linked construct, and will continue to exert some effect on cells.

4.3.3.2.2 Pro-inflammatory response

Relatively low level of both IL-6 and IL-8 were detected at all timepoints up to 4 hours. Direct comparison between cells exposed to cross-linker and negative control showed comparable levels of both chemokines released (figure 4.16). This suggests that at timepoints relevant to direct contact between cells and cross-linker (i.e. during $CaCl_2$ application for cross-linkage), no significant pro-inflammatory effects against C20A4 was observed.

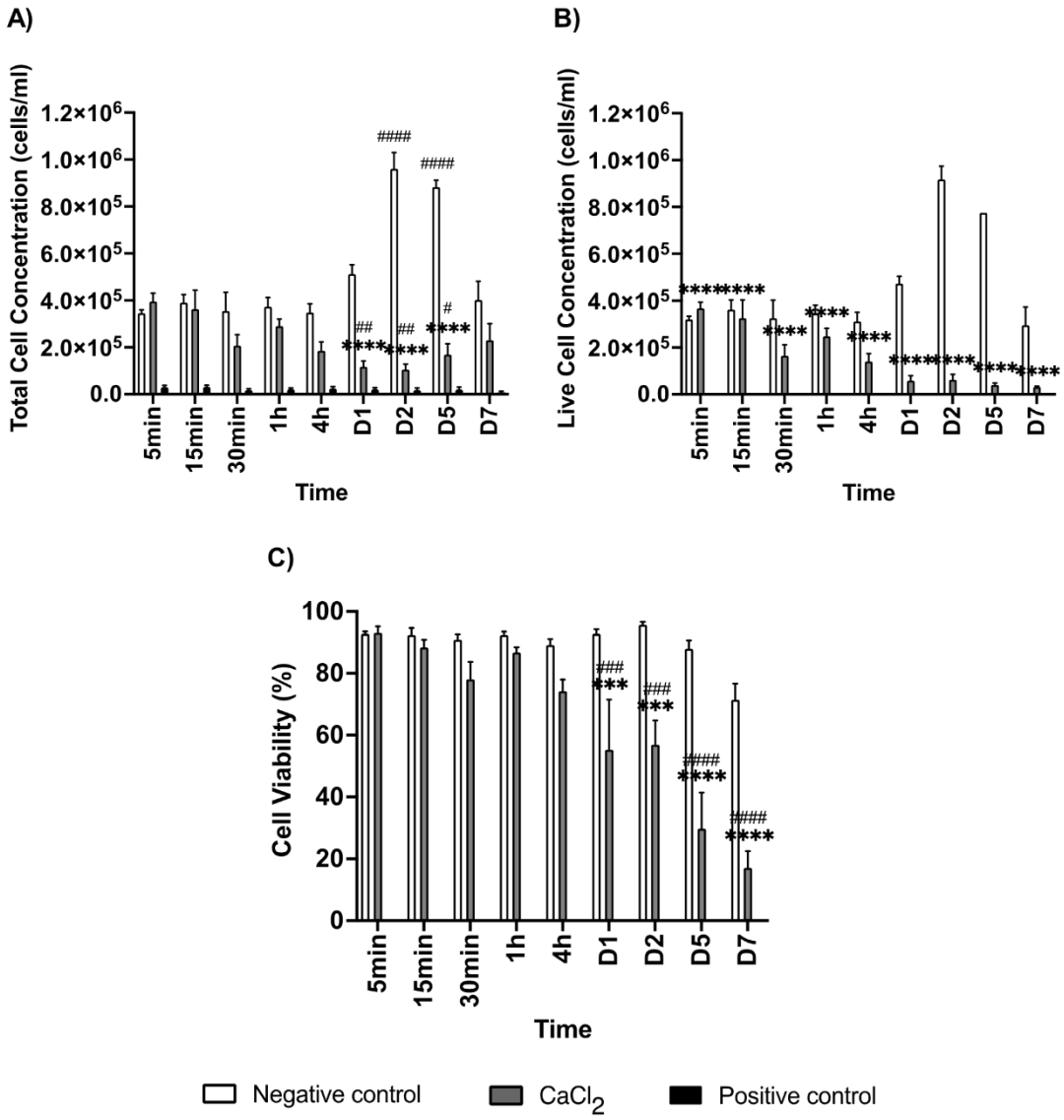

Figure 4.15 Cytotoxicity of C20A4 exposed to cross-linker 0.1M calcium chloride. *The effect of 0.1M calcium chloride ($CaCl_2$) were tested against 2D C20A4 monocultures up to 7 days using erythrosin B assay. Total cell concentration (A), live cell concentration (B) and cell viability (C) were assessed. Positive control was 0.1% Triton X. Mean±SEM is presented. N=3. Comparison between negative control and $CaCl_2$ or positive control denoted by * and timepoint comparison of 5min v 15min to day 7 for each culture condition by #. Statistical significance is presented as: p<0.05 */#, p<0.01 **/##, p<0.001 ***/### and p<0.0001 ****/####. Statistical significance reached between negative and positive control for total and live cell concentrations and cell viability at all timepoints (p<0.001/0.0001; not shown).*

It was interesting to note that IL-6 and IL-8 release in negative control at latter timepoints far exceeded that of cells exposed to $CaCl_2$. However, live cell concentration of cells exposed to $CaCl_2$ was significantly reduced compared to negative control, reduced cell number may account for the reduced level of pro-inflammatory response measured. Chemokine release per cell calculations are shown next to permit further examination.

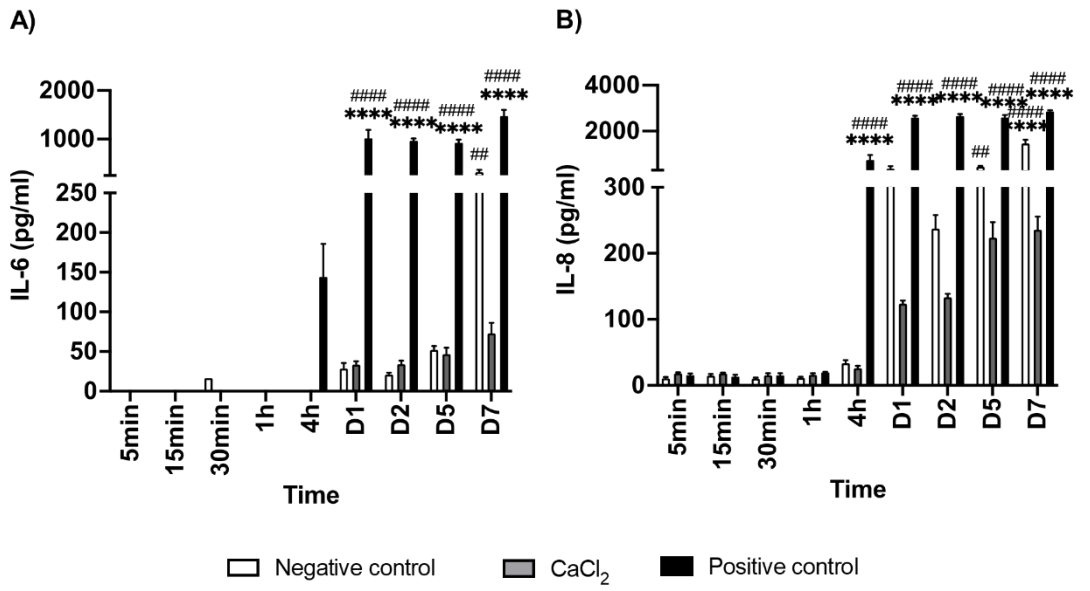

Figure 4.16 Pro-inflammatory effect of cross-linker calcium chloride ($CaCl_2$) on C20A4 2D monoculture over 7 days. *C20A4 was exposed to 0.1M $CaCl_2$ between 5 minutes and 7 days. IL-6 (A) and IL-8 (B) release were measured with ELISA. Positive control was LPS. Mean±SEM is presented. N=3. Comparisons are denoted as follows: between negative control and $CaCl_2$ or positive control at each timepoint (*) and timepoint comparison with 5min v 15min – day 7 for each culture condition (#). Statistical significance denoted as: $p<0.05$ */#, $p<0.01$ **/##, $p<0.001$ ***/### and $p<0.0001$ ****/####.*

When adjusted for cell numbers, increased IL-6 and IL-8 release per cell was seen in cells exposed to the cross-linker compared with negative control, opposite to the trend seen when the total amount of chemokine measured were compared (figure 4.17). This indicates that whilst the pro-inflammatory effects of cross-linker exposure remained low at up to 4 hours, between day 1 and 5, cells were exhibiting a measurable pro-inflammatory response when exposed to $CaCl_2$. On day 7 however, the levels of both chemokine with the negative control overtaken that of cells exposed to $CaCl_2$. Taking into consideration marked cytotoxic effects on day 7, this likely represents cellular dysfunction and dysregulation with a diminished capacity to mount a pro-inflammatory response.

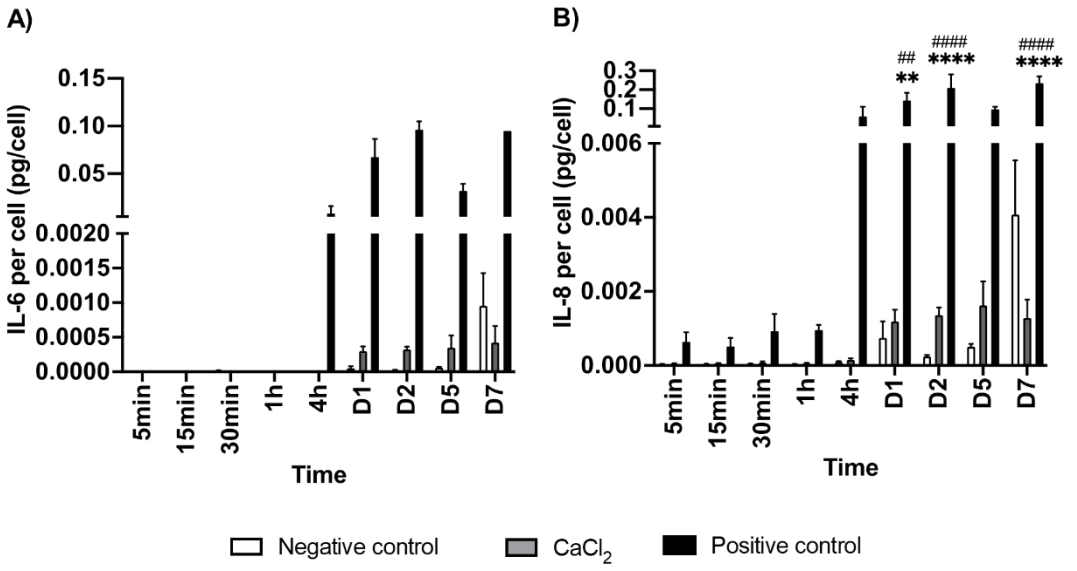

Figure 4.17 Pro-inflammatory effect per cell of 0.1M calcium chloride ($CaCl_2$) on C20A4 2D monoculture over 7 days. *IL-6 (A) and IL-8 (B) release were measured with ELISA, and chemokine released per cell were calculated relative to total cell number at each timepoint. Positive control was LPS. Mean±SEM is presented. N=3. Statistical significance between negative control and $CaCl_2$ or positive control are denoted by * and timepoint comparisons D1 v D2-21 of each cell conditions by #: p<0.05 */#, p<0.01 **/##, p<0.001 ***/### and p<0.0001 ****/####..*

4.3.3.2.3 Cell morphology

In view of the time- and dose-dependent cytotoxic effects of the cross-linker $CaCl_2$ against HFF-1, the lowest $CaCl_2$ concentration (0.1M) was taken forward for further testing against C20A4. C20A4 appeared relatively more resistant to the influence of 0.1M $CaCl_2$ upon the cell morphology, especially at earlier timepoints (figure 4.18). Cell morphology of C20A4 were relatively well-preserved at the 5 and 15 minutes exposure, coinciding with the high cell viabilities observed (figure 4.15C). Relatively more subtle morphological changes were seen at 30 minutes and 1 hour, and this precedes progressively marked alterations to cell morphology at 4 hours and beyond. The morphological changes were coupled with an overall reduction in total cell numbers, a stark contrast to the cell over-confluency with the negative controls at each respective timepoint. Overall, this illustrates the time-dependent cytotoxic effects of 0.1M $CaCl_2$ against C20A4, corroborating with data from the erythrosin B exclusion assay and together supports the limitation of cross-linker exposure duration to minimise cytotoxicity against C20A4.

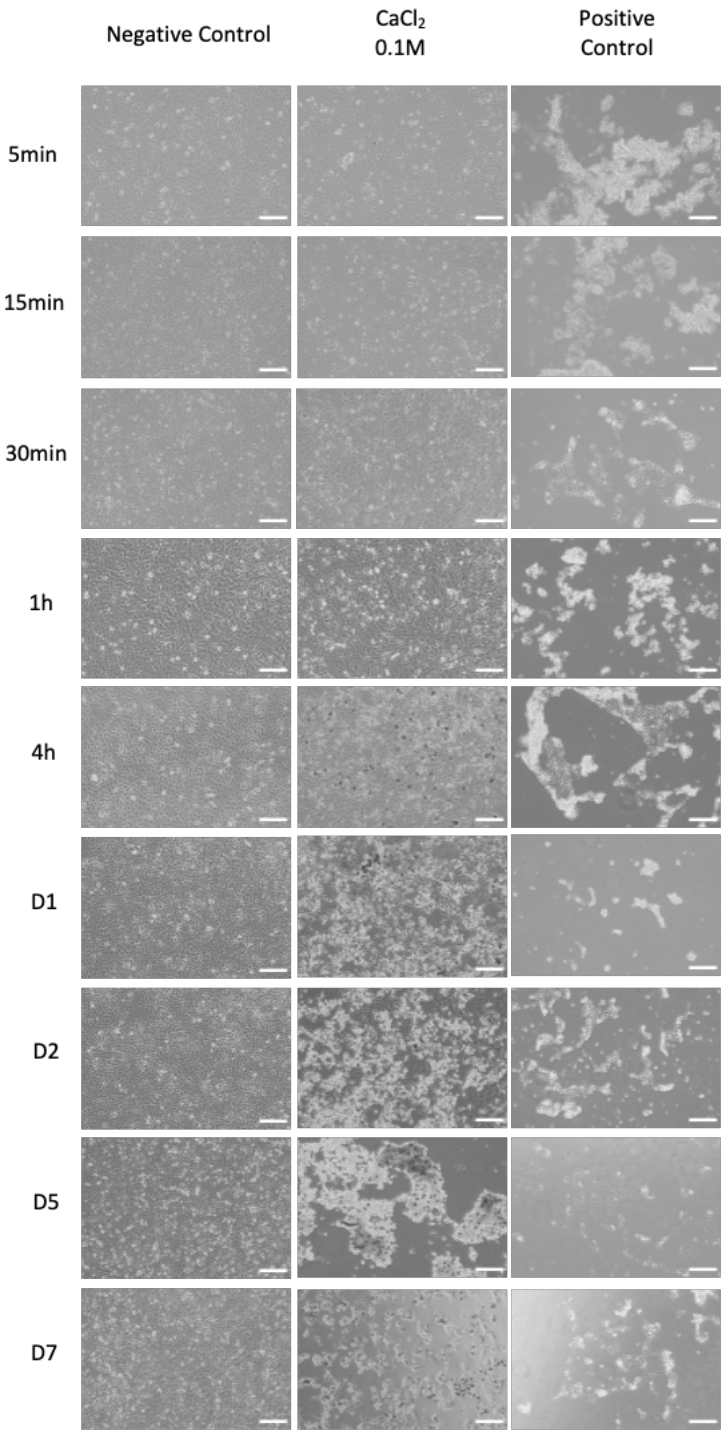

Figure 4.18 Light microscopy of the effect of 0.1M $CaCl_2$ cross-linker against C20A4 2D monoculture over 7 days. *Scale bars represent 200μm.*

4.3.3.3 Section summary and further discussion - cross-linker toxicity testing

Gelation of the nanocellulose:alginate bio-ink is a necessary step in creating a 3D bio-printed cartilage construct, and is therefore incorporated in the development of the 3D *in vitro* model. As such, the cytotoxic and pro-inflammatory effects from cells exposed to the cross-linker agent should be considered in addition to effects from bio-ink material alone.

Both HFF-1 and C20A4 demonstrated time-sensitive, adverse biological impact when exposed to the cross-linker $CaCl_2$. Whilst C20A4 was more tolerant of the cytotoxic effects of 0.1M $CaCl_2$ than HFF-1, and no significant pro-inflammatory response was detected at up to 4 hours, reduced viability was noted as early as 30 minutes following $CaCl_2$ application. Therefore, the result from the cross-linker toxicity study strongly supports the use of the lowest concentration of cross-linker, and restricting the time of cross-linker application where feasible.

Calculations for chemokine release per cell considered the use of both total and live cell concentration. Total cell concentration was chosen as it more closely reflected cell numbers over the study period at each timepoint. In contrast, the use of live cell concentration may falsely magnify effects measured. Whilst both approaches carry limitations, due to the varied cell numbers between exposures and negative control, as well as over time, chemokine release per cell approach provided an additional view into cellular behaviour.

4.3.4 Cross-linkage time definition

Following on from the biological experiments in this chapter, the next two sections focus on the gelation process with the Nanocellulose:Alginate bio-ink. As depicted in figure 4.1, the minimum cross-linkage time was first defined for the creation of discs-shaped pellets using silicon molds (detailed in section 2.11). This will be followed by rheological studies which examined the real-time material alteration when exposed to the cross-linker, $CaCl_2$, over a 12 hour study period (described in section 2.12).

4.3.4.1 Determination of minimum gelation time in silicon molds

Initial testing evaluated three types of pulp-derived nanocellulose and three $CaCl_2$ concentrations. There is a clear trend of shorter cross-linking time with higher $CaCl_2$ concentrations (table 4.2). Cross-linking duration was consistent with different types of pulp-derived nanocellulose, except with 0.5M $CaCl_2$ where CNF:Alginate required a shorter cross-linking time.

Table 4.2 Summary of minimum cross-linking duration (minutes) for pulp-derived Nanocellulose:Alginate bio-inks. *Bio-inks were cross-linked within silicon molds to create 8mm wide circular disc-shaped pellets using 100µl bio-ink and 600µl of $CaCl_2$. The minimum time required for gelation was defined as reaching five consecutive complete gelations with no residual un-crosslinked bio-ink. Testing was conducted at 1 minute intervals.*

Bio-ink	**Cross-linker $CaCl_2$ concentration**		
	0.1M	**0.5M**	**1.0M**
NCB:Alginate	15	11	6
CNC:Alginate	15	11	6
CNF:Alginate	15	9	6

The same study was repeated with the three forms of tunicate-derived nanocellulose, each variably functionalised, as described previously in table 3.1. Collectively, considering results from both the cross-linker toxicity testing and the gelation testing with pulp-derived nanocellulose, the decision to proceed with 0.1M $CaCl_2$ for all subsequent testing was taken. The results from table 4.2 confirms the suitability of the lowest $CaCl_2$ concentration as viable from a gelation perspective. It did not incur substantially longer cross-linker application times, which would in turn negatively impact cells biologically.

Proceeding with the tunicate-derived Nanocellulose:Alginate bio-inks, the study showed a trend of increasing cross-linking duration, from ETC (pre-enzymatically treated) to CTC (carboxymethylated), ending with TTC (TEMPO-mediated oxidised) requiring the longest cross-linking time (table 4.3). Broadly there was no difference in cross-linking time between the use of culture media versus ddH_2O for the reconstitution of alginate. This result therefore supports the use of culture media for the reconstitution of alginate for all future bio-ink creation and testing, with the intention of limiting potential cytotoxic effects from the hypotonic ddH_2O.

Table 4.3 Summary of minimum cross-linking duration (minutes) for tunicate-derived Nanocellulose:Alginate bio-inks.

Bio-inks	Solvent for Alginate	
	Media	Sterile ddH_2O
ETC:Alginate	15	15
TTC:Alginate	18	20
CTC:Alginate	17	17

4.3.4.2 Rheological study of gelation of ETC:Alginate bio-ink with $CaCl_2$

4.3.4.2.1 Gelation, viscoelasticity and oscillatory time sweeps

Whilst the previous study (section 4.3.4.1) identified the time required to achieve a physical hydrogel state sufficiently robust to withstand manual manipulation and handling for the purpose of *in vitro* model culture, it was recognised that ongoing application of $CaCl_2$ would prolong the cross-linking process. This would lead to constructs of altered physical and mechanical properties, which in turn impacts cell behaviour. In addition to presentation and discussion of results, the next section aimed to provide a succinct background in relevant concepts in material science and rheology to aid results interpretation.

Rheological study in this project initiated with an attempt to quantitatively define the gel point of the bio-ink. This can be delineated *via* oscillatory time sweep testing, which offers real-time monitoring of viscoelastic property changes in a material [280]. The bio-ink, sandwiched between two parallel plates, are subjected to sinusoidal stress by a motor on one end, with the resultant strain measured by a sensor on the other. As cross-linker is applied in the periphery of the bio-ink between the parallel plates, cross-linkage occurs as Ca^{++} diffuses through the bio-ink radially from outside in. In this experiment, measurements were taken every three seconds for a 12-hour study period, permitting detailed examination of the temporal change of viscoelastic properties and therefore gelation kinetics.

The relevance of applying the study of viscoelastic properties was not solely because rheology offered a form of dynamic mechanical testing well-suited to the study of material gelation [280]. In tissue engineering, the design of biomaterials serves to enable and potentially control cell function and cell fate, whereby the bio-ink or hydrogel

sought to mimic the extracellular matrix in the human body. In the past decade or so, numerous studies highlighted that controlling material stiffness, and more recently viscoelastic properties, are crucial in their influence across a spectrum of cellular behaviours. This meant that altering material mechanical properties can directly influence cell migration [281], proliferation and apoptosis [282] ,and stem cell fate and function [283-285].

Viscoelasticity, possessed by the majority of tissue in the human body [286], confers materials both viscous and elastic characteristics. A purely elastic material, when subjected to stress (amount of force applied to a unit of area), warps and stores the deformational energy until the stress is removed, which then springs back to its original state [287]. A purely elastic material is therefore considered 'solid', with the stretched spring being a classic analogy. This elastic material behaviour is measured by the elastic or storage modulus (G'), defined as the ratio of stress to strain.

Strain is defined as the degree of deformation that results from stress, or the applied force. The viscous or loss modulus (G") is a measure of the viscous or 'liquid' behaviour of a material, defined as the ratio of strain to rate of stress. A viscous material will dissipate the stress applied, often as heat, and upon removal of the deformational stresses, will remain in the deformed state. In other words, the strain (or deformation) becomes permanent.

4.3.4.2.2 Gel point

The gel point offered a quantitative definition of the sol-gel transition when the ETC:Alginate bio-ink was exposed to $CaCl_2$. Rheologically, the gel point is a recognised state in gelation kinetics and is denoted at the modulus crossover, i.e. when the storage modulus overtakes loss modulus, or vice versa. Mathematically, it is otherwise defined as when tan δ, calculated as the ratio of loss modulus to storage modulus and otherwise known as the viscoelasticity function, equates to one.

Initial pilot study conducted with the pulp-derived NCB:Alginate bio-ink concluded that the bio-ink is a visco-elastic solid. This corroborated with results from the tunicate-derived ETC:Alginate bio-inks (figure 4.19). Despite exhibiting viscoelastic properties, as the storage moduli of the uncrosslinked bio-inks were greater than their loss moduli prior to contact with the cross-linker, this implied that the uncrosslinked

bio-ink was a visco-elastic solid and therefore using the gel point to define complete cross-linkage was not feasible.

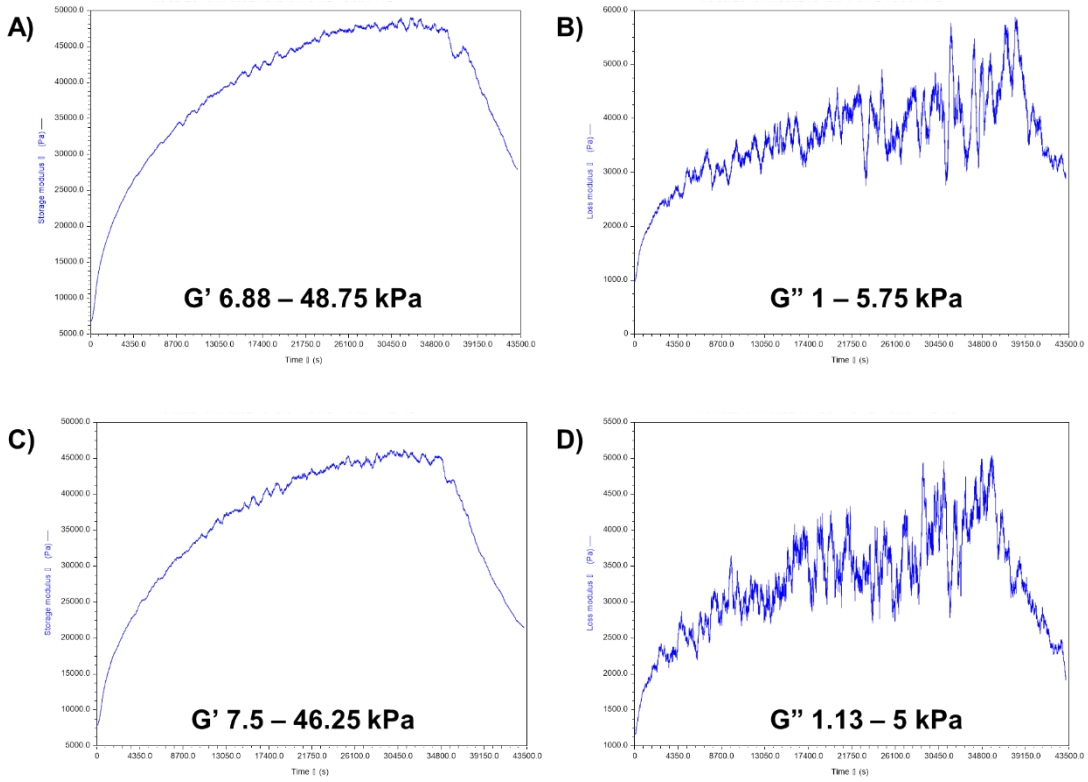

Figure 4.19 Oscillatory time sweeps of ETC:Alginate (media) and ETC:Alginate (ddH$_2$O) bio-inks exposed to 0.1M calcicum chloride. *Time sweeps were conducted over 12 hours at 1Pa and 1Hz. Frequency sweeps were between 0.01-1Hz. Storage (G') and loss (G") modulus were recorded at 3s intervals. N=3. Data smoothing and visualisation was performed via the TRIOS software to permit preliminary analysis. A+B (top row) represent ETC:Alginate (media) and C+D (bottom row) ETC:Alginate (ddH$_2$O). A+C (left) showed G' and B+D (right) G" of one repetition. Range of G' and G" presented in text.*

4.3.4.2.3 Real-time monitoring of storage modulus during cross-linkage

To examine the gelation kinetics of the ETC:Alginate bio-inks, the times required to reach the plateau of storage modulus (G'), and 50% of G' plateau were calculated (figure 4.20) [288]. The times required for both were not significantly distinct when comparing bio-inks with alginate reconstituted in media versus ddH$_2$O ($p>0.05$). This suggests that altering the alginate solvent did not infer significant mechanical property differences following bio-ink cross-linkage. As cell behaviour can be influenced by the viscoelastic properties of the hydrogel, this result could imply that should significant cytotoxic and pro-inflammatory effects be detected in future 3D *in vitro* model (chapter 6 and 7), the choice of alginate solvent is less likely to be a dominant variable.

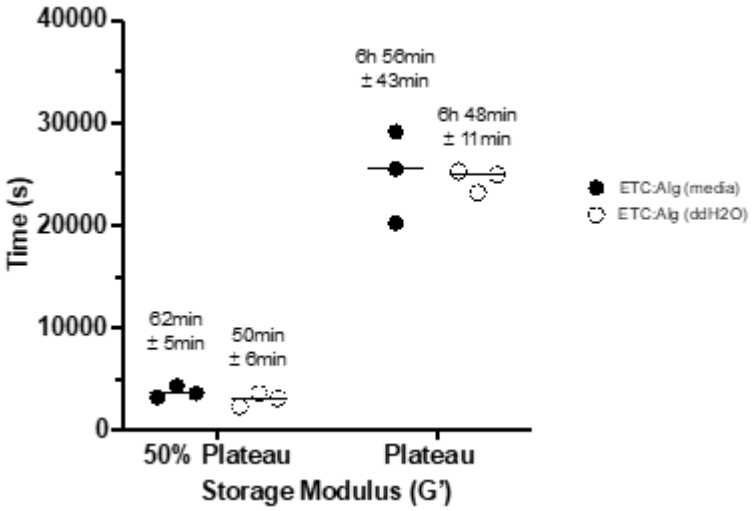

Figure 4.20 Time to reach plateau and 50% plateau of storage modulus of ETC:Alginate bio-inks. *Dot plots of rheological time-sweep study comparing bio-inks ETC:Alginate (media) and ETC:Alginate (ddH_2O) cross-linked with 0.1M $CaCl_2$. Mean±SEM is described in text. N=3.*

Further characterisation of the bio-ink and gelation kinetics is shown in figure 4.21, where G' at timepoints tested in the cross-linker toxicity testing were highlighted. Bio-inks made of both alginate solvents showed a greater change in G' at earlier timepoints with a steeper gradient seen, compared to timepoints nearer the G' plateau, in keeping with what is expected following an external gelation method. Using media or ddH_2O as solvent for alginate did not significantly alter the G' of the bio-inks when cross-linked, although variance was greater with ddH_2O, at up to 4 hours. The variance of G' of ETC:Alginate (media) widened nearing G' plateau, more closely resembled that seen with ETC:Alginate (ddH_2O) (figure 4.21). This may be related to the material confluence or the presence of minute air bubbles, both could lend the bio-ink a degree of heterogeneity. However, overall, the results confirmed consistency between bio-ink formulations, a positive attribute for the intended application as a 3D *in vitro* model.

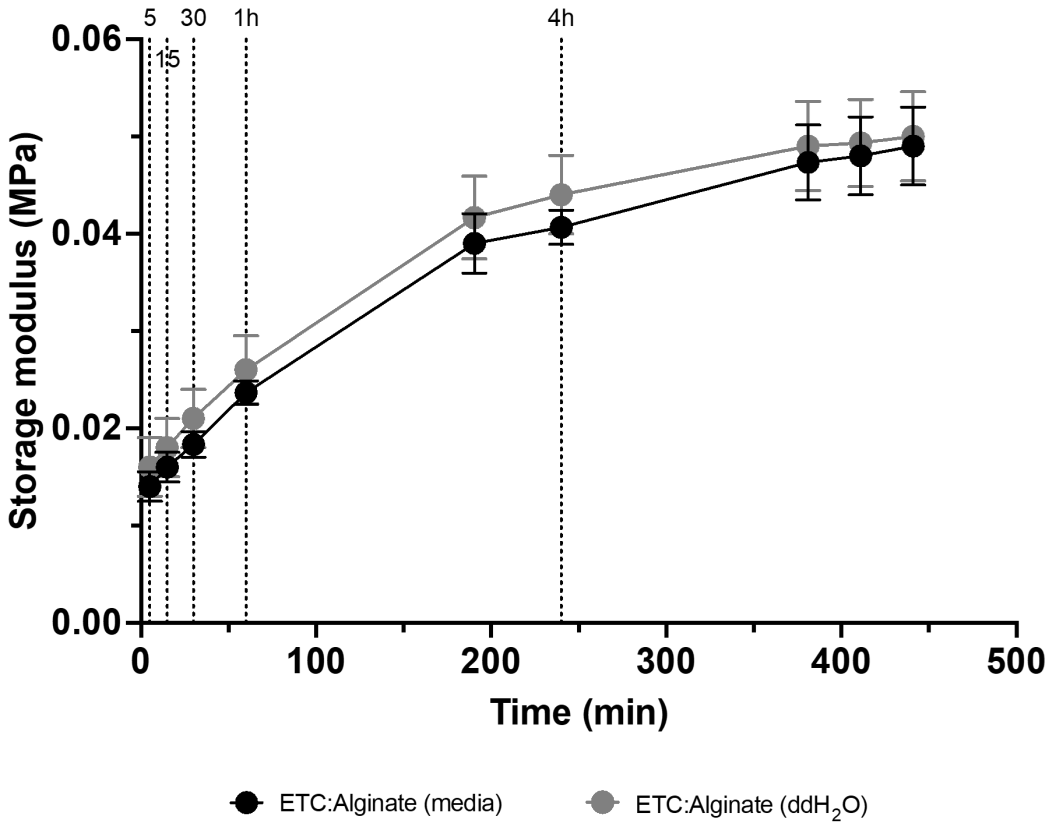

Figure 4.21 Storage modulus of ETC:Alginate bio-inks over time when exposed to 0.1M calcium chloride. *Gelation kinetics were studied using time-sweep test. Two bio-inks (ETC:Alginate (media) and ETC:Alginate (ddH_2O)) were tested. Storage modulus (G') was measured over time. Vertical dotted lines represent timepoints used in cross-linker toxicity testing, and includes 5, 15, 30 minutes, 1 hour and 4 hours. Additional timepoints plotted, from left to right, include 50% G' plateau, G' plateau, G' plateau + 30minutes and G' plateau + 1h. Mean±SEM is presented. N=3.*

4.4 Chapter Summary and Conclusion

This chapter examined the cytotoxic and pro-inflammatory effects of both alginate (material) and $CaCl_2$ (cross-linker) on both human dermal fibroblast (HFF-1) and human chondrocyte (C20A4) cell lines in 2D culture. Non-cell-based gelation and rheological studies further defined the minimum cross-linking time required and bio-ink gelation kinetics, respectively. Table 4.4 summarises the key findings of this chapter and relevant items to be taken forward for future *in vitro* model development and testing. The final bio-ink formulation for ETC:Alginate (media) and protocol for the production of bio-ink and the 3D *in vitro* models are detailed in the SOP (Appendix 1).

Furthermore, whilst the gel point could not be defined due to the predominant elastic behaviour of the pre-crosslinked bio-ink (objective 6), the minimum gelation time required to create a hydrogel suitable for use in the 3D *in vitro* model was achieved (objective 5). Studying the rate and magnitude of change in storage modulus upon application of $CaCl_2$ provided additional information regarding material behaviour and consistency. Variance, although not significantly pronounced, was observed and could account for a degree of divergence in cell behaviour in future studies.

Taking all data acquired in this chapter into consideration, which included both cell-based and non-biological gelation studies, the parameters for cross-linking were defined, supporting the attainment of chapter objective 7 (to select the optimal $CaCl_2$ concentration and duration of application) (table 4.4).

Table 4.4 Summary of chapter conclusions and take-on messages.

Conclusions	
Sterility	• UV-sterilised culture grade alginate met sterility threshold.
Material biological effects	• No adverse cytotoxic or pro-inflammatory effects detected when HFF-1 and C20A4 were exposed to alginate in 2D culture.
Cross-linker biological effects	• Time- and dose-dependent cytotoxic and pro-inflammatory effects of $CaCl_2$ were observed on HFF-1 in 2D culture, with 0.1M causing least adverse effects. • Viability of C20A4 was preserved (>70%) when exposed to 0.1M $CaCl_2$, for up to 4 hours.
Model creation	• Silicon molds were successfully applied to create cross-linked bio-ink 3D pellets for use as an *in vitro* model for future testing.
Gelation: **Bench-top + Rheology Study**	• Bench cross-linking time of ETC:Alginate bio-ink with 0.1M $CaCl_2$ defined at 15 minutes using silicon mold system. • Pre-crosslinked ETC:Alginate bio-ink held predominantly viscoelastic solid properties and sol-gel transition could not be defined rheologically. • Comparison of media and ddH_2O as solvents for alginate showed no significant difference in gelation kinetics and storage modulus.
Recommendations	
• UV-treated alginate to be reconstituted in media for bio-ink ETC:Alginate. • Creation of 3D *in vitro* model to utilise silicon molds yielding 8mm wide cross-linked discs. • Cross-linking of ETC:Alginate bio-ink to be conducted with 0.1M $CaCl_2$ for 15 min.	

Chapter 5: Hyaluronic acid – additive bio-ink material: Establishing sterility, its biological effects on HFF-1 and C20A4 cell lines and cross-linkage behaviour

5.1 Introduction

The focus of this chapter is the alternative additive bio-ink component, hyaluronic acid (HA). This is the third of three results chapters detailing investigations of the effects of each bio-ink component when tested individually (chapters 3-5). This will be followed by the development of an advanced *in vitro* model (appendix 1) and testing of the final hybrid bio-ink formulations (chapter 6-7).

HA is a native extra-cellular matrix (ECM) molecule, first isolated from tissue in 1934. It is found in various biological tissue types and fluids, but is particularly abundant in connective tissues such as the cartilage and skin [237, 289]. As a hydrophilic, linear, non-sulfated, natural polysaccharide, not only does the ability of HA to retain water confers physical properties that makes it an attractive biomaterial for hydrogel creation, the inclusion of HA enhances biomimicry due to its role in cellular processes such as cell adhesion, proliferation and inflammation [289]. As such, HA is increasingly adopted in tissue engineering. However, to enable hydrogel creation, modifications of HA are needed to grant cross-linking abilities, with a host of cross-linking methods described in the literature, ranging from chemical, physical to ionic cross-linking [290-292]. An example includes the tyramine-substituted HA (T-HA). It can be cross-linked via an oxidative reaction with hydrogen peroxide (H_2O_2) and horseradish peroxidase (HRP) [291]. Whilst differing T-HA content, H_2O_2 and HRP concentrations can produce tunable hydrogel of varying stiffness and visco-elasticity, an attractive proposition to permit the selection of hydrogel compositions most appropriate for the intended tissue regeneration, it is important to recognise the associated potential altered biological impact. From a toxicological perspective, it is pivotal to define the specific form and concentration of HA used, and the parameters of the cross-linkage processes where relevant, to enable realistic exposure testing scenarios specific to end-product application and to improve reproducibility of studies undertaken.

The work of this chapter builds upon previous research that developed bio-inks consisting of nanocellulose and T-HA, cross-linked with H_2O_2. Bio-inks containing T-HA demonstrated suitable rheological (flow for 3D-printing) and mechanical properties, with superior chondrogenicity (chondrocyte proliferation and ECM formation) when compared with bio-inks made of nanocellulose and alginate (unpublished data). In contrast to alginate, two concentrations of T-HA were identified

as suitable for further testing, instead of one. Therefore, both T-HA concentrations were tested in this chapter.

The aims of this chapter were three-fold:

i. To assess the cytotoxic and pro-inflammatory effects of HA against HFF-1 and C20A4 cell lines.
ii. To define the optimal cross-linking process of the bio-ink containing nanocellulose (ETC) and HA, with respect to developing a 3D *in vitro* model.
iii. To define the final bio-ink formulation containing both nanocellulose (ETC) and HA.

The aims were met *via* the following objectives:

1. To ensure standardised material preparation procedures for HA.
2. To establish material sterility of HA over 21 days.
3. To assess the cytotoxicity and pro-inflammatory response of HFF-1 and C20A4 cell lines when exposed to HA.
4. To assess the cytotoxicity and pro-inflammatory effects of cross-linker H_2O_2 against HFF-1 and C20A4 cell lines.
5. To define the minimum gelation time required, relating to aim (ii).
6. To define the gel point of bio-ink containing ETC and HA when cross-linked with suitable cross-linker reagent.
7. To select the optimal HA concentration between 0.006g/ml and 0.012g/ml, relating to aim (ii) and (iii).

5.2 Methods

All methods used in this chapter were previously described in Chapter 2 (Materials and Methods), except for the sterilisation and material preparation procedures for T-HA which are detailed below. Sections referenced to Chapter 2 are as specified. Figure 5.1 outlines the workflow of this chapter. The chapter begins with the testing of T-HA, followed by the non-tyramine-substituted HA (N-HA).

5.2.1 Concentrations of HA

Two concentrations of HA were used in this chapter, which are denoted as follows: 0.006g/ml (low) and 0.012g/ml (high). The basis from which the concentrations were selected are detailed in section 2.3.1, based upon previous research.

5.2.2 Sterilisation and material preparation of HA

Two forms of HA were tested: T-HA and N-HA. Both T-HA and N-HA were supplied in powder form and reconstituted as detailed in section 5.2.2.1 and 2.3.3.3, respectively.

T-HA was made from the commercially available Corgel® BioHydrogel 5% Gel Kit. The T-HA stock solution (30mg/ml) was first created with tyramine-substituted sodium hyaluronate and HRP in PBS (both supplied within the Gel Kit), and subsequently diluted to required concentrations.

N-HA was also acquired from LifeCore Biomedical, Inc., and is supplied as sodium hyaluronate, i.e. without tyramine-substitution. The rationale behind the selection of the specific form of N-HA was discussed in section 2.3.2.3. As N-HA can be directly reconstituted solely with in-house solvents, N-HA was reconstituted as needed at the desired concentration, without the need of prior creation of a HA stock solution.

5.2.2.1 Sterilisation and material preparation of T-HA

T-HA was classed as a research-grade product derived from GMP batches with low bioburden, in accordance with the manufacturer. Sterilisation procedure was undertaken prior to any material handling, following a protocol developed by the research group (unpublished). Sterilisation involved treating the T-HA powder to UV-

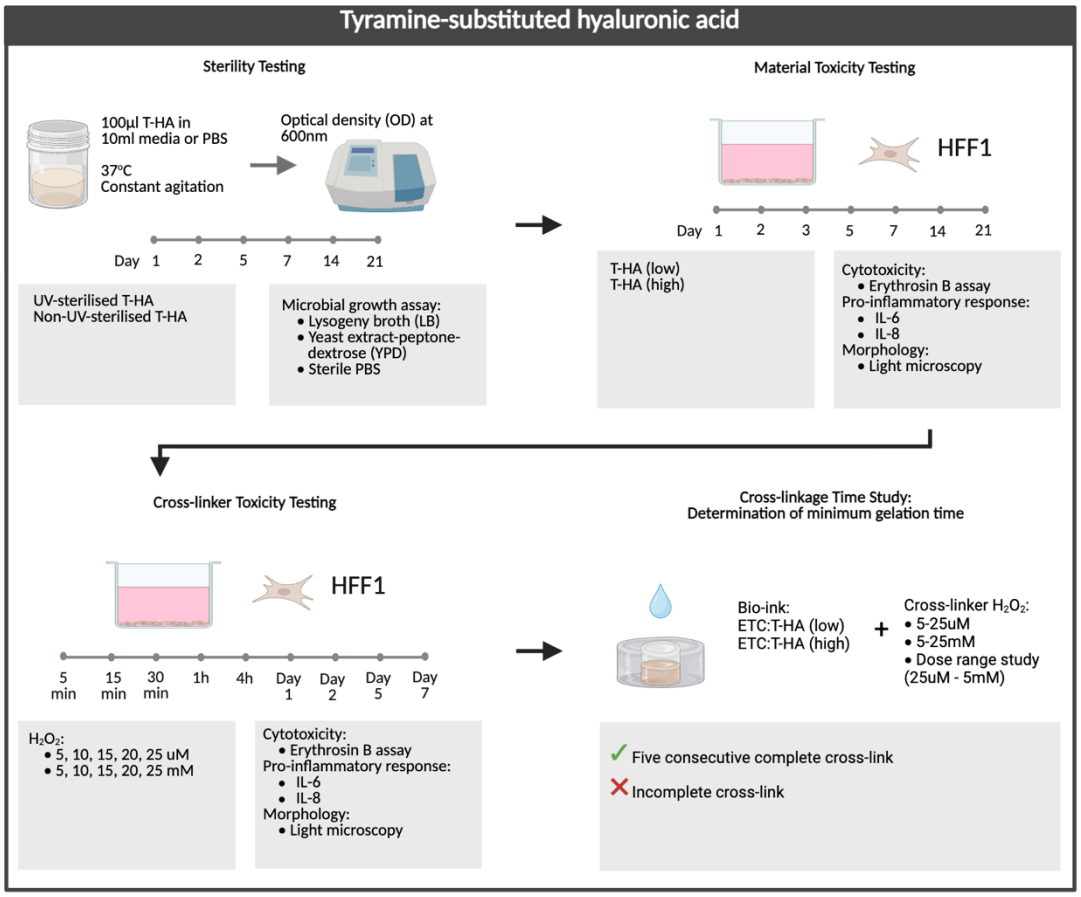
Tyramine-substituted hyaluronic acid
Sterility Testing
100µl T-HA in
10ml media or PBS
37°C
Constant agitation
Optical density (OD) at
600nm
Day 1 2 5 7 14 21
UV-sterilised T-HA
Non-UV-sterilised T-HA
Microbial growth assay:
• Lysogeny broth (LB)
• Yeast extract-peptone-dextrose (YPD)
• Sterile PBS
Material Toxicity Testing
HFF1
Day 1 2 3 5 7 14 21
T-HA (low)
T-HA (high)
Cytotoxicity:
• Erythrosin B assay
Pro-inflammatory response:
• IL-6
• IL-8
Morphology:
• Light microscopy
Cross-linker Toxicity Testing
HFF1
5 min 15 min 30 min 1h 4h Day 1 Day 2 Day 5 Day 7
H2O2:
• 5, 10, 15, 20, 25 uM
• 5, 10, 15, 20, 25 mM
Cytotoxicity:
• Erythrosin B assay
Pro-inflammatory response:
• IL-6
• IL-8
Morphology:
• Light microscopy
Cross-linkage Time Study:
Determination of minimum gelation time
Bio-ink:
ETC:T-HA (low)
ETC:T-HA (high)
+
Cross-linker H2O2:
• 5-25uM
• 5-25mM
• Dose range study
(25uM - 5mM)
✓ Five consecutive complete cross-link
✗ Incomplete cross-link

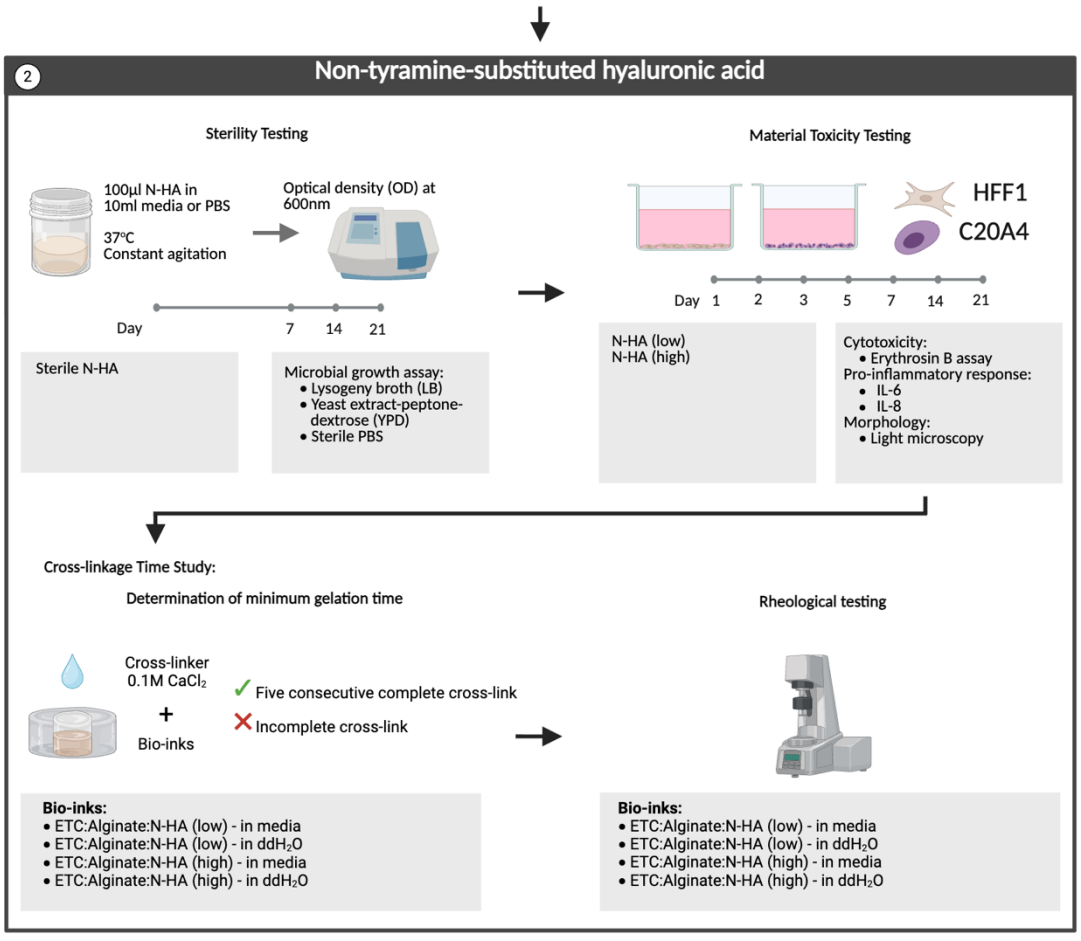
2
Non-tyramine-substituted hyaluronic acid
Sterility Testing
100µl N-HA in
10ml media or PBS
37°C
Constant agitation
Optical density (OD) at
600nm
Day 7 14 21
Sterile N-HA
Microbial growth assay:
• Lysogeny broth (LB)
• Yeast extract-peptone-dextrose (YPD)
• Sterile PBS
Material Toxicity Testing
HFF1
C20A4
Day 1 2 3 5 7 14 21
N-HA (low)
N-HA (high)
Cytotoxicity:
• Erythrosin B assay
Pro-inflammatory response:
• IL-6
• IL-8
Morphology:
• Light microscopy
Cross-linkage Time Study:
Determination of minimum gelation time
Cross-linker
0.1M CaCl2
+
Bio-inks
✓ Five consecutive complete cross-link
✗ Incomplete cross-link
Rheological testing
Bio-inks:
• ETC:Alginate:N-HA (low) - in media
• ETC:Alginate:N-HA (low) - in ddH2O
• ETC:Alginate:N-HA (high) - in media
• ETC:Alginate:N-HA (high) - in ddH2O
Bio-inks:
• ETC:Alginate:N-HA (low) - in media
• ETC:Alginate:N-HA (low) - in ddH2O
• ETC:Alginate:N-HA (high) - in media
• ETC:Alginate:N-HA (high) - in ddH2O

Figure 5.1 Schematic of chapter 5 workflow. *Chapter 5 are broadly categorised based on the material tested, initiating with tyramine-substituted hyaluronic acid (T-HA), followed by non-tyramine-substituted hyaluronic acid (N-HA). Investigations of T-HA included sterility testing, material toxicity testing, cross-linker toxicity testing and determination of minimum gelation time as the cross-linkage time study. Investigations of N-HA also included sterility testing and material toxicity testing, and cross-linkage time studies consisted of both determination of minimum gelation time and rheological testing. For sterility testing, T-HA (UV-sterilised and untreated) and N-HA (sterile) were incubated in lysogeny broth (LB), yeast extract-peptone-dextrose (YPD) or sterile PBS, at 37°C under constant agitation. Optical density was measured at 600nm. T-HA was tested on day 1, 2, 5, 7, 14 and 21, whilst an abbreviated schedule was applied for N-HA consisting of day 7, 14 and 21. This was followed by material +/- cross-linker toxicity testing for both HA forms. T-HA and the cross-linker hydrogen peroxide (H_2O_2) were tested against HFF-1, whilst N-HA was tested against HFF-1 and C20A4, all as 2D monocultures at specified timepoints depicted in figure. For both material and cross-linker toxicity testing, cytotoxicity (erythrosin B assay), pro-inflammatory effects (IL-6 and IL-8 release) and morphology (light microscopy) were assessed. Bio-inks consisting of both T-HA or N-HA were subjected to cross-linkage study to determine the minimum gelation time. Bio-inks with N-HA proceeded to further rheological testing. Created with BioRender.com.*

C at 254nm for one hour within a laminar flow hood. This was performed within the supply container with the lid removed.

Reconstitution of T-HA was then performed, following manufacturer's instructions. To create a 30mg/ml T-HA stock solution, 8.33ml of HRP in PBS (10U/ml; as supplied) was added to 250mg of T-HA powder. Contents were mixed well with a spatula for approximately 15-20minutes at room temperature to ensure full dissolution and a homogenous stock solution. The resultant material concentrations in the T-HA stock solution are: 30mg/ml T-HA; 10U/ml HRP. The T-HA stock solution was stored at 4°C, with parafilm cover of the lid, and hence forth handled in sterile conditions.

To enhance sterility, attempts were trialled to create smaller batches of HA stock solution as needed. The rationale being that maintenance of sterility would be superior in powder form versus in solution. This was, however, unsuccessful due to high static build-up of the supplied T-HA powder, with subsequent loss of T-HA content during attempts to aliquot the powder. The use of a static eliminator was trialled and despite some reduction in static build-up, it did not mitigate the loss of T-HA. Therefore, to ensure the full use of the supplied T-HA, both sterilisation and reconstitution were performed within the supplied container.

All T-HA used in this chapter were of the UV-treated T-HA, prepared as described above, except for the untreated T-HA used in the material sterility testing. The 'untreated T-HA' stock solution was created in the same manner as above, but without the UV-C treatment step.

5.2.2.2 Material preparation of N-HA

N-HA was supplied as a powder, in sterile condition. As such, no additional sterilisation step was required. Material preparation involving N-HA was previously described in section 2.3.3.3.

5.2.3 Material sterility testing

The protocols for microbial growth testing, and bacterial isolation when optical density exceeds 0.1 were described in section 2.6. Incubation in three culture media (LB, YPD and sterile PBS) was conducted in the same manner as with sterility testing of nanocellulose and alginate.

For T-HA, 100µl of the HA stock solution (30mg/ml) was used. For N-HA, 100µl of N-HA reconstituted in sterile ddH_2O at the high concentration was used. By testing against the higher N-HA concentration, if sterility was proven, sterility of HA at the lower concentration could be inferred.

Regarding timepoints, testing was extended to 21 days from previous published protocols to account for the full study period. Whilst T-HA was subjected to the full testing timepoints, which included day 1, 2, 5, 7, 14 and 21, testing of N-HA underwent an abbreviated schedule of day 7, 14 and 21 only. Due to material cost implications, it was surmised that should sterility be maintained at latter timepoints, sterility at earlier timepoints was implied.

5.2.4 Toxicity testing of material (T-HA and N-HA) and cross-linker (H_2O_2) on HFF-1 cell line

The cytotoxic and pro-inflammatory effects of each material or cross-linker were tested independently against both the HFF-1 and C20A4 cell lines in 2D monocultures. This included assessment using the erythrosin B exclusion assay, ELISA to assess IL-6 and IL-8 release, and light microscopy to visualise the impact on cell morphology.

The time course of material and cross-linker toxicity testing was kept consistent amongst various bio-ink components tested. Timepoints for material toxicity testing

included day 1, 2, 3, 5 and 7 (acute) and day 14 and 21 (chronic). For cross-linker toxicity testing, there was nine timepoints tested which were 5, 15 and 30 minutes, 1 and 4 hours, and 1, 2, 5 and 7 days. The rationale behind the choice of timepoints for cross-linker toxicity testing was previously explained in section 4.2.3.

A summary of chemicals (including concentrations) and cell types tested in material and cross-linker toxicity testing undertaken in chapter 5 is provided in table 5.1 and figure 5.1. Material and cross-linker toxicity testing initiated with T-HA and H_2O_2 against HFF-1. As a result of the cytotoxic effects of H_2O_2 at concentrations required to achieve cross-linkage, the application of T-HA and H_2O_2 was deemed futile and therefore further material and cross-linker testing against C20A4 was rendered irrelevant and was not undertaken.

In material toxicity testing, T-HA involved the dilution of T-HA stock solution in culture media, whilst N-HA involved direct reconstitution in media at desired concentrations. For cross-linker toxicity testing, H_2O_2 were diluted in media at desired concentrations. All material and cross-linker in media used for toxicity testing were made immediately prior to exposures.

Table 5.1 Summary of chemicals and cell types tested in material and cross-linker toxicity testing of hyaluronic acid (HA) and hydrogen peroxide (H_2O_2). *Two forms of HA were tested: tyramine-substituted HA termed T-HA and non-tyramine-substituted HA termed N-HA.*

	Material		**Cross-linker**
	T-HA	**N-HA**	**H_2O_2**
Cell types	HFF-1	HFF-1 + C20A4	HFF-1
Chemical Concentration	high + low	high + low	5, 10, 15, 20, 25μM 5, 10, 15, 20, 25mM

5.2.4.1 H_2O_2

All H_2O_2 used in this chapter was obtained from Sigma-Aldrich (30% (w/w) in H_2O with stabiliser; product code H1009, 5ml). To enhance consistency, only H_2O_2 in bottles opened within seven days was used. This was in recognition of the more rapid oxidation of H_2O_2 after bottle opening with the potential loss of potency, thereby introducing variability and potentially impacting results measured.

Concentration ranges tested were based on previous research that investigated nanocellulose:T-HA bio-inks cross-linked by H_2O_2 (unpublished). This consisted of 5,

10, 15, 20 and 25 at μM and mM ranges. The μM was applied for studies with cellular components, whilst the mM range was used for cell-free experiments such as rheological or testing of mechanical properties as it produced stiffer and stronger constructs. To understand their biological impact and explore their potential application to the intended *in vitro* model for biocompatibility testing, both μM and mM H_2O_2 ranges were tested in the cross-linker toxicity testing against HFF-1.

5.2.4.2 Cell culture

Cell culture methodologies for HFF-1 and C20A4 in 2D monocultures were detailed in section 2.7.

5.2.4.3 Erythrosin B exclusion assay

The erythrosin B exclusion assay was used to assess cytotoxicity in all 2D monocultures conducted in this chapter. The assay methodology was previously described in section 2.8.2.

5.2.4.4 ELISA

For the assessment of pro-inflammatory response, quantification of IL-6 and IL-8 released was performed using ELISA. Its methodology was described in section 2.8.3.

5.2.4.5 Light microscopy

Cell morphology was examined using light microscopy as detailed in section 2.8.4.

5.2.5 Gelation of Nanocellulose:HA bio-ink

The study of gelation of Nanocellulose:HA bio-inks was staged, in the same manner as that in chapter 4 examining Nanocellulose:Alginate bio-inks. Determination of the minimum gelation time to create a standardised 8mm wide circular disc with 100μl bio-ink in a silicon mold was first undertaken. This enabled selection of the optimal bio-ink formulations and cross-linker reagent and concentration required to progress to the next phase of rheological testing.

Bio-inks were created following protocols described in sections 2.3 and 2.4, detailing procedures including material sterilisation and preparation, concentrations of material used, material mixing and bio-ink preparatory steps. Based upon results from chapter 3, all nanocellulose used in this chapter was tunicate-derived ETC in a single concentration, detailed in section 2.3.1. Both forms of cross-linkage studies were performed in a similar manner to that in chapter 4, differing only in the bio-inks and cross-linkers tested.

5.2.5.1 Determination of minimum gelation time in silicon molds

Methodologies and rationale behind the testing and definition of the minimum gelation time in silicon molds are detailed in section 2.11 and section 4.3.4.1, respectively.

Table 5.2 and 5.3 summarises the bio-inks tested, which are also depicted in figure 5.1. This can be broadly categorised into bio-inks using T-HA and N-HA, constituting table 5.2 and 5.3 respectively.

Testing initiated with T-HA, beginning with bio-inks made solely of nanocellulose and T-HA. These were cross-linked with H_2O_2. Both the μM and mM concentration ranges were tested, mirroring concentrations examined in cross-linker toxicity testing. Due to incomplete gelation with 25μM which was the highest concentration within the μM range (table 5.4), a dose range study was undertaken to gain information bridging the concentration gap between the μM and mM ranges. All concentrations tested were shown in table 5.2. Due to the broad concentration gap (25μM – 5mM), concentrations tested were set at 1mM interval between 1-4mM, and approximating serial halving for concentrations below 1mM to encompass a representative spread of concentrations.

Due to results and conclusions drawn from investigations related to T-HA, which will be expanded upon in section 5.3.1, the transition towards a triple component bio-ink was trialled. The pilot testing was conducted using T-HA, but with the addition of alginate and was cross-linked by 0.1M $CaCl_2$. This was the same concentration of cross-linker used for the bio-ink ETC:Alginate in chapter 4. Variables in the pilot testing are summarised in table 5.2.

Due to the success of the pilot testing of the triple component bio-ink, transition towards the use of N-HA was made, which will be detailed and further discussed in

section 5.3.1.4. The cross-linkage study parameters for bio-inks using N-HA are detailed in table 5.3.

Table 5.2 Overview of bio-inks, solvents and cross-linkers tested in the study of minimum gelation time in silicon molds with bio-inks containing tyramine-substituted hyaluronic acid (T-HA). *Two forms of nanocellulose were used: pulp-derived nanocellulose blend (NCB) and tunicate-derived enzymatically pre-treated nanocellulose (ETC). Components denote the hybrid nature of the bio-ink compositions. Two T-HA concentrations were tested, denoted as low for 0.006g/ml and high for 0.012g/ml. *denotes concentrations tested as a dose range study.*

Two component			**Triple component (pilot testing)**		
Bio-inks	**Solvent**	**[H_2O_2]**	**Bio-inks**	**Solvent**	**[$CaCl_2$]**
NCB:T-HA (low) ETC:T-HA (low) ETC:T-HA (high)	ddH_2O	25μM 5, 10, 15, 20, 25mM *37.5, 75, 125, 250, 500μM, 1, 2, 3, 4mM	ETC:Alginate:T-HA (low) ETC:Alginate:T-HA (high)	ddH_2O media	0.1M

Table 5.3 Overview of bio-inks, solvents and cross-linkers tested in the study of minimum gelation time in silicon molds with bio-inks containing non-tyramine-substituted hyaluronic acid (N-HA). *Nanocellulose used was enzymatically pre-treated and tunicate-derived, denoted as ETC. N-HA was tested in a high (0.012g/ml) and low (0.006g/ml) concentration.*

Triple component		
Bio-inks	**Solvent**	**[$CaCl_2$]**
ETC:Alginate:N-HA (low) ETC:Alginate:N-HA (high)	ddH_2O media	0.1M

5.2.5.2 Rheological study of gelation

Rheological study in the forms of oscillatory time sweep experiment was conducted in a similar manner to that in chapter 4. Bio-inks and cross-linker tested were refined from previous studies in this chapter, and were the same as that tabulated in table 5.3. Experimental and data analysis methodologies were previously described in sections 2.12.2, 2.12.3 and 2.12.4. Overall, four bio-inks were tested to compare the material performance between the high and low N-HA concentrations, and between the use of media versus sterile ddH_2O as solvents for alginate and N-HA.

5.3 Results and Discussion

As two forms of HA were investigated in series, results and discussion are discussed beginning with T-HA (section 5.3.1), followed by N-HA (section 5.3.2).

5.3.1 Tyramine-substituted hyaluronic acid

5.3.1.1 Material sterility testing

Microbial growth assay was performed to compare between T-HA as supplied (untreated) versus T-HA that was sterilised by UV treatment.

All culture conditions maintained OD less than 0.1 threshold, denoting sterility, except for the untreated T-HA cultured in YPD. This suggests that the sterility of sterilised T-HA was maintained for the full study period in all media types (figure 5.2).

Whilst untreated T-HA maintained sterility in LB for up to 21 days, a rise in OD above 0.1 was seen on day 14 and 21 in YPD, although this was not statistically significant. The results indicate that there was a positive effect of UV treatment with regards to sterility, as the rise in OD in YPD at latter timepoints was not seen in UV-treated samples. As LB and YPD preferentially support the growth of bacteria and yeast respectively, the results indicate that the likely contaminant of T-HA was a form of yeast, although bacterial isolation did not yield positive growth. Nonetheless, exact identification of the contaminating microbe was not strictly relevant for the project as untreated T-HA will not be used in culture conditions and for the advanced *in vitro* model. The potential of material agglomeration as a cause of rise in OD was deemed less likely due to the consistently low OD when T-HA was cultured in sterile PBS.

Statistical testing performed included comparison between sterilised and untreated samples at each timepoint, between negative control and sterilised or untreated samples at each timepoint, and time course comparison of each culture condition between day 1 and day 2 – 21. There was no statistically significant difference for all comparisons and across all timepoints.

Overall, the results are in line with the information provided from the manufacturer, whereby T-HA was considered a ‘clean’ material with low bio-burden, but not defined as sterile. Based on these results, UV-treatment of T-HA was confirmed as a necessary material preparatory step and that the resultant material was suitable for culture for up

to 21 days. To account for potential chemical alterations from UV-treatment and the downstream impact on material behaviour including gelation, all T-HA used in the project will be UV-treated regardless if the material was used in cell-based or cell-free studies.

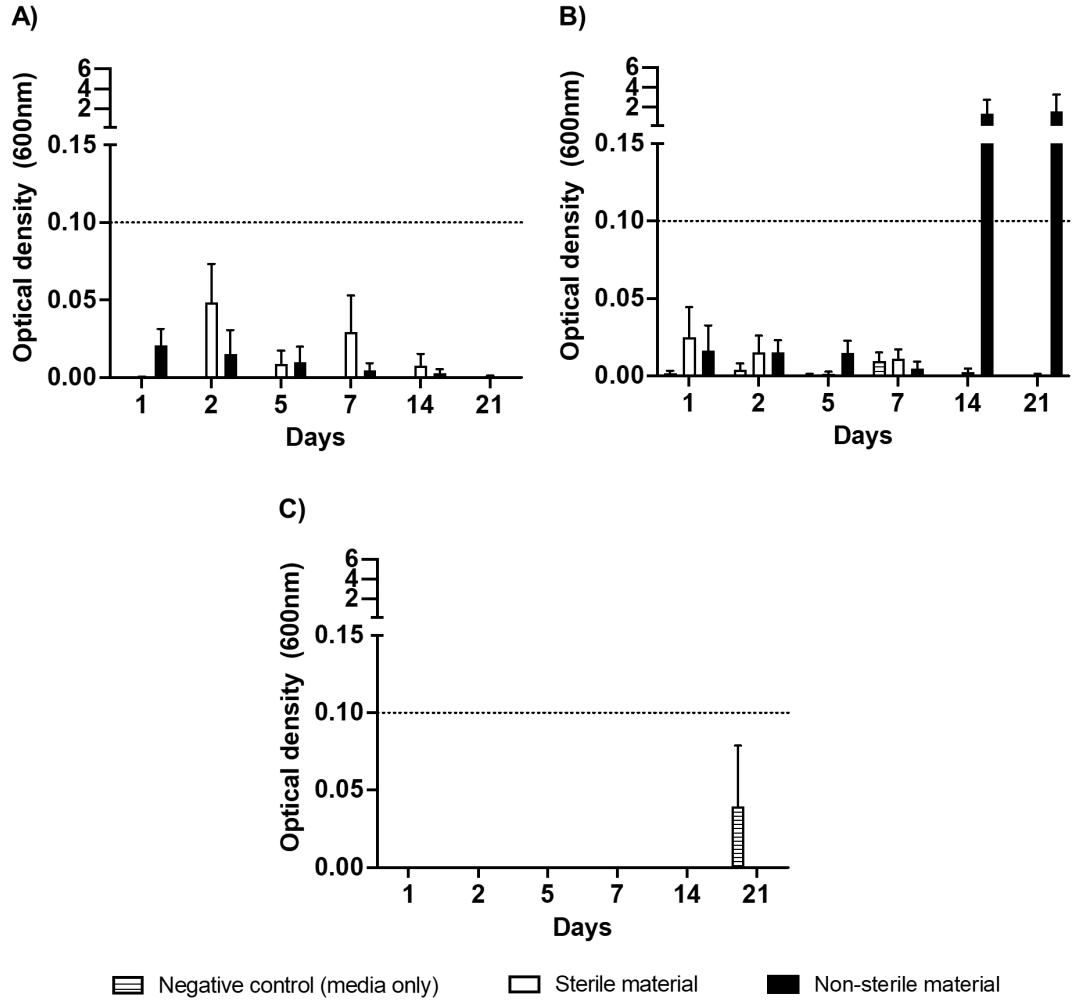

Figure 5.2 Sterility testing of tyramine-substituted hyaluronic acid (T-HA). *Assessment of sterility and material effects of T-HA on optical density in A) lysogeny broth (LB), B) yeast extract-peptone-dextrose (YPD) and C) sterile PBS. UV-sterilised and non-sterilised T-HA in LB, YPD or sterile PBS were incubated at 37°C under constant agitation over 21 days. Media or PBS without T-HA served as negative control. Optical density measured at 600nm. Accepted arbitrary threshold for sterility at <0.1 denoted by horizontal dotted line. Mean±SEM is shown. N=3.*

5.3.1.2 Material toxicity testing

The cytotoxic and pro-inflammatory effects of T-HA were assessed using the erythrosin B exclusion assay and measuring the levels of IL-6 and IL-8 released, beginning with the HFF-1 cell line (human dermal fibroblast).

As detailed in section 2.3.1, two concentrations (0.006g/ml and 0.012g/ml) will be simply referred to as ‘low’ and ‘high’ in all subsequent descriptions. For example, T-HA at 0.006g/ml will be referred to as ‘T-HA (low)’.

5.3.1.2.1 Cytotoxicity

HFF-1 exposed to T-HA demonstrated lower total and live cell concentrations than the negative control at all timepoints, although this was not statistically significant (figure 5.3A/B). The reduced cell concentrations may be due to increased media viscosity with the addition of T-HA, adversely impacting cellular access to nutrients and oxygen by diffusion. This could explain the dose-dependent effect, whereby T-HA (high) was associated with greater media viscosity as well as more marked reduction in cell concentrations. Nonetheless, the trend of total and live cell concentrations of HFF-1 exposed to T-HA followed that of negative control albeit at a lower level. There was a rise between day 1 and day 14, followed by a decline on day 21, most likely the result of over-confluence. The latter, however, was not seen with T-HA (high), presumably due to a lower cell concentration and not reaching the threshold of over-confluency to cause the subsequent drop in cell concentrations. Despite a reduction in total and live cell concentrations, cell viability was not significantly reduced when HFF-1 was exposed to T-HA when compared to negative control throughout the study period. Taken together, the results suggests that cells exposed to T-HA, in both concentrations, did not experience significant cytotoxicity, but did display a reduction in cell proliferation when compared to the negative control.

In terms of seeking a superior T-HA concentration based on the cytotoxicity data, comparison between the high and low concentrations of T-HA showed no statistically significant difference in total and live cell concentrations and cell viability at all timepoints (figure 5.3). The advantage of T-HA (low) over T-HA (high) in terms of greater cell concentrations and therefore greater degree of cell proliferation, may be subject to the system's effects (i.e. 2D culture), and is not necessarily translatable to 3D models.

5.3.1.2.2 Pro-inflammatory response

Comparison between HFF-1 exposed to T-HA versus negative control showed that whilst IL-6 release was consistently lower in exposures conditions, HFF-1 exposed to T-HA released greater levels of IL-8 on day 2-7 (figure 5.4). However, there was no statistically significant difference at all timepoints, with either high or low T-HA concentrations. Considering temporal change, a general rising trend was observed with

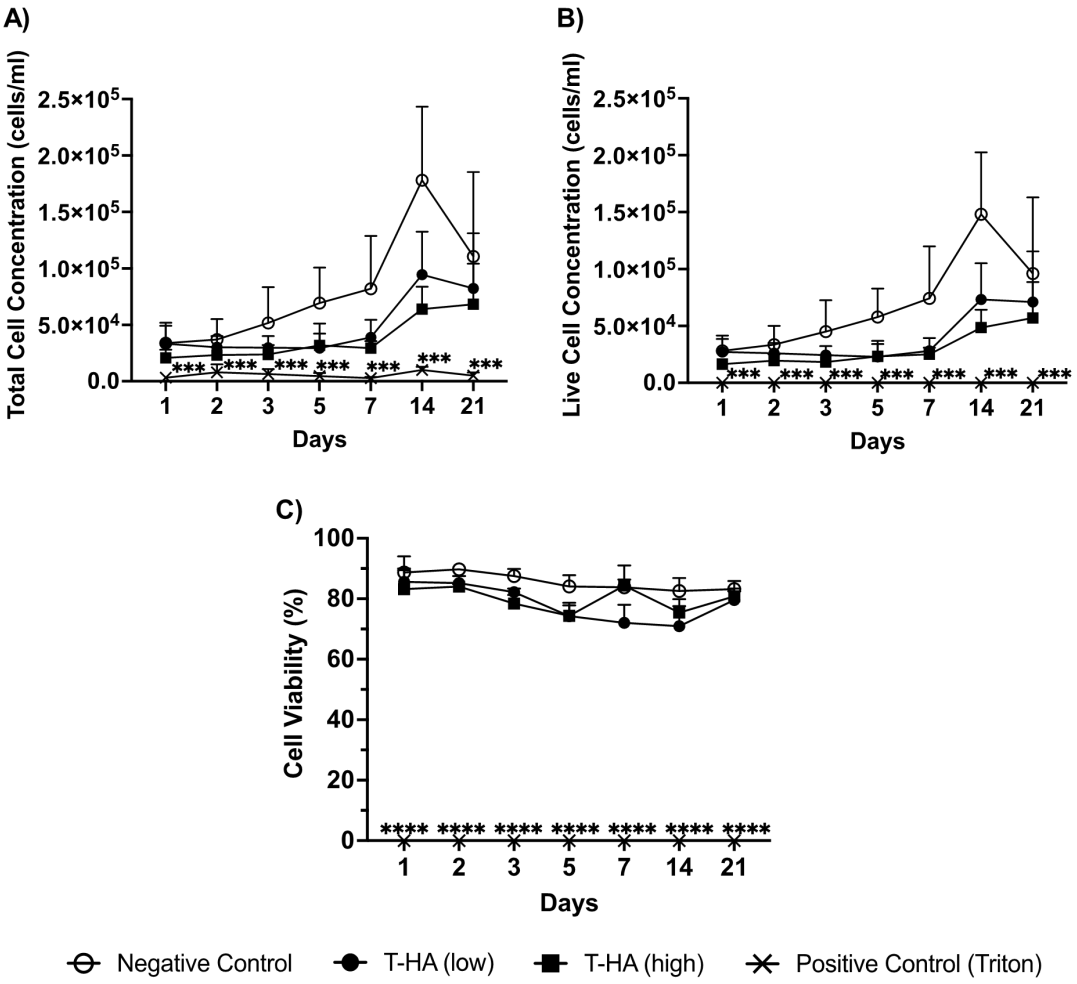

Figure 5.3 Cytotoxicity of 2D monoculture of HFF-1 exposed to tyramine-substituted hyaluronic acid (T-HA) over 21 days. *Two T-HA concentrations were tested, denoted as 0.006g/ml (low) and 0.012g/ml (high). Total (A) and live (B) cell concentration and cell viability (C) were assessed with erythrosin B assay. Positive control was 0.1% Triton X-100. Mean±SEM is presented. N=3. Comparison between negative control and T-HA (low), T-HA (high) or positive control at each timepoint were denoted by *, and timepoint comparisons of each culture conditions by #. Statistical significance is shown as: p<0.05 */#, p<0.01 **/##, p<0.001 ***/### and p<0.0001 ****/####.*

both chemokines, with all cellular conditions. There was a sharp rise on day 14, reaching statistical significance on day 21 when compared to chemokine levels on day 1 ($p<0.0001$). Interpretation of chemokine levels between negative control and exposures, and changes over time, is limited by the varying cell concentrations and therefore cell numbers between culture conditions and timepoints. Rise in chemokines levels measured could be due to cell activation, or increased cell numbers, or both. Therefore, to account for this, chemokine levels per cell was evaluated to offer an additional perspective in the next section (figure 5.5).

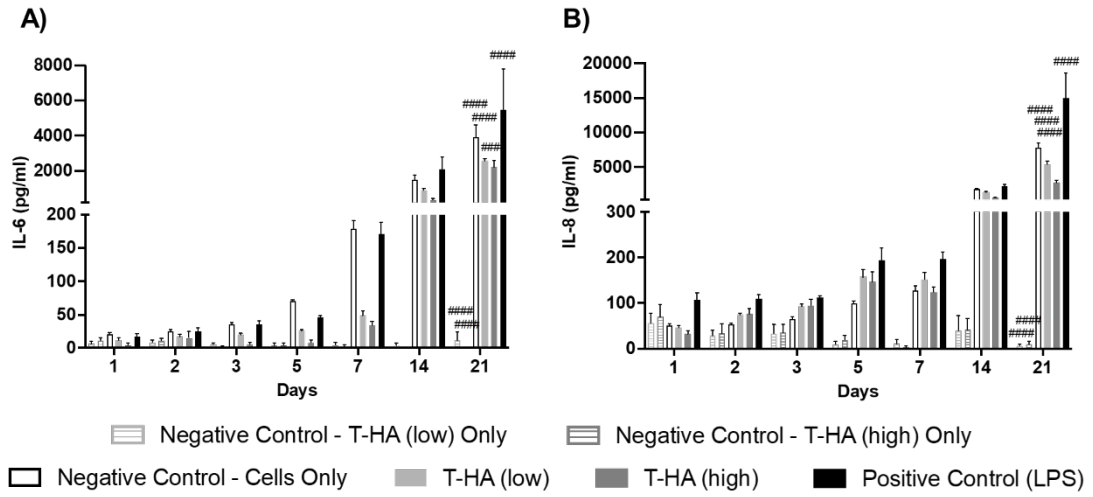

Figure 5.4 Pro-inflammatory effect of tyramine-substituted hyaluronic acid (T-HA) on HFF-1 2D monoculture over 21 days. *Two T-HA concentrations were tested, denoted as 0.006g/ml (low) and 0.012g/ml (high). IL-6 (A) and IL-8 (B) release were measured with ELISA. Negative control consisted of HFF-1 2D monoculture without material exposure, termed 'negative control – cells only'. Positive control was LPS 1μg/ml. Material interference on assay was investigated with material treated to the same experimental conditions, termed 'negative control – T-HA only', which included both T-HA concentrations. Mean±SEM is presented. N=3. Statistical significance on timepoint comparisons D1 v D2-21 of each culture conditions are denoted by: p<0.05 #, p<0.01 ##, p<0.001 ### and p<0.0001 ####.*

Considering still the total amount of chemokines measured, direct comparison of the high and low concentrations of T-HA showed no difference in IL-6 and IL-8 release across all timepoints ($p>0.05$) (figure 5.4). This suggests that the two T-HA concentrations tested did not produce a varied pro-inflammatory response by HFF-1.

The impact of material interference on the ELISA was also assessed by treating cell-free T-HA under the same experimental and culture conditions before measuring the levels of each chemokine at the same timepoints. Overall, relatively low but detectable levels of both chemokines were seen across the study period to suggest a degree of material interference of the assay. However, chemokines levels remained low throughout, and from day 5 onwards, levels were markedly below all cellular conditions. Whilst timepoint comparison revealed statistically significant changes in both chemokines between day 1 and 21, for both material concentrations tested ($p<0.0001$), taken together, it was concluded that biologically significant material interference of the assay was not present.

The application of per cell adjustment did not alter the overall pattern of results. Direct comparison of IL-6 and IL-8 release per cell between the two tyramine-substituted HA concentrations showed no statistically significant difference to infer superiority.

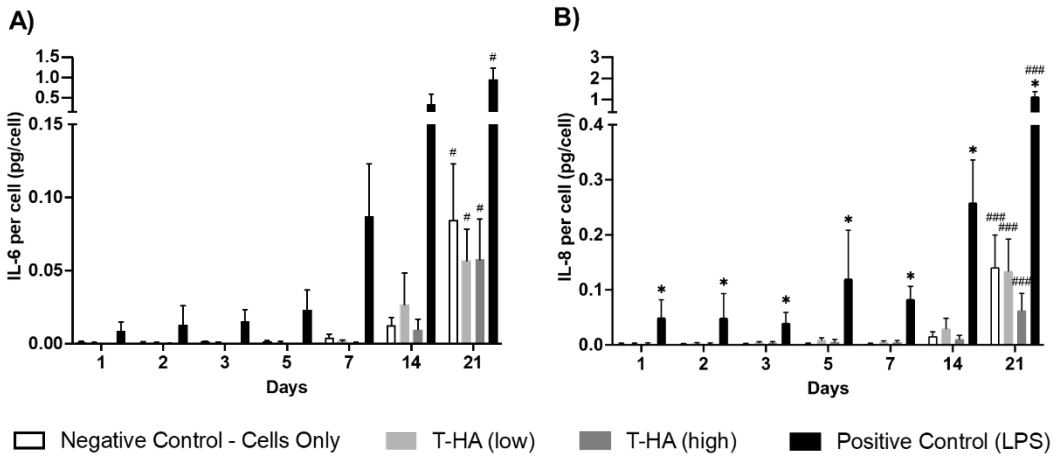

Figure 5.5 Pro-inflammatory effect per cell of tyramine-substituted hyaluronic acid (T-HA) on HFF-1 2D monoculture over 21 days. *Two T-HA concentrations were tested, denoted as 0.006g/ml (low) and 0.012g/ml (high). IL-6 (A) and IL-8 (B) release were measured with ELISA, and chemokine released per cell were calculated relative to total cell number at each timepoint. Negative control consisted of HFF-1 2D monoculture without material exposure, termed 'negative control – cells only'. Positive control was LPS 1µg/ml. Mean±SEM is presented. N=3. Comparisons between negative control and T-HA or positive control at each timepoint is denoted by *, and timepoint comparison within each culture condition between day 1 and day 2-21 by #. Statistical significance conditions are denoted by: p<0.05 */#, p<0.01 **/##, p<0.001 ***/### and p<0.0001 ****/####.*

When compared with negative control, there were no statistically significant difference in IL-6 or IL-8 release per cell with HFF-1 exposed to T-HA, at both concentrations. This suggests that T-HA did not stimulate a pro-inflammatory response when applied to HFF-1 over a 21 day period.

Time course review did reveal a rising trend of IL-6 and IL-8 release per cell over time. This was noted in all culture conditions, with a statistically significant rise on day 21 ($p<0.05$ for IL-6, $p<0.001$ for IL-8). This suggests that cells were activated on day 21 in this model, regardless of T-HA or LPS treatment or lack of, indicating the need for further model development at latter timepoints.

5.3.1.2.3 Cell morphology

The impact on cell morphology of HFF-1 exposed to two concentrations of T-HA was assessed by light microscopy. There was a general trend of increasing cell confluence over time, mirroring the rise in total cell concentration (figure 5.6). Whilst examination with the erythrosin B exclusion assay demonstrated greater total and live cell concentrations in the negative control, light microscopy images showed that HFF-1s cultured in T-HA looked comparable to cells in negative control. Shadows and dark 'clumps' were seen in culture conditions containing T-HA, which were more apparent

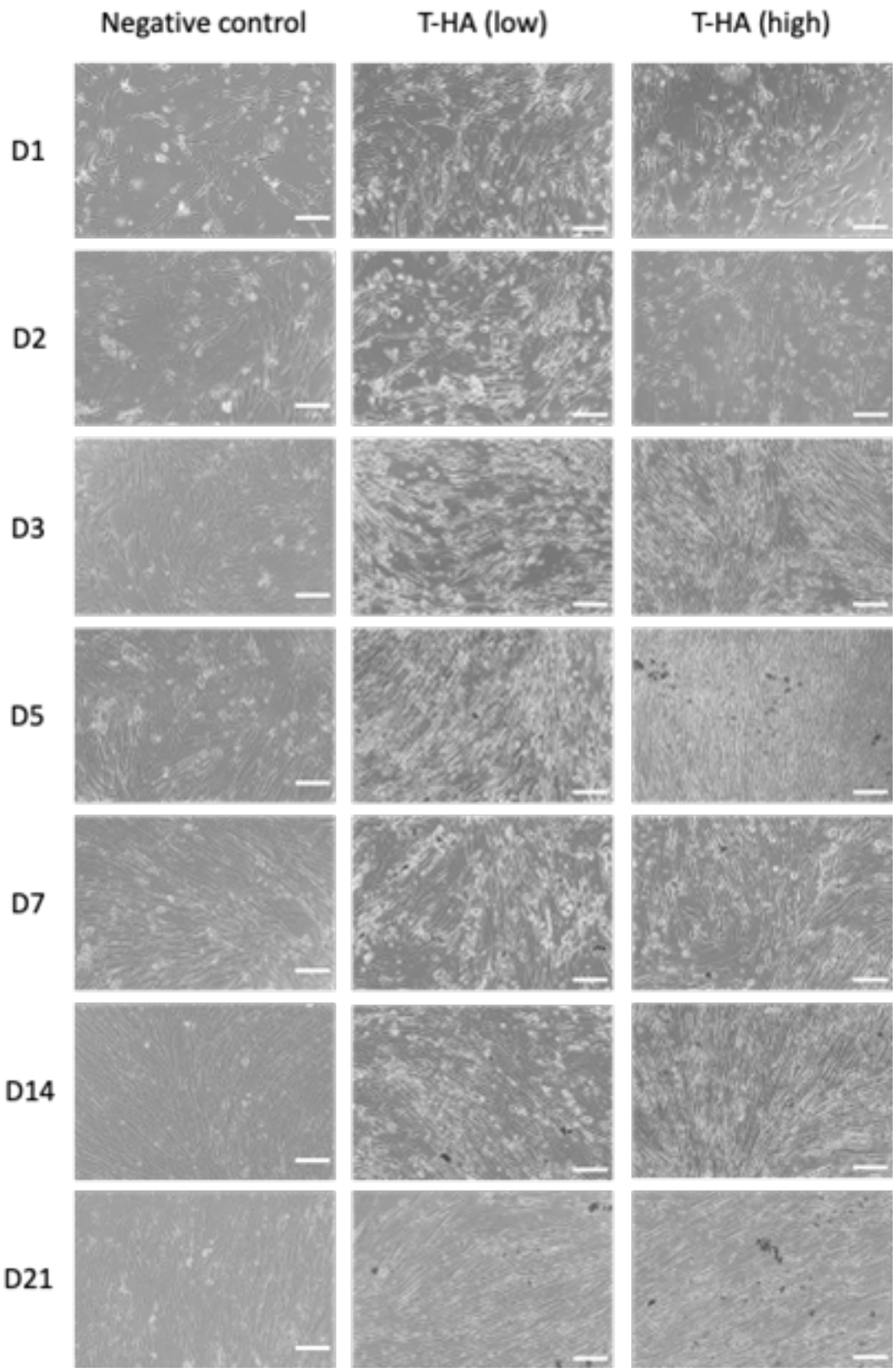

Figure 5.6 Light microscopy of effect of tyramine-substituted hyaluronic acid (T-HA) on HFF-1 2D monoculture over 21 days. *Two T-HA concentrations were tested, denoted as 0.006g/ml (low) and 0.012g/ml (high). Negative control constitutes HFF-1 2D culture without T-HA exposure. Scale bars represent 200μm.*

at latter timepoints with prolonged culture. These reflect the material effects on the media with potential increase in viscosity and a degree of heterogeneity with 'gel clump' formation with prolonged culture at 37°C. There also appeared to be a greater amount of extra-cellular matrix production in cells exposed to T-HA, causing enhanced contrast in light microscopy images. This may be explained by an increase in chondrogenicity in cells exposed to T-HA (unpublished data from the research group). Overall, cell morphology was not significantly altered and a rise in cell proliferation can be appreciated when HFF-1 was exposed to T-HA. There was also no marked difference between cells exposed to the high or low concentration of T-HA. This result suggests that T-HA at the concentrations used in the bio-ink did not induce gross adverse cytotoxic effects against HFF-1 in 2D culture.

5.3.1.2.4 Section summary – material toxicity testing

In summary, T-HA did not demonstrate cytotoxic or pro-inflammatory effects with preserved cell morphology when exposed to HFF-1, although cell proliferation was hindered which may be due to a systems effect from the model. Comparison between the high and low concentration of T-HA were mostly comparable, except for an advantage of greater cell proliferation with T-HA (low) although this maybe specific to the system in 2D culture. Data also suggest further development of the model at latter timepoints maybe indicated, due to over-confluency with subsequent reduction in cell numbers as well as cell activation with marked pro-inflammatory response.

5.3.1.3 Cross-linker toxicity testing

This section details the results of the assessment of the cytotoxic and pro-inflammatory effects of H_2O_2, the cross-linker for T-HA, and its impact on cell morphology against the HFF-1 cell line. Results are presented with the μM range first, followed by the mM range.

5.3.1.3.1 Cytotoxicity

HFF-1 in the negative control displayed an overall rising trend of total and live cell concentrations up to day 5, followed by a small decline, although this was not statistically significant. This may reflect that confluency was reached at day 5, with

time course comparison showing a statistically significant rise on day 5 when compared to at 5 minutes ($p<0.001$). However, cell viability in negative control was preserved and remained between 80-95% during the study period (figure 5.7).

When exposed to 5-25 μM H_2O_2, the total and live cell concentrations of HFF-1 were similar to that of negative control, both displaying greater variance on day 5 and 7. On the other hand, cell viability showed a statistically significant reduction with the application of H_2O_2. This was the case for all five μM concentrations at all timepoints tested. However, direct comparison between the five H_2O_2 μM concentrations did not reveal any statistically significant difference for total and live cell concentration and cell viability over time ($p>0.05$).

Positive control (0.1% Triton X-100) also led to a statistically significant reduction in total cell concentration on day 5, and reduction in live cell concentration at all timepoints. Live cell concentration and cell viability with positive control were zero at all timepoints from 15min to day 7, and was not depicted in figure 5.7.

These results demonstrate that cytotoxic effects against HFF-1 were detectable even at the lower μM H_2O_2 range. At the lowest concentration of 5μM, cell viability maintained at levels above 70% up to 4 hours application.

Next, the effects of the mM range of H_2O_2 against HFF-1 is discussed (figure 5.8). Compared to the μM range, cytotoxic effects were significantly more pronounced when exposed to 5-25mM H_2O_2, and a dose-dependent trend was observed.

Total cell concentration was reduced when HFF-1 were exposed to the mM range of H_2O_2. This was statistically significant at all timepoints for the majority of concentrations tested: 10 and 15mM $p<0.05$, 20 and 25mM $p<0.01$. Associated reductions in live cell concentration were also dose-dependent, and was a more sensitive measure compared to total cell concentrations: 5mM $p<0.05$, 10 and 15mM $p<0.001$, 20 and 25mM $p<0.0001$. These findings were consistent at all timepoints tested and was not shown in figure 5.8.

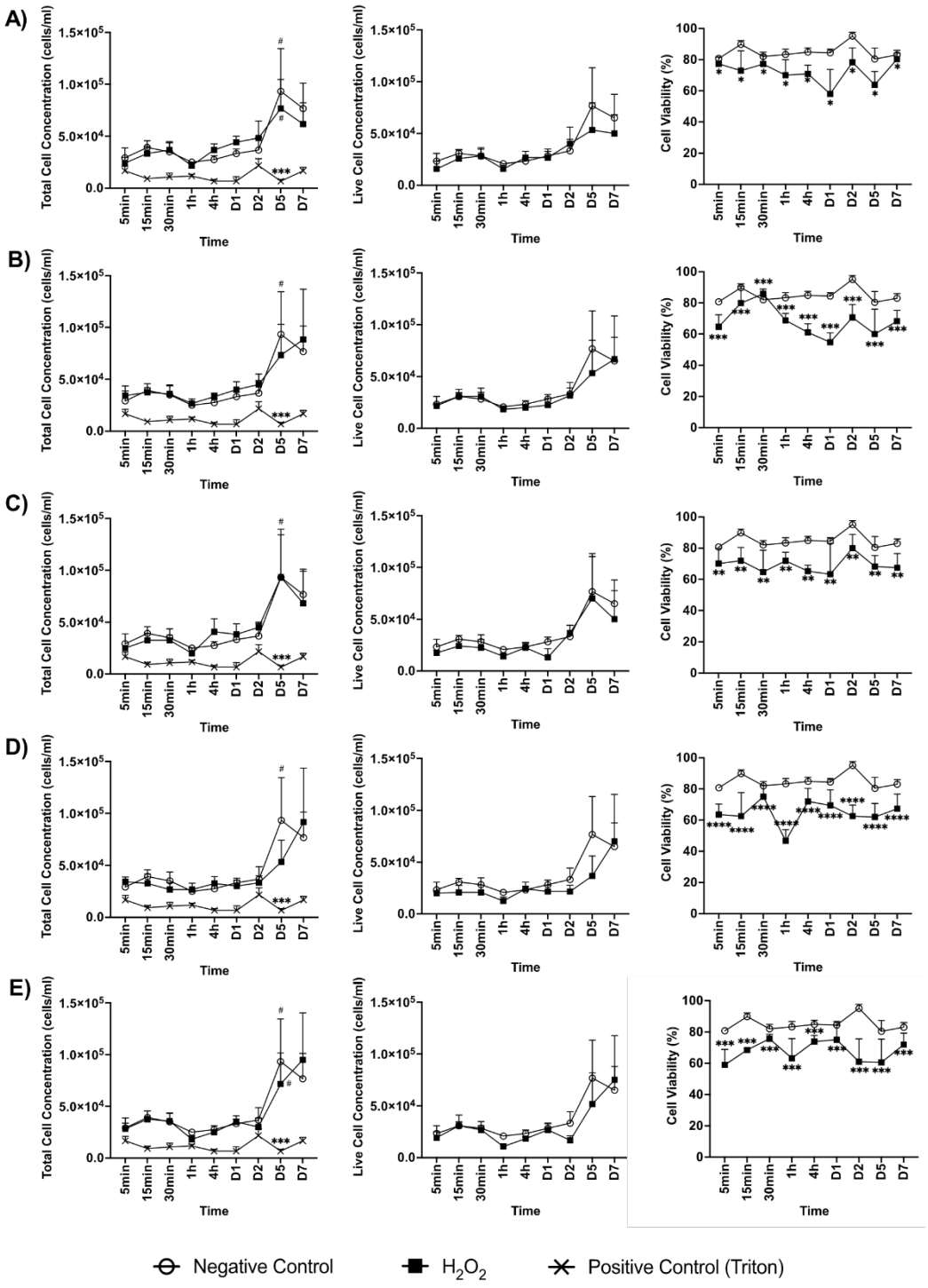

Figure 5.7 Cytotoxicity of cross-linker hydrogen peroxide (H_2O_2) 5-25μM against 2D HFF-1 monoculture over 21 days. *The effects of 5 (A), 10 (B), 15 (C), 20 (D) and 25 (E) μM H_2O_2 were assessed using erythrosin B assay. Total cell concentration (left column), live cell concentration (middle) and cell viability (right) were assessed. Negative control was HFF-1 2D monoculture alone, and positive control was 0.1% Triton X-100. Mean±SEM is presented. N=3. Comparison between negative control and H_2O_2 is denoted by ∗and timepoint comparison of 5min v 15min to day 7 for each culture condition by #. Statistical significance is presented as: p<0.05 ∗/#, p<0.01 ∗∗/##, p<0.001 ∗∗∗/### and p<0.0001 ∗∗∗∗/####.*

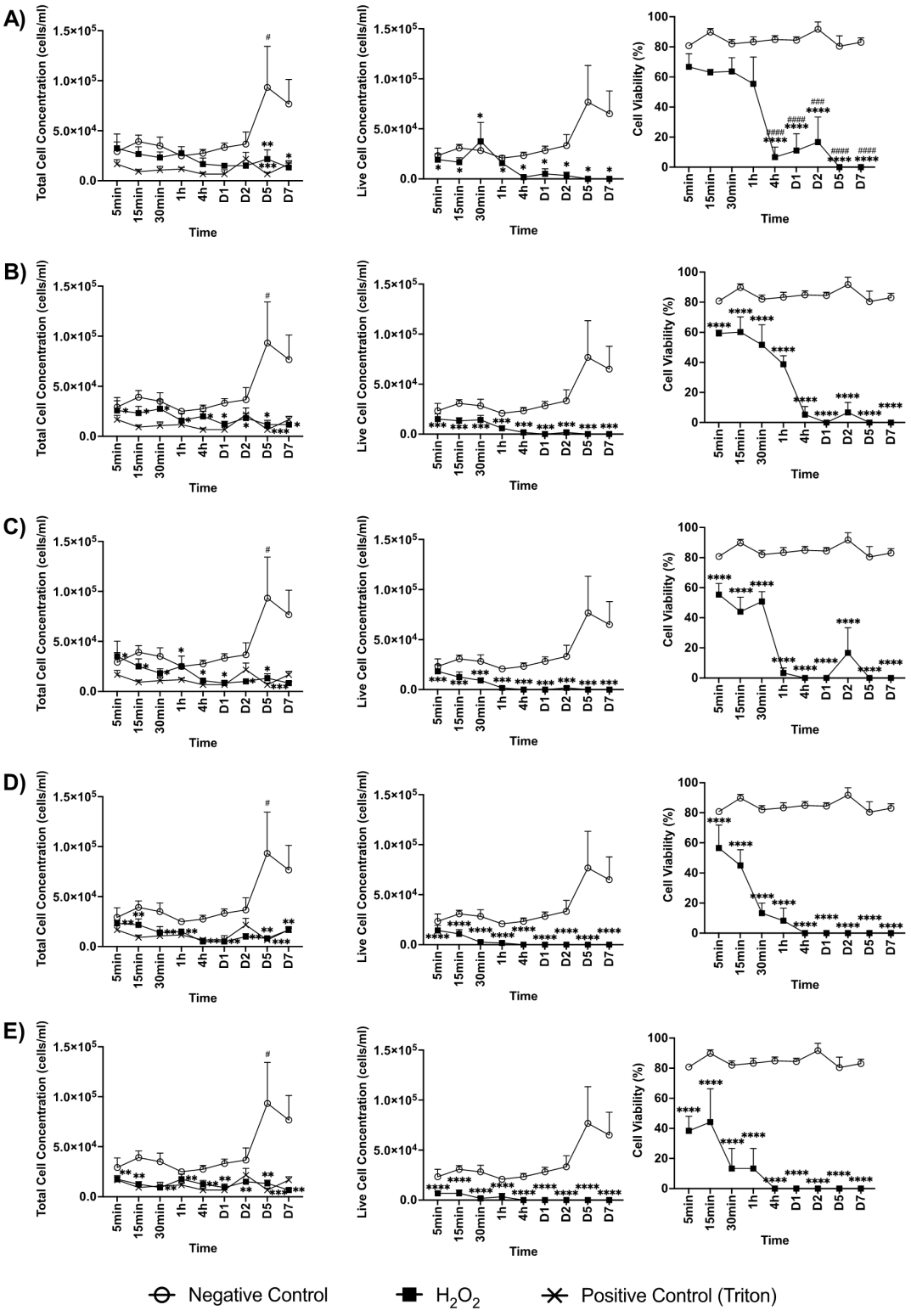

Figure 5.8 Cytotoxicity of cross-linker hydrogen peroxide (H_2O_2) 5-25mM against 2D HFF-1 monoculture over 21 days. *The effect of 5 (A), 10 (B), 15 (C), 20 (D) and 25 (E) mM H_2O_2 were assessed using erythrosin B assay. Total cell concentration (left column), live cell concentration (middle) and cell viability (right) were assessed. Negative control was HFF-1 2D monoculture alone, and positive control was 0.1% Triton X-100. Mean±SEM is presented. N=3. Comparison between negative control and H_2O_2 is denoted by ∗and timepoint comparison of 5min v 15min to day 7 for each culture condition by #. Statistical significance is presented as: p<0.05 ∗/#, p<0.01 ∗∗/##, p<0.001 ∗∗∗/### and p<0.0001 ∗∗∗∗/####.*

Cell viability followed a similar trend, demonstrating that with increasing H_2O_2 concentration, shorter periods of cross-linker application were able to induce cytotoxicity with cell viability below 50%. The timepoints at which cell viability fell below 50% for each H_2O_2 concentration were: 5minutes for 25mM, 15minutes for 20mM, 1 hour for 10 and 15mM and 4 hours for 5mM.

Although time course comparison of total cell concentration, live cell concentration and cell viability showed overall minimal statistically significant changes over time with all mM concentrations, trends of reduction in cell viability was present at all mM concentrations. This demonstrates a time-dependent effect, in addition to dose-dependency.

On the whole, HFF-1 experienced notable cytotoxic effects when exposed to H_2O_2. A clear time- and dose-dependent effect was observed at 5-25mM range, whilst a lesser but still detectable cytotoxic effect was seen at 5-25μM range. This raised questions regarding the suitability of H_2O_2 as a cross-linker agent in constructs that both encapsulates and interfaces with cells. This is further discussed in future sections following examination of other biological indicators and gelation kinetics.

5.3.1.3.2 Pro-inflammatory response

The effects of H_2O_2 in the μM range is first considered. Levels of IL-6 and IL-8 released by HFF-1 in all culture conditions were relatively low between 5 minutes and 4 hours. This was followed by a rise between day 1 and 7, which was statistically significant on day 2-7 for both chemokines ($p<0.0001$) (figure 5.9).

Upon initial analysis, without adjustment for total cell counts, IL-6 release was comparable between with negative controls and exposures to 5-25μM H_2O_2, at all timepoints ($p>0.05$). Comparison between the five H_2O_2 concentrations in the μM range also showed no statistically significant difference in terms of IL-6 and IL-8 release ($p>0.05$).

Chemokine release per cell was then assessed (figure 5.10). A similar trend of rising IL-6 and IL-8 over time were seen, for all culture conditions, reaching statistical significance with IL-6 on day 5 and 7 ($p<0.0001$). However, HFF-1 did not demonstrate significant pro-inflammatory effects when exposed to H_2O_2 in the μM

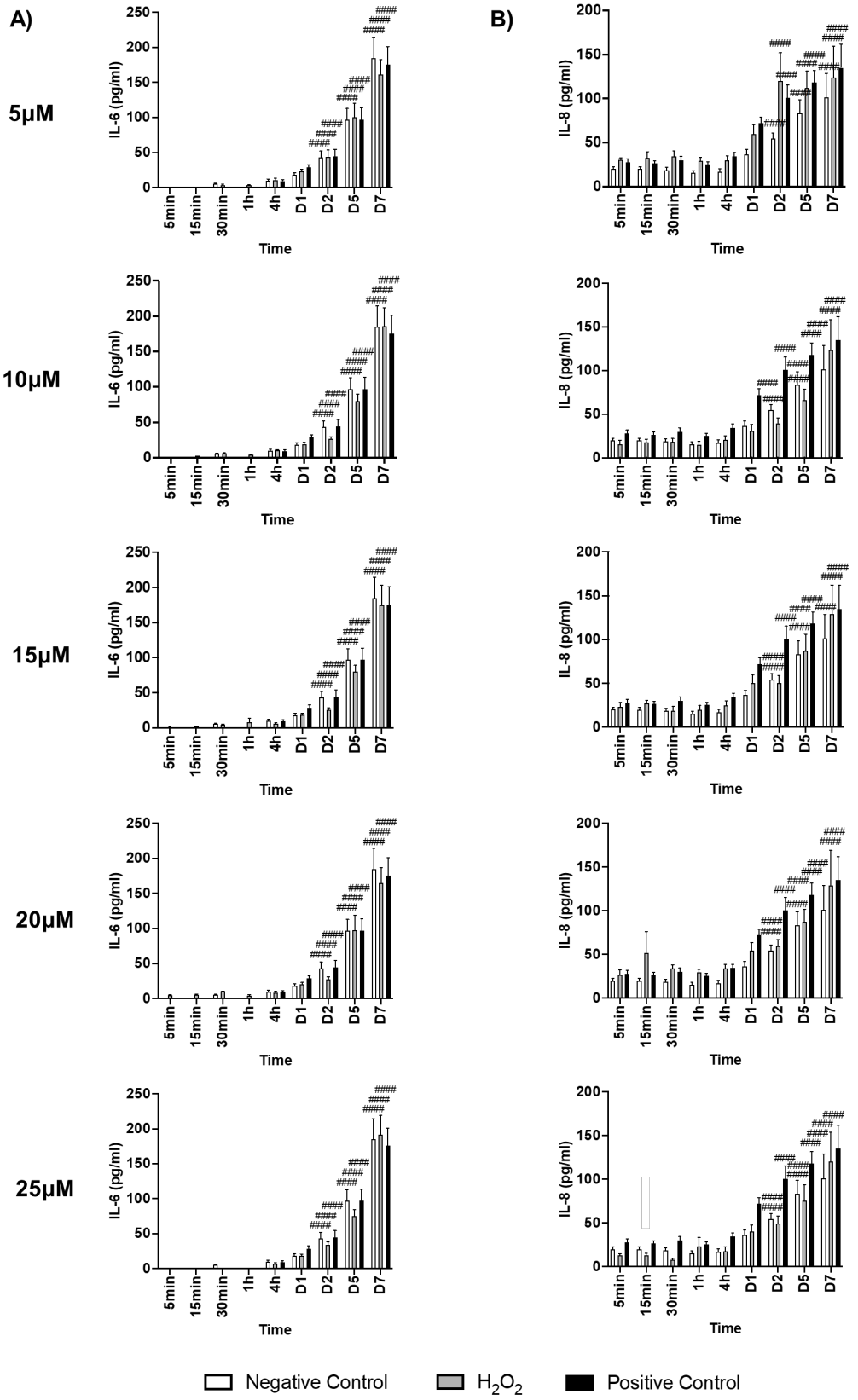

Figure 5.9 Pro-inflammatory effect of cross-linker hydrogen peroxide (H_2O_2) 5-25µM on HFF-1 2D monoculture. *HFF-1 was exposed to H_2O_2 at 5, 10, 15, 20 and 25µM for 5, 15, 30 minutes, 1, 4 hours and 1, 2, 5 and 7 days. IL-6 (A) and IL-8 (B) release were measured with ELISA. Positive control was LPS 1µg/ml. Mean±SEM is presented. N=3. Statistical significance of timepoint comparison between 5min and 15min – day 7 for each culture condition are denoted by: $p<0.05$ #, $p<0.01$ ##, $p<0.001$ ### and $p<0.0001$ ####.*

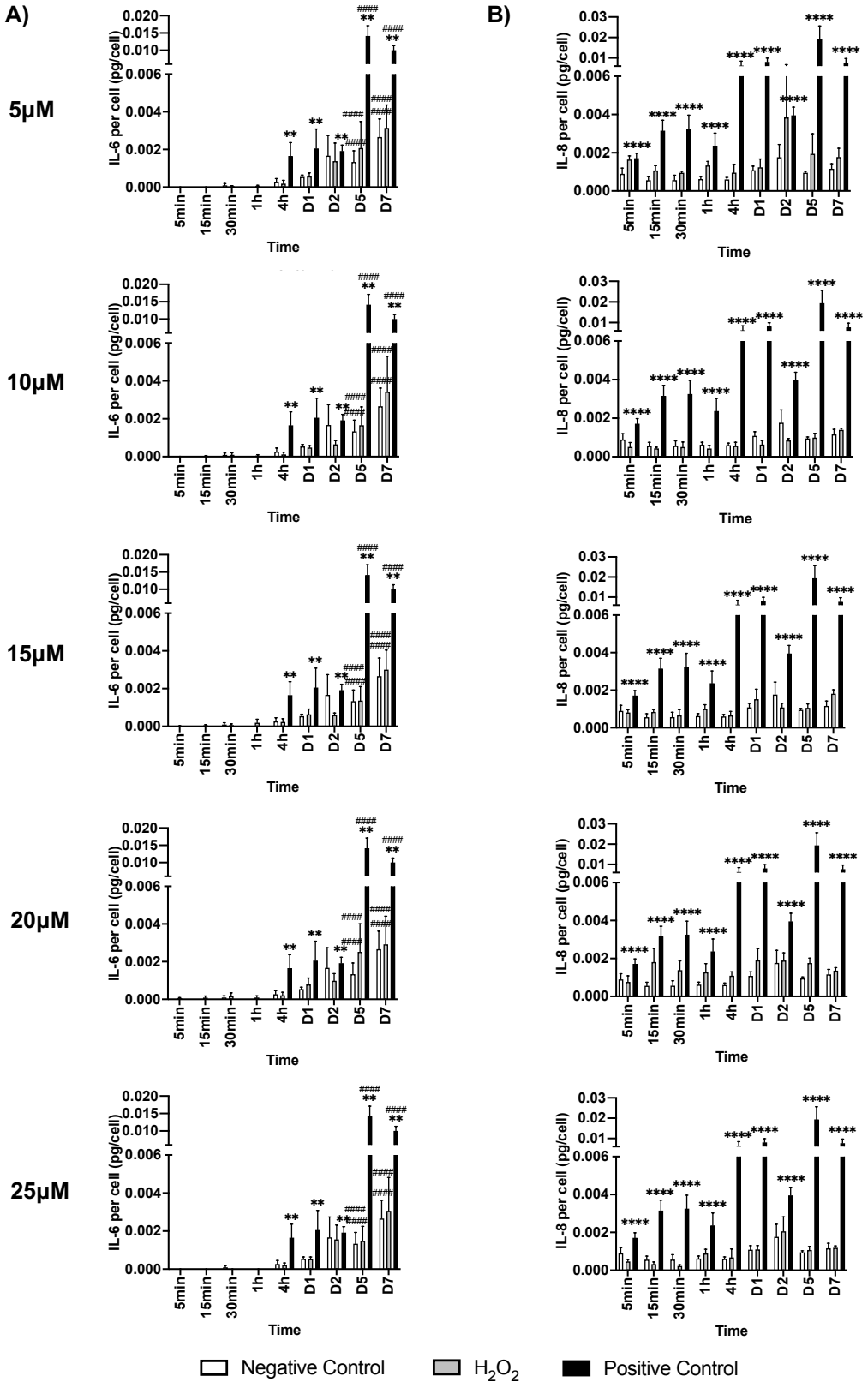

Figure 5.10 Pro-inflammatory effect per cell of cross-linker hydrogen peroxide (H_2O_2) 5, 10, 15, 20 and 25µM on HFF-1 2D monoculture over 7 days. *IL-6 (A) and IL-8 (B) release were measured with ELISA, and chemokine released per cell were calculated relative to total cell number at each timepoint. Positive control was LPS 1µg/ml. Mean±SEM is presented. N=3. Statistical significance between negative control and H_2O_2 or positive control are denoted by ∗ and timepoint comparisons 5min v 15min-7 days of each cell conditions by #: p<0.05 ∗/#, p<0.01 ∗∗/##, p<0.001 ∗∗∗/### and p<0.0001 ∗∗∗∗/####.*

ranges, although cells could be activated as seen in the positive control. Similar to consideration of total chemokine release, comparisons between the concentrations of the μM range did not show significant differences in IL-6 or IL-8 release per cell ($p>0.05$).

HFF-1 when exposed to all five H_2O_2 concentrations in the mM range displayed a significant reduction in IL-6 release when compared to negative control, which was statistically significantly at all timepoints ($p<0.01$) (figure 5.11). Taking into consideration the heightened cytotoxicity with H_2O_2 in the mM range as discussed in section 5.3.1.3.1, such findings are likely due to the absence of viable cells, or altered cell state. IL-6 was non-detectable across all timepoints with 15mM, 20mM and 25mM H_2O_2. A low level of IL-6 was detected on day 2 with 10mM H_2O_2, but was otherwise non-detectable. The lowest concentration tested in the mM range, 5mM, showed low level of IL-6 during the study period.

In terms of IL-8, HFF-1 exposed to 5-25mM H_2O_2 demonstrated a detectable, but relatively low and static levels throughout the study period. From day 1 onwards, whilst levels of IL-8 with HFF-1 exposed to H_2O_2 remained comparatively low, those with the negative control rose between day 1 and 7. Direct comparison of IL-8 levels from HFF-1 exposed to the five mM H_2O_2 concentrations did not show any statistically significant difference ($p>0.05$).

Chemokine release per cell was then evaluated in a similar manner to before, for HFF-1 exposed to 5-25mM H_2O_2. Extremely low to non-detectable levels of IL-6 were seen with HFF-1 exposed to 5-25mM, consistent with results considering total chemokine release, as well as with known cytotoxic effects of H_2O_2 in the mM range. Interestingly, heightened release of IL-8 was seen in per cell calculations. Although this was intermittent at varied timepoints and concentrations with no discernible trend or pattern. Nonetheless, this is likely to reflect cellular dysfunction of the remaining viable cells.

Overall, both the μM and mM ranges of H_2O_2 showed no clear demonstratable pro-inflammatory effects against HFF-1 in 2D culture. This finding is likely to be confounded by the cytotoxic effects against HFF-1, with minimal viable cells present to mount a response.

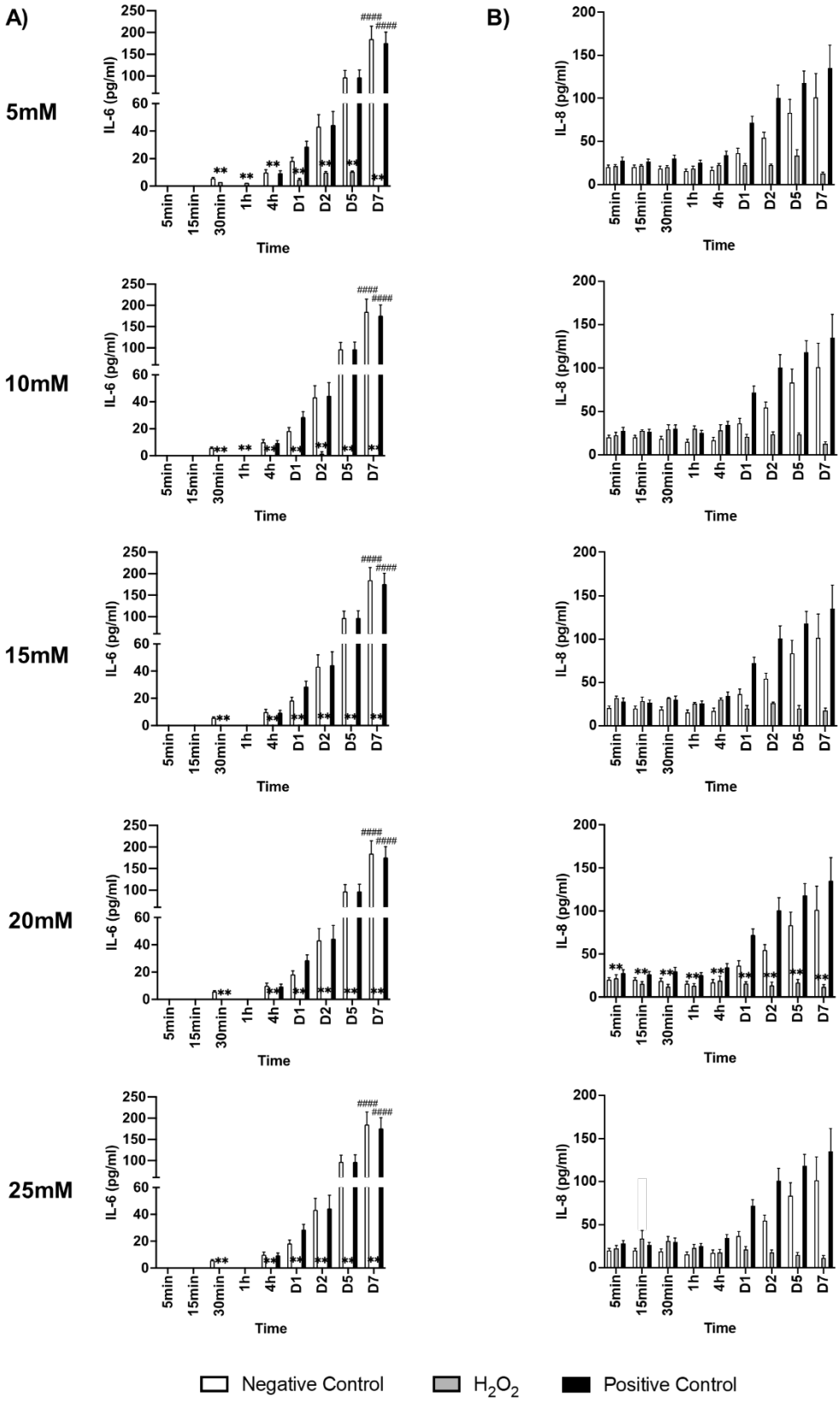

Figure 5.11 Pro-inflammatory effect of cross-linker hydrogen peroxide (H_2O_2) 5-25mM on HFF-1 2D monoculture. *HFF-1 was exposed to H_2O_2 at 5, 10, 15, 20 and 25mM for 5, 10, 15 minutes, 1, 4 hours and 1, 2, 5 and 7 days. IL-6 (A) and IL-8 (B) release were measured with ELISA. Positive control was LPS 1µg/ml. Mean±SEM is presented. N=3. Statistical significance between negative control and H_2O_2 or positive control are denoted by * and timepoint comparisons 5min v 15min-7 days of each cell conditions by #. p<0.05 */#, p<0.01 **/##, p<0.001 ***/### and p<0.0001 ****/####.*

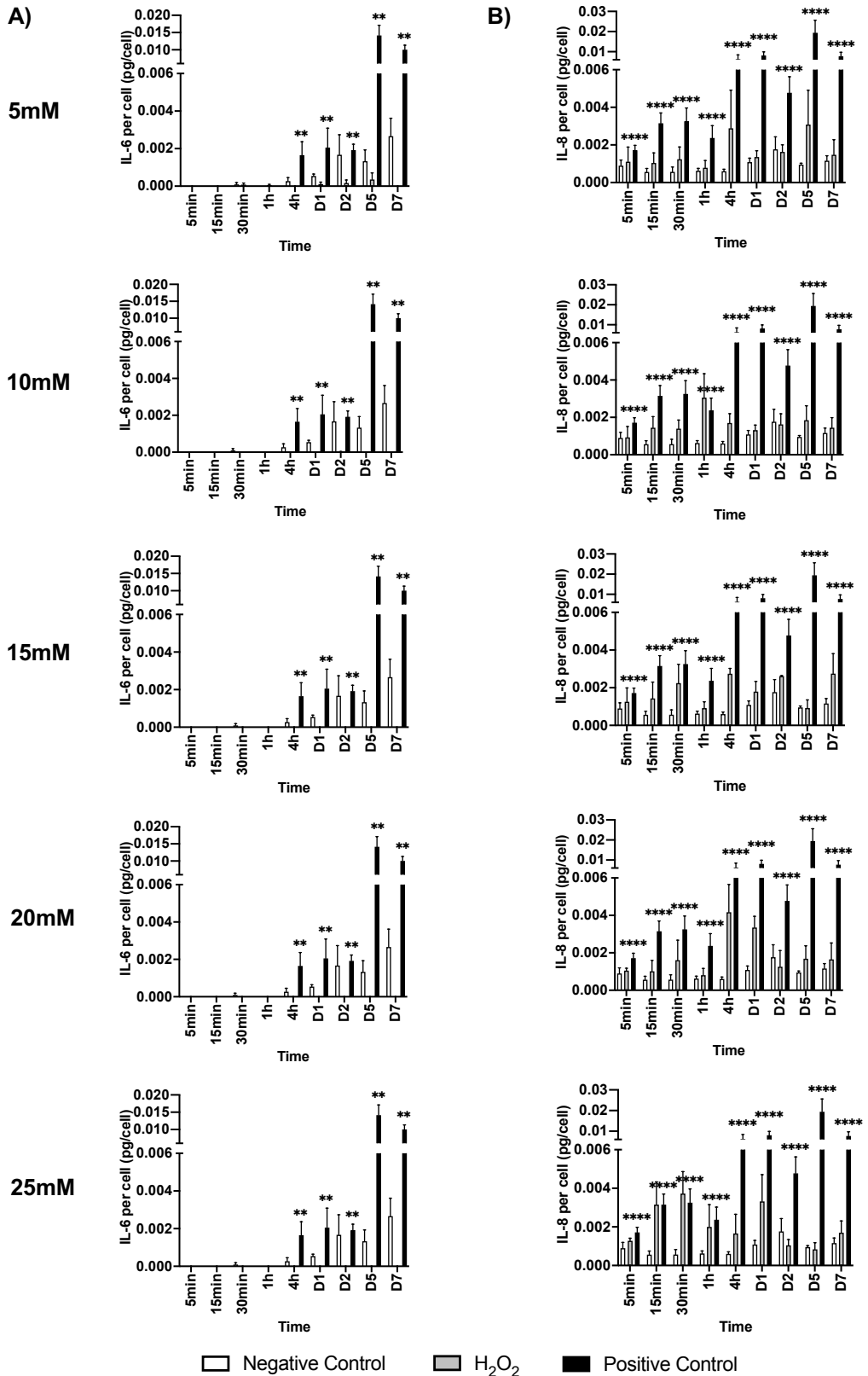

Figure 5.12 Pro-inflammatory effect per cell of cross-linker hydrogen peroxide (H_2O_2) 5-25mM on HFF-1 2D monoculture over 7 days. *IL-6(A) and IL-8(B) release were measured with ELISA, and chemokine released per cell was calculated relative to total cell number at each timepoint. Positive controls was LPS 1μg/ml. Mean±SEM is presented. N=3. Statistical significance between negative control and H_2O_2 or positive control are denoted by: $p<0.05$ *, $p<0.01$ **, $p<0.001$ *** and $p<0.0001$ ****.*

5.3.1.3.3 Cell morphology

The impact of H_2O_2 on the cell morphology of HFF-1 was assessed with light microscopy. Considering negative controls first, the comparable morphological appearance and cell densities at all timepoints under 1 day were as expected, as this encompassed a relatively short timeframe from a cell culture perspective. Following which, a gradual rise in cell density was observed, reaching confluence on day 7.

The most notable finding was the significant difference in cell morphology between HFF-1 exposed to H_2O_2 in the μM versus mM range (figures 5.13 and 5.14). On the other hand, cell morphology within each concentration range remained fairly similar between the five concentrations tested.

HFF-1 exposed to 5-25μM H_2O_2 maintained their cell morphology, with no significant difference in cell densities observed when compared with negative control across all timepoints up to day 7.

In contrast, HFF-1 exposed to 5-25mM H_2O_2 displayed evidence of cell death as early as at 30 minutes of exposure, whilst altered cell morphology could be appreciated even sooner at 15 minutes. The beginnings of the loss of spindle-like morphology were seen, heralding subsequent cell death. A dose- and time-dependent trend of greater morphological changes with higher H_2O_2 concentrations was also observed. Furthermore, cell death appeared relatively consistent from 1hour of exposure at the mM range, across all concentrations.

On the whole, the findings on light microscopy were consistent with that elicited with the erythrosin B exclusion assay. This result therefore corroborates with the cytotoxicity data and supports the conclusion that H_2O_2 at 5-25mM resulted in significant cytotoxicity.

5.3.1.3.4 Section summary – cross-linker toxicity testing

Studies pertaining to the toxicity of cross-linker H_2O_2 against HFF-1 showed marked cytotoxicity at the higher 5-25mM range. Whilst the lower 5-25μM range demonstrated relatively well-preserved cell morphology and a lack of pro-

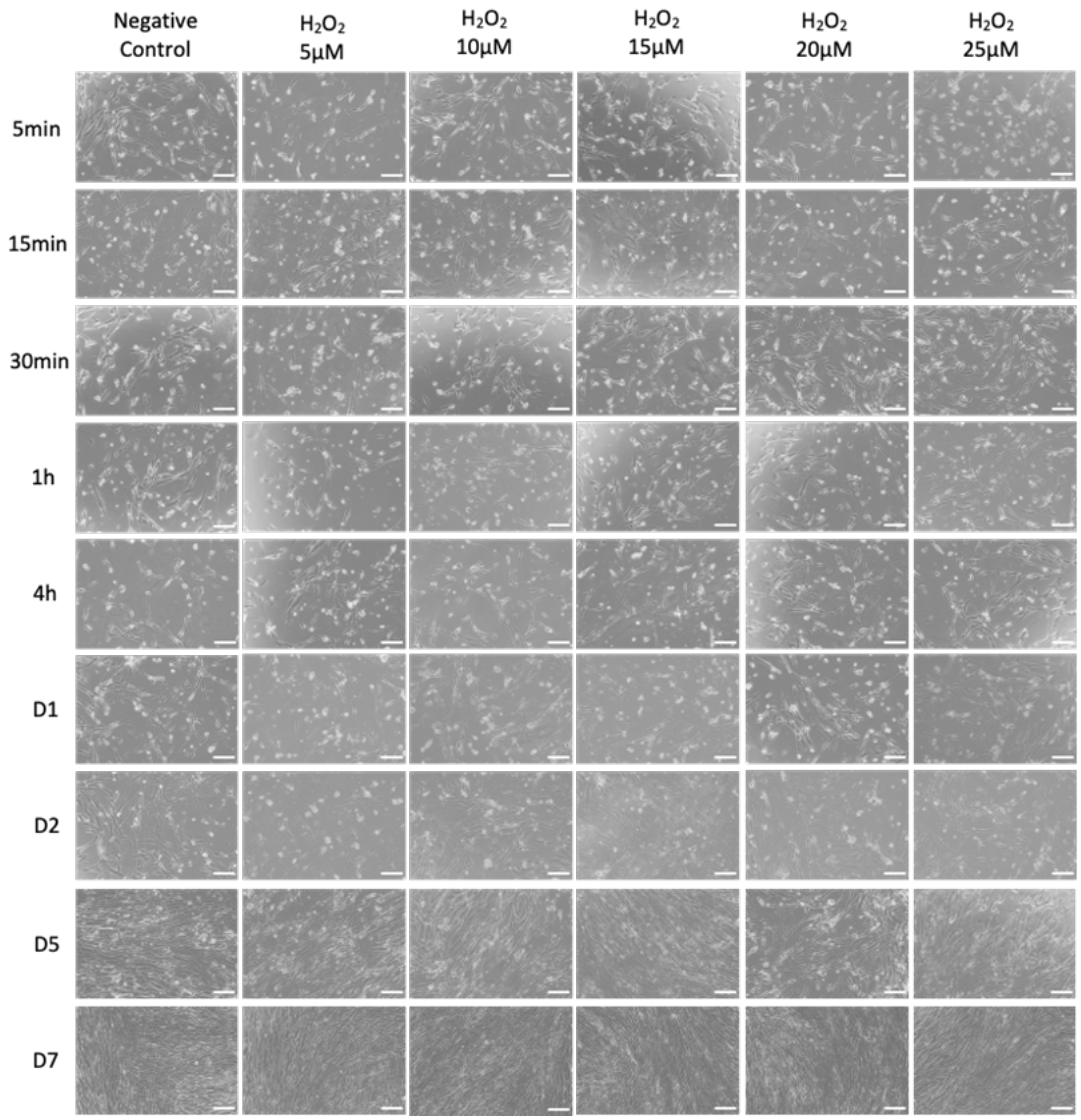

Figure 5.13 Light microscopy of HFF-1 cell line exposed to hydrogen peroxide (H_2O_2) at 5-25µM in 2D monoculture over 7 days. *Five H_2O_2 concentrations were tested: 5, 10, 15, 20, 25µM for 5, 15, 30 minutes, 1, 4 hours and 1, 2, 5 and 7 days. Negative control constitutes HFF-1 2D culture without H_2O_2 exposure. Scale bars represent 200µm.*

inflammatory response from HFF-1, there was a reduction in cell viability to suggest a degree of cytotoxicity in this concentration range. In view of the overarching aim of achieving tissue-engineered cartilage constructs, H_2O_2 at 5-25mM was deemed unsuitable for use as a cross-linker due to unacceptable adverse effect on cells.

In parallel to the cross-linker toxicity testing, cross-linkage time studies were also conducted and will be presented in the next section. Conclusions from both the biological and cell-free cross-linkage datasets will be discussed jointly in subsequent section 5.3.1.5. This will include the rationale behind why further testing of both T-HA and H_2O_2 against the C20A4 cell line was not conducted.

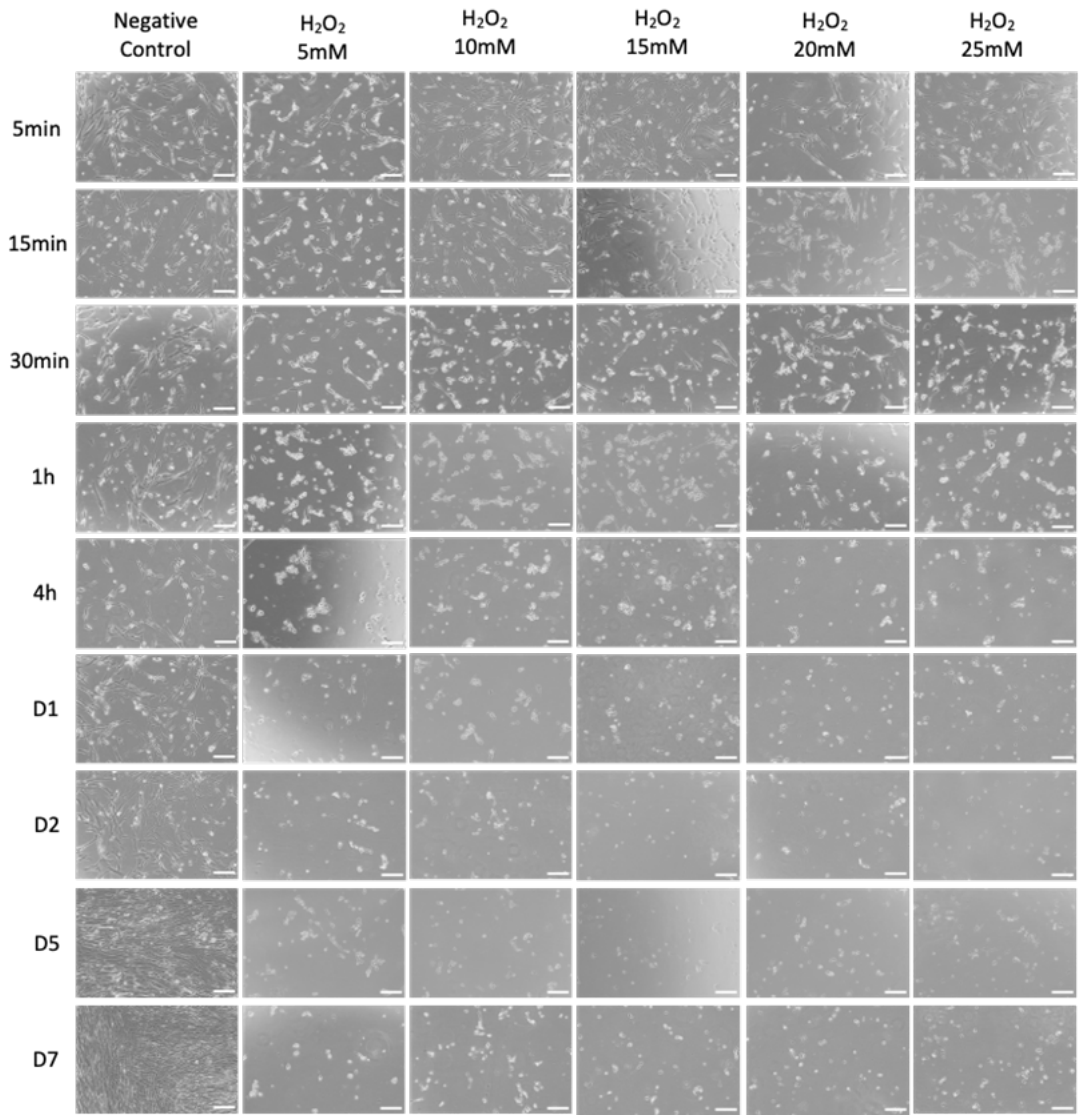

Figure 5.14 Light microscopy of HFF-1 cell line exposed to hydrogen peroxide (H_2O_2) at 5-25 mM in 2D monoculture over 7 days. *Five H_2O_2 concentrations were tested: 5, 10, 15, 20, 25mM for 5, 15, 30 minutes, 1, 4 hours and 1, 2, 5 and 7 days. Negative control constitutes HFF-1 2D culture without H_2O_2 exposure. Scale bars represent 200μm.*

5.3.1.4 Cross-linkage definition

5.3.1.4.1 Determination of minimum gelation time in silicon molds

In line with the approach taken with the cross-linker toxicity testing, both H_2O_2 concentration ranges were tested to determine their respective minimum gelation times using the silicon mold system. Initial testing begun with the bio-ink consisting of pulp-derived NCB and T-HA (low). The results are shown in table 5.4. Cross-linkers in the 2-25 mM range consistently achieved gelation, and therefore created cross-linked

Table 5.4 Summary of minimum cross-linking duration (minutes) for Nanocellulose:Tyramine-substituted hyaluronic acid (T-HA) bio-inks. *Bio-inks tested consisted of nanocellulose and T-HA. T-HA at concentration of 0.006g/ml was denoted as 'low' and of 0.012g/ml as 'high'. Three bio-inks tested were: i) Pulp-derived nanocellulose blend (NCB) with T-HA termed 'NCB:T-HA (low)', ii) + iii) Tunicate-derived enzymatically pre-treated nanocellulose (ETC) with T-HA at low and high T-HA concentrations termed 'ETC:T-HA (low)' and 'ETC:T-HA (high)', respectively. Bio-inks were cross-linked within silicon molds to create 8mm wide circular disc-shaped pellets of 100µl bio-inks and 600µl cross-linker hydrogen peroxide (H_2O_2) at specified concentrations. The minimum time required for gelation was defined as reaching five consecutive complete gelation with no residual uncross-linked bio-ink. N=5 for samples which failed to achieve gelation. Testing was conducted at 1 minute intervals in mM range of H_2O_2 and hourly for µM range. 'X @24h' represents failure to achieve gelation at 24 hours of cross-linker application.*

Bio-ink	**Cross-linker H_2O_2 concentration**					
	µM	**mM**				
	25µM	**5mM**	**10mM**	**15mM**	**20mM**	**25mM**
NCB:T-HA (low)	X @24h	12	10	9	9	9
ETC:T-HA (low)	X @24h	12	-	-	-	-
ETC:T-HA (high)	X @24h	55	-	-	-	-

hydrogel discs suitable for use in the advanced 3D *in vitro* model. Higher H_2O_2 concentration was associated with faster gelation time, although this plateaued above 15mM. In contrast, the highest µM concentration at 25µM did not succeed in fully cross-linking the 100µl bio-ink in the silicon molds, despite prolonged application at 24 hours (n=5). Further testing at lower µM concentrations was not conducted as it was anticipated that they will not achieve gelation.

As experiments were conducted in parallel, results from prior experiments were taken into consideration, permitting a focused approach with each sequential step of testing. As shown in table 5.4, the bio-inks consisting of tunicate-derived nanocellulose ETC and T-HA at both high and low concentrations were tested next. The bio-inks tested were based upon the selection of ETC and non-superiority between the high and low T-HA concentration, as described in section 3.3.2 and 5.3.1.2.4 respectively. Cross-linker concentration was rationalised to include the highest of the µM and lowest of the mM range, i.e. 25µM and 5mM H_2O_2. The former assumed that lower concentrations will not achieve gelation should 25µM proved unsuccessful. The latter was based on cross-linker cytotoxicity testing, whereby higher concentration would lead to more severe cytotoxicity. This was not warranted when gelation was achieved with a lower and 'safer' concentration.

The results indicated that the change of nanocellulose form did not alter the unsuccessful outcome when 25µM H_2O_2 was used (table 5.4). On the other hand, 5mM

Table 5.5 Summary of minimum cross-linkage duration (minutes) for Nanocellulose:Tyramine-substituted hyaluronic acid (ETC:T-HA (low)) bio-ink with cross-linker hydrogen peroxide (H_2O_2) between 37.5µM – 4mM. *This study assessed gelation time with H_2O_2 between previously studied concentration ranges. Cross-linker concentrations tested were: 37.5, 75, 125, 250 and 500 µM and 1, 2, 3 and 4mM H_2O_2. T-HA concentration for the bio-ink was 0.006g/ml and denoted as 'low'. Bio-inks were cross-linked within silicon molds to create 8mm wide circular disc-shaped pellets of 100µl bio-inks and 500µl H_2O_2. The minimum time required for gelation was defined as reaching five consecutive complete gelation with no residual uncross-linked bio-ink. Testing was conducted at 1 minute intervals in mM range of H_2O_2 and hourly for µM range. 'X @24h' represents failure to achieve gelation at 24 hours of cross-linker application.*

	Cross-linker H_2O_2 concentration				
µM	**37.5µM**	**75µM**	**125µM**	**250µM**	**500µM**
	X @24h				5 hours
mM	**-**	**1mM**	**2mM**	**3mM**	**4mM**
	-	49	42	26	22

was able to cross-link the same bio-ink, with the low T-HA concentration, with the same gelation time of 12 minutes. Interestingly, the increase in T-HA concentration led to a markedly longer gelation time at 55 minutes. This may reflect the influence of higher HA content upon diffusion of H_2O_2 across the bio-ink. In this case, due to the time-dependent cytotoxic effects of H_2O_2, as demonstrated in section 5.3.1.3, decision was taken to continue testing using the bio-ink ETC:T-HA (low) to limit cross-linker application duration and the associated adverse cellular effects.

Having established that 25µM H_2O_2 cannot achieve gelation and that 5mM H_2O_2 can cross-link the bio-ink ETC:T-HA (low) in a reasonable timeframe, there remained a wide concentration gap where the effectiveness of H_2O_2 to achieve gelation was unknown. To bridge this gap, an abbreviated dose range study was conducted to explore the gelation time for H_2O_2 between 25µM and 5mM (table 5.5).

Concentrations required to limit the cross-linker exposure time to under one hour or 30 minutes were 1mM and 3mM H_2O_2, respectively. Both of which were associated with unfavourable cytotoxicity to support their application in an *in vitro* model or for tissue engineering purposes.

Taken together, this gelation time study established that H_2O_2 was ineffective or non-biocompatible with the proposed bio-ink and hydrogel creation system at the 25µM – 5mM concentrations tested.

To achieve the goal of incorporating HA in a nanocellulose-based bio-ink whilst circumventing the issue with cross-linkage using H_2O_2, several potential strategies were considered and are now discussed.

As concentrations of T-HA, HRP and H_2O_2 can all influence the cross-linking process and therefore gelation time, one option was to explore beyond the single HRP and two T-HA concentrations tested. However, this could be counter-intuitive as the T-HA and HRP concentrations for the bio-ink, and H_2O_2 concentrations as cross-linker were based on previous research investigating alternative bio-ink performance parameters. Expanding beyond previously tested T-HA and HRP concentrations would require future rheological and mechanical testing to confirm suitability and may not prove fruitful.

Furthermore, cross-linkage with HRP and H_2O_2 is a relatively common cross-linking strategy for T-HA, with reports of use of 100μM – 1mM H_2O_2 in the literature [289]. As the current study encompassed and extended beyond this concentration range, this indicates that the concentrations tested were in line with published studies and further exploration was of uncertain value. The work of Abu-Hakmeh *et al* investigated 2% w/v (i.e. 20mg/ml) T-HA hydrogels cross-linked with 900μM H_2O_2 and 0.06-0.24U/ml HRP. With increasing HRP concentrations, gelation time was reduced (from 60 to 3 minutes), and stiffer and stronger constructs were produced [289]. In another study, 2% w/v T-HA cross-linked hydrogel was created with 0.12U/ml HRP and 0.5-1mM H_2O_2 [293]. At three weeks of culture, mechanical degradation and significant decline in cell numbers were seen. Between the H_2O_2 concentration range tested, it was found that higher H_2O_2 concentration was protective of hydrogel degradation in culture.

For context, the bio-ink in this study consisted of T-HA at 30mg/ml and a significantly greater HRP concentration at 10U/ml. Although the work of Abu-Hakmeh *et al* found that raising HRP concentration reduced gelation time at 900μM H_2O_2, the bio-ink tested in this study required a much higher H_2O_2 concentration to achieve adequate cross-linkage. It must be considered that varying geometry of the desired construct and different systems in which the cross-linker is applied can affect gelation time, and therefore studies are not directly comparable. Nonetheless, they provide an indication that further testing *via* the adjustment of T-HA, HRP and H_2O_2 concentration may not prove successful and supported consideration of alternative strategies.

A potential option which retains the use of T-HA is to employ other cross-linking modalities. An example would be to cross-link with UV light, which requires the addition of a photosensitiser such as riboflavin [291]. However, the cellular impact with the application of both the UV light and photosensitiser is unknown and maybe unfavourable. There are also logistical considerations to applying UV treatment on cell-encapsulated bio-inks whilst maintaining sterile and culture conditions. As such, this was not adopted for further testing.

Taking an altogether different approach, the concept of hybrid or composite bio-inks are frequently adopted to bring together advantages of different material, and is common in the field of tissue engineering [100]. Silva *et al* investigated a hybrid bio-ink made of HA, cellulose nanocrystal and tropoelastin [294]. In this work intended for tissue engineering applications, nanocellulose was introduced to improve HA hydrogel stability and tropoelastin to enhance material elasticity.

Pertaining back to the goal of achieving a nanocellulose-based bio-ink incorporating HA for biomimicry, but required cross-linking abilities, it was hypothesised that a triple component bio-ink to include alginate could be cross-linked with $CaCl_2$. The bio-ink used in trial testing consisted of nanocellulose (ETC), HA (T-HA) and alginate, cross-linked with 0.1M $CaCl_2$. All component parts were previously investigated in chapter 3-5 and demonstrated satisfactory sterility and toxicity profiles. Table 5.6 demonstrates proof of concept, with successful cross-linkage achieved. The gelation time was 21 minutes with the low T-HA concentration. An unexpected finding was the much prolonged gelation time for the bio-ink containing the high T-HA concentration using media as the solvent. Additional technical replicates were conducted (n=10), confirming the findings. Therefore, the results supported the transition towards a triple component bio-ink consisting of ETC, alginate and HA, crosslinked with 0.1M $CaCl_2$.

Table 5.6 Summary of minimum cross-linkage duration (minutes) for triple component bio-inks Nanocellulose:Alginate:Tyramine-substituted hyaluronic acid (T-HA) with cross-linker calcium chloride ($CaCl_2$). *Bio-inks tested consisted of tunicate-derived enzymatically pre-treated nanocellulose (ETC) and T-HA at two concentrations (0.006g/ml - 'low' and 0.012g/ml - 'high'). Bio-inks were cross-linked within silicon molds to create 8mm wide circular disc-shaped pellets of 100µl bio-inks and 600µl $CaCl_2$ 0.1M. The minimum time required for gelation was defined as reaching five consecutive complete gelation with no residual uncross-linked bio-ink. Testing was conducted at 1 minute intervals up to 45 minutes, beyond which testing was at 5 minutes interval.*

Bio-inks	**Solvent for Alginate**	
	Media	**Sterile ddH_2O**
ETC:Alginate:T-HA (low)	21	21
ETC:Alginate:T-HA (high)	90 (n=10)	41

5.3.1.5 Section summary – tyramine-substituted hyaluronic acid

Investigations undertaken to understand the effects of T-HA have established sterility with UV-treatment, and the lack of cytotoxic or pro-inflammatory effects when exposed to HFF-1 in 2D monoculture. Study of the biological impact and effectiveness in cross-linking with H_2O_2 unfortunately demonstrated incompatibility with the current 3D *in vitro* model creation system.

Whilst 5-25mM H_2O_2 was associated with significant cytotoxicity, reduction in cell proliferation was witnessed with 5-25μM, despite maintenance of cell morphology and no gross cytotoxic or pro-inflammatory effects observed based upon the erythrosin B exclusion assay and release of IL-6 and IL-8. As a minimum of 3mM H_2O_2 was required to achieve gelation within 30 minutes, the associated cytotoxicity rendered the model creation system incompatible.

The results also demonstrated that increasing T-HA concentration prolongs gelation time, an undesirable trait due to the time-dependent cytotoxic effects of the cross-linker, with the lower T-HA concentrations selected for model creation purposes. On the other hand, variation of HRP concentration to influence gelation time has been discussed and is unlikely to alter the conclusion that cross-linkage with T-HA, HRP and H_2O_2 is incompatible with the existing model creation system.

Expanding upon the cellular effects of H_2O_2, as a reactive oxygen species, its genotoxic and cytotoxic effects are well-documented in the literature [295, 296]. At sub-lethal concentrations, H_2O_2 can act as secondary messengers for various physiological stimuli and influence signal transduction pathways [295]. It is also a powerful inducer of apoptosis, although the dose range varies according to cell types. The application of H_2O_2 can trigger several interacting, but mechanically distinct cell death pathways. These may be distinguished, for example, with caspase 9 activation signifying the initiation of apoptosis, NFκB with oxidative stress and possible DNA damage, and p53, the dysregulation of cell cycle and proliferation[296]. The predominantly adverse effects of H_2O_2 across dose range, taken together with the demonstrable cytotoxic effects against HFF-1 (one of two cell types of the intended co-culture *in vitro* model) implies that even if a feasible T-HA and HRP concentrations can permit the use of a lower H_2O_2 concentration with a shorter cross-linkage time, negative cellular impact is to be expected. This therefore supports the notion to move away from the T-HA,

HRP and H_2O_2 cross-linkage system. Keeping in mind the intended end-application of tissue engineering, which will produce larger volume constructs (such as the human ear cartilage framework), longer cross-linkage duration is likely required, further limiting the application of H_2O_2 as a safe cross-linking agent.

For 3D bioprinting, an optimal compromise is needed between bio-compatibility (sustaining encapsulated cell viability pre- and post-print, and supporting host cell migration post-implantation), favourable rheological (flow for printing) and mechanical properties (strength and flexibility post-print and post-cross-linkage). This compromise is described as the 'biofabrication window' paradigm [297]. The results from this study highlighted above re-iterates the opposing nature and conditions required within the 'biofabrication window'.

In order to extend the 'biofabrication window', parameters could be adjusted or exchange within the bio-ink and cross-linker system. In this case, the addition of alginate cross-linked with $CaCl_2$ was trialled with a successful proof of concept. This led to the major transition in the project with the introduction of the triple component bio-ink. Consequentially, this led to the next section of this chapter investigating a non-tyramine-substituted form of HA (N-HA). As native human HA does not contain the modification of tyramine-substitution, when the need to cross-link with HRP and H_2O_2 was no longer, there was a strong basis to adopt a more biologically relevant form of HA. Furthermore, in recognition of the benefit of a sterile material source supply, as is the case with tunicate-derived nanocellulose, sterility was added as a selection criterion. Finally, due to the aforementioned transition, material toxicity and cross-linker toxicity testing against C20A4 and rheological testing of T-HA-based bio-inks were not conducted.

5.3.2 Non-tyramine-substituted hyaluronic acid

The core differences between T-HA and N-HA were that the latter was supplied sterile, and more closely mimic native human cartilage HA with no gross chemical modification such as tyramine-substitution, and was of a higher molecular weight. The rationale behind and selection process of N-HA was detailed in section 2.3.2.3.

Assessment of N-HA followed the same approach as with nanocellulose, alginate and N-HA. Sterility testing and material toxicity testing against both HFF-1 and C20A4

cell lines were conducted. Cross-linker toxicity testing did not require repetition as 0.1M $CACl_2$ was used. This was the same cross-linker and concentration as defined with Nanocellulose:Alginate bio-ink, and cross-linker toxicity results against both cell types are as detailed in section 4.3.3. Cross-linkage time definition studies, in the forms of determination of minimum gelation time in silicon molds, as well as rheological studies were performed to understand the material behaviour of this triple component bio-ink formulation. Whilst results are presented sequentially to mirror chapter 4 and section 5.3.1 (T-HA), successful gelation within silicon molds using the new N-HA was initially confirmed, prior to detailed material testing.

5.3.2.1 Material sterility testing

As N-HA was supplied sterile, the material was not subjected to UV-sterilisation, and therefore was tested as supplied. An abbreviated testing schedule with latter timepoints was adopted, with the assumption that sterility at latter timepoints infer sterile conditions at earlier timepoints.

Whilst OD remained below the 0.1 threshold for 21 days in both LB and sterile PBS, the OD was on the cusp of 0.1 on day 21 when cultured in YPD (figure 5.15). A greater variance was noted (mean OD±SEM was 0.106±0.021). Of note, the rise in OD was also observed in the cultured negative control of YPD media (Mean OD ± SEM was 0.138 ± 0.011), although this was not seen in fresh YPD not subjected to culture over time (figure 5.15B). In comparison to contaminated pulp-derived nanocellulose (figure 3.5), the rise in OD with N-HA was slight, just breaching the 0.1 threshold. The OD associated with N-HA was also below that of cultured negative control. Bacterial isolation of all samples exceeding OD of 0.1 did not yield microbial growth at 21 days. The coloured nature of YPD and batch-to-batch variability may be contributory to the slight rise in OD observed. Taken together, the results did not indicate N-HA material contamination, and therefore remain suitable for use.

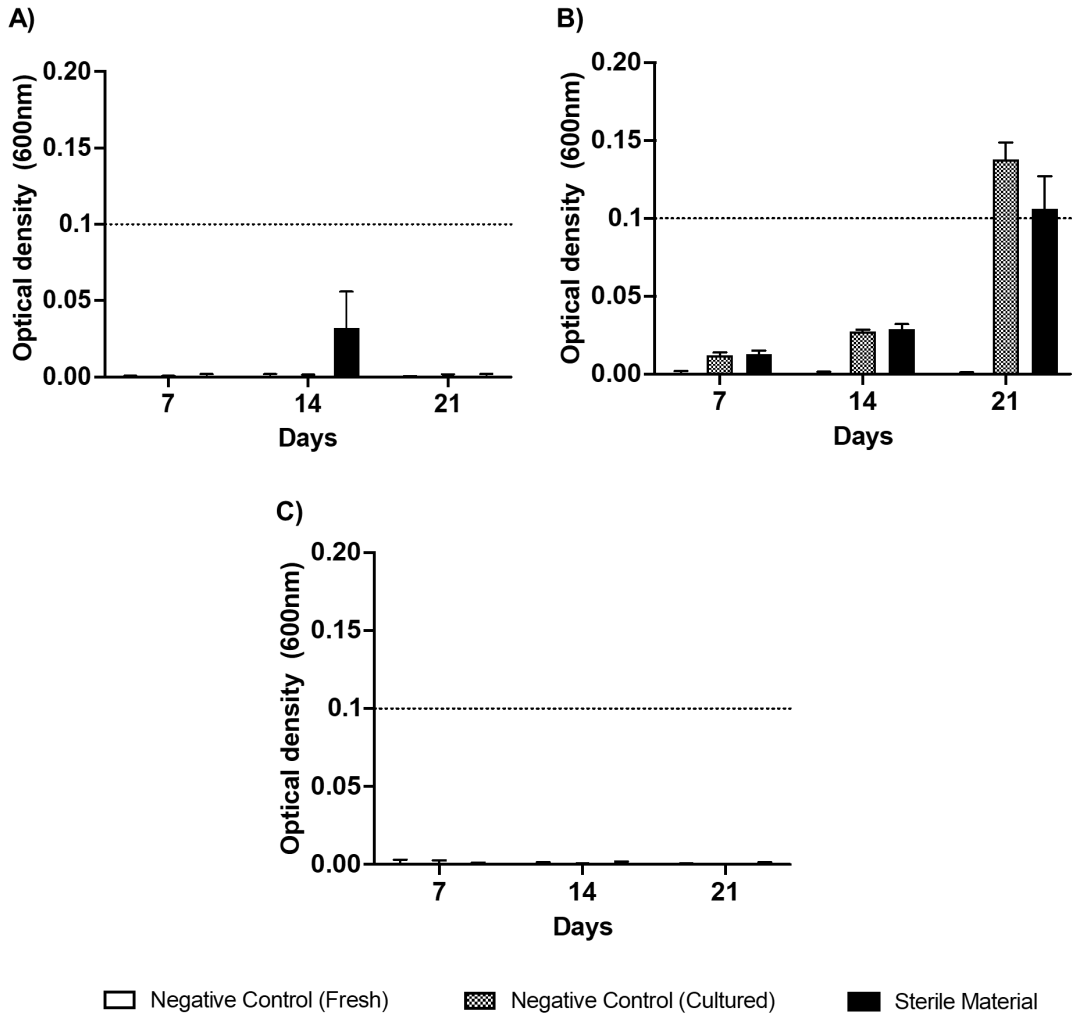

Figure 5.15 Sterility testing of non-tyramine-substituted hyaluronic acid (N-HA). *Assessment of sterility and material effects of N-HA on optical density in A) lysogeny broth (LB), B) yeast extract-peptone-dextrose (YPD) and C) sterile PBS. N-HA in LB, YPD or sterile PBS were incubated at 37°C under constant agitation over 21 days. Media or PBS without N-HA served as negative control, which included both uncultured (fresh) and cultured conditions. Optical density measured at 600nm. Accepted arbitrary threshold for sterility at <0.1 denoted by horizontal dotted line. Mean±SEM. N = 3.*

5.3.2.2 Material toxicity testing

In the same manner as with T-HA, both high and low concentrations were tested for material toxicity. This was performed against both cell types, HFF-1 (human dermal fibroblast) and C20A4 (human chondrocyte) cell lines. Cytotoxicity was assessed using the erythrosin B exclusion assay, pro-inflammatory effects *via* quantification of IL-6 and IL-8 release and cell morphology visualised with light microscopy.

5.3.2.2.1 HFF-1 cell line (human dermal fibroblast)

5.3.2.2.1.1 Cytotoxicity

The trends seen with total and live cell concentration were similar to that with T-HA (figure 5.3A/B and 5.16A/B). There was an increasing trend between day 1 and day 14, which was statistically significant for cells exposed to N-HA and negative control on day 7 and 14, when compared to day 1. This was followed by a decline in both cell concentrations and cell viability on day 21, likely a result of over-confluence (figure 5.16C).

A divergence was noted, in both total and live cell concentrations, from day 7 onwards. Cell concentrations were in descending order: greatest in negative control, followed by N-HA (low) and lowest with N-HA (high). This suggests that cell proliferation was hindered with increasing N-HA exposure. However, direct comparison between negative control and N-HA exposures, and between the two concentrations of N-HA, did not reveal statistically significant differences.

Despite a reduction in total and live cell concentrations with HFF-1 exposed to N-HA, cell viability remained comparable between negative control and exposure scenarios (figure 5.16C). As previously discussed with T-HA, N-HA was also reconstituted in media resulting in marked viscosity and this may have served as a contributory factor towards altered cell behaviour such as cell proliferation. Whilst it cannot be defined within the remit of this study if altered cell concentrations were the effect of the viscosity of the media alone, nonetheless cell viability was preserved when exposed to N-HA. Indeed, cell viability was more similar between negative control and cells exposed to N-HA (figure 5.16C) versus cells exposed to T-HA (figure 5.3C). It was concluded that N-HA was biocompatible with HFF-1 for the purpose of this project.

In terms of comparison between the two concentrations of N-HA, despite a higher total and live cell concentration with N-HA (low), there was no statistically significant difference between N-HA (high) and N-HA (low). As such, it was concluded that neither concentrations (0.006g/ml and 0.012g/ml) of N-HA caused significant cytotoxicity when exposed to HFF-1 in 2D culture for up to 21 days.

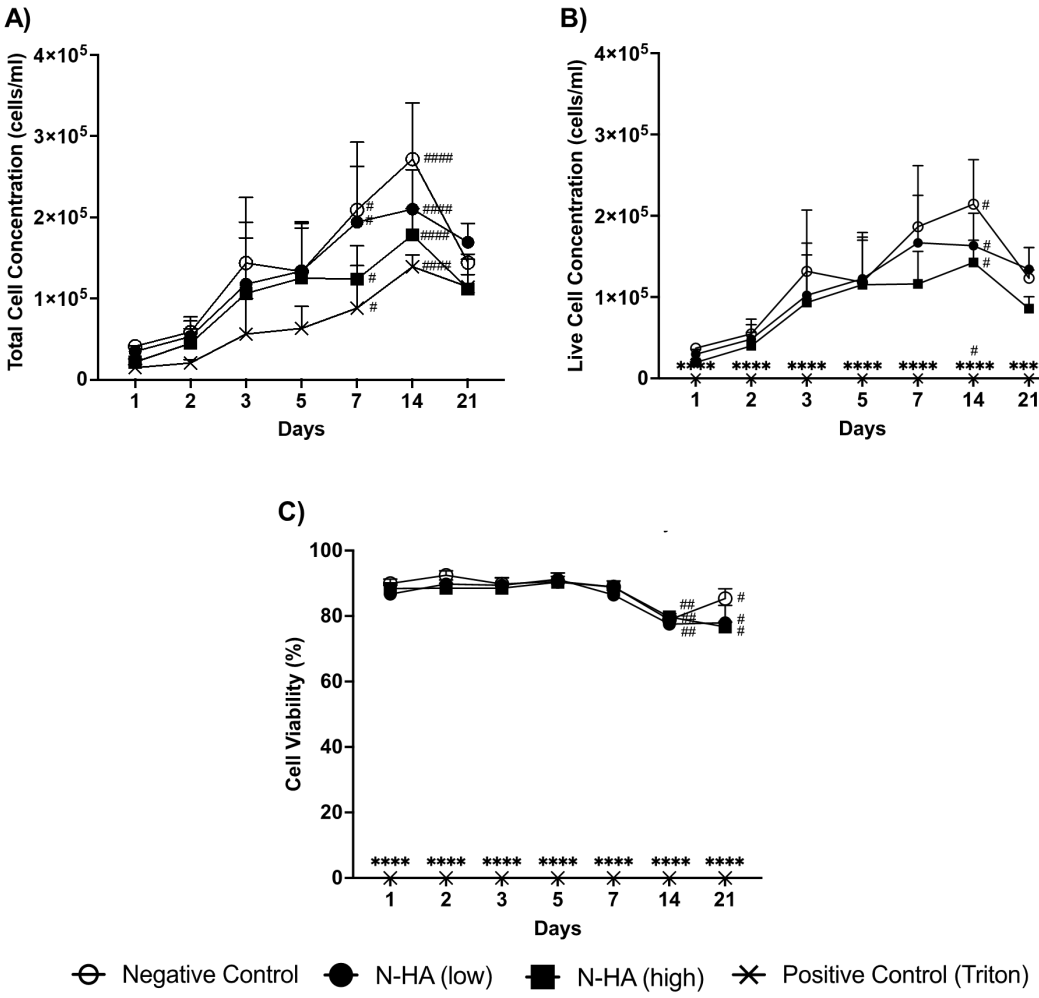

Figure 5.16 Cytotoxicity of HFF-1 exposed to non-tyramine-substituted hyaluronic acid (N-HA) in 2D monoculture over 21 days. *Two N-HA concentrations were tested, denoted as 0.006g/ml (low) and 0.012g/ml (high). Total (A) and live (B) cell concentration and cell viability (C) were assessed with erythrosin B assay. Positive control was 0.1% Triton X-100. Mean±SEM is presented. N=3. Comparison between negative control and N-HA (low), N-HA (high) or positive control at each timepoint were denoted by *, and timepoint comparisons of each culture conditions by #. Statistical significance is shown as: p<0.05 */#, p<0.01 **/##, p<0.001 ***/### and p<0.0001 ****/####.*

5.3.2.2.1.2 Pro-inflammatory response

For IL-6, all culture conditions demonstrated a rising trend over time, with a statistically significant rise on day 21 ($p<0.0001$) (figure 5.17A). The amount of IL-6 released when HFF-1 was exposed to N-HA in both concentrations were lower than negative control in day 1-3, before reaching similar levels between day 5 and 14. HFF-1 exposed to N-HA appeared activated and released greater amounts of IL-6 than negative control on day 21. However, there was no statistically significant difference between cells exposed to N-HA versus negative control at all timepoints. IL-6 levels were also comparable between those associated with N-HA (high) and N-HA (low)

throughout the study period, indicating no significant difference between the two N-HA concentrations.

Trends with IL-8 were akin to those with IL-6. An increase in IL-8 levels over time was observed, with statistical significance reached on day 14 and day 21 (figure 5.17B). There was no significant difference between negative control and both N-HA concentrations, as well as no difference between the two concentrations of N-HA. This was the case across all timepoints tested.

Material interference on the assay was examined with a cell-free, material only control. IL-6 was non-detectable on day 2 through to 14. Although extremely low levels of IL-6 were detected on day 1 (1.41pg/ml) and day 21 (2.97pg/ml). With IL-8, measurable but consistently low levels of IL-8 were detected. With both chemokines, when compared to cellular conditions, the non-detectable to low levels detected deemed any material interference as negligible in effect.

What was observed with both chemokines was higher levels with HFF-1 exposed to N-HA versus negative controls on day 21. Similar to previous experiments examining IL-6 and IL-8 release, chemokine release per cell was calculated to take into account the varied cell number across different cell culture conditions and timepoints (figure 5.18).

Overall, IL-6 and IL-8 demonstrated similar trends. Levels of both chemokines rose over time, with a statistically significant increase reached on day 21. With comparably high levels of IL-6 and IL-8 with the negative control and N-HA exposures, this level of chemokine may reflect the status and limitation of the model at this latter timepoint. I.e. cells were activated, possibly secondary to over-confluence, and would benefit from further model optimisation.

Comparison between the negative control and N-HA exposures showed relatively similar chemokine levels throughout the study period to suggest N-HA did not produce a pro-inflammatory effect against HFF-1 in 2D culture for up to 21 days. Interestingly, chemokine levels were noted to be higher on day 14 in exposures conditions than in negative control. This was associated with greater variance with IL-6, and a greater increase than negative control with IL-8. However, statistical significance was not reached. Furthermore, direct comparison between the high and low concentration of N-HA showed no significant difference.

Taken together, N-HA did not induce a pro-inflammatory response with HFF-1 in 2D culture for up to 21 days.

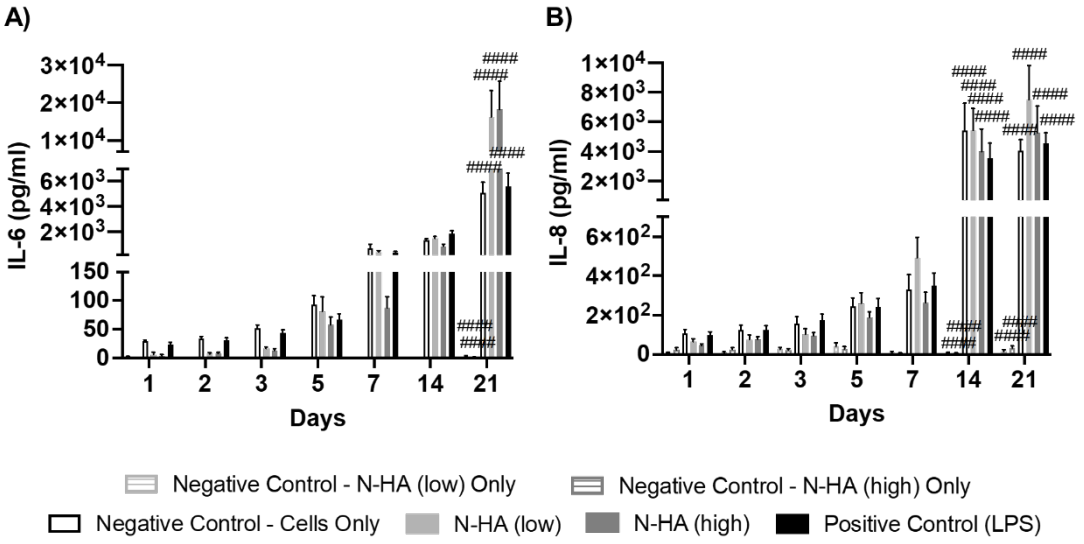

Figure 5.17 Pro-inflammatory effect of non-tyramine-substituted hyaluronic acid (N-HA) on HFF-1 2D monoculture over 21 days. *Two N-HA concentrations were tested, denoted as 0.006g/ml (low) and 0.012g/ml (high). IL-6 (A) and IL-8 (B) release were measured with ELISA. Negative control consisted of HFF-1 2D monoculture without material exposure, termed 'negative control – cells only'. Positive control was LPS 1μg/ml. Material interference on assay was investigated with material treated to the same experimental conditions, termed 'negative control – N-HA only', which included both N-HA concentrations. Mean±SEM is presented. N=3. Statistical significance on timepoint comparisons D1 v D2-21 of each culture conditions are denoted by: p<0.05 #, p<0.01 ##, p<0.001 ### and p<0.0001 ####.*

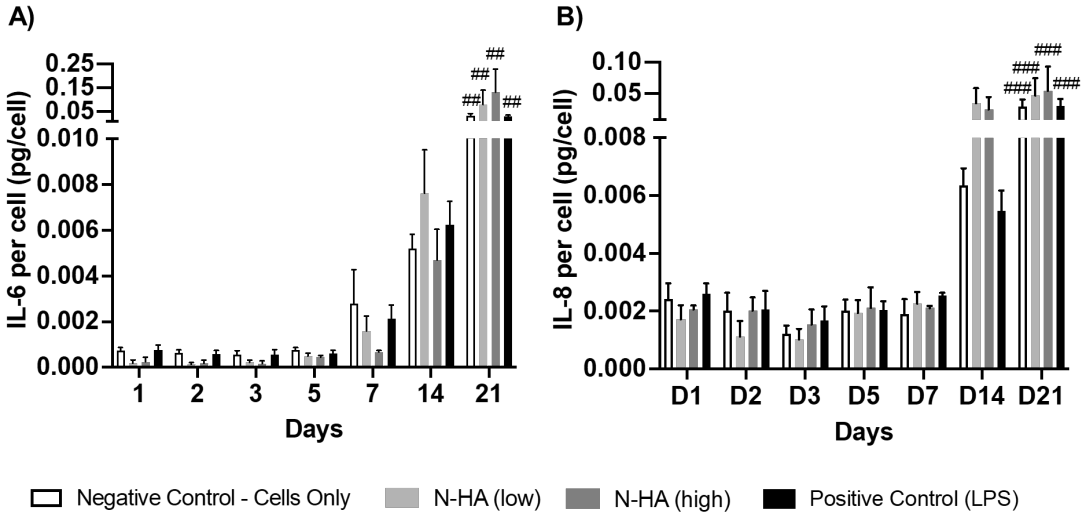

Figure 5.18 Pro-inflammatory effect per cell of non-tyramine-substituted hyaluronic acid (N-HA) on HFF-1 2D monoculture over 21 days. *Two N-HA concentrations were tested, denoted as 0.006g/ml (low) and 0.012g/ml (high). IL-6 (A) and IL-8 (B) release were measured with ELISA, and chemokine released per cell were calculated relative to total cell number at each timepoint. Negative control consisted of HFF-1 2D monoculture without material exposure, termed 'negative control – cells only'. Positive control was LPS 1μg/ml. Mean±SEM is presented. N=3. Statistical significance for timepoint comparisons within each culture condition between day 1 and day 2-21 are denoted by #: p<0.05 #, p<0.01 ##, p<0.001 ### and p<0.0001 ####.*

5.3.2.2.1.3 Cell morphology

Following a similar trend as seen in the erythrosin B exclusion assay, light microscopy images showed a rise in cell densities over time reflecting the increase in total cell concentration (figure 5.19). Comparison between both concentrations of HA revealed that with the higher HA concentration, cell confluence was reached at a later timepoint on day 14, as opposed to day 7 with the lower HA concentration. Mirroring results seen in the erythrosin B exclusion assay, a somewhat lower cell confluency can be appreciated on day 21 in the negative control and with N-HA (low). This likely reflects a drop in cell viability with over-confluence at earlier timepoint in culture. Cell morphology was maintained through the study period with the application of N-HA in both concentrations.

5.3.2.2.2 C20A4 cell line (human chondrocyte)

The effect of N-HA on the C20A4 cell line was tested in 2D monoculture. Testing included both the high and low N-HA concentrations, and they were assessed in the same vein as material toxicity testing against HFF-1.

5.3.2.2.2.1 Cytotoxicity

Total and live cell concentrations of C20A4 showed similar trends across the 21 day study period. A peak in total and live cell concentration was reached sooner with negative control (day 3), compared to N-HA (low) on day 5 and N-HA (high) on day 14. Both total and live cell concentrations were greater in negative control versus with C20A4 exposed to both concentrations of HA, which was statistically significant across all timepoints (figure 5.20 A/B). Total and live cell concentrations were higher with N-HA (low) compared to N-HA (high), although the divergence narrowed at latter timepoints. Despite this, there was no statistically significant difference between both concentrations of N-HA in terms of total and live cell concentration, nor with cell viability. Interestingly, despite varied total and live cell concentrations between negative control and HA exposures, cell viability remained comparable between all three conditions with no statistically significant difference between N-HA exposures and negative control at all timepoints (figure 5.20C).

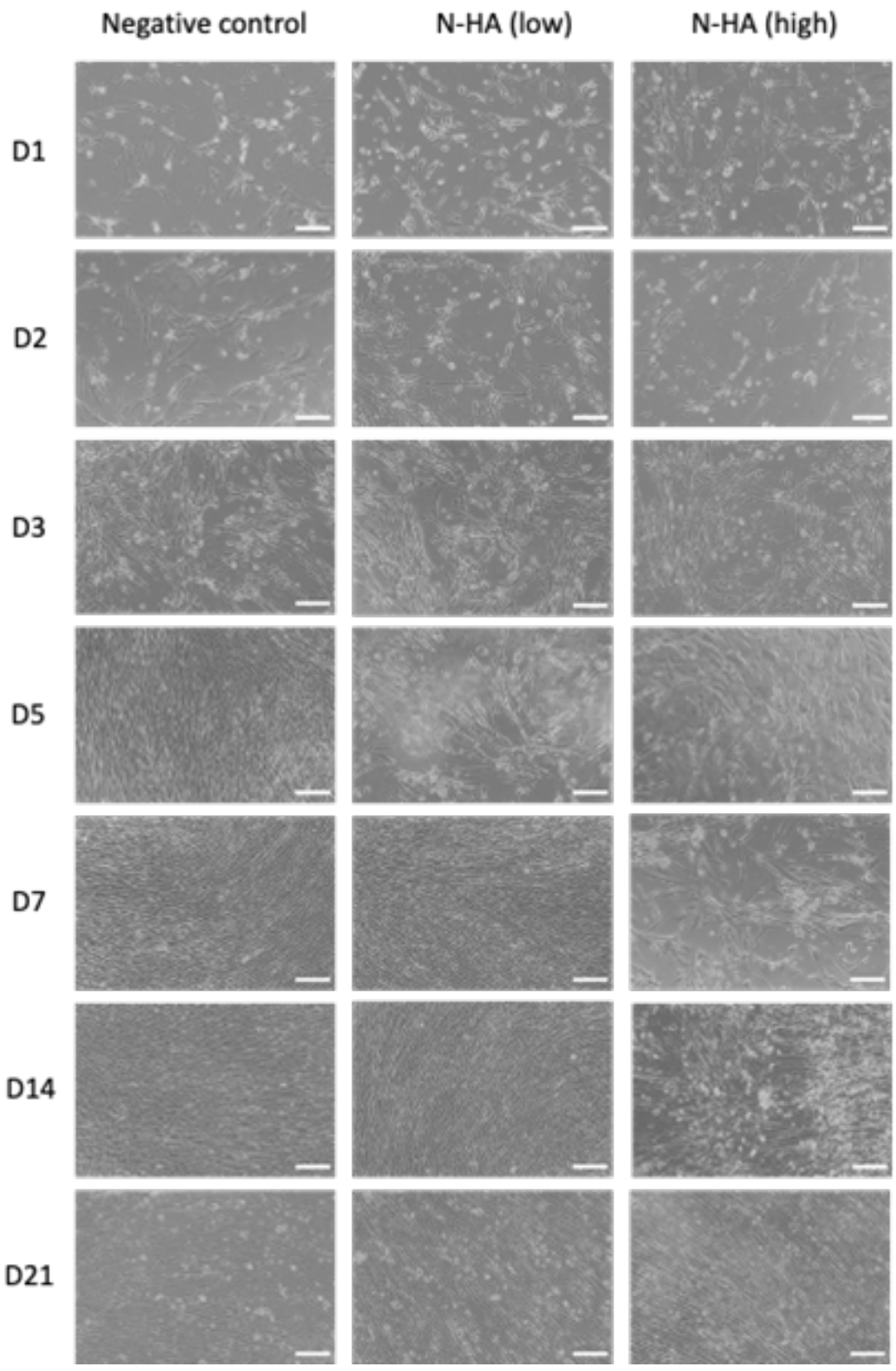

Figure 5.19 Light microscopy of effect of non-tyramine-substituted hyaluronic acid (N-HA) on HFF-1 2D monoculture over 21 days. *Two N-HA concentrations were tested: 0.006g/ml (low) and 0.012g/ml (high). Negative control constitutes HFF-1 2D culture without N-HA exposure. Scale bars represent 200μm.*

Taken together, this suggests an inhibitory effect on cell proliferation of N-HA against C20A4 when exposed in 2D monoculture. It may be possible that the increased viscosity of media inherent to the inclusion of N-HA impacts nutrient and oxygen diffusion and thereby adversely affect cell growth and behaviour. Indeed, higher N-HA concentration, yielding a more viscous media, was associated with slower and lower levels of cell proliferation. Of note, cell viability throughout the study period remained comparable between N-HA exposures, including the high N-HA concentration and negative control. This suggests that cells were relatively healthy and did not display gross cytotoxic effects when exposed to N-HA, despite reduced cell numbers. It is difficult to distinguish in this setting the effect of media viscosity versus true cytotoxic effects of the material (N-HA) per se. Nonetheless, preserved cell

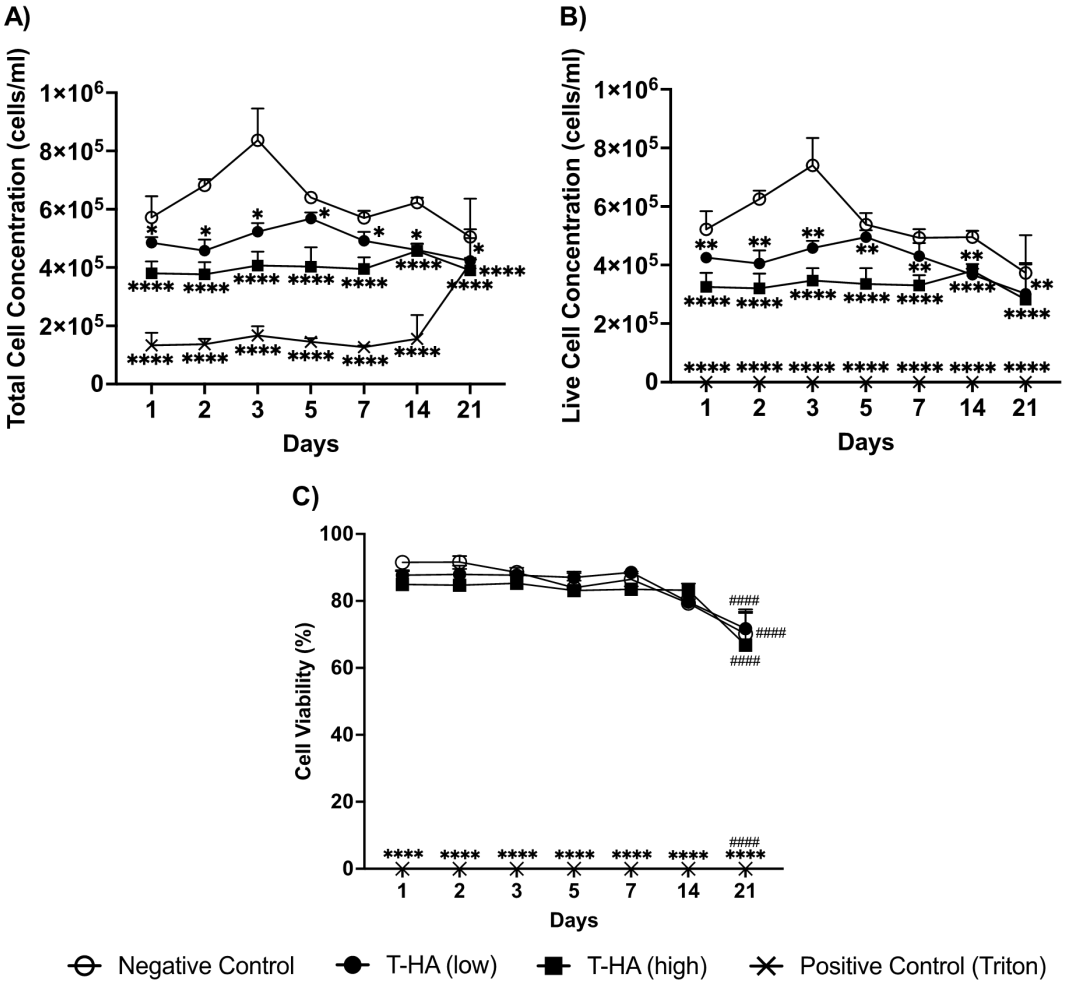

Figure 5.20 Cytotoxicity of C20A4 exposed to non-tyramine-substituted hyaluronic acid (N-HA) in 2D monoculture over 21 days. *Two N-HA concentrations were tested, denoted as 0.006g/ml (low) and 0.012g/ml (high). Total (A) and live (B) cell concentration and cell viability (C) were assessed with erythrosin B exclusion assay. Positive control was 0.1% Triton X-100. Mean±SEM is presented. N=3. Comparison between negative control and N-HA (low), N-HA (high) or positive control at each timepoint were denoted by *, and timepoint comparisons of each culture conditions by #. Statistical significance is shown as: p<0.05 */#, p<0.01 **/##, p<0.001 ***/### and p<0.0001 ****/####.*

viability in cells exposed to N-HA suggests that N-HA is biocompatible with C20A4 with respect to cell viability, despite reduced growth when exposed in a 2D culture scenario.

5.3.2.2.2.2 Pro-inflammatory response

Both IL-6 and IL-8 demonstrated lower levels of chemokine release from C20A4 exposed to both concentrations of N-HA compared to negative control at all timepoints ($p>0.05$; figure 5.21).

Time course comparison showed an overall rising trend with time, with statistically significant increase reached on day 21 when compared with day 1. This was the case for both chemokines, and with all cell-containing culture conditions. This likely reflect limitation of the model, with known over-confluence reached at latter timepoints.

Whilst chemokine levels released were greater with the higher N-HA concentration versus the lower concentration, this was not a marked increase and was not statistically significant at all timepoints.

Material interference of the ELISA assay was evaluated using cell-free, material-only negative controls. Similar to previous results with T-HA as detailed in section 5.3.1.2.2, extremely low to non-detectable levels of IL-6 were seen throughout the study period with N-HA. Whilst a low level of IL-8 was measured in the cell-free, material-only negative control, levels were far below that of cell-containing conditions (figure 5.21B) and deemed not biologically significant in terms of impact of results of the material toxicity testing.

Overall, the results suggests that N-HA in both concentrations did not induce a significant pro-inflammatory effect from C20A4 cell line. However, in view of the varied cell number between negative control and cells exposed to HA, as well as over time, chemokine released per cell was calculated to aid further analysis in the next section.

Regarding chemokine released per cell, there remained no statistically significant difference between cells exposed to N-HA, in either concentration, versus negative control at all timepoints (figure 5.22). Positive control with LPS was able to induce a pro-inflammatory response with a marked rise in IL-6 and IL-8 release per cell. This demonstrated that whilst C20A4 has the ability to mount a pro-inflammatory response,

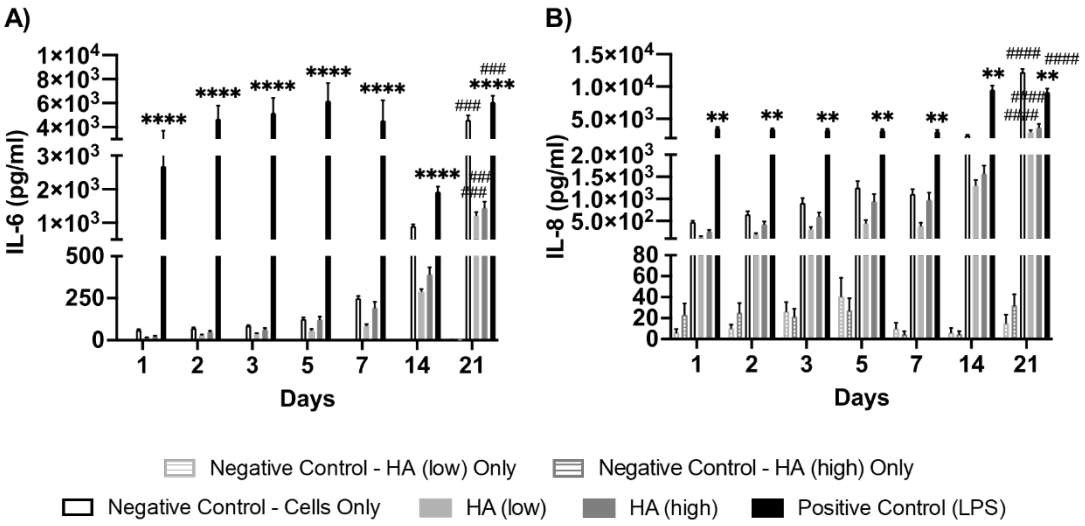

Figure 5.21 Pro-inflammatory effect of non-tyramine-substituted hyaluronic acid (N-HA) on C20A4 2D monoculture over 21 days. *Two N-HA concentrations were tested, denoted as 0.006g/ml (low) and 0.012g/ml (high). IL-6 (A) and IL-8 (B) release were measured with ELISA. Negative control consisted of C20A4 2D monoculture without material exposure, termed 'negative control – cells only'. Positive control was LPS 1μg/ml. Material interference on assay was investigated with material treated to the same experimental conditions, termed 'negative control – HA only', which included both N-HA concentrations. Mean±SEM is presented. N=3. Comparison between negative control and HA (low), HA (high) or positive control at each timepoint were denoted by ∗, and timepoint comparisons of each culture conditions by #. Statistical significance is shown as: p<0.05 ∗/#, p<0.01 ∗∗/##, p<0.001 ∗∗∗/### and p<0.0001 ∗∗∗∗/####.*

the exposure to N-HA at 0.006g/ml and 0.012g/ml concentrations did not elicit pro-inflammatory effects as measured by IL-6 and IL-8 release.

In addition, whilst the difference in chemokine levels between high and low N-HA concentrations was more apparent with chemokine per cell calculations, there was no statistically significant difference between the two HA concentrations to indicate superiority.

Time course comparison revealed the same findings as when total chemokine release was considered. I.e. A significant rise in both chemokine released per cell was seen on day 21, although IL-6 and IL-8 levels from C20A4 exposed to N-HA remained lower than that seen in negative control.

Overall, the results indicate that exposure of N-HA against C20A4 did not induce a pro-inflammatory response in the forms of IL-6 and IL-8 release. Whilst there is a suggestion that the lower concentration of HA produced lower levels of IL-8 released per cell, this did not reach statistical significance. Therefore, comparison between concentrations of N-HA did not show superiority.

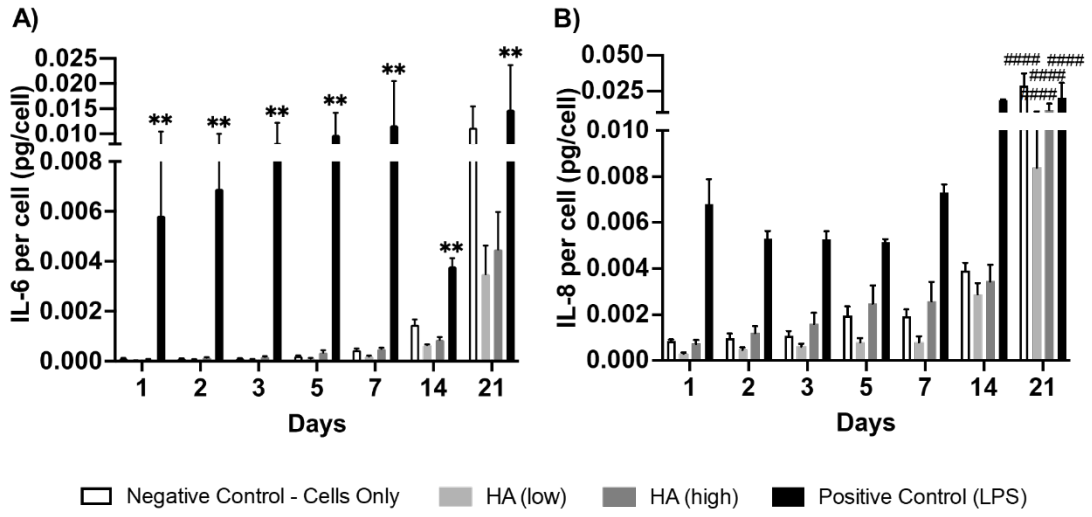

Figure 5.22 Pro-inflammatory effect per cell of non-tyramine-substituted hyaluronic acid (N-HA) on C20A4 2D monoculture over 21 days. *Two N-HA concentrations were tested, denoted as 0.006g/ml (low) and 0.012g/ml (high). IL-6 (A) and IL-8 (B) release were measured with ELISA, and chemokine released per cell were calculated relative to total cell number at each timepoint. Negative control consisted of C20A4 2D monoculture without material exposure, termed 'negative control – cells only'. Positive control was LPS 1μg/ml. Mean±SEM is presented. N=3. Comparison between negative control and HA (low), HA (high) or positive control at each timepoint were denoted by *, and timepoint comparisons of each culture conditions by #. Statistical significance is shown as: p<0.05 */#, p<0.01 **/##, p<0.001 ***/### and p<0.0001 ****/####.*

5.3.2.2.2.3 Cell morphology

Cell densities of C20A4 exposed to N-HA were appreciably less than that in negative control at each timepoint. This was quantified with the erythrosin B exclusion assay but also demonstrated qualitatively with light microscopy images (figure 5.23). Nonetheless, cell morphology of C20A4 exposed to N-HA at both concentrations was maintained, albeit demonstrating lower rates of cell proliferation.

Regarding change over time with the negative control, to mimic the cell concentration of the tissue-engineered construct, seeding density of C20A4 was relatively high, yielding confluence on day 1. Peak cell density was reached on day 3, as seen on light microscopy. This matched the trend seen with the erythrosin B exclusion assay for total cell concentration (figure 5.20A). An appreciable reduction in cell density beyond day 3 could be seen, likely a result of over-confluency of cells impacting cell proliferation.

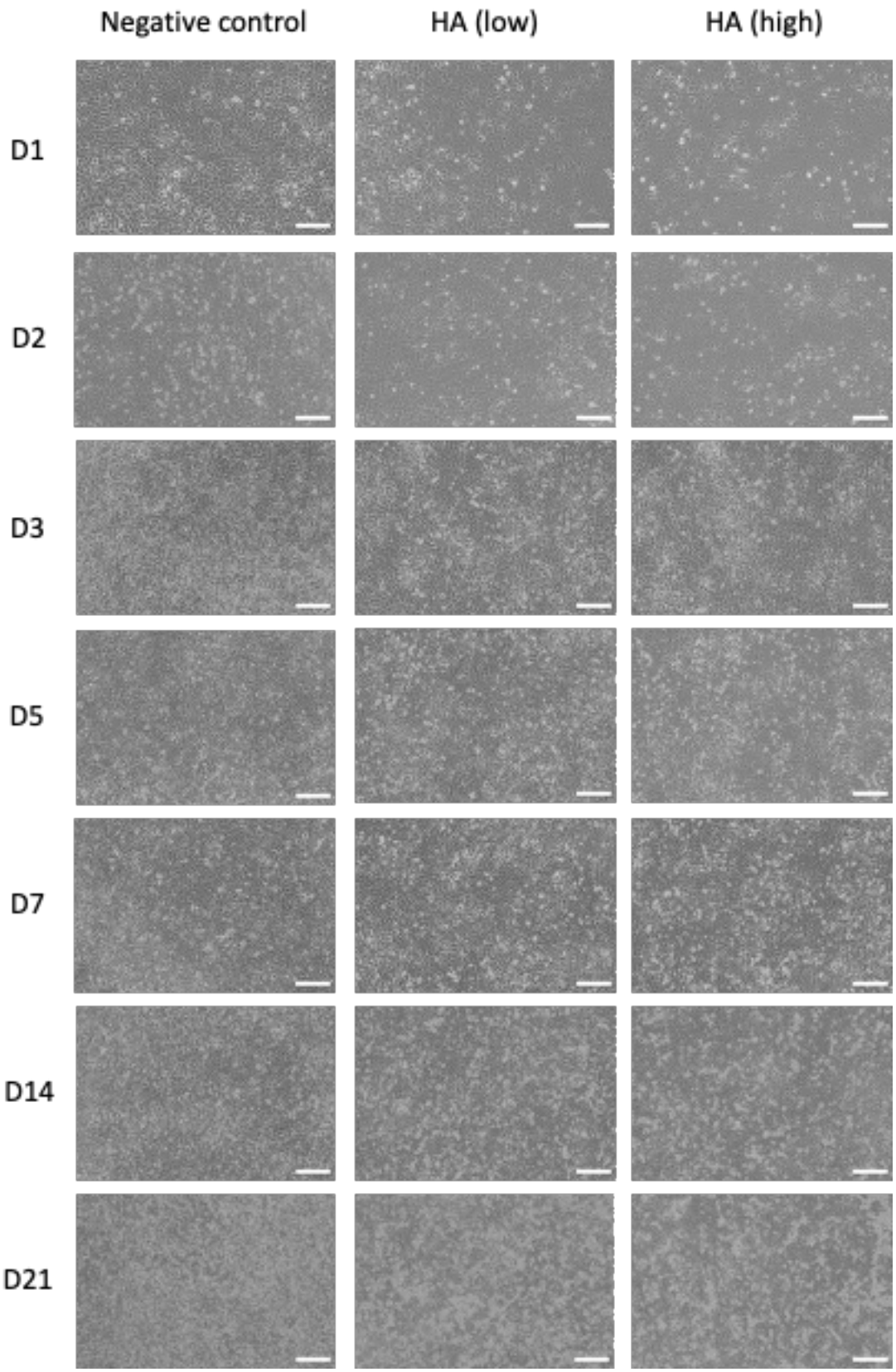

Figure 5.23 Light microscopy of effect of non-tyramine-substituted hyaluronic acid (N-HA) on C20A4 2D monoculture over 21 days. *Two N-HA concentrations were tested: 0.006g/ml (low) and 0.012g/ml (high). Negative control constitutes C20A4 2D culture without HA exposure. Scale bars represent 200μm.*

5.3.2.2.3 Section summary – material toxicity testing

Overall, HFF-1 and C20A4 exposed to N-HA at both concentrations did not display cytotoxicity or pro-inflammatory response. N-HA is therefore suitable for use in the advanced *in vitro* model for further testing of the nanocellulose-based hybrid bio-inks. With regards to N-HA concentrations, there was no clear evidence to suggest superiority. Although N-HA (low) was associated with greater cell proliferation as assessed with the erythrosin B exclusion assay and light microscopy, this may be secondary to the effects of media viscosity in a 2D culture system and is therefore not conclusive of the low concentration offering an advantage in terms of material effects.

5.3.2.3 Cross-linkage time definition

Four bio-inks containing N-HA were subjected to cross-linkage time studies. The bio-inks varied by N-HA concentrations (high and low), and the use of media or sterile ddH_2O as solvent for alginate and N-HA.

Determination of the minimum gelation time in silicon molds was conducted in the same manner as in chapter 4 for ETC:Alginate bio-inks and section 5.3.1.4.1 for bio-inks containing T-HA. This sought to determine the minimum cross-linker application time to achieve gelation of the 100µl bio-ink in an 8mm wide silicon mold to produce cross-linked hydrogel discs for use in the advanced *in vitro* model.

Subsequent rheological testing aimed to define the gel point (a rheologically defined state at which viscoelastic liquid transitions to a viscoelastic solid, or vice versa), and to undertake real-time monitoring of the storage modulus upon cross-linker application. The latter provides information on the temporal evolution of a rheological parameter of the bio-ink during cross-linkage. Through deeper understanding of the material (bio-ink) behaviour, the aim is to select an optimal bio-ink formulation for the triple component version bio-ink.

5.3.2.3.1 Determination of minimal gelation time in silicon molds

The results showed that bio-inks with higher N-HA concentration required longer gelation time. Media as the solvent was also associated with longer gelation time compared to ddH_2O, but showed less variability compared to bio-inks using T-HA

(table 5.7). The minimum gelation time for the bio-ink ETC:Alginate:N-HA (low) in media crosslinked with 0.1M $CaCl_2$ was 25 minutes.

In order to limit cross-linker application time, avoid osmotic cytotoxicity, and in view of the lack of superiority between N-HA concentrations in material toxicity testing, the triple component bio-ink using the low N-HA concentrations with media currently stands as the optimal formulation to take forward. Further characterisation of the bio-ink behaviour when exposed to 0.1M $CaCl_2$ will be examined next with rheological testing.

Table 5.7 Summary of minimum cross-linkage duration (minutes) for triple component bio-inks Nanocellulose:Alginate:Non-tyramine-substituted hyaluronic acid (N-HA) with cross-linker calcium chloride ($CaCl_2$). *Bio-inks tested consisted of tunicate-derived enzymatically pre-treated nanocellulose (ETC) and N-HA at two concentrations (0.006g/ml - 'low' and 0.012g/ml - 'high'). Bio-inks were cross-linked within silicon molds to create 8mm wide circular disc-shaped pellets of 100µl bio-inks and 600µl $CaCl_2$ 0.1M. The minimum time required for gelation was defined as reaching five consecutive complete gelation with no residual uncross-linked bio-ink. Testing was conducted at 1 minute intervals.*

Bio-inks	**Solvent for Alginate**	
	Media	**Sterile ddH_2O**
ETC:Alginate:N-HA (low)	25	19
ETC:Alginate:N-HA (high)	36	24

5.3.2.3.2 Rheological study of gelation of ETC:Alginate:N-HA bio-inks with $CaCl_2$

5.3.2.3.2.1 Gel point

Rheological studies initiated with attempts to define the gel point. As the gel point is defined at the point of modulus crossover, this was not feasible with all four bio-inks tested. As shown in figure 5.24, the storage moduli exceeded the loss moduli at time zero, prior to cross-linker application. This indicates that the un-crosslinked bio-inks were, in rheological terms, visco-elastic solids and therefore does not undergo the liquid-to-solid transition. This result mirrored that of Nanocellulose:Alginate bio-inks (section 4.3.4.2). As such, the next step was to further understand bio-ink behaviour with oscillatory time sweep experiments for real-time monitoring with cross-linker application.

5.3.2.3.2.2 Real-time monitoring of storage modulus during cross-linkage

Assessing times required to reach plateau and 50% of plateau of storage modulus (G') showed mostly comparable results amongst the four bio-inks tested, although greater variance was seen in bio-inks made with media (figures 5.25 and 5.26). The time to 50% G' plateau for ETC:Alginate:N-HA (high) in media was particularly short at 9 minutes compared to 32-36 minutes for other bio-inks. Likewise, the time to plateau for ETC:Alginate:N-HA (low) in media was prolonged at 10 hours 36 minutes, compared to 6 hours 8-39 minutes with other bio-ink formulations.

The results suggests that increased heterogeneity may be present with the use of higher N-HA concentrations, as well as the use of media as solvent. The former was of lesser consequence due to prior experimental testing supporting the move away from the use of higher N-HA concentration to reduce cross-linker application time and the associated cytotoxicity.

As to the bio-ink ETC:Alginate:N-HA (low) in media, material behaviour at 50% plateau of G' at 33 minutes of cross-linker application was reasonably consistent across the three replicates. This was the more relevant material state as the cross-linker application time is directly applicable to what would be used in the advanced *in vitro* model. Whilst the variance at the plateau point for this bio-ink was high, the decision was taken not to conduct further technical repeats as conclusion was adequately drawn from the data and the result will not alter conclusions drawn.

Similar to bio-inks without HA as examined in chapter 4 (section 4.3.4.2), the rate of change of G' over time for the triple component bio-inks displayed a faster rate of increase initially, which gradually slowed before reaching a plateau (figure 5.26). Increased variance in G' was observed in bio-inks reconstituted with media at 4 hours and beyond, which was not seen in bio-inks reconstituted with ddH_2O, or with all bio-inks when exposed to cross-linker for under one hour. Whilst this may be of interest for further research, for the purpose of this project, as the cross-linker application time will be limited to the time required to achieve complete gelation to produce hydrogel discs for use in the advanced *in vitro* model, the relevance of high variance with prolonged cross-linker exposure was not directly applicable to this project.

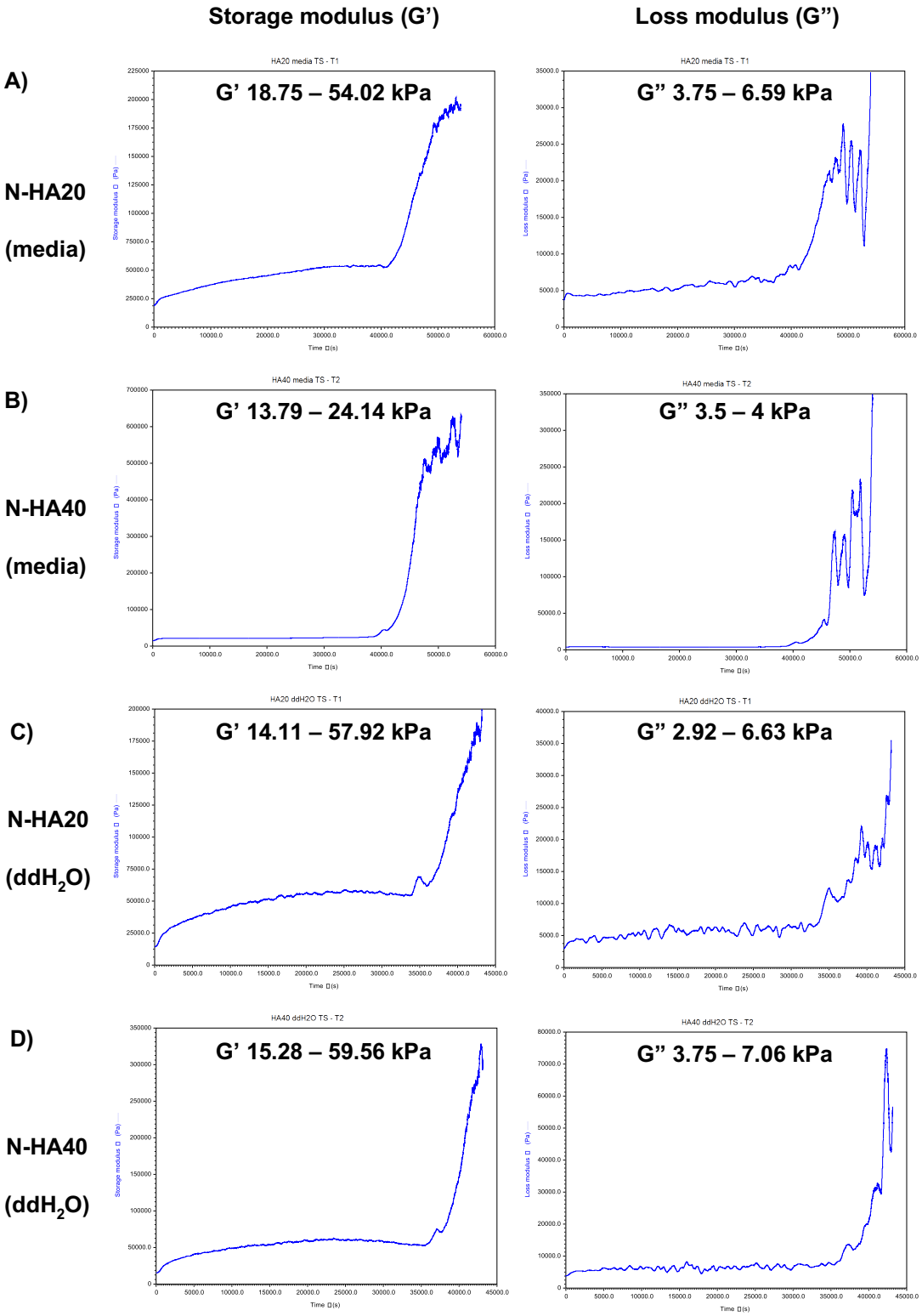

Figure 5.24 Oscillatory time sweeps of ETC:Alginate:Non-tyramine-substituted hyaluronic acid (N-HA) (media) and ETC:Alginate:N-HA (ddH_2O) bio-inks exposed to 0.1M calcium chloride ($CaCl_2$). *All bio-inks tested contained nanocellulose (ETC), alginate and N-HA. Concentrations of N-HA were 0.006g/ml (low, N-HA20) and 0.012g/ml (high, N-HA40). Alginate and N-HA were reconstituted in culture media (media) or sterile double-distilled water (ddH_2O). Four bio-inks tested were: A) ETC:Alginate:N-HA (low) in media, B) ETC:Alginate:N-HA (high) in media, C) ETC:Alginate:N-HA (low) in ddH_2O, and D) ETC:Alginate:N-HA (high) in ddH_2O. Time sweeps were conducted over 12 hours at 1Pa and 1Hz. Frequency sweeps were between 0.01-1Hz. Storage (G') and loss (G") modulus were recorded at 3s intervals, and denoted in left and right columns respectively. N=3. Data smoothing and visualisation was performed via the TRIOS software to permit preliminary analysis.*

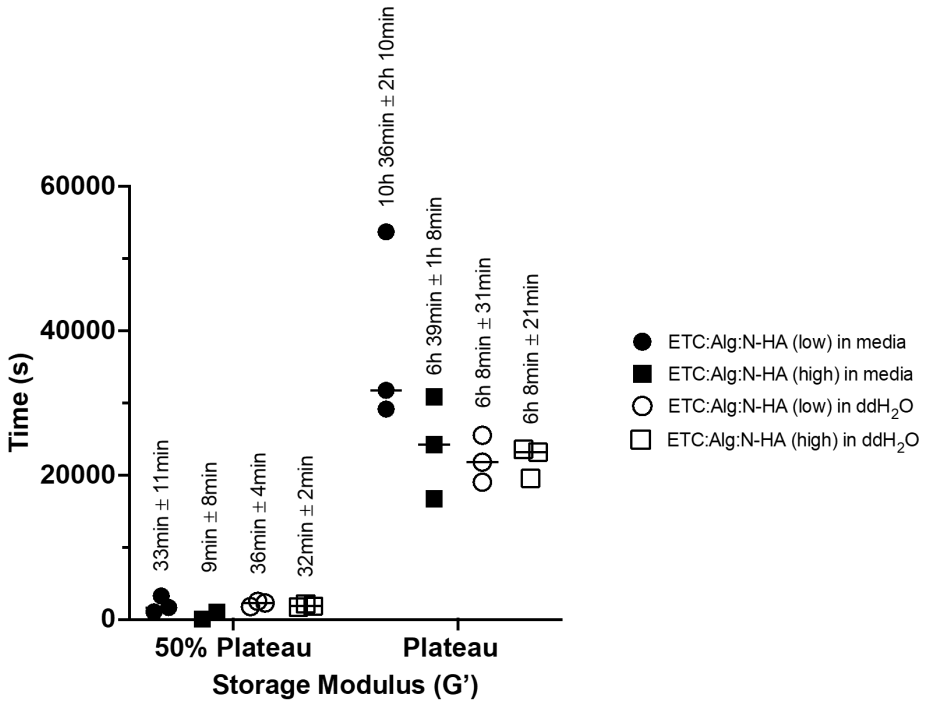

Figure 5.25 Time to reach plateau and 50% plateau of storage modulus of ETC:Alginate:Non-tyramine-substituted hyaluronic acid (N-HA)bio-inks. *Dot plot of rheological time-sweep study comparing four bio-inks, all cross-linked with 0.1M $CaCl_2$. Bio-inks differ in two ways: i) two N-HA concentrations, denoted as low (0.006g/ml) and high (0.012g/ml); and ii) solvent for alginate and N-HA in media or sterile double-distilled water (ddH_2O). Mean±SEM is described in text. N=3.*

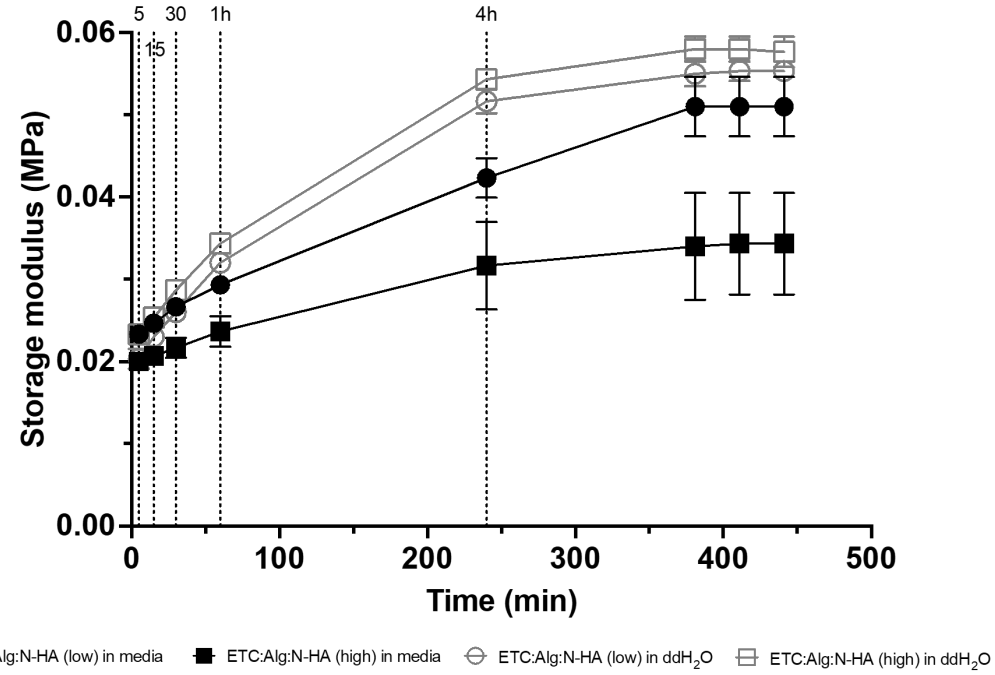

Figure 5.26 Storage modulus of ETC:Alginate:Non-tyramine-substituted hyaluronic acid (N-HA) bio-inks over time when exposed to 0.1M calcium chloride ($CaCl_2$). *Gelation kinetics were studied using time-sweep test. Four bio-inks were tested, which varied as follows: i) solvents for alginate and N-HA were media and sterile double-distilled water (ddH2O); ii) high (0.012g/ml) and low (0.006g/ml) concentration of N-HA. Storage modulus (G') was measured over time. Vertical dotted lines represent timepoints used in cross-linker toxicity testing, and includes 5, 15, 30 minutes, 1 hour and 4 hours. Additional timepoints plotted, from left to right, include 50% G' plateau, G' plateau, G' plateau + 30minutes and G' plateau + 1h. Mean±SEM is presented. N=3.*

Interestingly, bio-inks with higher N-HA concentration demonstrated opposite effects in terms of G' when reconstituted in ddH_2O or media. For bio-inks reconstituted in ddH_2O, G' was greater in the bio-ink with the higher N-HA concentration. In contrast, when reconstituted in media, G' was higher in the bio-ink with the lower N-HA concentration. This pattern was consistent over time, for over 8 hours of cross-linker exposure. A potential cause of the observed difference may be the chemical and salt content in media, and their impact on the ionic cross-linkage of the hydrogel. In addition, a higher N-HA content is likely to alter Ca^{++} diffusion, necessary to effect the gelation process. It was, however, unexpected that bio-inks with a lower N-HA content had a higher G', as is the case when reconstituted in media. With G' being a physical property parameter of the cross-linked hydrogel, this result emphasises the importance to control for variables due to their potential effects on the physical properties of the cross-linked bio-ink and potential downstream cellular effects.

5.3.2.3.3 Section summary – cross-linkage time definition

Overall, the gelation studies showed that using a lower N-HA concentration necessitated a shorter exposure time to cross-linker. On the other hand, whilst differences were elicited between bio-inks with varying N-HA contents and solvent used, the material behaviour of all bio-inks exhibited a similar temporal profile when exposed to 0.1M $CaCl_2$. Examining the specific downstream effects as a result of such differences was outside the remit of this project.

Given the parallel trends in material behaviour, it was concluded from this work that the lower N-HA concentration will be used to enable shorter cross-linker exposure time, and thereby limiting its associated adverse biological effects in terms of cytotoxicity and pro-inflammatory effects. Furthermore, media was selected as the solvent for alginate and N-HA for reasons discussed in chapter 4, namely to avoid the effect of osmotic cytolysis.

5.3.2.4 Section summary – Non-tyramine-substituted hyaluronic acid

The introduction of the triple component bio-ink brought alongside an alternative form of HA, N-HA. Material sterility and toxicity testing was both supportive of its use, for up to 21 days. Further sterilisation steps were not necessary as N-HA was supplied

sterile and sterility was confirmed in the microbial growth assay, despite a higher variance on day 21. Material toxicity testing showed no adverse cytotoxic or pro-inflammatory effects of N-HA against both the HFF-1 and C20A4 cell lines in 2D monoculture for up to 21 days.

The biological data did not indicate a strong preference towards the high or low N-HA concentrations. However, it was clear that the low N-HA concentration was associated with a shorter gelation time from the cross-linkage time studies. Considering the time-dependent toxicity profile of $CaCl_2$, it is preferable to keep cross-linker application time to the minimum. As such, the adoption of the low N-HA concentration could be recommended based on data from this section.

5.4 Chapter Summary and Conclusion

This chapter sought to better understand the effects of HA, with respect to creating a nanocellulose-based bio-ink inclusive of this native ECM substance. Testing was also performed to support the creation of a cross-linked hydrogel for use in an advanced 3D *in vitro* model for testing of the finalised bio-ink formulations in a co-culture model. Experimental studies followed the same systematic approach as adopted for the assessment of nanocellulose and alginate (chapter 3 + 4). A summary of results and conclusions drawn to take forward, referred to as recommendations, is shown in table 5.8.

The major findings in this chapter were the difficulty in harmonising the effects of H_2O_2 as a cross-linker, specifically between minimising adverse biological effects on cells and its effectiveness as a cross-linker to achieve gelation. This directly led to several key transitions in this chapter: i) transition from a nanocellulose:T-HA bio-ink to a triple component bio-ink incorporating alginate and cross-linked with $CaCl_2$; ii) conversion to a non-tyramine-substituted HA (N-HA) for better biomimicry to avoid unnecessary chemical modification; iii) the adoption of a sterile source of N-HA, afforded due to the need for a new HA source. Along the same vein, although material toxicity testing did not yield a strong contender between the high and low N-HA concentrations, based on the premise of limiting cross-linker application duration and associated cytotoxicity, it was concluded that the low N-HA concentration will be taken forward for future work as it required shorter cross-linker application time. Finally, for the creation of hydrogel discs for use in the advanced *in vitro* model, the work from this chapter showed that the previously developed silicon molds used with the Nanocellulose:Alginate bio-inks was also effective with the triple-component bio-ink, albeit with a longer gelation time.

In summary, to achieve a nanocellulose-based bio-ink containing HA, based on both biological and cross-linkage studies undertaken in this chapter, the final bio-ink formulation was defined as ETC:Alginate:N-HA (low) in media. To create hydrogel discs for use in the advanced 3D *in vitro* model, the bio-ink will be cross-linked with 0.1M $CaCl_2$ for 25 minutes in silicon molds.

Table 5.8 Summary of chapter conclusions and take-on messages.

Conclusions	
Tyramine-substituted HA	***Cross-linker effects - cytotoxicity + minimum gelation time:*** • Significant time- and dose-dependent cytotoxic effects of 5-25mM H_2O_2 on HFF-1 in 2D culture, therefore unsuitable for use. • Viability of HFF-1 preserved when exposed to 5-25μM H_2O_2, but failed to achieve gelation at 24 hours, therefore also unsuitable. • Dose range study of H_2O_2 (25μM – 5mM) on gelation time confirmed lack of appropriate concentration with satisfactory biological and gelation effects, thereby excluding T-HA and H_2O_2 for *in vitro* model.
Triple component bio-ink	• Pilot testing of triple component bio-ink consisting of nanocellulose, alginate and T-HA was successful in achieving gelation with 0.1M $CaCl_2$ within acceptable timeframe, leading to transition to this approach. • Alternative sterile non-tyramine-substituted HA introduced to mimic native human cartilage HA.
Non-tyramine-substituted HA	***Gelation studies to determine minimum cross-linkage time:*** • Cross-linking time of ETC:Alginate:N-HA (low) bio-ink in media with 0.1M $CaCl_2$ defined at 25 minutes. • Low N-HA concentration selected for advanced *in vitro* model, based on shorter cross-linker exposure time required and therefore reduced cytotoxic effects from cross-linker. ***Rheological studies:*** • Pre-crosslinked ETC:Alginate:N-HA bio-ink held predominantly viscoelastic solid properties and therefore gel point cannot be defined rheologically, the same as bio-inks without HA. • Comparison of media and ddH_2O as solvents for alginate and HA, and between high and low HA concentrations showed no significant difference in gelation kinetics and storage modulus.
Recommendations	
• HA to be used in final bio-ink formulations: sterile non-tyramine-substituted HA, at low concentration (0.006g/ml) and reconstituted in media. • Transition to triple component bio-ink (ETC:Alginate:N-HA (low) in media). • *In vitro* model creation with silicon molds, in the same manner as bio-inks without HA. • Cross-linking of ETC:Alginate:N-HA (low) bio-ink in media with 0.1M $CaCl_2$ for 25 min.	

Chapter 6: Advanced 3D *in vitro* model for bio-ink toxicity testing

6.1 Introduction

This chapter addresses the thesis aim of assessing the cytotoxic and pro-inflammatory effects of nanocellulose-based bio-inks intended for cartilage 3D bio-printing. This chapter builds upon results from the preceding chapters (chapters 3, 4, 5), namely, the refinement of bio-ink formulations and the development of advanced 3D *in vitro* models. Two bio-inks for testing were defined from chapter 4 and 5, ETC:Alginate in media and ETC:Alginate:N-HA (low) in media, respectively. Regarding the advanced 3D *in vitro* models, there is a chondrocyte-encapsulated monoculture model to investigate cell-material interactions. A co-culture model, consisting of chondrocyte-encapsulation coupled with surface-seeding with dermal fibroblast, to mimic the surgically implanted cartilage tissue engineered implant *in vivo*. To supplement the co-culture model, a fibroblast mono-culture model was created to understand the material-host interaction and the contribution of fibroblast to the co-culture system. An SOP was developed for the creation of the optimised bio-inks and the advanced 3D *in vitro* models, and this is presented in appendix 1.

Conventional 2D culture benefits from higher reproducibility, lower cost and relative ease of endpoint analysis. However, they are limited by the absence of a biomimetic 3D cell environment with resultant altered cell-to-cell connectivity, cell polarity and gene and protein expression profiles, in turn negatively impacting their predictability as a model for testing of therapeutic products. Commonly used 3D cultures, in the context of tissue engineering, often lacks multi-cellular representation to mimic the *in vivo* scenario. In contrast, increasing numbers of advanced 3D co-culture models, such as those applied for the study of cancer therapies, incorporates fibroblast in recognition of its structural influences with ECM deposition, and paracrine effects on cell growth, migration and the metabolic and immune profile of the local tissue microenvironment[298-300]. Fibroblast is a key cell type relevant in wound healing and the foreign body reaction, and its inclusion in the co-culture model aims to address this gap in current efforts within the field of tissue engineering.

The overall objective of developing and applying advanced 3D *in vitro* co-culture systems is to better select optimal material and processes during product development, with clinical translation in mind. This is important because drug and medicinal therapy development is extremely resource-intensive with a high attrition rate. The availability

of clinically relevant advanced 3D *in vitro* models bridges the gap between 2D culture models and *in vivo* studies. Thus, offering species-specific biological testing, in line with the 3R's movement and the concept of Safe-by-Design by reducing the amount of animal studies required, and taking into consideration biological safety data during product development, respectively.

The aims of this chapter were:

i) To establish the cytotoxic and pro-inflammatory effects of bio-inks ETC:Alginate in media, and ETC:Alginate:N-HA (low) in media against HFF-1 and C20A4 cell lines.
ii) To identify the optimal nanocellulose-based bio-ink formulation for cartilage tissue engineering based on biological evaluation.

Both aims were met *via* the objective below:

1. To assess the cytotoxicity and pro-inflammatory response of HFF-1 and C20A4 in advanced 3D *in vitro* monocultures and co-culture models when exposed to nanocellulose-based bio-inks.

6.2 Methods

The advanced 3D *in vitro* models were created in accordance with the SOP (appendix 1). Figure 6.1 illustrates the parameters of the cytotoxicity and pro-inflammatory response studies, including the two bio-inks tested, the investigations and cellular system applied (chondrocyte and fibroblast monocultures + co-culture). There were seven timepoints over 21 days, the same as with material toxicity testing (chapter 3 - 5). In concordance with past material toxicity testing and to permit joint data interpretation, media exchange was performed in the same manner with 500µl exchange on day 7 and day 14 (section 2.13). Therefore, supernatant-based assays, which includes the LDH assay and ELISA, used a dilution factor of 2 and 4 for day 14 and day 21, respectively. As described in section 2.13, the negative control for each assay was 2D cell culture devoid of bio-ink material. Material interference was accounted for with a material only, cell-free control created in the same manner as described in the SOP and subjected to the same experimental culture conditions. Positive control for cytotoxicity was 0.1% Triton X-100, which was performed with the live/dead staining, and for pro-inflammatory effects, 1µg/ml LPS was used. To

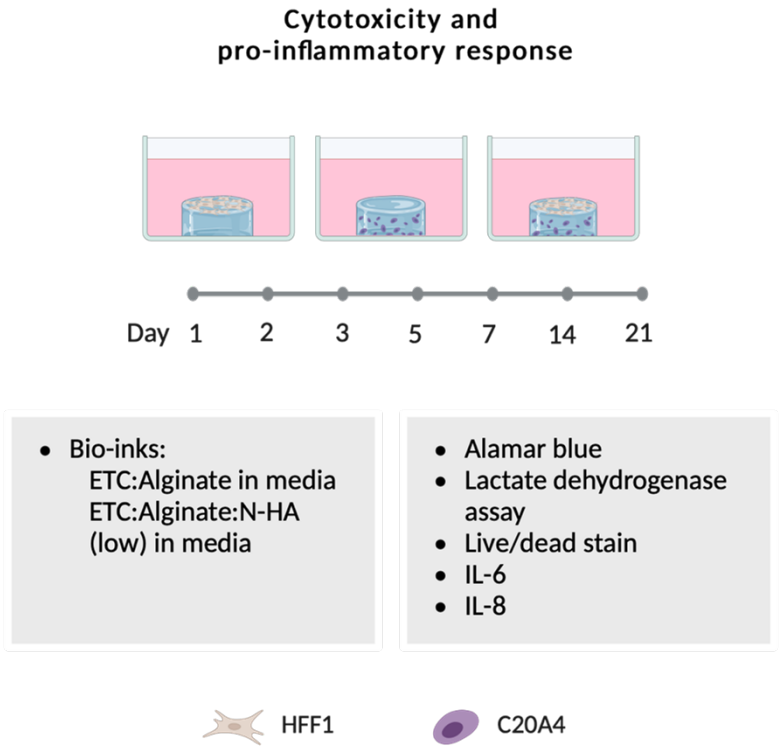

Figure 6.1 Schematic of chapter 6 workflow. *Assessment of cytotoxicity and pro-inflammatory responses with chondrocyte and fibroblast in 3D monoculture and co-culture systems. Created with biorender.com.*

address chapter aim (ii), direct comparison of quantitative endpoint testing between the two bio-inks was also performed.

6.2.1 Alamar blue assay

The alamar blue assay uses cellular metabolic activity as a measure of cell proliferation and cytotoxicity. As a non-toxic form of similar metabolism-based assays (e.g. MTT assay), the alamar blue assay has been widely adopted since its introduction in 1993[301]. The principle of the assay is the colour change that the blue, non-fluorescent resazurin undergoes when it is taken up into the cytosol of live cells and reduced to the red and highly fluorescent resorufin. The conversion of resazurin to resofurin is measured by absorbance or fluorescence, whereby the intensity of colour or fluorescence denotes the amount of metabolic activity within the cell population. Therefore, with no standard unit of measure for absorbance or fluorescence intensity, it is the relative change in absorbance or fluorescence values that infers the degree of cell viability or proliferation. The latter is often shown as the relative fluorescent unit (RFU), calculated against the negative control (cells devoid of chemical exposure). Fluorescence reading was selected in this study over colorimetric change as it confers greater sensitivity[301].

The procedure for the assay was conducted with shielding from direct light due to light sensitivity of the alamar blue reagent. The alamar blue reagent was pre-warmed to room temperature prior to use. The staining solution was prepared at the ratio of 1:9 of alamar blue reagent and culture media (e.g. 100µl alamar blue reagent with 900µl culture media). Prior to adding the staining solution to samples, culture media in each 24 well plate wells were removed, and samples subjected to a wash step with 1ml of PBS per sample. The staining solution was then added to each sample (1ml per sample) and incubated for 3 hours at 37°C. Fluorescence was read following transfer of 100µl of staining solution to black 96 well plates. With fluorescence readings, black microplates were used instead of transparent plates to minimise signal interference from adjacent wells. Three reading replicas were performed per sample, and the excitation and emission settings were 544nm and 590nm respectively. The fluorescence unit (FU) for each sample was calculated by averaging the three reading replicas and subtracting the mean of FU of blank wells.

With advanced 3D *in vitro* models, the negative controls consisted of 2D monocultures of HFF-1 and C20A4 without bio-ink exposure. However, due to the inherent differences between 2D v 3D culture, they were not directly comparable. Therefore, the relative fluorescence unit (RFU) is calculated against the fluorescence value of day 1 using equation 6.1. The lack of a reference material with known cytotoxic and pro-inflammatory profile that could act as a control scaffold to support 3D culture for comparison against the bio-ink is a common challenge in this context. Nonetheless, the 2D cell culture (negative control) provides an indication of cell behaviour over the study period. A 2D co-culture model was not performed, however, as it was deemed physiologically less relevant and therefore would not yield clinically relevant result. Material interference on the assay was accounted for using material-only, cell-free hydrogel discs, subjected to the same experimental conditions as the cultured models. Although the alamar blue reagent is considered non-toxic and marketed as permissive for longitudinal studies, the impact of retained Alamar blue reagent in the 3D system is unquantified. Therefore, a separate model was prepared for each timepoint. The study was conducted with biological triplicates.

Equation 6-1

$$\text{Relative Fluorescence Unit (RFU)} = \frac{\text{FU of samples (day2-21)}}{\text{FU of sample (day 1)}} \times 100$$

6.2.2 Lactate dehydrogenase assay

Methodology for the LDH assay was previously described in section 2.9.

6.2.3 Live/dead staining

Live/dead staining of samples was performed for the qualitative assessment of cytotoxicity using a commercial kit. The principle of the assay involves simultaneous staining of cells with calcein acetoxy-methyl-ester (calcein AM) and ethidium homodimer-1 (EthD-1)[302]. The non-fluorescent calcein AM permeates live cells, and is converted to the green fluorescent calcein by intracellular esterase activities, thereby selectively staining live cells green.

Conversely, EthD-1 is impermeable to live cells with intact cell membrane. EthD-1 permeates dead cells, upon which it binds to nucleic acid and produce a red fluorescence and staining dead cells (and cells with damaged cell membranes) red. All

procedures were performed with protection from direct light. The assay reagents were thawed to room temperature and previously optimised concentrations were used (performed by the research group – unpublished data). Both reagents were diluted in PBS to create the dye solution, at concentrations of 2µl/ml for calcein AM and 4µl/ml for EthD-1. For sample preparation, culture media which contained serum esterases was removed. Samples were subjected to three wash steps (1ml PBS per wash cycle per sample). Dye solution was added to the washed samples (600µl per sample per well) and incubated for 30 minutes at room temperature as per manufacturer's guidance. All procedural steps described thus far were performed in the tissue culture hood, following which, steps were performed in the standard laboratory bench. Following incubation, the dye solution was removed, and samples again washed with three cycles of PBS (1ml per wash cycle per sample). Samples were protected from light with foil, kept submerged in 1ml PBS to avoid desiccation and transferred immediately onto histology slides for imaging under the fluorescence microscope. The excitation and emission wavelength for aalcein AM and EthD-1 were 495/515nm and 495/632nm, respectively. Three biological replicates were performed, with three field of views taken per sample. Representative images are shown.

6.2.4 ELISA

The ELISA was used to quantify IL-6 and IL-8. Its methodology was previously described in section 2.8.3.

6.3 Results and Discussion

6.3.1 Cytotoxicity

Cytotoxicity was assessed quantitatively with the alamar blue assay and the LDH assay. This was complemented by live/dead staining of the models.

6.3.1.1 Alamar blue assay

The fluorescence intensity (FU) and RFU relative to day 1 are shown in figure 6.2 and 6.3, respectively. Overall, 2D culture displayed trends in cell proliferation and cytotoxicity in line with cell line characterisation (section 2.8.5). HFF-1 showed a rising trend of FU and RFU between day 1 and day 14 reflecting cell proliferation, which was statistically significant on day 7 and day 14 for FU readings, and day 14 for RFU. Both analyses showed a reduction in FU and RFU on day 21, reflective of over-confluence and a decline in cell viability and live cell numbers.

Similarly, the negative control for C20A4 in 2D culture showed similar cell proliferation and viability trends as in cell line characterisation. Due to the initial high seeding density to mimic the cell number within the advanced 3D *in vitro* model, cell confluence was reached sooner than with HFF-1. Both FU and RFU demonstrated a rising trend between day 1 and day 3, a plateau between day 3 and 5, and a gradual decline from day 7 onwards, with statistical significance reached at varying timepoints as shown in figure 6.2 and 6.3. As noted in the cell line characterisation, the decline in cell number and viability was due to over-confluence. Interestingly, the auto-detachment of the chondrocyte cell sheet did not occur in this experimental set-up. This was most likely a result of the altered culture medium exchange regime. With a relative rationing of nutrients, cell proliferation in this study was inhibited relative to conditions during cell line characterisation. As such, the threshold for cell sheet detachment was not reached.

In terms of bio-ink comparisons in the advanced 3D *in vitro* models, FU was overall lower with HFF-1 than with C20A4 or the co-culture model due to a significantly lower seeding density and therefore cell numbers. Cell proliferation was seen with HFF-1 in the acute timeframe, with a rise in FU and RFU between day 1 and 7. This rise peaked sooner on day 5 with the bio-ink containing HA, compared to day 7 for the

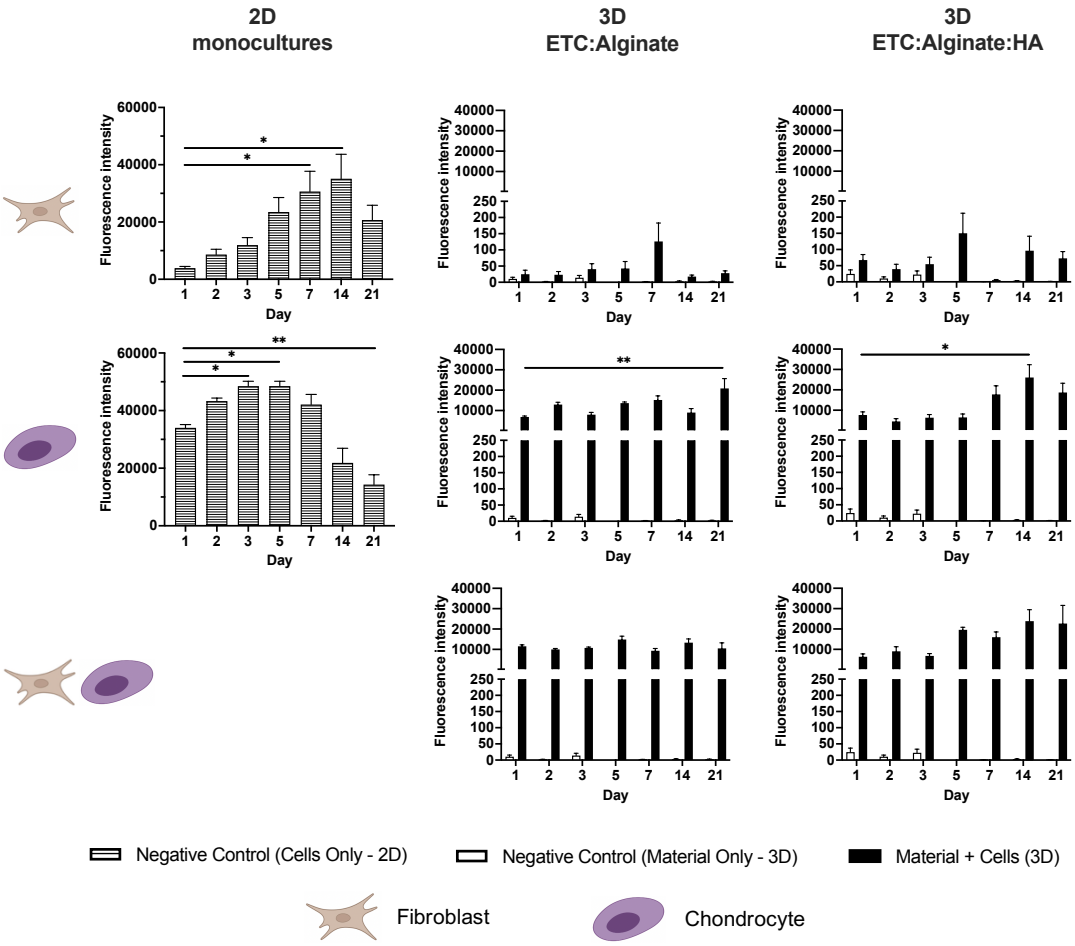

Figure 6.2 Alamar blue assay on chondrocyte (C20A4) and fibroblast (HFF-1) in 2D monocultures and 3D mono- and co-culture systems over 21 days. *Bio-inks tested in 3D systems were ETC:Alginate and ETC:Alginate:Hyaluronic Acid(HA). Top, middle and bottom rows are of fibroblast, chondrocyte and co-culture of both cell types, respectively. Mean±SEM of fluorescence intensity are represented. N=3. Statistical significance of timepoint comparisons against day 1 denoted by * ($p<0.05$ *, $p<0.01$ **).*

bio-ink without HA. This suggests that HA is supportive of fibroblast proliferation. However, beyond this peak, the metabolic activity from HFF-1 in the monoculture settings declined to varying degrees with both bio-inks, although it is beyond the remit of this study to ascertain the cause of this.

With the C20A4 monoculture 3D model, increasing cellular metabolic activity was observed with both bio-inks. A statistically significant rise in FU was reached, sooner with the bio-ink containing HA on day 14, followed by with the bio-ink without HA on day 21 (figure 6.2). This is reflected similarly when presented in RFU, with a statistically significant rise in RFU on day 14 with the bio-ink containing HA. This result is consistent with previous studies that showed that the bio-ink consisting of nanocellulose and HA supported chondrogenicity to a greater degree than bio-inks containing nanocellulose and alginate (unpublished data). The study here differs in that both bio-ink tested contained alginate.

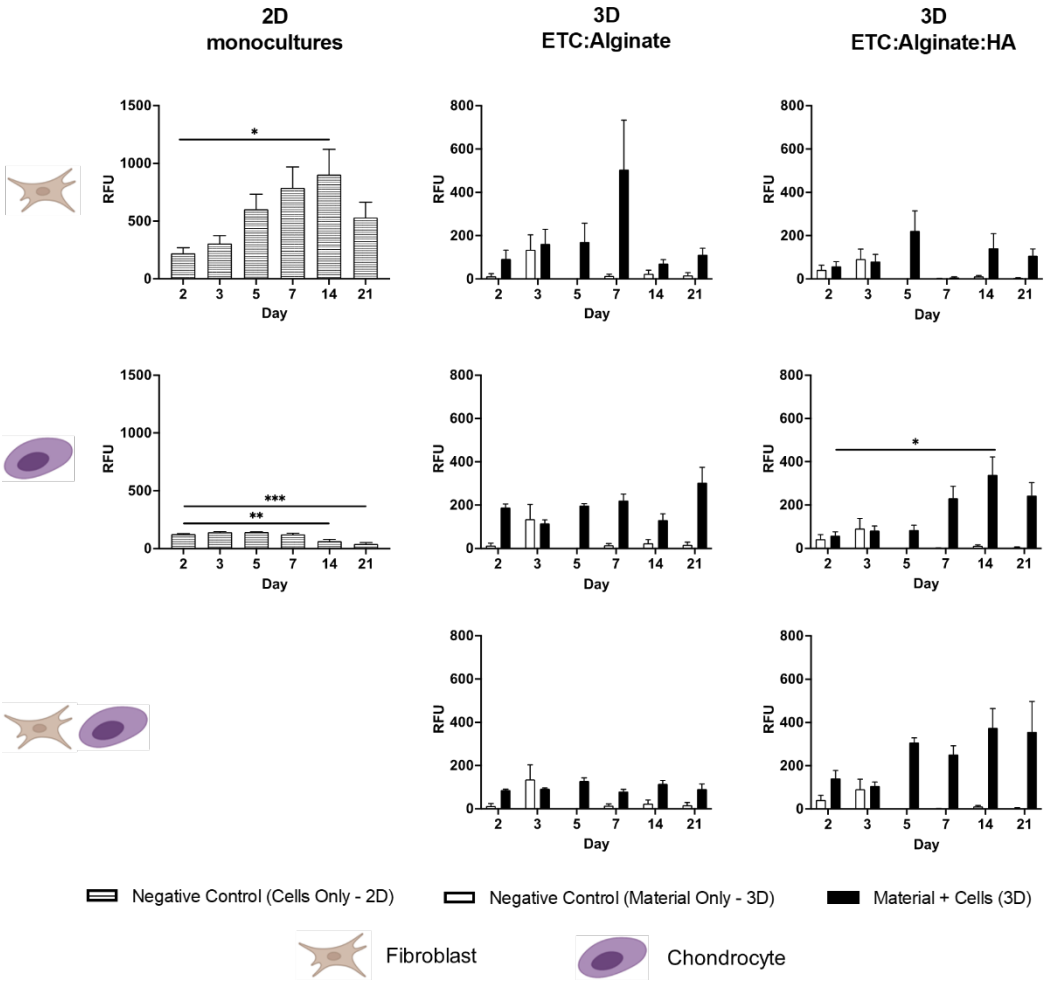

Figure 6.3 Relative fluorescent unit (RFU) of alamar blue assay on chondrocyte and fibroblast in 2D monocultures and 3D mono- and co-culture systems over 21 days. *Bio-inks tested in 3D systems were ETC:Alginate and ETC:Alginate:Hyaluronic Acid(HA). RFU were calculated relative to fluorescence intensity value on day 1. Top, middle and bottom rows are of fibroblast, chondrocyte and co-culture of both cell types, respectively. Mean±SEM of RFU are represented. N=3. Statistical significance of timepoint comparisons against RFU on day 2 denoted by * ($p<0.05$ *, $p<0.01$ **, $p<0.001$ ***).*

Interestingly, the co-culture model showed an earlier rise in RFU coupled with marginally lower FU levels when compared to the C20A4 3D monoculture. This indicates that whilst cell proliferation occurred at a faster rate initially in the co-culture model, the overall cellular metabolic activity of the system over the period of 21 days remained less than that of the C20A4 3D monoculture system. Whilst the exact mechanism for the difference observed cannot be defined at this point, the data suggests that there is a degree of cellular cross-talk, and the presence of fibroblast influenced the C20A4 proliferation profile with both bio-inks.

The impact of the bio-ink material on the assay was tested with the cell-free material-only negative control, conducted for all 3D systems. Fluorescence intensity measured was overall low. There was no statistically significant difference across all timepoints with both bio-inks for FU and RFU, reflecting no significant change over time. This

indicates that prolonged culture of the cross-linked bio-ink did not enhance material interference on the assay.

6.3.1.2 Lactate dehydrogenase assay

Considering firstly the cytotoxicity profile in the 2D negative controls, there was a statistically significant rise in LDH on day 21 with both HFF-1 and C20A4. This is concurrent to a reduction in RFU in both cell lines at the same timepoint. Taken together, along with cell line characterisation data (section 2.8.5), the findings all reflect cytotoxicity at the latter timepoint due to over-confluence. The rise in LDH, however, precedes the decline in cellular metabolic activity measured in the Alamar blue assay, reflecting the presence of cellular dysfunction at earlier timepoints. This demonstrates the benefit and recommended practice of incorporating at least two assessment method for each toxicity endpoint[303].

With the LDH assay, material interference was relatively more apparent compared with the alamar blue assay. LDH levels in the cell-free bio-ink only material controls were notable on day 14 and day 21, whilst remaining detectable at lower levels at earlier timepoints (figure 6.4). Its relevance is discussed below with each *in vitro* model.

In the case of the HFF-1 3D monocultures, the levels of LDH from the exposure conditions were comparable to the cell-free control. Therefore, it was concluded that no significant cytotoxicity was observed in the HFF-1 monoculture model over the 21-day period. Nonetheless, FU and RFU in the 3D model was reduced at the chronic timepoints compared to day 5 indicating a reduced level of cellular metabolic activity in the systems, which warrants caution in data interpretation and potentially further investigation for future model applications.

On the other hand, a statistically significant rise in LDH on day 21 was noted across both the C20A4 monoculture and co-culture 3D systems, with both bio-inks. Despite a greater degree of material interference on the assay on day 21, the levels of LDH measured in the cellular were interpretated as indicative of cytotoxicity on day 21 for both models and bio-inks. The greatest degree of cytotoxicity on day 21 was with the bio-ink ETC:Alginate in media tested in the co-culture system. Taken together, with the superior cell proliferation profile seen with the bio-ink containing HA with the

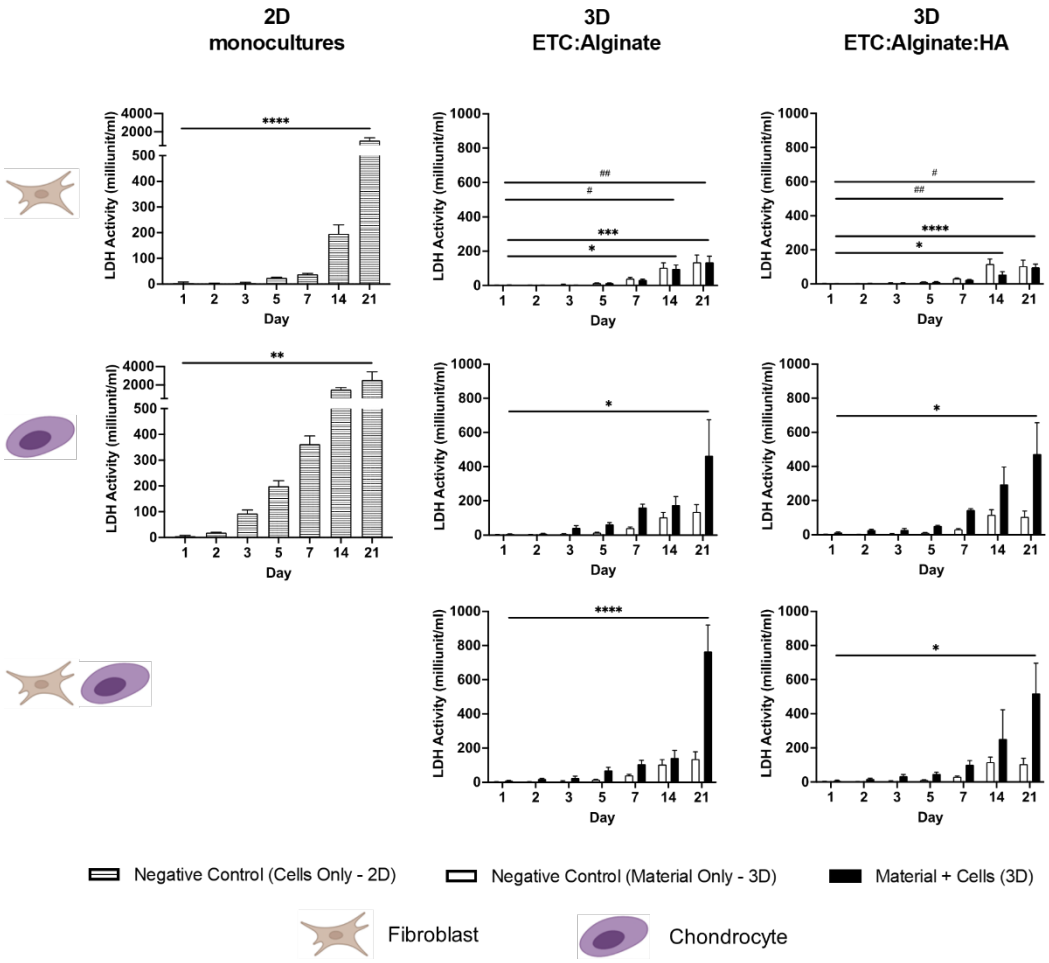

Figure 6.4 Lactate dehydrogenase assay on chondrocyte (C20A4) and fibroblast (HFF1) in 2D monocultures and 3D mono- and co-culture systems over 21 days. *Bio-inks tested in 3D systems were ETC:Alginate and ETC:Alginate:Hyaluronic Acid(HA). Top, middle and bottom rows are of fibroblast, chondrocyte and co-culture of both cell types, respectively. Mean±SEM are represented (n=3). Statistical significance of timepoint comparisons against day 1: of 3D cellular systems denoted by ∗, and of material only negative control by # (p<0.05 ∗/#, p<0.01 ∗∗/##, p<0.001 ∗∗∗/###, p<0.0001 ∗∗∗∗/####).*

alamar blue assay, the bio-ink ETC:Alginate:N-HA (low) in media was found to be superior in terms of cytotoxicity.

Furthermore, differences were observed in the trends and levels of LDH measured over time between the C20A4 monoculture and co-culture 3D models, and with both bio-inks. Although the differences were less marked compared with the alamar blue assay, nonetheless, the differences indicate varied cell behaviour and response in both cellular systems, which signifies cell-to-cell interaction between the chondrocyte and fibroblast in the co-culture system. This illustrates the merit of the co-culture model in the context of creating an advanced 3D *in vitro* model aimed at understanding the biological impact of nanocellulose-based bio-inks for tissue engineering purposes.

In terms of model development, the heightened LDH levels on day 21 could indicate model limitation, which would benefit from further characterisation and development.

On the other hand, chondrocytes were seeded at $3x10^6$ cells/ml, which was considered at the lower end of the spectrum of seeding densities of bio-inks intended for cartilage tissue engineering in the literature (section 2.8.5.2). A relatively high chondrocyte density is considered desirable due to the dependence on chondrocyte proliferation and ECM production to enhance the mechanical properties of the tissue engineered implant. There is currently a lack of consensus regarding the superiority between *ex vivo* cell expansion and pre-seeding implants with the desired number of chondrocytes, versus post-implant fabrication cultivation in a bioreactor to achieve the desired implant characteristics[304, 305]. This is in part due to challenges with chondrocyte dedifferentiation and loss of functionality during *ex vivo* expansion, and the volume required to populate a full-size cartilage implant for human application. Furthermore, the tissue engineered implant is intended to last the lifetime of the recipient, and crucially maintaining its form (shape) when used for facial reconstruction. As such, it is of great interest to further our understanding of the cellular behaviour and proliferation profile in the long term, for which the advanced 3D *in vitro* co-culture model could be further characterised and developed for this purpose.

6.3.1.3 Live/dead staining

Live/dead staining was conducted permitting both qualitative assessment of cytotoxicity and visualisation of live and dead cells in the advanced 3D *in vitro* models. The findings from live/dead staining of 2D mono-cultures of HFF-1 and C20A4, which served as negative control of the advanced 3D *in vitro* models (i.e. without bio-ink exposure) were in line with both cell line characterisation and the alamar blue and LDH assays (figure 6.5). HFF-1 demonstrated cell proliferation over time, with increasing confluency observed. A greater number of dead cells was seen on day 21 with HFF-1, reflecting findings of the LDH assay. As for C20A4, cell confluency was seen from day 1, as with cell line characterisation. This was associated with a relatively greater number of dead cells at earlier timepoints. Nonetheless, a general trend of increasing number of dead cells was seen with the C20A4 cell line. Although the 2D cultures tolerated the augmented culture media exchange regime without cell sheet auto-detachment, which occurred during cell line characterisation, it did not tolerate the multiple wash steps very well for the live/dead staining procedure. As such, the live/dead staining showed evidence of the partial lifting of the C20A4 cell sheet.

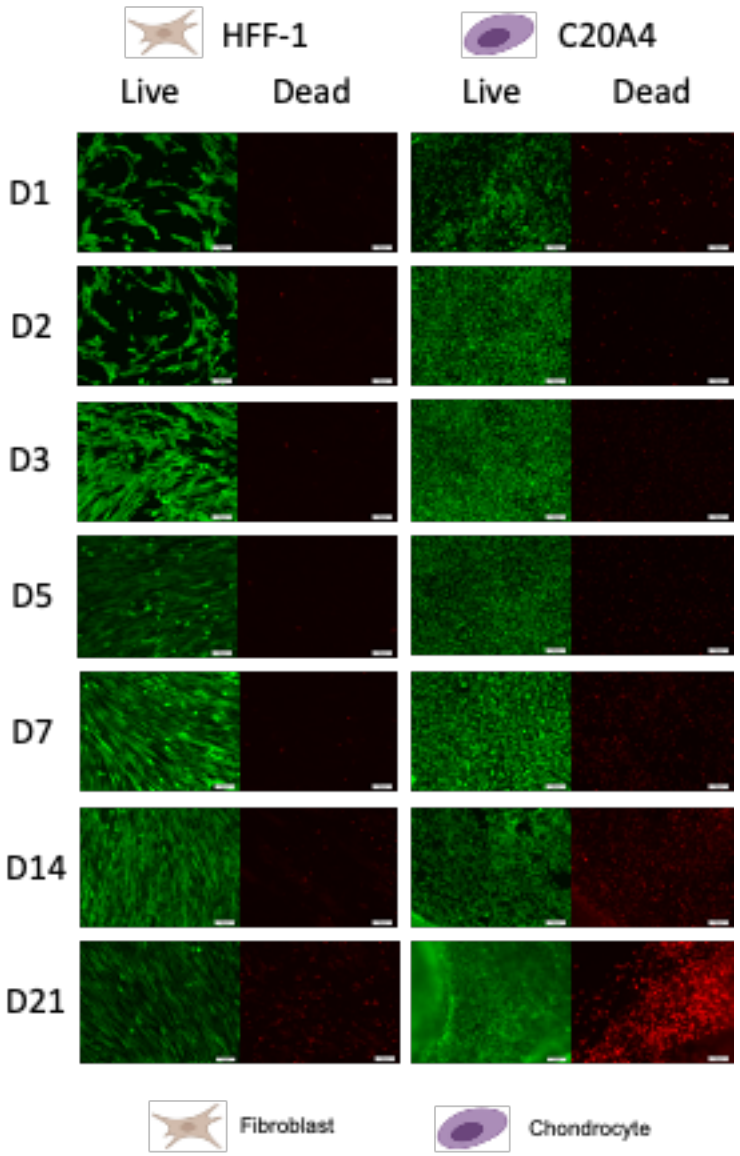

Figure 6.5 Live/dead staining of human dermal fibroblast (HFF-1) and human chondrocyte (C20A4) cell lines in 2D cultures over 21 days. *Cell culture without bio-ink exposure served as negative control for toxicity testing of bio-inks. Live/dead staining was conducted with calcein AM and ethidium homodimer-1 which stains live and dead cells fluorescent green and red, respectively. Scale bars represent 100μm.*

As for the advanced 3D *in vitro* models, the results were broadly in keeping with the findings of the alamar blue and LDH assay. The seeding density discrepancy between HFF-1 and C20A4 was apparent during visualisation, with a much lower number of live fibroblasts seen on day 1 and throughout the study period (figure 6.6 and 6.7). Whilst an overall increase in live cell numbers could be appreciated between day 1 and 7 with HFF-1, the live cell number or density appeared relatively static with the C20A4 monoculture and co-culture models. The trends in cellular metabolic activity, and the differences seen between bio-inks or between systems were less apparent with the live/

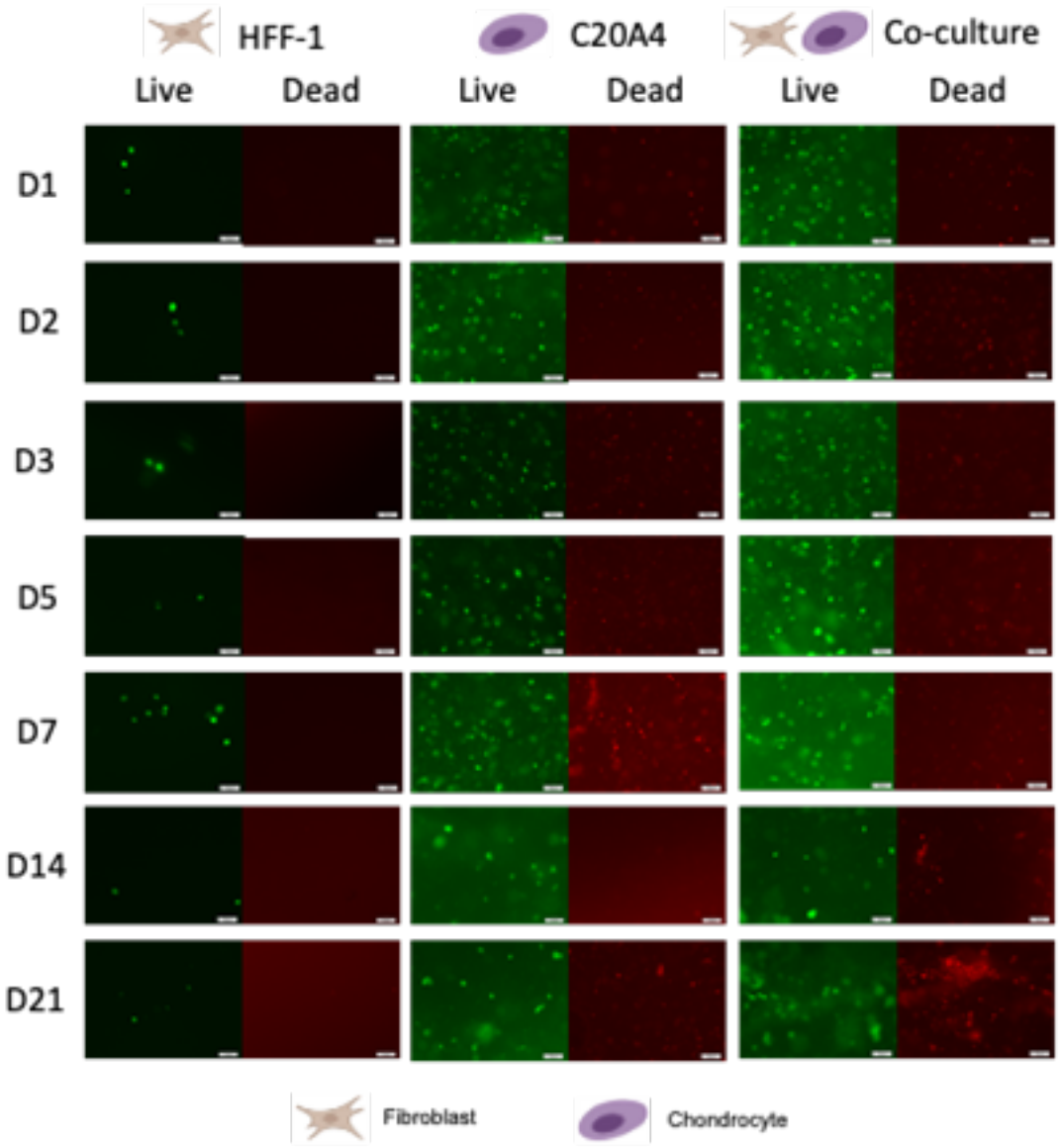

Figure 6.6 Live/dead staining of advanced 3D in vitro models of human dermal fibroblast (HFF-1) and human chondrocyte (C20A4) mono- and co-culture with bio-ink ETC:Alginate in media. *A nanocellulose-based bio-ink, consisting of enzymatically pre-treated nanocellulose fibrils (ETC) and alginate reconstituted in media, was used to create the advanced 3D in vitro models. Three models were tested over 21 days: surface-seeded fibroblast (left), chondrocyte-encapsulated (mid) and co-culture of both surface-seeded fibroblast and chondrocyte encapsulation (right). Live/dead staining was conducted with calcein AM and ethidium homodimer-1, which stain live and dead cells fluorescent green and red, respectively. Scale bars represent 100μm.*

dead staining. Indeed, a relative reduction in cell numbers, both live and dead, was noted at the chronic timepoints (day 14 and day 21) with the live/dead staining. This produced a seemingly conflicting results when compared with the alamar blue and LDH assay. However, this may be due to alterations in the diffusion of the live/dead staining solution across the 8mm 100µl seeded hydrogel discs. ECM production by chondrocytes, and to a lesser extent by fibroblasts, may have hindered the efficacy of the live/dead staining solution. It was noted that the live/dead staining was effective

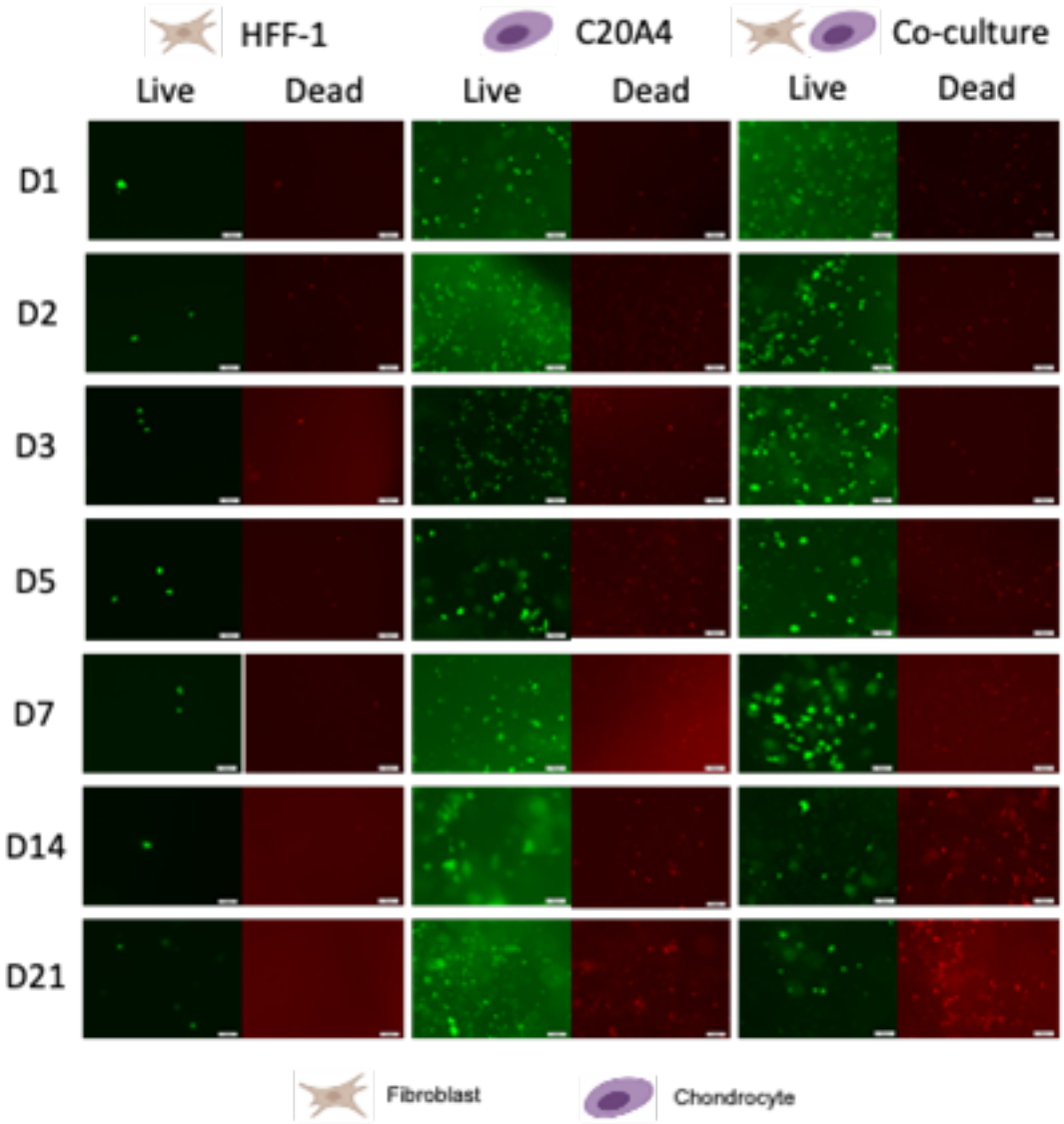

Figure 6.7 Live/dead staining of advanced 3D in vitro models of human dermal fibroblast (HFF-1) and human chondrocyte (C20A4) mono- and co-culture with bio-ink ETC:Alginate:N-HA (low) in media. *A nanocellulose-based bio-ink, consisting of enzymatically pre-treated nanocellulose fibrils (ETC), alginate and non-tyramine-substituted hyaluronic acid (N-HA) at low concentration (6mg/ml) reconstituted in media, was used to create the advanced 3D in vitro models. Three models were tested over 21 days: surface-seeded fibroblast (left), chondrocyte-encapsulated (mid) and co-culture of both surface-seeded fibroblast and chondrocyte encapsulation (right). Live/dead staining was conducted with calcein AM and ethidium homodimer-1, which stain live and dead cells fluorescent green and red, respectively. Scale bars represent 100μm.*

on the 2D cell cultures at day 21. Therefore, future application of live/dead staining for the advanced 3D *in vitro* model will require optimisation. As the incubation period for the staining solution (3 hours) was near the upper end of the manufacturer's guidance (30 minutes to 4 hours), other variables for optimisation could include reagent concentration, incubation duration and temperature.

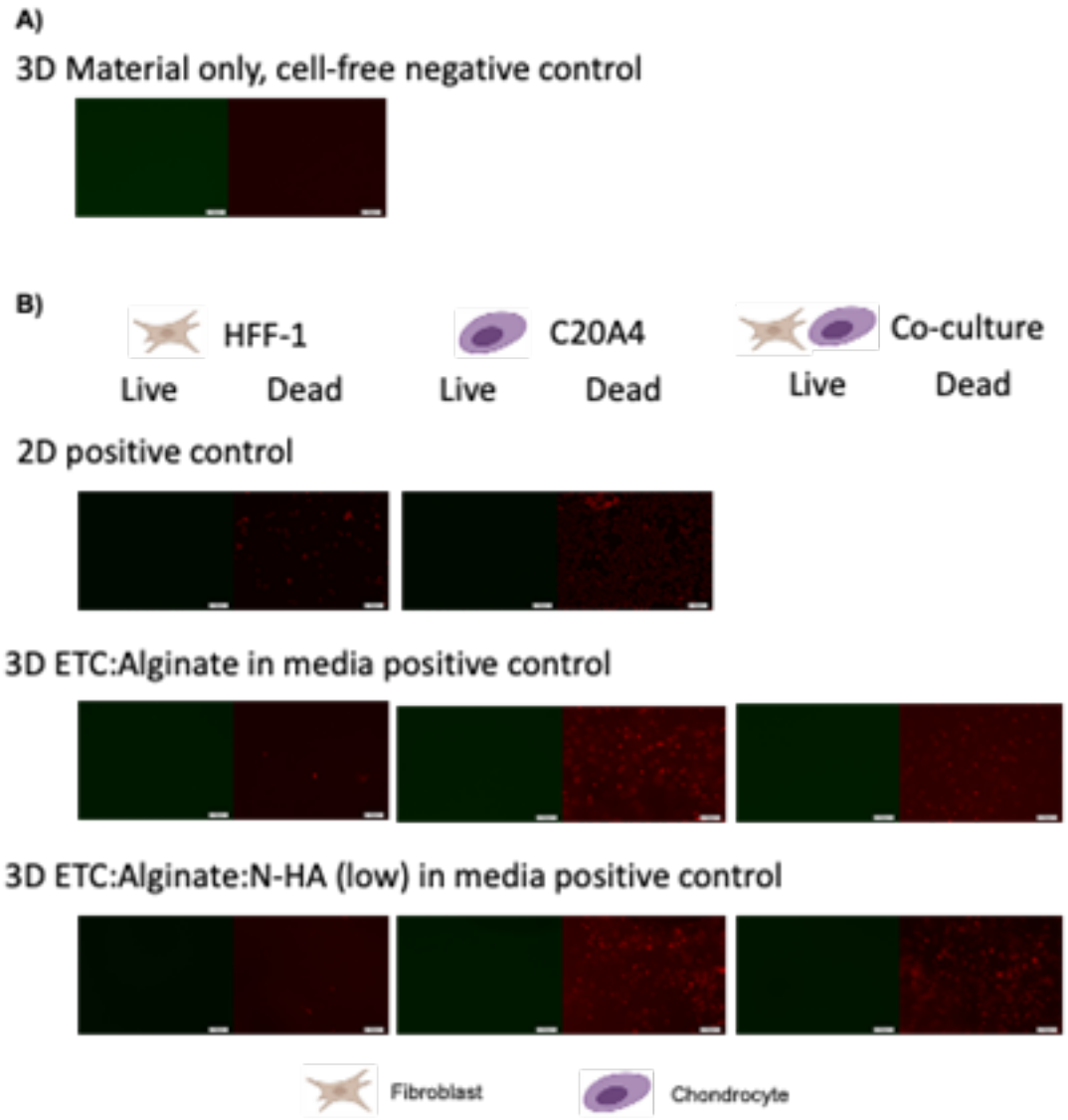

Figure 6.8 Live/dead staining of negative and positive controls of advanced 3D in vitro models of human dermal fibroblast (HFF-1) and human chondrocyte (C20A4) mono- and co-culture. *Two nanocellulose-based bio-inks were tested: ETC:Alginate in media (consisted of enzymatically pre-treated nanocellulose fibrils (ETC) and alginate), and ETC:Alginate:N-HA (low) in media (consisted of ETC, alginate and non-tyramine-substituted hyaluronic acid (N-HA) at low concentration (6mg/ml)), both reconstituted in media. Three models were tested: surface-seeded fibroblast (left), chondrocyte-encapsulated (mid) and co-culture of both surface-seeded fibroblast and chondrocyte encapsulation (right). Live/dead staining was conducted with calcein AM and ethidium homodimer-1, which stain live and dead cells fluorescent green and red, respectively. Scale bars represent 100μm. Positive control was 0.1% Triton X-100. (A) represents a cell-free material only negative control. (B) represents cell-based systems controls. 2D positive controls refers to 2D cell culture without bio-ink exposure. Positive controls for all three 3D mono- and co-culture models, made with both bio-inks, are shown.*

Lastly, positive and negative controls with regards to the live/dead staining were reviewed. Cell-free material only controls did not show false positive results (figure 6.8A). Regarding positive control, 0.1% Triton X-100 was effective in achieve 100% cytotoxicity, with no live cells seen in both 2D monocultures, and all 3D cellular models with both bio-inks, across all three cellular systems, and at all timepoints. As the results of all positive and negative material controls were consistent, singular representative images are shown.

6.3.1.4 Comparison of bio-inks for cytotoxicity

To address the chapter aim (ii) of identifying the optimal bio-ink formulation for cartilage tissue engineering, figure 6.9 aims to facilitate the comparison between the two bio-inks. It presents the same dataset illustrated in figures 6.2, 6.3 and 6.4, but for the purpose of simplicity, negative controls are not shown.

The bio-ink containing HA was associated with higher measures of FU and RFU in most part, indicating that this bio-ink enhanced cell proliferation with greater cell metabolic activity measured. A notable exception was with the HFF-1 3D monoculture on day 7, although greater variance was present. Nonetheless, the RFU associated with the bio-ink containing HA in the co-culture system was significantly greater than that of the bio-ink without HA at all timepoints, supporting the conclusion drawn above.

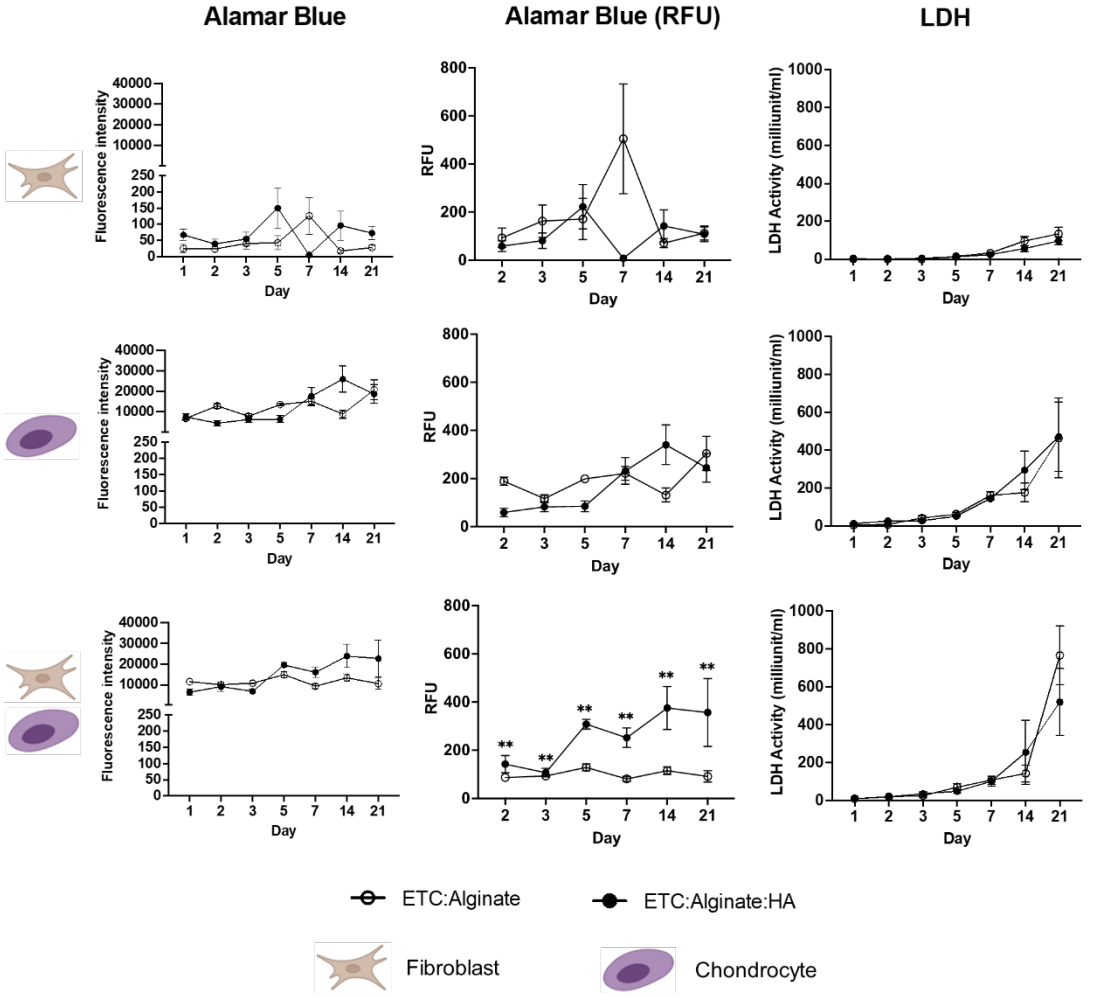

Figure 6.9 Comparison of bio-inks ETC:Alginate and ETC:Alginate:HA on alamar blue and lactate dehydrogenase assay in 3D chondrocyte and fibroblast mono- and co-culture systems over 21 days. *Top, middle and bottom rows are of fibroblast, chondrocyte and co-culture of both cell types, respectively. Mean±SEM are represented. N=3. Statistical significance of comparisons between bio-inks at each timepoint are denoted by * ($p<0.05$ *, $p<0.01$ **).*

The LDH levels however were comparable between the two bio-inks, except for day 21 in the co-culture system, although increased variance was noted also.

Overall, based on the cytotoxicity data from the alamar blue assay, the LDH assay and live/dead staining, the nanocellulose-based bio-ink containing both alginate and HA was deemed superior in terms of enhanced cell proliferation and non-inferiority in terms of cytotoxicity. This was in line with previous studies which showed that HA was supportive of chondrogenicity (unpublished data). There was also an indication of cellular cross-talk in the co-culture model, with a relative but low level of inhibition of cell metabolic activities. In conclusion, the bio-ink ETC:Alginate:N-HA (low) in media was recommended to be taken forward for further testing based on cytotoxicity assessment.

6.3.2 Pro-inflammatory response

6.3.2.1 Interleukin-6

Both cell types in the 2D negative controls were activated with statistically significantly elevated IL-6 levels measured at the chronic timepoints (day 14 and day 21) (figure 6.10A). This is likely secondary to over-confluence, as identified during cell line characterisation and with concurrent cytotoxicity. Of note, the culture media exchange regime was augmented in this study to mimic the experimental conditions during material toxicity testing. HFF-1 was relatively more tolerant of this change compared to C20A4, with C20A4 demonstrating higher levels of IL-6 release compared with cell line characterisation. As commented in the cytotoxicity assays, the auto-detachment of the C20A4 cell sheet did not occur with the augmented media exchange conditions, although cells showed a heightened pro-inflammatory state in 2D culture conditions.

In 3D conditions, IL-6 was non-detectable in the HFF-1 monoculture system with both bio-inks at all timepoints, except for the positive control with the bio-ink without HA on day 21. It could be considered that HFF-1 was not activated as tested within the advanced 3D *in vitro* model when exposed to either bio-ink, although caution is taken given the relatively low seeding density. Nonetheless, a pro-inflammatory response was witnessed on day 21 with the bio-ink ETC:Alginate in media when cells were further stimulated with LPS in the positive control.

As for chondrocytes, a pro-inflammatory response was detected with heightened IL-6 release in both the monoculture and co-culture 3D systems on day 14 and day 21. The most marked rise was seen with the bio-ink without HA when tested in the co-culture model, although statistically significant increases in IL-6 were found with both bio-inks in both mono- and co-culture systems (figure 6.10B). Differences in the levels and trends of IL-6 release over time across the two bio-inks and the C20A4 monoculture and co-culture systems were more apparent, when compared to the cytotoxic assays (alamar blue and LDH assay). Again, this indicates varied cellular response to both bio-inks, and to the same bio-ink but when cultured in a mono-culture versus co-culture system.

Interestingly, in the co-culture model, IL-6 release on day 14 and day 21 was markedly less with the bio-ink containing HA than the bio-ink without. This is despite a slightly higher fluorescence intensity measured in the alamar blue assay. This suggests that despite heightened cell proliferation in the bio-ink containing HA, cells were not as strongly activated into a pro-inflammatory state as with the bio-ink without HA. Furthermore, when considering the bio-ink containing HA, the levels of IL-6 were less in the co-culture model than in the monoculture model, indicating the influence of the fibroblast with cell-to-cell interactions.

Material interference on the assay was deemed negligible with extremely low to non-detectable levels of IL-6 with the material only control throughout the study period.

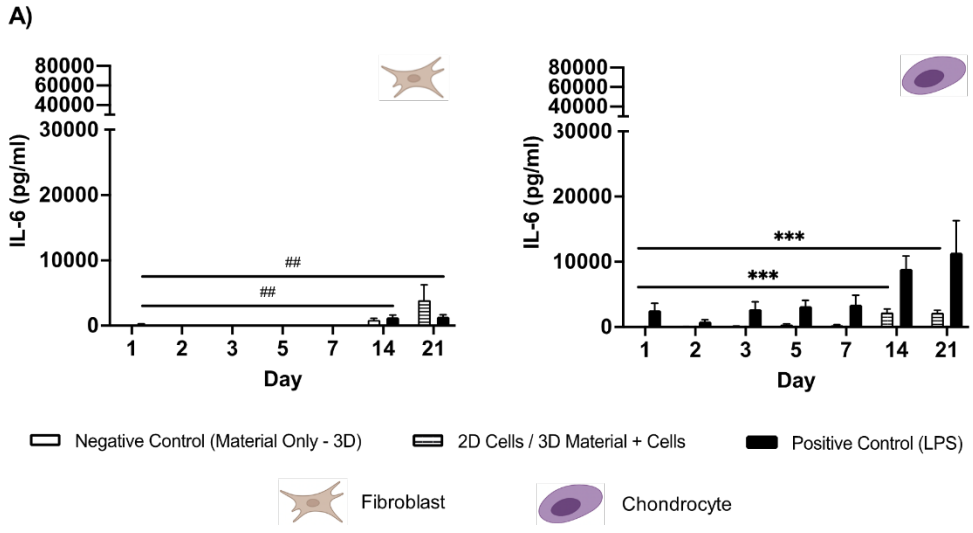

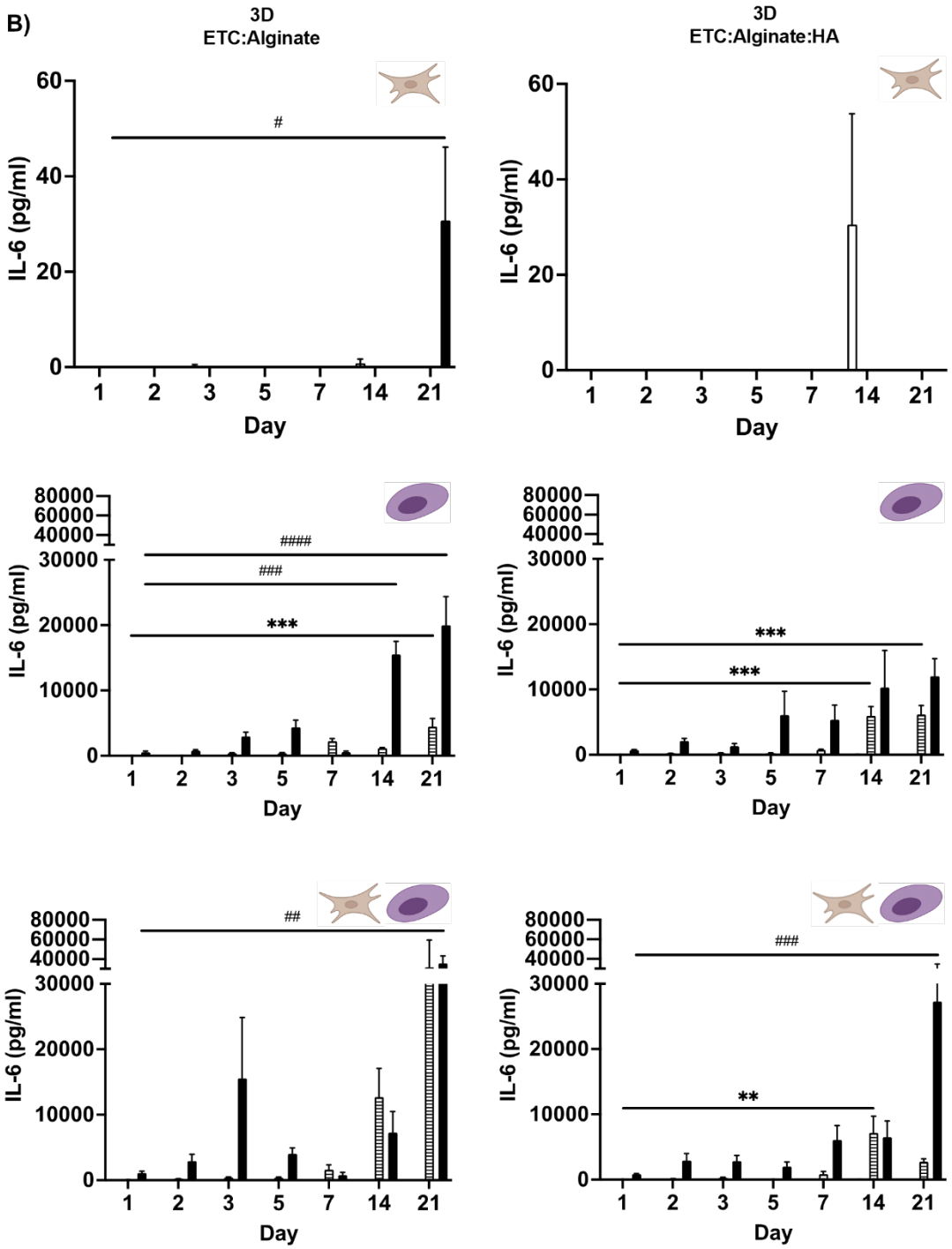

Figure 6.10 Interleukin-6 release by chondrocyte and fibroblast in 2D monocultures and 3D mono- and co-cultures over 21 days. *(A) represents 2D cell only negative controls consisting of monocultures of HFF-1 (left) and C20A4 (right). (B) represents bio-inks tested in 3D systems. Two bio-inks tested were ETC(nanocellulose):Alginate in media and ETC:Alginate:Non-tyramine substituted hyaluronic Acid (N-HA) (low) in media. Top, middle and bottom rows are of fibroblast, chondrocyte and co-culture of both cell types, respectively. IL-6 release was measured with ELISA and the mean±SEM are represented. N=3. Positive control was 1μg/ml LPS. Statistical significance of timepoint comparisons against day 1: of 3D cellular systems denoted by *, and of positive controls (LPS) by # (p<0.05 */#, p<0.01 **/##, p<0.001 ***/###, p<0.0001 ****/####).*

6.3.2.2 Interleukin-8

In parallel with IL-6 release profile in the 2D negative controls, IL-8 release by both HFF-1 and C20A4 in negative controls rose over time with statistically significant increases on day 14 and day 21 (figure 6.11A). When compared with cell line characterisation (section 2.8.5), IL-8 levels were comparable until day 21 with HFF-1 and day 14 with C20A4 where levels in the current study exceeded that seen in cell line characterisation. This suggests that both cell types were activated into a pro-inflammatory state at the chronic timepoints in 2D cultures with the augmented media exchange regime.

With the 3D *in vitro* models, an increasing trend of IL-8 release over time was observed across all three cellular systems and with both bio-inks (figure 6.11B). The greatest increase was with the bio-ink containing HA in the C20A4 monoculture system on day 14. The peak in IL-8 in systems containing C20A4 showed a lag in bio-inks without HA, reaching the peak on day 21, versus on day 14 with bio-inks containing HA. This may be explained by the slower cell proliferation observed with HA-free bio-inks, and therefore a delay in reaching a state of activation if this was due to over-confluence. Also, with the bio-ink containing HA, the presence of fibroblast appeared to have augmented the pro-inflammatory response detected within the co-culture system with lower levels of IL-8 when compared to the C20A4 mono-culture system. Interestingly, this was not the case with the bio-ink consisting of nanocellulose and alginate only.

Finally, as with IL-6, whilst material interference with the ELISA was detected with IL-8 using the cell-free material-only control, the levels of IL-8 were relatively low. This was despite a time-dependent rise with the material control over the 21 days. Overall, the low level of material intereference detected did not affect interpretation of the assay.

6.3.2.3 Comparison of bio-inks for pro-inflammatory effect

Along the same vein as section 6.3.1.4, the pro-inflammatory effect of the two bio-inks is compared directly in figure 6.12. It is the same dataset as shown in figure 6.10 and 6.11, but the negative and positive controls are not shown.

Overall, the IL-6 and IL-8 release profiles were comparable between the two bio-inks across all three cellular 3D systems, with no statistically significant difference

detected. A divergence in the pro-inflammatory status was seen on day 14 between the two bio-inks. Higher levels of IL-6 and IL-8 levels were measured with the bio-ink containing HA, despite taking into account the greater variance seen on day 14. Nonetheless, on day 21, the pro-inflammatory effects between the two bio-inks returned to similar levels. This was the case except with IL-6 measured in the co-culture system with the bio-ink without HA.

In conclusion, the data indicates that on day 14, the bio-ink containing HA was associated with cell activation with heightened levels of IL-8, in conjunction with greater levels cell proliferation as measured with the alamar blue assay. However, this effect was not sustained, and on day 21, the pro-inflammatory response induced by both bio-inks were indistinct and superiority between the bio-inks cannot be conferred.

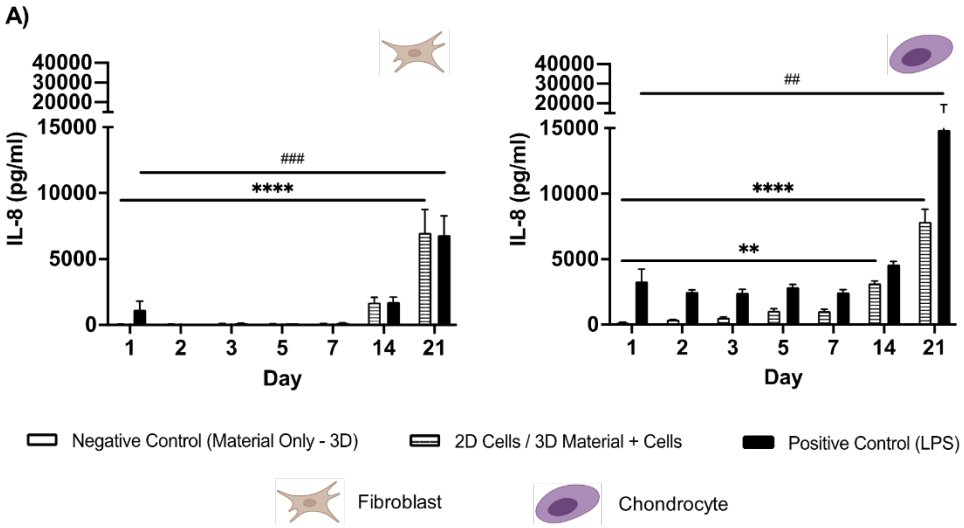

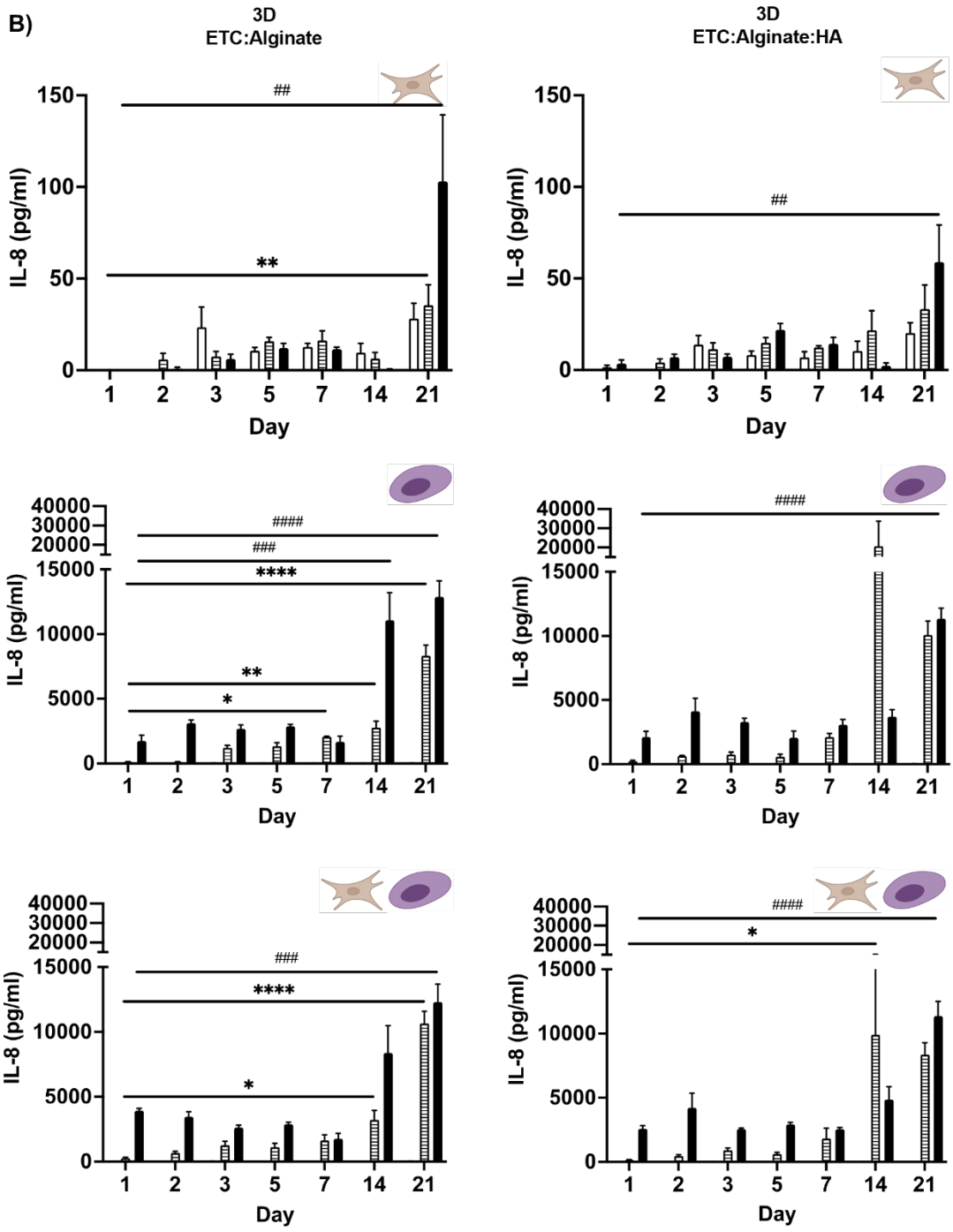

Figure 6.11 Interleukin-8 release by chondrocyte and fibroblast in 2D monocultures and 3D mono- and co-cultures over 21 days. *(A) represents 2D cell only negative controls consisting of monocultures of HFF-1 (left) and C20A4 (right). (B) represents bio-inks tested in 3D systems. Two bio-inks tested were ETC(nanocellulose):Alginate in media (left) and ETC:Alginate:Non-tyramine substituted hyaluronic Acid (N-HA) (low) in media (right). Top, middle and bottom rows are of fibroblast, chondrocyte and co-culture of both cell types, respectively. IL-8 release was quantified with ELISA. Mean±SEM are represented. N=3. Positive control was 1µg/ml LPS. Statistical significance of timepoint comparisons against day 1: of 3D cellular systems denoted by *, and of positive controls (LPS) by # (p<0.05 */#, p<0.01 **/##, p<0.001 ***/###, p<0.0001 ****/####).*

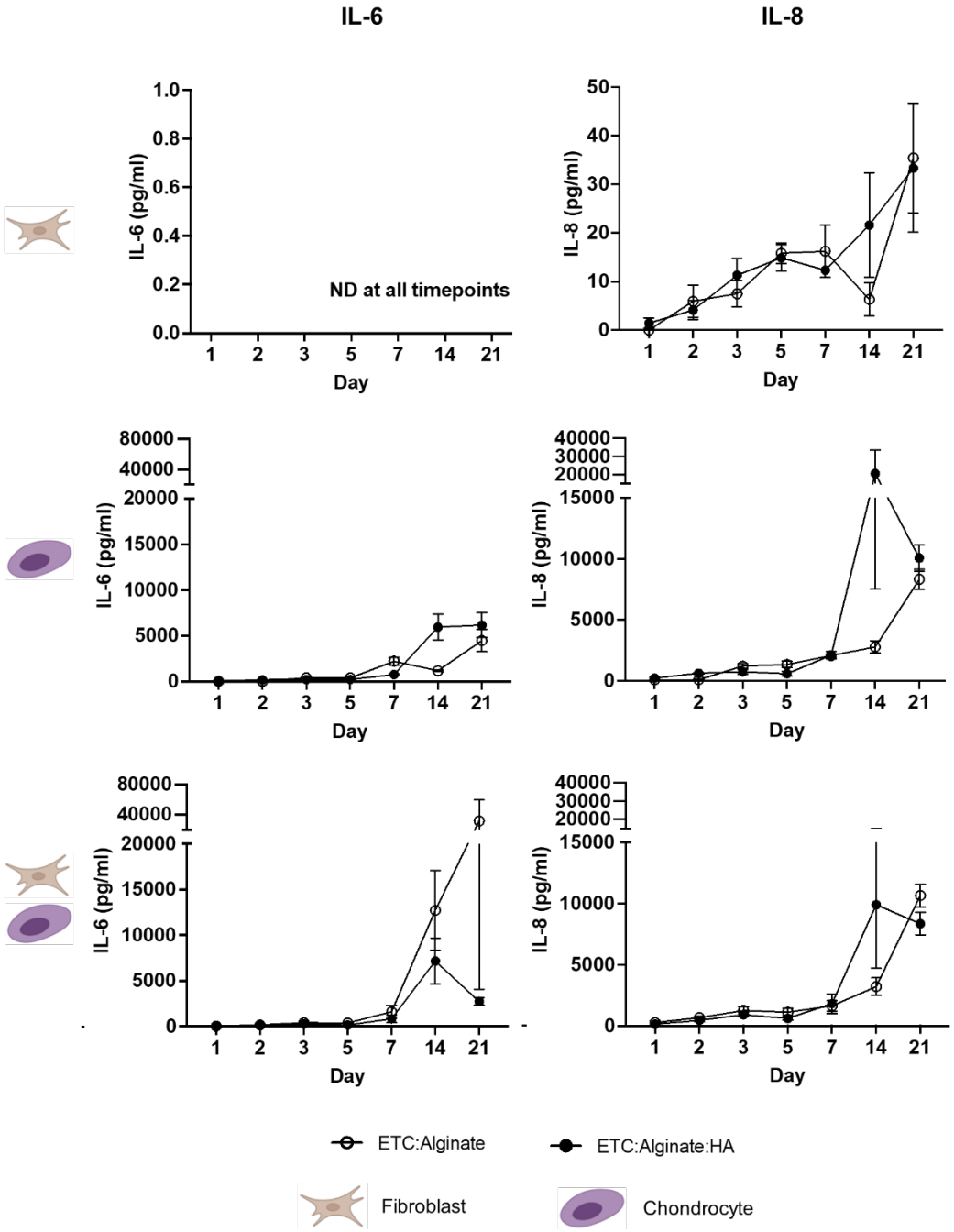

Figure 6.12 Comparison of IL-6 and IL-8 release between bio-inks ETC:Alginate and ETC:Alginate:HA in 3D chondrocyte and fibroblast mono- and co-culture over 21 days. *Top, middle and bottom rows are of fibroblast, chondrocyte and co-culture of both cell types, respectively. Mean±SEM are represented. N=3. Non-detectable levels denoted as ND. Statistical significance of comparisons between bio-inks at each timepoint are denoted by ∗(p<0.05 ∗, p<0.01 ∗∗).*

6.4 Chapter Summary and Conclusion

This chapter evaluated the cytotoxic and pro-inflammatory effects of two nanocellulose-based bio-inks in three advanced 3D *in vitro* models. Both bio-inks contained alginate, and differed by the inclusion of HA. A summary of results and conclusion is presented in table 6.1. Overall, the data supports the use of the bio-ink containing HA (ETC:Alginate:N-HA (low) in media) for further testing for the application of cartilage tissue engineering, due to the enhanced cell proliferation profile. This is in line with previous studies that suggests the inclusion of HA promotes chondrogenicity (unpublished data). Raised cytotoxicity and pro-inflammatory response were observed at the chronic timepoints. This could be due to intrinsic (high chondrocyte seeding density) or extrinsic factors (augmented culture media exchange regime). A decline in the health of cell state can be observed in alternative *in vitro* model at chronic timepoints in the literature. Cheng *et al* examined adult mouse brain neural stem cells cultured in a chitosan-cellulose nanofibril hydrogel in an *in vitro* model[220]. Cell viability and proliferation was assessed with the CCK-8 assay, which demonstrated maximal cell proliferation on day 21 followed by a decline in cell viability on day 28. This decline on day 28 was seen across all experimental groups (chitosan without nanocellulose, and with varying nanocellulose content), which may indicate an inherent model limitation. Further optimisation and characterisation of the *in vitro* models will be beneficial. Varied cellular response observed between the C20A4 monoculture and co-culture systems when exposed to the same bio-ink indicates cellular cross-talk and modulation with the presence of fibroblast in the co-culture system. This highlights the potential value in further developing multi-cellular advanced 3D *in vitro* models for the purpose of biological testing intended for tissue engineering product development.

Table 6.1 Summary of chapter conclusions and take-on messages.

Conclusions	
Cytotoxicity	• Bio-ink containing HA showed greater cell metabolic activity reflecting enhanced cell proliferation, compared to bio-ink without HA • Non-superiority between two bio-inks based on LDH assay • Despite maintained cell metabolic activity, increased cytotoxicity was seen on day 21 with the LDH assay
Pro-inflammatory effects	• Non-superiority between two bio-inks based on IL-6 and IL-8 release • Rise in pro-inflammatory effects at chronic timepoints (day 14 and day 21) across all three cellular models
Recommendations	
• Bio-ink ETC:Alginate:N-HA (low) in media is the bio-ink of choice. • Rise in cytotoxicity and pro-inflammatory effects on day 21 warrant further optimisation and characterisation	

Chapter 7: Characterisation of advanced 3D *in vitro* models *via* transcriptomic study

7.1 Introduction

This chapter is focused upon the further characterisation of the advanced 3D *in vitro* models for its biological relevance and mechanisms. A challenge in this regard is the ability to extract live cells or produce high quality cell lysates for downstream assays. To date, in-house attempts at live cell extraction from cross-linked bio-ink was unsuccessful, and low yields achieved with RNA extraction. Material interference could also render certain methodologies unsuitable, or assays and data invalid. For example, residual bio-ink material in cell suspensions would be a relative contraindication to the application of fluorescence-activated cell sorting due to the risks of clogging and inaccuracies.

Recent advances in gene expression analysis technologies offer the opportunity to assess the global response of the advanced 3D *in vitro* models and the bio-ink of interest. The Nanostring nCounter® Analysis System (Nanostring) is a multi-plexed, panel-based platform that can measure up to 800 genes in a single sample. It benefits from a relatively low RNA input requirement, increased number of target genes compared to quantitative real-time polymerase chain reaction (qRT-PCR), does not require reverse transcription for cDNA (as needed with qRT-PCR, microarrays and RNA-sequencing, thereby reducing the risk of errors and the introduction of bias), and the relative ease of data analysis (as compared with RNA-sequencing)[306]. Its application for model characterisation could potentially permit the assessment across a spectrum of toxicological endpoints whilst overcoming restrictions posed by cell encapsulation and material costs. In turn, this approach may further address the aim of the thesis, to assess the biocompatibility of nanocellulose-based bio-ink for cartilage tissue engineering in an advanced 3D *in vitro* model.

The aims of this chapter were therefore two folds:

i. To optimise RNA extraction from the advanced 3D *in vitro* models.
ii. To characterise and assess the global response of the advanced 3D *in vitro* models with the bio-ink ETC:Alginate:N-HA (low) in media using Nanostring for gene expression analysis.

The aims were met *via* the following objectives:

1. To optimise cell extraction from cross-linked hydrogel models.
2. To optimise RNA extraction from advanced 3D *in vitro* models.

3. To undertake a gene expression analysis for the assessment of the global response of the advanced 3D *in vitro* models with the bio-ink ETC:Alginate:N-HA (low) in media using Nanostring.

7.2 Methods

The workflow of this chapter begins with the pilot testing and optimisation of the RNA extraction processes, followed by the application of Nanostring for the assessment of global response of the advanced 3D *in vitro* models. This is illustrated in figure 7.1.

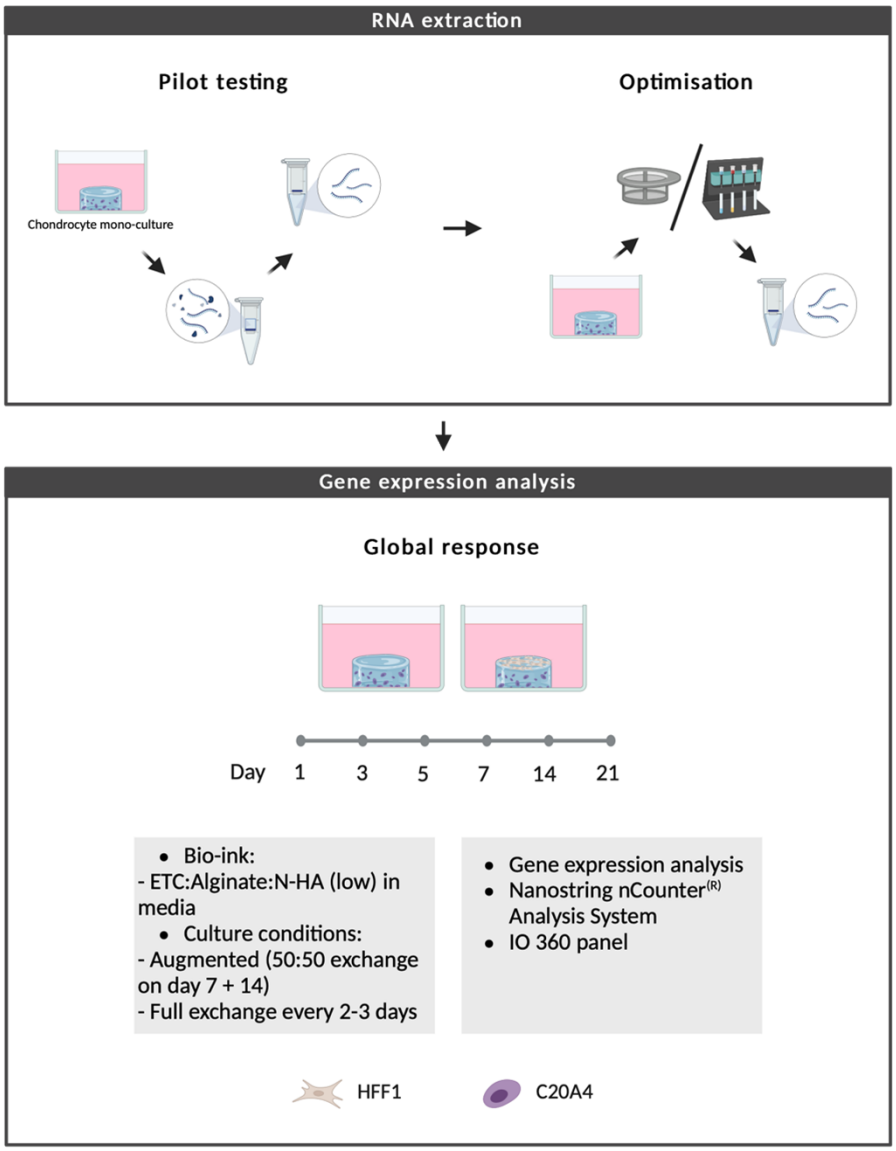

Figure 7.1 Schematic of chapter 7 workflow. *Part 1 centres on RNA extraction. Pilot testing of an adapted RNA extraction protocol intended for organoids was conducted using the chondrocyte monoculture 3D in vitro model. Subsequent optimisations included the trials of cell strainers and magnetic-activated cell sorting. N=1. Part 2 involved the application of the Nanostring nCounter® Analysis System to conduct gene expression analysis of the advanced 3D in vitro models over 21 days. The bio-ink tested consisted of an enzymatically pre-treated nanocellulose fibril (ETC), alginate and a non-tyramine-substituted form of hyaluronic acid (N-HA), reconstituted in media. The chondrocyte mono-culture and co-culture system with the addition of dermal fibroblast were compared, in addition to comparison of the two culture conditions. The IO360 panel was used. N=3. Created with biorender.com.*

7.2.1 Chemical and reagents

Table 7.1 List of chemicals and reagents used in chapter 7 (exclusive of those listed in table 2.1).

Material	**Brand (Cat No.)**
200µl tube strips (for qubit assay)	Invitrogen (Q33252)
2-mercaptoethanol	Sigma-Aldrich (M6250)
Agilent rna 6000 nano kit	Agilent (5067-1511)
All prep dna/rna mini kit	Qiagen (80204)
Bovine serum albumin (BSA)	Sigma-Aldrich A7906
CD44 antibody, anti-human, vioblue®	Miltenyi Biotec (130-113-899)
CD15 antibody, anti-human, APC	Miltenyi Biotec (130-114-008)
Ethylenediaminetetraacetic acid (EDTA)	Sigma-Aldrich (E9884)
ERbb-2 (CD340) antibody, anti-human, PE, reafinity^{tm}	Miltenyi Biotec (130-124-473)
Hybridization buffer + prep pack	Nanostring
Qiashredder	Qiagen (79656)
Quant-it^{tm} ribogreen reagent and rna assay kit	Invitrogen (R11490)
Qubit^{tm} rna high sensitivity assay	Invitrogen (Q32852)
Rnasezap^{tm} rnase decontamination solution	Invitrogen (AM9780)
Rneasy mini kit	Qiagen 74106
3M Sodium acetate	Thermo Scientific (R1181)
Sodium azide	Sigma-Aldrich (S2002)
Tryple^{tm} express enzyme (1x), no phenol red	Gibco 12604013

7.2.2 General material and equipment

Table 7.2 List of material and equipment used in chapter 7 (exclusive of those listed in table 2.2).

Material	**Brand (Cat No.)**
2100 Bioanalyzer instrument	Agilent
2100 Bioanalyzer laptop	Agilent
BD^{tm} CYTOMETER SETUP & TRACKING BEADS KIT	BD Biosciences (642412)
Depc-trearted water (nuclease-free)	Invitrogen (AM9915G)
FACS tube – falcon round bottom polystyrene tube	Falcon (352052)
Falcon^{tm} cell strainers, 40µm	Falcon (352340)
Falcon^{tm} cell strainers, 70µm	Falcon (352350)
LS columns	Miltenyi Biotec (130-042-401)
Macs® multistand	Miltenyi Biotec (130-042-303)
Nanophotometer^{tm} np80 uv/vis spectrophotometer	Implen
Ncounter cartridge	Nanostring
Ncounter® sprint profiler	Nanostring
Cytek Aurora	Cytek Biosciences
Pierce^{TM} tissue strainers, 250µm, 2.5ml	Thermo Scientific (87791)
Polystyrene test tubes – falcon^{tm} round-bottom	Falcon (10579511)
Quadromacs^{tm} separator	Miltenyi Biotec (130-090-976)
Qubit^{TM} 4 Fluorometer	Invitrogen

7.2.3 Optimisation of RNA extraction

Previous in-house attempts to achieve cell suspensions for RNA extraction included the use of the TissueRuptor II (Qiagen) for mechanical sample disruption, and cellulase and/or ethylenediaminetetraacetic acid (EDTA) to dissociate cells from the nanocellulose-based hydrogel and reverse the chemical cross-linkage of alginate, respectively (unpublished data). Due to poor yield from previous attempts, alternative methodology was explored. Pilot testing was conducted with an adapted RNA extraction protocol intended for organoids (unpublished), and two commercial RNA extraction kits was trialled. With some initial success with the generation of preliminary data for RNA yield and an understanding of feasibility and potential challenges, further optimisation was undertaken to maximise RNA yield in terms of quantity and quality.

With chondrocyte being the key cell of interest for cartilage tissue engineering, and a markedly lower fibroblast seeding density and therefore an anticipated low yield, the chondrocyte monoculture 3D *in vitro* model was chosen for pilot testing and the optimisation of RNA extraction. The optimised RNA extraction method was then applied for the global response assessment of the advanced 3D *in vitro* models with Nanostring. As detailed in chapter 6, the bio-ink ETC:Alginate:N-HA (low) in media was used. Outcomes for RNA extraction relates to the yield from a single sample, unless otherwise specified, which namely involved fibroblast monoculture models where pooling of samples was performed.

7.2.3.1 Pilot testing for RNA extraction

An overview of the pilot testing for RNA extraction is illustrated in figure 7.2. Due to the step-wise nature of the protocol and varied commercial kits tested, the methodology is broken down into each component part and detailed separately (sections 7.2.3.1.1 - 7.2.3.1.7). Selected elements which proved successful were taken forward for the final RNA extraction protocol as described in the SOP (appendix 1).

The pilot testing initiated with step 1, sample homogenisation. The chondrocyte-encapsulated cross-linked hydrogel pellet was homogenised *via* enzymatic and mechanical means with the application of trypLE (an animal origin-free trypsin-like enzyme) and pipetting the sample up and down through a 1000µl pipette tip (section

7.2.3.1.1). This produced a suspension of cells and bio-ink, confirmed *via* light microscopy and the erythrosin B assay (section 7.2.3.1.2).

Initial trial of RNA extraction utilised the serial application of QIAshredder and the RNeasy Mini Kit as previously applied for 2D cell cultures (section 7.2.3.1.3). Clogging of the RNeasy spin column was noted. Unfortunately, quantification using the NanoPhotometer™ NP80 UV/Vis spectrophotometer did not yield detectable levels of RNA (section 7.2.3.1.4).

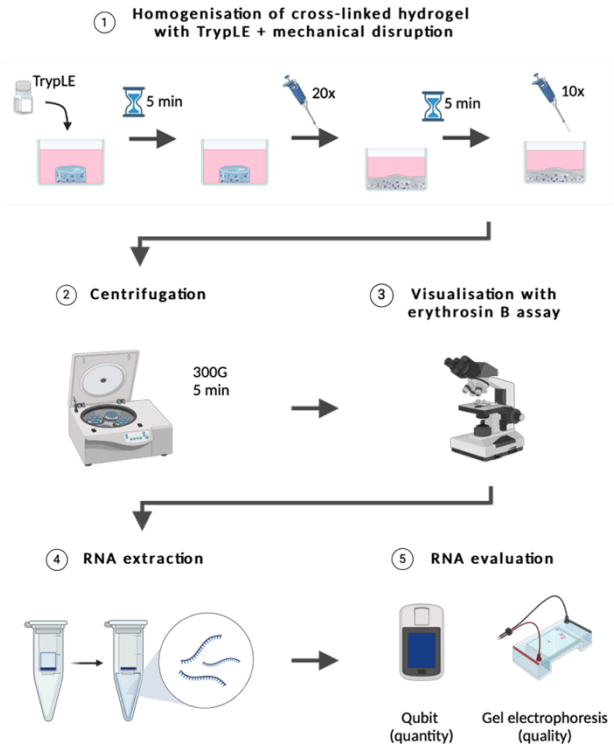

Figure 7.2 Schematic of the pilot testing for RNA extraction. *Step 1 involved the enzymatic and mechanical homogenisation of the chondrocyte-encapsulated cross-linked hydrogel disc constituting the advanced 3D in vitro model. Step 2 is the centrifugation step to achieve a cell pellet, which was visualised in step 3 with the erythrosin B assay. Bio-ink residuals remained through step 2 and 3. RNA extraction was performed using the spin column technique (step 4), quantified using the Qubit assay and assessed for quality with gel electrophoresis (step 5). Created with BioRender.com.*

As such, an alternative commercial kit as specified in the organoid DNA/RNA extraction protocol was trialled next (AllPrep DNA/RNA Mini Kit) (section 7.2.3.1.5). In recognition of the low yield, the Qubit™ RNA High Sensitivity Assay was used for quantification (section 7.2.3.1.6). The Qubit assay offered a greater degree of assay sensitivity (0.2-200ng/µl) when compared to the NanoPhotometer (1-16,500ng/µl), although the NanoPhotometer was still used for purity ratios assessment (A260:A280 and A260:A230). Gel electrophoresis was conducted to assess RNA integrity (section

7.2.3.1.7). The methods of pilot testing are hereby described and the results expanded upon in section 7.3.1.

7.2.3.1.1 Sample homogenisation

Prior to RNA extraction, the sample (cell-seeded cross-linked hydrogel disc) was homogenised to create a suspension of cells and bio-ink material. Each sample was washed with 1ml PBS and incubated with 1ml of trypLE at 37^{o}C for 5 minutes. The sample was then mechanically disrupted by pipetting up and down (trituration) through a 1000µl pipette tip 20 times. The sample was incubated for a further 5 minutes and a repeat of trituration 10 times. The trypLE was neutralised with the addition of 1ml culture media. All well contents were transferred to a 15ml tube for centrifugation at 300G for 5 minutes. Whilst this would typically create a cell pellet, in this case, phase separation was achieved with the denser biomaterial and cells at the base without a cell pellet. The supernatant was removed, leaving the cell suspension with residual bio-ink material ready for the next step.

7.2.3.1.2 Erythrosin B dye exclusion assay

The application of the erythrosin B exclusion assay in this context was simply to visualise the amount of cells and bio-ink content following sample homogenisation, or any sample treatment, prior to RNA extraction. The method was adapted from the erythrosin B exclusion assay used for cell counting and cell viability assessment as described in section 2.8.2. Due to the lack of a cell pellet, the supernatant following centrifugation was carefully removed, and culture media added to achieve a total volume of 1ml and mixed by pipetting up and down. The erythrosin B exclusion assay was then followed as previously described and assessed under light microscopy.

7.2.3.1.3 RNA extraction method 1

Prior to RNA extraction, equipment and bench top was wiped down with RNaseZAP. The QIAshredder and RNeasy Mini Kit was used following the manufacturer's instructions, except for minor adaptations mostly inferred by the additional sample volume due to the bio-ink material and the inability to achieve a cell pellet.

The sample was prepared as described in section 7.2.3.1.1. Buffer RLT (600µl) from the RNeasy Mini Kit was added to the sample and mixed by pipetting up and down.

This was transferred to the QIAshredder and centrifuged at 8,000G for 2 minutes for further homogenisation. The flow-through from the QIAshredder was used with the RNeasy Mini Kit.

Ethanol 70% was added at 1:1 volume ratio and mixed well, which supports the selective binding of RNA to the RNeasy spin column membrane. This was then added to the RNeasy Mini spin column (maximum 700µl loading volume as per manufacturer's guidance), and centrifuged at 8,000G for 15 seconds. The flow-through was discarded, and the remainder of the sample was added to the same spin column as recommended by the manufacturer to capture RNA on the same spin column membrane. It was noted that not all 700µl of samples will 'flow-through' in one centrifugation sample, but repeat centrifugation at the same speed and duration ensured all sample flows-through the membrane.

The next step was to add 700µl Buffer RW1 to the same RNeasy spin column and repeat centrifugation at 8,000G for 15 seconds, discarding the flow-through. Next, 500µl Buffer RPE was added to the spin column and centrifuged at 8,000G. This step was performed twice, initially for 15 seconds, and again for 2 minutes, discarding the flow-through after each step. The optional step aimed at removing any residual Buffer RPE was performed, which involved further centrifugation of the spin column placed in a new collection tube at 17,000G for 1 minute.

To elute the RNA, 30µl RNase-free water was added to the spin column which has been transferred to a new collection tube, and centrifuged at 8,000G for 1 minute. Again, the optional step to maximise RNA yield was undertaken which involved adding the eluate back to the spin column and repeating the centrifugation step.

7.2.3.1.4 RNA quantification and purity assessment with NanoPhotometer

The Implen NanoPhotometer® NP80 was used to determine the purity ratios A260:A280 and A260:A230. It was also initially used to estimate RNA quantity during the pilot testing of RNA extraction. The NanoPhotometer was used in accordance with manufacturer's guidance. Prior to use, the sample window was cleaned and a blank control using RNAse-free water was performed. The RNA sample volume used was 1µl. The absorbance ratios denote clarity, with a ratio of between 1.8-2.0 considered satisfactory.

7.2.3.1.5 RNA extraction method 2

The second attempt at RNA extraction differed from the first (as described in section 7.2.3.1.3) with the addition of β-mercaptoethanol to the lysis buffer, mechanical homogenisation of the sample, and the use of the AllPrep DNA/RNA Mini Kit which included an additional DNA spin column.

Prior to RNA extraction, equipment and bench top was again wiped down with RNaseZAP. The manufacturer's instruction was followed in the most part for the AllPrep DNA/RNA Mini Kit, except for similar adaptations made to account for the additional sample volume due to the bio-ink material.

The sample as prepared from section 7.2.3.1.1 was used. The lysis buffer was 10µl β-mercaptoethanol per 1ml RLT lysis buffer. Each sample was mixed with 600µl lysis buffer. Further homogenisation was performed by passing the sample through a 21G needle at least five times. The sample was then added to the AllPrep DNA spin column and centrifuged at 8,000G for 30 seconds. Any residual sample retained in the DNA spin column was transferred to a new DNA spin column and centrifuged in the same manner. As such, two DNA spin columns were required per sample. All flow-through containing RNA was collated and 70% ethanol was added at 1:1 volume ratio. This was then added to the AllPrep RNeasy spin column and centrifuged at 10,000G for 15 seconds, with flow-through discarded. Due to added sample volume, all flow-through from the DNA spin column was added to the same RNeasy spin column and processed as described to ensure all RNA from the single sample was captured in one membrane. The RNeasy spin column was then washed by adding 700µl RW1 buffer and centrifuged at 8,000G for 15 seconds, followed by two cycles of 500µl of RPE buffer centrifuged at 8,000G for 15 seconds, then for 2 minutes. The RNeasy spin column was transferred to a new collection tube and centrifuged at 10,000G for 1 minute to dry the membrane. To elute the RNA, 40µl of RNase-free water was added to the RNeasy spin column placed in a new collection tube, and centrifuged at 8,000G for 1 minute. The optional step to maximise RNA yield was performed as standard, which involved placing the eluate back into the RNeasy spin column and repeating the final centrifugation step.

7.2.3.1.6 RNA quantification with Qubit

The Qubit™ RNA High Sensitivity Assay Kit was used for RNA quantification. It is a fluorescence-based technique whereby the dye binds selectively to RNA. RNA concentration is determined by comparing the fluorescence values of samples against known standard concentrations. It was applied as specified for pilot testing, and for all samples intended for gene expression analysis with Nanostring. The kit was used in accordance with the manufacturer's guidance.

RNA samples were thawed prior to quantification and kept on ice when not in use. All assay solutions were allowed to come to room temperature prior to use. The working solution was prepared by mixing the supplied reagent and buffer in 1:200 ratio. Two kit standards were prepared with 10µl standard and 190µl working solution. RNA samples were prepared with 1µl sample and 199µl working solution. Both standards and samples (10µl each) were added to a fresh 200µl tube strips, incubated for 2 minutes at room temperature and RNA concentration read using the Qubit™ Flex fluorometer.

7.2.3.1.7 RNA quality assessment with gel electrophoresis

The assessment of RNA integrity was performed with agarose gel electrophoresis. In principle, RNA samples were loaded into an agarose gel. An electrical current is applied to the gel, which causes the negatively charged RNA to migrate towards the positive electrode. Smaller fragments will migrate faster, with separation of RNA fragments according to size. The resulting bands were visualised using a UV transilluminator and compared to the RNA ladder.

7.2.3.2 Optimisation of RNA extraction

Building on from the pilot testing, the goal of optimisation was to attain RNA from the advanced 3D *in vitro* models suitable for Nanostring application. The objectives of optimisation were:

1) Reduce the amount of residual bio-ink and achieve a purer cell suspension;

2) Cell sorting to distinguish between chondrocytes and fibroblast populations from the co-culture model;

3) Improve RNA yield in terms of quantity, quality (i.e. integrity) and purity.

A step-wise approach, as outlined in figure 7.3, was taken to systematically select the optimal option and exclude unsuccessful conditions. This formed a series of experiments, one through six, divided into four sequential steps:

1) Homogenisation of cross-linked hydrogel;

2) Cell extraction and cell sorting;

3) RNA extraction;

4) RNA purification.

As there was variable overlap of methods used in the pilot testing and optimisation, table 7.3 aims to provide clarity by listing methods in each group. Items listed under optimisation represent methods not already included under pilot testing.

The various components of RNA extraction taken forward from pilot testing are sample homogenisation (section 7.2.3.1.1), erythrosin B exclusion assay (section 7.2.3.1.2), assessment of purification ratio using the NanoPhotometer (section 7.2.3.1.4), RNA extraction (section 7.2.3.1.5) and quantification using the Qubit assay (section 7.2.1.1.6). These methods were applied for all RNA extractions undertaken from this section onwards, with additional procedures hereby described.

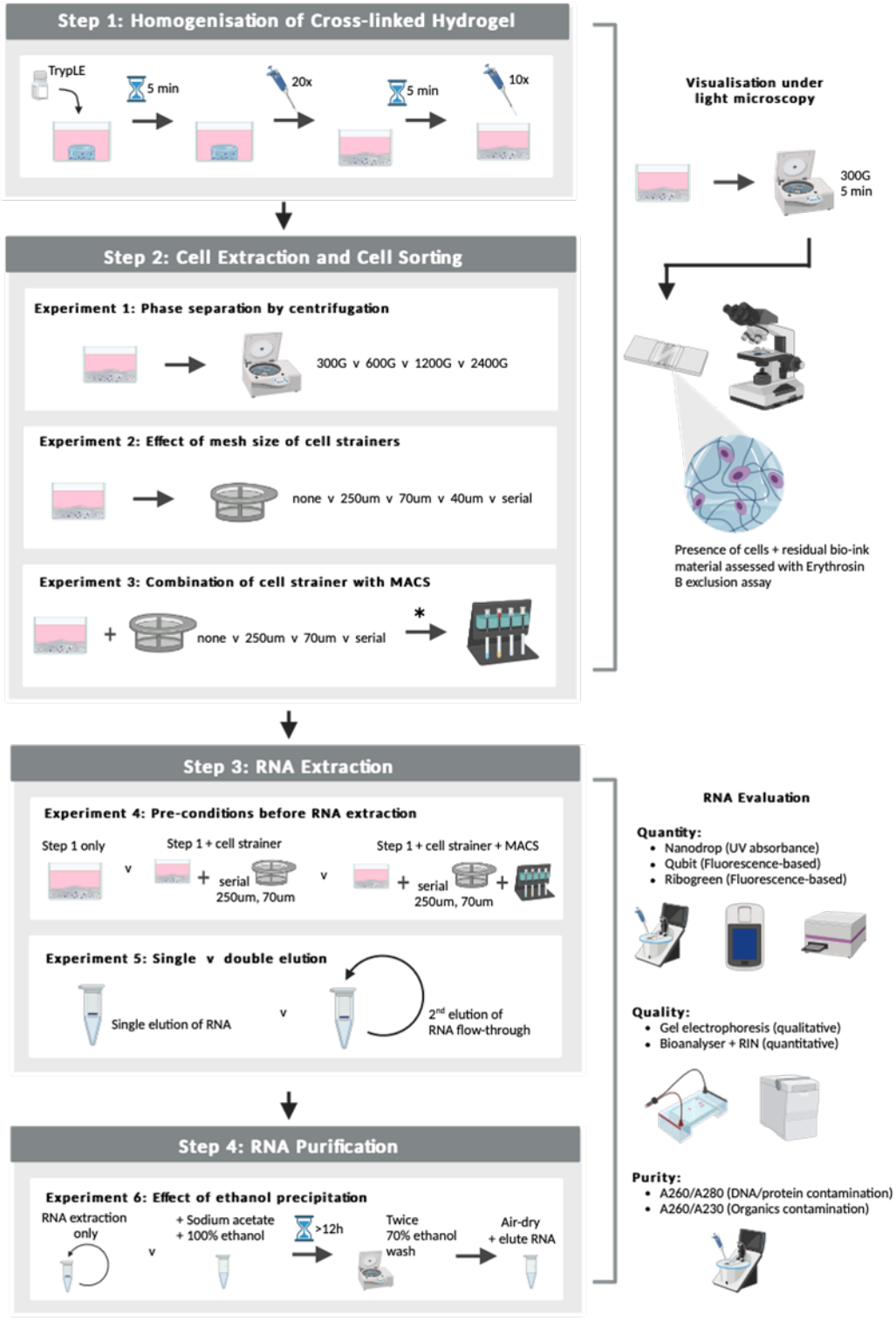

Figure 7.3 Schematic of optimisation for RNA extraction. *Testing undertaken during optimisation are listed as experiment 1-6. Step 1: Homogenisation of cross-linked hydrogel. Step 2: Cell extraction and cell sorting. This included experiment 1: phase separation by centrifugation; experiment 2: effect of cell strainer mesh sizes; and experiment 3: effect of cell strainer and mesh sizes with MACS. To enable MACS, the expression of CD markers in chondrocyte and fibroblast cell lines was confirmed by flow cytometry as part of experiment 3, denoted by *. Step 3: RNA extraction. This entailed experiment 4: comparison of three pre-conditions, and experiment 5: comparison of single versus double RNA elution. Step 4: RNA purification through ethanol precipitation, with experiment 6: comparison of RNA yield pre- and post-ethanol precipitation. Right-sided illustrations depict evaluation methodologies of the corresponding steps. N=1. Created with biorender.com.*

Table 7.3 Methods used in pilot testing and optimisation of RNA extraction.

Steps	Pilot Testing	Optimisation
1. Homogenisation of cross-linked hydrogel	• Application of TrypLE™ Express and trituration • Visualisation with erythrosin B exclusion assay	Nil addition
2. Cell extraction and cell sorting	Not performed	• Phase separation by centrifugation: 300G, 600G, 1200G, 2400G • Cell strainer: 250µm, 70µm, 40µm • Magnetic-activated cell sorting (MACS) • Flow cytometry: CD44, CD350, CD15
3. RNA extraction	• Test 1: -QIAshredder -RNeasy kit • Test 2: -Homogenisation with 21G needle -AllPrep DNA/RNA kit	• All performed with Test 2 methodology • Comparison of 3 conditions: i) homogenisation only as per step 1 ii) condition (i) plus serial cell strainers (250µm and 70µm) iii) condition (ii) plus MACS using CD44 • Comparison of single vs double elution
4. RNA purification	Not performed	• Ethanol precipitation • Comparison of pipetting versus vortex in wash step
5. RNA evaluation	• Nanodrop spectrophotometer • Qubit • Gel electrophoresis	• Ribogreen • Bioanalyser (RIN)

7.2.3.2.1 Experiment 1: phase separation

Sample was prepared as described in section 7.2.3.1.1. Culture media was added to reach a total volume of 5ml and pipetted up and down for mixing. A range of

centrifugation forces was tested at 300, 600, 1200 and 2400G at 4°C for 5 minutes. Supernatant was removed and inspection for cell pellet performed. The dense bio-ink and cell material was resuspended in media to achieve a total volume of 1ml and assessed using the erythrosin B exclusion assay as described in section 7.2.3.1.2.

7.2.3.2.2 Experiment 2: effect of mesh size of cell strainer

The mesh sizes of cell strainer tested were 250, 70 and 40µm. An additional test of serial application of cell strainers from wide to narrow pores was also investigated. This was adapted from a protocol intended for organoid cultures, which involved passing the sample through a 250µm cell strainer, then 70µm and 40µm.

Sample was prepared as described in section 7.2.3.1.1 up to and including the step of neutralisation of trypLE with media. The prepared sample was added to cell strainers. The flow-through was collected in falcon tubes and centrifuged at 300G at 4°C for 5 minutes. The supernatant was discarded, and due to the lack of a cell pellet, the suspension containing bio-ink material and cells was resuspended with media to reach a total volume of 1ml. Visualisation was performed with the erythrosin B exclusion assay (section 7.2.3.1.2).

7.2.3.2.3 Experiment 3: combination of cell strainer with MACS

The primary goal of MACS was to separate the chondrocytes and fibroblast from the co-culture model to permit assessment of the relative influence of each cell type in the differential gene expression analysis. It was hypothesised that the application of MACS may also reduce the amount of residual bio-ink, leading to higher purity of the cell suspension.

The workflow for the trial of MACS was: 1) confirmation of suitability of CD markers for each cell type with flow cytometry (section 7.2.3.2.3.1), and 2) testing of MACS together with the cell strainers (experiment 3; section 7.2.3.2.3.2).

MACS is an immunomagnetic cell separation technique. Target cells are labelled with a magnetic particle specific for a cell surface (CD) marker. When the cell suspension is passed through the MACS LS column placed within the MACS separator, powerful magnets within the MACS separator cause the magnetically labelled cells to be

retained in the LS column, with flow-through of the unlabelled cells. Cells are then retrieved from the LS column by removing it from the magnetic field. Therefore, a cell-specific CD marker distinct for each cell type was required with MACS.

An initial literature search revealed a paucity of cell line-specific CD markers. As such, the search criteria were broadened to include human-specific cell types. The majority of CD markers was reported as dually expressed by both cell types, and therefore not suitable for cell sorting purposes. These included CD9, CD10, CD14, CD29, CD39, CD44, CD47, CD49b, CD49c, CD54, CD71, CD73, CD90, CD105, CD106, CD140b, CD146, CD151 and CD166 [307-329].

The use of transmembrane glycoproteins, CD44 and CD54, with human articular chondrocytes for MACS was reported by Hamada *et al*[318]. CD44 is a receptor for HA, whilst CD54 is also known as intercellular adhesion molecule-1 (ICAM-1). Whilst both are recognised chondrocyte markers[307], they are also expressed in fibroblast. As CD44 human microbeads are available for MACS, this was selected to test for positive selections of both cell types. To isolate a single cell type, CD340 for chondrocyte and CD15 for fibroblast were chosen for their reported preferential expression in their respective cell types [309]. Antibodies used for cell labelling are listed in table 7.4.

7.2.3.2.3.1 Flow cytometry

Flow cytometric analysis was used to assess whether the CD markers were expressed by the C20A4 and HFF-1 cell lines. To avoid influence of bio-ink material, cells from 2D cultures were used (as detailed in section 2.7). Staining with the fluorophore-labelled antibodies for the three selected cell markers was performed and analysed with the flow cytometer. The staining protocol involved transferring $1x10^5$ cells to a fluorescence-activated cell sorting (FACS) tube, centrifugation to achieve a cell pellet and the supernatant discarded. The cell pellet was resuspended in 200µl FACS buffer (0.2% w/v bovine serum albumin (BSA), 0.05% sodium azide in PBS) and incubated with 2µl of each antibody stain for 30 minutes on ice shielded from light. The cell suspension was washed by adding 2ml of FACS buffer, centrifugation to achieve a cell pellet, removal of the supernatant and resuspension in 200µl of FACS buffer. Centrifugation steps were performed at 515G at 4°C for 7 minutes. The labelled cells were then analysed on the Cytek Aurora flow cytometer immediately for the expression of CD15, CD44 and CD340.

With the unstained control, parameters for forward scatter (FSC) reflecting cell size and side scatter (SSC), a measure of cell granularity, were set. Following which, the individual fluorophore channel was set for each of the three antibodies used (table 7.4). These settings were applied for the full experiment. For each run, 10,000 events were acquired for the population of interest. Quality control (QC) for the flow cytometer was assured using the BD^{TM} Cytometer Setup & Tracking Beads Kit. This was performed as the first step, which involved adding one drop of the beads to 300µl of sheath fluid and initiating the QC programme.

Table 7.4 Antibodies for flow cytometric analysis.

Antibody	**Fluorochrome**	**Lasers and Wavelength / Excitation-Emission (nm)**	**Detection Channel (NovoCyte)**	**Isotype**	**Clone**	**Company (Catalog no.)**
CD15 Anti-human	APC	651/660	R1A	Mouse IgM	VIMC6	Miltenyi Biotec (130-114-008)
CD44 Anti-human	VioBlue	400/455	V3A	Mouse IgG1κ	DB105	Miltenyi Biotec (130-113-899)
ErbB-2 (CD340) Anti-human	PE	565/578	B4A	Recombinant human IgG1	REA1232	Miltenyi Biotec (130-124-473)

Data acquisition was performed with the SpectroFlo® (Cytek Biosciences). Data analysis was performed using FlowJo 10.8.1 (Tree star, Oregon, USA). An example of the gating strategy applied is shown in figure 7.4. The first gating was performed to select live cells and exclude debris based on size and granularity using the FSC v SSC density plot (figure 7.4A). Doublets with higher forward scatter were then excluded, with the selection of single cells using the FSC height versus area density plot (figure 7.4B). The gated population, which excluded debris and doublets, were used to generate histograms for each fluorophore (figure 7.4C). The median fluorescence intensity (MFI) of positive cells was used to evaluate the expression of specific CD markers by each cell population.

Compensation controls with single-stained samples for each antibody was performed to account for fluorescence spillover in this multi-colour experiment. Compensation for potential spectral overlap of the three fluorophores in mixed stain samples aimed to reduce false positive results. The positive and negative events of the single-stained runs were gated, labelled, and a compensation matrix was generated using the FlowJo software 10.8.1. This was applied to all flow cytometry data acquired prior to analysis.

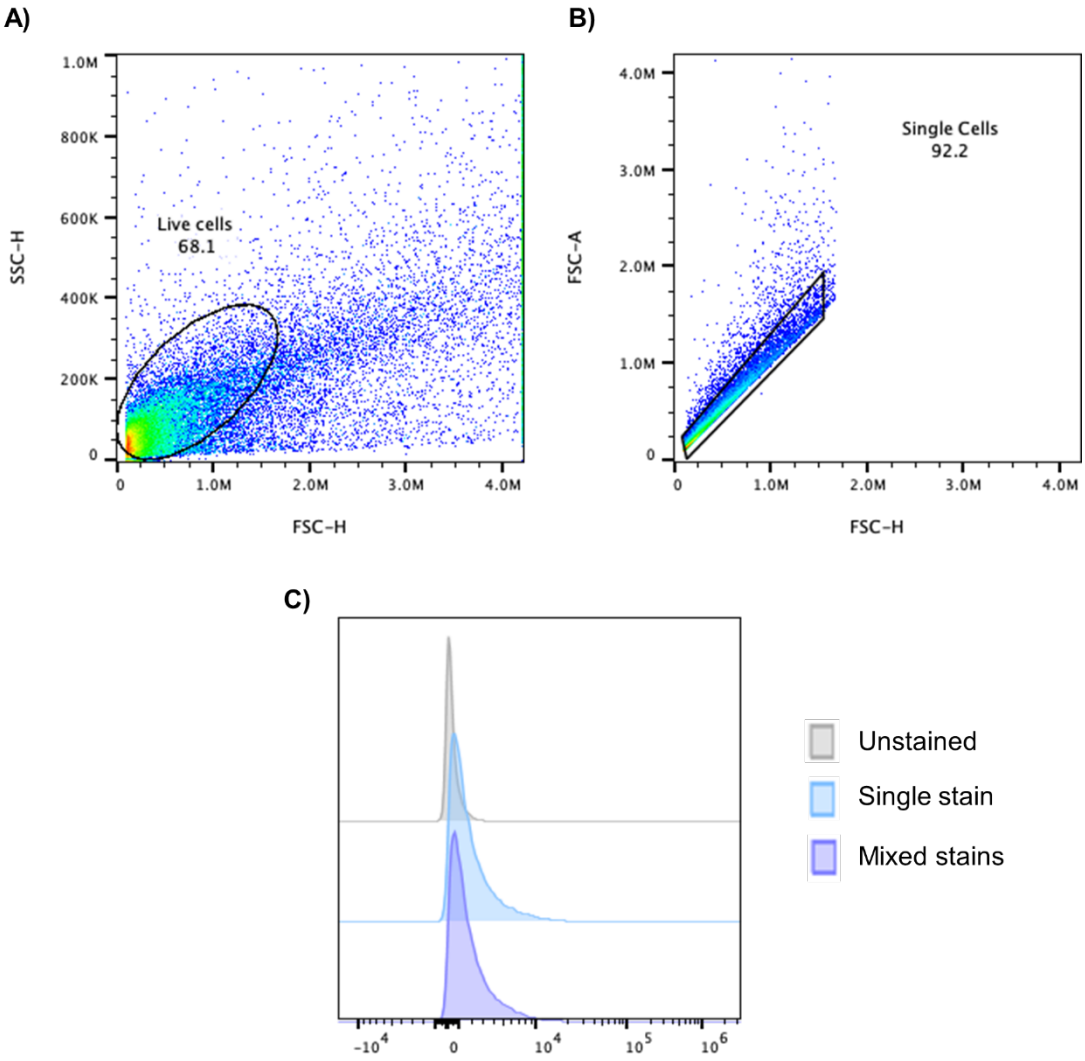

Figure 7.4 Example of gating strategy applied for flow cytometric analysis with CD44 expression by C20A4 cell line. *A) Density plot to identify cells of interest with gating of live cells based on their size with forward scatter (FSC) and granularity with side scatter (SSC). B) FSC height v area density plot used for doublet exclusion, with gating of single cells. C) Histogram demonstrating CD44 expression by C20A4: unstained (grey), single stain with anti-human CD44 (blue) and mixed stains (CD15, CD44, CD340) (purple). N=1.*

7.2.3.2.3.2 Combination of cell strainer with MACS

Following the confirmation of CD44 expression by the C20A4 cell line (results detailed in section 7.3.4), experiment 3 continued to compare sample preparation

conditions with the use of both cell strainers and MACS. Samples were prepared as described in section 7.2.3.1.1, up to and including the step of neutralisation of trypLE with culture media. The four conditions for cell strainers tested were: i) no cell strainer, ii) 250µm, iii) 70µm, and iv) serially with 250µm then 70µm cell strainers. MACS was then applied using CD44 microbeads following all four cell strainer conditions.

The MACS procedure was performed as per manufacturer's guidance with adaptations to account for the residual bio-ink and lack of cell pellet. The LS column was inserted into the MACS separator housing the magnets. The LS column was rinsed with 2ml MACS buffer (0.5% BSA, 2mM EDTA in PBS, pH 7.2), allowing this to run through. Concurrently, the strained sample was centrifuged at 300G at 4°C for 5 minutes, and the supernatant was discarded. The sample was mixed with 20µl of CD44 microbeads and 80µl of MACS buffer, and incubated at 4°C for 15 minutes shielded from light. The sample was then washed with 2ml MACS buffer and centrifuged at 300G at 4°C for 10 minutes. The supernatant was removed and the sample resuspended in 500µl of MACS buffer and added to the LS column. A top-up of 5ml MACS buffer was added to aid visualisation of the passage of the sample through the LS column. The flow-through consisting of unlabelled cells was collected. Once the sample and added buffer has passed through the LS column, the column was removed from the MACS separator. The positively selected cells were retrieved by flushing the cells out of the LS column with 5ml of MACS buffer. The cell suspension containing CD44+ chondrocytes was assessed with the erythrosin B exclusion assay as described in section 7.2.3.1.2.

7.2.3.2.4 Experiment 4: pre-conditions before RNA extraction

Optimisation thus far was assessed with the erythrosin B exclusion assay. The visualisation of the amount of cells and residual bio-ink material provided an indication of the efficacy of each variable tested, guiding their selection. As the final objective was RNA extraction, the assessment from experiment 4 onwards was changed to RNA quantification for a more precise comparison of methodologies tested.

Experiment 4 built on results from experiment 1 through 3, and was the first experiment evaluating RNA yield. Three sample preparation methodologies were tested:

i) sample homogenisation only (as described in section 7.2.3.1.1),

ii) sample homogenisation followed by serial cell strainers of 250μm and 70μm (sections 7.2.3.1.1 and 7.2.3.2.2), and

iii) the same as (ii), with the addition of MACS using CD44 for positive selection of cells (as described in section 7.2.3.2.3.2).

RNA extraction was performed as described in section 7.2.3.1.5. RNA quantification was performed with the Qubit assay (section 7.2.3.1.6), and purity ratios (A260:A280 and A260:A230) were assessed with the NanoPhotometer (section 7.2.3.1.4). Three biological replicates were performed.

7.2.3.2.5 Experiment 5: single versus double elution

Experiment 5 assessed the impact of the optional procedural step of the AllPrep DNA/RNA Mini Kit of double elution to increase RNA yield. Samples were prepared as per condition (ii) in section 7.2.3.2.4. RNA extraction was performed as described in section 7.2.3.1.5, with the final step of elution performed (termed double elution), or not performed (termed single elution). Assessment of RNA quantity and purity with the Qubit assay and the NanoPhotometer was performed as described in section 7.2.3.1.6 and 7.2.3.1.4, respectively. Nine biological replicates were performed.

7.2.3.2.6 Experiment 6: ethanol precipitation

The relevance of ethanol precipitation for RNA extraction was: i) to concentrate the extracted RNA to allow sample preparation at the required concentration for the application with Nanostring, and ii) to improve the purity of the RNA extracted. Samples were prepared as per condition (ii) in section 7.2.3.2.4, and RNA extraction with double elution as per section 7.2.3.2.5.

The ethanol precipitation was performed following an in-house protocol (unpublished). A tenth volume of sodium acetate was added to the extracted RNA. Ethanol (100%) was then added at 2.5x volume inclusive of sodium acetate, and the sample mixed by vortex. The sample was stored at -20^{o}C overnight for RNA precipitation. Although the protocol specified between one hour to overnight for the RNA precipitation step, in view of the anticipated low yield, overnight precipitation was selected. The RNA sample was centrifuged at 12,000G at 4^{o}C for 20 minutes, and

the supernatant was discarded. The RNA was washed by adding 500µl of 70% ethanol, mixed by vortexing, centrifuged at 12,000G at 4°C for 10 minutes and the supernatant was discarded. The wash step was performed twice. The RNA pellet was allowed to air dry. Once dry, the RNA pellet was dissolved in the desired volume of RNase free water.

The Qubit assay and NanoPhotometer were used to quantify and measure the purity ratios of the RNA pre- and post-ethanol precipitation respectively (as described in section 7.2.3.1.6 and 7.2.3.1.4). Three biological replicates were performed.

7.2.3.2.7 Trial of RNA extraction for HFF-1 3D monoculture model

Following optimisation of the full RNA extraction process with the chondrocyte monoculture model (as described in section 5.8.4.3 of the SOP in appendix 1), RNA extraction from the fibroblast monoculture model was trialled.

Initial quantification using the Qubit assay (section 7.2.3.1.6) did not yield detectable levels of RNA. In view of the low seeding density, the pooling of 10 fibroblast samples was performed. The same procedural steps were followed, except for the collation of flow-through from the DNA spin column. These were processed through a single RNeasy spin column to retain all RNA from 10 samples into a single RNeasy column membrane.

Due to undetectable levels of RNA of the pooled sample with the Qubit assay which has a detection range of 0.2-200ng/µl (assay range 4-200ng), a more sensitive assay, the Quant-it™ RiboGreen® Reagent and RNA Assay Kit (Ribogreen), was used. This kit can be applied in two ranges for low or broad detection ranges. The low range assay with a sensitivity range of 0.1-5ng/µl (assay range 1-200ng RNA) was used, and the assay was performed as per manufacturer's guidance. All kit components were allowed to come to room temperature before use. The RNA reagent, which is the fluorescent RNA stain, was shielded from light at all times. The TE buffer was first added to a 96 well microplate. Standards (maximum 100ng/ml with two-fold serial dilution) and 1µl RNA samples were added to the TE buffer to create a final volume of 50µl per well. The RNA dye reagent was diluted 2000 fold in the TE buffer and 50µl was added to each standard and sample well and incubated at room temperature for 5 minutes shielded from light. Fluorescence was measured using a microplate reader with an

excitation/emission of 482/520nm. The instrument's gain was adjusted such that the highest RNA concentration yielded a fluorescence intensity near the instrument's maximum range (i.e. 85%). This ensured all sample readings fall within the detection range of the fluorometer. Data analysis was performed by first subtracting the mean fluorescence value from the blank wells. The corrected data was then used to generate a standard curve against which the RNA concentration of samples was calculated from. Three technical replicate was performed with a single biological replicate consisting of the pooling of ten fibroblast-seeded 3D *in vitro* models.

7.2.3.2.8 Section summary – optimisation of RNA extraction

Results of each experiment for the optimisation of RNA extraction are detailed in sections 7.3.1 – 7.3.7. The final protocol for RNA extraction based on these results are detailed in section 5.8.4.3 of the SOP (appendix 1). This RNA extraction protocol was used for all RNA samples intended for Nanostring application.

7.2.4 Characterisation of advanced 3D *in vitro* models with gene expression analysis

To further elucidate the biological effects of the nanocellulose-based bio-ink in the advanced 3D *in vitro* model, gene expression analysis was performed with the use of Nanostring. The study parameters were illustrated in figure 7.1. The optimal bio-ink inclusive of alginate and HA (ETC:Alginate:N-HA (low) in media) was selected for testing (rationale detailed in section 5.3.2). The fibroblast monoculture 3D *in vitro* model was excluded due to unsuccessful RNA extraction (section 7.3.8). The bio-ink was tested in both the chondrocyte monoculture and co-culture models, permitting evaluation of the influence of the fibroblast in the co-culture system. Applying the same experimental conditions in chapter 6, the augmented culture media exchange regime (sections 2.13 and 6.2) was used to supplement the cytotoxicity and pro-inflammatory response dataset with the gene expression analysis. An optimal culture media exchange regime was also included, involving full media exchange every 2 - 3 days, to permit characterisation of the model without the potential deleterious effect of restricted nutrients and waste products removal. Nanostring uses a single-use cartridge-based sample loading system, with each cartridge taking 12 biological

samples. The timepoints selected for this study were rationalised, in conjunction with the experimental conditions described above, to maximise the use of available sample slots and facilitate condition comparisons for differential gene expression analysis. Six timepoints were included over the full 21-day study period, covering both acute (day 1, 3, 5, 7) and chronic timepoints (day 14 and 21).

7.2.4.1 Nanostring nCounter analysis system

Nanostring is an automated, panel-based gene expression quantification system which utilises molecular barcodes and digital counting technologies to provide analysis of up to 800 target genes in a single sample simultaneously. The principle of the assay is illustrated in figure 7.5. RNA is first bound to a gene-specific capture and reporter probe through a hybridization step (step 1), creating a 'target probe complex'. Each reporter probe contains a six-spot fluorescent barcode made of a combination of four colours. Each gene is assigned a specific colour combination, creating a unique identification for each target gene. The purification step removes excess unbound capture and reporter probes (step 2). The sample is then loaded onto the Nanostring cartridge, where the target probe complex is immobilised to the cartridge slide surface (step 3). This process is aided by the biotinylated capture probe, which interacts with the streptavidin-coated slide. Once immobilised, the target probe complexes are laid flat and aligned on the slide surface *via* the application of an electric current in a microfluidic system (step 4). A digital image is captured of the slide containing multiple gene-specific target probe complexes (step 5), and digital counting of each colour barcode combinations provides the direct transcript count (step 6).

Nanostring carries over 150 human-relevant panels covering a variety of conditions and biological processes. As there was no specific panel for tissue engineering, regenerative medicine or relevant cartilage-related conditions, a literature search was conducted for cartilage tissue engineering which used nanocellulose-based biomaterial with the search terms of RNA, PCR and differential gene expression. This generated a list of 88 potential gene of interest with which the top 10 Nanostring panels with the best coverage were identified. In-depth review of these suggested that the PanCancer IO360 panel, although designed to investigate immune-oncology, with its broad scope covering 770 genes across 25 biological processes (e.g. cell proliferation, cytotoxicity,

cytokine and chemokine signalling and metabolic stress) was most suitable for the intention of the chapter aims.

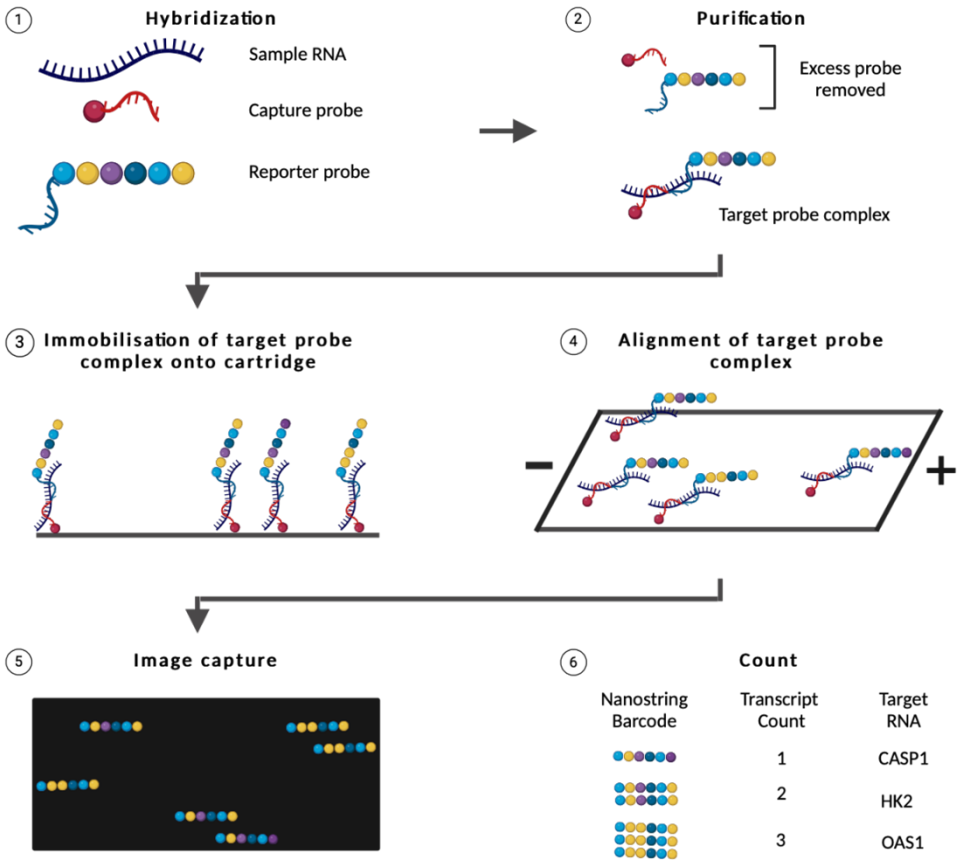

Figure 7.5 Schematic of the Nanostring nCounter Analysis System experimental procedure. *Step 1: Hybridization of sample RNA with target-specific capture and reporter probes, creating unique target probe complex. Step 2: Purification of the sample removed excess capture and reporter probes. Step 3: Sample is added to the Nanostring cartridge where target probe complex immobilises onto the slide surface. Step 4: Alignment of the target probe complex is performed by the application of an electric current. Step 5: Image capture of the immobilised target probe complex yields image with fluorescent barcodes. Step 6: Digital counting of the unique barcodes provides direct count of individual transcripts. Created with BioRender.com.*

The RNA input was standardised to 60ng using the lowest RNA yield across all samples. This met the manufacturer's input recommendation of 50ng-300ng. The Qubit assay was used to calculate loading sample quantity due to the enhanced accuracy of the fluorescence-based assay. All RNA samples were prepared as described in the SOP (appendix 1). Quantification was performed with the Qubit assay (section 7.2.3.1.6). Purity was assessed with the NanoPhotometer (section 7.2.3.1.4). Specifically for Nanostring application and quality control purposes, to avoid repetitive freeze / thaw cycles of RNA samples, the sample was reconstituted to a target

concentration of 12ng/µl. Separate aliquots for QC (4µl) and Nanostring application (6µl) were prepared.

7.2.4.2 RNA integrity assessment

RNA integrity assessment involved the determination of the RIN and DV200 of all RNA samples intended for Nanostring application. This was performed using the RNA 6000 Nano Kit with the Agilent 2100 Bioanalyzer. The bioanalyzer is an automated microfluidics-based electrophoresis system and it employs a chip-based system which can house up to 12 samples. The principle of the assay is akin to the gel electrophoresis (as described in section 7.2.3.1.7). The electrophoretic assay quantifies the sizing of RNA fragments in a digital format. It is more sensitive and precise than gel electrophoresis and provides additional information such as the DV200 (% of RNA fragments greater than 200 nucleotide).

The procedure begun with the preparation of the chip priming station (supplied by Agilent) as per the manufacturer's guidance. Preparation of the RNA ladder involved heating at 70^{o}C for precisely 2 minutes to denature the ladder and immediately cooling the RNA ladder on ice. Next, the gel was prepared by placing the RNA gel matrix into a spin filter and centrifuged at 1500G for 10 minutes at room temperature. The RNA dye concentrate was added to the RNA gel matrix at a ratio of 1µl dye to 62µl filtered gel, and vortexed to mix. This was then centrifuged at 13000G for 10 minutes at room temperature, and loaded onto the RNA chip placed within the chip priming station. Next, 5µl of the RNA marker was added to each sample and ladder well. The RNA ladder and sample was added next at 1µl each. The chip was vortexed horizontally at 2400rpm for 1 minute in the IKA vortex, and ran in the 2100 Bioanalyzer immediately. The RIN and DV200 values were recorded directly from the Bioanalyzer software for each sample.

7.2.4.3 Nanostring experimental procedure

The hybridization master mix was first created by adding 70µl of the supplied hybridization buffer to the thawed Reporter CodeSet tube. The hybridization mix (8µl) was then added to each tube of a 12 tube strip, followed by 5µl of RNA sample (60ng) and 2µl of Capture ProbeSet. A new pipette tip was used for each sample to minimise

cross-contamination and errors. The content was mixed by flicking and a brief spin. The contents were then incubated at 65ºC for 20 hours in a thermal cycler for the hybridization reaction.

On the following day, the Nanostring cartridge was prepared 15 minutes prior to use by removal from the -20ºC freezer to return to room temperature. The samples were used immediately following the hybridization reaction. The volume of samples was checked by pipetting to account for evaporation during the hybridization process. RNase-free water was added to each sample to reach a total volume of 35µl. The sample (33µl) was then loaded onto the Nanostring cartridge as per the manufacturer's guidance with the inclusion of an air bubble. The cartridge was then loaded onto the Nanostring SPRINT Profiler for analysis.

7.2.4.4 Nanostring data analysis

7.2.4.4.1 Raw data appraisal with the Nanostring nSolver analysis software

The raw data, which consists of raw digital counts of each transcript, was exported and analysed using the Nanostring nSolver analysis software 4.0. Raw data appraisal, including QC assessment and data normalisation was performed using the advanced analysis package. Internal QC was ensured using the default parameters as recommended by Nanostring. This included the assessment of imaging (% of FOV registration), binding density, positive control linearity and positive control limit of detection. Normalisation of the raw data was performed using the 20 internal housekeeping genes of the IO360 panel and the nSolver normalisation module. Log2 transformed normalised data was used for all subsequent differential gene expression analysis.

7.2.4.4.2 Volcano plots of DEGs

Visualisation of DEGs in the forms of volcano plots was performed using GraphPad Prism v10. DEGs were identified by comparing the co-culture model on day 3, 5, 7, 14 and 21 in optimal culture conditions against baseline on day 1. Differential expression was defined as a log2 fold change of greater than 1.5 or less than -1.5, with a negative log10 Benjamini-Hochberg adjusted p-value of less than 0.05. All reference to DEGs in future refers to those identified as described in this section.

7.2.4.4.3 Nanostring pathway score

The nanostring pathway score was calculated *via* the proprietary nSolver software function using Principal Component Analysis (PCA) principles. It condenses data of all genes within a pathway into a single score. Scaling of each gene's expression by its variance was first performed so that scores are comparable. The first principle component (PC) of all genes within a pathway was then calculated. Genes are weighted by how much they contribute to the first PC, and then multiplied by their expression. This focused the pathway score on genes that varies the most within the pathway and makes the score more sensitive. By default, the PCs are zero-centered. The Nanostring algorithm includes a step which orientates the matrix such that the pathway scores provide an indication of whether the overall expression within the pathway is above or below the mean. Individual gene variance and significance of such variance are not considered. Instead, focus is placed on genes within the pathway that changes the most (i.e. first PC). In totality, the Nanostring pathway score is a high-level overview of each of the 25 pathways (also known as functional annotations) on the IO360 panel. It provides an indication of the effect of the variable tested on each pathway, and whether gene expression is increased or decreased compared to the reference group. In this case, the model was characterised *via* comparison of the model on day 3 to 21 against baseline on day 1.

7.2.4.4.4 Heatmap of DEGs

Heatmaps of DEGs were created using the z scores of each gene and GraphPad Prism v10. The z score represents the gap between a data point and the mean of a dataset, and is expressed in terms of standard deviations. It is calculated with equation 7.1.

Normalised mRNA counts were used throughout. For each target gene, x represents the datapoint for which the Z score is calculated for, and μ and σ are the mean and standard deviation of mRNA counts of the target gene across all timepoints and conditions.

Equation 7-1

$$Z\ score = \frac{x - \mu}{\sigma}$$

x = mRNA count
μ = mean of mRNA count
σ = standard deviation of mRNA count

7.2.4.4.5 Analysis of DEGs overlap over time

The degree of overlap of DEGs during the time course of the model characterisation study was illustrated using DiVenn, an online visualisation tool (available from https://divenn.tch.harvard.edu)[330]. This produces clusters of DEGs based on the timepoints at which the genes were differentially expressed.

7.2.4.4.6 Functional enrichment analysis with protein-protein interactions

Network visualisation was performed to demonstrate known and predicted protein-protein interactions (PPI) using the STRING database v12. The STRING database encompasses over 59 million proteins across many organisms. Both physical or direct PPIs, as well as functional interactions (i.e. proteins which interacts without physically binding), are evidenced, with data sources benchmarked against the KEGG pathway maps[331].

DEGs were first converted to Ensembl gene IDs (ENSG) using the online g:Convert function of g:Profiler (available from https://biit.cs.ut.ee/gprofiler/convert). The ENSGs of all DEGs were then inputted into the online STRING database using the multiple proteins setting (available from https://string-db.org/cgi/input?sessionId=behMcCHgI4VH&input_page_active_form=multiple_identifiers). Settings selected were homosapiens, clustering to k-means with a high confidence threshold (0.700) and textmining off, in accordance with advice from Iain Perry, a bioinformatician. This resulted in a human-relevant PPI network based on the experimentally defined DEGs.

To further annotate this network, the STRING output was exported to Cytoscape, a bioinformatics software platform (available from https://cytoscape.org). GO terms were mapped to the PPI network, and redundant GO terms removed using the ClueGO Cytoscape add-on[332]. The thickness of linkage lines of the network corresponds with the STRING 'combined' scores. This denotes the confidence in the interaction, i.e. how strongly STRING deems an interaction to be true based on its evidence base. It does not indicate the strength or specificity of the PPI.

7.2.4.4.7 Over-representation analysis

Over-representation analysis (ORA) is a widely applied method to detect statistically significantly enriched biological pathways from large scale gene expression data by

linking genes to known biological pathways. An ORA compares the DEGs against pre-defined gene sets of numerous known biological pathways, and assesses if the DEGs are disproportionately represented in a pathway compared to a random selection of genes. I.e. If the DEGs are over-represented than what would be expected by chance.

The g:Profiler is an online platform with multiple functions for the characterisation and manipulation of gene lists (available from https://biit.cs.ut.ee/gprofiler/gost). It utilises varied data sources encompassing biological pathways (KEGG, Reactome and WikiPathways), regulatory motif matches (TRANSFAC), tissue specificity (Human Protein Atlas), protein complexes (CORUM) and human disease phenotypes (Human Phenotype Ontology) [333]. The g:GOSt function was used to undertake the ORA using an unordered list of DEGs, separated into those which were up- or down-regulated. DEGs were converted to Ensembl gene IDs and inputted into the g:GOSt function. Default settings were used whilst selecting for homo sapiens. The term size was adjusted to between 1 and 1000 to produce more discrete pathway terms. The GO terms output was then exported to ReviGO (available from http://revigo.irb.hr). It served to condense multiple GO terms which essentially define the same pathway into an overarching term[334]. In addition, the intersection ratio was calculated for the top 10 GO terms for the up- and down-regulated DEGs. This represents the number of DEGs divided by the number of genes for each GO term. Therefore, an intersection ratio of 1 implies that the DEGs encompasses the entire gene set (100%) for a particular GO term.

7.2.4.4.8 Log fold change of RNA count over time

The normalised RNA transcript count or log2 fold change over time are visualised using GraphPad Prism v10. In addition to the data from the co-culture model in optimal culture conditions, data from the C20A4 monoculture models and comparison between the augmented and optimal culture media regime are shown.

7.3 Results and Discussion

The results from this chapter is divided into three sections: i) pilot testing of RNA extraction, ii) optimisation of RNA extraction and iii) characterisation of advanced 3D *in vitro* model with gene expression analysis with Nanostring.

7.3.1 Results of pilot testing of RNA extraction

The initial homogenisation step using trypLE and mechanical disruption was adapted from an RNA extraction protocol intended for organoids due to the parallels of cell encapsulation within a material. This proved successful in breaking down the cross-linked hydrogel with live cells seen under light microscopy (figure 7.6A/B).

A key difference between the samples when compared to the organoids was the use of Matrigel in the organoid creation. This accounts for the lack of phase separation between material and cells and therefore the lack of a cell pellet with the samples. Matrigel is a commercially available reconstituted basement membrane preparation developed from mouse sarcoma, and is commonly applied in 3D cultures systems. It is in liquid state at 4^{o}C, but gels at 22-37^{o}C (i.e. at room and physiological temperatures). When centrifugation is performed at 4^{o}C, the Matrigel returns to its liquid state during centrifugation, thereby supporting cell and material separation and cell pelleting. On the other hand, the partially homogenised bio-ink does not have this property and centrifugation alone did not separate the bio-ink and encapsulated cells (figure 7.6B).

Nonetheless, pilot testing continued with the trial of firstly a protocol intended for 2D cell culture, and subsequently one intended for organoid DNA and RNA extraction. Two commercial RNA kits were tested, with the core difference being the added DNA spin column application in the second trial. Clogging of the spin column membrane was noted with both kits. It was found that the use of the DNA spin column filtered bio-ink material with RNA content contained within the flow-through, leading to successful RNA extraction.

In part, because of the anticipated low yield, the spin column technique for RNA extraction was preferred over the use of the TRIzol reagent, another widely used RNA extraction technique. The former minimises user-dependent variability and therefore reduce potential errors which may impact RNA yield, including its purity and quality.

The first trial of RNA extraction was based on protocols for 2D cell cultures, utilising the Qiagen QIAShredder and RNeasy kit for homogenisation and RNA extraction, respectively. Clogging of the RNeasy spin column membrane was seen with residual sample above the membrane after centrifugation. Repeated centrifugation in the same spin column was successful in ensuring complete sample flow-through across the spin column membrane, but quantification with the NanoPhotometer showed no measurable RNA. As RNA is captured by and eluted from the RNeasy column membrane, it is likely that the bio-ink residual has deposited on the membrane and negatively impacted on RNA capture and elution.

The second RNA extraction protocol trialled was intended for organoid cultures. It differed from the first protocol with homogenisation by repeated passage via a 21G needle, the addition of β-mercaptoethanol to the lysis buffer and the use of the AllPrep

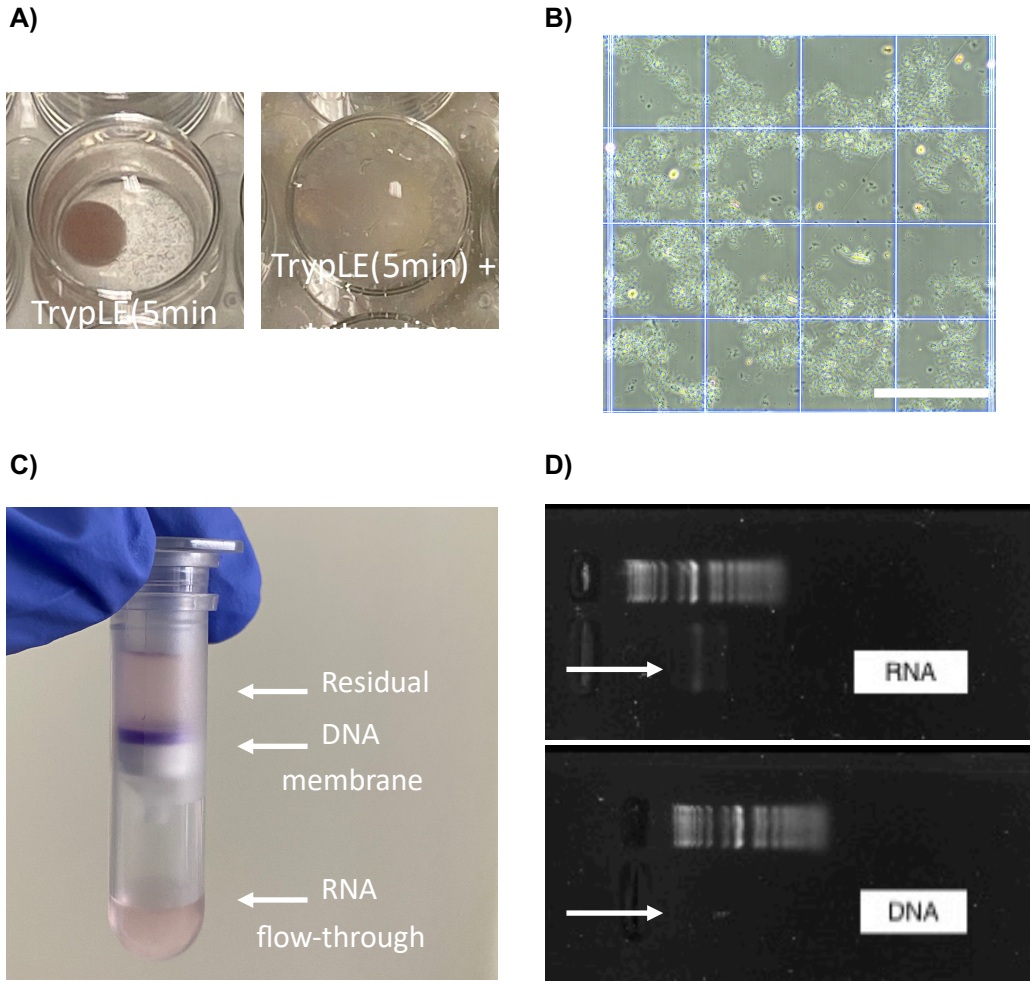

Figure 7.6 Pilot testing results. *(A) Breakdown of cross-linked pellet upon application of TrypLE and mechanical agitation. (B) Erythrosin B assay of cell suspension after application of TrypLE and mechanical agitation. Scale bar = 300μm. (C) Evidence of clogging of spin column membrane with residual sample above membrane. (D) Agarose gel electrophoresis RNA and DNA. Top row is the RNA/DNA ladder, and bottom row is the sample (white arrow). N=1.*

DNA/RNA Kit. As described in section 7.2.3.1.5, the AllPrep DNA/RNA kit involved the passage of biological sample through the DNA column initially, with DNA captured in the DNA column membrane. The flow-through containing RNA was then passed through the RNA column, where RNA was captured in the column membrane. Although the RNA spin columns from both Qiagen kits used in pilot testing were the same, the reason that RNA extraction was successful with the AllPrep kit was likely because the DNA column membrane served to filter the bio-ink material. Clogging of the DNA column was seen, in the same manner as with the RNA column in pilot testing 1 (figure 7.6C). The transfer of the residual sample that has not flowed through to a new DNA column for centrifugation, rather than repeating centrifugation is also a crucial step. In combination, this permitted full utilisation of biological sample, and no clogging of the RNA column membrane was seen as in pilot test one. A satisfactory quantity and quality RNA were eluted. Quantification with qubit showed 500ng RNA and integrity assessment using gel electrophoresis showed two clear ribosomal bands, albeit faint due to low quantity (figure 7.6D). DNA was non-detectable on gel electrophoresis. In conclusion, methodologies from pilot test two were then taken forward for optimisation.

7.3.2 Experiment 1: Phase separation by centrifugation

Phase separation by centrifugation was first trialled to achieve a purer cell sample. This is important to reduce residual bio-ink interference of downstream procedures and assays. The magnetic-activated cell sorting (MACS) was intended to support cell sorting, and residual bio-ink may block the MACS LS columns through which the cell suspension pass through for cell isolation.

A range of centrifugation forces tested (300, 600, 1200 and 2400G for 5 minutes) all failed to produce a cell pellet. Visualisation with the erythrosin B exclusion assay confirmed the lack of material and cell separation (figure 7.7). Under light microscopy, live cells were seen alongside copious amount of bio-ink material.

Interestingly higher centrifugation forces were associated with greater amount of bio-ink material. Whilst the goal of applying higher centrifugation forces was to bring the denser cells to pellet at the base, it appears that higher forces were associated with a

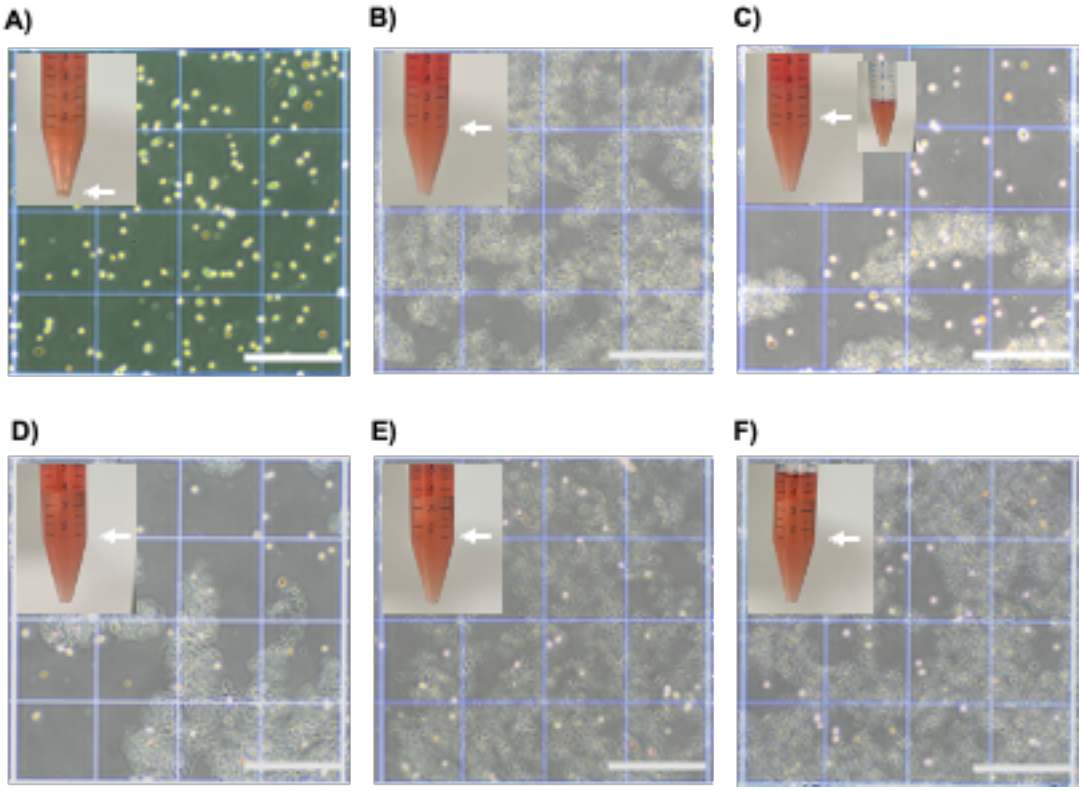

Figure 7.7 Experiment 1: phase separation by centrifugation. *Light microscopy with erythrosin B assay applied to cross-linked pellet treated with trypLE and mechanical agitation. Inset image showed cell and/or material suspension following centrifugation, with arrow denoting cell pellet (A) or level of phase separation (B-F). In C), images of suspension before and after supernatant is removed are shown to more clearly demonstrate level of phase separation. A) Cell only 300G using 2D chondrocyte monoculture. B) Material only 300G (cross-linked hydrogel disc). C-F) Consists of cells and materials. Centrifugation speed for each were: C) 300G, D) 600G, E) 1200G and F) 2400G. Scale bar = 300μm. N=1.*

more concentrated amount of bio-material in the denser portion. As such, 300G was chosen for future work, with the most favourable ratio of cells and residual bio-ink, although further optimisation was indicated to further reduce material interference.

7.3.3 Experiment 2: Effect of mesh sizes of cell strainers

The use of cell strainers was recommended for clinical tissue samples prior to MACS application to minimise the clogging of LS columns. As such, experiment 2 evaluated its application with the advanced 3D *in vitro* models and included the trial of various mesh pore sizes.

Overall, the cell and material suspensions passed through each cell strainer rapidly with no gross amount of material collected above the mesh. However, a marked reduction in both cells and material was seen with the use of 40μm cell strainer under microscopy (figure 7.8D). This likely accounts for the similar result with the serial application of strainers (figure 7.8E). The differences between the 250μm and 70μm

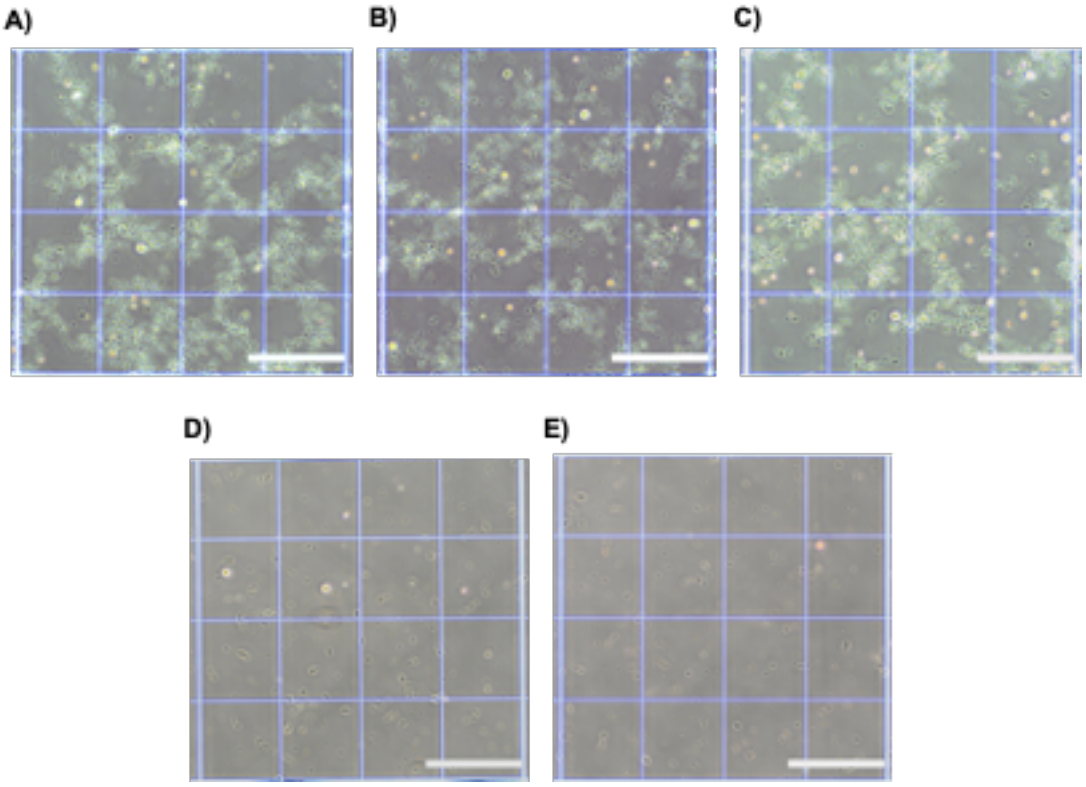

Figure 7.8 Experiment 2: effect of mesh size of cell strainers. *Light microscopy with erythrosin B assay applied to cross-linked pellet treated with trypLE and mechanical agitation, and a variety of cell strainers. A) No cell strainer. B) 250µm. C) 70µm. D) 40µm. E) Serial - 250µm, 70µm, 40µm. Scale bar = 300µm. N=1.*

cell strainer, and when no cell strainer was used were relatively subtle. Due to known challenge of low RNA yield, the use of 40µm was excluded as it will reduce RNA quantity significantly. Both the 250µm and 70µm cell strainer was taken forward for further testing.

7.3.4 Experiment 3: Combination of cell strainer with MACS

To permit MACS, the selection of a suitable CD marker was assessed with flow cytometry. Subsequently, the results of its application together with cell strainers were discussed.

7.3.4.1 Flow cytometry

The expression of three CD markers were evaluated. The expression of CD44 was observed in both cell types, although more pronounced in fibroblast (figures 7.9B + 7.10G) compared with the chondrocytes (figures 7.9A + 7.10G). Although CD15 was selected for the isolation of fibroblast, its expression was not detected in fibroblast (figures 7.9E + 7.10H), nor chondrocytes (figures 7.9D + 7.10H). On the other hand,

CD340 was chosen to isolate chondrocytes. It was found to be dually expressed by both cell types, with comparable MFI observed between both fibroblast

(figures 7.9H + 7.10I) and chondrocytes (figures 7.9G + 7.10I).

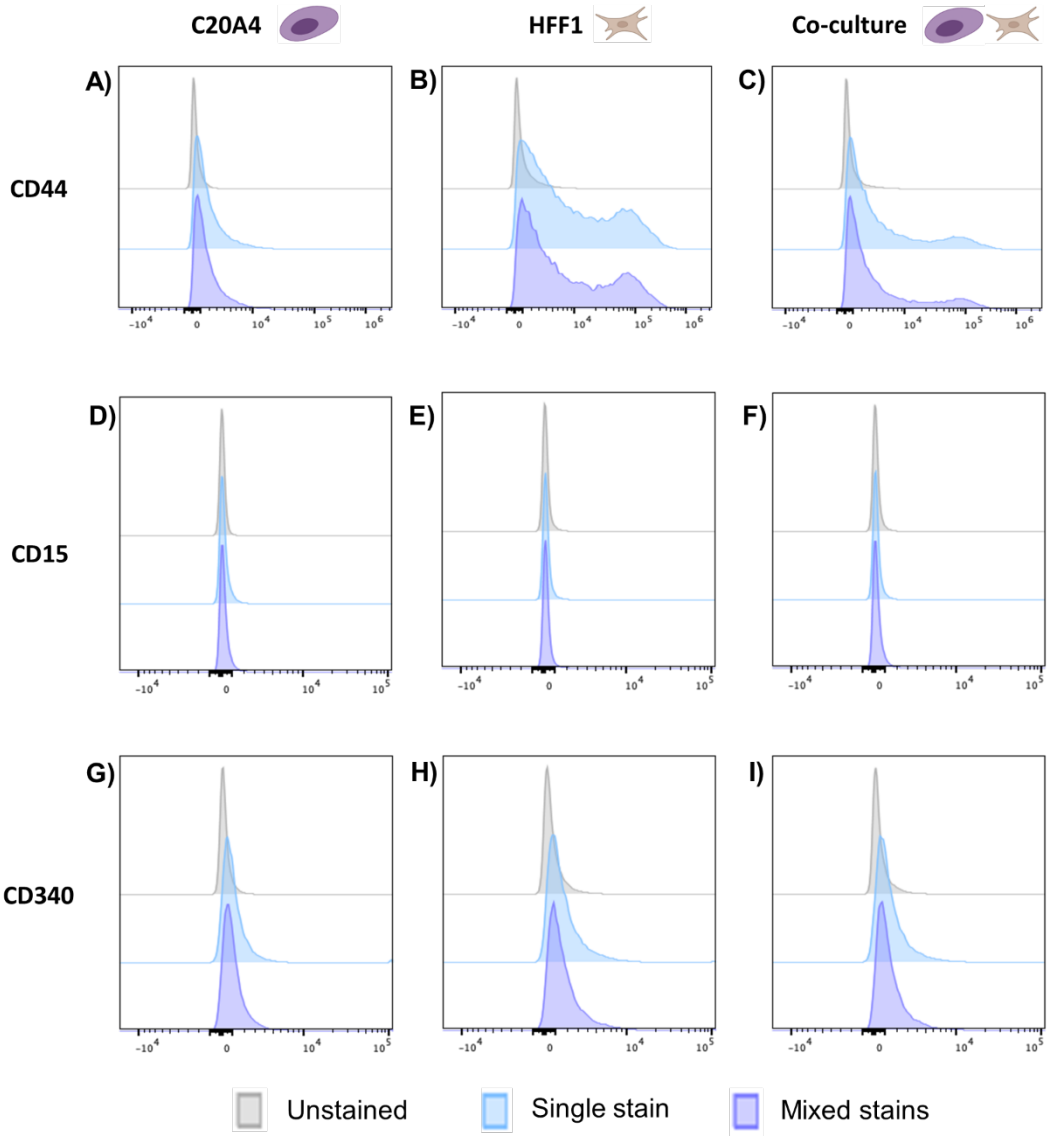

Figure 7.9 Histograms of CD44, CD15 and CD340 expression on C20A4, HFF-1 and as a co-culture. *The expression of CD44 (top row), CD15 (mid) and CD340 (bottom) was determined using flow cytometry. Both single cell types (left – chondrocytes C20A4; mid – fibroblast HFF-1) and mixed cell types mimicking co-culture cell suspension (right) were tested. N=1.*

Taken together, the CD44 and CD340 could be used to positively select both chondrocytes and fibroblasts for MACS purposes. Due to its higher levels of expression, and availability of antibody-specific MACS microbeads, CD44 was selected for further testing. Based on the flow cytometric data, the tested CD markers was not suitable for use in the isolation of single cell types. Nonetheless, MACS was further tested for its potential to reduce bio-ink residuals to improve RNA yield.

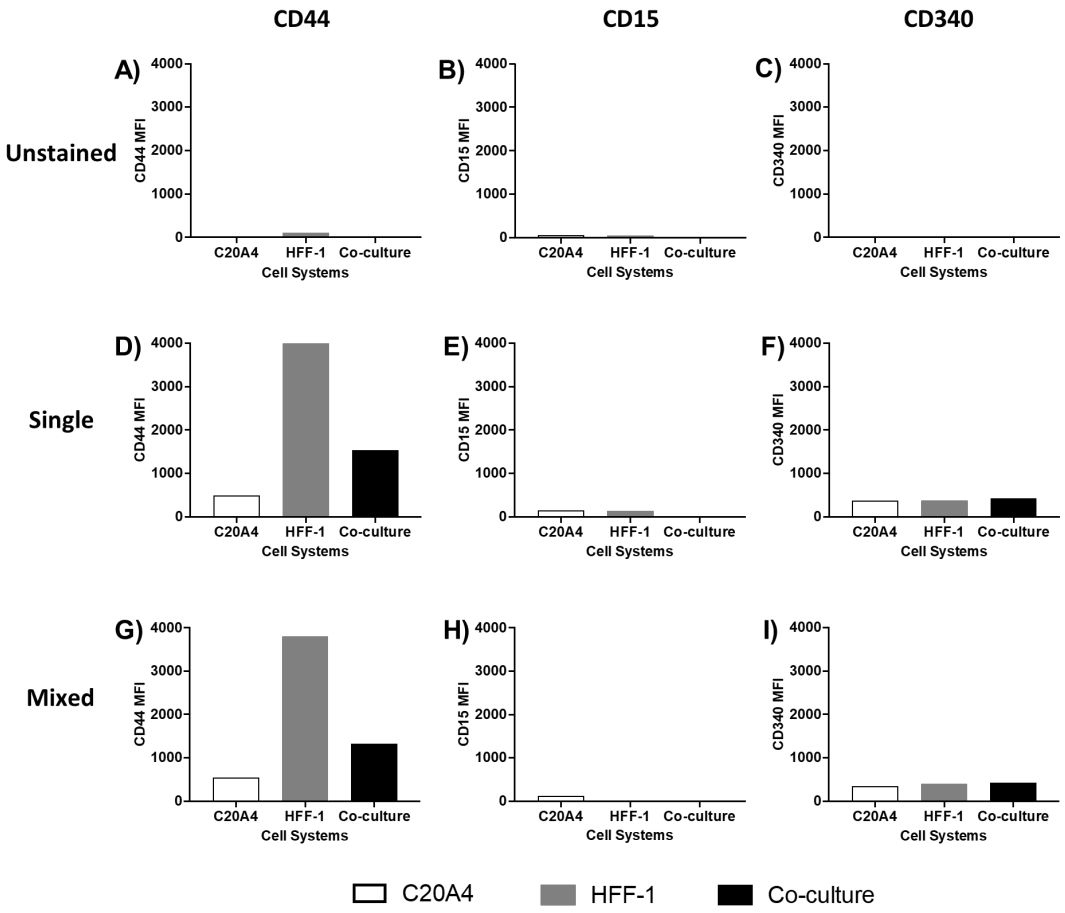

Figure 7.10 Expression of CD44, CD15 and CD340 on chondrocytes and fibroblast. *The median fluorescence intensity of CD44, CD15 and CD340 were determined using flow cytometry of chondrocytes (C20A4), fibroblasts (HFF-1) and as a co-culture. N=1.*

7.3.4.2 Combination of cell strainers with MACS

Building on from experiment 2 which tested various mesh pore sizes of cell strainers, with the exclusion of 40µm, experiment 3 tested four conditions: i) no cell strainer, ii) 250µm, iii) 70µm and iv) serial cell strainers with 250µm then 70µm, all followed by MACS using CD44 for positive selection.

The variance of the time required for samples to pass through the MACS LS columns was immediately apparent depending on the mesh sizes of the cell strainers. The shortest passage was under 30 minutes, with the serial application of cell strainers of 250µm and 70µm (figure 7.11E). The second fastest was with 70µm strainer alone, followed by 250µm. The slowest passage lasted approximately 2 hours 30 minutes, where no cell strainer was used. In contrast, when tested using chondrocytes cell suspension from 2D culture only, i.e. without bio-ink, the duration for passage through

the MACS column was only 3 minutes (data not shown). This indicates the direct effect of the bio-ink in the prolonged duration required.

Inspection of the cell suspension achieved with MACS using the erythrosin B exclusion assay revealed a significant reduction in bio-ink material following MACS. However, this was associated with reduced cell numbers also, with no gross difference between the three combinations of cell strainers (figure 7.11B-D). Interestingly, the sample without cell strainers showed the least amount of bio-ink material when processed through MACS (figure 7.11A).

With no superiority between different cell strainer options based on light microscopy imaging, the serial application of cell strainers with 250μm and 70μm was chosen for subsequent experiments because it led to the shortest duration required for passage through the MACS column. This implies reduced residual bio-ink material which will be beneficial for downstream assays. The reduction in cell processing time would also limit potential negative impact on cells when outside of culture conditions prior to RNA extraction.

7.3.5 Experiment 4: Comparison of pre-conditions for optimal RNA yield

Building on previous work, experiment 4 in step 3 (Figure 7.3) aimed to compare the following three conditions of sample preparation for RNA extraction:

1) Sample preparation with trypLE and mechanical disruption (step 1 in Figure 7.3; section 7.2.3.1.1);

2) Same as (1), with the addition of serial applications of cell strainers of 250um and 70um (based on results from experiment 2);

3) Same as (2), with the addition of using MACS with CD44 microbeads for positive cell selection (based on results from experiment 3).

The three pre-conditions were assessed quantitatively based on RNA yield. In terms of RNA quantity, despite two outliers (one each in condition 1 and 2), sample preparatory pre-condition 2 was superior, providing the maximal RNA yield (figure 7.12A).

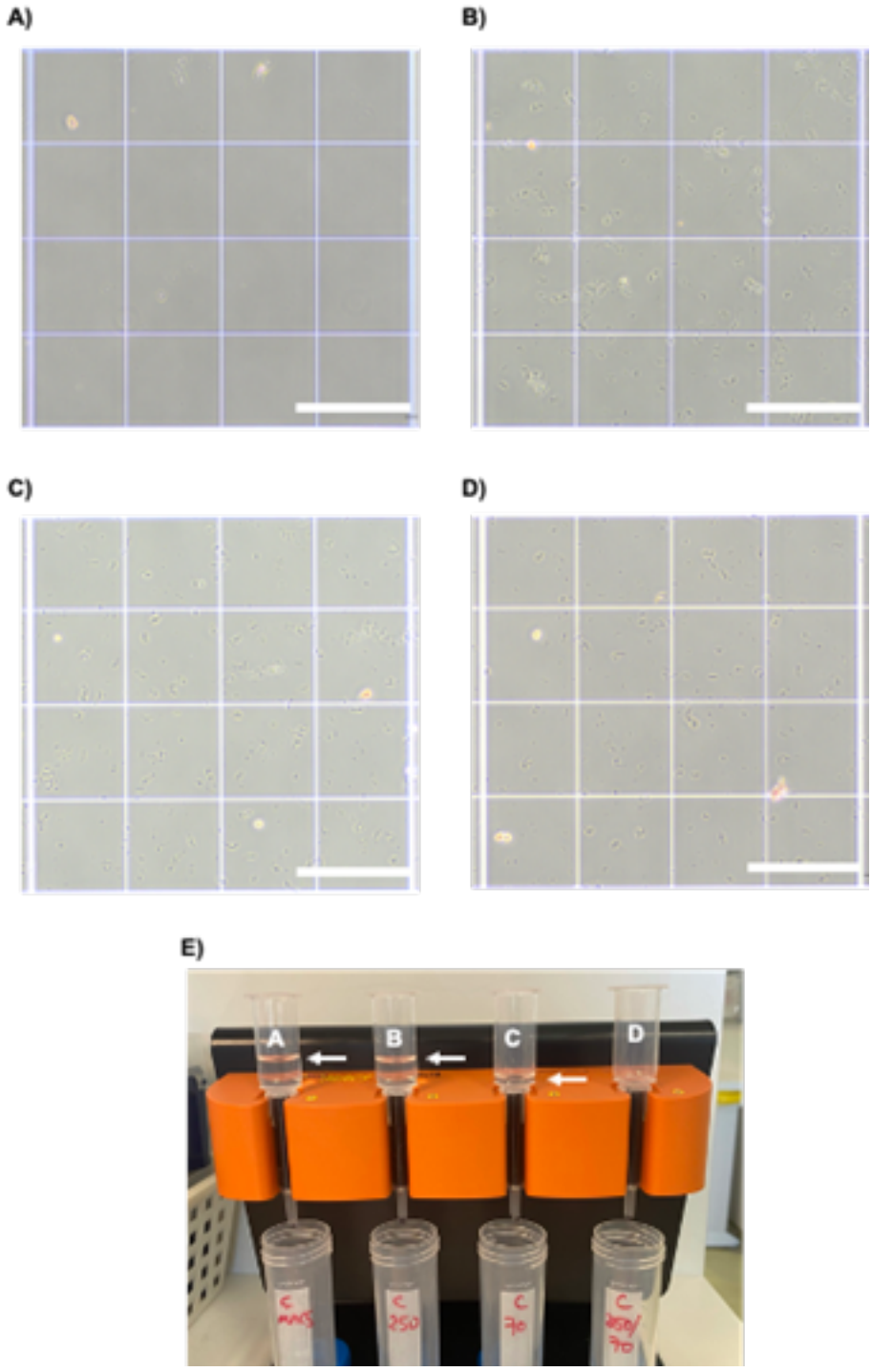

Figure 7.11 Experiment 3: combination of cell strainer with MACS. *A-D: Light microscopy with erythrosin B assay applied to samples processed through a variety of cell strainers followed by MACS using CD44. A) No cell strainer. B) 250μm. C) 70μm. D) 250μm and 70μm serially. Scale bar = 300μm. N=1. Image E shows the variable sample volumes above MACS LS columns at 30 minutes, denoted by arrows. The letters (A-D) corresponds to the cell strainers used for light microscopy imaging. This demonstrates the different rate at which samples pass through columns, and in order of quickest to slowest: 1) 250μm and 70μm serially, 2) 70μm, 3) 250μm and 4) no cell strainer.*

In terms of sample purity, this was assessed using the A260:A280 and A260:A230 ratio as determined with the NanoPhotometer. The common wavelength is based on the peak absorbance of nucleic acid at 260nm. Conversely, proteins and organic compounds with phenol groups absorb UV light strongly at 280nm, whilst organic compounds such as phenol, TRIzol and chaotropic salts absorb light at 230nm. As such, the A260:A280 ratio is used to determine protein contamination of RNA samples. Pure RNA samples would carry an A260:A280 ratio of around 2.0, with a lower ratio indicating contamination. The A260:A230 ratio, on the other hand, indicates organic contaminants of compounds described above. Values of less than 1.8 indicates marked contamination and is likely to adversely impact downstream processes including reverse transcription, although this is not required for the Nanostring application.

The A260:A280 ratio was overall satisfactory indicating no significant protein contamination, although heightened variance with samples treated with pre-condition 3 was noted (figure 7.12B). However, a markedly low A260:A230 ratio was seen across all samples (figure 7.12C). This indicates contamination with organic compounds which could include phenol, TRIzol and salts and will require addressing. Although not formally tested, guanidine thiocyanate contained within the lysis buffer of the AllPrep DNA/RNA Mini Kit lysis could be a source of contamination.

Based on these results, sample preparatory condition 2 (trypLE and mechanical disruption followed by serial cell strainers application without MACS) was selected for further testing. For future work, further optimisation to incorporate MACS would

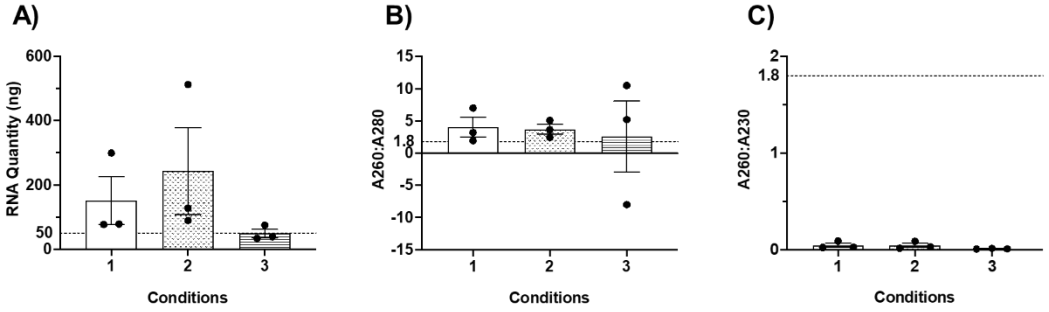

Figure 7.12 Experiment 4: RNA quantity and purity between three pre-conditions for RNA extraction. *Prior to RNA extraction, 3D monoculture models with chondrocytes were treated as follows: Condition 1 - sample treated with tryple and mechanical agitation. Condition 2 – sample treated as condition 1, with subsequent passage serially through cell strainers of 250μm and 70μm mesh sizes. Condition 3 – sample treated as condition 2, with subsequent positive cell selection with MACS using CD44. Mean±SEM is presented in A-C. N=3. A) RNA extracted were quantified using Nanodrop. Horizontal dotted line denotes RNA quantity of 50ng, which was the recommended amount for Nanostring application. B+C) RNA purity was assessed with nanodrop ratios A260:A280 and A260:A230, which are presented in B and C respectively. Horizontal dotted line denotes the minimum desired ratio value of 1.8.*

be beneficial due to the ability to cell sort and to isolate the chondrocyte and fibroblast cell populations for downstream assays. Due to time and resource constraints, the MACS strategy was not taken further. Cell dissociation is the procedural element most likely to impact the success of MACS. Alternative strategies for further testing may include alternative cell dissociation reagents, methods to dissolve cross-linked hydrogel and clinical tissue cell extraction protocols.

7.3.6 Experiment 5: Comparison of single versus double RNA elution

Experiment 5 entailed the testing of double-elution of RNA to achieve a higher yield as recommended as an optional step with the Qiagen AllPrep DNA/RNA kit (section 7.2.3.2.5). As anticipated, double elution increased RNA yield for all samples tested (figure 7.13A). The mean percentage increase in RNA quantity following double elution was 121.1%, with SEM of 53.8%. As such, this optional step was included in the optimised RNA extraction protocol as standard. The assessment of purity ratios A260:A280 and A260:A230 displayed little change before and after double elution (figure 7.13B/C). The need to reduce organics contamination remained, reflected by a low A260:A230, and are described in the next section.

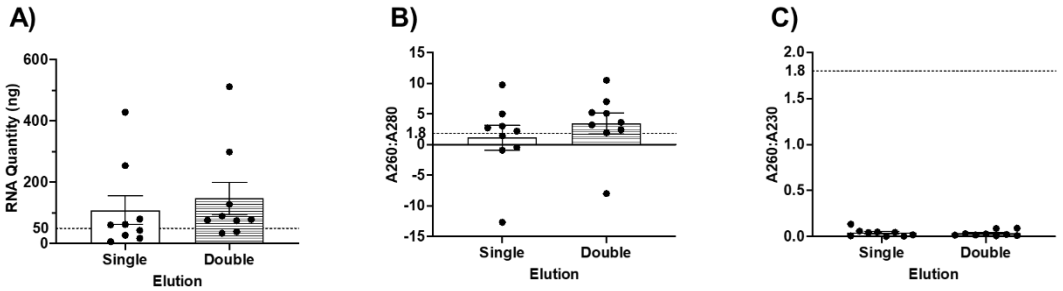

Figure 7.13 Experiment 5: single vs double RNA elution. *RNA extracted from 3D monoculture models with chondrocytes were evaluated by nanodrop before and after double elution. Mean±SEM is presented. N=9. A) RNA quantity in ng. Horizontal dotted line represents 50ng, the recommended amount for Nanostring application. B+C) A260:A280 ratio and A260:A230 ratios respectively. Horizontal dotted lines represent ratio value of 1.8, the minimum recommended value for RNA purity.*

7.3.7 Experiment 6: Ethanol precipitation

The effect of ethanol precipitation was assessed in experiment 6. This aimed to: i) increase RNA concentration, and ii) improve purity as measured by A260:A230. For the application of Nanostring, RNA concentration of 12ng/µl was required (total 60ng in 5µl). Whilst total RNA quantity from a single sample was sufficient, the RNA concentration was often less than 12ng/µl and below what was needed, therefore requiring concentration. Regarding RNA purity, the mean A260:A230 following

double elution was 0.03 (SEM 0.01). This was far below the ratio value of 2.0 expected of pure RNA, and with uncertain downstream impact against Nanostring application, required improvement.

Ethanol precipitation was successful in achieving both aims. Whilst an attrition of RNA quantity was seen, with a 3.1-13.3 percentage loss of RNA yield following ethanol precipitation (figure 7.14A), the required higher RNA concentration was achieved (figure 7.14B). An improved A260:A230 ratio was also realised, with no adverse changes to the A260:A280 ratio (figure 7.14C/D).

Experiment 6 concludes the series of tests for the optimisation of the RNA extraction process. In summary, an optimised sample preparation, RNA extraction and ethanol precipitation protocol was produced and is detailed in section 5.8.4.3 in the SOP in appendix 1. This protocol was used for all samples intended for Nanostring application, and was inclusive of all steps from the point of harvest and up to but not including quality control testing of samples which will be described next.

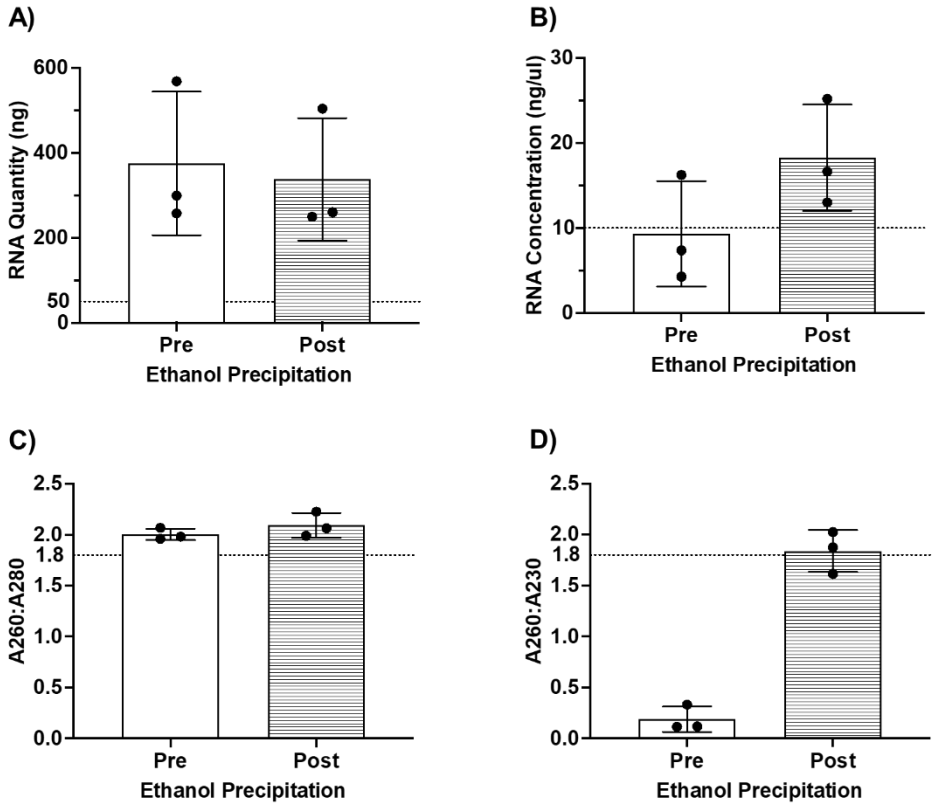

Figure 7.14 Experiment 6: effect of ethanol precipitation. *RNA extracted from 3D monoculture models with chondrocytes were evaluated by nanodrop before and after ethanol precipitation. Mean±SEM is presented. N=3. A) RNA quantity in ng. Horizontal dotted line represents 50ng, the recommended amount for Nanostring application. B) RNA concentration in ng/µl. Horizontal dotted line represents 10 ng/µl, the recommended concentration for Nanostring application. C+D) A260:A280 ratio and A260:A230 ratios respectively. Horizontal dotted lines represent ratio value of 1.8, the minimum recommended value for RNA purity.*

7.3.8 Trial of RNA extraction for HFF-1 3D monoculture model

With a finalised RNA extraction protocol based on experimental studies using the chondrocyte monoculture 3D model, the protocol was applied to the fibroblast monoculture model to determine its feasibility. A foreseen challenge was the low yield with fibroblast due to the ten-fold reduction in cell numbers between the two cell types in the co-culture model. The cell numbers seeded per pellet were $1x10^5$ for chondrocytes and $1x10^4$ for fibroblasts.

Following an initial non-detectable level of RNA with a single sample, the pooling of ten samples was tested. The RNA extraction as per the SOP was followed, except to reduce the number of spin columns used, the maximum volume of sample was added to the DNA and RNeasy spin columns. Nine RNA spin columns were used. RNA extracted from each RNeasy column were evaluated individually following the step of double elution. It was assessed with the NanoPhotometer only to reduce sample attrition. The results are shown in table 7.5. RNA quantity was variable across samples, with an inconsistent A260:A280 including multiple negative values which contrasts with past experience with chondrocytes. It was deemed that RNA quantity fell below the detection range of the NanoPhotometer yielding unintelligible results.

Table 7.5 RNA quantity and purity from fibroblast monoculture model assessed with Nanodrop.

RNeasy column	Concentration (ng/µl)	Quantity (ng)	A260:A280	A260:A230
1	0.32	12.8	0.615	0.003
2	1.32	52.8	6.60	0.005
3	2.20	88	-55	0.011
4	0.28	11.2	0.538	0.002
5	1.44	57.6	1.895	0.012
6	0.08	3.2	0.40	0.002
7	1.16	46.4	-5.80	0.02
8	0.52	20.8	-6.50	0.009
9	0.28	11.2	0.875	0.005

Therefore, the nine RNA samples were pooled, vortexed to mix and re-assessed with the NanoPhotometer. This yielded an RNA concentration of 1.08ng/µl in 310µl,

equating to a total of 334.8ng. Both purity ratios were sub-optimal with an A260:A280 of -6.75, and A260:A230 of 0.008.

Ethanol precipitation was then performed immediately with the pooled RNA sample. The resultant RNA pellet was much different to that extracted from the chondrocyte. The pooled fibroblast sample produced a larger pellet with a jelly-like appearance (figure 7.15), which required over 3 hours to air dry prior to re-constitution.

In order to achieve the desired RNA concentration of 10ng/µl required for Nanostring application, the RNA pellet was reconstituted in 20µl of RNase-free water. The resultant RNA was viscous, to an extent that it could not be reliably transferred using a 10µl pipette despite the use of reverse pipetting. Nonetheless, assessment with the NanoPhotometer demonstrated an RNA concentration of 2.32ng/µl, equating to 46.4ng, and A260:A280 and A260:A230 values of 2.32 and 0.095 respectively. However, multiple factors including the variable and sub-optimal purity ratios suggestive of the presence of contaminants, together with a low RNA quantity at the cusp of the NanoPhotometer's detection range, were expected to impact the accuracy of quantification with such a spectroscopy-based technique. Quantification using the Qubit RNA High Sensitivity assay, a more accurate fluorescence-based quantification techniques, showed non-detectable levels of RNA from the pooled sample.

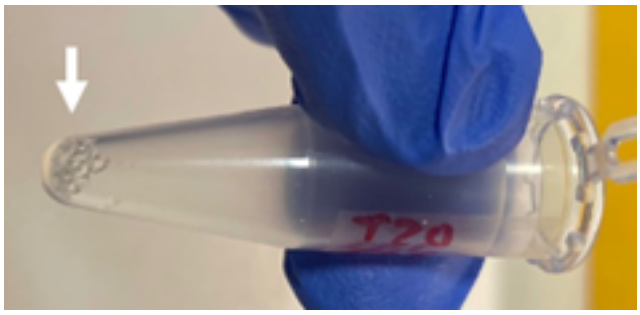

Figure 7.15 RNA pellet following ethanol precipitation prior to reconstitution. *Image illustrates the relatively large and viscous consistency of RNA pellet from pooled RNA samples from ten fibroblast monoculture 3D models. N=1.*

As such, a more sensitive fluorescence-based RiboGreen assay with a detection range of 0.1-5ng/µl, was used to quantify the RNA content of the pooled fibroblast sample. The RNA concentration of ten pooled fibroblast monoculture 3D *in vitro* models was 0.14ng/µl in 50µl, equating to 7.1ng, far below the recommend minimum quantity of 50ng for Nanostring applications. Therefore, it was concluded that it was not feasible

to extract RNA reliably from the fibroblast monoculture models and they were excluded from the gene expression testing with Nanostring.

7.3.9 Quality control evaluation of RNA samples for Nanostring

Table 7.6 and figure 7.16 summarises the QC data of the 60 samples used in the Nanostring assay. Overall, QC parameters following ethanol precipitation were all within the recommended range for use with Nanostring. There was sufficient quantity of RNA from each individual sample as quantified with the Qubit assay (figure 7.16B). The integrity of the RNA was very good with a RIN above 8 on average (figure 7.16C) and the DV200 far exceeded the recommended threshold from Nanostring of >50% (figure 7.16D). The purity of samples was also satisfactory and above 1.8 for both A260:A280 and A260:A230 (figures 7.16E/F).

Table 7.6 Quality control outcomes of RNA intended for Nanostring application. *Mean±SEM. N=3.*

		Ethanol precipitation	
		Pre-	**Post-**
Quantity (ng)	**Nanodrop**	722.3 ± 73.6	597.5 ± 63.4
	Qubit	-	673.3 ± 75.4
Integrity	**RIN**	-	8.5 ± 0.1
	DV200	-	92.6 ± 0.7
Purity	**A260:A280**	2.10 ± 0.02	1.96 ± 0.02
	A260:A230	0.21 ± 0.03	1.83 ± 0.05

The QC data for each sample used with Nanostring, including values pre- and post-ethanol precipitation are shown in figures 7.17, 7.18 and 7.19. A spread of RNA quantity was seen (figure 7.17B) which was not related to the duration of culture. Nonetheless, RNA extracted by the optimised protocol demonstrated good RNA integrity throughout. Contaminants affecting the A260:A230 purity ratio was much improved with ethanol precipitation, although there remained some variability (figure 7.19B).

Advice sought directly from Nanostring suggested that the assay is compatible with RNA of a wide range of quality conditions, with emphasis placed on standardisation of RNA input quantity and a minimum DV200 value of 50%. Increased input quantity

was recommended should DV200 falls below the recommended level, although this was not the case with the sample set (figure 7.18B).

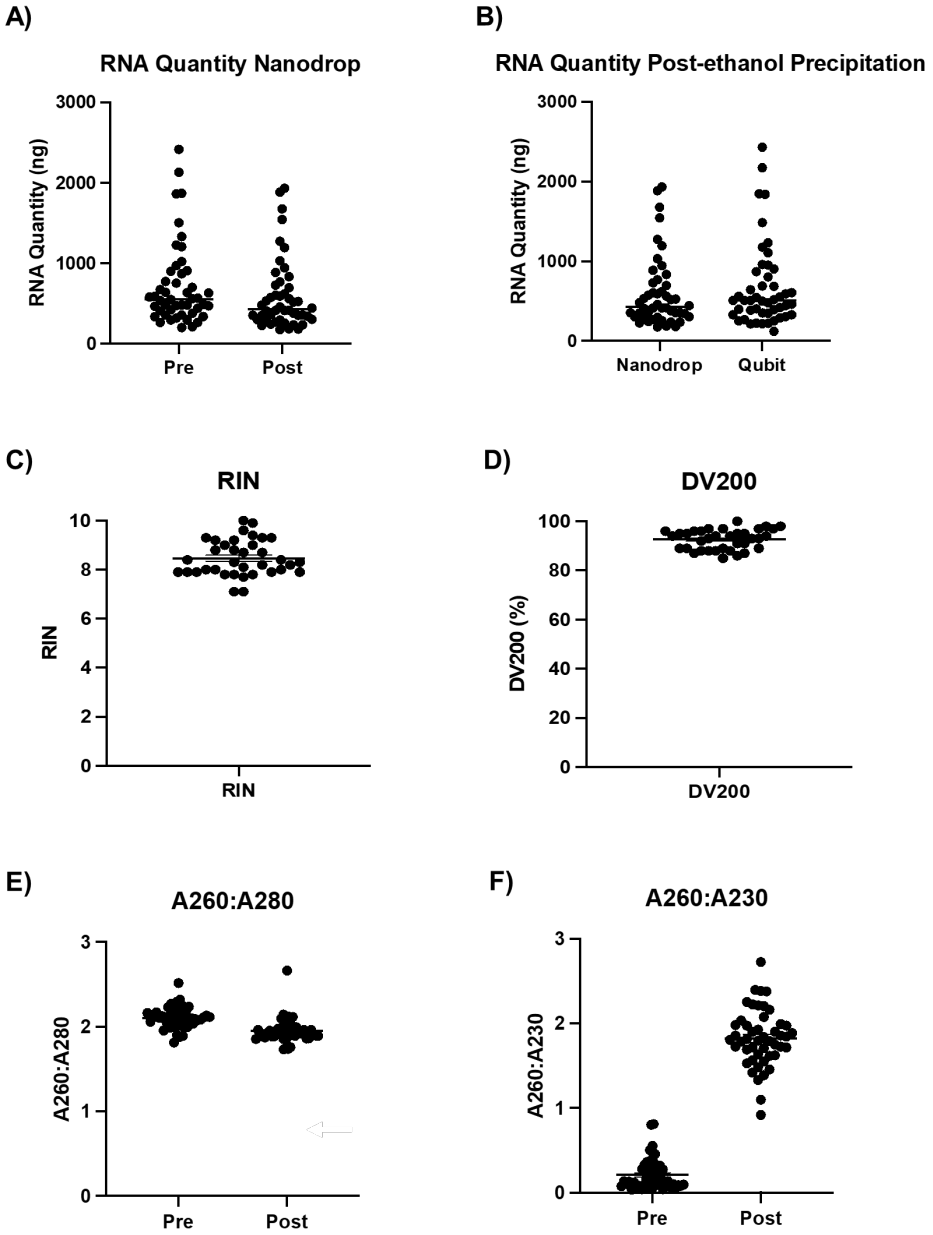

Figure 7.16 Quality control assessment of RNA samples for Nanostring application. *Samples include chondrocyte monoculture and co-culture with the addition of fibroblast, in ETC:Alginate:HA, covering timepoints day 1, 3, 5, 7, 14, 21. Mean±SEM is presented. N=3. A) RNA quantity in ng before and after ethanol precipitation, as measured by nanodrop. B) RNA quantity in ng following ethanol precipitation as measured with nanodrop and qubit assay. C) RNA Integrity Number (RIN) and D) DV200, both measured by Agilent 2000 bioanalyzer. E) A260:A280 and F) A260:A230, both measured by nanodrop.*

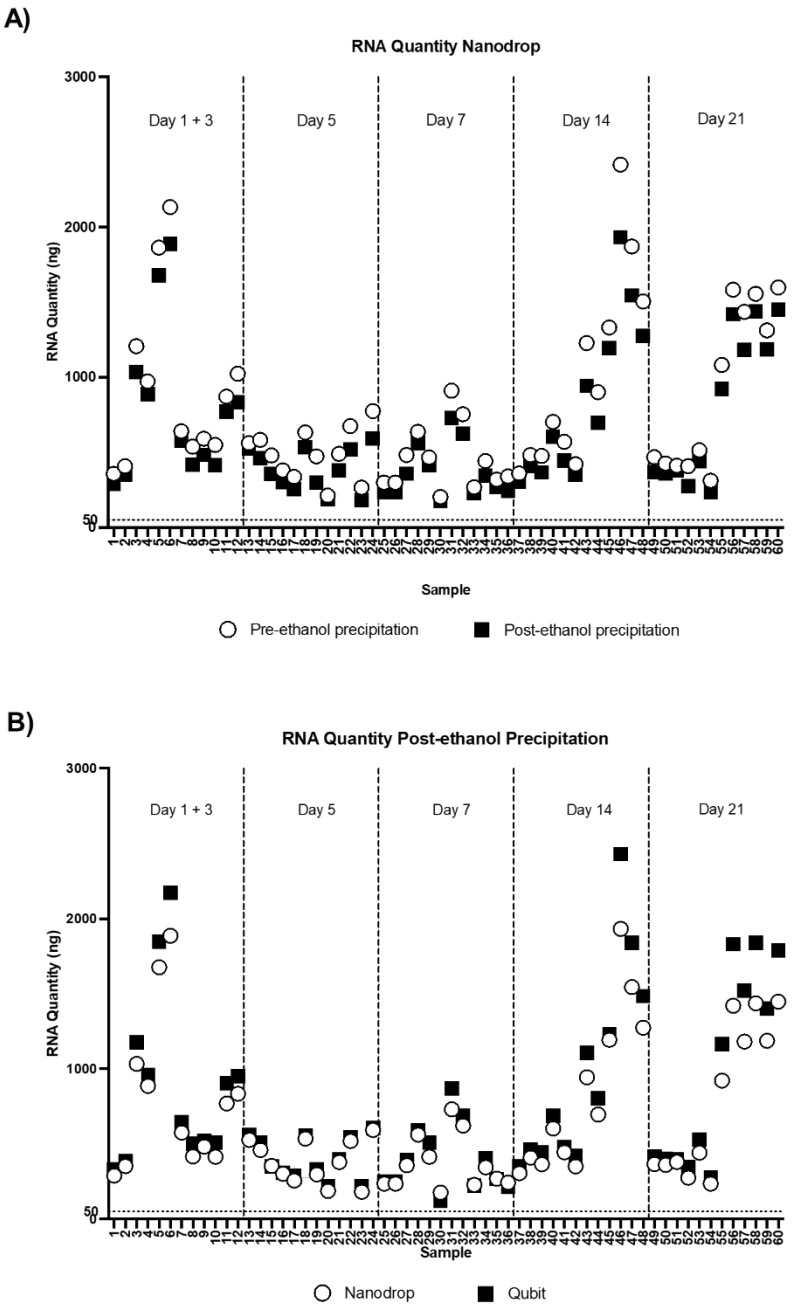

Figure 7.17 RNA quantification for Nanostring application. *Individual quantification values of all samples of RNA extracted from 3D in vitro models used in Nanostring is presented. Samples include chondrocyte monoculture and co-culture with the addition of fibroblast, covering timepoints day 1, 3, 5, 7, 14, 21 and 3 biological repetitions. A) RNA quantity in ng before and after ethanol precipitation, as measured by nanodrop. B) RNA quantity in ng following ethanol precipitation as measured with nanodrop and qubit assay. Horizontal dotted lines in A + B represent 50ng, the recommended amount for Nanostring application.*

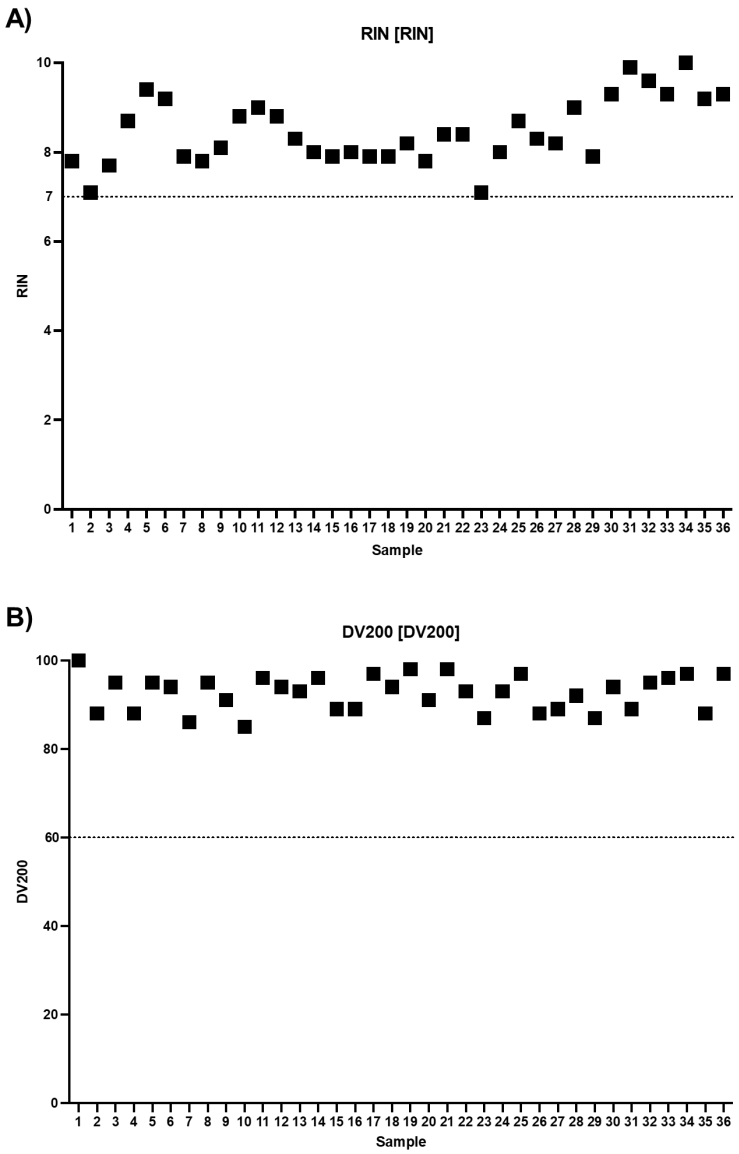

Figure 7.18 RIN and DV200 of RNA samples used in Nanostring*. Individual RNA integrity measurements of all samples of RNA extracted from 3D in vitro models used in Nanostring, following ethanol precipitation, is presented. Values were measured with the Agilent 6000 bioanalyser. Samples include chondrocyte monoculture and co-culture with the addition of fibroblast, covering timepoints day 1, 3, 5, 7, 14, 21 and 3 biological repetitions. A) RNA Integrity Number (RIN) is presented. Horizontal dotted line denotes RIN score of 7, above which reflects good quality RNA. B) DV200 is presented, where horizontal dotted lines represent 60% , the recommended minimum threshold for Nanostring application.*

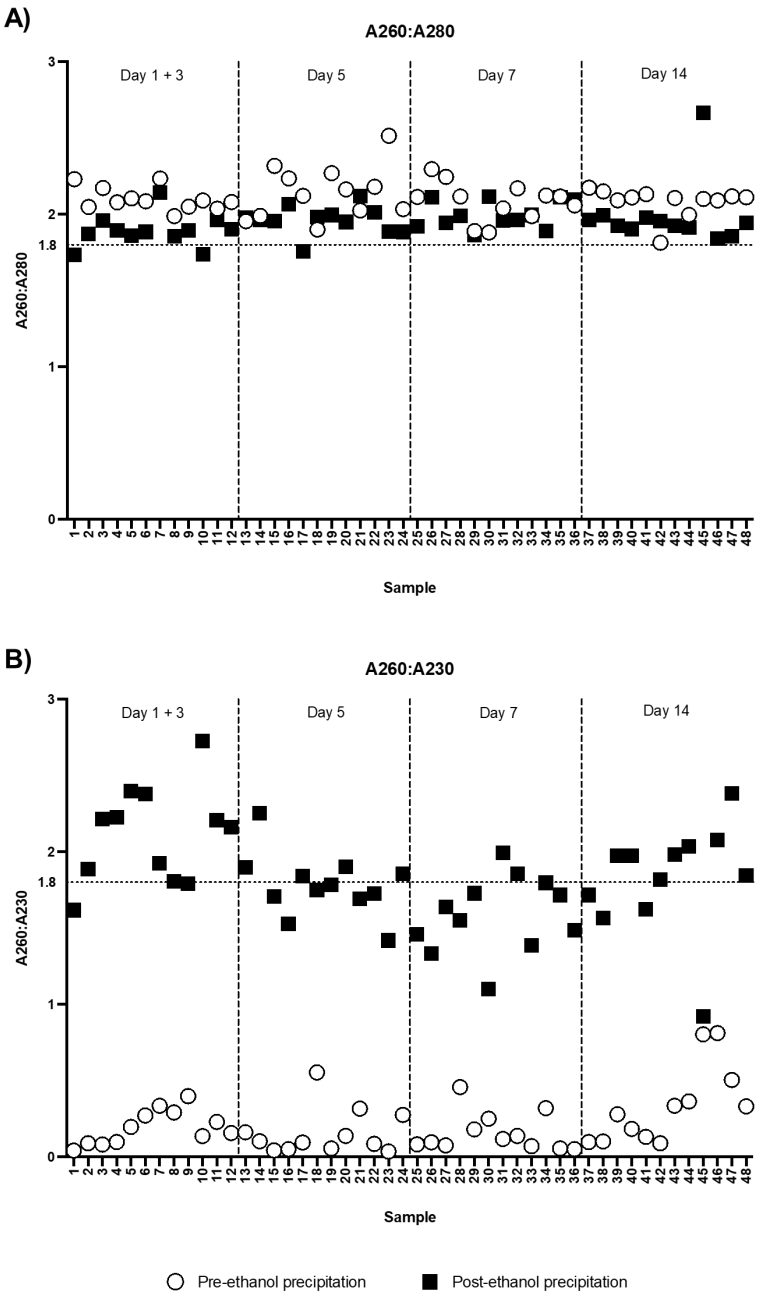

Figure 7.19 RNA purity assessment for Nanostring application. *Purity assessments, A260:A280m and A260:A230 measured by nanodrop, of all samples of RNA extracted from 3D in vitro models used in Nanostring, before and after ethanol precipitation, is presented. Samples include chondrocyte monoculture and co-culture with the addition of fibroblast, covering timepoints day 1, 3, 5, 7, 14, 21 and 3 biological repetitions. A) A260:A280 is presented. B) A260:A230 is presented. Horizontal dotted line denotes ratio value of 1.8.*

7.3.10 Differential gene expression analysis for global response assessment

The Nanostring IO360 panel assessed 770 genes across 25 biological functions as defined by Nanostring. Differential gene expression analysis was performed for the characterisation of the advanced 3D *in vitro* co-culture model in optimal culture media condition. Comparison was made of models in day 3 to day 21 of culture, compared to baseline on day 1. Seventy-seven DEGs were identified across the study period, representing 10% of all genes investigated. DEGs were visualised in volcano plots which demonstrated a clear trend of increasing numbers of both up and down-regulated DEGs over time, with up-regulated DEGs outnumbering those which were down-regulated throughout the timecourse study (figure 7.20).

To denote biological significance of the DEGs, it is helpful to consider the biological processes in which the DEGs were involved in. The Nanostring pathway scores offer a high-level overview of changes to genes within a pathway, although it is worth noting that the gene set per pathway was defined by Nanostring specific to the panel selected. Although the IO360 panel was geared towards the investigation of immune-oncology, it offered the maximum coverage of over 50 potential genes of interest identified from the literature relating to nanocellulose-based biomaterial for cartilage tissue engineering. Examination of the pathway scores revealed that the vast majority of pathways were enriched compared to baseline on day 1 (figure 7.21). This mirrors the dominance of up-regulated DEGs seen in the volcano plots (figure 7.20).

7.3.10.1 Nanostring pathway scores and pathway heatmap

Two pathways (cell proliferation and DNA damage repair) demonstrated initial negative pathway scores indicating reduced expression in the pathway genes during the acute timepoints. Cells in the advanced 3D *in vitro* model by default was subjected to much cell handling. This included trypsination for cell harvest from 2D culture, mechanical stress from mixing of the cell suspension with the bio-ink (in particular for chondrocytes) and chemical exposure to the cross-linker $CaCl_2$ during model creation. The reduced pathway score for cell proliferation on day 3 and day 5 when compared against day 1 may reflect the lag phase of cell growth where cells were acclimatising to the new culture condition following cell disturbance during model creation, and therefore demonstrating limited cell division. This is consistent with a relatively static

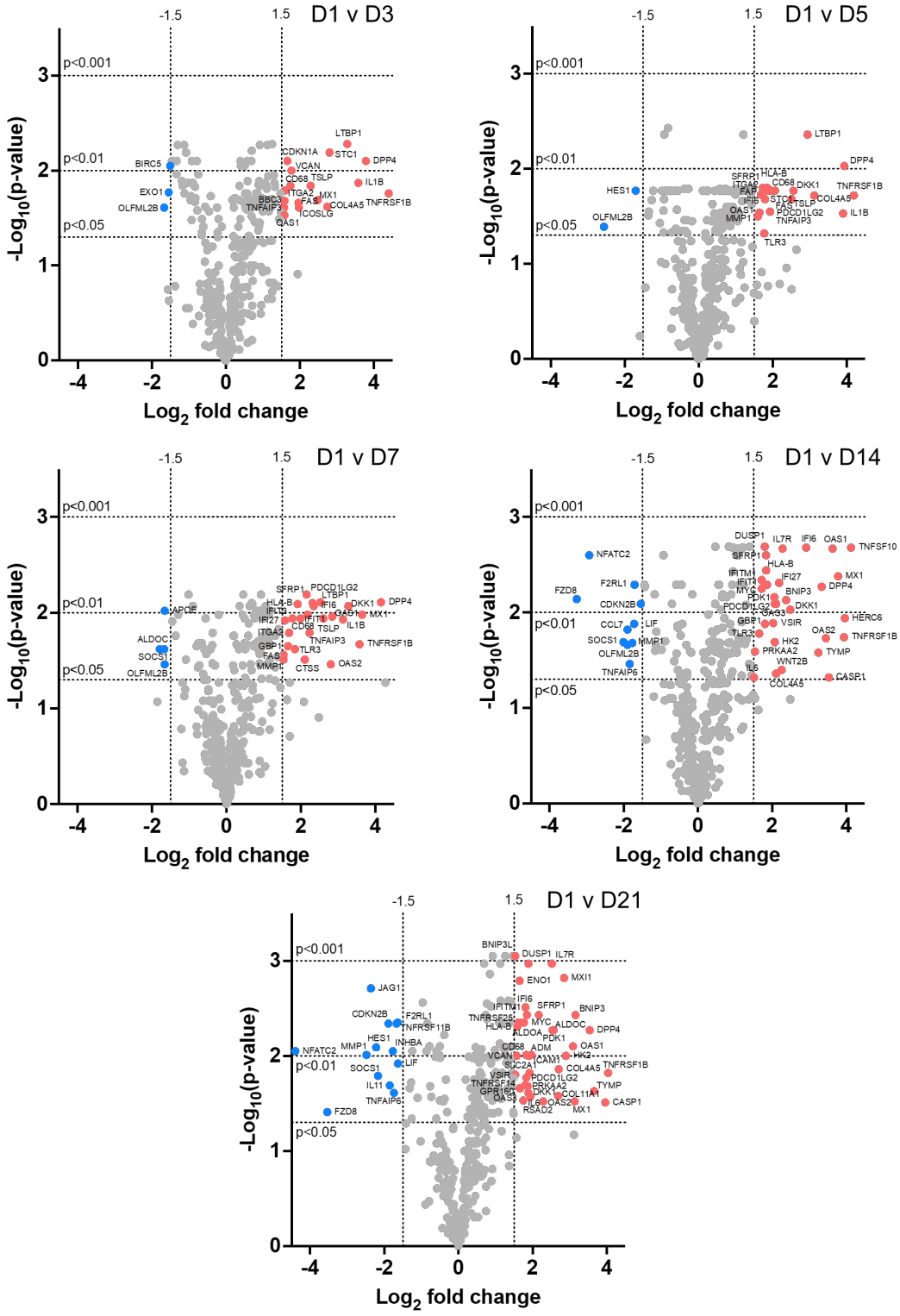

Figure 7.20 Differentially expressed genes in human chondrocytes and fibroblast in a nanocellulose-based advanced 3D in vitro co-culture model over 21 days. *Gene expression from day 3 to day 21 was compared against day 1 as baseline using the Nanostring nCounter® IO360 panel. Differentially expressed genes (DEGs) were defined as log2 fold change >1.5 (pink) or <-1.5 (blue) with a p_{adj} <0.05. Non-DEGs are illustrated in grey. Vertical dotted lines denote log2 fold change 1.5 or -1.5, and horizontal doted lines indicates a -log10 p value of 1.3 (p<0.05), 2 (p<0.01) and 3 (p<0.001). N=3.*

RFU on day 2 and 3 with the Alamar Blue assay from chapter 6 (figure 6.3). Similarly, the increased cell proliferation pathway score at latter timepoints mirrored the rise in RFU confirming increased cellular metabolic activity associated with cell proliferation.

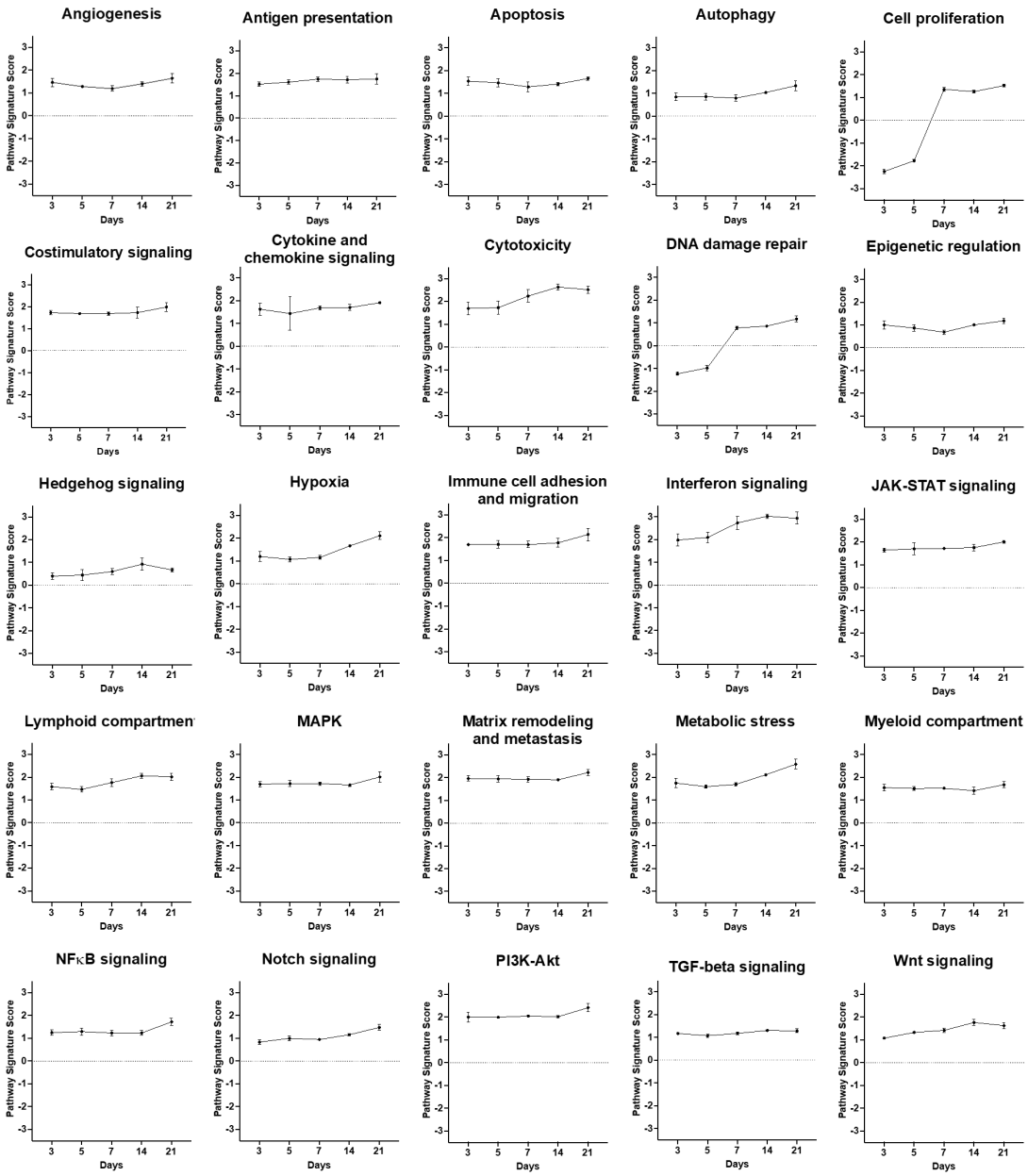

Figure 7.21 Pathway scores of advanced 3D in vitro co-culture model with chondrocyte and fibroblast over time. *Gene expression analysis was performed using the Nanostring nCounter IO360 panel. Day 3 to 21 were compared to baseline on day 1. Pathway scores were calculated as the first principal component of the normalised expression of genes of each pathway. Increased scores signify pathways most perturbed and indicates increased expression compared to baseline. Highlighted pathways denote those where DEGs represented >15% of genes in each pathway. N=3.*

Most pathways displayed a relatively flat trend in their pathway score over time, indicating that gene expression was increased from day 1 to day 3, but remained relatively consistent thereafter until day 21. However, pathway enrichment was seen with a rising pathway score at chronic timepoints (day 14-21) with cytotoxicity, hypoxia, interferon signaling and metabolic stress pathways. Table 7.7 ranks the 25 Nanostring pathways in accordance with the number of DEGs represented within each defined gene set. This further highlight JAK-STAT and co-stimulatory signaling as pathways of interest which were enriched at chronic timepoints. The matrix remodelling and metastasis pathway also contained a high number of DEGs and merits further investigation. As an *in vitro* model mimicking cartilage tissue engineering, increased gene expression relevant for ECM production is a desirable feature.

Table 7.7 Pathways ranked by the number of differentially expressed genes using the Nanostring IO360 panel. *Differential gene expression analysis was performed of day 3 to 21 against baseline on day 1. DEGs were defined as log2 fold change of >2.5/<-1.5. N=3.*

Pathway	**No. of DEGs**	**No. of genes in pathway**
Interferon signaling	14	64
Cytotoxicity	13	52
Lymphoid compartment	9	84
Metabolic stress	9	84
JAK-STAT signaling	8	58
Matrix remodelling + metastasis	8	55
Co-stimulatory signaling	7	88
Hypoxia	7	43
PISK-Akt	7	100
Immune cell adhesion and migration	6	88
Myeloid compartment	6	75
Wnt signaling	6	33

Pathway	**No. of DEGs**	**No. of genes in pathway**
Angiogenesis	5	35
Apoptosis	5	38
Cell proliferation	5	50
Cytokine and chemokine signaling	4	96
MAPK	4	76
NK-κB signaling	4	38
TGF-β signaling	4	21
Antigen presentation	3	61
Notch signaling	3	25
Autophagy	2	23
DNA damage repair	1	34
Epigenetic regulation	1	17
Hedgehog signaling	1	21

To further contextualise the observed DEGs, a heat map was created to simultaneously display their up- or down-regulation over time and groupings based on the Nanostring pathways (figure 7.22). Each small square represents a single sample, with three biological replicates per timepoint. Overall, the data displayed a good degree of

consistency across biological replicates, with Wnt2B showing greater variability on day 5.

The DEGs involved in the four pathways which displayed increased pathway scores at chronic timepoints was considered next with respect to the pathway heatmap. It was interesting to note that DEGs relevant for interferon signaling displayed maximal up-regulation around day 7 and 14, heralding that seen in cytotoxicity, hypoxia and metabolic stress on day 14 and 21. At even earlier timepoints, DEGs in the co-stimulatory signaling and JAK-STAT signaling pathways were noted to be most up-regulated between day 3 and 7.

Whilst the majority of DEGs within the cytotoxicity, hypoxia and metabolic stress pathways were up-regulated at chronic timepoints, a handful of DEGs were up-regulated in the acute period (day 3-5) suggestive of varying mechanistics at play between the acute and chronic time period. Such DEGs included *LIF*, *BBC3*, *CDKN1A* and *CDKN2B* (figure 7.22).

7.3.10.2 Influence of time on DEGs

Therefore, to better visualise the influence of time on all DEGs identified across the 21 day study period, DiVenn, a web-based visualisation tool was used to create a modified version of a Venn diagram to illustrate how DEGs clustered based on time. Unsurprisingly, the largest clusters were found on day 14 and 21, and day 21 alone (figure 7.23). Of the 77 DEGs, only three genes were consistently differentially expressed throughout the 21 day study period. The majority (39 out of 77) were differentially expressed only at chronic timepoints (day 14 + 21). A relative minority was differentially expressed acutely between day 3 and day 7 (16 out of 77), with the remaining 19 DEGs variably differentially expressed across the 21 days. It was also observed that only 2 out of 77 DEGs were variably up- and down-regulated over time, leaving the vast majority being consistently up- or down-regulated throughout the study period when deemed statistically significant. Taken together, this indicates that different biological processes were activated or at play at different times with a clear distinction between acute and chronic timepoints.

Thus far, the high-level overview and data visualisation served to identify several

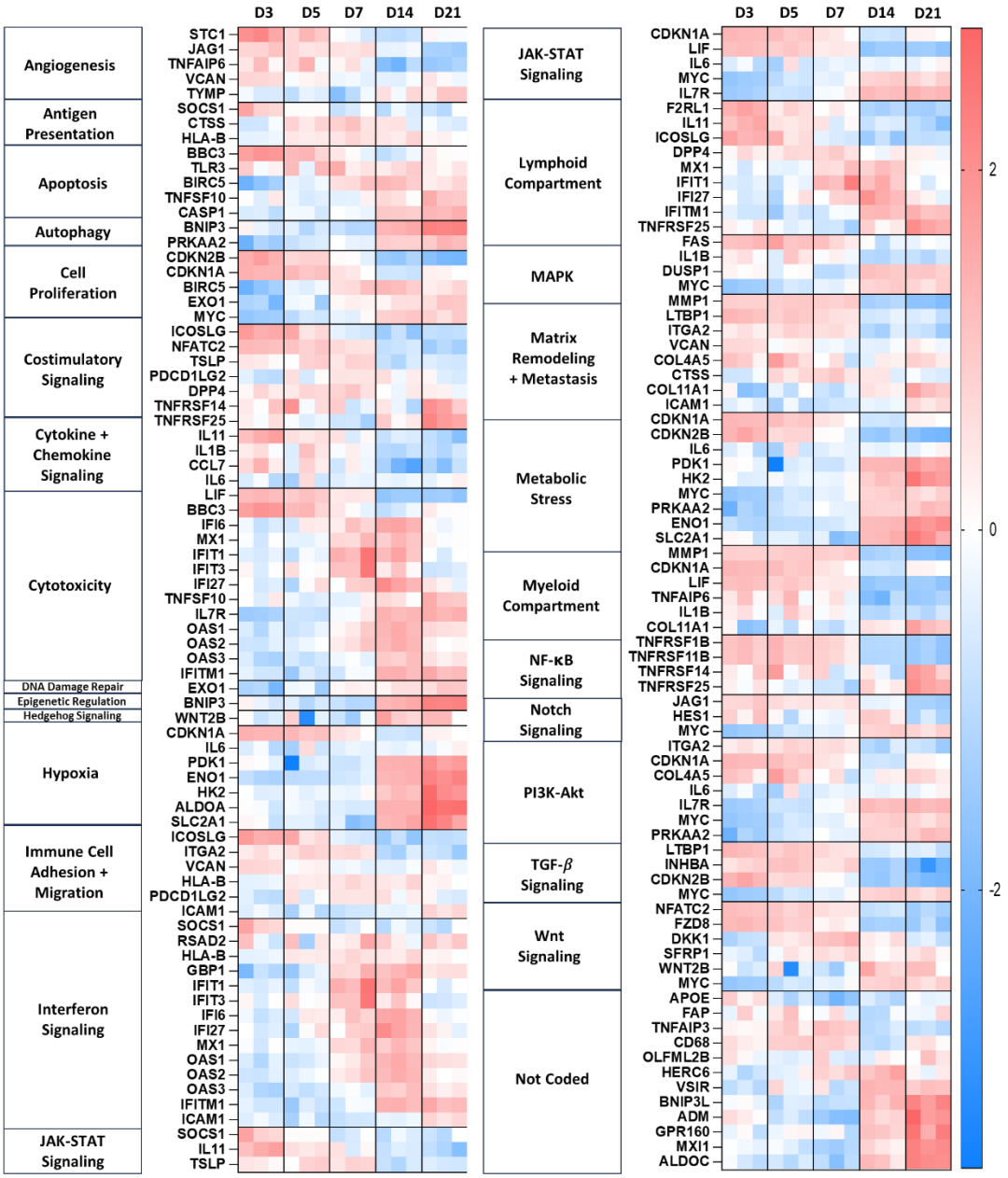

Figure 7.22 Heatmap of differentially expressed genes (DEGs) with human chondrocytes and fibroblast in a nanocellulose-based advanced 3D in vitro co-culture model over 21 days. *The advanced 3D in vitro model consists of human chondrocyte(C20A4)-encapsulated and human fibroblast(HFF-1) surface-seeded cross-linked nanocellulose-based bio-ink with alginate and hyaluronic acid additives. Gene expression from day 3 to day 21 was compared against day 1 as baseline using the Nanostring nCounter®Analysis System. Differentially expressed genes (DEGs) were defined as log2 fold change >1.5/<-1.5 with a p_{adj} <0.05, and presented as z-scores and functionally annotated in accordance with the Nanostring IO360 panel. Red indicates up-regulation and blue represents down-regulation. N=3.*

biological functions including interferon signaling, cytotoxicity, hypoxia and metabolic stress as enhanced on day 14 and 21 as compared to baseline on day 1. Expression of genes relevant to cell proliferation was found to be reduced on day 3-5 prior to an increase at latter timepoints, corroborating with cell metabolic data indicating enhanced cell proliferation between day 7-21. The matrix remodelling and

metastasis pathway was also enriched, which may be of particular relevance with regards to ECM production in cartilage regeneration.

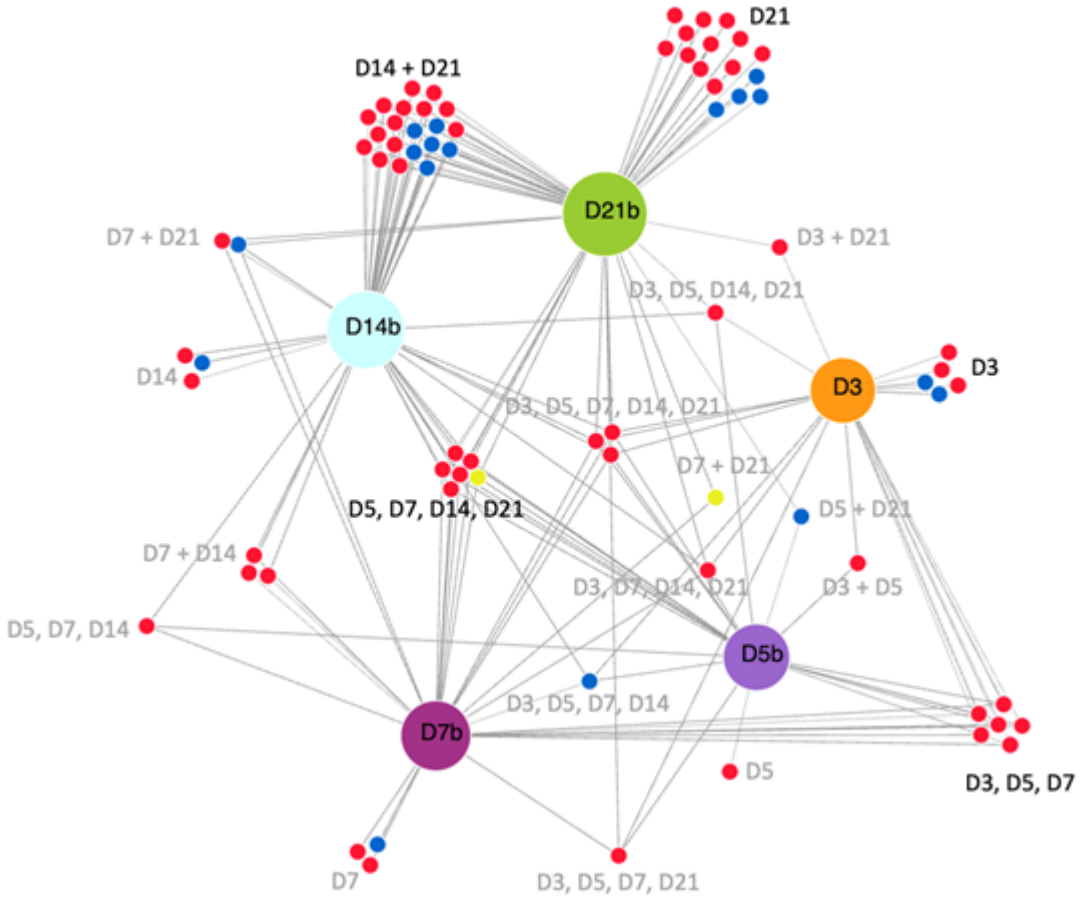

Figure 7.23 Overlapping differentially expressed genes in advanced 3D in vitro co-culture model across time. *Gene expression from day 3 to day 21 were compared against day 1 as baseline using the Nanostring nCounter IO360 panel. Red denotes up-regulated DEGs, blue for down-regulated and yellow for up- and down-regulated DEGs. Each cluster denotes a common set of DEGs across specified timepoints. Clusters of ≥5 DEGs are highlighted in bold.*

7.3.10.3 Functional enrichment analysis

To further derive biological significance from the differential gene analysis, functional enrichment analysis was performed against the 77 DEGs in the forms of an over-representation analysis (ORA), as well as an exploration of relevant protein-protein interactions using the STRING database. This approach differs from the analysis of the Nanostring pathway scores where the gene sets of each pathway were defined by and therefore limited to what was selected by Nanostring to represent the condition or biological process of interest. In contrast, the ORA and STRING analysis draws from a multitude of data sources of known biochemical maps. Key data sources include Gene Ontology (GO), the Kyoto Encyclopedia of Genes and Genomes (KEGG), Reactome and WikiPathways. This is a common approach for high-throughput omics

studies, such as RNA-sequencing. However, due to the limited number of genes investigated with Nanostring (770 versus hundreds of thousands in a transcriptome), the volume of DEGs input from this study was relatively less. As such, it was not feasible to clearly delineate exact mechanistics or biological pathways activated in the advanced 3D *in vitro* model due to insufficient data input to fully characterise a biochemical pathway. Nonetheless, the ORA and STRING analysis highlights and focuses the biological processes of interest in greater detail compared to what could be offered by the Nanostring pathway score alone.

Considering the protein-protein interactions first with STRING analysis, five GO biological processes terms were aligned with the DEGs from the co-culture model. These confirmed pathways of interest identified based on the Nanostring pathway scores, and narrowed the relevant biological processes, highlighting genes of interest.

Whilst the Nanostring pathway score highlighted interferon signaling as enhanced during intermediate timepoints (day 7-14), the STRING analysis further focuses the relevant GO term to 'response to type I interferon' (figure 7.24), with 10 DEGs highlighted *via* STRING largely corresponding with those in the Nanostring pathway. The STRING analysis also suggests the extrinsic apoptosis pathway as a possible mechanism for cytotoxicity, although this was based on four DEGs amongst which there were no direct protein-protein interaction (figure 7.24), and therefore should be interpretated with caution. Hypoxia was another biological term dually highlighted in the STRING analysis and Nanostring pathway scores. All six DEGs identified *via* STRING were up-regulated at the chronic timepoints to suggest that the effect or response to hypoxia was limited to day 14 - 21 of culture.

Finally, the STRING analysis revealed two further GO terms related to cell signaling, in addition to type I interferon. These were tumour necrosis factor and cytokine-mediated signaling. All of which have a role in influencing a range of physiological processes including cell proliferation, apoptosis, inflammation and modulation of immune responses.

Whilst the scope of the STRING analysis focused on protein-protein interactions, both direct (with physical binding) or functional (without), the ORA examined more broadly the potential biological inference of DEGs without limiting this to PPIs solely. Up- or down-regulated DEGs were used as input, and the ORA statistically examines

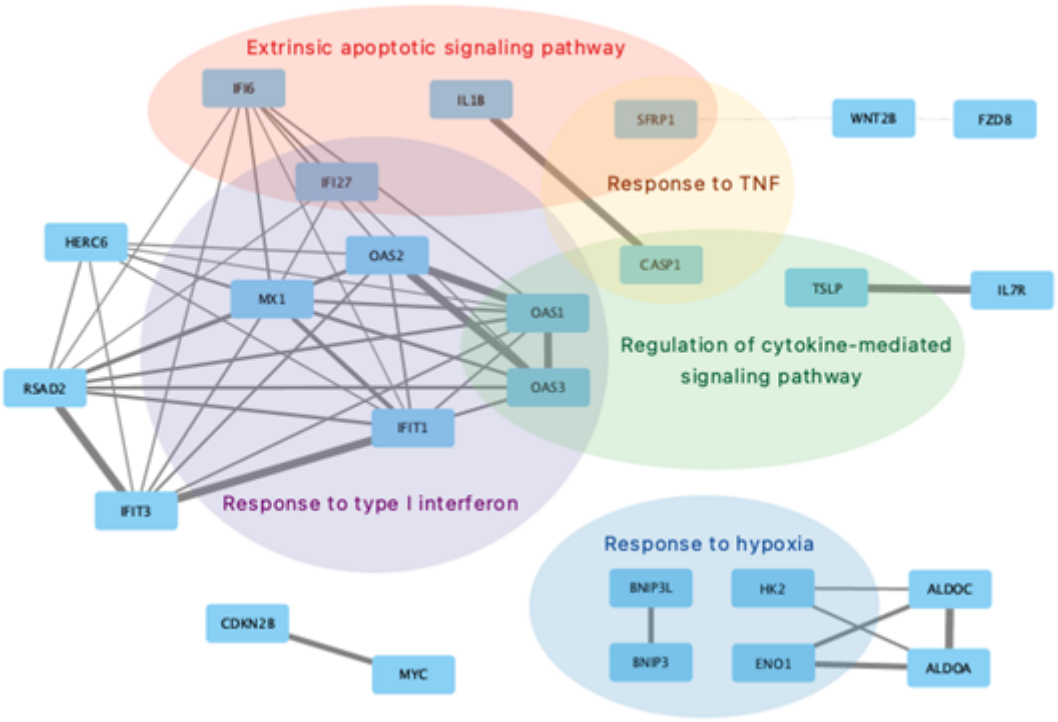

Figure 7.24 Protein-protein association networks from differentially expressed genes in the advanced 3D in vitro co-culture models of nanocellulose-based bio-ink. *DEGs were analysed using the STRING database which demonstrates known and predicted functional and physical protein-protein interactions (PPI). Linkage line thickness reflects the 'combined' score of interactions, with thicker lines indicating stronger probability of interaction. Gene Ontology (GO) terms were mapped to PPIs using ClueGO with Cytoscape to aid biological interpretation.*

for differentially expressed components of a vast range of biological pathways based on databases including the Gene Ontology (GO).

The Gene Ontology Consortium is a major bioinformatics initiative which provides a framework to represent gene and gene products with ordered and defined vocabularies. As the largest information source on the functions of genes, there are over 40,000 GO terms across three domains eloquently described by Huntley *et al*: *"1) molecular functions a gene product performs, 2) the biological processes it is involved in, and 3) the cellular components it is located in"*[335].

Although the ORA yielded numerous potential biological terms of interest based on the initial ORA output with the g:Profiler (figure 7.25A), closer inspection of DEGs overlaid with biochemical maps such as the KEGG pathway found too few DEGs represented per pathway to derive meaningful conclusions (data not shown). This is reflected by low intersection ratios ranging between 0.008 and 0.044 across both up- and down-regulated DEGs (figure 7.25B). The exception was the GO term 2'-5'-oligoadenylate synthetase activity with an intersection ratio of one. This means 100%

of the gene set for this GO term was represented by the DEGs, and it will be further discussed subsequently.

Regarding GO terms dominating the ORA output, the top 10 GO terms were defined, with the application of ReviGO to condense redundant terms (figure 7.25B). The common themes identified from the Nanostring pathway scores, STRING analysis and ORA were cytokine signaling (in particular, type I interferon and tumour necrosis factor), apoptosis, hypoxia (or response to oxygen levels) and extracellular matrix. All of which were up-regulated. Down-regulated DEGs formed the minority of DEGs identified from the co-culture model (17 out of 77), with the top 10 GO terms illustrated in figure 7.25B. They carried similarly low intersection ratios and cytokine activity and responses also featured as a key theme.

Exploring deeper into individual DEGs, the effect of culture media conditions, and the influence of fibroblast in the co-culture model as compared to the chondrocyte 3D monoculture were further examined.

7.3.10.4 Gene expression analysis of cytokine signaling

Gene functions were consulted *via* the GeneCards database unless specifically referenced. GeneCards is an online database with vast coverage of tens of thousands of genes coupled with gene-specific information integrating multi-sources including genomics, transcriptomics, proteomics and clinical data[336].

7.3.10.4.1 Interleukin-6

Gene expression for IL-6, relevant to the pro-inflammatory response, was first examined. IL-6 demonstrated congruence between the elevated levels of IL-6 release measured with ELISA and gene expression on day 14 and 21 (figures 6.10 + 7.26A). Although the rise in *IL-6* expression only reached statistical significance at chronic timepoints, the log2 fold change was relatively elevated at around 1.5 throughout the study period. This suggests that the co-culture model was activated in a pro-inflammatory state throughout the 21 days, with an increasing magnitude observed over time. The effect of culture media conditions was also found to have a statistically significant impact. Unsurprisingly, the optimal culture media condition (i.e. full media exchange every 2-3 days) was associated with reduced levels of *IL-6* expression, especially at chronic

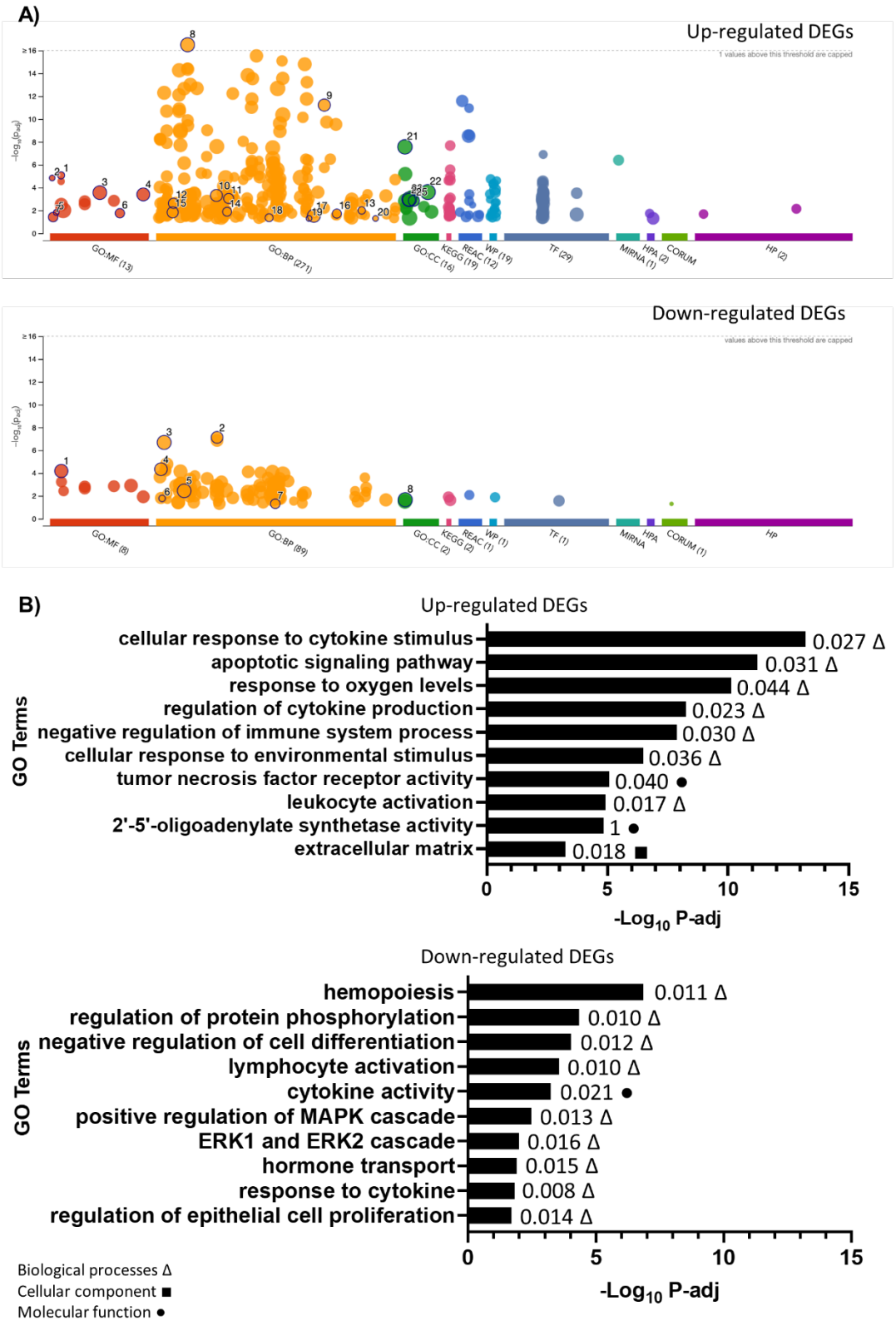

Figure 7.25 Over-representation analysis of differentially expressed genes in the advanced 3D in vitro co-culture model. *A) Graphical representation of ORA output using up- and down-regulated DEGs performed with g:Profiler. B) Top 10 GO terms identified by ORA and condensed with ReviGO with the removal of redundant GO terms. Negative log10 adjusted p value of 1.3 represents an adjusted p value of 0.05, 2 (p=0.01) and 3 (p=0.001). The intersection ratio of each DEG is specified with each GO term. Δ/■/● denote the GO term category as defined in the figure legend.*

timepoints. This was seen with both the chondrocyte monoculture and co-culture models. This highlights that insufficient nutrients and persistence of cellular waste products promoted a pro-inflammatory response. In contrast, when comparing the monoculture and co-culture models, although some variation was detected over time in both culture media conditions, statistical significance was not reached. This may be due to the relative low cell concentration of fibroblasts to effect a measurable change in gene expression, especially in the absence of cell isolation to interrogate gene expression specific to each cell type. Moreover, this may also indicate that the cell-cell interactions between chondrocytes and fibroblasts in the co-culture model did not yield detectable levels of changes in the gene expression of chondrocytes.

7.3.10.4.2 Ligand-receptor pairs

When considering intercellular signaling, the ligand-receptor pair is a well-established class of interaction which could be examined based on gene co-expression[337]. Armingol *et al* described the inference of cell-cell interactions based on activities of paired gene expression, with the 'sender' cell displaying gene expression for the ligand and the 'receiver' cell showing gene expression of the relevant receptor. Interactions between different cells could be in the manner of paracrine, juxtacrine or endocrine signaling.

The interleukin 6 receptor (*IL-6R*) encodes the sub-unit of the IL-6 receptor complex. Its gene expression levels remained static throughout the study period with no significant change over time, between culture media conditions, nor between monoculture and co-culture systems (figure 7.26C/D). Taken together with the elevated levels of IL-6 in terms of both gene expression and the measured cytokine, this data could reflect that IL-6 did not act in an autocrine manner, i.e. it did not induce a cellular response on the same cell. This is in line with the understanding that *IL-6R* expression is limited primarily to hepatocytes and some immune cells, thereby directing the actions of IL-6[338].

7.3.10.4.3 Interleukin-11 and transforming growth factor-beta

The difference in gene expression between ligand and receptor was similarly observed with interleukin-11 (*IL-11*) and its receptor subunit alpha (*IL-11RA*). A statistically

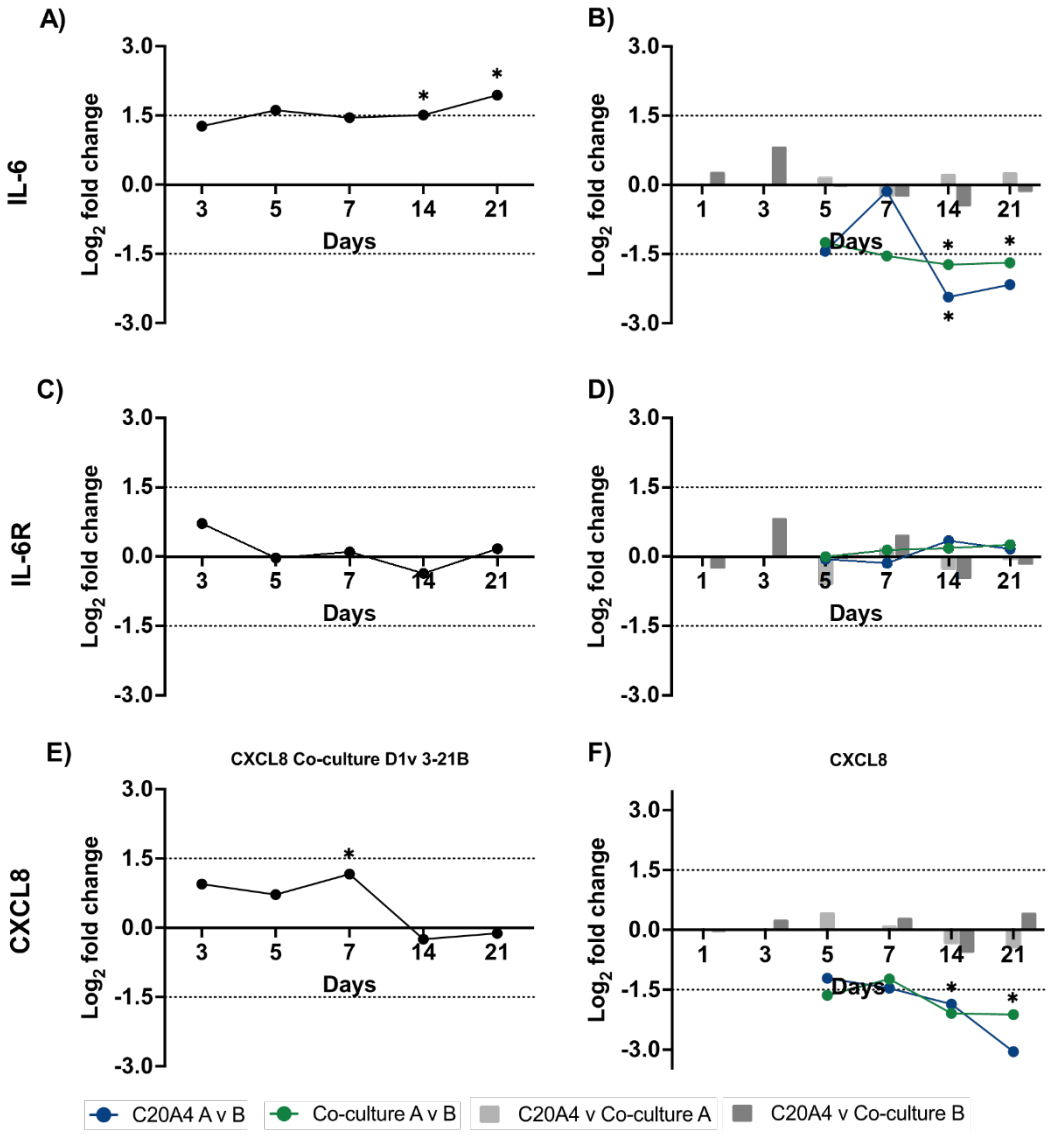

Figure 7.26 Change in gene expression of pro-inflammatory cytokines and its receptor over time. *Differential gene expression was examined in advanced 3D in vitro models using the Nanostring IO360 panel. Log2 fold change for: A+B) interleukin-6 (IL-6), C+D) IL-6 receptor (IL-6R), and E+F) CXCL8 (IL-8) are shown representing 3 biological replicates. Timepoint comparisons between day 3-21 against day 1 as baseline in the co-culture model in optimal culture media condition are shown on the left. Culture media conditions representing augmented regime (A) versus optimal regime (B), and chondrocyte monoculture versus co-culture with fibroblast in both culture media conditions were compared at each timepoint on the right. Statistical significance is denoted by * ($p<0.05$) and the horizontal dotted lines represent log2 fold change of >1.5 or <-1.5.*

significant reduction in *IL-11* expression was observed on day 14 and 21, but not with *IL-11RA* (figure 7.27A-D). First isolated in 1990, IL-11 is a member of the IL-6 cytokine family, with an as yet unclear physiological function[339]. Recent discoveries hint at its pleiotropic effects upon multiple tissue types with both pro- and anti-inflammatory properties and a regulatory role in tissue homeostasis [339-342]. The biological relevance of IL-11 on chondrocyte function are currently actively investigated with a focus on articular chondrocytes. Articular chondrocytes were found to release IL-11 when induced by transforming growth factor-beta 1 (TGF-β1)[343, 344].

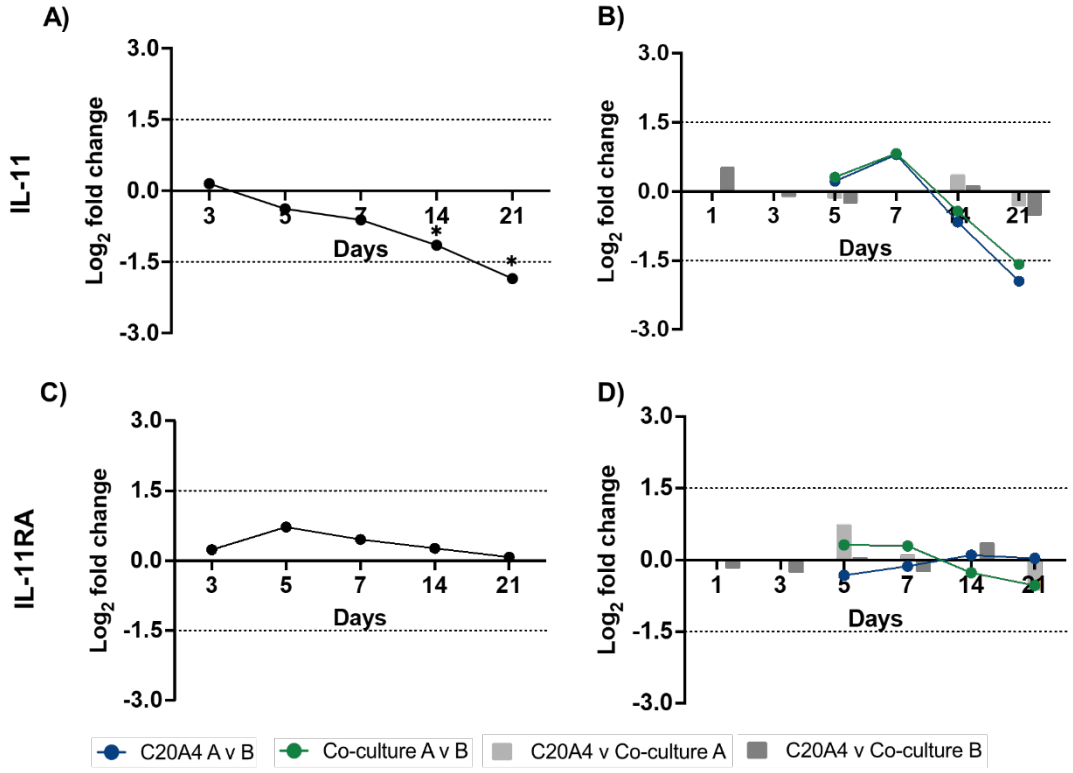

Figure 7.27 Change in gene expression of IL-11 cytokine-receptor pairs over time. *Differential gene expression was examined in advanced 3D in vitro models using the Nanostring IO360 panel. Log2 fold change for: A+B) interleukin-11 (IL-11) and C+D) IL-11 receptor subunit alpha (IL-11RA). Timepoint comparisons between day 3-21 against day 1 as baseline in the co-culture model in optimal culture media condition are shown on the left. Culture media conditions representing augmented regime (A) versus optimal regime (B), and chondrocyte monoculture versus co-culture with fibroblast in both culture media conditions were compared at each timepoint on the right. Statistical significance is denoted by * ($p<0.05$) and the horizontal dotted lines represent log2 fold change of >1.5 or <-1.5.*

Cell-specificity in the expression of the receptor gene *IL-11RA* by chondrocytes and bone cells (osteoblasts, osteocytes and osteoclasts) potentially indicates the essential role of IL-11 in joint physiology and diseases and its function in an autocrine manner[342, 345]. Patients with osteoarthritis were found to have high levels of IL-11 in their joint synovial fluids, with primary chondrocytes from such patients strongly influenced by IL-11 with the potent activation of the Jak/STAT3 signaling pathway[343]. However, as mentioned, the mechanism of action of IL-11 remains to be elucidated. An earlier study by Maier *et al* found that chondrocytes stimulated by IL-11 demonstrated an enhanced production of the tissue inhibitor of metalloproteinases and therefore infers a potential protective role against ECM degradation[344].

Given the action of TGF-β1 as an inducer of IL-11 production, genes relevant to TGF-β in the advanced 3D *in vitro* model were examined. The expression of *TGF-β1* was

found to be statistically significantly reduced throughout the study when compared to baseline on day 1, although it did not reached the threshold of log2 fold changes to be considered a DEG (figure 7.28A). TGF-β1, TGF-β2 and TGF-β3 are isoforms transcribed from different genes and chromosomes, but acts on the same receptor and signaling pathways[346]. TGF-β is a multi-functional cytokine expressed by most cell types, with broad regulatory effects influencing cellular processes such as cell cycle progression, differentiation and migration, as well as tissue and immune homeostasis including bone formation, angiogenesis and haematopoiesis [347, 348]. In the context of wound healing, its therapeutic role has been tested in multiple studies demonstrating accelerated wound healing with its topical or systematic applications[347].

Current evidence suggests that TGF-β1 and TGF-β2 carries pro-fibrotic effects, with neutral or anti-fibrotic actions conferred to TGF-β3[346, 349]. In the current study, the gene expression of the three isoforms of TGF-β were variably expressed, with statistically significant changes seen with *TGF-β1* and *TGF-β2*, although this was within the threshold of log2 fold change of 1.5 to -1.5. Such effects were unperturbed by culture media conditions (figure 7.28A-F). On the other hand, *CDKN2B* and *IHNBA* were two DEGs identified in the co-culture model with relevance to TGF-β. *CDKN2B* encodes a cyclin-dependent kinase inhibitor, serving to control cell cycle G1 progression. It is dramatically induced by TGF-β, and may have a role in TGF-β-induced growth inhibition. The expression of this gene was significantly reduced at chronic timepoints, with culture media conditions producing a low level but statistically significant effect (figure 7.28G+I). Whilst there is insufficient data to visualise entire biochemical pathways, the reduced expression of *CDKN2B*, a TGF-β-induced growth inhibitor, was observed in parallel to a rise in cell proliferation at chronic timepoints (figures 6.2 + 6.3). Furthermore, *INHBA*, which encodes a member of the TGF-β superfamily of proteins, was significantly augmented at chronic timepoints in the co-culture model in optimal culture media condition (figure 7.28 H+J). *IL-11*, *CDKN2B* and *INHBA* as DEGs, as well as the statistically significant altered gene expression of *TGF-β1* and *TGF-β2*, revealed commonality of maximal gene expression augmentations at chronic timepoints. Their shared occupation in the TGF-β signaling pathway together with the relevance of TGF-β in wound healing and fibrosis, which has a keen implication in the function of tissue engineered cartilage

implants *in vivo*, would suggest that this may be an area of interest for further exploration.

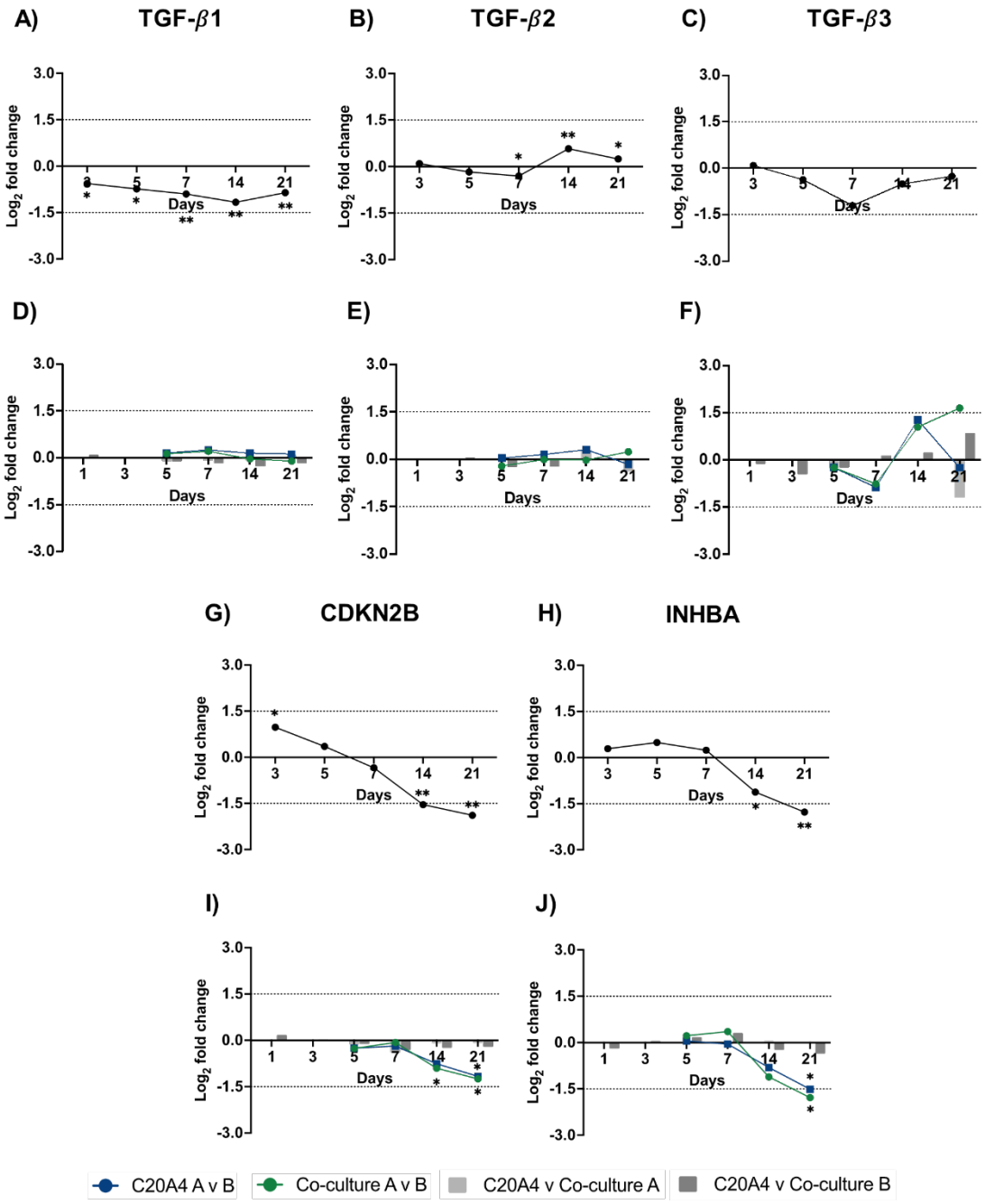

Figure 7.28 Change in gene expression of TGF-β-relevant genes over time. *Differential gene expression was examined in advanced 3D in vitro models using the Nanostring IO360 panel. Log2 fold change for: A+D) transforming growth factor-β1 (TGF-β1), B+E) TGF-β2, C+F) TGF-β3, G+I) cyclin dependent kinase inhibitor 2B (CDKN2B), and H+J) inhibin subunit beta A (INHBA). Timepoint comparisons between day 3-21 against day 1 as baseline in the co-culture model in optimal culture media condition are shown in A-C and G-H. Culture media conditions representing augmented regime (A) versus optimal regime (B), and chondrocyte monoculture versus co-culture with fibroblast in both culture media conditions were compared at each timepoint in D-F and I-J. Statistical significance is denoted by * ($p<0.05$) and the horizontal dotted lines represent log2 fold change of >1.5 or <-1.5.*

7.3.10.4.4 Interleukin-8

In contrast to *IL-6*, *CXCL8* which encodes IL-8 was not a DEG in the co-culture model. A statistically significant rise in its gene expression was witnessed on day 7, before its decline back to baseline level on day 14 and 21 (figure 7.26E). This is an interesting finding as it contrasted with the measured levels of IL-8 using ELISA, which demonstrated a time-dependent response with rising cytokine levels detected over time (figure 6.11B). Notably, figure 6.11B illustrates IL-8 levels in the co-culture model in the augmented culture media condition with reduced media exchange, whilst figure 7.26E belonged to the co-culture model with optimal culture media conditions. Examining the effects of culture media conditions revealed similar effects to those seen with *IL-6*, with the optimum culture media conditions associated with reduced expression of *CXCL8* (figure 7.26B+F). Taken together, the data could suggest that IL-6 production in the model was more sensitive to culture media conditions than IL-8. Data from the step-wise characterisation of the *in vitro* models in chapter 6 and 7 supports the use of the optimal culture media conditions for future investigations and applications.

7.3.10.4.5 Tumour necrosis factor

'Tumour necrosis factor (TNF) receptor activity' and 'response to TNF' were highlighted as of interest by the ORA and STRING analysis respectively. The co-culture model in optimal culture media condition yielded nine DEGs relevant to TNF signaling. They are broadly categorised under: i) TNF receptors, ii) TNFSF10-related, and iii) TNF-α.

The gene expression of tumour necrosis factor receptor superfamily member 1B (TNFRSF1B) was significantly up-regulated throughout day 3 to 21 when compared to baseline on day 1 (figure 7.29A). The encoded receptor mediates the metabolic effects of TNF-α, with both pro- and anti-apoptotic effects reported. *TNFRSF14* and *TNFRSF25* were up-regulated too, but to a lower magnitude and only at chronic timepoints (figure 7.29B/C). The TNF signaling network is complex and consists of bi-directional stimulatory and inhibitory pathways, and may be best served interrogated with a true high-throughput technique such as RNA-sequencing to permit the visualisation of gene expression patterns across the entire pathway. Nonetheless,

the current data showed a rise in the expression of *TNFRSF14* and *TNFRSF25* in chronic timepoints. They are associated with the pro-inflammatory response and the induction of apoptosis, possibly through NFκB activation, respectively. Paired with an observed rise in pro-inflammatory cytokines and cytotoxicity measured, the latter in the forms of LDH release (sections 6.3.1 and 6.3.2), it would be interesting to further investigate the role and impact of TNF in the advanced 3D *in vitro* model.

Notably, whilst most DEGs were found to be up-regulated at chronic timepoints, the *Fas* gene was differentially expressed during the acute phase between day 3 and 7 (figure 7.29G). Also known as *TNFRSF6*, the Fas cell surface death receptor gene encodes a death domain-containing receptor and has a central role in the regulation of programmed cell death. It functions to trigger a downstream caspase cascade towards apoptosis, including the formation of a death-inducing signaling complex that includes the Fas-associated death domain protein (FADD), caspase 8 and caspase 10. FADD is an apoptotic adaptor protein which can be recruited by a host of receptors including Fas and TNFRSF25, gene expression for both were up-regulated in the co-culture model, albeit at differing timepoints (figure 7.29 C/G). FADD functions to mediate cell apoptosis, but its gene expression did not mirror the rise in the *Fas* receptor gene in the acute timeframe or otherwise (figure 7.29H). Despite not seeing a downstream effect beyond the acute up-regulation of the *Fas* gene, future elucidation may pick apart its biological relevance especially in the acute phase. Due to the necessitated cell handling and the cross-linker chemical exposure during model creation, or indeed with the intended biofabrication of a 3D-printed cartilage implant, a degree of cell stress is anticipated. Whether the observed up-regulation of *Fas* reflects this inevitable state, if there are downstream implications as to the health condition and function of chondrocytes, and whether this translates to quantifiable or clinically relevant effects remain to be seen.

A further grouping of DEGs relevant to TNF was those related to the TNF superfamily member 10 (*TNFSF10*). The protein ligand encoded by *TNFSF10* preferentially induces apoptosis in transformed and tumour cells, and of note, does not cause cell death in normal cells despite heightened expression. It binds to the receptor encoded by *TNFRSF10B*, which then triggers the activation of the caspase cascade including caspase 8, an initiator caspase involved in the extrinsic apoptosis pathway and caspase 3, an effector caspase common to both intrinsic and extrinsic apoptosis. Up-regulation

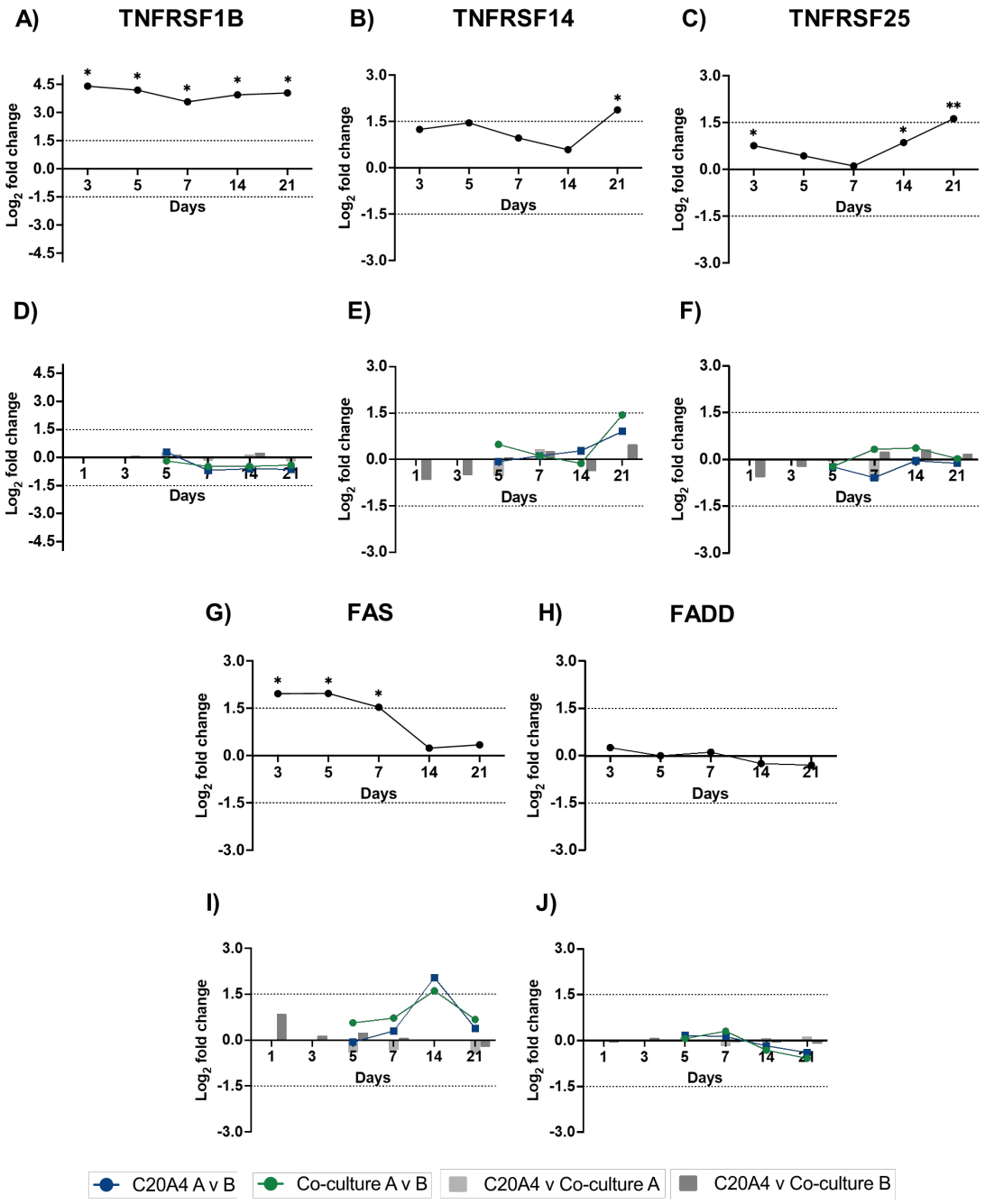

Figure 7.29 Change in gene expression of TNF receptors over time. *Differential gene expression was examined in advanced 3D in vitro models using the Nanostring IO360 panel. Log2 fold change for: A+D) tumour necrosis factor receptor superfamily member 1B (TNFRSF1B), B+E) TNFRSF14, C+F) TNFRSF25, G+I) Fas cell surface death receptor (FAS), and H+J) Fas-associated via death domain (FADD). Timepoint comparisons between day 3-21 against day 1 as baseline in the co-culture model in optimal culture media condition are shown in A-C and G-H. Culture media conditions representing augmented regime (A) versus optimal regime (B), and chondrocyte monoculture versus co-culture with fibroblast in both culture media conditions were compared at each timepoint in D-F and I-J. Statistical significance is denoted by ∗(p<0.05) and ∗∗(P<0.01). The horizontal dotted lines represent log2 fold change of >1.5 or <-1.5.*

of the ligand and receptor was observed in the co-culture model, albeit only *TNFSF10* was deemed differentially expressed at the chronic timepoints at markedly elevated levels with log2 fold changes of greater than 4 ($p<0.01$ on day 14 and $p<0.001$ on day 21) (figure 7.30A). Due to its expression in normal tissues, it is difficult to draw

conclusions based on what was observed. To add to this, TNFSF10 also binds to three decoy receptors which renders the ligand muted in the induction of apoptosis.

These decoy receptors included TNFRSF10C, which was investigated but showed non-detectable levels of gene expression, TNFRSF10D and TNFRSF11B. The latter

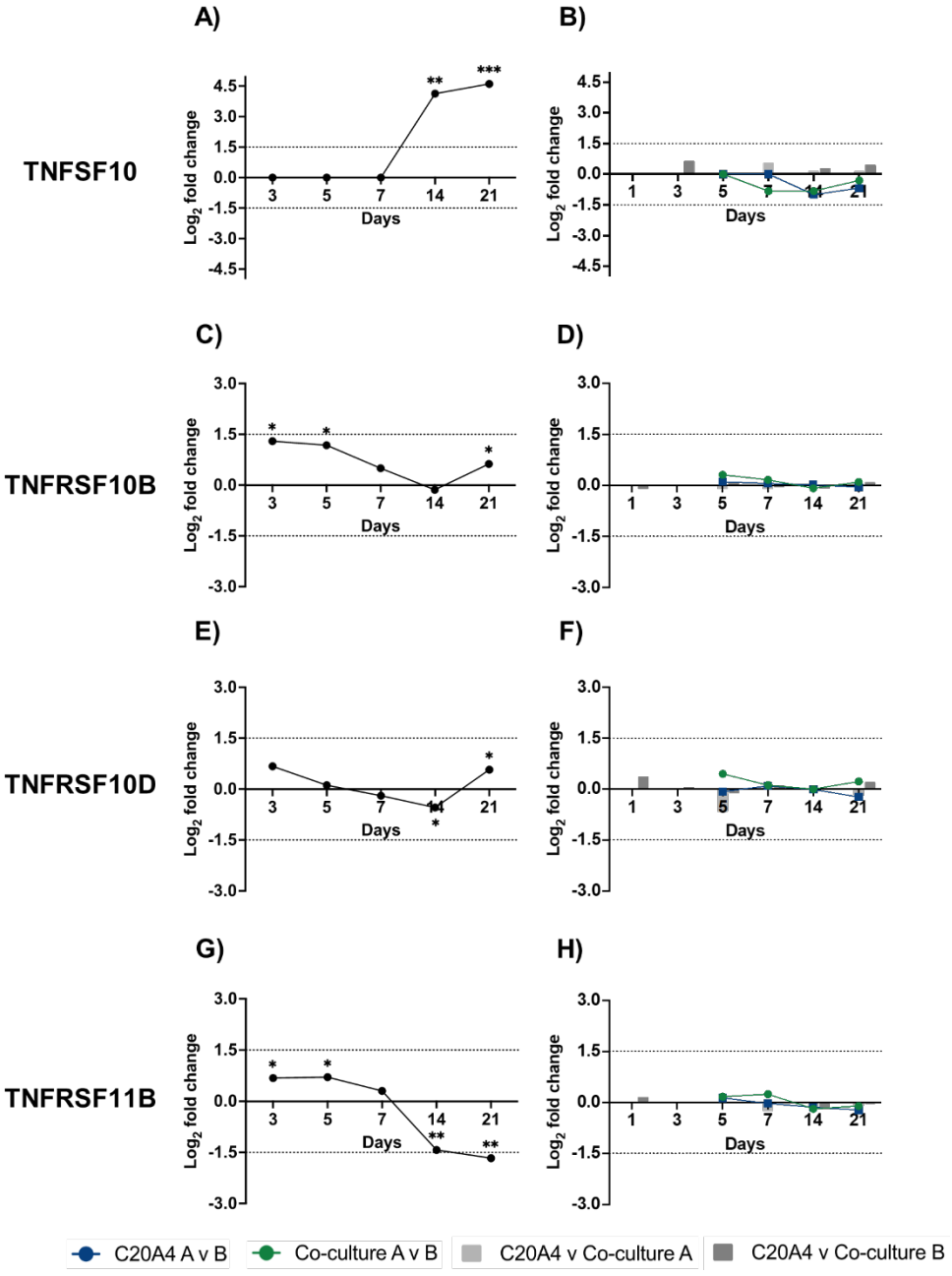

Figure 7.30 Change in gene expression of TNFSF10 and its related receptors over time. *Differential gene expression was examined in advanced 3D in vitro models using the Nanostring IO360 panel. Log2 fold change for: A+B) tumour necrosis factor superfamily member 10 (TNFSF10), C+D) tumour necrosis factor receptor superfamily member 10B (TNFRSF10B), E+F) TNFRSF10D, and G+H)TNFRSF11B. Timepoint comparisons between day 3-21 against day 1 as baseline in the co-culture model in optimal culture media condition are shown in A,C,E,G. Culture media conditions representing augmented regime (A) versus optimal regime (B), and chondrocyte monoculture versus co-culture with fibroblast in both culture media conditions were compared at each timepoint in B,D,F,H. Statistical significance is denoted by * ($p<0.05$), ** ($p<0.01$) and *** ($p<0.001$). The horizontal dotted lines represent log2 fold change of >1.5 or <-1.5.*

pair, whilst demonstrated statistically significant changes when compared to day 1, were variably up- and down-regulated over time and did not reach the threshold for differential expression for the most part (figure 7.30 E/G).

The final group relates to TNF-α, a potent pro-inflammatory cytokine with a critical role in the immune system. Although mostly secreted by activated macrophages, T cells and natural killer cells, TNF-α is also secreted by chondrocytes[350]. Although studied in the context of articular joint pathophysiology, TNF-α was found to inhibit cartilage matrix synthesis, promote matrix metalloproteinases activity thereby hasten cartilage degradation, and inhibit chondrogenesis *via* the NFκB pathway. As such, its action can directly influence the functionality and performance of a tissue-engineered cartilage implant.

In the co-culture model, two genes encoding TNF-alpha induced proteins (TNFAIP) were differentially expressed. *TNFAIP3* encodes an enzyme which inhibits NFκB activation and TNF-mediated apoptosis, and was found to be significantly up-regulated in the acute phase (figure 7.31A). *TNFAIP6* conversely was down-regulated at chronic timepoints (figure 7.31B). It encodes a member of the hyaluronan-binding protein family which serves as a key regulator of ECM organisation during tissue remodelling. It influences the assembly of hyaluronan in the ECM, affecting ECM stability and cell migration. Finally, the intercellular adhesion molecule 1 (*ICAM1*) was found to be up-regulated on day 21 (figure 7.31C). The expression of *ICAM1* can be induced by a variety of pro-inflammatory mediators including TNF-α, but also IL-6, IL-1β and interferon-γ (IFN-γ)[351], with which an increase in IL-6 was observed at chronic timepoints (figure 7.26A).

Furthermore, the DEGs were, in the most part, not unduly influenced by culture media conditions (figures 7.29 D/E/F/I, 7.30 B/D/F/H, and 7.31 D/E). This suggests that activities in the TNF signaling mechanisms reflect inherent model properties. Although it is difficult to disentangle the effects of the nanocellulose-based bio-ink based on the current data alone, it would be interesting to quantify the amount of TNF-α and other proteins relevant to TNF signaling, and correlate this with chondrocyte viability and function.

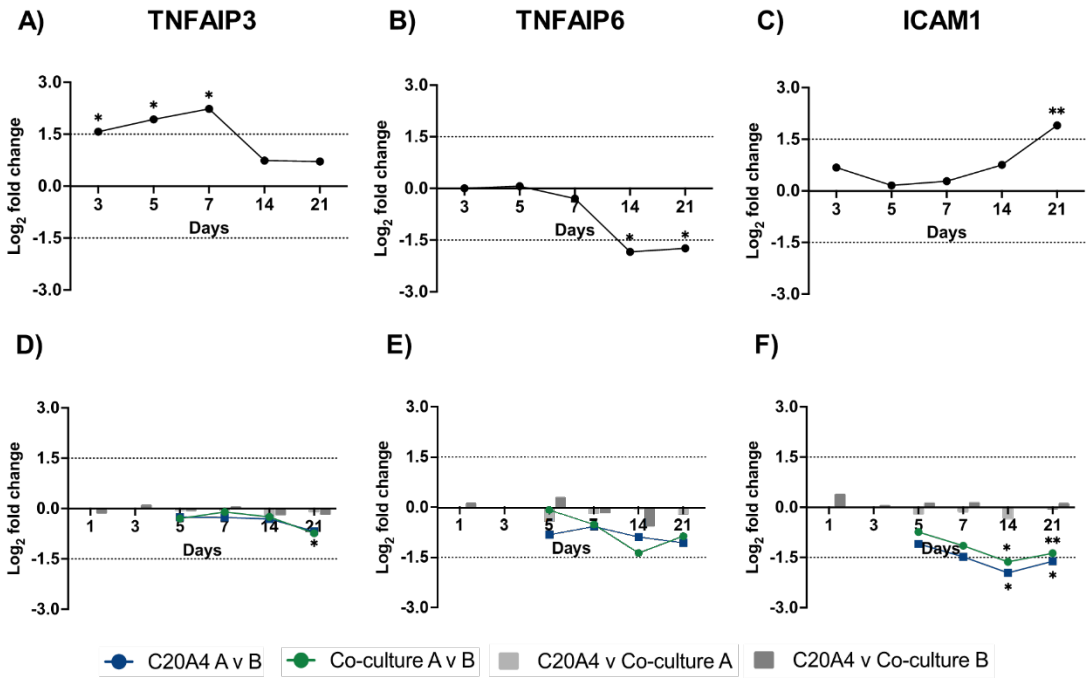

Figure 7.31 Change in gene expression of TNF-α-related DEGs over time. *Differential gene expression was examined in advanced 3D in vitro models using the Nanostring IO360 panel. Log2 fold change for: A+D) tumour necrosis factor alpha-induced protein 3 (TNFAIP3), B+E) TNFAIP6 and C+F) intercellular adhesion molecule 1 (ICAM1). Timepoint comparisons between day 3-21 against day 1 as baseline in the co-culture model in optimal culture media condition are shown in A-C. Culture media conditions representing augmented regime (A) versus optimal regime (B), and chondrocyte monoculture versus co-culture with fibroblast in both culture media conditions were compared at each timepoint in D-F. Statistical significance is denoted by * ($p<0.05$) and ** ($p<0.01$). The horizontal dotted lines represent log2 fold change of >1.5 or <-1.5.*

7.3.10.4.6 Response to type I interferon

Response to type I interferon was identified as a relevant GO term in the functional enrichment analysis on protein-protein interactions. Of the ten DEGs highlighted, *IFIT1*, *IFIT3* and *RSAD2*, and *OAS1*, *OAS2* and *OAS3* had the strongest probability of being true PPIs based on their STRING combined scores, also indicated by the thickness of the interlinkage lines (figure 7.24).

Type I interferon is a key component of the innate immune system, where a core function is its defence against viral pathogens[352]. The innate immune system relies on rapid antigen recognition through pattern recognition receptors (PRR), examples of which include NOD-like receptors and toll-like receptors (TLR)[353]. In the co-culture model, the gene expression of the nucleotide-binding oligomerization domain containing 2 (NOD2) nod-like receptor and TLR4 were non-detectable and non-differentially expressed, respectively (data not shown). The expression of *TLR3* however was up-regulated throughout the study period (figure 7.32G). In the context

of viral infection where its function is more clearly defined, it serves as a PRR for pathogen-associated molecular patterns (PAMP) where the recognition of double-stranded RNA induces the activation of NFκB pathway and production of type I interferons. Whilst appreciating the lack of complete visualisation of the NFκB pathway, a statistically significant but low-level increased gene expression of NFκB2 was observed, but not with NFκB1 (figure 7.32 H+I). Following the release of type I interferons, its downstream effects are mediated through the binding to its respective receptors, which triggers intracellular signaling *via* the JAK/STAT pathway, leading to the transcription of hundreds of interferon-stimulated genes (ISGs)[354]. Six ISGs (*IFIT1, IFIT3, RSAD2, OAS1, OAS2, OAS3*) were identified as differentially expressed in the co-culture model. All of which were up-regulated and may indicate the presence and effects of type I interferon upon the model (figures 7.32 A-C and 7.33 A-C).

The 2'-5'-oligoadenylate synthetase (OAS) 1, 2 and 3 are interferon-induced double-stranded RNA-binding enzymes with a key role in interferon-driven antiviral activity[355, 356]. Whilst response against viral infection is a core function of type I interferon and its downstream effector enzymes and ISGs, they are also involved more broadly within the immune system and exerts their effects on a multitude of cellular processes which could be influential in the context of tissue engineering. The *OAS1-3* gene set is of particular interest in this study because it is the only GO term with a high intersection ratio, with 100% of the gene set for the GO term "2'-5'-oligoadenylate synthetase activity" differentially expressed. The broader reach of the effects of OAS reported in the literature includes cell differentiation, cell cycle and growth control, inflammation and apoptosis[355-357]. With reference to the impact of OAS on the differentiation process of various cell types in the context of cartilage regeneration, differential OAS activity was shown in neocartilage in a perinatal murine model[358]. Maor *et al* demonstrated that maximal activity of OAS was detected in proliferating, undifferentiated pre-chondrocytes, whilst the level of activity was reduced in fully differentiated chondrocytes. This is indicative of an area worthy of further exploration as maintaining chondrocyte functionality and the avoidance or at least the control of de-differentiation of chondrocytes, especially with primary chondrocytes *ex vivo*, remains a challenge in the field of cartilage tissue engineering.

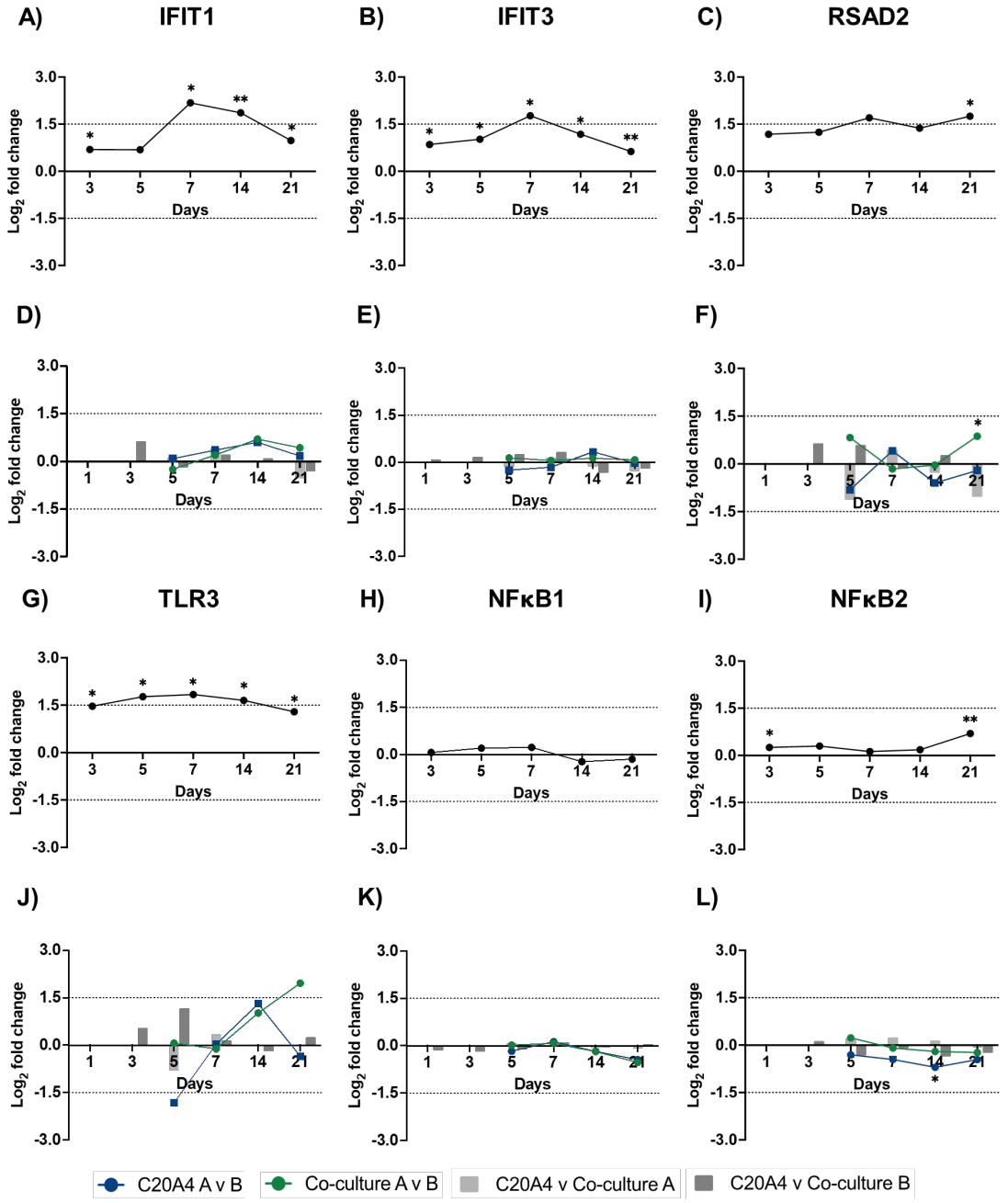

Figure 7.32 Change in gene expression of DEGs relevant to response to type I interferon over time. *Differential gene expression was examined in advanced 3D in vitro models using the Nanostring IO360 panel. Log2 fold change for: A+D) interferon-induced protein with tetratricopeptide repeats 1 (IFIT1), B+E) IFIT3, C+F) radical S-adenosyl methionine domain containing 2 (RSAD2), G+J) toll like receptor 3 (TLR3), H+K) nuclear factor kappa B subunit 1 (NFκB1), and I+L) NFκB2. Timepoint comparisons between day 3-21 against day 1 as baseline in the co-culture model in optimal culture media condition are shown in A-C/G-I. Culture media conditions representing augmented regime (A) versus optimal regime (B), and chondrocyte monoculture versus co-culture with fibroblast in both culture media conditions were compared at each timepoint in D-F/J-L. Statistical significance is denoted by * ($p<0.05$) and ** ($p<0.01$). The horizontal dotted lines represent log2 fold change of >1.5 or <-1.5.*

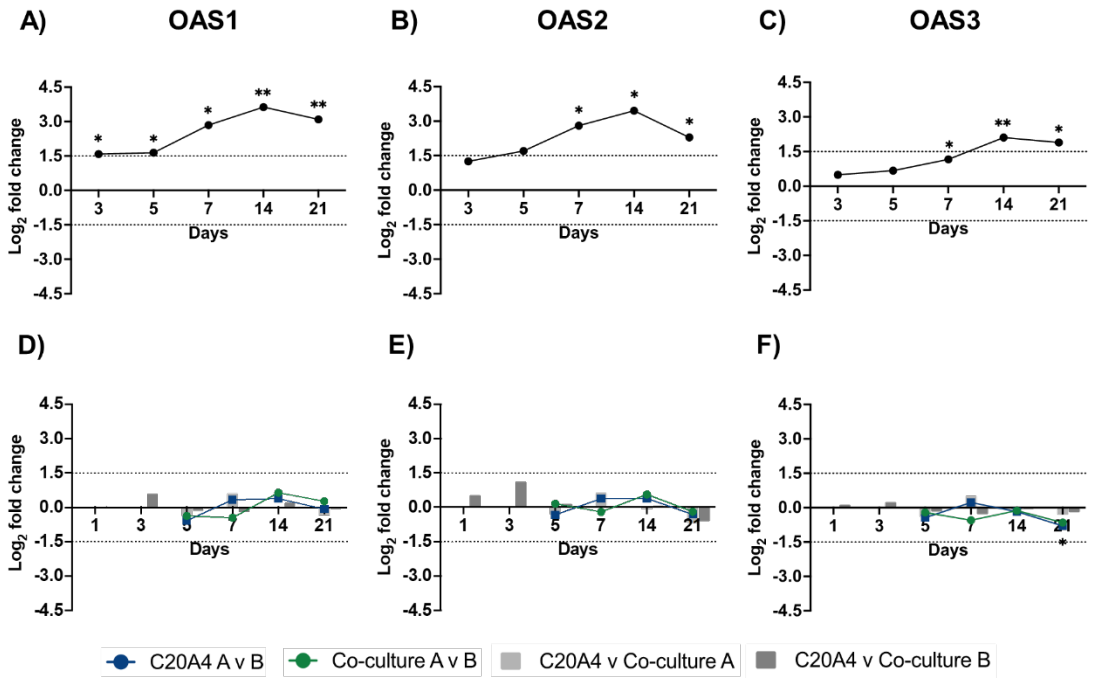

Figure 7.33 Change in gene expression of DEGs relevant to 2'-5'oligoadenylate synthetase (OAS) over time. *Differential gene expression was examined in advanced 3D in vitro models using the Nanostring IO360 panel. Log2 fold change for: A+D) 2'-5'-oligoadenylate synthetase (OAS1), B+E) OAS2 and C+F) OAS3. Timepoint comparisons between day 3-21 against day 1 as baseline in the co-culture model in optimal culture media condition are shown in A-C. Culture media conditions representing augmented regime (A) versus optimal regime (B), and chondrocyte monoculture versus co-culture with fibroblast in both culture media conditions were compared at each timepoint in D-F. Statistical significance is denoted by * ($p<0.05$) and ** ($p<0.01$). The horizontal dotted lines represent log2 fold change of >1.5 or <-1.5.*

7.3.10.4.7 Interleukin-1-beta and caspases

Interleukin-1β (IL-1β) and cysteine aspartate-specific protease 1 (CASP1) was another strong protein-protein interaction identified by the STRING analysis in the co-culture model. Both were significantly up-regulated with log2 fold changes of greater than 3, seen at the acute timepoints with *IL-1β* and chronic timepoints with *CASP1* (figure 7.34 A/B).

IL-1β is a potent pro-inflammatory cytokine with broad biological functions. It mediates inter-cellular communications in innate and adaptive immune responses, and is also involved in cell proliferation, differentiation and apoptosis. In osteoarthritis, increased levels of IL-1β were found to impact mitochondrial activity, and together with TNF-α, could exacerbate the expression of matrix metalloproteinases (MMPs) and aggrecanases which promotes cartilaginous matrix degradation[359, 360]. IL-1β is produced as an inactive precursor, pro-IL-1β, which cannot bind its intended receptor

IL-1R[361]. Caspase 1 proteolytically cleaves the full-length pro-IL-1β, thereby converting it to its active form IL-1β. It was interesting to note that the marked up-regulation of *IL-1β* precedes that of *CASP1* in the *in vitro* model.

Furthermore, caspase 1 also requires activation from its precursor form. This involves the formation and activation of the inflammasome, a multi-protein signaling complex consisting of caspase 1 and a NOD-like receptor. Using the nucleotide-binding domain, leucine-rich-containing family, pyrin domain-containing-3 (NLRP3) as an example for a well-known inflammasome, it could be observed that the DEGs in the co-culture model demonstrated biological activities along the cell signaling pathway relevant to the release of IL-1β.

The NLRP3 inflammasome forms part of the innate immune system which mediates the activation of caspase 1 and the release of IL-1β *via* sequential priming and activation signals[362]. The priming signal is triggered by PAMPs after the activation of toll-like receptors or by pro-inflammatory cytokines, leading to the activation of the transcription factor NFκB with the synthesis of NLRP3 and pro-IL-1β. Multiple factors are involved in the NFκB pathway for the priming signal, such as caspase 8, FADD and NOD1/2. The activation signal then serves to activate the inflammasome and caspase 1, culminating in the resultant biologically active IL-1β. A variety of molecular or cellular stimuli could act as the activation signal which includes extracellular ATP, mitochondrial dysfunction, reactive oxygen species, through to bacterial or fungal toxins, RNA viruses and particulate matter. In the co-culture model, up-regulated genes, inclusive of those with statistically significant increases but below the threshold for differential gene expression, included *TLR3* (figure 7.32G), NFκB2 (figure 7.32I), *FAS* (figure 7.29G), *CASP8* (figure 7.34C), *CASP1* (figure 7.34B) and *IL-1β* (figure 7.34A). These findings were found to be relatively independent of the effects of augmented culture media conditions, except for *IL-1β* (figure 7.29I, 7.32J/L and 7.34D/E/F).

Further examination of the caspase family showed a statistically significant rise in the expression of *CASP8*, which encodes an initiator caspase of the extrinsic apoptosis pathway (figure 7.34C). This was coupled with the down-regulation of the gene for

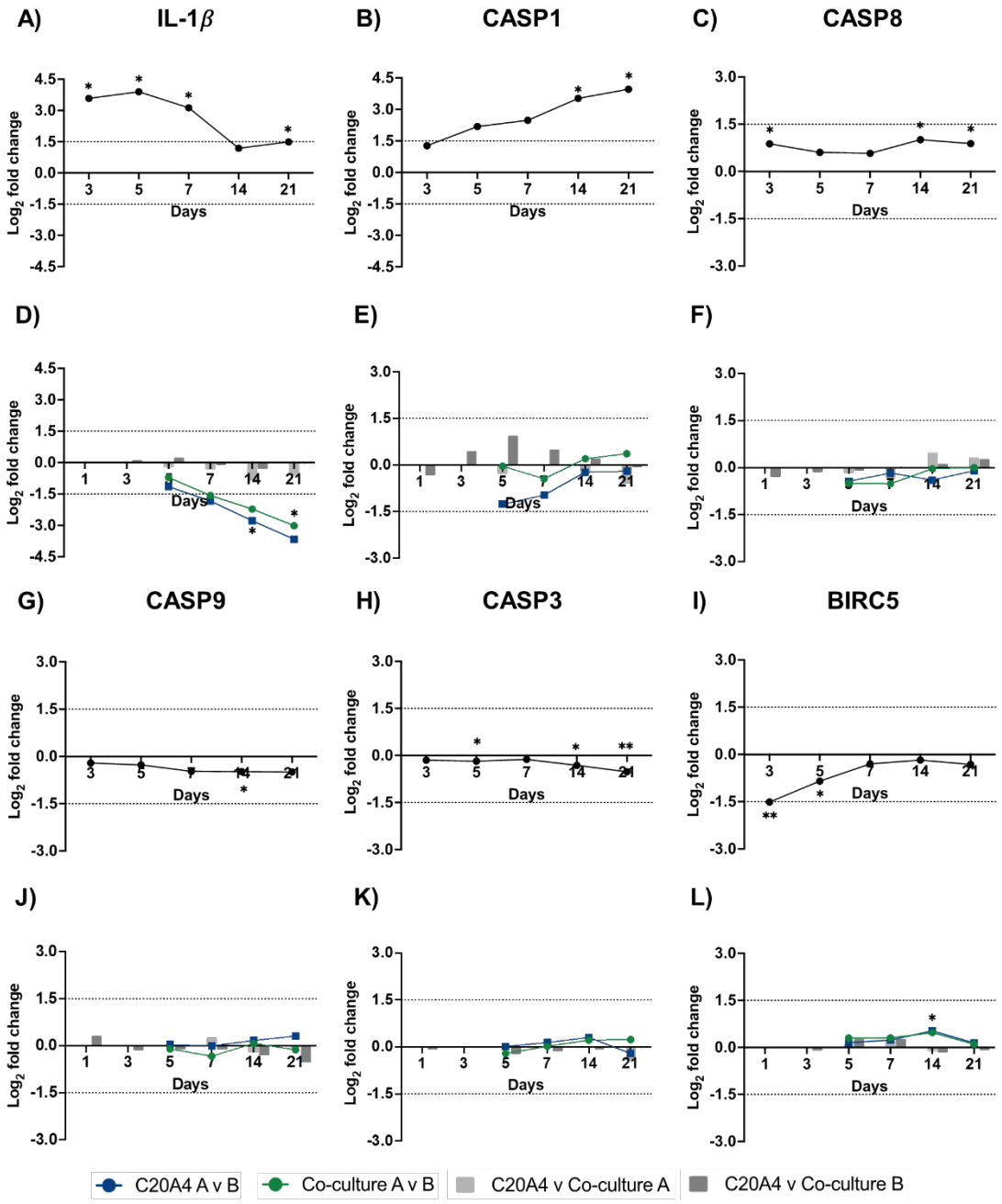

Figure 7.34 Change in gene expression of IL-1β and caspase-related genes over time. *Differential gene expression was examined in advanced 3D in vitro models using the Nanostring IO360 panel. Log2 fold change for: A+D) interleukin-1β (IL-1β), B+E) caspase 1 (CASP1), C+F) CASP8, G+J) CASP9, H+K) CASP3, and I+L) baculoviral IAP repeat containing 5 (BIRC5). Timepoint comparisons between day 3-21 against day 1 as baseline in the co-culture model in optimal culture media condition are shown in A-C/G-I. Culture media conditions representing augmented regime (A) versus optimal regime (B), and chondrocyte monoculture versus co-culture with fibroblast in both culture media conditions were compared at each timepoint in D-F/J-L. Statistical significance is denoted by * ($p<0.05$) and ** ($p<0.01$). The horizontal dotted lines represent log2 fold change of >1.5 or <-1.5.*

the initiator caspase of the intrinsic pathway, *CASP9* (figure 7.34G). This underlies the identification of the GO term extrinsic apoptosis through the ORA and STRING analysis. However, *CASP3*, which encodes the effector caspase of both apoptosis pathways, was relatively unchanged with a statistically significantly reduced levels of gene expression detected on day 5, 14 and 21 (figure 7.34H). Apart from *CASP1*, the

log2 fold change of all genes encoding caspases did not reach the threshold of >1.5 or <-1.5. Furthermore, *BIRC5* encodes an inhibitor of caspase 3 and is a member of the family of inhibitor of apoptosis (IAP). It was interesting to note that its gene expression was significantly reduced on day 3 and day 5, potentially reflective of cell stress or injury during the acute timepoints.

7.3.10.4.8 Section summary – gene expression analysis of cytokine signaling

Cytokine signaling is a complex, multi-directional and multi-tiered process which regulates a broad spectrum of physiological and pathological processes. The application of Nanostring enabled a more global assessment of gene expression in the advanced 3D *in vitro* model than what would be feasible with qPCR techniques due to technical restrictions imposed by RNA sample input. The differential gene analysis confirmed the findings of a pro-inflammatory response with elevated IL-6 gene expression. Although biochemical pathways cannot be fully assessed, the study identified 77 DEGs amongst 770 examined and these highlighted interferon signaling, tumour necrosis factor signaling and the extrinsic apoptosis pathways as potential areas of interest. The gene expression of several cytokines (IL-6, IL-8 and IL-1β) were found to be sensitive to culture media conditions with increased gene expression and therefore a heightened pro-inflammatory state was found to be associated with nutrient deprivation. However, numerous signaling pathway genes, including DEGs and statistically significantly augmented genes within log2 fold changes of 1.5 to -1.5, did not demonstrate altered gene expression in the restricted media regime (an extrinsic factor), suggestive of inherent effect or characteristics of the *in vitro* model.

7.3.10.5 Gene expression analysis of extra-cellular matrix

The extra-cellular matrix is a 3-dimensional network critical in its function to provide the physical and biochemical microenvironment where cells reside. In the context of 3D-bioprinting, this is initially composed of the bio-ink used as the cell carrier. Over time, functional resident cells, in this case chondrocytes, will secrete ECM components which further augments the cell physical niche. How this evolves over time, at both molecular and microscopic levels, can directly impact cellular functions and implant performance *in vivo*.

Multiple GO terms relevant to ECM were identified from the STRING analysis and ORA. These included 'ECM organisation', 'ECM binding', 'ECM cellular component disassembly' and simply 'ECM'. Together, there were 34 DEGs with ECM-relevant GO terms identified in the co-culture model in optimal culture condition. Of these, 14 DEGs correlated with genes in the MatrisomeDB 2.0 and are listed in table 7.8. The MatrisomeDB is a database that cross-references genomic and proteomic data specific for ECM and ECM-associated proteins. It integrates both *in vivo* and *in silico* data to produce an ECM atlas of various tissue types[363, 364]. DEGs corresponding to the core matrisome genes are discussed.

Table 7.8 Extra-cellular matrix-relevant DEGs in the MatriosomeDB.

Core Matrisome Genes		**Matrisome-associated Genes**	
Collagen	*COL4A5* *COL11A1*	**Secreted factors**	*IL-2* *IL-4* *IL-6* *SFRP1* *WNT2B* *WNT5A*
Proteoglycan	*VCAN*	**Regulators**	*CTSS* *MMP1*
Glycoprotein	*FAP* *LTBP1* *TNFAIP6*		

COL4A5 and *COL11A1* are both genes encoding collagen sub-units which were up-regulated and deemed beneficial for cartilage tissue engineering (figure 7.35 A/B/D/E). Multiple sub-types of collagen are found in human cartilage, with type 2, 4 and 11 being most abundant and therefore most studied[365]. The specificity of collagen genes examined was pre-selected based on the Nanostring IO360 panel. For future research, the expression of *COL2A1* (type II collagen) will be of particular interest in the regeneration of cartilage.

Versican is a member of the aggrecan/versican proteoglycan family and is a major component of ECM. It binds HA and plays an important role in tissue morphogenesis and maintenance. Its gene expression (*VCAN*) was significantly up-regulated throughout the study period, showing a bimodal pattern with maximal increases on day 3 and day 21, when compared to baseline on day 1 (figure 7.35C). For future

research, the gene expression for aggrecan (*ACAN*), also an HA-binding proteoglycan with a role in resisting compressive forces, will be of interest.

Other core matrisome genes encoding glycoproteins were *FAP, LTBP1* and *TNFAIP6*. The latter was previously discussed in section 7.3.10.4.5. The fibroblast activation protein alpha (*FAP*) gene encodes an integral membrane gelatinase. In association with dipeptidyl peptidase 4 (DPP4), a transmembrane glycoprotein, or with integrins (which are transmembrane receptors), FAP participates in the peri-cellular proteolysis of ECM and facilitates cell adhesion and migration through the ECM. Taken together, the up-regulation of both *FAP* and *DPP4* suggests cell adhesion and migration within the nanocellulose-based hydrogel. Confirmation could be performed in the forms of real-time imaging to track cell migration. The confirmation of cell adhesion on the nanocellulose-based bio-ink would substantiate one of several benefits of employing naturally-derived bio-ink material, as synthetic materials are known to lack cell-binding capabilities which in turn alters cellular function.

LTBP1 encodes a member of the latent TGF-β binding proteins. It controls integrin-dependent TGF-β activation, maintains it in a latent state, and is considered a driver in fibrosis. Although *LTBP1* was found to be up-regulated across the study period, the magnitude of up-regulation was relatively reduced in the chronic timepoints. Understanding the biological mechanisms which drives fibrosis will be instrumental to maximising the performance and longevity of tissue engineered implants *in vivo*.

Finally, TNFAIP6 is a member of the HA-binding protein family and is a key regulator of ECM organisation. As discussed previously, TNFAIP6 is induced by TNF-α. Its down-regulation on day 14 and 21 could suggest that its expression is not induced. Whilst the expression of most ECM-relevant DEGs were not overly influenced by culture media conditions, the expression of *TNFAIP6* was seen to be further reduced in optimal culture media condition, which suggests, in difference to *FAP* and *DPP4*, the action of TNFAIP6 may not be inherent to the *in vitro* model and could be related to a partly pathologic state induced by deficient nutrients and presence of TNF-α.

Overall, the glimpse of ECM-relevant DEGs in the study suggests that the *in vitro* model utilising a nanocellulose-based bio-ink with alginate and HA additives were supportive of collagen production, ECM formation and cell adhesion and migration, although work is required for validation of these findings.

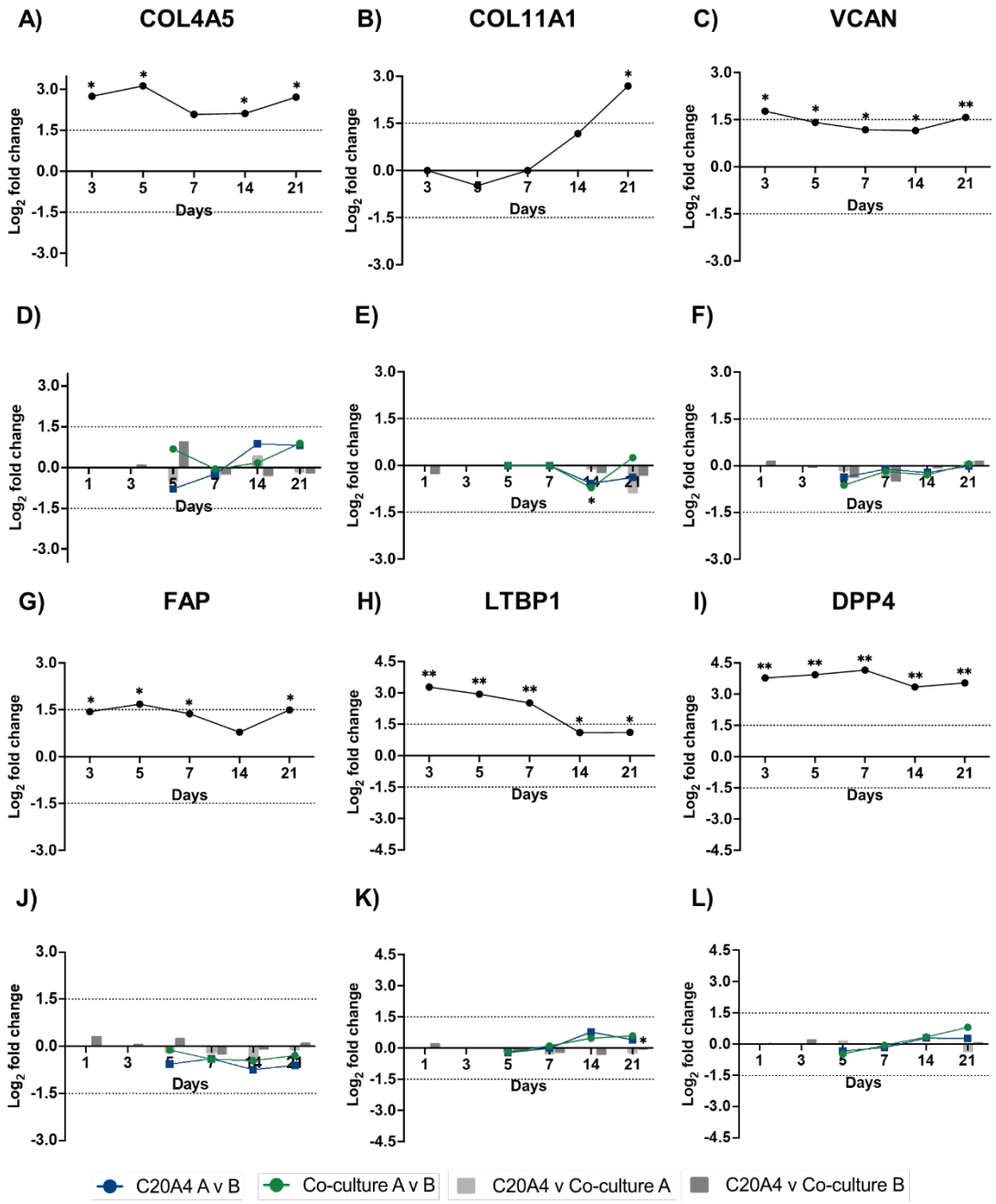

Figure 7.35 Change in gene expression of core matriosomeDB DEGs over time. *Differential gene expression was examined in advanced 3D in vitro models using the Nanostring IO360 panel. Log2 fold change for: A+D) collagen type IV alpha 5 chain (COL4A5), B+E) collagen type XI alpha 1 chain (COL11A1), C+F) versican (VCAN), G+J) fibroblast activation protein alpha (FAP), H+K) latent-transforming growth factor beta-binding protein 1 (LTBP1), and I+L) dipeptidyl peptidase 4 (DPP4) are shown. Timepoint comparisons between day 3-21 against day 1 as baseline in the co-culture model in optimal culture media condition are shown in A-C/G-I. Culture media conditions representing augmented regime (A) versus optimal regime (B), and chondrocyte monoculture versus co-culture with fibroblast in both culture media conditions were compared at each timepoint in D-F/J-L. Statistical significance is denoted by * ($p<0.05$) and ** ($p<0.01$). The horizontal dotted lines represent log2 fold change of >1.5 or <-1.5.*

7.3.10.6 Gene expression analysis for response to hypoxia

Response to hypoxia was the final common theme revealed from the ORA and STRING analysis. The inter-related nature of hypoxia and cellular metabolism in chondrocyte physiology means that they are best considered in parallel. A brief account of relevant chondrocyte metabolism is provided prior to the discussion of DEGs pertaining to hypoxia.

Cartilage is avascular and oxygenation occurs *via* diffusion from the capillary network with which the cartilage is in contact with. In the case of articular cartilage, which constitutes a significant body of research into chondrocyte function and regeneration, oxygen is derived from the synovial (joint) fluid and subchondral bone[366]. As such, the physiologic microenvironment of the chondrocyte is relatively hypoxic compared to other well-vascularised tissue types, such as muscle and bone[367]. Oxygen levels in cartilage were reported to be between less than 1% to 6%, in comparison to 13% in arterial blood, with reduced levels of oxygen detected in zones deeper within the cartilage structure[367].

Under hypoxic conditions, ATP generation by cells are usually via glycolysis, hence the traditional term 'anaerobic glycolysis'[368]. It is a less efficient means of energy generation as oxidative phosphorylation yields 36 molecules of ATP for each single molecule of glucose, contrasting with glycolysis which yields only 2 ATP molecules[368].

Under normal physiological conditions, chondrocytes have adapted to its native hypoxic microenvironment, and cartilage tissue generally demonstrate low metabolic activity and extracellular matrix turnover[369]. In healthy chondrocytes, over 75% of cellular ATP is generated through glycolysis, rather than *via* mitochondrial oxidative phosphorylation[369, 370]. In early pathophysiological states such as mild osteoarthritis, cells transition to a metabolically more active state for the regeneration and repair of ECM. It temporarily adopts oxidative phosphorylation to meet the increased metabolic demands of enhanced cell proliferation and ECM production[369]. However, as disease progresses, the energy requirements are no longer met despite the metabolic shift and mitochondrial dysfunction ensues and ATP generation *via* glycolysis resumes with a running metabolic deficit. Alongside inflammation with disease progression, a vicious cycle of increasing oxidative stress in a lactate dehydrogenase-mediated manner

causes mitochondrial DNA damage and loss of membrane integrity with worsening mitochondrial dysfunction, leading to eventual cell senescence and/or cell death[366, 371].

The hypoxia-inducible factor 1 subunit alpha (*HIF1A*) was discovered in the mid-1990s[372]. It is a key transcriptional regulator for cellular and systemic homeostatic response to hypoxia. With adequate oxygen levels, the encoded alpha subunit of the HIF1 transcription factor is degraded as soon as it is synthesised, but in hypoxia (eg. <5% oxygen tension), HIF-α forms a complex with HIF-β, translocate to the nucleus and activates the transcription of target genes. The rise in *HIF1A* on day 21 in the co-culture model indicates the presence of a hypoxia-driven response in cells. Whilst this rise in *HIF1A* was statistically significant, the log2 fold change was relatively modest and *HIF1A* did not constitute a DEG (figure 7.36A).

Studies have suggested that in hypoxia, HIF1A acts to convert ATP generation from oxidative to glycolytic processes. In the context of osteoarthritis, HIF-1 was found to drive ATP production *via* anaerobic means by metabolically active chondrocytes in diseased states. It acts to increase levels of pyruvate dehydrogenase kinase 1, encoded by *PDK1*, which promotes anaerobic glycolysis[370]. PDK1 acts to inhibit pyruvate dehydrogenase, a mitochondrial multi-enzyme complex, thereby impacting the Kreb cycle and leads to the down-regulation of aerobic respiration. PDK1 has a critical role in the cellular response to hypoxia and is thought to be protective against hypoxic and oxidative stress. It was found to be significantly up-regulated on day 14 and 21 of the co-culture model (figure 7.36G).

Four DEGs encoding glycolytic enzymes (*ALDOA, ALDOA, ENO1* and *HK2*) shared the PPI under the GO term of 'response to hypoxia' in the STRING analysis. They were also significantly up-regulated at chronic timepoints, reflecting a change in chondrocyte metabolism in parallel with cells responding to hypoxia (figure 7.36B/C/H/I). *ALDOA* and *ALDOC* encode aldolase A and C respectively, which are isozymes that catalyse the same chemical reaction but have varied catalytic efficiencies allowing differential regulation of the reaction. *ENO1* encodes enolase 1 which is involved in hypoxia tolerance. Elevated expression of hexokinase 2, encoded by *HK2*, was found to be associated with joint pathologies, and its up-regulation at chronic timepoints in the co-culture model could reflect similar altered cellular glucose metabolism as seen in cartilage injury. Hexokinase is an evolutionarily conserved

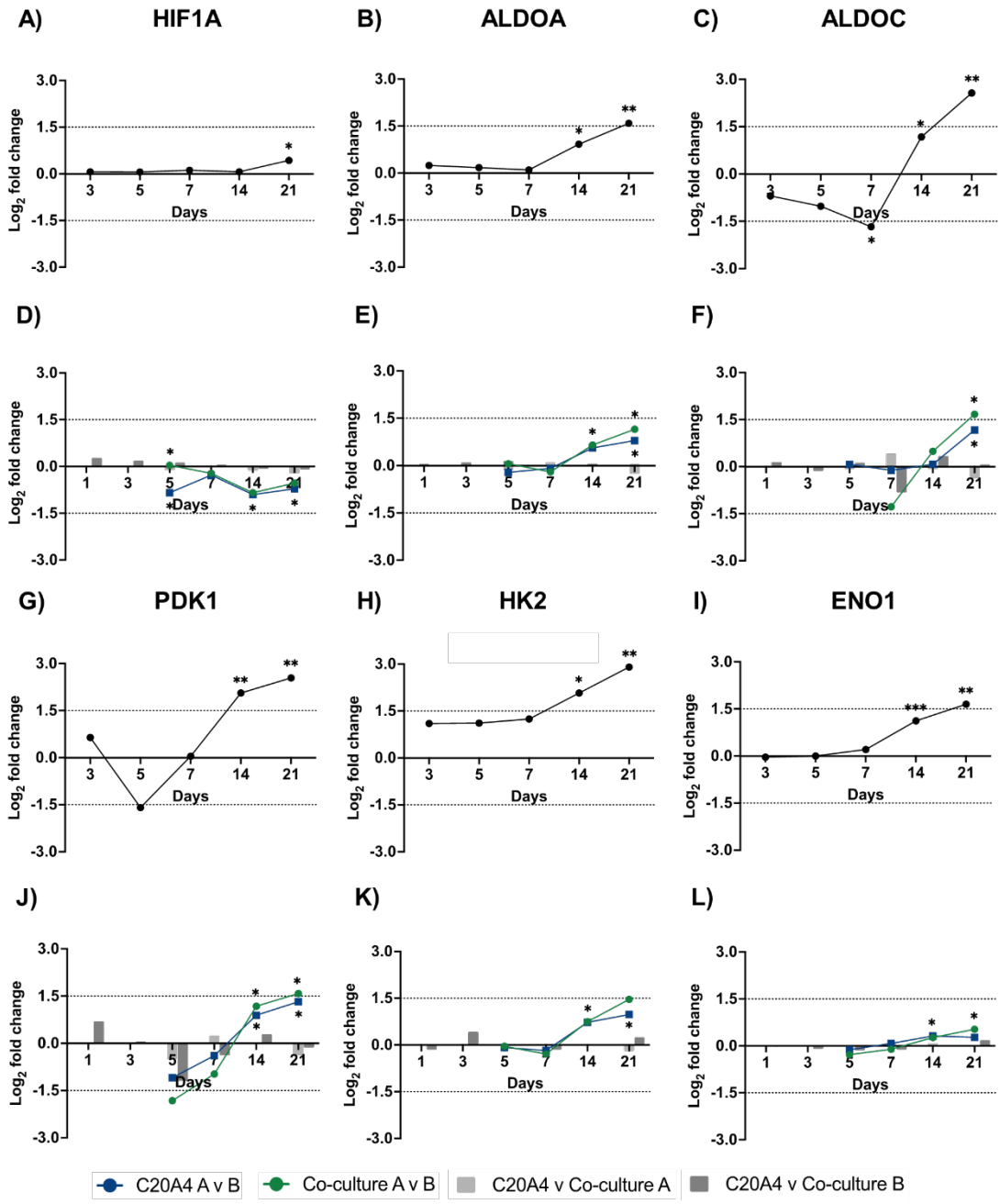

Figure 7.36 Change in gene expression of hypoxia-relevant DEGs over time. *Differential gene expression was examined in advanced 3D in vitro models using the Nanostring IO360 panel. Log2 fold change for: A+D) hypoxia inducible factor 1 subunit alpha (HIF1A), B+E) aldolase, fructose-bisphosphate A (ALDOA), C+F) aldolase, fructose-bisphosphate C (ALDOC), G+J) pyruvate dehydrogenase kinase 1 (PDK1), H+K) hexokinase 2 (HK2), and I+L) enolase 1 (ENO1) are shown. Timepoint comparisons between day 3-21 against day 1 as baseline in the co-culture model in optimal culture media condition are shown in A-C/G-I. Culture media conditions representing augmented regime (A) versus optimal regime (B), and chondrocyte monoculture versus co-culture with fibroblast in both culture media conditions were compared at each timepoint in D-F/J-L. Statistical significance is denoted by * ($p<0.05$), ** ($p<0.01$) and *** ($P<0.001$). The horizontal dotted lines represent log2 fold change of >1.5 or <-1.5.*

intracellular glucose sensor[367]. Hexokinases catalyses the conversion of glucose to glucose-6-phosphate (G6P), which is the first step of glucose metabolism common to both the glycolytic and oxidative phosphorylation pathways[370]. It acts as an important regulator of cellular glucose metabolism, and its levels and activity are increased in

joint pathology. The expression of *HK2* was found to be increased in primary human chondrocytes in severe osteoarthritis with elevated G6P levels confirmed with metabolomic study[373]. *HK2* expression was up-regulated by TGF-β in osteoarthritis[374], whilst increased *HK2* expression was associated with raised IL-6, IL-8 and MMPs expression in human fibroblast-like synoviocytes in rheumatoid arthritis[375].

Another PPI for the response to hypoxia was with *BNIP3* and *BNIP3L*. Together with *BBC3*, the three DEGs encode proteins associated with the pro-apoptotic BCL2 protein and are involved with mitochondrial function. BCL2 interacting protein 3 (BNIP3) and BNIP3-like (BNIP3L) form a complex that localises to the mitochondria, acting as a key regulator to induce mitophagy[376, 377]. Mitophagy is a form of autophagy which involves the removal of dysfunctional or excess mitochondria. It serves to preserve mitochondrial function and limit the production of reactive oxygen species (ROS). This is important because ROS activates pro-inflammatory pathways, such as NFκB, which up-regulates cytokines such as IL-6, IL-1β and TNF-α and matrix metalloproteinases, whilst limiting the production of glycoasaminoglycans and type II collagen[367]. Together this disturbs the balance between catabolic and anabolic activities, with resultant matrix degradation as seen in arthritic diseases with loss of cartilage and would be detrimental in the context of cartilage tissue engineering. This underlies the key role of the mitochondria in cartilage homeostasis. In terms of stimulus, mitophagy occurs in response to adverse physiological stimulus such as hypoxia and nutrient deprivation. Studies have confirmed the role of HIF1A in the transcriptional up-regulation of BNIP3L-mediated mitophagy in response to hypoxia[376]. The paired up-regulation of *BNIP3* and *BNIP3L* in the co-culture model at chronic timepoints suggests a cellular response at the mitochondrial level to physiological stressors, possibly hypoxia-driven given the rise in *HIF1A*.

Interestingly, all DEGs associated with the response to hypoxia, except for *HIF1A*, demonstrated an up-regulation of gene expression in the optimal culture media condition when compared with the augmented media regime (figure 7.36 E/F/J/K/L). This is in sharp contrast to previously examined DEGs in the co-culture model, whereby the augmented culture media regime with nutrient restriction was usually associated with up-regulation of gene expressions. Whilst *HIF1A* infers direct cellular response to hypoxia, the other DEGs discussed in this section relates to cellular metabolism. This observation therefore could potentially be explained by the increased

metabolic demand associated with the increased cell proliferation associated with the optimal culture media condition. Increasing cell stress in turn leading to the up-regulation of metabolically-relevant DEGs. Whilst it is feasible that increased cell proliferation in the optimal culture media condition leads to increased ECM production, which in turn limits oxygen diffusion within the *in vitro* model, the data from the culture media effects would suggest otherwise (figure 7.36D).

Finally, *BBC3* encodes the BCL2 binding component 3 which is a pro-apoptotic member of the BCL-2 family of proteins. It acts to increase mitochondrial outer membrane permeability and induce apoptosis. It was significantly up-regulated on day 3 and 5, but not at chronic timepoints (figure 7.37C). As such, this protein is unlikely to be involved in the processes relating to the altered metabolism in hypoxia seen mostly at chronic timepoints. It may participate in cell disturbance associated with cell handling during model creation given its early up-regulation.

Overall, in tissue engineering, whilst there are growing evidence of hypoxic conditions supporting chondrogenic differentiation of mesenchymal stromal cells (MSCs) during the expansion or differentiation phase of culture, a recent systematic review also

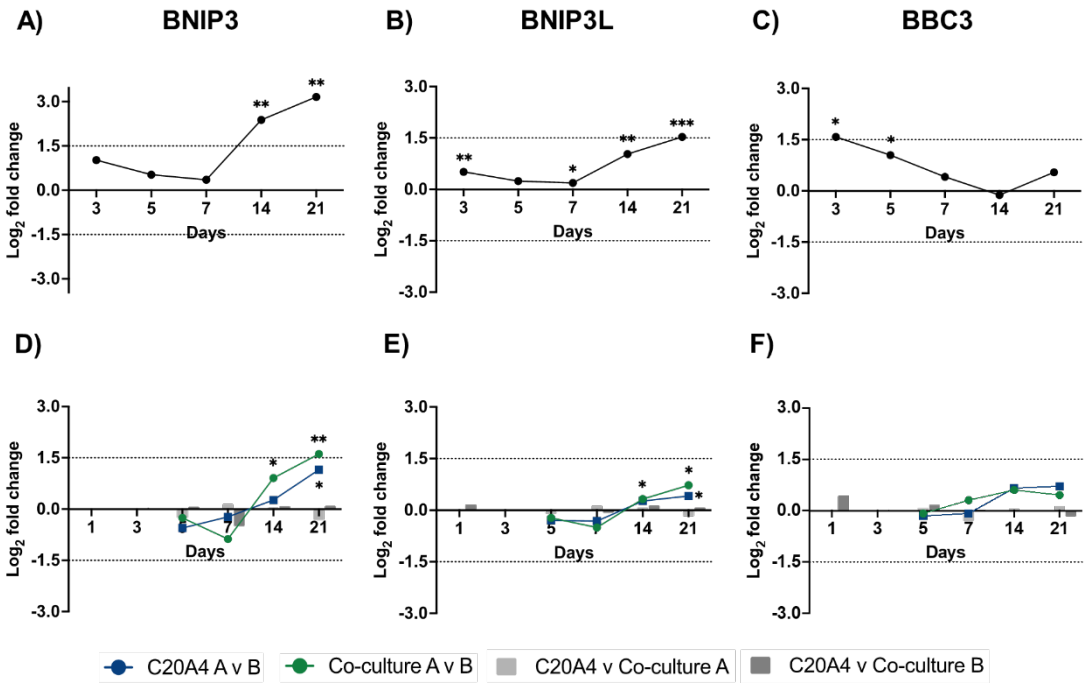

Figure 7.37 Change in gene expression of BCL2-related DEGs over time. *Differential gene expression was examined in advanced 3D in vitro models using the Nanostring IO360 panel. Log2 fold change for: A+D) BCL2 interacting protein 3 (BNIP3), B+E) BCL2 interacting protein 3 like (BNIP3L), and C+F) BCL2 binding component 3 (BBC3) are shown. Timepoint comparisons between day 3-21 against day 1 as baseline in the co-culture model in optimal culture media condition are shown in A-C. Culture media conditions representing augmented regime (A) versus optimal regime (B), and chondrocyte monoculture versus co-culture with fibroblast in both culture media conditions were compared at each timepoint in D-F. Statistical significance is denoted by * ($p<0.05$), ** ($p<0.01$) and *** ($P<0.001$). The horizontal dotted lines represent log2 fold change of >1.5 or <-1.5.*

revealed that this was not always substantiated in proteomic studies and continuous hypoxic conditions have yielded mixed results[372, 378, 379]. The interplay between hypoxia and cellular metabolism, in quiescent versus metabolically active chondrocytes, the control of chondrocyte differentiation, and phenotype and functional maintenance during prolonged culture are complex and therapeutic targets to augment cartilage regeneration remain a work in progress. Nonetheless, the differential gene expression analysis revealed a temporal effect of the model's response to hypoxia and metabolism. This indirectly indicates the dynamic nature of the model as illustrated by the rising metabolic activity with the alamar blue assay in chapter 6. Further research is required to understand the optimal oxygen tension and metabolic state most conducive to cartilage regeneration for product development.

7.4 Chapter Limitations and Summary

The purpose of this chapter was to further characterise the advanced 3D *in vitro* model for the purpose of biocompatibility testing and product and process improvement as relevant to cartilage tissue engineering. Notably, the technical challenge of cell extraction from cross-linked hydrogel samples directly limits the feasibility of downstream assays for the assessment of toxicological endpoints.

Considerations for these included western blotting for genotoxicity assessment testing for proliferating cell nuclear antigen (PCNA), poly-ADP-ribose polymerase (PARP) and phosphor-52, and the examination for the presence of micronuclei in binucleated cells using the cytokinesis-block micronucleus assay. Alternatively, oxidative stress could be assessed *via* the determination of the levels of activity of anti-oxidant enzymes such as superoxide dismutase and peroxiredoxin and the levels of anti-oxidant peptide, glutathione. With the proposed, commonly used assay techniques, residual bio-ink in the samples is likely to cause material interference and interfere with the validity of the results. Furthermore, the cell extraction process may cause adverse biological effects introducing potential confounding variables.

In-situ techniques were explored, including imaging using confocal microscopy and immunohistochemistry (IHC) assessment, although both were unsuccessful. With both techniques, the goal included the characterisation of the model in a 3D manner to understand cell distribution and cellular state in the model's peripheries and center. Initial trials with confocal microscopy including the application of Z-stack did not produce useable images (data not shown). A combination of factors hindered the application of confocal microscopy, such as sub-optimal stain penetration and time constraints for the attainment of representative z-stacks in cultured samples. IHC was also trialled but difficulty was encountered to produce reliable fixation to permit slicing for IHC staining and imaging purposes. Standard and augmented protocols for formalin fixation and paraffin embedding did not overcome the technical barrier of achieving thin slices of the soft hydrogel sample (data not shown).

As such, efforts were focused upon the optimisation of RNA extraction, given an initial successful pilot testing. Following a series of optimisation studies, the objective of RNA extraction was achieved, with the yield of good quality (integrity) RNA with acceptable purity and adequate, albeit low, quantity. The next step was to rationalise

the application of the extracted RNA. RNA sequencing, whilst being a high-throughput technique permitting the sequencing of thousands of transcripts and therefore a wealth of information, it also requires additional sample processing (e.g. reverse transcription for cDNA), additional RNA input quantity and expert bioinformatics support. As such, a panel-based technique was preferred, where both qPCR array and Nanostring was considered. Technical advantages (namely lower RNA input quantity) and the multiplex capabilities of up to 800 genes led to the selection of Nanostring as the technique of choice.

A limitation of the study is the lack of fibroblast isolation and therefore the assessment of the influence of each cell type upon the co-culture model. Whilst the comparison of the chondrocyte monoculture and co-culture models offered some insight, the assessment of the material-host interaction using fibroblast was absent.

Nonetheless, the application of differential gene analysis using the Nanostring technology permitted a broader characterisation of the advanced *in vitro* models. The result substantiated the rise in pro-inflammatory response noted in the direct measurement of the cytokines with ELISA, whilst DEGs relevant to ECM and response to hypoxia revealed model characteristics congruent to what would be anticipated in a model of cartilage regeneration. The study demonstrated a clear temporal effect with varying biological processes and signaling pathways enriched at acute and chronic timepoints. In particular, the TNF and interferon signaling pathways may be of research interest due to their up-regulation in the model.

The use of a panel-based technique with broad gene and biological process coverage, whilst providing a global overview of the *in vitro* model, the granular data required to visualise complete biochemical pathways were lacking. For example, the Nanostring human inflammation panel consist of 249 genes, whereas the IO360 panel of 770 genes encompassed 25 biological processes with an average coverage of 54 genes per biological process (range 17-100 target genes per biological process). In this case, differential gene analysis permitted the identification of target genes and biological processes of interest, but was not suited for the delineation of specific pathway components of interest to generate detailed hypothesis for further testing.

Overall, this chapter generated a reliable RNA extraction strategy for the advanced 3D *in vitro* model, contributing to the creation of the SOP (appendix 1). A global assessment of the advanced 3D *in vitro* model was undertaken, with multiple variables examined including the effects of time, culture media conditions and comparison between mono- and co-culture systems. This data provides an indication of the biological effects of the nanocellulose-based bio-ink with respect to cartilage tissue engineering, whilst establishing model characterisation data to enable future model modifications or further testing.

Chapter 8: Discussion

This thesis aimed to address the biocompatibility of nanocellulose-based bio-inks intended for cartilage tissue engineering, for facial reconstruction purposes. The goals were to create an advanced 3D *in vitro* model, with which biological testing of the nanocellulose-based bio-ink was conducted against human chondrocytes and human dermal fibroblasts. A secondary aim was to refine the bio-ink formulation and cross-linkage processes based on optimal biological effects.

The creation of the *in vitro* model was preceded by assessment of the three bio-ink components (nanocellulose, alginate and hyaluronic acid) which encompassed sterility testing, biological testing of their cytotoxic and pro-inflammatory effects and with the latter two components, their cross-linkage behaviour. Sterility was established using a microbial growth assay. Cytotoxicity was assessed using the erythrosin B exclusion assay and with cell morphology for cells in 2D culture, and the alamar blue assay and LDH assay for cells in 3D culture. The pro-inflammatory effects were determined with the quantification of IL-6 and IL-8 with ELISA. The biological effects of each bio-ink components parts were assessed individually initially, in accordance with the pre-cautionary principle in toxicology. Further evaluation of the *in vitro* model was conducted with differential gene expression analysis using Nanostring following the successful trial of RNA extraction from the cross-linked hydrogel models.

The study defined the final bio-ink formulation to consist of ETC (nanocellulose), alginate and non-tyramine-substituted HA in the low concentration reconstituted in media, and a standardised cross-linkage method with 0.1M $CaCl_2$ over 25 minutes in a silicon mold. Whilst superiority of the bio-ink inclusive of HA was seen with heightened cellular metabolic activity, all models demonstrated a rise in LDH and pro-inflammatory cytokines indicative of cell activation and cell stress on day 21, with further model development and characterisation warranted. An SOP was produced for the creation of the advanced 3D *in vitro* model, as well as several endpoint assessment techniques directly applicable to the model. The study also confirmed the suitability of Nanostring for differential gene expression analysis, which identified several areas of interest for further investigations.

8.1 Data generated based on the pre-cautionary principle

Tissue engineering is a multi-disciplinary field which thrives on the cross-pollination of skills and knowledge across a wide spectrum of specialties[380]. This spans disciplines

such as cell biology, material sciences, bioengineering and surgery. Whilst a TEP intended for market are subject to regulatory toxicological assessment to ensure safety and biocompatibility, the pairing of *in vitro* toxicology and regenerative medicine during early to mid-point product development does not appear to be a common occurrence. As such, the assessment of the biological effects of bio-ink candidates in line with the pre-cautionary principle is relatively less commonly found in the literature. The next sections detail new and original contributions to existing knowledge as relevant to 3D bioprinting cartilage using a nanocellulose-based bio-ink.

8.1.1 Pro-inflammatory effects of tunicate-derived nanocellulose

Whilst nanocellulose are generally considered to be of limited toxicity, studies have shown potential adverse biological effects depending on their physical characteristics, exposure routes and administered dosage[206]. In tissue engineering, modern bio-inks are often composite in nature, especially for those incorporating nanocellulose in order to incorporate polymers capable of gelation to achieve a stable construct[100]. The overwhelming majority of studies investigating cell viability and cytotoxicity of nanocellulose-based bio-ink involves that of the composite bio-ink. As such, there is a relative paucity of direct comparisons of different nanocellulose forms, nor assessments of nanocellulose alone (i.e. free from other bio-ink additives) against an end-application relevant cell type, in this case, chondrocyte.

The direct comparison of the cytotoxic and pro-inflammatory effects of three forms of variably functionalised tunicate-derived nanocellulose fibrils (enzymatically pre-treated (ETC), TEMPO-mediated oxidised (TTC) and carboxymethylated (CTC)) against the C20A4 cell line (human chondrocyte) in chapter 3 identified ETC as the least pro-inflammatory form across all timepoints. This filled a knowledge gap in the literature and permitted the selection of ETC as the nanocellulose form to take forward for further investigation.

As nanocellulose is currently explored as a bio-ink candidate for a variety of tissue regeneration, such as bone, nerve, skin, corneal and vascular tissues, specific tests against relevant cell types would be prudent to ensure results validity. This could be expanded to include composite tissue regeneration, such as joint replacement with bone and cartilage cell types, or vascularised tissue constructs including both the primary cell type supplemented by vascular endothelial cells.

Inflammation, beyond the acute phases of wound healing, can be a key determinant of success of an implanted tissue-engineered cartilage construct. Potential alternative cellular analytical methods and the investigative strategy taken in this project is hereby further discussed.

Techniques relevant to the evaluation of pro-inflammatory effects in the *in vitro* setting can include the ELISA and Western blot analysis, providing quantification of various cytokines and pro-inflammatory mediators, as well as qRT-PCR and RNA sequencing for gene expression analysis. In this project, due to the number of material and cross-linker options (forms and concentrations), a focused selection of cytokine and chemokine (IL-6 and IL-8) were used to determine the suitability of various materials (chapters 3, 4, 5). The presence of marked pro-inflammatory response would indicate potential hazards, supporting the use of more favourable materials options.

In order to gain a more holistic inflammatory profile of the *in vitro* cell systems, the combined assessment of pro-inflammatory (e.g. IL-6, IL-8, IL-1β, TNF-α and IL-18) and anti-inflammatory mediators (e.g. IL-10, IL-4 and IL-37) would prove beneficial. Although not undertaken in this project in view of the planned global assessment of the cell systems *via* differential gene analysis, this approach would be most applicable in the toxicological testing of the bio-inks in the advanced 3D *in vitro* models (chapter 6). The strategy of using a broader panel-based testing early vs a focused examination using key cytokines of cell systems are each associated with their respective benefits, limitations and resource requirements. In this project, the use of IL-6 and IL-8 permitted the refinement of the bio-ink and the cross-linkage process, whilst the differential gene analysis with Nanostring highlighted multiple potential cell signalling pathways of interest which guides future proteomic-based studies to validate findings and deepen understanding of the roles of relevant biochemical pathways (chapter 7).

8.1.2 Time- and dose-dependent cytotoxicity of $CaCl_2$ and H_2O_2

$CaCl_2$ is a commonly employed ionic cross-linker for bio-inks incorporating alginate. A variety of concentration has been reported in the literature ranging from 0.1 to 1.0M applied across various bio-ink systems, with application times in the range of minutes but occasionally reported in hours[212, 219, 221, 223, 224]. To appropriately account for the biological effects of the *in vitro* model, toxicity induced *via* the fabrication process must be taken into consideration. The cytotoxic and pro-inflammatory effects of $CaCl_2$

against HFF-1 and C20A4 cells lines, at dosage and timescale relevant for cross-linkage for the purposes of the *in vitro* model as reported in chapter 4, has not been previously reported. Similarly the effects of H_2O_2 against HFF-1, a known inducer of genotoxic and cytotoxic effects in mammalian cells, as studied in chapter 5, provided crucial data which led to the transition towards a triple component bio-ink as described in the SOP (appendix 1) and subsequent testing as used in the advanced 3D *in vitro* model in chapter 6 and 7.

8.2 Standardisation of bio-ink components

The conversion of bio-ink material contents from ratios to concentrations was particularly helpful to permit comparisons of singular variables and determination of its effects. Whilst not necessarily a novel principle, bio-ink formulations in ratios are relatively common in the field of tissue engineering[223, 224, 227]. As highlighted in chapter 2, ratio-derived bio-ink formulations have varying concentrations of all bio-ink components, each of which can contribute to altered material behaviour. In chapter 5, the comparison of two HA concentrations, by merit of the conversion to a concentration-based formulation, permitted direct comparison of the biological and cross-linkage dataset for the selection of the optimal HA concentration for bio-ink and *in vitro* model creation. This approach is likely to support future bio-ink developments whilst ensuring reproducibility.

8.3 Creation of an advanced 3D *in vitro* model

The application of a standardised and characterised advanced 3D *in vitro* model for the purpose of biological testing of bio-inks intended for 3D bioprinting is a novel concept. Whilst many studies in the field of tissue engineering evaluate cell viability and cytotoxicity associated with biomaterials (3D printed or casted) with cell metabolic assays (e.g. the MTT assay), immunostaining (e.g. live/dead staining) or other techniques, the system parameters including cell densities and hydrogel dimensions may vary depending on the assay employed and are therefore specific to the assessment in question and are not standardised. Timepoints employed for characterisation or endpoint assessment are also relatively limited compared to the current study.

The value of an advanced 3D *in vitro* model developed for a specific application is its reproducibility, and in bridging a gap between an overly simplistic *in vitro* model and *in vivo* studies. As highlighted previously, the successful clinical translation of a TEP requires examination of many variables and combinations of variables, which may be time- and cost-prohibitive. The availability of an advanced *in vitro* model could potentially accelerate future developments of the bio-ink and bio-fabrication process by streamlining products relevant for further testing in an *in vivo* setting. The *in vitro* model can also support additional testing to elucidate mechanisms behind observed biological effects.

Indeed, the development of complex *in vitro* models (CIVMs) are on the rise and has been adopted in a variety of settings. Its use as cancer models may be an apt analogy as new oncology therapies carry the lowest success rate of proceeding from phase I trial to FDA approval across all sectors at 3.4% (2000-2015)[381].

A recent survey conducted by the EU Reference Laboratory for alternatives to animal testing (EURL ECVAM) in 2021 found growing interest in CIVMs. This is reflected by a four-fold increase of publications related to CIVMs annually (2014-2018), international institutions investing in CIVMs (e.g. Horizon 2020 and Innovative Health Initiative (formerly known as the Innovative Medicines Initiative) in the EU, and the National Centre for Advancing Translational Sciences and Food and Drug Administration in the US), and their applications in pharmaceutical companies including GSK, AstraZeneca and Pfizer.

CIVMs are developed to mimic a variety of physiological conditions and microenvironments, with wide ranging applications from disease modelling such as with cancer models to therapy development including drug screening. They can be tailored to be human-specific, permit control over specific experimental variables, be highly reductive to best support high-throughput assays (e.g. for screening high volume of chemicals), or be highly complex to more closely mimic *in vivo* microenvironment which can serve to establish mechanisms. It supports the 3Rs movement for the replacement, reduction and refinement of animals used in research. However, CIVMs lack whole organism representation and therefore, in its current form, seeks to complement animal studies. It may provide an avenue for individualised medicine by using patient's own cells for model creation which addresses variation in

patient phenotypes. Validation of CIVMs is recognised to be an important pre-requisite for their recognition and adoption in the regulatory setting in the EURL ECVAM 2021 survey and remains an area of evolution.

8.4 RNA extraction and transcriptomic study with Nanostring

In parallel to advances in CIVMs, technological progressions in the field of transcriptomics could be leveraged to catapult efforts in tissue engineering. Alongside increasing ease and utilisation of RNA-sequencing, the vast accumulation of data yielded the availability of a human atlas of cell transcriptomes[382] and the Compendium for Biomaterial Transcriptomics (cBiT), a repository of biomaterial-based transcriptomic dataset which details cell and biomaterial interactions [383]. Together, they represent powerful data resources to map native human biology processes against which pathological or tissue engineered processes could be compared with. Although not employed in this study, spatial transcriptomics and single cell transcriptomics may prove insightful, particularly in distinguishing cell behaviour at the core of a TEP construct reflecting the primary cell function, in this case, the chondrocyte; whilst the ability to identify individual cells such as the fibroblast, in the periphery of the TEP construct, can shed light on processes relevant to implant integration and foreign body reaction.

Relating to this study, a key contribution is the successful development of an RNA extraction protocol from the cross-linked hydrogel construct as detailed in chapter 8. Low yield in terms of quantity was a common finding when compared to previous in-house attempts. High variance in quantitative polymerase chain reaction (qPCR) data was observed in past studies, although this may not be attributed to RNA quality (unpublished data). The RNA yield in the current study, whilst of good integrity as represented by an average RIN score of 8.5, was limited by low quantity. Despite a relatively low RNA input quantity, differential gene analysis using Nanostring showed good concordance across the biological replicates.

To date, qPCR and RNA sequencing are key techniques in small scale and genome-wide gene expression studies, respectively. The Nanostring nCounter System offers an alternative which examines hundreds of genes. As discussed in chapter 7, it benefits from a low RNA input requirement, which suited the current advanced 3D *in vitro* model well. However, its panel-based nature, similar to qPCR, carries the inherent

limitation of the examination of known gene targets only. Furthermore, as of early 2024 when the Nanostring experiment was conducted, of the hundred or so available Nanostring panels, none was geared towards regenerative medicine. Whilst custom panels or gene additions were available, the cost-benefit ratio rapidly deteriorates with increasing number of target genes added. Based on the transcriptomic study data in chapter 7, it can be concluded that Nanostring is an excellent application as a multiplexed gene expression analysis technology compatible with RNA extracted from the advanced 3D *in vitro* model in this study. With the appropriate selection of Nanostring panel, it is more efficient in generating greater volume of data output when compared with qPCR methods, and does not require specialist bioinformatics expertise for data analysis as is the case with RNA-sequencing. However, due to the incomplete interrogation of the transcriptome and the broad range of biological processes covered with the IO360 panel, it was difficult to derive definitive conclusions regarding pathway enrichment. As such, it is proposed that RNA sequencing may be a good option to identify biological processes of interest which could offer new insight or identify novel genes of interest, following which Nanostring panels relevant to specific biological processes (e.g. inflammation) are employed for efficiency.

8.5 Material characterisation and lack of reference material

Material characterisation in the forms of detailed physico-chemical characterisation, of both the raw form of nanocellulose and as a composite triple component bio-ink, is crucial to support toxicological data[268, 384, 385]. Whilst this is outwith the remit of this study, its relevance is recognised and work is underway to address this need. In TEPs, further complexity is introduced from the biofabrication process. For example, cross-linkage parameters can alter scaffold porosity which directly impacts biological function such as gas exchange, nutrient transport, cell migration and neovascularisation[386, 387]. I.e. the biological effects measured is specific not only for the raw nanoparticle and composite bio-ink formulation, but also with the system tested.

Drasler *et al* described four widely accepted, salient points with regards to *in vitro* approaches for hazards assessment of nanomaterials[384]. This included material characterisation, the use of realistic dosage and exposure conditions, the use of positive and negative controls and a multiple endpoint approach together with multiple assays

for each endpoint. The authors highlighted that a benefit of employing controls is to support intra- and inter-laboratory comparisons. In culmination, these approaches serve to enhance results reproducibility, relevance and validity, and are considered good practice.

In the context of tissue engineering, cells are often encapsulated within the cross-linked biomaterial, as is the case in the advanced 3D *in vitro* model in this study. As such, there are inherent challenges in achieving a negative control. As is commonly described in the literature, the use of 2D cell culture devoid of material exposure was used as the negative control[224, 226, 231]. However, differences in 2D versus 3D cell culture automatically deem results not directly comparable. This raises the topic of a reference material, with stable and defined physico-chemcial properties and validated toxicological data for specific toxicological endpoints and assessment methodologies. Appreciation of the relative lack of reference engineered nanomaterials and efforts to address this is emerging, such as with material groups including metals and metal oxides, and gold nanoparticles[388-390].

Although in the relative minority, studies evaluating nanocellulose-based biomaterial for cartilage tissue engineering purposes have used surrogate materials as controls. Examples include the use of a sterile Eppendorf lid cultured in media [227], and the Gore® Dualmesh biomaterial made of polytetrafluoroethylene (ePTFE)[232]. Whilst both substitutions may offer advantages over 2D cell culture, the discernible difference with tissue-engineered implants are that the material is designed to be bioactive and support cell growth and differentiation for tissue regeneration, in contrasts to traditional synthetic implants which are designed to be inert. Using ear reconstruction as an example, whilst Medpor, a polyethylene implant that currently serves as a standard of care for patients undergoing total ear reconstruction when autologous (patient's own) cartilage is not used, for the reasons outlined, it would not be an ideal reference material for said purposes as the material was not designed to be a cell carrier. An alternative could be Matrigel, a widely utilised basement membrane preparation established from mouse sarcoma. Its thermosensitive gelation properties, achieving a solid gel state at physiological temperatures (37^{o}C) and transitions to a liquid state at cool temperatures (<10^{o}C), could simultaneously support 3D *in vitro* modelling and remove the need for cross-linkage and reduce potential adverse effects from cell dissociation procedures. Nonetheless, it would require detailed

characterisation to establish its cytotoxic and pro-inflammatory effects against relevant cell types, specific experimental parameters and methodologies for endpoint testing.

8.6 Future directions

Whilst *in vitro* toxicology is not classically embedded amongst the multi-disciplinary team in tissue engineering, TEPs as a form of advanced therapy medicinal products are subjected to product development challenges as with pharmaceuticals and regulatory toxicology when ready for market. Therefore, an awareness and considered adoption of current advances in *in vitro* toxicology may potentially enhance and expedite efforts in tissue engineering towards clinical translation.

Table 8.1 illustrates potential avenues for future work, and are categorised as follows: i) Model development - to enhance the complexity and relevance of the advanced 3D *in vitro* model;

ii) Model application - to expand the application of the *in vitro* model for the investigations of alternative facets relevant to cartilage tissue engineering, and

iii) Investigative modalities – to explore alternative assessments modalities of the *in vitro* model.

Despite over twenty years of research and development involving tissue-engineered cartilage specifically for head and neck applications, there is a predominance of *in vitro* and *in vivo* studies with nude mice, whilst progress towards clinical translation is limited to phase I/IIa clinical trials[391]. Anatomical sites relevant for tissue-engineered cartilage in the head and neck include the ear, nose, eyelid, larynx and trachea. Total ear or tracheal reconstruction may represent the most challenging clinical scenarios.

The publication of the first clinical application in 2008, and its five year follow-up in 2014, of a tissue-engineered, decellularized trachea from a human donor populated with the recipient patient's own epithelial cells and MSC-derived chondrocytes invited much interest in the field of regenerative medicine[43, 392]. In the ensuing years, investigations were conducted regarding the efficacy and ethical concerns surrounding this case. Airway reconstruction carries potential for significant morbidity and mortality. It is a high-risk site, and albeit with an unmet clinical need, alternative head and neck sites, such as the ear, may be associated with a relatively more limited

Table 8.1. Future work proposed.

Future work	
Model development	• Use of human or alternative factors to achieve non-animal-derived model - e.g. substitution of FBS with human platelet lysate, trypsin with accutase. • Incorporate immune modelling *in vitro* – with the introduction of immune cells; e.g. with Transwell inserts for indirect contact. • Explore the effects of fluid flow on model characteristics – e.g. with microfluidic system to mimic capillary blood flow surrounding *in vivo* implant.
Model application	• 3D bioprinting – to 3D print models instead of casting with mold to more closely mimic the end-application scenario; printing parameters can be tested (e.g. printing speed, sheer rate, nozzle diameters). • Use of autologous (patient's own) cells – instead of cell lines to identify patient-specific responses. • Investigate known culture conditions associated with heightened chondrogenesis – e.g. hypoxic conditions, mechanical agitation, growth factors.
Investigative modalities	• In-situ live cell imaging – e.g. laser scanning confocal microscopy to track cell migration and proliferation. • RNA-sequencing – with single cell or spatial RNA sequencing to investigate cell-material and material-host interactions. • Investigation of other toxicological endpoints – e.g. oxidative stress and genotoxicity. • Model functionality – e.g. ECM formation

morbidity and mortality profile. Furthermore, rigorous scientific conduct in line with the Good Clinical Practice which provides a framework and international standard for the design, conduct, recording and reporting are mandatory of all clinical trials.

Notable clinical studies of tissue engineered cartilage for ear reconstruction included Zhou *et al*'s study in 2018[393] and more recently the AuriNovo trial in 2023. The former described the use of expanded ear chondrocytes from patients with microtia (congenital malformation of the ear) with a composite synthetic scaffold consisting of PCL, PGA and PLA[393]. This study involving five patients with microtia demonstrated cartilage formation and acceptable aesthetic outcomes at 2.5 years, but lack further longitudinal follow-up. Theoretically, eventual cell fate of chondrocytes expanded from congenitally dysplastic tissue following implantation is uncertain, despite adequacy during *in vitro* expansion. Furthermore, whilst synthetic compounds offered enhanced tunability, mechanical strength and lack potential batch-to-batch variability

associated with organic materials, there is a greater potential for heightened foreign body response following implantation which can be particularly detrimental in reconstruction where lifelong shape maintenance is key. Between 2021 and 2023, two patients with microtia were recruited in the AuriNovo trial (ClinicalTrials.gov ID NCT04399239). This US-based Phase I/IIa trial utilised a 3D-bioprinted collagen hydrogel scaffold seeded with patient's own ear chondrocytes. The latest update of the trial, which was sponsored by 3DBio Therapeutics, was from March 2024 *via* ClinicalTrials.gov, which stated that the study was terminated citing "*company decision, not safety related*".

Taken together, the above highlights that the influential factors associated with the success of a tissue engineered product is multi-factorial. Factors worthy of consideration for successful clinical translation may include ensuring optimal cell source for stable and functional cell phenotype, minimising foreign body response such as with the use of natural biomaterials or augmentation of synthetic compound, and prudent navigation of commercial, academic and clinical collaborations.

Chapter 9: Appendix

Appendix 1: Standard operating procedure for the creation of advanced 3D *in vitro* models

Appendix 1 refers to the standard operating procedure (SOP) for the creation of advanced 3D *in vitro* models for toxicity testing of nanocellulose-based bio-inks intended for cartilage 3D bio-printing. The laboratory methodologies to create the advanced *in vitro* models have been described previously in the thesis, but as separate components across chapters 3 to 5. Building on this, the methodology is presented here in its entirety in SOP form. This is preceded by a summary of the research conducted in this thesis which informed the SOP, which are outlined in appendix 1.1. The process to create the advanced 3D *in vitro* models is illustrated in appendix 1.2. The SOP is presented in appendix 1.3.

A detailed outline of the four key parts of the SOP (appendix 1.3) is as follows:

i. Cell culture procedures for both the HFF-1 and C20A4 cell lines.
ii. Creation of two bio-inks: i) ETC:Alginate in media, and ii) ETC:Alginate:N-HA (low) in media.
iii. Creation of the cell-seeded hydrogel discs to create three culture models: i) HFF-1 surface-seeded monoculture, ii) C20A4-encapsulated monocultures, and iii) a co-culture model combining (i) and (ii). This can be applied with either bio-inks described in (ii).
iv. Tests and assays applied to the advanced 3D *in vitro* models created by the SOP for toxicity testing. This includes the alamar blue assay, ELISA, LDH assay and RNA extraction. Methods and assays including the modifications of techniques required for the 3D *in vitro* models are described.

Appendix 1.1 Summary of recommendations informing SOP creation

The stages and rationale for the selection of specific materials or procedures are illustrated in appendix 1.2, and hereby outlined for clarity. Due to the interconnected nature of bio-ink formulations, cross-linkers and the cross-linking system using silicon molds, despite being represented sequentially in appendix 1.2, some studies relating to these parts occurred in parallel. Sections referenced here in appendix 1.1 refer to sections within the main thesis (i.e. not the SOP/appendix).

Stage 1 refers to the selection of the nanocellulose form, with autoclave-sterilised pulp-derived nanocelluloses excluded due to non-sterility at latter timepoints (section 3.3.1). ETC was chosen between three forms of tunicate-derived nanocellulose as it was the least pro-inflammatory based on IL-6 and IL-8 release profiles (section 3.3.2.2). Stage 2 focused on the selection of the cross-linker agent and its concentration. $CaCl_2$ was first tested as the cross-linker for alginate. Amongst three $CaCl_2$ concentrations, the lowest concentration (0.1M) was selected due to the dose- and time- dependent cytotoxicity profile against HFF-1, and preserved viability with C20A4 with 0.1M $CaCl_2$ (section 4.3.3).

Stages 3 to 7 described efforts to create a nanocellulose-based bio-ink inclusive of HA, a native human cartilage component. Bio-inks of nanocellulose and T-HA were unsuccessfully cross-linked with the cross-linker H_2O_2 at low concentrations (section 5.3.1.4), whilst high H_2O_2 concentrations were associated with unacceptable cytotoxicity (section 5.3.1.3). Therefore, the concept of a triple component bio-ink was introduced. This was successfully piloted, leading to the creation of the bio-ink ETC:Alginate:N-HA (low) in media for cross-linkage with 0.1M $CaCl_2$. As part of this transition, a non-tyramine-substituted form of HA was introduced to more closely mimic native HA. Two HA concentrations were tested. The low N-HA concentration was selected due to equivocal cytotoxic and pro-inflammatory profiles (section 5.3.2.2), but markedly shortened cross-linkage time requirement (section 5.3.2.3), thereby limiting cross-linker toxicity. This leads to the definition of the cross-linker application time, which was defined at 15 minutes for the bio-ink ETC:Alginate in media (section 4.3.4.1) and 25 minutes for ETC:Alginate:N-HA (low) in media (section 5.3.2.3.1), both cross-linked with 0.1M $CaCl_2$.

The final part of the SOP involved cell seeding. Due to the low physiological cell density of HFF-1, three cell densities were examined during cell line characterisation, which identified $2x10^4$ cells/cm^2 (mid) as the most suitable (section 2.8.5.1), and therefore adopted for the SOP.

Appendix 1.2 Schematic for the creation of the SOP for advanced 3D *in vitro* models for the testing of bio-inks intended for cartilage tissue engineering

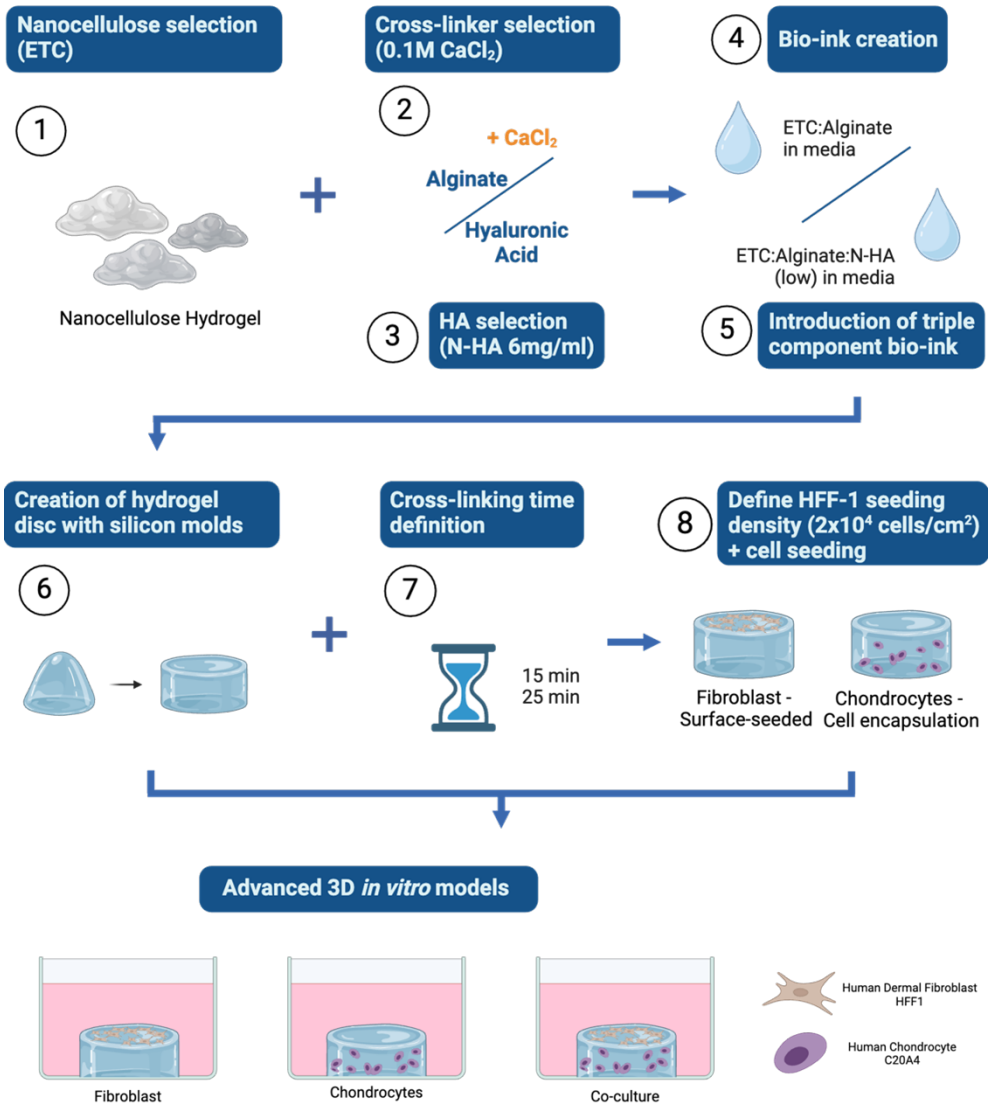

Each stage (numbered) represents prior studies which informed material or procedural choices for the final SOP. **Stage 1** – Enzymatically pre-treated nanocellulose (ETC) was chosen amongst 6 nanocelluloses due to its sterility and optimal pro-inflammatory profile. Stage 2-7 are inter-linked elements although presented sequentially. **Stage 2** – 0.1M $CaCl_2$ was chosen as it was the least cytotoxic amongst 3 concentrations tested whilst remaining effective as a cross-linker. **Stage 3** – Non-tyramine-substituted hyaluronic acid (N-HA) at the low concentration (6mg/ml) was taken forward as the HA form and concentration of choice due to its suitable cytotoxic, pro-inflammatory and gelation profiles. This was selected amongst two forms of HA in two

concentrations. **Stage 4 + 5** – Two final bio-inks were created to incorporate nanocellulose and alginate, with a triple component bio-ink version which includes HA. Both bio-inks are cross-linked with 0.1M $CaCl_2$. **Stage 6** – Dome-shaped hydrogel pellets were modified to be disc-shaped using silicon molds to support surface cell seeding of fibroblast. **Stage 7** – Definition of cross-linking time using bio-ink defined in stage 4 and cross-linker in stage 2, in the system described in stage 6. **Stage 8** – HFF-1 cell seeding density was defined via cell line characterisation of three cell densities. Cell seeding was performed with surface seeding with HFF-1 to mimic the material-host interaction and cell encapsulation with C20A4 for the cell-material interaction. Created with BioRender.com.

Appendix 1.3 SOP

This project has received funding from the Royal College of Surgeons of England, the Blond McIndoe Research Foundation, Action Medical Research and the VTCT Foundation.

Standard Operating Procedure (SOP)

Guidance Document:

Creation of an Advanced 3D *In Vitro* Model for the Testing of Nanocellulose-based Bio-inks for Cartilage Tissue Engineering

Adapted from the PATROLS SOP, Meldrum K *et al* (Under the European Union's Horizon 2020 research and innovation programme. Grant agreement 218539; available from https://www.patrols-h2020.eu/publications/sops/SOP-library-pdfs/3101-Guidance-Document-for-cell-culture-of-lung-epithelial-cell-line-A549-.pdf?m=1636040463& - accessed 18.02.2025)

Authored by:

Cynthia de Courcey[1], Kirsty Meldrum[1], Laurence Hill[2], Matthew Turner[2], Thomas Jovic[2,3], Alethea Tang[4], Laura Thomas[4], Iain S Whitaker[2,3], Martin J D Clift[1]

[1]In Vitro Toxicology Group, Institute of Life Science 1, Faculty of Medicine, Health and Life Sciences, Swansea University, Swansea, UK

[2]The Reconstructive Surgery & Regenerative Medicine Research Group (ReconRegen), Institute of Life Science 1, FMHLS, Swansea University, Swansea, UK

[3]The Welsh Centre for Burns & Plastic Surgery, Morriston Hospital, Swansea, UK

[4]Inherited Tumour Syndromes Research Group, Institute of Life Science 1, Faculty of Medicine, Health and Life Sciences, Swansea University, Swansea, UK

Reviewed by:

n/a

Document history:

Version	Approval Date	Description	Authors of Change
1.0	23.02.2025	Initial document	Cynthia de Courcey

Contents

1 Introduction

Tissue engineering aims to overcome the risks and limitations of current reconstructive options for individuals with cartilage tissue loss, such as from trauma, cancer or congenital conditions. With 3D bioprinting, the patient's own cells are loaded into a biomaterial (bio-ink), and is printed layer-by-layer to create precise, bespoke cartilage implants, which can then be used for facial reconstruction[1,2].

Nanocellulose is a relatively new bio-ink candidate[3]. It is a natural material with shear-thinning and mechanical properties, particularly relevant in the context of extrusion-based 3D printing and as a material scaffold, respectively[4]. While nanocellulose demonstrates overall favourable biocompatibility, *in vitro* studies available are mostly focused on raw material and pulmonary models relevant to occupational exposures[5,6]. Establishing the biological effects of nanocellulose-based bio-ink, as an implantable material, is now of heightened interest.

The development of a physiologically relevant, advanced 3D *in vitro* model aims to aid: i) toxicity testing of the bio-ink, and ii) further research for the refinement of bio-ink formulations and processes relevant to 3D bio-printing. In reconstruction, the surgically-created implantation pocket is characterised by active immunological and inflammatory processes, influenced by both the effects of cell-material and material-host interactions, and wound healing. As such, a co-culture model was created to mimic the *in vivo* scenario, with chondrocyte-encapsulated cross-linked bio-ink reflecting the cartilage implant. This model also includes surface-seeding with dermal fibroblast to simulate the material-host interface. Toxicity testing with the advanced 3D *in vitro* model are in line with the movement of 3R's, permitting the selection or refinement of materials and processes based on *in vitro* biological data, prior to *in vivo* studies.

1.1 Scope and limitations

This SOP describes the procedures required for an advanced 3D *in vitro* model, developed specifically for the toxicity testing of nanocellulose-based bio-inks for the creation of tissue-engineered cartilage implants *via* extrusion-based 3D bio-printing. The scope and limitations are described as specific to the four parts of the SOP.

1.1.1 Cell culture

Part 1 of the SOP details the cell culture procedures for the human dermal fibroblast (HFF-1) and human chondrocyte (C20A4) cell lines intended for their application to create an advanced 3D *in vitro* model.

The scope of this SOP refers to cell culture procedure, up to but not including the stage of cell seeding for the creation of the advanced 3D *in vitro* model.

Limitations:

As stated by the supplier, the C20A4 cell line may display altered cell function and loss of cell marker expression beyond 10 passages. Use of C20A4 therefore is recommended to be within 10 passages from supply. Cell line characterisation was performed up to, and inclusive of P10.

1.1.2 Creation of bio-inks

Part 2 of the SOP details the preparation of two bio-inks. The two bio-inks detailed are: i) ETC:Alginate in media, and ii) ETC:Alginate:N-HA (low) in media. Both bio-inks utilises the common components of ETC (a tunicate-derive nanocellulose fibril which is enzymatically pre-treated) and alginate. The material form and concentrations for nanocellulose and alginate in both bio-inks are the same. The two bio-ink differ only by the incorporation of N-HA in bio-ink (ii).

The physico-chemcial properties of individual bio-inks, as well as the mechanical properties of the cross-linked construct, can both influence cellular behaviour, and therefore potentially the results of toxicity testing. As such, the bio-ink formulation and preparatory procedures should be standardised and defined for clarity and reproducibility. Whilst future adaptation of the SOP can

be made for alternative bio-inks formulation, this is outwith the scope of this SOP. With bio-ink formulatory changes, adjustments of model creation processes may be required.

1.1.3 Creation of an advanced 3D *in vitro* model

Part 3 of the SOP relates to the creation of an advanced 3D *in vitro* model. As described in section 1.1, there are three models:

i. Human dermal fibroblast mono-culture (HFF-1)
   - Surface-seeded 

   - Material-host interaction


Fibroblast

ii. Human chondrocyte mono-culture (C20A4)
   - Cell-encapsulated 

   - Material-cell interaction

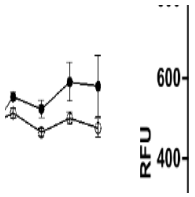

iii. Co-culture
   - Surface seeded fibroblast
   - Chondrocyte-encapsulated


Co-culture

The SOP also includes the procedure for the creation of silicon molds.

Limitations:

The model was characterised for use for up to 21 days. However, heightened pro-inflammatory response was noted on day 21 in the chondrocyte monoculture and co-culture models. This is suggestive of cell activation at latter timepoints which may be related to a relatively high chondrocyte cell seeding density for cell culture purposes. However, the chondrocyte seeding density chosen for the SOP is in the lower end of the spectrum of seeding densities in the literature, specific for cartilage tissue engineering[7,8,9,10,11,12,13]. Interpretation of data at latter timepoints should be undertaken with caution.

1.1.4 Implementation

Part 4 of the SOP refers to several assays and methods relevant for toxicity testing as applied to the advanced *in vitro* models developed with this SOP. This includes the alamar blue assay, ELISA, LDH assay and RNA extraction. Whilst all assays and methods followed manufacturer's guidance in most parts, adapted techniques and methods are described. This is predominantly related to the 3D nature of the *in vitro* models, where efforts to reduce the interference of residual bio-ink material are required.

Limitations:

All assays and techniques were applied to models of up to 21 days culture.

RNA extraction described in the SOP was successfully applied for transcriptomic studies using the Nanostring technology. However, RNA yield is relatively low for the chondrocyte monoculture and co-culture models (Mean±SEM 337±83ng per model), as compared to conventional 2D cell culture models. Pooling of samples is recommended should endpoint testing require greater quantities of RNA. In addition, RNA extraction was unsuccessful for the fibroblast monoculture. This is likely a result of relatively low cell numbers due to a low cell seeding density, and challenges in cell extraction from the bio-ink material.

2 Terms and definitions

Bio-ink – composite material which represent bio-inks used for 3D bioprinting, and for the creation of *in vitro* models in the SOP.

Cross-linker – chemical that acts to cause gelation of the bio-ink

Hydrogel disc – standardised 8mm diameter, 100μl cross-linked bio-ink.

Model – cell-seeded versions of hydrogel disc.

Sample – cell-seeded hydrogel disc from experimental studies (i.e. same as 'model', but subjected to experimental conditions; used for endpoint testing).

3 Abbreviations

Table 1 Abbreviations

Abbreviations	In full
3D	3-dimensional
ATCC	American Type Culture Collection
$CaCl_2$	Calcium chloride
CCM	Complete culture medium
CO_2	Carbon dioxide
ddH_2O	Double-distilled water
DMEM	Dulbecco's modified eagle medium
DMSO	Dimethyl sulfoxide
DNA	Deoxyribonucleic acid
EDTA	Ethylenediaminetetraacetic acid
ELISA	Enzyme linked immunosorbent assay
ETC	Enzymatically pre-treated nanocellulose
FBS	Fetal bovine serum
HA	Hyaluronic acid
LDH	Lactate dehydrogenase
N-HA	Non-tyramine-substituted hyaluronic acid
PBS	Phosphate buffered saline
RNA	Ribonucleic acid
SOP	Standard operating procedure
TB	Trypan blue
UV-C	Ultraviolet-C

4 Principle of the Method

4.1 Cell culture

This SOP aims to standardise cell culture procedures for the maintenance and expansion of HFF-1 and C20A4 cell lines in tissue culture flasks, and methods for their cryopreservation. This is divided into the following stages:

1. Thawing and culturing cryopreserved cells
2. Subculturing cells
3. Cryopreserving cells
4. Cell counting and cell viability assessment

Stage 4 is performed using the erythrosin B exclusion assay. Unless otherwise specified, cell culture procedures described applies for both cell lines, due to common methodologies.

4.2 Preparation of bio-inks

Standardised procedures for the creation of two nanocellulose-based bio-inks are described. This includes the sterilisation of alginate, and preparatory steps for both bio-inks. The two bio-inks are termed:

1. ETC:Alginate in media
2. ETC:Alginate:N-HA (low) in media

4.3 Creation of an advanced 3D *in vitro* model

This SOP covers the creation of the following three *in vitro* models:

1. HFF-1 (human dermal fibroblast) monoculture model
2. C20A4 (human chondrocyte) monoculture model
3. Co-culture model

The procedure for the creation of silicon molds used to shape the hydrogel discs to create each model is also included.

4.4 Implementation

The methodologies relevant to, including adapted or added steps to manufacturer’s guidance, are described for the following assays and procedure:

1. Alamar blue assay
2. ELISA / LDH assay
3. RNA extraction

5 Description of the Method

5.1 Biological setting

All procedures should be performed under sterile conditions in a laboratory-based setting of Biological Safety Level 1 conditions or above.

The two cell lines are:

- Human chondrocyte:
  The C20A4 cell line was derived from human rib cartilage and is available from Sigma-Aldrich (SCC041). Additional information is available from: https://www.merckmillipore.com/GB/en/product/C20A4-Human-Chondrocyte -Cell-Line,MM_NF-SCC041

- Human dermal fibroblast:
  The HFF-1 cell line was established from human skin and is available from ATCC (SCRC-1041™). Additional information could be found from: https://www.atcc.org/products/scrc-1041

5.2 Chemicals and reagents

Table 2 Chemicals and reagents

Materials	Brand (Cat No.)	1	2	3	4
0.05% Trypsin-EDTA solution	Gibco® (5300-054)	Y		Y	
100% ethanol		Y	Y	Y	Y
β-mercaptoethanol	Sigma-Aldrich (M6250)				Y
Calcium chloride dihydrate	Sigma-Aldrich (C7902)			Y	
DMEM (1X Dulbecco's Modified Eagle Medium); [+] 4.5g/l D-glucose, L-Glutamine; [-] pyruvate	Gibco® (41965)	Y	Y	Y	Y
DMSO		Y			
Elastosil® RT 601 A/B	Wacker			Y	

Materials	Brand (Cat No.)	1	2	3	4
Erythrosin B stain	Logos Biosystem (L13002)	Y		Y	
FBS	Gibco® (10270-106)	Y	Y	Y	Y
PBS pH 7.4 1X, $MgCl_2$ + $CaCl_2$ free	Gibco® (14190-094)	Y		Y	Y
Penicillin/Streptomycin 10,000 U/ml	Gibco® (15140-122)	Y	Y	Y	Y
Qiagen AllPrep DNA/RNA MiniKit	Qiagen (80204)				Y
RNAse ZAP	Invitrogen (AM9780)				Y
Sodium acetate (3M), pH 5.2	Thermo Scientific (R1181)				Y
Sodium alginate*	Sigma-aldrich (W201502)		Y		
Sodium hyaluronate* - Sterile research-grade (molecular weight 1.59x10^6Da) (N-HA)	Lifecore Biomedical, Inc (HA15MS)		Y		
TrypLE™ Express Enzyme (1X), no phenol red	Gibco (12604)				Y
Trypsin-EDTA		Y		Y	
ETC*	Ocean TuniCell AS				Y
Virkon (Rely+On™ Virkon® Powder)	Du Pont	Y	Y	Y	Y

5.3 Apparatus and equipment

All tissue culture consumables were purchased from Greiner Bio-One, UK, unless otherwise specified.

Table 3 Apparatus and equipment

Apparatus and equipment	Brand (Cat No.)	1	2	3	4
Autoclave			Y	Y	
Bijou container (sterile, 7ml)			Y		
Cell counter		Y		Y	
Cell culture flask (T25, T75, T175)		Y			
Cell strainer (70μm)	Corning (CLS431751)				Y
Centrifuge		Y			Y
Centrifuge tubes (15ml, 50ml, 50ml skirted)		Y	Y	Y	Y
Cryovial		Y			
Eppendorf tube (1.5ml)		Y			Y
Filter Unit (sterile, 0.22μm Millex™-GP)	Millipore (SLGPM33RS)	Y		Y	Y

Apparatus and equipment	Brand (Cat No.)	1	2	3	4
Forceps, metal				Y	Y
Freezing container (Mr frosty™)	Thermo Scientific (5100-0001)	Y			
Haemocytometer		Y			
Incubator (37°C, 5% CO_2 ISO class 2 hepa filter)	NUAIRE™ DHD Autoflow	Y		Y	Y
Light microscope	Olympus (CKX53)	Y			
Liquid nitrogen dewar		Y			
Luer-lock connector	*			Y	
Micropipettes (P1000, P200, P100, P20)		Y	Y	Y	Y
Needle (21G)					Y
Parafilm			Y		
Pipette controller		Y			
Pipette dropper				Y	Y
Pipette tips (non-filtered sterile, 1000µl, 200µl, 20µl)		Y			Y
Scale (bench top)					Y
Scale (in laminar flow hood)			Y	Y	
Skin biopsy punch tool (8mm)	**				Y
Spatula, metal, small			Y	Y	Y
Static eliminator (Ionizer100A)	Ohaus				Y
Serological pipettes (sterile 5, 10, 25ml)		Y		Y	
Syringe (1ml, 10ml; 1ml luerlock, 5ml luerlock)			Y	Y	Y
Tissue (Kleenex)					Y
Tissue culture hood (laminar class II, with UV-C function)	Scanlaf Mars	Y			
Tissue strainers (Pierce™ 250µm)	Thermo scientific (87791)				Y
Tissue well plate (12, 24 wells)	Greiner Bio-One	Y		Y	Y
Vortex				Y	Y
Waterbath (37°C)		Y			Y
Weighing boat (large, disposable)	**				Y

*Provided by ReconRegen

**Provided by IVTG

5.4 Reporting of protected elements

To the best of our knowledge, this SOP does not contain the use of material, procedures, or otherwise, associated with patent restrictions, specific licenses, material transfer agreements or commercial purchase requirements.

5.5 Health and safety precautions

Standard safety procedures, protocols, manufacturer's instructions and good laboratory practice should be followed, including local departmental or institutional policies. Review and adherence to guidelines relating to the health and safety precautions relevant to the laboratory work environment and undertaking of mammalian cell culture from the European Agency for Safety and Health at Work are recommended (available from: https://osha.europa.eu/en/safety-and-health-legislation/european-guidelines, accessed 18.02.2025). Attention should also be given to all health and safety precautions stated in material or product safety data sheets (SDS) for chemicals used within the SOP.

5.6 Nanomaterials used and associated handling procedures

ETC is the only nanomaterial used in the SOP. It is a tunicate-derived nanocellulose fibril which is enzymatically pre-treated. It is manufactured by Ocean Tunicell, and supplied in 2.5-3.5% ETC in cell culture grade pyrogen- and endotoxin-free water. Precautions should be undertaken as stated in the product safety data sheet.

5.7 Reagent preparation

5.7.1 CCM

Complete cell culture medium is made with the addition of the following to the DMEM:

- 1% Penicillin-Streptomycin (equivalent to Penicillin 100U/ml, Streptomycin 100μg/ml) – antibiotic to reduce the risk of bacterial contamination
- 10% FBS – added to basal media (DMEM) to achieve complete culture medium

Correspondingly, for a 500ml bottle of DMEM media, add:

- 5ml of Penicillin-Streptomycin
- 50ml of FBS

Pre-warming of all three elements is not required for supplementation.Thorough mixing is performed before use. Supplemented culture medium is stored at 4°C, and used within 3 months.

5.7.2 Freezing medium

The freezing medium is made by adding 10% (v/v) DMSO to the CCM. For example, 1ml of freezing medium would consists of 900μl media and 100μl DMSO. Freezing medium should be freshly prepared immediately prior to use.

5.7.3 $CaCl_2$

1. Make up 1.0M $CaCl_2$ stock solution (e.g. for 30ml of 1.0M solution, add 30ml sterile ddH_2O to 4.41g). Mix by vortex.
2. Filter 1.0M $CaCl_2$ stock solution using a sterile 0.22μm Millex™-GP Filter Unit and 10ml syringe.
3. Make up 0.1M $CaCl_2$ stock solution by diluting filtered 1.0M $CaCl_2$ stock solution (e.g. for 40ml of 0.1M solution, add 4ml of 1.0 M $CaCl_2$ to 36ml of sterile ddH_2O). Mix by vortex.
4. All $CaCl_2$ stock solutions are stored at 4°C.

5.8 Procedures

Decontaminate all equipment, including tissue culture hood and lab benches with 70% ethanol prior to use. Equipment and cells in their containers taken into tissue culture hood are disinfected in the same manner. Ensure the lid and openings of vials and bottles placed in the waterbath are above the waterline and not submerged to minimise the risk of contamination. Local laboratory policies should be followed for waste disposal. Centrifugation is performed at room temperature, unless otherwise specified, and correctly balanced.

5.8.1 Cell culture

5.8.1.1 Thawing and culturing of cryopreserved cells

1. Pre-warm CCM to 37^{o}C in a waterbath (approximately 20-30 minutes).
2. Ensure all required equipment are placed in the tissue culture hood, to minimise delay in cell handling after thawing.
3. Remove the cryovial of cells from liquid nitrogen and thaw immediately in a waterbath at 37^{o}C.
4. Monitor the cryovial regularly and proceed to the next step immediately once the vial contents are thawed (approximately 1-2 minutes).
5. Inside a tissue culture hood, transfer the cryovial contents into a sterile 15ml centrifuge tube using a 1000μl micropipette.
6. Into the same 15ml centrifuge tube, add 10ml of pre-warmed CCM. This should be performed gradually to reduce osmotic shock and preserve cell viability.
7. Gently mix the cell suspension and CCM by pipetting up and down several times, taking care to avoid the introduction of air bubbles.
8. Centrifuge the tube at 300G for 3 minutes to achieve a cell pellet. See table 4 for centrifugation requirements for HFF-1 and C20A4 cell lines.
9. Return the tube to the tissue culture hood, and pour away the supernatant, which contains residual DMSO, leaving behind the cell pellet.
10. The cell pellet is suspended in 1ml CCM, and 10μl placed in a 1.5ml Eppendorf for cell counting.

11. The remainder of the 1ml cell suspension is then diluted with 9ml of CCM, and gently mixed.
12. Cell counting is performed using the erythrosin B exclusion assay to determine the total and live cell concentration and cell viability (see section 5.8.1.4).
13. The cell suspension is transferred to a T75 tissue culture flask for HFF-1 and T175 flask for C20A4 cell lines.
14. The flask is incubated at 37^{o}C and 5% CO_2 in a humidified environment.
15. Cells is inspected under light microscopy at 24 hours, alongside the exchange of fresh CCM to remove non-viable cells.
16. Subsequent exchange of fresh CCM is performed every 2-3 days for C20A4, and twice a week for HFF-1 or when pH decreases, whichever is sooner.
17. Cell confluency is monitored regularly to avoid over-confluency. Cell passage or cryopreservation are recommended when 90% confluency is reached for C20A4 cell lines, and full confluency for HFF-1, as specified from the cell line product sheets.

Notes:

- To maximise cell viability, ensure rapid and complete thawing of cryopreserved cells.
- Ensure appropriate water levels in incubator to achieve a humidified environment for optimal cell culture conditions.
- Where available, record the passage number from the supplier.
- With step 13, follow supplier's guidance regarding the size of the tissue culture flask size for the first thawing and culturing of commercially purchased cell lines. For cell line maintenance and expansion purposes, the culture flask size recommendation is based on the anticipated cell number required for the *in vitro* model. As a greater number of chondrocytes is required, the T175 culture flask is used. CCM is added to culture flasks prior to the addition of cell suspension (volumes are as recommended by the supplier, and is typically 5ml for T25, 15ml for T75 and 25ml for T175). Inspection of the cells under light microscopy is recommended prior to incubation.

- With step 16, low pH is indicated by the colour change from red towards yellow with decreasing pH due to the presence of phenol red as a pH indicator.

Table 4 Centrifugation parameters, seeding densities, confluency threshold for sub-culturingm and sub-culturing ratios for HFF-1 and C20A4 cell lines as recommended by cell line suppliers

	HFF-1	C20A4
Centrifugation parameters	270G for 5 minutes	300G for 2 minutes
Seeding densities	$0.8x10^4$ cells/cm^2	$1.3x10^4$ cells/cm^2
Confluency at which sub-culturing recommended	'confluency'	90%
Sub-culturing split ratios	1:5 –1:7	1:8 – 1:10

5.8.1.2 Sub-culturing cells

1. Refer to table 4 for recommended confluency levels at which sub-culturing should be performed for each cell line.
2. Pre-warm trypsin-EDTA solution and CCM in a waterbath at 37^{o}C.
3. Ensure all required equipment are placed in the tissue culture hood.
4. Discard the CCM.
5. Cells are washed with three cycles of PBS to remove residual serum which can inhibit the action of trypsin-EDTA.
6. Trypsin-EDTA is added to the flask and allowed to incubate at 37^{o}C for 3-5 minutes. A volume of 3-5ml of trypsin-EDTA for T75 and 5-8ml for T175 tissue culture flasks are recommended.
7. The flask is inspected under light microscopy for cell detachment.
8. When cells are fully detached from the flask, add double the volume of CCM to the trypsin-EDTA. For example, if 5ml of trypsin-EDTA was used, 10ml of CCM is added at this step. The serum in CCM acts to neutralise the action of trypsin-EDTA.
9. Gently rotate the flask to mix the cell suspension with the added CCM.

10. Transfer flask contents into a conical centrifuge tube by pouring or pipetting (15ml tube for T75; 50ml for T175).
11. Centrifuge the tube as specified in table 4 to achieve a cell pellet.
12. Gently pour away and discard the supernatant.
13. Resuspend the cell pellet in CCM (1ml for cells grown in T75; 3ml for cells in T175). Pipette up and down until the cells are fully re-suspended with no visible cell pellet or agglomerates.
14. Cell counting is performed using the erythrosin B exclusion assay and haemocytometer (see section 5.8.1.4).
15. Cells are plated at the recommended split ratio (see table 4), or desired seeding density.
16. Return the flask to the incubator (37^{o}C, 5% CO_2, humidified).
17. Exchange of fresh pre-warmed CCM should be undertaken every 2-3 days for C20A4 and twice a week or when pH decreases with HFF-1 cell lines. Regular inspections of cells to monitor for confluence, cell morphology and CCM condition are performed.

Notes:

- With step 1, sub-culturing is undertaken approximately every 3-5 days, with slower growth and longer periods between sub-culturing for cells recovering from cell cryopreservation, or with lower seeding densities.
- With step 4, CCM can be discarded by pouring directly into a waste container, taking care to avoid splashbacks from the waste fluid. Alternatively, it can be removed by pipetting. The adherent cell layer should not be disturbed by the pipette tip.
- With step 5, for each rinse cycle, add PBS to the flask (same volume as CCM for each flask size) with a pipette, and discard in the same manner as described in step 4.
- With step 7, the flask can be tapped gently on the side (with the palm of your hand) to encourage cell detachment. Cell detachment is confirmed macroscopically, and also microscopically where cell will be rounded and floating.
- With step 8, prolonged exposure to trypsin-EDTA will adversely impact cell surface proteins and the ability of cells to adhere.

5.8.1.3 Cryopreserving cells

1. Cell detachment and cell counting follows the same steps as described in section 5.8.1.2 from step 1 to step 14 (inclusive).
2. Add to the cell suspension the desired amount of freezing media and transfer into a cryovial.
3. Store the cryovial overnight in a Mr frosty™ freezing container at -80°C, before transfer into liquid nitrogen for long term storage the following day.

Notes:

- Cryopreservation should be performed at earlier passages where able, and passage number should always be recorded.
- With step 2, cells are cryopreserved at approximately double the minimum cell seeding density or as desired (see table 4).
- Due to the high cell number required for C20A4 for future *in vitro* model work, cell numbers cryopreserved should be recorded with reference to tissue culture flask size intended upon thawing (eg. T75 or T175).
- Where able, storage of cells in separate liquid nitrogen dewars will act as a fail-safe should one storage vessel fails.

5.8.1.4 Cell counting and cell viability assessment (with erythrosin B exclusion assay and haemocytometer)

1. Cell counting utilises the re-suspended cell pellet following centrifugation (see section 5.8.1.2 step 13).
2. From the cell suspension described in step 1, transfer 10µl into an Eppendorf.
3. Clean the haemocytometer and the glass cover slip with 70% ethanol, and dry thoroughly.
4. Place the cover slip onto the haemocytometer, moistened with exhaled breath. Apply light pressure whilst sliding the cover slip back and forth a few millimeters until adherent.
5. Set up the light microscope.

6. Prepare the sample by adding 10μl of erythrosin B stain and mixing the sample by pipetting up and down several times (i.e. 1:1 ratio of sample and erythrosin B stain).
7. Load 10μl of the mixed stain and cell sample onto the haemocytometer, ensuring full dispersion across the 9 large squares.
8. Count the number of live and dead cells in the 4 large squares using a cell counter and light microscope (see figure 1). Cells situated at the borders of the large square are counted as shown in figure 1. Live cells are unstained and dead cells are stained pink.
9. Cell concentration in cells/ml is calculated using equation 1. The number of cells counted referred to the total number of cells counted across the four large squares. The dilution factor refers to the dilution of the cell sample with the erythrosin B stain (in this case, the dilution factor is 2, based on a 1:1 ratio as described in step 6). The number of squares counted is 4. Live and dead cells concentrations are calculated using the number of live or dead cells counted. The total cell concentration is calculated using the sum of the live and dead cells counted.

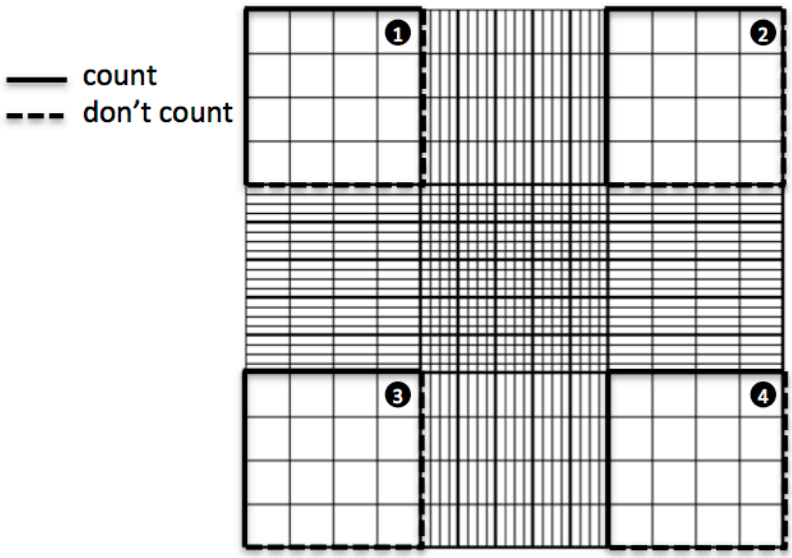

Figure 1: Haemocytometer and cell counting[14]. The large squares are labelled 1-4, situated at the outer corners of the figure. Cells that fall within the 4 large squares are counted. For cells that sits on the borders of the large square, only cells that sits along two edges are counted. It is customary to keep this consistent amongst the four large squares. This is illustrated in the figure, with bold lines across the top and left-sided borders where cells are counted.

Equation 1 $$\text{Cell concentration (cells/ml)} = \text{No. of cells counted} \times \frac{\text{Dilution factor}}{\text{No. of squares counted}} \times 10^4$$

10. For calculations of cell sample dilutions for cell seeding, the following equation can be applied following cell counting. By setting the desired cell concentration (C_2) and volume (V_2), the volume required to dilute the sample (V_1) is determined *via* equation 2:

Equation 2 $$C_1V_1 = C_2V_2$$

C_1 = Concentration of the cell sample (cells/ml)
V_1 = Volume of the cell sample (ml)
C_2 = Concentration desired (cells/ml)
V_2 = Volume desired (ml)

5.8.2 Preparation of bio-inks

CCM is prepared as described in section 5.7.1. With both bio-inks, the alginate +/- HA stock solution is prepared first, followed by the addition of nanocellulose (ETC). The measurement of alginate and N-HA powders is performed on a scale within a bench top laminar flow hood to maintain sterility.

Both ETC and N-HA are supplied sterile, and are used or reconstituted as supplied. Culture grade alginate powder is sterilised with UV-C application as described by Al-Sabah *et al*[15].

Table 5 lists the concentrations of each material as supplied and within the bio-ink, based upon previous research by Jessop *et al* on nanocellulose-based bio-inks combined with alginate[2], and by Jovic *et al* when combined with HA *(*unpublished data). The bio-ink material concentrations take into account the cell suspension required to create the final *in vitro* model. Therefore, it is important to define the volume for cell suspension to ensure the correct material concentration is reached. For example, 3.75ml bio-ink contains 3ml of ETC, leaving 750μl volume for the stock solution of alginate +/- N-HA, and the cell suspension. This is typically split with 500μl for the stock solution of

alginate +/- HA, and 250µl for the cell suspension. Material and cell suspension handling is performed with care and patience due to high material viscosity and high cell density.

The principles of the bio-ink preparatory steps are similar with both bio-inks. However, the addition of N-HA markedly increases material viscosity for the alginate and N-HA stock solution. As such, the preparation of both bio-inks is described separately, with additional techniques and tips included for the triple component bio-ink.

Table 5 Summary of bio-ink material concentrations as supplied and within the bio-ink.

Material	Supply concentration	Bio-ink concentration
ETC	25 mg/ml	20 mg/ml
Alginate	Powder	5 mg/ml
N-HA	powder	6 mg/ml

5.8.2.1 ETC:Alginate in media

1. Add the required amount of alginate powder into a 50ml skirted centrifuge tube.
2. Apply UV-C (germicidal light at 254nm) to the alginate powder with the lid removed in a tissue culture hood for 1 hour for sterilisation.
3. Reconstitute the alginate powder in the required amount of CCM. Mixing is performed with a spatula, and warmed in a waterbath at 37^{o}C for 20 minutes to aid dissolution (20 minutes). This is repeated as needed.
4. When there are no visible residual powder or heterogeneity of the alginate solution, store at 4^{o}C overnight and re-mixed with a spatula the following day before use.
5. Transfer the required amount of alginate stock to a smaller vessel for the bio-ink (e.g. a 7ml sterile bijou container), using a 1ml or 5ml syringe.
6. Add ETC directly to the bijou, and mix with an electric mixer.

7. Remove air bubbles by centrifugation at 1000G in 5 minutes cycles, followed by gentle mixing with a spatula. This is repeated until there are no visible air bubbles.
8. Seal the container with parafilm, and store at 4°C.

Notes:

- Sterile ETC is supplied in gel format at 2.5%-3.5%, in cell grade, pyrogen free water, in 3ml syringes. It is used as supplied.
- With step 5, for ease of material handling, it is recommended that no more than 4ml of bio-ink is created using a 7ml bijou. The material mixing process can cause overspill should the volume be too great.
- With step 6, the addition of ETC in smaller aliquot is recommended, e.g. 1ml at a time. Care is taken to minimise the introduction of air bubbles, as well as to avoid material loss when using the electric mixer.

5.8.2.2 ETC:Alginate:N-HA (low) in media

1. Add 1.5x the required amount of alginate powder into a 50ml skirted centrifuge tube.
2. Apply UV-C (germicidal light at 254nm) to the alginate powder with the lid removed in a tissue culture hood for 1 hour for sterilisation.
3. Apply the static eliminator to the N-HA powder to reduce static (approximately 30 seconds).
4. Add the required amount of N-HA powder into a sterile 7ml bijou container.
5. Add the required amount of UV-treated alginate powder to the same bijou container.
6. Reconstitute the alginate / N-HA powders with the required amount of CCM.
7. Seal the alginate / N-HA stock solution with parafilm and store at 4°C overnight.
8. On the following day, add the required volume of ETC directly to the alginate / N-HA stock solution.
9. Mixing of the ETC and the alginate / N-HA stock solution is performed with an electric mixer.

10. Remove air bubbles by centrifugation at 1000G in 5 minutes cycles, followed by gentle mixing with spatula. This is repeated until there are no visible air bubbles.
11. Seal the bio-ink container with parafilm, and store at 4^{o}C.

Notes:

- Due to the high cost associated with N-HA, the correct amount of alginate / N-HA stock solution is made in the 7ml bijou for the intended bio-ink volume. I.e. a larger quantity of alginate / N-HA stock solution is not made.
- Step 3 is performed to limit the loss of N-HA powder due to static. The application of the static eliminator improves but not fully remove this issue. As such, alginate is added to N-HA in this sequence to minimise the need to transfer the N-HA powder between containers.
- With step 6, it is important to do this in a gradual manner (e.g. adding 100μl at a time). Mixing with a spatula will initially create a paste. As more solvent is added, a viscous solution is achieved. Once this is the case, the solution is warmed in a waterbath at 37^{o}C in 20 minutes interval in between mixing. This is continued until all visible powders are dissolved and there is homogeneity of the viscous solution.
- With steps 8 + 9, the addition of ETC in small aliquots is recommended (e.g. 1ml at a time). Care is taken to minimise the introduction of air bubbles, as well as to avoid material loss when using the electric mixer.

5.8.3 Creation of an advanced 3D *in vitro* model

Each model uses 100µl of bio-ink. As the two monoculture models uses different cell seeding methodologies (surface-seeding with HFF-1, and cell encapsulation with C20A4), the procedures are described separately. Creation of the silicon molds is a common procedure, and is therefore described first. Preparation of the cross-linker (0.1M $CaCl_2$) is detailed in section 5.7.3. All sections apart from 5.8.3.1 is performed under sterile conditions in the tissue culture hood. All hydrogel discs and models should be handled gently by lifting or pushing with a spatula and forceps. The models should not be picked up directly with forceps as it will deform or disintegrate.

5.8.3.1 Creation of silicon molds

1. Use a 5ml syringe to add the required amount of Elastosil® RT 601 part A to a large weighing dish placed directly on a scale.
2. Add to part A, the Elastosil® RT 601 part B using a pipette dropper.
3. Mix part A + B mixture vigorously manually using a 1000µl pipette tip (approximately 30 seconds).
4. Add the mixture to a 24 well plate (1 ml per well), using a 5ml syringe.
5. Allow to set overnight in room temperature (see figure 2A).
6. On the following day, lift out the silicon disc using metal forceps and a small metal spatula (see figure 2B).
7. Cut out the centre of the silicon mold using an 8mm skin biopsy punch tool (see figure 2C/D), to create a donut-shaped mold. Discard the centre circular piece.
8. Sterilise the silicon molds with a single cycle of autoclaving.

Notes:

- With step 1, note that Elastosil® RT 601 part A is very viscous.
- With step 2, the addition of Elastosil® RT 601 part B should proceed drop by drop to reach a part A:part B ratio of 15:1.
- With step 5, the air bubbles within the silicon mixture will dissipate overnight during the setting process.
- With step 6, the elasticity of the silicon allows the mold to be eased away from the walls of the well plate slightly. Remove the molds from

the well plate by easing the mold away from the wall of the well with metal forceps. Then slide a small metal spatula in this gap. Continue until the spatula reaches the base of the well, after which the mold should come out easily. Take care to avoid damage to the mold, especially in the center.

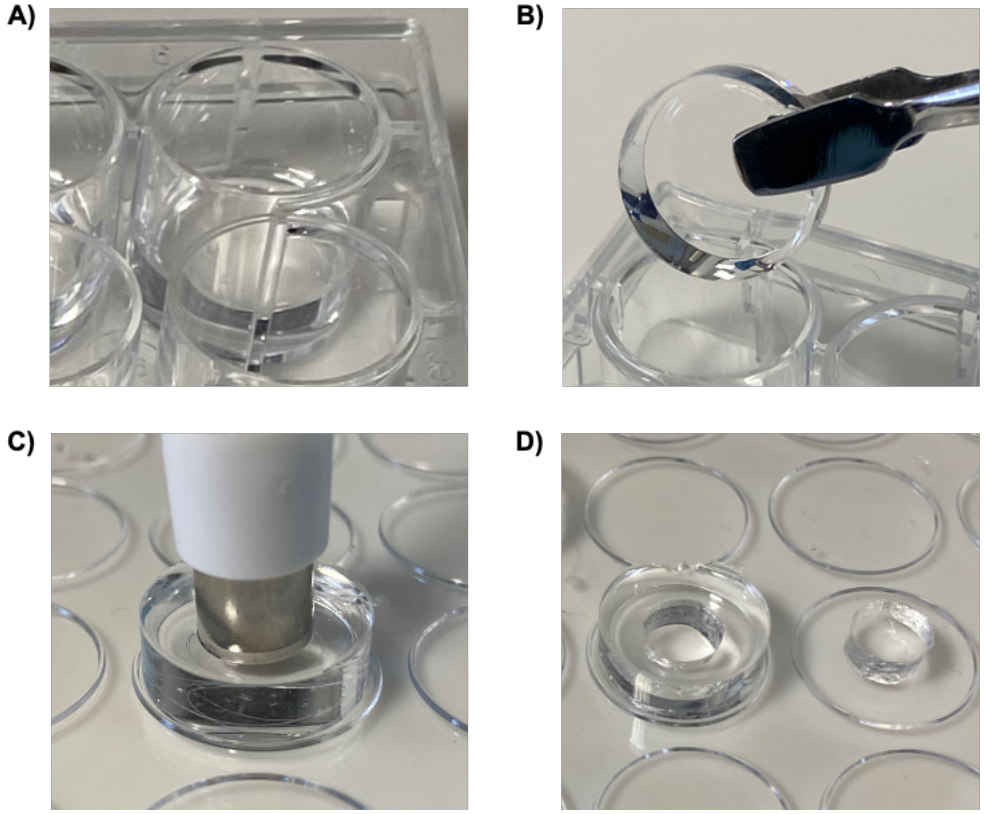

Figure 2 Creation of silicon molds. Elastosil® RT 601 A+B was mixed in 15:1 ratio (A:B), and added to a 24 well plate (1ml per well). This is allowed to set overnight at room temperature (A). The silicon discs were lifted off the well plate the following day (B). The mold was created by applying an 8mm skin punch biopsy tool centrally (C), thereby creating a donut-shaped mold (D).

5.8.3.2 Creation of the HFF-1 monoculture model

1. Place the silicon mold into the centre of each well in a 12 well plate (one mold per model), and press down firmly. Check for adherence of the mold.
2. Add 100µl bio-ink (as prepared in section 5.8.2) into the centre of the mold using a 1ml syringe.

3. Smooth the surface of the bio-ink within the mold using a 200μl pipette tip.
4. Add 600μl of cross-linker (as prepared in section 5.7.3) onto the bio-ink, ensuring the droplet remain on the silicon mold (see figure 3A).
5. Remove the cross-linker with a pipette after the defined cross-linkage time. This is performed at 15 minutes for bio-ink ETC:Alginate in media, and at 25 minutes for bioink ETC:Alginate:N-HA (low) in media.
6. During the cross-linkage time (step 5), prepare a 24 well plate by adding 1ml PBS per well per model.
7. Immediately following the removal of the cross-linker (step 5), ease the silicon mold off the well plate.
8. Transfer the hydrogel disc to the 24 well plate using a spatula and submerge in PBS (as prepared in step 6).
9. A total of 3 washes with 1ml PBS is performed with the hydrogel discs using a pipette dropper, to remove residual crosslinker.
10. Hydrogel discs are kept submerged in PBS whilst the HFF-1 cell suspension is prepared.
11. Prepare the HFF-1 cell suspension at $1x10^5$ cells/ml by following sections 5.8.1.2 step 1-14 for cell detachment, and section 5.8.1.4 for cell counting. The volume of cell suspension is calculated at 100μl per model.
12. Place fresh molds onto a fresh 12 well plate, as described in step 1.
13. Carefully transfer the hydrogel disc in PBS from step 10 into the inside of the fresh molds (one hydrogel disc per mold). The flat basal surface of the hydrogel disc should now be the apical surface. (see figure 3B).
14. Add 100μl of the HFF-1 cell suspension (as prepared in step 11) on top of each hydrogel disc.
15. Incubate the models at 37°C for 2 hours.
16. Remove the cell suspension by pipetting. Take care to avoid disturbing the seeded model cell surface.
17. Carefully lift the silicon mold off the well plate to retrieve the seeded model.
18. Transfer the model to a new 24 well plate, submerged in 1ml of CCM.

19. The model is ready for use, and is incubated at 37°C.
20. Exchange of CCM is performed every 2-3 days.

Notes:

- With step 1, note that the mold has a flat surface (basal surface) and a slightly concave surface (apical). Ensure that the molds are placed with the flat (basal) surface against the base of the well plate, as otherwise it will not adhere correctly. Adherence is confirmed by turning the well plate upside down. The mold will remain in place and not fall off.
- With step 4, due to the slight concavity of the apical surface of the silicon mold, a larger volume of cross-linker could be applied and retained above the bio-ink and within the silicon mold.
- Depending on the number of models required, it is recommended that all cell-free hydrogel discs are created first, which will allow cell seeding for all models to be performed in one sitting.
- With step 11, the seeding density of HFF-1 is 20,000 cells/cm^2 (based on histological studies of dermal fibroblast from human skin biopsies[16] and cell line characterisation (unpublished data)). The surface area of an 8mm diameter hydrogel disc is calculated using the geometric equation: area = πr^2, where r is the radius (0.4cm). The area of each model is therefore 0.503cm^2. The number of cells per model is 10,053 (i.e. 20,000 x 0.503). As the cell suspension is delivered at 100µl per model, the cell concentration required is 10,053 cells per 100µl, i.e. $1x10^5$ cells/ml.
- With steps 12-16, the mold is used to control the area in which cell seeding occurs. New molds and well plates are used in step 13 to minimise contamination with cross-linkers, and to ensure a dry well plate surface for mold adherence. Therefore, 2 silicon molds are required per model.
- With step 13, take note that the hydrogel disc is placed ‘upside down’. The hydrogel disc was flipped such that the flat and smooth basal surface achieved during cross-linkage can be used for cell seeding, and therefore will become the apical surface.

- With step 14, the cell suspension volume is chosen to ensure the full cell suspension remained within the central well of the donut-shaped silicon mold and not overspill onto the outer surface of the silicon mold. such as in the case with cross-linker application. This is to ensure targeted cell seeding onto the hydrogel discs.

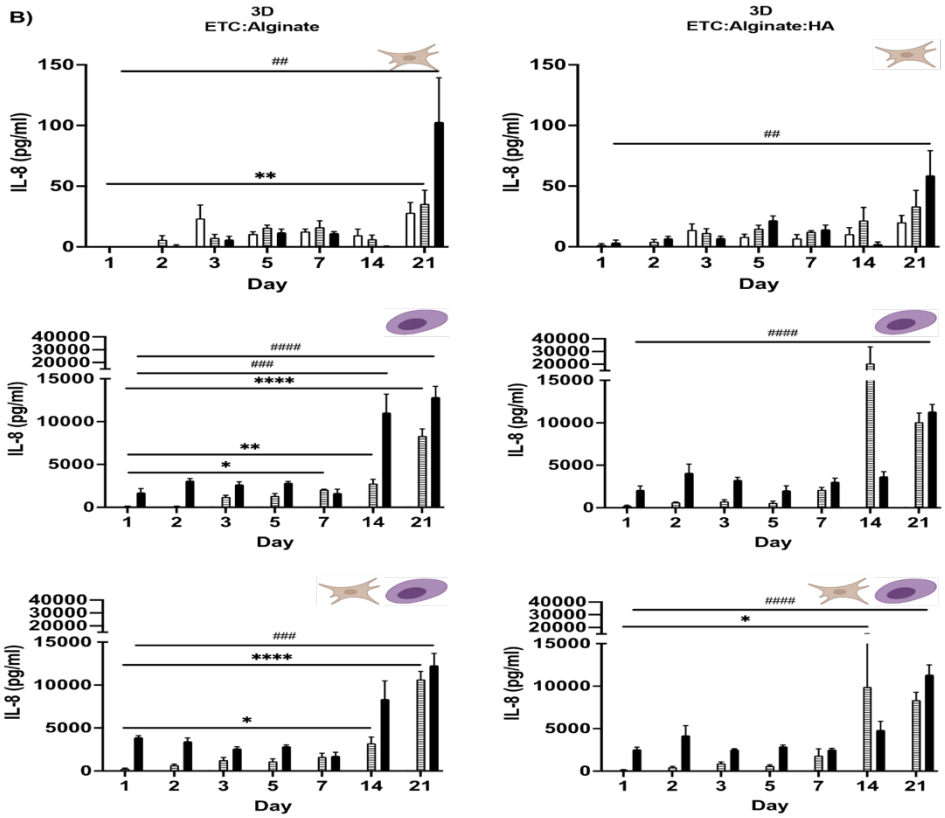

Figure 3 Creation of cell-free hydrogel discs. Bio-ink (100µl) is added to the centre of silicon molds placed in a 12 well plate. The cross-linker (600µl) is added on top of the bio-ink (A) and removed following the desired cross-linkage duration. The silicon mold is lifted from the plate and the hydrogel discs eased off the molds. Figure B illustrates the smooth basal surface of the hydrogel disc, and figure C the relatively irregular apical surface.

5.8.3.3 Creation of the C20A4 monoculture model

1. Remove the bio-ink (as prepared in section 5.8.2) from 4°C storage, and allow to come to room temperature during step 2.
2. Prepare the C20A4 cell suspension via trypsinisation and cell counting as described in sections 5.8.1.2 steps 1-14 and section 5.8.1.4. See notes for the required cell concentration.
3. Transfer the required amount of bio-ink into a 5ml luerlock syringe.

4. Add the cell suspension to the 5ml syringe with a 200μl micropipette.
5. Mix the bio-ink and cell suspension by passaging the bio-ink between two 5ml syringes with a luer-lock connector. Take care to minimise the introduction of air bubbles (expelling them as needed). Passage slowly and gently with a minimum of 20 passages to homogenise the bio-ink and cell suspension.
6. Place molds into a 12 well plate and ensure adherence (see section 5.8.3.2 step 1).
7. Transfer the C20A4-seeded bio-ink (prepared in step 5) into a 1 ml syringe, using a luer-syringe connector.
8. Add 100μl of the C20A4-seeded bio-ink into the centre of each mold (with a 1ml syringe).
9. Smooth the bio-ink surface using a 200μl pipette tip.
10. Add 600μl of cross-linker to the bio-ink, and allow to cross-link for 15 minutes for bio-ink ETC:Alginate in media, and for 25 minutes for bioink ETC:Alginate:N-HA (low) in media.
11. During cross-linkage time (step 10), prepare a fresh 24 well plate by adding 1ml PBS per well per model.
12. Remove the cross-linker when the cross-linkage time is complete, using a pipette.
13. Carefully lift the silicon mold off the well plate and retrieve the seeded model.
14. Transfer and submerge the model in PBS in the 24 well plate prepared in step 11.
15. Complete a total of 3 PBS washes of the models by removing the PBS and adding 1ml of fresh PBS for each cycle.
16. Transfer the model to a new tissue culture plate and submerge in 1ml media.
17. The model is ready for use, and is incubated at 37^{o}C.
18. Exchange of CCM is performed every 2-3 days.

Notes:

- With step 2, please note that the cell concentration of the cell suspension to be mixed with the bio-ink takes into account the material

volume in the bio-ink. The target cell seeding density is $3x10^6$ cells/ml[15]. For 3.75ml of bio-ink, the cell suspension volume is 250μl (3ml ETC, 500μl alginate +/- N-HA). Therefore, the total number of cells in 3.75ml of bio-ink is $1.125x10^7$ (i.e. $3x10^6$ x 3.75). The cell suspension would contain $1.125x10^7$ cells in 250μl, i.e. $4.5x10^7$ cells/ml.

- With step 3, take up the bio-ink from the 7ml bijou container with a nonuer-lock 1 ml syringe. The bio-ink is then transferred to a 5ml syringe *via* a luer-lock connector. Take care to avoid the introduction of air bubbles. When taking up bio-ink from the bijou containter directly, avoid using a luer-lock syringe, which leads to the trapping and loss of bio-ink within the luer-lock mechanism. To minimise the introduction of air bubbles, first take up a small amount of bio-ink (0.1ml) into the syringe. Pull back the plunger and re-advance this slowly to fill the tip and/or body of the syringe with the bio-ink. This is performed repeatedly and regularly to minimise the amount of air bubbles introduced into the system.
- With step 4, the cell suspension is added directly to the tip of the 5ml syringe of bio-ink. This is performed slowly and carefully. Concomitant gradual withdrawal of the 5ml syringe plunger as the cell suspension is being added ensures that the cell suspension does not overspill and is taken up fully into the syringe.
- With step 18, due to the high initial seeding density of C20A4, the pH of CCM reduces more rapidly at latter timepoints. This is reflected by the alteration of CCM colour from red to yellow, due to the pH indicator in CCM (phenol red). As such, the exchange of CCM is performed typically every 3 days between day 1 – 10, and every 2 days beyond. This details the maintenance of the model in culture conditions. Please note that the exchange of CCM in experimental conditions will be specified should it differs from the SOP.

5.8.3.4 Creation of the Co-culture model

1. A C20A4 seeded model is first created following all steps described in section 5.8.3.3.

2. The HFF-1 cell suspension and seeding procedure is as described in section 5.8.3.2 steps 11-18.
3. The model is ready for use and is incubated at 37°C.
4. Exchange of CCM is performed every 2-3 days.

Notes:

- See notes in section 5.8.3.3 relating to the frequency of exchange of CCM and high C20A4 cell seeding density.

5.8.4 Implementation

5.8.4.1 Alamar blue assay

The model was successfully applied with the alamar blue assay for the assessment of metabolic activity of live cells as an indicator of cell proliferation and cytotoxicity. Although the manufacturer's guidance of the alamar blue assay implied that the assay is non-destructive and can be used repeatedly with the same model over time, there remains uncertainty regarding how this translates to a 3D model where residual alamar blue reagent may be retained within the hydrogel disc. As such, each timepoint was assigned one model (i.e. 7 models for 7 timepoints).

5.8.4.2 ELISA / LDH assay

For assays which require supernatants, including the ELISA and LDH assay, the supernatant is centrifuged to pellet and remove residual cellular or biomaterial debris. This is performed prior to the assays, and coordinated to reduce the number of freeze-thaw cycles of the supernatants. Centrifugation is performed at 100G for 1 minutes, and the supernatant is transferred to a fresh 1.5ml Eppendorf.

5.8.4.3 RNA extraction

Bench work for RNA extraction requires thorough decontamination of all work area and equipment by wiping down with RNAse ZAP before starting. This includes micropipettes and tip boxes. All centrifugation in this section is performed at 4°C.

Sample preparation prior to RNA extraction:

1. Add PBS to a 24 well plate (1ml per well per sample).
2. Transfer and submerge samples in PBS in the 24 well plate (one sample per well).
3. Exchange PBS with 1ml of pre-warmed TrypLE.
4. Incubate the sample in TrypLE at 37°C for 5 minutes.
5. Mechanically disrupt the sample by pipetting the sample in TrypLE up and down 20x using 1000µl micropipette. Take care to avoid the introduction of air bubbles. The sample should visibly disintegrate (see figure 4).
6. Return the sample for incubation for a further 5 minutes at 37°C.
7. Triturate the sample again by pipetting up and down 10x.
8. Add 1ml CCM to each sample to neutralise the action of TrypLE, and mix by pipetting up and down 5x.
9. Transfer the well contents to a fresh 15ml centrifuge tube.
10. Rinse the well with 1ml CCM, and add this to the same centrifuge tube as step 9.
11. Filter the sample serially first with a 250µm strainer, placed over a 15ml centrifuge tube.
12. Filter the sample again with a 70µm strainer, placed over a 50ml centrifuge tube.
13. Transfer the sample to a 15ml centrifuge tube.
14. Centrifuge the sample at 300G for 5 minutes to achieve phase separation.
15. Aspirate and discard the supernatant using a 1000µl micropipette, taking care to leave behind the denser material / cell suspension at the bottom of the centrifuge tube.

Notes:

- With steps 11 + 12, a small amount of sample will be retained by the strainers.
- Step 13 is performed to permit ease of control and sample visualisation in step 15.

- With step 14, please note that there is no cell pellet. The cells are contained within the dense material seen achieved with phase separation.
- Sample preparation is performed immediately prior to RNA extraction. Please ensure all reagents and equipment required for RNA extraction is ready prior to performing sample preparation.
- Step 1-10 is performed within a tissue culture hood. Step 11-15 can be performed on a standard laboratory bench.
- An optional step could be performed at the end of sample preparation to visualise cells under light microscope with 10µl of sample and a haemocytometer.

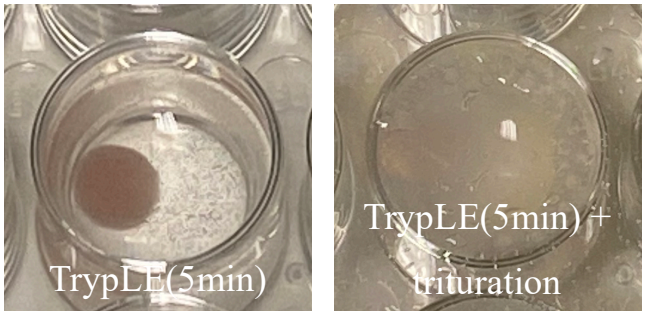

Figure 4 Appearance of the sample pre- (left) and post- (right) mechanical disruption by trituration following incubation in TrypLE.

RNA extraction:

1. Prepare the lysis buffer by adding 10µl β-mercaptoethanol per 1ml RLT lysis buffer (i.e. for 10ml of RLT lysis buffer, add 100µl β-mercaptoethanol). This is performed in a fume hood. Vortex to mix.
2. Add 600µl RLT lysis buffer (with β-mercaptoethanol) to prepared sample, and pipette up and down to mix.
3. Homogenise the sample by passing contents through a 21G needle (green) at least 5x. Take care to limit the introduction of air bubbles.
4. Transfer the homogenised sample to an AllPrep DNA spin column placed in a 2ml collection tube. Close the lid and centrifuge at 8000G for 30 seconds. The sample volume will exceed that of the DNA spin

column, therefore fill the first DNA spin column to around 4mm from the lid (approximately 700μl), and centrifuge. Transfer the residual sample remaining in the first DNA spin column (not the collection tube) to a new DNA spin column (see figure 5). Add to this the remaining sample not yet subjected to centrifugation.

5. Collate all flow-through from step 4 into one 2ml collection tube.
6. Discard the two used DNA spin columns.
7. Estimate the total volume of flow-through from step 5 with a pipette.
8. Add 1:1 volume of 70% ethanol to the flow-through collated in step 5 and mix well by pipetting.
9. Transfer 700μl of the sample from step 8 to a RNeasy spin column placed in a new 2ml collection tube, and centrifuge at 10,000G for 15 seconds.
10. Discard the flow-through, and gently tap the collection tube on tissue paper to dry.
11. Continue step 9 and 10 using the same RNeasy spin column until all samples from step 8 is processed.
12. Add 700μl RW1 buffer to the RNeasy spin column, and centrifuge at 8000G for 15 seconds to wash the spin column. Discard flow-through.
13. Add 500μl RPE buffer to the RNeasy spin column, and centrifuge at 8000G for 15 seconds to wash the spin column. Discard flow-through.
14. Add 500μl RPE buffer to the RNeasy spin column, and centrifuge at 8000G for 2 minutes. Discard flow-through.
15. Transfer the RNeasy spin column to a new 2ml collection tube, and centrifuge at 10,000G for 1 minute.
16. Transfer the RNeasy spin column to a new 1.5ml collection tube.
17. Add 40μl DEPC-treated RNAse-free water to the RNeasy spin column (in the new 1.5ml collection tube). Close the lid and centrifuge at 8000G for 1 minute to elute the RNA.
18. Transfer the the flow-through from step 17 back into the same RNeasy spin column (in the same 1.5ml collection tube) and repeat centrifugation at 8000G for 1 minute to maximise RNA yield.

19. Quantification of RNA concentration using the Qubit™ RNA HS Assay Kit is recommended for an initial estimation of RNA quantity.

Notes:

- With step 3, a 1ml syringe is sufficiently narrow to fit within a 15ml centrifuge tube. Ideally, a luer-lock syringe would avoid the risk of needle dislodgment during passages, but this is not essential.
- With step 4, due to the lack of a cell pellet and additional volume from the bio-ink material following sample preparation, one sample will typically require two DNA spin columns.
- Trials to extract DNA through the kit's instruction with samples prepared as described in the SOP were unsuccessful. As such, the DNA spin columns are discarded in step 6. However, the processing of samples through the DNA spin column was a necessary step, as direct RNA extraction using the RNA spin column was also unsuccessful.
- Step 11 is an additional step compared to manufacturer's instruction to account for increased sample volume. By using the same RNeasy spin column, RNA from one sample is captured in a single spin column membrane.
- Follow manufacturer's kit instruction from step 12 onwards, using the AllPrep DNA/RNA Mini Kit (Qiagen).
- Step 15 is an optional step in the manufacturer's instruction to dry the membrane. Manufacturer's instruction stated to centrifuge at full speed. This is standardised to 10,000G in this SOP.
- Step 18 is an optional step in the manufacturer's instruction, and is incorporated as standard in the SOP to maximise RNA yield.
- With step 19, the quantification of RNA content in the sample is recommended which aids the estimation of reconstitution volume following ethanol precipitation. Due to the relatively low yield, the Qubit™ RNA HS Assay is recommended over nanodrop due to improved accuracy with the Qubit's assay's higher sensitivity range. Both methods require 1μl of sample.

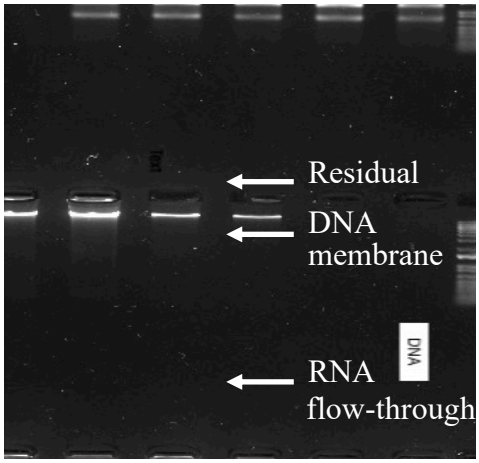

Figure 5 Photo demonstrating residual sample in the DNA spin column following centrifugation, with flow-through containing RNA in the collection tube.

Ethanol precipitation:

1. Ensure RNA samples are kept on ice when not processing.
2. Estimate the volume of RNA sample using a micropipette, taking care to avoid the introduction of air bubbles.
3. Add 1/10th volume of sodium acetate to the RNA sample (e.g. for 40μl of sample, add 4μl of sodium acetate).
4. Add 2.5x volume of 100% ethanol to the sample (inclusive of the addition of sodium acetate; i.e. for 40μl sample and 4μl sodium acetate, the volume of ethanol is 2.5 x (40+4) = 2.5 x 44 = 110μl).
5. Mix the sample by pipetting.
6. Store the sample at -20^{o}C overnight for RNA precipitation.
7. Ensure a supply of 70% ethanol at -20^{o}C for use the following day.
8. On the following day, centrifuge the sample at 12,000G for 20 minutes.
9. Pour away and discard the supernatant.
10. Add 500μl ice cold 70% ethanol to the sample. Vortex briefly to mix and centrifuge at 12,000G for 10 minutes.
11. Repeat step 9 and 10.

12. Pour away and discard the supernatant, and allow the RNA pellet to air dry.
13. When the pellet and collection tube is dry, dissolve the RNA pellet in the desired amount of RNAse-free water (e.g. 20μl). Ensure all RNA is captured by repeatedly coating the sides of the collection tube with the RNAse-free water, especially where the pellet was sited. Continue for a brief period beyond the point when the RNA pellet is no longer visible.

Notes:

- Extracted RNA is immediately subjected to ethanol precipitation to minimise the number of freeze-thaw cycles.
- With step 6, whilst RNA precipitation can be performed within the range of 1 hour to overnight, the latter was chosen as standard due to the anticipated low yield in terms of quantity.
- Note that 70% and 100% ethanol remain in liquid phase at -20^{o}C (step 6 + 7).
- With step 12, any liquid droplet within the collection tube separate to the RNA pellet is removed by dragging the droplet to the rim using a 200μl pipette tip. The droplet is absorbed by gentle tapping onto a tissue. To reduce contamination, the collection tube is placed on its side on top of and covered lightly by tissue. The air-dry process requires several hours, and is checked half hourly after 2 hours to avoid delay to step 13.
- The volume in which the RNA pellet is dissolved in (step 13) will depend on the end-application and the desired RNA concentration. For example, 4μl could be reserved for quality control purposes (1μl each for nanodrop (A260:A280 for DNA/protein contamination, and A260:A230 organics contaminations), Qubit^{TM} RNA HS Assay (quantity) and BioAnalyzer (RIN), and an additional 1μl as buffer). The residual RNA is aliquoted as needed for analysis. The purpose of aliquoting is to reduce the number of freeze-thaw cycles to preserve the quality of RNA.

5.9 Quality control and acceptance criteria

Not applicable.

6 Data analysis and reporting of data

Not applicable.

7 Publications

Not applicable.

8 References

1.Thomas DJ, Jessop Z & Whitaker I. 2018. *3D bioprinting for reconstructive surgery techniques and applications.* 1st edition. Woodhead Publishing.

2. Jessop, Z. M., A. Al-Sabah, N. Gao, S. Kyle, B. Thomas, N. Badiei, K. Hawkins and I. S. Whitaker (2019). "Printability of pulp derived crystal, fibril and blend nanocellulose-alginate bioinks for extrusion 3D bioprinting." Biofabrication 11(4): 045006.

3. Tarassoli, S. P., Z. M. Jessop, T. Jovic, K. Hawkins and I. S. Whitaker (2021). "Candidate Bioinks for Extrusion 3D Bioprinting-A Systematic Review of the Literature." Front Bioeng Biotechnol 9: 616753.

4.Markstedt, K., A. Mantas, I. Tournier, H. Martinez Avila, D. Hagg and P. Gatenholm (2015). "3D Bioprinting Human Chondrocytes with Nanocellulose-Alginate Bioink for Cartilage Tissue Engineering Applications." Biomacromolecules 16(5): 1489-1496.

5. Lopes, V. R., C. Sanchez-Martinez, M. Stromme and N. Ferraz (2017). "In vitro biological responses to nanofibrillated cellulose by human dermal, lung and immune cells: surface chemistry aspect." Particle and Fibre Toxicology 14.

6. Endes, C., S. Camarero-Espinosa, S. Mueller, E. J. Foster, A. Petri-Fink, B. Rothen-Rutishauser, C. Weder and M. J. Clift (2016). "A critical review of the current knowledge regarding the biological impact of nanocellulose." J Nanobiotechnology 14(1): 78.

7. Chia, S. H., B. L. Schumacher, T. J. Klein, E. J. Thonar, K. Masuda, R. L. Sah and D. Watson (2004). "Tissue-engineered human nasal septal cartilage using the alginate-recovered-chondrocyte method." Laryngoscope 114(1): 38-45.

8. Chung, C. and J. A. Burdick (2008). "Engineering cartilage tissue." Adv Drug Deliv Rev 60(2): 243-262.

9. Reuther, M. S., V. W. Wong, K. K. Briggs, A. A. Chang, Q. T. Nguyen, B. L. Schumacher, K. Masuda, R. L. Sah and D. Watson (2012). "Culture of human septal chondrocytes in a rotary bioreactor." Otolaryngol Head Neck Surg 147(4): 661-667.

10. Cigan, A. D., B. L. Roach, R. J. Nims, A. R. Tan, M. B. Albro, A. M. Stoker, J. L. Cook, G. Vunjak-Novakovic, C. T. Hung and G. A. Ateshian (2016). "High seeding density of human chondrocytes in agarose produces tissue-engineered cartilage approaching native mechanical and biochemical properties." J Biomech 49(9): 1909-1917.

11. Angelozzi, M., L. Penolazzi, S. Mazzitelli, E. Lambertini, A. Lolli, R. Piva and C. Nastruzzi (2017). "Dedifferentiated Chondrocytes in Composite Microfibers As Tool for Cartilage Repair." Front Bioeng Biotechnol 5: 35.

12. O'Connell, G. D., A. R. Tan, V. Cui, J. C. Bulinski, J. L. Cook, M. Attur, S. B. Abramson, G. A. Ateshian and C. T. Hung (2017). "Human chondrocyte migration behaviour to guide the development of engineered cartilage." J Tissue Eng Regen Med 11(3): 877-886.

13. Vedicherla, S. and C. T. Buckley (2017). "Rapid Chondrocyte Isolation for Tissue Engineering Applications: The Effect of Enzyme Concentration and Temporal Exposure on the Matrix Forming Capacity of Nasal Derived Chondrocytes." Biomed Res Int 2017: 2395138.

14.Figure of haemocytometer. Available from https://www.hemocytometer.org/hemocytometer-protocol/ (Accessed on 18.02.2025)

15. Al-Sabah, A., S. E. A. Burnell, I. N. Simoes, Z. Jessop, N. Badiei, E. Blain and I. S. Whitaker (2019). "Structural and mechanical characterization of crosslinked and sterilised nanocellulose-based hydrogels for cartilage tissue engineering." Carbohydr Polym 212: 242-251.

16. Gunin, A. G., N. K. Kornilova, O. V. Vasilieva and V. V. Petrov (2011). "Age-related changes in proliferation, the numbers of mast cells, eosinophils, and cd45-positive cells in human dermis." J Gero

Chapter 10: References

1. Faces C. The face equality campaign – the evidence: the incidence and prevalence of disfigurement. [Available from: https://www.changingfaces.org.uk/education/health/patient-needs/statistics.
2. Gomoll AH, Minas T. The quality of healing: articular cartilage. Wound Repair Regen. 2014;22 Suppl 1:30-8.
3. Tew S, Redman S, Kwan A, Walker E, Khan I, Dowthwaite G, et al. Differences in repair responses between immature and mature cartilage. Clin Orthop Relat Res. 2001(391 Suppl):S142-52.
4. Uppal RS, Sabbagh W, Chana J, Gault DT. Donor-site morbidity after autologous costal cartilage harvest in ear reconstruction and approaches to reducing donor-site contour deformity. Plast Reconstr Surg. 2008;121(6):1949-55.
5. Nagata S. Modification of the stages in total reconstruction of the auricle: Part IV. Ear elevation for the constructed auricle. Plast Reconstr Surg. 1994;93(2):254-66; discussion 67-8.
6. Nagata S. Modification of the stages in total reconstruction of the auricle: Part III. Grafting the three-dimensional costal cartilage framework for small concha-type microtia. Plast Reconstr Surg. 1994;93(2):243-53; discussion 67-8.
7. Nagata S. Modification of the stages in total reconstruction of the auricle: Part II. Grafting the three-dimensional costal cartilage framework for concha-type microtia. Plast Reconstr Surg. 1994;93(2):231-42; discussion 67-8.
8. Nagata S. Modification of the stages in total reconstruction of the auricle: Part I. Grafting the three-dimensional costal cartilage framework for lobule-type microtia. Plast Reconstr Surg. 1994;93(2):221-30; discussion 67-8.
9. Ohara K, Nakamura K, Ohta E. Chest wall deformities and thoracic scoliosis after costal cartilage graft harvesting. Plast Reconstr Surg. 1997;99(4):1030-6.
10. Wallace CG, Mao HY, Wang CJ, Chen YA, Chen PK, Chen ZC. Three-dimensional computed tomography reveals different donor-site deformities in adult and growing microtia patients despite total subperichondrial costal cartilage harvest and donor-site reconstruction. Plast Reconstr Surg. 2014;133(3):640-51.
11. Zhang Q, Zhang R, Xu F, Jin P, Cao Y. Auricular reconstruction for microtia: personal 6-year experience based on 350 microtia ear reconstructions in China. Plast Reconstr Surg. 2009;123(3):849-58.
12. Osorno G. Autogenous rib cartilage reconstruction of congenital ear defects: report of 110 cases with Brent's technique. Plast Reconstr Surg. 1999;104(7):1951-62; discussion 63-4.
13. Lewin S. Complications after Total Porous Implant Ear Reconstruction and Their Management. Facial Plast Surg. 2015;31(6):617-25.
14. Pruthi G, Bansal K, Jain V, Kumar Koli D. Retrospective study of treatment outcomes with implant retained auricular prostheses at a tertiary referral care centre. J Oral Biol Craniofac Res. 2020;10(3):266-75.
15. Ronde EM, Esposito M, Lin Y, van Etten-Jamaludin FS, Bulstrode NW, Breugem CC. Long-term complications of microtia reconstruction: A systematic review. J Plast Reconstr Aesthet Surg. 2021;74(12):3235-50.
16. Langer R, Vacanti JP. Tissue engineering. Science. 1993;260(5110):920-6.
17. research Gv. Tissue engineering market size, share & trends analysis report by application (cord blood & cell banking, cancer, GI & gynecology, dental, orthopedics, musculoskeletal, & spine), by region, and segment forecasts, 2020-2027 2019 [Available from: https://www.grandviewresearch.com/industry-analysis/tissue-engineering-and-regeneration-industry.
18. Stampoultzis T, Karami P, Pioletti DP. Thoughts on cartilage tissue engineering: A 21st century perspective. Curr Res Transl Med. 2021;69(3):103299.
19. Cao Y, Vacanti JP, Paige KT, Upton J, Vacanti CA. Transplantation of chondrocytes utilizing a polymer-cell construct to produce tissue-engineered cartilage in the shape of a human ear. Plast Reconstr Surg. 1997;100(2):297-302; discussion 3-4.
20. Yi HG, Choi YJ, Jung JW, Jang J, Song TH, Chae S, et al. Three-dimensional printing of a patient-specific engineered nasal cartilage for augmentative rhinoplasty. J Tissue Eng. 2019;10:2041731418824797.
21. Mendelson A, Ahn JM, Paluch K, Embree MC, Mao JJ. Engineered nasal cartilage by cell homing: a model for augmentative and reconstructive rhinoplasty. Plast Reconstr Surg. 2014;133(6):1344-53.
22. Pomerantseva I, Bichara DA, Tseng A, Cronce MJ, Cervantes TM, Kimura AM, et al. Ear-Shaped Stable Auricular Cartilage Engineered from Extensively Expanded Chondrocytes in an Immunocompetent Experimental Animal Model. Tissue Eng Part A. 2016;22(3-4):197-207.

23. Luo X, Zhou G, Liu W, Zhang WJ, Cen L, Cui L, et al. In vitro precultivation alleviates post-implantation inflammation and enhances development of tissue-engineered tubular cartilage. Biomed Mater. 2009;4(2):025006.
24. Luo X, Liu Y, Zhang Z, Tao R, Liu Y, He A, et al. Long-term functional reconstruction of segmental tracheal defect by pedicled tissue-engineered trachea in rabbits. Biomaterials. 2013;34(13):3336-44.
25. Liu Y, Zhou GD, Cao YL. Recent Progress in Cartilage Tissue Engineering-Our Experience and Future Directions. Engineering. 2017;3(1):28-35.
26. Emara A, Shah R. Recent update on craniofacial tissue engineering. J Tissue Eng. 2021;12:20417314211003735.
27. Liu Y, Li D, Yin Z, Luo X, Liu W, Zhang W, et al. Prolonged in vitro precultivation alleviates post-implantation inflammation and promotes stable subcutaneous cartilage formation in a goat model. Biomed Mater. 2016;12(1):015006.
28. Haisch A. Ear reconstruction through tissue engineering. Adv Otorhinolaryngol. 2010;68:108-19.
29. Kamil SH, Vacanti MP, Aminuddin BS, Jackson MJ, Vacanti CA, Eavey RD. Tissue engineering of a human sized and shaped auricle using a mold. Laryngoscope. 2004;114(5):867-70.
30. Christophel JJ, Chang JS, Park SS. Transplanted tissue-engineered cartilage. Arch Facial Plast Surg. 2006;8(2):117-22.
31. Yanaga H, Imai K, Tanaka Y, Yanaga K. Two-stage transplantation of cell-engineered autologous auricular chondrocytes to regenerate chondrofat composite tissue: clinical application in regenerative surgery. Plast Reconstr Surg. 2013;132(6):1467-77.
32. Yanaga H, Imai K, Fujimoto T, Yanaga K. Generating ears from cultured autologous auricular chondrocytes by using two-stage implantation in treatment of microtia. Plast Reconstr Surg. 2009;124(3):817-25.
33. Weidenbecher M, Tucker HM, Awadallah A, Dennis JE. Fabrication of a neotrachea using engineered cartilage. Laryngoscope. 2008;118(4):593-8.
34. Weidenbecher M, Tucker HM, Gilpin DA, Dennis JE. Tissue-engineered trachea for airway reconstruction. Laryngoscope. 2009;119(11):2118-23.
35. Schwarz S, Koerber L, Elsaesser AF, Goldberg-Bockhorn E, Seitz AM, Durselen L, et al. Decellularized cartilage matrix as a novel biomatrix for cartilage tissue-engineering applications. Tissue Eng Part A. 2012;18(21-22):2195-209.
36. Huang BJ, Hu JC, Athanasiou KA. Cell-based tissue engineering strategies used in the clinical repair of articular cartilage. Biomaterials. 2016;98:1-22.
37. Lim HC, Park YB, Ha CW, Cole BJ, Lee BK, Jeong HJ, et al. Allogeneic Umbilical Cord Blood-Derived Mesenchymal Stem Cell Implantation Versus Microfracture for Large, Full-Thickness Cartilage Defects in Older Patients: A Multicenter Randomized Clinical Trial and Extended 5-Year Clinical Follow-up. Orthop J Sports Med. 2021;9(1):2325967120973052.
38. ClinicalTrials.gov. Phase III Study to Evaluate Safety and Effectiveness of NOVOCART 3D Plus vs. Microfracture in Knee Cartilage Defects (N3D) 2012 [Available from: https://clinicaltrials.gov/ct2/show/NCT01656902.
39. Tschugg A, Diepers M, Simone S, Michnacs F, Quirbach S, Strowitzki M, et al. A prospective randomized multicenter phase I/II clinical trial to evaluate safety and efficacy of NOVOCART disk plus autologous disk chondrocyte transplantation in the treatment of nucleotomized and degenerative lumbar disks to avoid secondary disease: safety results of Phase I-a short report. Neurosurg Rev. 2017;40(1):155-62.
40. Weber AE, Locker PH, Mayer EN, Cvetanovich GL, Tilton AK, Erickson BJ, et al. Clinical Outcomes After Microfracture of the Knee: Midterm Follow-up. Orthop J Sports Med. 2018;6(2):2325967117753572.
41. Wasyleczko M, Sikorska W, Chwojnowski A. Review of Synthetic and Hybrid Scaffolds in Cartilage Tissue Engineering. Membranes (Basel). 2020;10(11).
42. Evans JT, Evans JP, Walker RW, Blom AW, Whitehouse MR, Sayers A. How long does a hip replacement last? A systematic review and meta-analysis of case series and national registry reports with more than 15 years of follow-up. Lancet. 2019;393(10172):647-54.
43. Macchiarini P, Jungebluth P, Go T, Asnaghi MA, Rees LE, Cogan TA, et al. Clinical transplantation of a tissue-engineered airway. Lancet. 2008;372(9655):2023-30.
44. Hawkes N. Macchiarini case: seven researchers are guilty of scientific misconduct, rules Karolinska's president. BMJ. 2018;361:k2816.
45. Paolo Macchiarini is not guilty of scientific misconduct. Lancet. 2015;386(9997):932.

46. Fulco I, Miot S, Haug MD, Barbero A, Wixmerten A, Feliciano S, et al. Engineered autologous cartilage tissue for nasal reconstruction after tumour resection: an observational first-in-human trial. Lancet. 2014;384(9940):337-46.
47. Irawan V, Sung TC, Higuchi A, Ikoma T. Collagen Scaffolds in Cartilage Tissue Engineering and Relevant Approaches for Future Development. Tissue Eng Regen Med. 2018;15(6):673-97.
48. Zhang Q, Lu H, Kawazoe N, Chen G. Pore size effect of collagen scaffolds on cartilage regeneration. Acta Biomater. 2014;10(5):2005-13.
49. Gobbi A, Whyte GP. Long-term Clinical Outcomes of One-Stage Cartilage Repair in the Knee With Hyaluronic Acid-Based Scaffold Embedded With Mesenchymal Stem Cells Sourced From Bone Marrow Aspirate Concentrate. Am J Sports Med. 2019;47(7):1621-8.
50. Lin H, Beck AM, Shimomura K, Sohn J, Fritch MR, Deng Y, et al. Optimization of photocrosslinked gelatin/hyaluronic acid hybrid scaffold for the repair of cartilage defect. J Tissue Eng Regen Med. 2019;13(8):1418-29.
51. Whu SW, Hung KC, Hsieh KH, Chen CH, Tsai CL, Hsu SH. In vitro and in vivo evaluation of chitosan-gelatin scaffolds for cartilage tissue engineering. Materials Science & Engineering C-Materials for Biological Applications. 2013;33(5):2855-63.
52. Chen S, Chen W, Chen Y, Mo X, Fan C. Chondroitin sulfate modified 3D porous electrospun nanofiber scaffolds promote cartilage regeneration. Mater Sci Eng C Mater Biol Appl. 2021;118:111312.
53. Zhou F, Zhang X, Cai D, Li J, Mu Q, Zhang W, et al. Silk fibroin-chondroitin sulfate scaffold with immuno-inhibition property for articular cartilage repair. Acta Biomater. 2017;63:64-75.
54. Kim JS, Kim TH, Kang DL, Baek SY, Lee Y, Koh YG, et al. Chondrogenic differentiation of human ASCs by stiffness control in 3D fibrin hydrogel. Biochem Biophys Res Commun. 2020;522(1):213-9.
55. Balakrishnan B, Banerjee R. Biopolymer-based hydrogels for cartilage tissue engineering. Chem Rev. 2011;111(8):4453-74.
56. Vega SL, Kwon MY, Burdick JA. Recent advances in hydrogels for cartilage tissue engineering. Eur Cell Mater. 2017;33:59-75.
57. Yang J, Zhang YS, Yue K, Khademhosseini A. Cell-laden hydrogels for osteochondral and cartilage tissue engineering. Acta Biomater. 2017;57:1-25.
58. Asghari F, Samiei M, Adibkia K, Akbarzadeh A, Davaran S. Biodegradable and biocompatible polymers for tissue engineering application: a review. Artif Cells Nanomed Biotechnol. 2017;45(2):185-92.
59. Singhvi MS, Zinjarde SS, Gokhale DV. Polylactic acid: synthesis and biomedical applications. Journal of Applied Microbiology. 2019;127(6):1612-26.
60. Fan W, Yuan L, Li J, Wang Z, Chen J, Guo C, et al. Injectable double-crosslinked hydrogels with kartogenin-conjugated polyurethane nano-particles and transforming growth factor beta3 for in-situ cartilage regeneration. Mater Sci Eng C Mater Biol Appl. 2020;110:110705.
61. Sancho-Tello M, Forriol F, Martin de Llano JJ, Antolinos-Turpin C, Gomez-Tejedor JA, Gomez Ribelles JL, et al. Biostable scaffolds of polyacrylate polymers implanted in the articular cartilage induce hyaline-like cartilage regeneration in rabbits. Int J Artif Organs. 2017;40(7):350-7.
62. Fu TS, Wei YH, Cheng PY, Chu IM, Chen WC. A Novel Biodegradable and Thermosensitive Poly(Ester-Amide) Hydrogel for Cartilage Tissue Engineering. Biomed Research International. 2018;2018.
63. Gartner LP. Textbook of histology. Fifth edition. ed. Philadelphia, PA: Elsevier; 2021. xi, 611 pages p.
64. Brown DS, Eames BF. Emerging tools to study proteoglycan function during skeletal development. Methods Cell Biol. 2016;134:485-530.
65. Zhang L, Hu J, Athanasiou KA. The role of tissue engineering in articular cartilage repair and regeneration. Crit Rev Biomed Eng. 2009;37(1-2):1-57.
66. Anderson CE, Ludowieg J, Harper HA, Engleman EP. The Composition of the Organic Component of Human Articular Cartilage. Relationship to Age and Degenerative Joint Disease. J Bone Joint Surg Am. 1964;46:1176-83.
67. Benjamin M, Evans EJ. Fibrocartilage. J Anat. 1990;171:1-15.
68. Carriel V, Geuna S, Alaminos M. Ex Vivo and In Vivo Stem Cells-Based Tissue Engineering Strategies for Their Use in Regenerative Medicine. Stem Cells Int. 2018;2018:7143930.
69. Mata M, Milian L, Oliver M, Zurriaga J, Sancho-Tello M, de Llano JJM, et al. In Vivo Articular Cartilage Regeneration Using Human Dental Pulp Stem Cells Cultured in an Alginate Scaffold: A Preliminary Study. Stem Cells Int. 2017;2017:8309256.

70. Uhlin M, Mattsson J. In vitro or in vivo expansion before adoptive T-cell therapy? Immunotherapy. 2011;3(2):131-3.
71. Kusuhara H, Isogai N, Enjo M, Otani H, Ikada Y, Jacquet R, et al. Tissue engineering a model for the human ear: assessment of size, shape, morphology, and gene expression following seeding of different chondrocytes. Wound Repair Regen. 2009;17(1):136-46.
72. Xu JW, Zaporojan V, Peretti GM, Roses RE, Morse KB, Roy AK, et al. Injectable tissue-engineered cartilage with different chondrocyte sources. Plast Reconstr Surg. 2004;113(5):1361-71.
73. Isogai N, Asamura S, Higashi T, Ikada Y, Morita S, Hillyer J, et al. Tissue engineering of an auricular cartilage model utilizing cultured chondrocyte-poly(L-lactide-epsilon-caprolactone) scaffolds. Tissue Eng. 2004;10(5-6):673-87.
74. Semine AA, Damon A. Costochondral Ossification and Aging in 5 Populations. Human Biology. 1975;47(1):101-16.
75. Barchilon V, Hershkovitz I, Rothschild BM, Wish-Baratz S, Latimer B, Jellema LM, et al. Factors affecting the rate and pattern of the first costal cartilage ossification. Am J Forensic Med Pathol. 1996;17(3):239-47.
76. Lau AG, Kindig MW, Kent RW. Morphology, distribution, mineral density and volume fraction of human calcified costal cartilage. Acta Biomater. 2011;7(3):1202-9.
77. Schulz RM, Bader A. Cartilage tissue engineering and bioreactor systems for the cultivation and stimulation of chondrocytes. Eur Biophys J. 2007;36(4-5):539-68.
78. Natenstedt J, Kok AC, Dankelman J, Tuijthof GJ. What quantitative mechanical loading stimulates in vitro cultivation best? J Exp Orthop. 2015;2(1):15.
79. Knobloch TJ, Madhavan S, Nam J, Agarwal S, Jr., Agarwal S. Regulation of chondrocytic gene expression by biomechanical signals. Crit Rev Eukaryot Gene Expr. 2008;18(2):139-50.
80. Allen JL, Cooke ME, Alliston T. ECM stiffness primes the TGFbeta pathway to promote chondrocyte differentiation. Mol Biol Cell. 2012;23(18):3731-42.
81. Bougault C, Aubert-Foucher E, Paumier A, Perrier-Groult E, Huot L, Hot D, et al. Dynamic compression of chondrocyte-agarose constructs reveals new candidate mechanosensitive genes. PLoS One. 2012;7(5):e36964.
82. Sanz-Ramos P, Mora G, Ripalda P, Vicente-Pascual M, Izal-Azcarate I. Identification of signalling pathways triggered by changes in the mechanical environment in rat chondrocytes. Osteoarthritis Cartilage. 2012;20(8):931-9.
83. Hollister SJ. Porous scaffold design for tissue engineering. Nat Mater. 2005;4(7):518-24.
84. Bruzauskaite I, Bironaite D, Bagdonas E, Bernotiene E. Scaffolds and cells for tissue regeneration: different scaffold pore sizes-different cell effects. Cytotechnology. 2016;68(3):355-69.
85. Loh QL, Choong C. Three-dimensional scaffolds for tissue engineering applications: role of porosity and pore size. Tissue Eng Part B Rev. 2013;19(6):485-502.
86. Kyle S, Jessop ZM, Al-Sabah A, Whitaker IS. 'Printability' of Candidate Biomaterials for Extrusion Based 3D Printing: State-of-the-Art. Adv Healthc Mater. 2017;6(16).
87. Sanan A, Haines SJ. Repairing holes in the head: a history of cranioplasty. Neurosurgery. 1997;40(3):588-603.
88. Cronin TD. Use of a silastic frame for total and subtotal reconstruction of the external ear: preliminary reort. Plast Reconstr Surg. 1966;37(5):399-405.
89. Cronin TD, Greenberg RL, Brauer RO. Follow-up study of silastic frame for reconstruction of external ear. Plast Reconstr Surg. 1968;42(6):522-9.
90. Cronin TD, Ascough BM. Silastic ear construction. Clin Plast Surg. 1978;5(3):367-78.
91. Reinisch JF, Lewin S. Ear reconstruction using a porous polyethylene framework and temporoparietal fascia flap. Facial Plast Surg. 2009;25(3):181-9.
92. Wellisz T. Reconstruction of the burned external ear using a Medpor porous polyethylene pivoting helix framework. Plast Reconstr Surg. 1993;91(5):811-8.
93. Wellisz T. Clinical experience with the Medpor porous polyethylene implant. Aesthetic Plast Surg. 1993;17(4):339-44.
94. Eltom A, Zhong GY, Muhammad A. Scaffold Techniques and Designs in Tissue Engineering Functions and Purposes: A Review. Advances in Materials Science and Engineering. 2019;2019.
95. Chung C, Burdick JA. Engineering cartilage tissue. Adv Drug Deliv Rev. 2008;60(2):243-62.
96. Puppi D, Chiellini F, Piras AM, Chiellini E. Polymeric materials for bone and cartilage repair. Progress in Polymer Science. 2010;35(4):403-40.
97. Zhang X, Wu Y, Pan Z, Sun H, Wang J, Yu D, et al. The effects of lactate and acid on articular chondrocytes function: Implications for polymeric cartilage scaffold design. Acta Biomater. 2016;42:329-40.

98. Nayyer L, Patel KH, Esmaeili A, Rippel RA, Birchall M, O'Toole G, et al. Tissue engineering: revolution and challenge in auricular cartilage reconstruction. Plast Reconstr Surg. 2012;129(5):1123-37.
99. Bichara DA, O'Sullivan NA, Pomerantseva I, Zhao X, Sundback CA, Vacanti JP, et al. The tissue-engineered auricle: past, present, and future. Tissue Eng Part B Rev. 2012;18(1):51-61.
100. Tarassoli SP, Jessop ZM, Jovic T, Hawkins K, Whitaker IS. Candidate Bioinks for Extrusion 3D Bioprinting-A Systematic Review of the Literature. Front Bioeng Biotechnol. 2021;9:616753.
101. Moroni L, Boland T, Burdick JA, De Maria C, Derby B, Forgacs G, et al. Biofabrication: A Guide to Technology and Terminology. Trends Biotechnol. 2018;36(4):384-402.
102. Mota C, Puppi D, Chiellini F, Chiellini E. Additive manufacturing techniques for the production of tissue engineering constructs. J Tissue Eng Regen Med. 2015;9(3):174-90.
103. Placone JK, Engler AJ. Recent Advances in Extrusion-Based 3D Printing for Biomedical Applications. Adv Healthc Mater. 2018;7(8):e1701161.
104. Kuhnt T, Camarero-Espinosa S. Additive manufacturing of nanocellulose based scaffolds for tissue engineering: Beyond a reinforcement filler. Carbohydr Polym. 2021;252:117159.
105. Nguyen KT, West JL. Photopolymerizable hydrogels for tissue engineering applications. Biomaterials. 2002;23(22):4307-14.
106. Schoenmakers DC, Rowan AE, Kouwer PHJ. Crosslinking of fibrous hydrogels. Nat Commun. 2018;9(1):2172.
107. Miyata T, Uragami T, Nakamae K. Biomolecule-sensitive hydrogels. Adv Drug Deliv Rev. 2002;54(1):79-98.
108. Kuo CK, Ma PX. Ionically crosslinked alginate hydrogels as scaffolds for tissue engineering: part 1. Structure, gelation rate and mechanical properties. Biomaterials. 2001;22(6):511-21.
109. Sun JY, Zhao X, Illeperuma WR, Chaudhuri O, Oh KH, Mooney DJ, et al. Highly stretchable and tough hydrogels. Nature. 2012;489(7414):133-6.
110. Wilhelm J, Frey E. Elasticity of stiff polymer networks. Phys Rev Lett. 2003;91(10):108103.
111. Spicer CD. Hydrogel scaffolds for tissue engineering: the importance of polymer choice. Polymer Chemistry. 2020;11(2):184-219.
112. Mow VC, Ratcliffe A, Poole AR. Cartilage and diarthrodial joints as paradigms for hierarchical materials and structures. Biomaterials. 1992;13(2):67-97.
113. Askew MJ, Mow VC. Biomechanical Function of Collagen Fibril Ultrastructure of Articular-Cartilage. Journal of Biomechanical Engineering-Transactions of the Asme. 1978;100(3):105-15.
114. Charreau H, Cavallo E, Foresti ML. Patents involving nanocellulose: Analysis of their evolution since 2010. Carbohydr Polym. 2020;237:116039.
115. Trache D, Tarchoun AF, Derradji M, Hamidon TS, Masruchin N, Brosse N, et al. Nanocellulose: From Fundamentals to Advanced Applications. Front Chem. 2020;8:392.
116. Moon RJ, Schueneman GT, Simonsen J. Overview of Cellulose Nanomaterials, Their Capabilities and Applications. JOM. 2016;68(9):2383-94.
117. Thomas B, Raj MC, B AK, H RM, Joy J, Moores A, et al. Nanocellulose, a Versatile Green Platform: From Biosources to Materials and Their Applications. Chem Rev. 2018;118(24):11575-625.
118. Charreau H, Foresti ML, Vazquez A. Nanocellulose patents trends: a comprehensive review on patents on cellulose nanocrystals, microfibrillated and bacterial cellulose. Recent Pat Nanotechnol. 2013;7(1):56-80.
119. Eichhorn SJ, Dufresne A, Aranguren M, Marcovich NE, Capadona JR, Rowan SJ, et al. Review: current international research into cellulose nanofibres and nanocomposites. J Mater Sci. 2010;45:1-33.
120. Gómez H C, Serpa A, Velásquez-Cock J, Gañán P, Castro C, Vélez L, et al. Vegetable nanocellulose in food science: A review. Food Hydrocolloids. 2016;57:178-86.
121. Kim JH, Lee D, Lee YH, Chen W, Lee SY. Nanocellulose for Energy Storage Systems: Beyond the Limits of Synthetic Materials. Adv Mater. 2019;31(20):e1804826.
122. Dufresne A. Nanocellulose Processing Properties and Potential Applications. Current Forestry Reports. 2019;5(2):76-89.
123. Tamo AK. Nanocellulose-based hydrogels as versatile materials with interesting functional properties for tissue engineering applications. J Mater Chem B. 2024;12(32):7692-759.
124. Chen PH, Liao HC, Hsu SH, Chen RS, Wu MC, Yang YF, et al. A novel polyurethane/cellulose fibrous scaffold for cardiac tissue engineering. RSC Adv. 2015;5:6932-9.
125. Phatchayaway PP, Khamkeaw A, Yodmuang S, Phisalaphong M. 3D bacterial cellulose-chitosan-alginate-gelatin hydrogel scaffold for cartilage tissue engineering. Biochem Eng J. 2022;184:108476.

126. Chen C, Xi Y, Weng Y. Recent Advances in Cellulose-Based Hydrogels for Tissue Engineering Applications. Polymers (Basel). 2022;14(16).
127. Durairaj V, Li P, Liljeström T, Wester N, Etula J, Leppänen I, et al. Functionalized Nanocellulose/Multiwalled Carbon Nanotube Composites for Electrochemical Applications. ACS Applied Nano Materials. 2021;4(6):5842-53.
128. Ferreira FV, Souza LP, Martins TMM, Lopes JH, Mattos BD, Mariano M, et al. Nanocellulose/bioactive glass cryogels as scaffolds for bone regeneration. Nanoscale. 2019;11:19842-9.
129. Patil TV, Patel DK, Dutta SD, Ganguly K, Santra TS, Lim KT. Nanocellulose, a versatile platform: From the delivery of active molecules to tissue engineering applications. Bioact Mater. 2022;9:566-89.
130. Li J, Wu C, Chu PK, Gelinsky M. 3D printing of hydrogels: Rational design strategies and emerging biomedical applications. Mater Sci Eng R. 2020;150:100543.
131. Wei Z, Wu CJ, Li R, Yu D, Ding Q. Nanocellulose based hydrogel or aerogel scaffolds for tissue engineering. Cellulose. 2021;28(12):7497-520.
132. Monfared M, Mawad D, Rnjak-Kovacina J, Stenzel MH. 3D bioprinting of dual-crosslinked nanocellulose hydrogels for tissue engineering applications. J Mater Chem B. 2021;9(31):6163-75.
133. Tamo AK, Tran TA, Doench I, Jahangir S, Lall A, David L, et al. 3D Printing of Cellulase-Laden Cellulose Nanofiber/Chitosan Hydrogel Composites: Towards Tissue Engineering Functional Biomaterials with Enzyme-Mediated Biodegradation. Materials (Basel). 2022;15(17).
134. Del Valle LJ, Diaz A, Puiggali J. Hydrogels for Biomedical Applications: Cellulose, Chitosan, and Protein/Peptide Derivatives. Gels. 2017;3(3).
135. Kamdem Tamo A, Doench I, Walter L, Montembault A, Sudre G, David L, et al. Development of Bioinspired Functional Chitosan/Cellulose Nanofiber 3D Hydrogel Constructs by 3D Printing for Application in the Engineering of Mechanically Demanding Tissues. Polymers (Basel). 2021;13(10).
136. Doench I, Ahn Tran T, David L, Montembault A, Viguier E, Gorzelanny C, et al. Cellulose Nanofiber-Reinforced Chitosan Hydrogel Composites for Intervertebral Disc Tissue Repair. Biomimetics (Basel). 2019;4(1).
137. Isikgora FH, Becer CM. Lignocellulosic biomass: a sustainable platform for the production of bio-based chemicals and polymers. Polym Chem. 2015;6:4497-559.
138. Gibson LJ. The hierarchical structure and mechanics of plant materials. J R Soc Interface. 2012;9(76):2749-66.
139. Ghorbani M, Roshangar L, Rad JS. Development of reinforced chitosan/pectin scaffold by using the cellulose nanocrystals as nanofillers: An injectable hydrogel for tissue engineering. Eur Polym J. 2020;130:109697.
140. Chayanun S, Soufivand AA, Faber J, Budday S, Lohwongwatana B, Boccaccini AR. Reinforcing Tissue-Engineered Cartilage: Nanofibrillated Cellulose Enhances Mechanical Properties of Alginate Dialdehyde–Gelatin Hydrogel. Adv Eng Mater. 2024;26(4):2300641.
141. Cui S, Zhang S, Coseri S. An injectable and self-healing cellulose nanofiber-reinforced alginate hydrogel for bone repair. Carbohydr Polym. 2023;300:120243.
142. Pomari AAN, Montanheiro TLA, Siqueira CP, Silva RS. Chitosan Hydrogels Crosslinked by Genipin and Reinforced with Cellulose Nanocrystals: Production and Characterization. Journal of Composites Science. 2019;3(3):84.
143. Tortorella S, Vetri Buratti V, Maturi M, Sambri L, Comes Franchini M, Locatelli E. Surface-Modified Nanocellulose for Application in Biomedical Engineering and Nanomedicine: A Review. Int J Nanomedicine. 2020;15:9909-37.
144. Rol F, Belgacem MN, Gandini A, Bras J. Recent advances in surface-modified cellulose nanofibrils. Progress in Polymer Science. 2019;88:241-64.
145. Ashammakhi N, Ahadian S, Xu C, Montazerian H, Ko H, Nasiri R, et al. Bioinks and bioprinting technologies to make heterogeneous and biomimetic tissue constructs. Mater Today Bio. 2019;1:100008.
146. Baniasadi H, Ajdary R, Trifol J, Rojas OJ, Seppala J. Direct ink writing of aloe vera/cellulose nanofibrils bio-hydrogels. Carbohydr Polym. 2021;266:118114.
147. Yadav C, Lee JM, Mohanty P, Li X, Jang WD. Graft onto approaches for nanocellulose-based advanced functional materials. Nanoscale. 2023;15(37):15108-45.
148. Solhi L, Guccini V, Heise K, Solala I, Niinivaara E, Xu W, et al. Understanding Nanocellulose-Water Interactions: Turning a Detriment into an Asset. Chem Rev. 2023;123(5):1925-2015.
149. Wang X, Wang Q, Xu C. Nanocellulose-Based Inks for 3D Bioprinting: Key Aspects in Research Development and Challenging Perspectives in Applications-A Mini Review. Bioengineering (Basel). 2020;7(2).

150. Norizan MN, Shazleen SS, Alias AH, Sabaruddin FA, Asyraf MRM, Zainudin ES, et al. Nanocellulose-Based Nanocomposites for Sustainable Applications: A Review. Nanomaterials (Basel). 2022;12(19).
151. Osorio-Madrazo A, Eder M, Rueggeberg M, Pandey JK, Harrington MJ, Nishiyama Y, et al. Reorientation of cellulose nanowhiskers in agarose hydrogels under tensile loading. Biomacromolecules. 2012;13(3):850-6.
152. George J, Sabapathi SN. Cellulose nanocrystals: synthesis, functional properties, and applications. Nanotechnol Sci Appl. 2015;8:45-54.
153. Mali P, Sherje AP. Cellulose nanocrystals: Fundamentals and biomedical applications. Carbohydr Polym. 2022;275:118668.
154. Shojaeiarani J, Bajwa DS, Chanda S. Cellulose nanocrystal based composites: A review. Composites Part C. 2021;5:100164.
155. Leong SL, Tiong SIX, Siva SP, Ahamed F, Chan CH, Lee CL, et al. Morphological control of cellulose nanocrystals via sulfuric acid hydrolysis based on sustainability considerations: An overview of the governing factors and potential challenges. J Environ Chem Eng. 2022;10(4):108145.
156. Mao J, Osorio-Madrazo A, Laborie MP. Preparation of cellulose I nanowhiskers with a mildly acidic aqueous ionic liquid: reaction efficiency and whiskers attributes. Cellulose. 2013;20:1829-40.
157. Xu Y, Xu Y, Deng W, Chen H, Xiong J. Extracting dialdehyde cellulose nanocrystals using choline chloride/urea-based deep eutectic solvents: A comparative study in NaIO(4) pre-oxidation and synchronous oxidation. Int J Biol Macromol. 2023;246:125604.
158. Douard L, Bras J, Encinas T, Belgacem MN. Natural acidic deep eutectic solvent to obtain cellulose nanocrystals using the design of experience approach. Carbohydr Polym. 2021;252:117136.
159. Zhu S, Sun H, Mu T, Li Q, Richel A. Preparation of cellulose nanocrystals from purple sweet potato peels by ultrasound-assisted maleic acid hydrolysis. Food Chem. 2023;403:134496.
160. Pang Z, Wang P, Dong C. Ultrasonic pretreatment of cellulose in ionic liquid for efficient preparation of cellulose nanocrystals. Cellulose. 2018;25(2):7053-64.
161. Haddis DZ, Chae M, Asomaning J, Bressler DC. Evaluation of steam explosion pretreatment on the cellulose nanocrystals (CNCs) yield from poplar wood. Carbohydr Polym. 2024;323:121460.
162. De France KJ, Yager KG, Chan KJW, Corbett B, Cranston ED, Hoare T. Injectable Anisotropic Nanocomposite Hydrogels Direct in Situ Growth and Alignment of Myotubes. Nano Lett. 2017;17(10):6487-95.
163. Jiang Y, J. Z, Shi H, Zhao G. Preparation of cellulose nanocrystal/oxidized dextran/gelatin (CNC/OD/GEL) hydrogels and fabrication of a CNC/OD/GEL scaffold by 3D printing. J Mater Sci. 2020;55(14):2618-35.
164. Eichhorn SJ. Cellulose nanowhiskers: promising materials for advanced applications. Soft Matter. 2011;7:303-15.
165. Dugan JM, Collins RF, Gough JE, Eichhorn SJ. Oriented surfaces of adsorbed cellulose nanowhiskers promote skeletal muscle myogenesis. Acta Biomater. 2013;9(1):4707-15.
166. Hosseinidoust Z, Alam MN, Sim G, Tufenkji N, van de Ven TG. Cellulose nanocrystals with tunable surface charge for nanomedicine. Nanoscale. 2015;7(40):16647-57.
167. Carter N, Grant I, Dewey M, Bourque M, Neivandt D. Production and Characterization of Cellulose Nanofiber Slurries and Sheets for Biomedical Applications. Front Nanotechnol. 2021;3:729743.
168. Ghilan A, Nicu R, Ciolacu DE, Ciolacu F. Insight into the Latest Medical Applications of Nanocellulose. Materials. 2023;16(12):4447.
169. Carneiro Pessan C, Silva Bernardes J, Bettini SHP, Leite ER. Oxidized cellulose nanofibers from sugarcane bagasse obtained by microfluidization: Morphology and rheological behavior. Carbohydr Polym. 2023;304:120505.
170. Yao C, Li F, Chen T, Tang Y. Green preparation of cellulose nanofibers via high-pressure homogenization and their film-forming properties. Ind Crops Prod. 2023;206:117575.
171. Marquez-Bravo S, Doench I, Molina P, Bentley FE, Tamo AK, Passieux R, et al. Functional Bionanocomposite Fibers of Chitosan Filled with Cellulose Nanofibers Obtained by Gel Spinning. Polymers (Basel). 2021;13(10).
172. Liu X, Jiang Y, Qin C, Yang S, Song X, Wang S, et al. Enzyme-assisted mechanical grinding for cellulose nanofibers from bagasse: energy consumption and nanofiber characteristics. Cellulose. 2018;25:7065-978.
173. Wang X, Chang CH, Jiang J, Liu Q, Liao YP, Lu J, et al. The Crystallinity and Aspect Ratio of Cellulose Nanomaterials Determine Their Pro-Inflammatory and Immune Adjuvant Effects In Vitro and In Vivo. Small. 2019;15(42):e1901642.

174. Kandhola G, Djioleu A, Rajan K, Labbé N, Sakon J, Carrier DJ, et al. Maximizing production of cellulose nanocrystals and nanofibers from pre-extracted loblolly pine kraft pulp: a response surface approach. Bioresourc Bioprocess. 2020;7:19.
175. Nagarajan KJ, Ramanujam NR, Sanjay MR, Siengchin S, Rajan BS, Basha KS, et al. A comprehensive review on cellulose nanocrystals and cellulose nanofibers: Pretreatment, preparation, and characterization. Polym Compos. 2021;42(4):1588-630.
176. Mishra RM, Sabu A, Tiwari SK. Materials chemistry and the futurist eco-friendly applications of nanocellulose: Status and prospect. J Saudi Chem Soc. 2018;22(8):949-78.
177. Masaoka S, Ohe T, Sakota N. Production of cellulose from glucose by Acetobacter xylinum. J Ferment Bioeng. 1993;75(1):18-22.
178. Ruka DR, Simon GP, Dean KM. Altering the growth conditions of Gluconacetobacter xylinus to maximize the yield of bacterial cellulose. Carbohydr Polym. 2012;89(2):613-22.
179. Klemm D, Kramer F, Moritz S, Lindstrom T, Ankerfors M, Gray D, et al. Nanocelluloses: a new family of nature-based materials. Angew Chem Int Ed Engl. 2011;50(24):5438-66.
180. Klemm D, Heublein B, Fink HP, Bohn A. Cellulose: fascinating biopolymer and sustainable raw material. Angew Chem Int Ed Engl. 2005;44(22):3358-93.
181. Blanco Parte FG, Santoso SP, Chou CC, Verma V, Wang HT, Ismadji S, et al. Current progress on the production, modification, and applications of bacterial cellulose. Crit Rev Biotechnol. 2020;40(3):397-414.
182. Czaja W, Krystynowicz A, Bielecki S, Brown RM, Jr. Microbial cellulose--the natural power to heal wounds. Biomaterials. 2006;27(2):145-51.
183. Frankel VH, Serafica GC, Damien CJ. Development and testing of a novel biosynthesized XCell for treating chronic wounds. Surg Technol Int. 2004;12:27-33.
184. Fu L, Zhang J, Yang G. Present status and applications of bacterial cellulose-based materials for skin tissue repair. Carbohydr Polym. 2013;92(2):1432-42.
185. Svensson A, Nicklasson E, Harrah T, Panilaitis B, Kaplan DL, Brittberg M, et al. Bacterial cellulose as a potential scaffold for tissue engineering of cartilage. Biomaterials. 2005;26(4):419-31.
186. Schumann DA, Wippermann J, Klemm DO, Kramer F, Koth D, Kosmehl H, et al. Artificial vascular implants from bacterial cellulose: preliminary results of small arterial substitutes. Cellulose. 2008;16:877-85.
187. Gorgieva S, Trcek J. Bacterial Cellulose: Production, Modification and Perspectives in Biomedical Applications. Nanomaterials (Basel). 2019;9(10).
188. Hu X, Song M, Li S, Chu Y, Zhang WX, Deng Z. TEMPO oxidized cellulose nanocrystal (TOCNC) scaffolded nanoscale zero-valent iron (nZVI) for enhanced chromium removal. Chemosphere. 2023;343:140212.
189. Luo H, Xiong G, Hu D, Ren K, Yao F, Zhu Y, et al. Characterization of TEMPO-oxidized bacterial cellulose scaffolds for tissue engineering applications. Mater Chem Phys. 2013;143(1):373-9.
190. Lan X, Ma Z, Szojka ARA, Kunze M, Mulet-Sierra A, Vyhlidal MJ, et al. TEMPO-Oxidized Cellulose Nanofiber-Alginate Hydrogel as a Bioink for Human Meniscus Tissue Engineering. Front Bioeng Biotechnol. 2021;9:766399.
191. Kamdem Tamo A, Doench I, Morales Helguera A, Hoenders D, Walther A, Madrazo AO. Biodegradation of Crystalline Cellulose Nanofibers by Means of Enzyme Immobilized-Alginate Beads and Microparticles. Polymers (Basel). 2020;12(7).
192. Saito T, Kimura S, Nishiyama Y, Isogai A. Cellulose nanofibers prepared by TEMPO-mediated oxidation of native cellulose. Biomacromolecules. 2007;8(8):2485-91.
193. Isogai A, Bergstrom L. Preparation of cellulose nanofibers using green and sustainable chemistry. Curr Opin Green Sustainable Chem. 2018;12:15-21.
194. Isogai A, Saito T, Fukuzumi H. TEMPO-oxidized cellulose nanofibers. Nanoscale. 2011;3(1):71-85.
195. Abdullaevich YS, Ergashovich YK, Abdukhalilovich SA, Shavkat o'g'li GI. Synthesis and characterization of sodium-carboxymethylcellulose from cotton, powder,microcrystalline and nanocellulose. Polym Eng Sci. 2022;62:677-86.
196. Juncu G, Stoica-Guzun A, Stroescu M, Isopencu G, Jinga SI. Drug release kinetics from carboxymethylcellulose-bacterial cellulose composite films. Int J Pharm. 2016;510(2):485-92.
197. Mosconi G, Formica ML, Palmab SD, Rojas R. Carboxymethylcellulose/layered double hydroxide dispersions for topical ocular delivery of non-steroidal anti-inflammatory drugs. New J Chem. 2024;48:406-15.
198. Singh RK, Singh AK. Optimization of Reaction Conditions for Preparing Carboxymethyl Cellulose from Corn Cobic Agricultural Waste. Waste Biomass Valor. 2013;4:129-37.

199. Klunklin W, Jantanasakulwong K, Phimolsiripol Y, Leksawasdi N, Seesuriyachan P, Chaiyaso T, et al. Synthesis, Characterization, and Application of Carboxymethyl Cellulose from Asparagus Stalk End. Polymers (Basel). 2020;13(1).
200. Chinga-Carrasco G, Syverud K. Pretreatment-dependent surface chemistry of wood nanocellulose for pH-sensitive hydrogels. J Biomater Appl. 2014;29(3):423-32.
201. Zhou Y, Saito T, Bergstrom L, Isogai A. Acid-Free Preparation of Cellulose Nanocrystals by TEMPO Oxidation and Subsequent Cavitation. Biomacromolecules. 2018;19(2):633-9.
202. Yin H, Song P, Chen X, Huang Q, Huang H. A self-healing hydrogel based on oxidized microcrystalline cellulose and carboxymethyl chitosan as wound dressing material. Int J Biol Macromol. 2022;221:1606-17.
203. Kono H, Tsukamoto E, Tajima K. Facile Post-Carboxymethylation of Cellulose Nanofiber Surfaces for Enhanced Water Dispersibility. ACS Omega. 2021;6(49):34107-14.
204. Thiangtham S, Runt J, Manuspiya H. Sulfonation of dialdehyde cellulose extracted from sugarcane bagasse for synergistically enhanced water solubility. Carbohydr Polym. 2019;208:314-22.
205. Fredricks JL, Jimenez AM, Grandgeorge P, Meidl R, Law E, Fan J, et al. Hierarchical biopolymer-based materials and composites. J Polym Sci. 2023;61(21):2585-632.
206. Endes C, Camarero-Espinosa S, Mueller S, Foster EJ, Petri-Fink A, Rothen-Rutishauser B, et al. A critical review of the current knowledge regarding the biological impact of nanocellulose. J Nanobiotechnology. 2016;14(1):78.
207. Lopes VR, Sanchez-Martinez C, Stromme M, Ferraz N. In vitro biological responses to nanofibrillated cellulose by human dermal, lung and immune cells: surface chemistry aspect. Particle and Fibre Toxicology. 2017;14.
208. Vital N, Cardoso M, Kranendonk M, Silva MJ, Louro H. Evaluation of the cyto- and genotoxicity of two types of cellulose nanomaterials using human intestinal cells and in vitro digestion simulation. Arch Toxicol. 2025;99(2):575-96.
209. Dong S, Hirani AA, Colacino KR, Lee YW, Roman M. CYTOTOXICITY AND CELLULAR UPTAKE OF CELLULOSE NANOCRYSTALS. Nano Life. 2012;2(3):1241006.
210. Harper BJ, Clendaniel A, Sinche F, Way D, Hughes M, Schardt J, et al. Impacts of chemical modification on the toxicity of diverse nanocellulose materials to developing zebrafish. Cellulose (Lond). 2016;23(3):1763-75.
211. Trachsel L, Johnbosco C, Lang T, Benetti EM, Zenobi-Wong M. Double-Network Hydrogels Including Enzymatically Crosslinked Poly-(2-alkyl-2-oxazoline)s for 3D Bioprinting of Cartilage-Engineering Constructs. Biomacromolecules. 2019;20(12):4502-11.
212. Sun C, Xie Y, Zhu H, Zheng X, Hou R, Shi Z, et al. Highly Electroactive Tissue Engineering Scaffolds Based on Nanocellulose/Sulfonated Carbon Nanotube Composite Hydrogels for Myocardial Tissue Repair. Biomacromolecules. 2023;24(12):5989-97.
213. Xu C, Zhang Molino B, Wang X, Cheng F, Xu W, Molino P, et al. 3D printing of nanocellulose hydrogel scaffolds with tunable mechanical strength towards wound healing application. J Mater Chem B. 2018;6(43):7066-75.
214. Amaral HR, Wilson JA, do Amaral R, Pascu I, de Oliveira FCS, Kearney CJ, et al. Synthesis of bilayer films from regenerated cellulose nanofibers and poly(globalide) for skin tissue engineering applications. Carbohydr Polym. 2021;252:117201.
215. Nizan NSNH, Zulkifli FH. Reinforcement of hydroxyethyl cellulose / poly (vinyl alcohol) with cellulose nanocrystal as a bone tissue engineering scaffold. J Polym Res. 2020;27:169.
216. Alexandrescu L, Syverud K, Gatti A, Chinga-Carrasco G. Cytotoxicity tests of cellulose nanofibril-based structures. Cellulose. 2013;20:1765-75.
217. Kummala R, Soto Veliz D, Fang Z, Xu W, Abitbol T, Xu C, et al. Human Dermal Fibroblast Viability and Adhesion on Cellulose Nanomaterial Coatings: Influence of Surface Characteristics. Biomacromolecules. 2020;21(4):1560-7.
218. Xu W, Molino BZ, Cheng F, Molino PJ, Yue Z, Su D, et al. On Low-Concentration Inks Formulated by Nanocellulose Assisted with Gelatin Methacrylate (GelMA) for 3D Printing toward Wound Healing Application. ACS Appl Mater Interfaces. 2019;11(9):8838-48.
219. Dutta SD, Hexiu J, Patel DK, Ganguly K, Lim KT. 3D-printed bioactive and biodegradable hydrogel scaffolds of alginate/gelatin/cellulose nanocrystals for tissue engineering. Int J Biol Macromol. 2021;167:644-58.
220. Cheng KC, Huang GF, Wei Y, Hsu SH. Novel chitosan-cellulose nanofiber self-healing hydrogels to correlate self-healing properties of hydrogels with neural regeneration effects. NPG Asia Materials. 2019;11:25.

221. Ojansivu M, Rashad A, Ahlinder A, Massera J, Mishra A, Syverud K, et al. Wood-based nanocellulose and bioactive glass modified gelatin-alginate bioinks for 3D bioprinting of bone cells. Biofabrication. 2019;11(3):035010.
222. Apelgren P, Amoroso M, Lindahl A, Brantsing C, Rotter N, Gatenholm P, et al. Chondrocytes and stem cells in 3D-bioprinted structures create human cartilage in vivo. PLoS One. 2017;12(12):e0189428.
223. Al-Sabah A, Burnell SEA, Simoes IN, Jessop Z, Badiei N, Blain E, et al. Structural and mechanical characterization of crosslinked and sterilised nanocellulose-based hydrogels for cartilage tissue engineering. Carbohydr Polym. 2019;212:242-51.
224. Jessop ZM, Al-Sabah A, Gao N, Kyle S, Thomas B, Badiei N, et al. Printability of pulp derived crystal, fibril and blend nanocellulose-alginate bioinks for extrusion 3D bioprinting. Biofabrication. 2019;11(4):045006.
225. Sinna J, Jeencham R, Mueangkhot P, Sophon S, Noralak P, Raksapakdee R, et al. Development of Poly(vinyl alcohol) Grafted Glycidyl Methacrylate/Cellulose Nanofiber Injectable Hydrogels for Meniscus Tissue Engineering. Polymers (Basel). 2023;15(21).
226. Patel DK, Dutta SD, Hexiu J, Ganguly K, Lim KT. Bioactive electrospun nanocomposite scaffolds of poly(lactic acid)/cellulose nanocrystals for bone tissue engineering. Int J Biol Macromol. 2020;162:1429-41.
227. Markstedt K, Mantas A, Tournier I, Martinez Avila H, Hagg D, Gatenholm P. 3D Bioprinting Human Chondrocytes with Nanocellulose-Alginate Bioink for Cartilage Tissue Engineering Applications. Biomacromolecules. 2015;16(5):1489-96.
228. Mariño MA, Oyarce K, Tobar C, del Río RS, Paredes MG, Pavez P, et al. Crosslinked oxidized-nanocellulose/chitosan hydrogels as a scaffold matrix for mesenchymal stem cell growth. Cellulose. 2024;31:363-79.
229. He X, Xiao Q, Lu C, Wang Y, Zhang X, Zhao J, et al. Uniaxially aligned electrospun all-cellulose nanocomposite nanofibers reinforced with cellulose nanocrystals: scaffold for tissue engineering. Biomacromolecules. 2014;15(2):618-27.
230. Catalan J, Norppa H. Safety Aspects of Bio-Based Nanomaterials. Bioengineering (Basel). 2017;4(4).
231. Pourbashir S, Shahrousvand M, Ghaffari M. Preparation and characterization of semi-IPNs of polycaprolactone/poly (acrylic acid)/cellulosic nanowhisker as artificial articular cartilage. Int J Biol Macromol. 2020;142:298-310.
232. Apelgren P, Samfors S, Saljo K, Molne J, Gatenholm P, Troedsson C, et al. Biomaterial and biocompatibility evaluation of tunicate nanocellulose for tissue engineering. Biomater Adv. 2022;137:212828.
233. Xeroudaki M, Rafat M, Moustardas P, Mukwaya A, Tabe S, Bellisario M, et al. A double-crosslinked nanocellulose-reinforced dexamethasone-loaded collagen hydrogel for corneal application and sustained anti-inflammatory activity. Acta Biomater. 2023;172:234-48.
234. Kyle S, Jessop ZM, Al-Sabah A, Hawkins K, Lewis A, Maffeis T, et al. Characterization of pulp derived nanocellulose hydrogels using AVAP(R) technology. Carbohydr Polym. 2018;198:270-80.
235. Nelson K, Retsina T. Innovative nanocellulose process breaks the cost barrier. TAPPI Journal. 2014;13(5):19-23.
236. Cowman MK, Lee HG, Schwertfeger KL, McCarthy JB, Turley EA. The Content and Size of Hyaluronan in Biological Fluids and Tissues. Front Immunol. 2015;6:261.
237. Snetkov P, Zakharova K, Morozkina S, Olekhnovich R, Uspenskaya M. Hyaluronic Acid: The Influence of Molecular Weight on Structural, Physical, Physico-Chemical, and Degradable Properties of Biopolymer. Polymers (Basel). 2020;12(8).
238. Strober W. Trypan Blue Exclusion Test of Cell Viability. Curr Protoc Immunol. 2015;111:A3 B 1-A3 B
239. Piccinini F, Tesei A, Arienti C, Bevilacqua A. Cell Counting and Viability Assessment of 2D and 3D Cell Cultures: Expected Reliability of the Trypan Blue Assay. Biol Proced Online. 2017;19:8.
240. Kim SI, Kim HJ, Lee HJ, Lee K, Hong D, Lim H, et al. Application of a non-hazardous vital dye for cell counting with automated cell counters. Anal Biochem. 2016;492:8-12.
241. Krause AW, Carley WW, Webb WW. Fluorescent erythrosin B is preferable to trypan blue as a vital exclusion dye for mammalian cells in monolayer culture. J Histochem Cytochem. 1984;32(10):1084-90.
242. Field FE, Roberts G, Hallowes RC, Palmer AK, Williams KE, Lloyd JB. Trypan blue: identification and teratogenic and oncogenic activities of its coloured constituents. Chem Biol Interact. 1977;16(1):69-88.

243. Kelly JW, Feagans WM, Parker JC, Jr., Porterfield JM. Studies on the Mechanism of Trypan Blue-Induced Congenital Malformations. I. Dye Fractions and Fetal Anomalies. Exp Mol Pathol. 1964;3:262-78.
244. Murphy KC, Weaver; Janeway, Charles Janeway's immunobiology. 9th ed: New York: Garland Science; 2017.
245. Kim A, Downer MA, Berry CE, Valencia C, Fazilat AZ, Griffin M. Investigating Immunomodulatory Biomaterials for Preventing the Foreign Body Response. Bioengineering (Basel). 2023;10(12).
246. Gunin AG, Kornilova NK, Vasilieva OV, Petrov VV. Age-related changes in proliferation, the numbers of mast cells, eosinophils, and cd45-positive cells in human dermis. J Gerontol A Biol Sci Med Sci. 2011;66(4):385-92.
247. Haydont V, Bernard BA, Fortunel NO. Age-related evolutions of the dermis: Clinical signs, fibroblast and extracellular matrix dynamics. Mech Ageing Dev. 2019;177:150-6.
248. Haydont V, Neiveyans V, Perez P, Busson E, Lataillade J, Asselineau D, et al. Fibroblasts from the Human Skin Dermo-Hypodermal Junction are Distinct from Dermal Papillary and Reticular Fibroblasts and from Mesenchymal Stem Cells and Exhibit a Specific Molecular Profile Related to Extracellular Matrix Organization and Modeling. Cells. 2020;9(2).
249. Zimmermann DR, Dours-Zimmermann MT, Schubert M, Bruckner-Tuderman L. Versican is expressed in the proliferating zone in the epidermis and in association with the elastic network of the dermis. J Cell Biol. 1994;124(5):817-25.
250. Miller CC, Godeau G, Lebreton-DeCoster C, Desmouliere A, Pellat B, Dubertret L, et al. Validation of a morphometric method for evaluating fibroblast numbers in normal and pathologic tissues. Exp Dermatol. 2003;12(4):403-11.
251. Chia SH, Schumacher BL, Klein TJ, Thonar EJ, Masuda K, Sah RL, et al. Tissue-engineered human nasal septal cartilage using the alginate-recovered-chondrocyte method. Laryngoscope. 2004;114(1):38-45.
252. Angelozzi M, Penolazzi L, Mazzitelli S, Lambertini E, Lolli A, Piva R, et al. Dedifferentiated Chondrocytes in Composite Microfibers As Tool for Cartilage Repair. Front Bioeng Biotechnol. 2017;5:35.
253. Reuther MS, Wong VW, Briggs KK, Chang AA, Nguyen QT, Schumacher BL, et al. Culture of human septal chondrocytes in a rotary bioreactor. Otolaryngol Head Neck Surg. 2012;147(4):661-7.
254. Vedicherla S, Buckley CT. Rapid Chondrocyte Isolation for Tissue Engineering Applications: The Effect of Enzyme Concentration and Temporal Exposure on the Matrix Forming Capacity of Nasal Derived Chondrocytes. Biomed Res Int. 2017;2017:2395138.
255. O'Connell GD, Tan AR, Cui V, Bulinski JC, Cook JL, Attur M, et al. Human chondrocyte migration behaviour to guide the development of engineered cartilage. J Tissue Eng Regen Med. 2017;11(3):877-86.
256. Cigan AD, Roach BL, Nims RJ, Tan AR, Albro MB, Stoker AM, et al. High seeding density of human chondrocytes in agarose produces tissue-engineered cartilage approaching native mechanical and biochemical properties. J Biomech. 2016;49(9):1909-17.
257. Homicz MR, McGowan KB, Lottman LM, Beh G, Sah RL, Watson D. A compositional analysis of human nasal septal cartilage. Arch Facial Plast Surg. 2003;5(1):53-8.
258. Vetter U, Heit W, Helbing G, Heinze E, Pirsig W. Growth of the human septal cartilage: cell density and colony formation of septal chondrocytes. Laryngoscope. 1984;94(9):1226-9.
259. Kuo J, Shi C, Cisewski S, Zhang L, Kern MJ, Yao H. Regional cell density distribution and oxygen consumption rates in porcine TMJ discs: an explant study. Osteoarthritis Cartilage. 2011;19(7):911-8.
260. Shapiro EM, Borthakur A, Kaufman JH, Leigh JS, Reddy R. Water distribution patterns inside bovine articular cartilage as visualized by 1H magnetic resonance imaging. Osteoarthritis Cartilage. 2001;9(6):533-8.
261. Kaja S, Payne AJ, Naumchuk Y, Koulen P. Quantification of Lactate Dehydrogenase for Cell Viability Testing Using Cell Lines and Primary Cultured Astrocytes. Curr Protoc Toxicol. 2017;72:2 26 1-2 10.
262. Kumar P, Nagarajan A, Uchil PD. Analysis of Cell Viability by the Lactate Dehydrogenase Assay. Cold Spring Harb Protoc. 2018;2018(6).
263. Cox MC, Mendes R, Silva F, Mendes TF, Zelaya-Lazo A, Halwachs K, et al. Application of LDH assay for therapeutic efficacy evaluation of ex vivo tumor models. Sci Rep. 2021;11(1):18571.
264. Griffin M, Naderi N, Kalaskar DM, Malins E, Becer R, Thornton CA, et al. Evaluation of Sterilisation Techniques for Regenerative Medicine Scaffolds Fabricated with Polyurethane Nonbiodegradable and Bioabsorbable Nanocomposite Materials. Int J Biomater. 2018;2018:6565783.

265. Boix-Lemonche GN, R. M.; Niemi, E. M.; Josifovska, N.; Johansen, S.; Moe, M. C.; Scholz, H.' Petrovski, G. Intracorneal Implantation of 3D Bioprinted Scaffolds Containing Mesenchymal Stromal Cells Using Femtosecond-Laser-Assisted Intrastromal Keratoplasty. Macromolecular Bioscience. 2023;23(2200422).
266. Gilljam KM, Stenlund P, Standoft S, Andersen SB, Kaaber K, Lund H, et al. Alginate and Nanocellulose Dressings With Extract From Salmon Roe Reduce Inflammation and Accelerate Healing of Porcine Burn Wounds. J Burn Care Res. 2023;44(5):1140-9.
267. Stenlund P, Enstedt L, Gilljam KM, Standoft S, Ahlinder A, Lundin Johnson M, et al. Development of an All-Marine 3D Printed Bioactive Hydrogel Dressing for Treatment of Hard-to-Heal Wounds. Polymers (Basel). 2023;15(12).
268. Foster EJ, Moon RJ, Agarwal UP, Bortner MJ, Bras J, Camarero-Espinosa S, et al. Current characterization methods for cellulose nanomaterials. Chem Soc Rev. 2018;47(8):2609-79.
269. Kjesbu JS, Zaytseva-Zotova D, Samfors S, Gatenholm P, Troedsson C, Thompson EM, et al. Alginate and tunicate nanocellulose composite microbeads - Preparation, characterization and cell encapsulation. Carbohydr Polym. 2022;286:119284.
270. Apelgren P, Amoroso M, Saljo K, Montelius M, Lindahl A, Stridh Orrhult L, et al. Vascularization of tissue engineered cartilage - Sequential in vivo MRI display functional blood circulation. Biomaterials. 2021;276:121002.
271. Amoroso MA, P.; Saljo, K.; Montelius, M.; Orrhult, L. S.; Engstrom, M.; Gatenholm, P.; Kolby, L. Functional and morphological studies of in vivo vascularization of 3D-bioprinted human fat grafts. Bioprinting. 2021;23(e00162).
272. Saljo K, Apelgren P, Stridh Orrhult L, Li S, Amoroso M, Gatenholm P, et al. Long-term in vivo survival of 3D-bioprinted human lipoaspirate-derived adipose tissue: proteomic signature and cellular content. Adipocyte. 2022;11(1):34-46.
273. Oskarsdotter K, Saljo K, Samfors S, Niemi EM, Li S, Simonsson S, et al. Autologous endothelialisation by the stromal vascular fraction on laminin-bioconjugated nanocellulose-alginate scaffolds. Biomed Mater. 2023;18(4).
274. Samfors SN, E. M.; Oskarsdotter, K.; Egea, C. V.; Mark, A.; Scholz, H.; Gatenholm, P. Design and biofabrication of a leaf-inspired vascularized cell-delivery device. Bioprinting. 2022;26(e00199).
275. Oskarsdotter K, Nordgard CT, Apelgren P, Saljo K, Solbu AA, Eliasson E, et al. Injectable In Situ Crosslinking Hydrogel for Autologous Fat Grafting. Gels. 2023;9(10).
276. K MJSV. Cross-linking in hydrogels - a review. American Journal of Polymer Science. 2014;4(2):25-31.
277. Ansar R, Saqib S, Mukhtar A, Niazi MBK, Shahid M, Jahan Z, et al. Challenges and recent trends with the development of hydrogel fiber for biomedical applications. Chemosphere. 2022;287(Pt 1):131956.
278. Tan J, Luo Y, Guo Y, Zhou Y, Liao X, Li D, et al. Development of alginate-based hydrogels: Crosslinking strategies and biomedical applications. Int J Biol Macromol. 2023;239:124275.
279. Hennink WEvN, C. F. Novel crosslinking methods to design hydrogels. Advanced drug delivery reviews. 2012;64:223-36.
280. Besiri IN, Goudoulas TB, Fattahi E, Becker T. Experimental Advances in the Real-Time Recording of Cross-Linking Alginate In Situ Gelation: A Review. Polymers (Basel). 2023;15(13).
281. Lo CM, Wang HB, Dembo M, Wang YL. Cell movement is guided by the rigidity of the substrate. Biophys J. 2000;79(1):144-52.
282. Kong HJ, Liu J, Riddle K, Matsumoto T, Leach K, Mooney DJ. Non-viral gene delivery regulated by stiffness of cell adhesion substrates. Nat Mater. 2005;4(6):460-4.
283. Engler AJ, Sen S, Sweeney HL, Discher DE. Matrix elasticity directs stem cell lineage specification. Cell. 2006;126(4):677-89.
284. Huebsch N, Arany PR, Mao AS, Shvartsman D, Ali OA, Bencherif SA, et al. Harnessing traction-mediated manipulation of the cell/matrix interface to control stem-cell fate. Nat Mater. 2010;9(6):518-26.
285. Huebsch N, Lippens E, Lee K, Mehta M, Koshy ST, Darnell MC, et al. Matrix elasticity of void-forming hydrogels controls transplanted-stem-cell-mediated bone formation. Nat Mater. 2015;14(12):1269-77.
286. Chaudhuri O, Cooper-White J, Janmey PA, Mooney DJ, Shenoy VB. Effects of extracellular matrix viscoelasticity on cellular behaviour. Nature. 2020;584(7822):535-46.
287. Janmey PA, Schliwa M. Rheology. Curr Biol. 2008;18(15):R639-R41.
288. Koshy ST, Desai RM, Joly P, Li J, Bagrodia RK, Lewin SA, et al. Click-Crosslinked Injectable Gelatin Hydrogels. Adv Healthc Mater. 2016;5(5):541-7.

289. Abu-Hakmeh A, Kung A, Mintz BR, Kamal S, Cooper JA, Lu XL, et al. Sequential gelation of tyramine-substituted hyaluronic acid hydrogels enhances mechanical integrity and cell viability. Med Biol Eng Comput. 2016;54(12):1893-902.
290. Khunmanee S, Jeong Y, Park H. Crosslinking method of hyaluronic-based hydrogel for biomedical applications. J Tissue Eng. 2017;8:2041731417726464.
291. Donnelly PE, Chen T, Finch A, Brial C, Maher SA, Torzilli PA. Photocrosslinked tyramine-substituted hyaluronate hydrogels with tunable mechanical properties improve immediate tissue-hydrogel interfacial strength in articular cartilage. J Biomater Sci Polym Ed. 2017;28(6):582-600.
292. Mattei G, Cacopardo L, Ahluwalia AA. Engineering Gels with Time-Evolving Viscoelasticity. Materials (Basel). 2020;13(2).
293. Toh WS, Lim TC, Kurisawa M, Spector M. Modulation of mesenchymal stem cell chondrogenesis in a tunable hyaluronic acid hydrogel microenvironment. Biomaterials. 2012;33(15):3835-45.
294. Silva CR, Babo PS, Mithieux S, Domingues RM, Reis R, Gomes ME, et al. Tuneable cellulose nanocrystal and tropoelastin-laden hyaluronic acid hydrogels. J Biomater Appl. 2019;34(4):560-72.
295. Kannan K, Jain SK. Oxidative stress and apoptosis. Pathophysiology. 2000;7(3):153-63.
296. Xiang J, Wan C, Guo R, Guo D. Is Hydrogen Peroxide a Suitable Apoptosis Inducer for All Cell Types? Biomed Res Int. 2016;2016:7343965.
297. Levato R, Jungst T, Scheuring RG, Blunk T, Groll J, Malda J. From Shape to Function: The Next Step in Bioprinting. Adv Mater. 2020;32(12):e1906423.
298. Vitale S, Calapa F, Colonna F, Luongo F, Biffoni M, De Maria R, et al. Advancements in 3D In Vitro Models for Colorectal Cancer. Adv Sci (Weinh). 2024;11(32):e2405084.
299. Mu P, Zhou S, Lv T, Xia F, Shen L, Wan J, et al. Newly developed 3D in vitro models to study tumor-immune interaction. J Exp Clin Cancer Res. 2023;42(1):81.
300. Rodrigues J, Heinrich MA, Teixeira LM, Prakash J. 3D In Vitro Model (R)evolution: Unveiling Tumor-Stroma Interactions. Trends Cancer. 2021;7(3):249-64.
301. Longhin EM, El Yamani N, Runden-Pran E, Dusinska M. The alamar blue assay in the context of safety testing of nanomaterials. Front Toxicol. 2022;4:981701.
302. Kummrow A, Frankowski M, Bock N, Werner C, Dziekan T, Neukammer J. Quantitative assessment of cell viability based on flow cytometry and microscopy. Cytometry A. 2013;83(2):197-204.
303. Dusinska M BS, Saunders M, Juillerat-Jeanneret L, Tran L, Pojana G, Marcomini A, Volkovova K, Tulinska J, Knudsen LE, Gombau L, Whelan M, Collins AR, Marano F, Housiadas C, Bilanicova D, Halamoda Kenzaoui B, Correia Carreira S, Magdolenova Z, Fjellsbø LM, Huk A, Handy R, Walker L, Barancokova M, Bartonova A, Burello E, Castell J, Cowie H, Drlickova M, Guadagnini R, Harris G, Harju M, Heimstad ES, Hurbankova M, Kazimirova A, Kovacikova Z, Kuricova M, Liskova A, Milcamps A, Neubauerova E, Palosaari T, Papazafiri P, Pilou M, Poulsen MS, Ross B, Runden-Pran E, Sebekova K, Staruchova M, Vallotto D, Worth A. . Towards an alternative testing strategy for nanomaterials used in nanomedicine: lessons from NanoTEST. . Nanotoxicology. 2015;9:118-32.
304. Monaco G, El Haj AJ, Alini M, Stoddart MJ. Ex Vivo Systems to Study Chondrogenic Differentiation and Cartilage Integration. J Funct Morphol Kinesiol. 2021;6(1).
305. O'Connell CD, Duchi S, Onofrillo C, Caballero-Aguilar LM, Trengove A, Doyle SE, et al. Within or Without You? A Perspective Comparing In Situ and Ex Situ Tissue Engineering Strategies for Articular Cartilage Repair. Adv Healthc Mater. 2022;11(24):e2201305.
306. Narrandes S, Xu W. Gene Expression Detection Assay for Cancer Clinical Use. J Cancer. 2018;9(13):2249-65.
307. Vinod E, Kachroo U, Rebekah G, Yadav BK, Ramasamy B. Characterization of human articular chondrocytes and chondroprogenitors derived from non-diseased and osteoarthritic knee joints to assess superiority for cell-based therapy. Acta Histochem. 2020;122(6):151588.
308. Sober SA, Darmani H, Alhattab D, Awidi A. Flow cytometric characterization of cell surface markers to differentiate between fibroblasts and mesenchymal stem cells of different origin. Arch Med Sci. 2023;19(5):1487-96.
309. Fabre H, Ducret M, Degoul O, Rodriguez J, Perrier-Groult E, Aubert-Foucher E, et al. Characterization of Different Sources of Human MSCs Expanded in Serum-Free Conditions with Quantification of Chondrogenic Induction in 3D. Stem Cells Int. 2019;2019:2186728.
310. Denu RA, Nemcek S, Bloom DD, Goodrich AD, Kim J, Mosher DF, et al. Fibroblasts and Mesenchymal Stromal/Stem Cells Are Phenotypically Indistinguishable. Acta Haematol. 2016;136(2):85-97.

311. Diaz-Romero J, Nesic D, Grogan SP, Heini P, Mainil-Varlet P. Immunophenotypic changes of human articular chondrocytes during monolayer culture reflect bona fide dedifferentiation rather than amplification of progenitor cells. J Cell Physiol. 2008;214(1):75-83.
312. Kienzle G, von Kempis J. Vascular cell adhesion molecule 1 (CD106) on primary human articular chondrocytes: functional regulation of expression by cytokines and comparison with intercellular adhesion molecule 1 (CD54) and very late activation antigen 2. Arthritis Rheum. 1998;41(7):1296-305.
313. Sudo K, Kanno M, Miharada K, Ogawa S, Hiroyama T, Saijo K, et al. Mesenchymal progenitors able to differentiate into osteogenic, chondrogenic, and/or adipogenic cells in vitro are present in most primary fibroblast-like cell populations. Stem Cells. 2007;25(7):1610-7.
314. Ichim TE, O'Heeron P, Kesari S. Fibroblasts as a practical alternative to mesenchymal stem cells. J Transl Med. 2018;16(1):212.
315. Mennan C, Garcia J, McCarthy H, Owen S, Perry J, Wright K, et al. Human Articular Chondrocytes Retain Their Phenotype in Sustained Hypoxia While Normoxia Promotes Their Immunomodulatory Potential. Cartilage. 2019;10(4):467-79.
316. Agorku DJ, Langhammer A, Heider U, Wild S, Bosio A, Hardt O. CD49b, CD87, and CD95 Are Markers for Activated Cancer-Associated Fibroblasts Whereas CD39 Marks Quiescent Normal Fibroblasts in Murine Tumor Models. Front Oncol. 2019;9:716.
317. Grogan SP, Barbero A, Diaz-Romero J, Cleton-Jansen AM, Soeder S, Whiteside R, et al. Identification of markers to characterize and sort human articular chondrocytes with enhanced in vitro chondrogenic capacity. Arthritis Rheum. 2007;56(2):586-95.
318. Hamada T, Sakai T, Hiraiwa H, Nakashima M, Ono Y, Mitsuyama H, et al. Surface markers and gene expression to characterize the differentiation of monolayer expanded human articular chondrocytes. Nagoya J Med Sci. 2013;75(1-2):101-11.
319. Alt E, Yan Y, Gehmert S, Song YH, Altman A, Gehmert S, et al. Fibroblasts share mesenchymal phenotypes with stem cells, but lack their differentiation and colony-forming potential. Biol Cell. 2011;103(4):197-208.
320. Ramirez JM, Bai Q, Pequignot M, Becker F, Kassambara A, Bouin A, et al. Side scatter intensity is highly heterogeneous in undifferentiated pluripotent stem cells and predicts clonogenic self-renewal. Stem Cells Dev. 2013;22(12):1851-60.
321. Unguryte A, Bernotiene E, Bagdonas E, Garberyte S, Porvaneckas N, Jorgensen C. Human articular chondrocytes with higher aldehyde dehydrogenase activity have stronger expression of COL2A1 and SOX9. Osteoarthritis Cartilage. 2016;24(5):873-82.
322. Lerbs T, Cui L, King ME, Chai T, Muscat C, Chung L, et al. CD47 prevents the elimination of diseased fibroblasts in scleroderma. JCI Insight. 2020;5(16).
323. Zeltz C, Primac I, Erusappan P, Alam J, Noel A, Gullberg D. Cancer-associated fibroblasts in desmoplastic tumors: emerging role of integrins. Semin Cancer Biol. 2020;62:166-81.
324. Desai S, Dooner M, Newberry J, Twomey-Kozak J, Molino J, Trivedi J, et al. Stable human cartilage progenitor cell line stimulates healing of meniscal tears and attenuates post-traumatic osteoarthritis. Front Bioeng Biotechnol. 2022;10:970235.
325. Ito M, Watanabe M, Ihara T, Kamiya H, Sakurai M. Increased expression of adhesion molecules (CD54, CD29 and CD44) on fibroblasts infected with cytomegalovirus. Microbiol Immunol. 1995;39(2):129-33.
326. Yellin MJ, Winikoff S, Fortune SM, Baum D, Crow MK, Lederman S, et al. Ligation of CD40 on fibroblasts induces CD54 (ICAM-1) and CD106 (VCAM-1) up-regulation and IL-6 production and proliferation. J Leukoc Biol. 1995;58(2):209-16.
327. Diaz-Romero J, Gaillard JP, Grogan SP, Nesic D, Trub T, Mainil-Varlet P. Immunophenotypic analysis of human articular chondrocytes: changes in surface markers associated with cell expansion in monolayer culture. J Cell Physiol. 2005;202(3):731-42.
328. Tai C, Xie Z, Li Y, Feng Y, Xie Y, Yang H, et al. Human skin dermis-derived fibroblasts are a kind of functional mesenchymal stromal cells: judgements from surface markers, biological characteristics, to therapeutic efficacy. Cell Biosci. 2022;12(1):105.
329. Covas DT, Panepucci RA, Fontes AM, Silva WA, Jr., Orellana MD, Freitas MC, et al. Multipotent mesenchymal stromal cells obtained from diverse human tissues share functional properties and gene-expression profile with CD146+ perivascular cells and fibroblasts. Exp Hematol. 2008;36(5):642-54.
330. Sun L, Dong S, Ge Y, Fonseca JP, Robinson ZT, Mysore KS, et al. DiVenn: An Interactive and Integrated Web-Based Visualization Tool for Comparing Gene Lists. Front Genet. 2019;10:421.

331. Szklarczyk D, Kirsch R, Koutrouli M, Nastou K, Mehryary F, Hachilif R, et al. The STRING database in 2023: protein-protein association networks and functional enrichment analyses for any sequenced genome of interest. Nucleic Acids Res. 2023;51(D1):D638-D46.
332. Bindea G, Mlecnik B, Hackl H, Charoentong P, Tosolini M, Kirilovsky A, et al. ClueGO: a Cytoscape plug-in to decipher functionally grouped gene ontology and pathway annotation networks. Bioinformatics. 2009;25(8):1091-3.
333. Raudvere U, Kolberg L, Kuzmin I, Arak T, Adler P, Peterson H, et al. g:Profiler: a web server for functional enrichment analysis and conversions of gene lists (2019 update). Nucleic Acids Res. 2019;47(W1):W191-W8.
334. Supek F, Bosnjak M, Skunca N, Smuc T. REVIGO summarizes and visualizes long lists of gene ontology terms. PLoS One. 2011;6(7):e21800.
335. Huntley RP, Sawford T, Martin MJ, O'Donovan C. Understanding how and why the Gene Ontology and its annotations evolve: the GO within UniProt. Gigascience. 2014;3(1):4.
336. Safran M, Dalah I, Alexander J, Rosen N, Iny Stein T, Shmoish M, et al. GeneCards Version 3: the human gene integrator. Database (Oxford). 2010;2010:baq020.
337. Armingol E, Officer A, Harismendy O, Lewis NE. Deciphering cell-cell interactions and communication from gene expression. Nat Rev Genet. 2021;22(2):71-88.
338. Weitz HT, Ettich J, Rafii P, Wittich C, Schultz L, Frank NC, et al. Interleukin-11 receptor is an alternative alpha-receptor for interleukin-6 and the chimeric cytokine IC7. FEBS J. 2025;292(3):523-36.
339. Du X, Williams DA. Interleukin-11: review of molecular, cell biology, and clinical use. Blood. 1997;89(11):3897-908.
340. Cook SA. Understanding interleukin 11 as a disease gene and therapeutic target. Biochem J. 2023;480(23):1987-2008.
341. Widjaja AA, Lim WW, Viswanathan S, Chothani S, Corden B, Dasan CM, et al. Inhibition of IL-11 signalling extends mammalian healthspan and lifespan. Nature. 2024;632(8023):157-65.
342. Kespohl B, Schumertl T, Bertrand J, Lokau J, Garbers C. The cytokine interleukin-11 crucially links bone formation, remodeling and resorption. Cytokine Growth Factor Rev. 2021;60:18-27.
343. Lokau J, Bollmann M, Garbers Y, Feist E, Lohmann CH, Bertrand J, et al. Transforming growth factor beta induces interleukin-11 expression in osteoarthritis. Cytokine. 2025;187:156863.
344. Maier R, Ganu V, Lotz M. Interleukin-11, an inducible cytokine in human articular chondrocytes and synoviocytes, stimulates the production of the tissue inhibitor of metalloproteinases. J Biol Chem. 1993;268(29):21527-32.
345. Fung KY, Louis C, Metcalfe RD, Kosasih CC, Wicks IP, Griffin MDW, et al. Emerging roles for IL-11 in inflammatory diseases. Cytokine. 2022;149:155750.
346. Wilson SE. TGF beta -1, -2 and -3 in the modulation of fibrosis in the cornea and other organs. Exp Eye Res. 2021;207:108594.
347. Chin D, Boyle GM, Parsons PG, Coman WB. What is transforming growth factor-beta (TGF-beta)? Br J Plast Surg. 2004;57(3):215-21.
348. Deng Z, Fan T, Xiao C, Tian H, Zheng Y, Li C, et al. TGF-beta signaling in health, disease, and therapeutics. Signal Transduct Target Ther. 2024;9(1):61.
349. Lee TY, Chin GS, Kim WJ, Chau D, Gittes GK, Longaker MT. Expression of transforming growth factor beta 1, 2, and 3 proteins in keloids. Ann Plast Surg. 1999;43(2):179-84.
350. Wang S, Kurth S, Burger C, Wirtz DC, Schildberg FA, Ossendorff R. TNFalpha-Related Chondrocyte Inflammation Models: A Systematic Review. Int J Mol Sci. 2024;25(19).
351. Miller MR, Landis HE, Miller RE, Tizabi Y. Intercellular Adhesion Molecule 1 (ICAM-1): An Inflammatory Regulator with Potential Implications in Ferroptosis and Parkinson's Disease. Cells. 2024;13(18).
352. Lamot L, Niemietz I, Brown KL. Methods for type I interferon detection and their relevance for clinical utility and improved understanding of rheumatic diseases. Clin Exp Rheumatol. 2019;37(6):1077-83.
353. Almeida-da-Silva CLC, Savio LEB, Coutinho-Silva R, Ojcius DM. The role of NOD-like receptors in innate immunity. Front Immunol. 2023;14:1122586.
354. Schoggins JW, Rice CM. Interferon-stimulated genes and their antiviral effector functions. Curr Opin Virol. 2011;1(6):519-25.
355. Justesen J, Hartmann R, Kjeldgaard NO. Gene structure and function of the 2'-5'-oligoadenylate synthetase family. Cell Mol Life Sci. 2000;57(11):1593-612.
356. Donovan J, Dufner M, Korennykh A. Structural basis for cytosolic double-stranded RNA surveillance by human oligoadenylate synthetase 1. Proc Natl Acad Sci U S A. 2013;110(5):1652-7.

357. Al-Modawi RN, Brinchmann JE, Karlsen TA. Multi-pathway Protective Effects of MicroRNAs on Human Chondrocytes in an In Vitro Model of Osteoarthritis. Mol Ther Nucleic Acids. 2019;17:776-90.
358. Maor G, Salzberg S, Silbermann M. The activity of 2,5-oligoadenylate synthetase, an interferon-induced enzyme, is coupled to the differentiation state of mouse condylar cartilage. Differentiation. 1990;44(1):18-24.
359. Lopez-Armada MJ, Carames B, Martin MA, Cillero-Pastor B, Lires-Dean M, Fuentes-Boquete I, et al. Mitochondrial activity is modulated by TNFalpha and IL-1beta in normal human chondrocyte cells. Osteoarthritis Cartilage. 2006;14(10):1011-22.
360. Choi WS, Lee G, Song WH, Koh JT, Yang J, Kwak JS, et al. The CH25H-CYP7B1-RORalpha axis of cholesterol metabolism regulates osteoarthritis. Nature. 2019;566(7743):254-8.
361. Afonina IS, Muller C, Martin SJ, Beyaert R. Proteolytic Processing of Interleukin-1 Family Cytokines: Variations on a Common Theme. Immunity. 2015;42(6):991-1004.
362. Kelley N, Jeltema D, Duan Y, He Y. The NLRP3 Inflammasome: An Overview of Mechanisms of Activation and Regulation. Int J Mol Sci. 2019;20(13).
363. Naba A, Clauser KR, Ding H, Whittaker CA, Carr SA, Hynes RO. The extracellular matrix: Tools and insights for the "omics" era. Matrix Biol. 2016;49:10-24.
364. Shao X, Gomez CD, Kapoor N, Considine JM, Grams C, Gao YT, et al. MatrisomeDB 2.0: 2023 updates to the ECM-protein knowledge database. Nucleic Acids Res. 2023;51(D1):D1519-D30.
365. Alcaide-Ruggiero L, Molina-Hernandez V, Granados MM, Dominguez JM. Main and Minor Types of Collagens in the Articular Cartilage: The Role of Collagens in Repair Tissue Evaluation in Chondral Defects. Int J Mol Sci. 2021;22(24).
366. Han J, Kim YH, Han S. Increased oxidative phosphorylation through pyruvate dehydrogenase kinase 2 deficiency ameliorates cartilage degradation in mice with surgically induced osteoarthritis. Exp Mol Med. 2025;57(2):390-401.
367. Zheng L, Zhang Z, Sheng P, Mobasheri A. The role of metabolism in chondrocyte dysfunction and the progression of osteoarthritis. Ageing Res Rev. 2021;66:101249.
368. Hollander JM, Zeng L. The Emerging Role of Glucose Metabolism in Cartilage Development. Curr Osteoporos Rep. 2019;17(2):59-69.
369. Adam MS, Zhuang H, Ren X, Zhang Y, Zhou P. The metabolic characteristics and changes of chondrocytes in vivo and in vitro in osteoarthritis. Front Endocrinol (Lausanne). 2024;15:1393550.
370. Pi P, Zeng L, Zeng Z, Zong K, Han B, Bai X, et al. The role of targeting glucose metabolism in chondrocytes in the pathogenesis and therapeutic mechanisms of osteoarthritis: a narrative review. Front Endocrinol (Lausanne). 2024;15:1319827.
371. Arra M, Swarnkar G, Ke K, Otero JE, Ying J, Duan X, et al. LDHA-mediated ROS generation in chondrocytes is a potential therapeutic target for osteoarthritis. Nat Commun. 2020;11(1):3427.
372. Murphy CL, Thoms BL, Vaghjiani RJ, Lafont JE. Hypoxia. HIF-mediated articular chondrocyte function: prospects for cartilage repair. Arthritis Res Ther. 2009;11(1):213.
373. Wu X, Liyanage C, Plan M, Stark T, McCubbin T, Barrero RA, et al. Dysregulated energy metabolism impairs chondrocyte function in osteoarthritis. Osteoarthritis Cartilage. 2023;31(5):613-26.
374. Wang C, Silverman RM, Shen J, O'Keefe RJ. Distinct metabolic programs induced by TGF-beta1 and BMP2 in human articular chondrocytes with osteoarthritis. J Orthop Translat. 2018;12:66-73.
375. Bustamante MF, Oliveira PG, Garcia-Carbonell R, Croft AP, Smith JM, Serrano RL, et al. Hexokinase 2 as a novel selective metabolic target for rheumatoid arthritis. Ann Rheum Dis. 2018;77(11):1636-43.
376. Li Y, Zheng W, Lu Y, Zheng Y, Pan L, Wu X, et al. BNIP3L/NIX-mediated mitophagy: molecular mechanisms and implications for human disease. Cell Death Dis. 2021;13(1):14.
377. Mauro-Lizcano M, Sotgia F, Lisanti MP. Mitophagy and cancer: role of BNIP3/BNIP3L as energetic drivers of stemness features, ATP production, proliferation, and cell migration. Aging (Albany NY). 2024;16(11):9334-49.
378. Lee HH, Chang CC, Shieh MJ, Wang JP, Chen YT, Young TH, et al. Hypoxia enhances chondrogenesis and prevents terminal differentiation through PI3K/Akt/FoxO dependent anti-apoptotic effect. Sci Rep. 2013;3:2683.
379. Ranmuthu CKI, Ranmuthu CDS, Wijewardena CK, Seah MKT, Khan WS. Evaluating the Effect of Hypoxia on Human Adult Mesenchymal Stromal Cell Chondrogenesis In Vitro: A Systematic Review. Int J Mol Sci. 2022;23(23).
380. da Silva RGL, Au L, Blasimme A. Organizational aspects of tissue engineering clinical translation: insights from a qualitative case study. Transl Med Commun. 2024;9(1):17.
381. Searson PC. The Cancer Moonshot, the role of in vitro models, model accuracy, and the need for validation. Nat Nanotechnol. 2023;18(10):1121-3.

382. Tabula Sapiens C, Jones RC, Karkanias J, Krasnow MA, Pisco AO, Quake SR, et al. The Tabula Sapiens: A multiple-organ, single-cell transcriptomic atlas of humans. Science. 2022;376(6594):eabl4896.
383. Hebels D, Carlier A, Coonen MLJ, Theunissen DH, de Boer J. cBiT: A transcriptomics database for innovative biomaterial engineering. Biomaterials. 2017;149:88-97.
384. Drasler B, Sayre P, Staeinhauser KG, Petri-Fink A, Rothen-Rutishauser B. In vitro approaches to assess the hazard of nanomaterials. NanoImpact. 2017;8:99-116.
385. Fadeel B, Fornara A, Toprak MS, Bhattacharya K. Keeping it real: The importance of material characterization in nanotoxicology. Biochem Biophys Res Commun. 2015;468(3):498-503.
386. Swingler S, Gupta A, Gibson H, Kowalczuk M, Heaselgrave W, Radecka I. Recent Advances and Applications of Bacterial Cellulose in Biomedicine. Polymers (Basel). 2021;13(3).
387. Mukasheva F, Adilova L, Dyussenbinov A, Yernaimanova B, Abilev M, Akilbekova D. Optimizing scaffold pore size for tissue engineering: insights across various tissue types. Front Bioeng Biotechnol. 2024;12:1444986.
388. Beltran-Huarac J, Zhang Z, Pyrgiotakis G, DeLoid G, Vaze N, Hussain SM, et al. Development of reference metal and metal oxide engineered nanomaterials for nanotoxicology research using high throughput and precision flame spray synthesis approaches. NanoImpact. 2018;10:26-37.
389. Nelson BC, Petersen EJ, Marquis BJ, Atha DH, Elliott JT, Cleveland D, et al. NIST gold nanoparticle reference materials do not induce oxidative DNA damage. Nanotoxicology. 2013;7(1):21-9.
390. Roebben G, Kestens V, Varga Z, Charoud-Got J, Ramaye Y, Gollwitzer C, et al. Reference materials and representative test materials to develop nanoparticle characterization methods: the NanoChOp project case. Front Chem. 2015;3:56.
391. Niermeyer WL, Rodman C, Li MM, Chiang T. Tissue engineering applications in otolaryngology-The state of translation. Laryngoscope Investig Otolaryngol. 2020;5(4):630-48.
392. Gonfiotti A, Jaus MO, Barale D, Baiguera S, Comin C, Lavorini F, et al. The first tissue-engineered airway transplantation: 5-year follow-up results. Lancet. 2014;383(9913):238-44.
393. Zhou G, Jiang H, Yin Z, Liu Y, Zhang Q, Zhang C, et al. In Vitro Regeneration of Patient-specific Ear-shaped Cartilage and Its First Clinical Application for Auricular Reconstruction. EBioMedicine. 2018;28:287-302.